

AN INDIVIDUAL CORE STRUCTURE OF A SANDWICH BEAM DUE TO THE “BROKEN LINE” THEORY OF THE SHEAR EFFECT–THREE-POINT BENDING

Krzysztof MAGNUCKI*, Ewa MAGNUCKA-BLANDZI**

*Łukasiewicz Research Network – Poznań Institute of Technology, Rail Vehicles Center, ul. Warszawska 181, 61-055 Poznań, Poland

**Institute of Mathematics, Poznań University of Technology, ul. Piotrowo 3a, 60-965 Poznań, Poland

krzysztof.magnucki@pit.lukasiewicz.gov.pl, ewa.magnucka-blandzi@put.poznan.pl

received 18 October 2023, revised 9 April 2024, accepted 6 May 2024

Abstract: The work concerns a sandwich beam with an individual core structure giving a shear effect exactly in accordance to the “broken line” theory. According to the general theoretical scheme of a planar cross section deformation, longitudinal displacements, strains and stresses are analytically formulated. Moreover, the unknown deformation function of the core, with consideration of the classical shear stress formula, is analytically derived. Based on the condition regarding the linear deformation function of the core, according to the “broken line” theory, the differential equation is obtained. The solution of this equation is the sought individual core structure. Then, the bending problem of a clamped sandwich beam under three-point bending is studied.

Key words: sandwich beam, individual core structure, “broken line” theory, bending, shear effect

1. INTRODUCTION

Sandwich structures initiated in the 20th century are contemporary intensively developed and improved. Carrera [1] presented a detailed review of theories used in analytical modeling of multi-layer structures, in particular Zig-Zag theory, taking into account 138 publications, including three from the 19th century. Magnucka-Blandzi and Magnucki [2] developed an analytical model of a simply supported sandwich beam with symmetrically varying mechanical properties of the core at its depth and determined the critical load of this beam. Based on the formulated optimization criterion with consideration of the critical load, the dimensionless effective parameters of the example beam were determined. Carrera and Brischetto [3], taking into account selected important articles on modeling layered structures, pointed out the advantages and certain imperfections of the theories used, presenting five comparative problems. They identified two main sources of error: geometric parameters (the length-to-thickness -ratio LTR) and mechanical parameters (the face-to-core-stiffness-ratio FCRS). Demasi [4] presented an extension of the generalized unified formulation (GUF) to the theory of higher order shear deformation considering thick-layer structures, taking into account the Advanced Higher Order Shear Deformation Theory and a fourth-order fully Zig-Zag theories. Grygorowicz et al [5] studied the sandwich beam buckling problem analytically and numerically with FEM. The mechanical properties of the core of this beam varied symmetrically along its depth. The analytical model of this beam takes into account linear and nonlinear shear deformation theory. Detailed critical load tests were carried out on sample beams. Sayyad and Ghugal [6] presented a detailed, comprehensive review of publications on bending, buckling and free vibration of sandwich beams, taking into account 515 works, from the 18th century to the present, related to these problems. Kędzia and Smoczyński [7] analytically investigated the buckling problem of a

rectangular polyethylene sandwich plate subjected to a magnetic field. The analytical model of this plate was developed taking into account the “broken line” theory. Critical loads and dynamic equilibrium paths for example plates were determined. Paczos et al. [8] studied analytically and experimentally the three-point bending of simply supported sandwich beams with an individual structure of the honeycomb core. This beam was manufactured using additive technology, and the elastic modulus of the core varied along its entire length. The test results determined using these two methods were compared with each other. Magnucka-Blandzi [9] developed an analytical model of a seven-layer beam with three-layer cladding. The central core and cladding cores are wavy structures. Detailed deflection and buckling tests were performed for the translated family of beams. Marczak [10] presented an analytical study of the vibration problem of sandwich panels with periodic facings, taking into account the broken line hypothesis. He examined the vibration problems of this plate taking into account two tolerance models and, based on the analysis of the calculation results, he indicated an easier and more precise model that contains fewer governing equations with fewer coefficients. Magnucki et al. [11] studied analytically and numerically FEM the bending problem of a simply supported homogeneous beam with a bisymmetric cross section under a generalized load. The analytical model of this beam was elaborated with consideration of the classical shear stress formula – called the Zhuravsky shear stress. Detailed calculations of the maximum deflection of the beam with sample cross sections were carried out using these two methods and their results were compared with each other. Icardi and Urraci [12] developed a generalization of physically-based fixed degrees of freedom 3-D zig-zag theories. The aim of this work was to prove that the choice of global and layerwise functions is immaterial whenever coefficients are recalculated exactly (via symbolic calculus) by the enforcement of interfacial stress continuity, boundary conditions and equilibrium in point form, as

prescribed by the elasticity theory. Sharei et al. [13] experimentally and numerically investigated the impact of low speeds on sandwich panels with a foam core reinforced with short hybrid fibers. They experimentally demonstrated a significant impact of core reinforcement with carbon, aramid and carbon-aramid hybrid fibers on the Young's modulus value from 100 to 180 percent. FEM numerical tests confirmed the experimental results, the differences amounted to approximately 9.1 percent. Montazeri and Safarabadi [14] conducted comparative tests on the mechanical properties of composite laminates to demonstrate the influence of hybridization of cut glass fibers and kenaf fibers of their core. They determined that the kenaf core laminate had the highest dent resistance and the best properties due to the energy absorbed. Moreover, the performed FEM numerical tests showed quite good agreement with the experimental results. Magnucki et al. [15] developed three analytical models of a sandwich beam and analytically and numerically FEM studied the bending, buckling and free vibration problems of this beam. Magnucki [16] presented the individual nonlinear deformation theory and its application to analytical modeling of homogeneous beams, sandwich beams and functionally graded beams. Lewandowski and Litewka [17] analytically presented the problem of harmonic vibrations of laminated plates in the von Karman geometrically non-linear regime, taking into account the refined zigzag theory. Montazeri et al. [18] presented experimental and numerical FEM studies of three-point bending of beams with six honeycomb structures and different Poisson's ratios obtained using 3D printing technology. They demonstrated that four novel honeycomb structures, designed by hybridizing hexagonal and re-entrant units, outperformed standard conventional honeycomb structures in terms of load-bearing capacity. Montazeri et al. [19] investigated experimentally and numerically in FEM the performance of hexagonal and concave honeycombs additively manufactured based on polylactic acid and thermoplastic polyurethane, subjected to three-point bending. Conventional and auxetic cellular structures filled with polyurethane were created using 3D printing technology. The obtained research results indicated positive performance of foam-filled thermoplastic polyurethane based auxetic structures. Magnucki and Magnucka-Blandzi [20] developed analytical model of an asymmetric sandwich beam with consideration of the classical shear stress formula, called the Zhuravsky shear stress, and analytically studied the bending problem of this beam under uniformly distribute load along its length. Magnucki et al. [21] analytically and numerically studied the bending problem of a sandwich beam with stepped layers thicknesses. The effect of this thickness stepped on the beam deflection is analyzed.

The subject of the work is a sandwich beam with a core of an individual structure, the influence of which on the deformation shape of a planar cross-section is special. The main purpose of the work is to analytically determine such a structure of this core that the deformation shape of the planar cross-section of this beam will be exactly in accordance with the "broken line" theory.

2. ANALYTICAL MODEL OF THE SANDWICH BEAM

The cross section of the typical sandwich beam of total depth h , faces thicknesses h_f , core thickness h_c and width b is shown in Fig. 1.

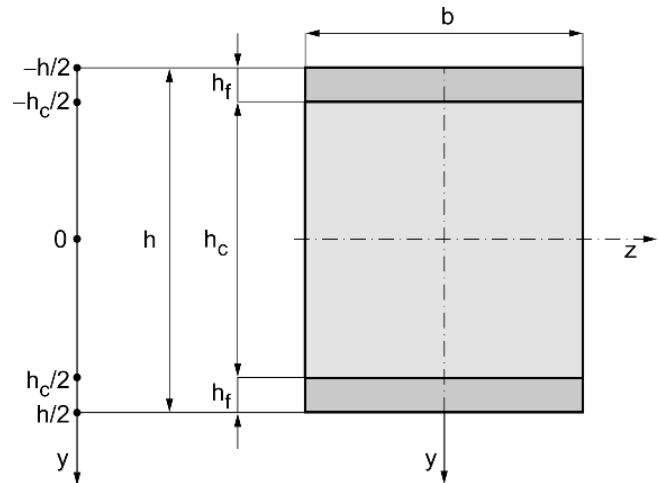


Fig. 1. Scheme of the cross section of the sandwich beam

The Young's modulus of successive layers is as follows:

- the upper face-sheet: $-1/2 \leq \eta \leq -\chi_c/2$

$$E(\eta) = E_f = \text{const}, \quad (1)$$

- the core: $-\chi_c/2 \leq \eta \leq \chi_c/2$

$$E(\eta) = E_f \cdot f_c(\eta), \quad (2)$$

- the lower face-sheet: $\chi_c/2 \leq \eta \leq 1/2$

$$E(\eta) = E_f = \text{const}, \quad (3)$$

where: $\eta = y/h$ – dimensionless coordinate, $\chi_c = h_c/h$ – dimensionless thickness of the core, $f_c(\eta)$ – unknown function of variability of Young's modulus along the thickness of the core fulfilling the condition $f_c(\pm \chi_c/2) = e_c$, and e_c – dimensionless coefficient of the core Young's modulus.

The general theoretical deformation of a planar cross section without shear effect in the faces of this beam, according to the paper [15], is shown in Fig. 2.

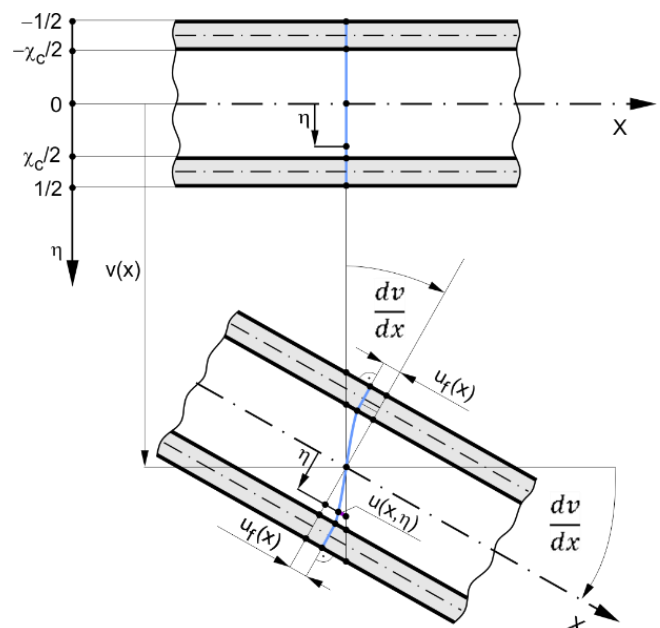


Fig. 2. Scheme of a planar cross section deformation of this beam

Considering Fig. 2 longitudinal displacements, strains and stresses in successive layers are written in the following form:

– the upper face-sheet: $-1/2 \leq \eta \leq -\chi_c/2$

$$u^{(uf)}(x, \eta) = -h \left[\eta \frac{dv}{dx} + \psi_f(x) \right], \quad (4)$$

$$\varepsilon_x^{(uf)}(x, \eta) = -h \left[\eta \frac{d^2v}{dx^2} + \frac{d\psi_f}{dx} \right], \quad \gamma_{xy}^{(uf)}(x, \eta) = 0, \quad (5)$$

$$\sigma_x^{(uf)}(x, \eta) = E_f \cdot \varepsilon_x^{(uf)}(x, \eta), \quad \tau_{xy}^{(uf)}(x, \eta) = 0, \quad (6)$$

– the core: $-\chi_c/2 \leq \eta \leq \chi_c/2$

$$u^{(c)}(x, \eta) = -h \left[\eta \frac{dv}{dx} - f_d^{(c)}(\eta) \cdot \psi_f(x) \right], \quad (7)$$

$$\varepsilon_x^{(c)}(x, \eta) = -h \left[\eta \frac{d^2v}{dx^2} - f_d^{(c)}(\eta) \cdot \frac{d\psi_f}{dx} \right], \quad (8)$$

$$\gamma_{xy}^{(c)}(x, \eta) = \frac{df_d^{(c)}}{d\eta} \cdot \psi_f(x), \quad (9)$$

$$\sigma_x^{(c)}(x, \eta) = E_f \cdot \varepsilon_x^{(c)}(x, \eta) \cdot f_c(\eta), \quad (10)$$

$$\tau_{xy}^{(c)}(x, \eta) = \frac{E_f}{2(1+\nu)} \cdot \gamma_{xy}^{(c)}(x, \eta) \cdot f_c(\eta), \quad (11)$$

– the lower face-sheet: $\chi_c/2 \leq \eta \leq 1/2$

$$u^{(lf)}(x, \eta) = -h \left[\eta \frac{dv}{dx} - \psi_f(x) \right], \quad (12)$$

$$\varepsilon_x^{(lf)}(x, \eta) = -h \left[\eta \frac{d^2v}{dx^2} - \frac{d\psi_f}{dx} \right], \quad \gamma_{xy}^{(lf)}(x, \eta) = 0, \quad (13)$$

$$\sigma_x^{(lf)}(x, \eta) = E_f \cdot \varepsilon_x^{(lf)}(x, \eta), \quad \tau_{xy}^{(lf)}(x, \eta) = 0, \quad (14)$$

where: $\psi_f(x) = u_f(x)/h$ – dimensionless displacement function, $f_d^{(c)}(\eta)$ – dimensionless deformation function of the core.

This dimensionless deformation function $f_d^{(c)}(\eta)$ of the core is formulated with consideration of the paper [16], especially the classical shear stress formula – called Zhuravsky shear stress

$$\tau_{xy}^{(cl)}(x, \eta) = S_z^{(c)}(\eta) \frac{T(x)}{b \cdot J_z}, \quad (15)$$

where: $S_z^{(c)}(\eta)$ – first moment of the selected part of the beam cross section, $T(x)$ – shear force, J_z – inertia moment of the cross section.

Taking into account the papers [15] or [16], the selected part of this beam cross section is shown in Fig. 3.

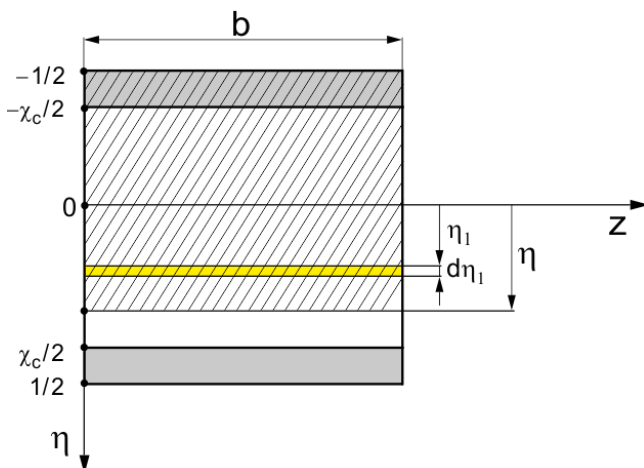


Fig. 3. Scheme of the selected part of this beam cross section

The first moment of the hatched area of the beam cross section (Fig. 3) with consideration of the Young's modulus is as follows:

$$S_z^{(c)}(\eta) = \bar{S}_z^{(c)}(\eta) \cdot b h^2, \quad (16)$$

where

$$\bar{S}_z^{(c)}(\eta) = \frac{1}{8} (1 - \chi_c^2) - J_c(\eta), \quad (17)$$

$$J_c(\eta) = \int_{-\chi_c/2}^{\eta} \eta_1 f_c(\eta_1) d\eta_1. \quad (18)$$

Equating the shear stress (11) to the classical shear stress formula (15) with consideration of the expression (16), after transformation, the derivative and the dimensionless function of the nonlinear deformation of a planar cross section of the core are obtained in forms:

$$\frac{df_d^{(c)}}{d\eta} = \frac{1 - \chi_c^2 - 8J_c(\eta)}{8C_0 f_c(\eta)}, \quad (19)$$

$$f_d^{(c)}(\eta) = \int \frac{1 - \chi_c^2 - 8J_c(\eta)}{8C_0 f_c(\eta)} d\eta, \quad (20)$$

where C_0 – constant.

This function according to the “broken line” theory, described in the paper [15], satisfies the following conditions:

$$\frac{df_d^{(c)}}{d\eta} = \frac{2}{\chi_c}, \quad \text{and} \quad f_d^{(c)}\left(\pm \frac{\chi_c}{2}\right) = \mp 1, \quad (21)$$

therefore, the constant C_0 is determined from the condition

$$\int_0^{\chi_c/2} \frac{1 - \chi_c^2 - 8J_c(\eta)}{8C_0 f_c(\eta)} d\eta = 1. \quad (22)$$

Based on the expression (19), with consideration of the first condition (21), the following equation is formulated

$$C_0 \frac{2}{\chi_c} f_c(\eta) = \frac{1}{8} (1 - \chi_c^2) - \int_{-\chi_c/2}^{\eta} \eta_1 f_c(\eta_1) d\eta_1. \quad (23)$$

Differentiating this equation and after simple transformation, the following differential equation is obtained

$$\frac{df_c}{f_c(\eta)} = -\frac{\chi_c}{2C_0} \eta. \quad (24)$$

The solution of this equation is the subject function of variability of Young's modulus along the thickness of the core in the following form

$$f_c(\eta) = \exp \left\{ \ln e_c + \frac{\chi_c}{4C_0} \left[\left(\frac{\chi_c}{2} \right)^2 - \eta^2 \right] \right\}. \quad (25)$$

This function satisfies the condition $f_c(\pm \chi_c/2) = e_c$.

Thus, the longitudinal displacements, strains and stresses of the core are as follows:

– the core: $-\chi_c/2 \leq \eta \leq \chi_c/2$

$$u^{(c)}(x, \eta) = -h \eta \left[\frac{dv}{dx} - \frac{2}{\chi_c} \cdot \psi_f(x) \right], \quad (26)$$

$$\varepsilon_x^{(c)}(x, \eta) = -h \eta \left[\frac{d^2v}{dx^2} - \frac{2}{\chi_c} \cdot \frac{d\psi_f}{dx} \right], \quad (27)$$

$$\gamma_{xy}^{(c)}(x, \eta) = \frac{2}{\chi_c} \cdot \psi_f(x), \quad (28)$$

$$\sigma_x^{(c)}(x, \eta) = -E_f h \cdot \eta \left[\frac{d^2v}{dx^2} - \frac{2}{\chi_c} \cdot \frac{d\psi_f}{dx} \right] \cdot f_c(\eta), \quad (29)$$

$$\tau_{xy}^{(c)}(x, \eta) = \frac{E_f}{1+\nu} \cdot \frac{1}{\chi_c} \cdot f_c(\eta) \cdot \psi_f(x). \quad (30)$$

3. THREE-POINT BENDING OF THE SANDWICH BEAM

The bending moment, according to its definition, for the subject sandwich beam is of the form

$$M_b(x) = bh^2 \left[J_M^{(uf)}(x) + J_M^{(c)}(x) + J_M^{(lf)}(x) \right], \quad (31)$$

$$\text{where: } J_M^{(uf)}(x) = \int_{-1/2}^{-\chi_c/2} \eta \sigma_x^{(uf)}(x, \eta) d\eta,$$

$$J_M^{(c)}(x) = \int_{-\chi_c/2}^{\chi_c/2} \eta \sigma_x^{(c)}(x, \eta) d\eta,$$

$$J_M^{(lf)}(x) = \int_{\chi_c/2}^{1/2} \eta \sigma_x^{(lf)}(x, \eta) d\eta.$$

Substituting the expressions (6), (14) and (28) into the above expression (31), after integration one obtains the equation

$$C_{vv} \frac{d^2 v}{dx^2} - C_{v\psi} \frac{d\psi_f}{dx} = -12 \frac{M_b(x)}{E_f b h^3}, \quad (32)$$

where dimensionless coefficients: $C_{vv} = 1 - \chi_c^3 + 12J_{c2}$,
 $C_{v\psi} = 3 \left(1 - \chi_c^2 + \frac{8}{\chi_c} J_{c2} \right)$, $J_{c2} = \int_{-\chi_c/2}^{\chi_c/2} \eta^2 f_c(\eta) d\eta$.

The elastic strain energy

$$U_{\varepsilon, \gamma} = \frac{1}{2} E_f b h \int_0^L \left[J_U^{(uf)}(x) + J_U^{(c)}(x) + J_U^{(lf)}(x) \right] dx, \quad (33)$$

$$\text{where: } J_U^{(uf)}(x) = \int_{-1/2}^{-\chi_c/2} \left[\varepsilon_x^{(uf)}(x, \eta) \right]^2 d\eta,$$

$$J_U^{(c)}(x) = \int_{-\chi_c/2}^{\chi_c/2} \left\{ \left[\varepsilon_x^{(c)}(x, \eta) \right]^2 + \frac{1}{2(1+\nu)} \left[\gamma_{xy}^{(c)}(x, \eta) \right]^2 \right\} f_c(\eta) d\eta,$$

$$J_U^{(lf)}(x) = \int_{\chi_c/2}^{1/2} \left[\varepsilon_x^{(lf)}(x, \eta) \right]^2 d\eta.$$

Substituting the expressions (5), (13), (27) and (28) into the above expression (33), after integration the elastic strain energy is of the form

$$U_{\varepsilon, \gamma} = \frac{1}{24} E_f b h^3 \int_0^L \left[C_{vv} \left(\frac{d^2 v}{dx^2} \right)^2 - 2 C_{v\psi} \frac{d^2 v}{dx^2} \frac{d\psi_f}{dx} + C_{\psi\psi} \left(\frac{d\psi_f}{dx} \right)^2 + C_{\psi} \frac{\psi_f^2(x)}{h^2} \right] dx, \quad (34)$$

where dimensionless coefficients: $C_{\psi\psi} = 12 \left(1 - \chi_c + \frac{4}{\chi_c^2} J_{c2} \right)$,
 $C_{\psi} = \frac{6}{1+\nu} \frac{4}{\chi_c^2} J_{c0}$, $J_{c0} = \int_{-\chi_c/2}^{\chi_c/2} f_c(\eta) d\eta$.

The work of the load

$$W = \int_0^L T(x) \frac{dv}{dx} dx, \quad (35)$$

where $T(x)$ – shear force.

Taking into account the principle of stationary total potential energy $\delta(U_{\varepsilon, \gamma} - W) = 0$, two differential equations of equilibrium of this sandwich beam is obtained in the following form:

$$C_{vv} \frac{d^4 v}{dx^4} - C_{v\psi} \frac{d^3 \psi_f}{dx^3} = -\frac{12}{E_f b h^3} \frac{dT}{dx}, \quad (36)$$

$$C_{vv} \frac{d^3 v}{dx^3} - C_{\psi\psi} \frac{d^2 \psi_f}{dx^2} + C_{\psi} \frac{\psi_f(x)}{h^2} = 0. \quad (37)$$

The equations (32) and (36) are equivalent, then, equations (32) and (37) are fundamental in the beam bending studies. Thus,

after simply transformation of these two equations, the one differential equation of the form is obtained

$$\frac{d^2 \psi_f}{dx^2} - \alpha^2 \frac{\psi_f(x)}{h^2} = -12 \frac{C_{v\psi}}{C_{vv} C_{\psi\psi} - C_{v\psi}^2} \frac{T(x)}{E_f b h^3}, \quad (38)$$

where $\alpha = \sqrt{\frac{C_{vv} C_{\psi\psi}}{C_{vv} C_{\psi\psi} - C_{v\psi}^2}}$ – dimensionless coefficient.

The three-point bending problem of this sandwich beam is analyzed in detail. The scheme of the beam of length L is shown in Fig. 4.

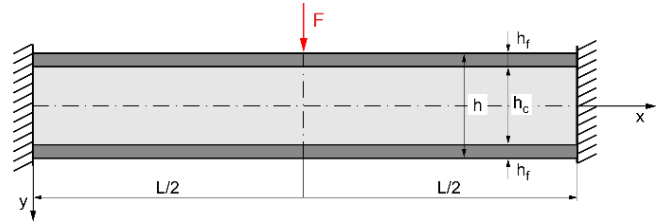


Fig. 4. Scheme of the three-point bending of the beam

The scheme of the left end-part of this beam with reactions is shown in Fig. 5.

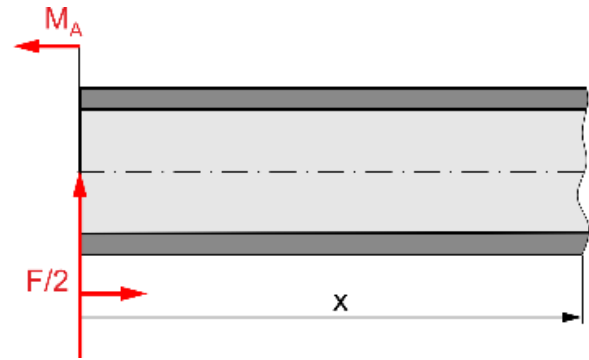


Fig. 5. Scheme of reactions in left end-part of this beam

Thus, the shear force and the bending moment in the left part of this beam ($0 \leq x \leq L/2$) are as follows:

$$T(x) = \frac{1}{2} F, \quad M_b(x) = -M_A + \frac{1}{2} Fx. \quad (39)$$

Consequently, the differential equation (38) with consideration of the expression (39a), in the dimensionless coordinate $\xi = x/L$, is in the following form

$$\frac{d^2 \psi_f}{d\xi^2} - (\alpha\lambda)^2 \cdot \psi_f(\xi) = -6 \frac{C_{v\psi}}{C_{vv} C_{\psi\psi} - C_{v\psi}^2} \lambda^2 \frac{F}{E_f b h}, \quad (40)$$

where λ – relative length of the beam.

The solution of this differential equation for the left part of this beam ($0 \leq \xi \leq 1/2$) is as follows

$$\psi_f(\xi) = \bar{\psi}_f(\xi) \cdot \frac{F}{E_f b h} \quad (41)$$

where

$$\bar{\psi}_f(\xi) = 6 \left\{ 1 - \frac{\sinh(\alpha\lambda\xi) + \sinh[(1-2\xi)\alpha\lambda/2]}{\sinh(\alpha\lambda/2)} \right\} \frac{C_{v\psi}}{C_{vv} C_{\psi\psi}}. \quad (42)$$

This function satisfy following conditions: $\bar{\psi}_f(0) = 0$ – clamped end, and $\bar{\psi}_f(1/2) = 0$ – middle of the beam.

The equation (32) with consideration of the expression (39b), in the dimensionless coordinate $\xi = x/L$, was written in the following form

$$C_{vv} \frac{d^2 \bar{v}}{d\xi^2} = C_{v\psi} \frac{d\psi_f}{d\xi} + 6(2\bar{M}_A - \xi) \lambda^2 \frac{F}{E_f b h}, \quad (43)$$

where: $\bar{v}(\xi) = v(\xi)/L$ – relative deflection of the beam, $\bar{M}_A = M_A/(FL)$ – dimensionless reaction moment.

This equation after integration is in the form

$$C_{vv} \frac{d\bar{v}}{d\xi} = C_3 + C_{v\psi} \psi_f(\xi) + 6 \left(2\bar{M}_A \xi - \frac{1}{2} \xi^2 \right) \lambda^2 \frac{F}{E_f b h}, \quad (44)$$

where the integration constant from the condition $d\bar{v}/d\xi|_0 = 0$ is equal to zero $C_3 = 0$, and the dimensionless reaction moment from the condition $d\bar{v}/d\xi|_{1/2} = 0$ is equal $\bar{M}_A = 1/8$.

Consequently, integrating this equation and taking into account the function (41) and the boundary condition $\bar{v}(0) = 0$, one obtains the function of the relative deflection of the beam

$$\bar{v}(\xi) = \tilde{v}(\xi) \cdot \frac{F}{E_f b h}, \quad (45)$$

where

$$\tilde{v}(\xi) = \left\{ 6 \left[\xi - \phi_\psi(\xi) \right] \frac{C_{v\psi}^2}{C_{vv} C_\psi} \frac{1}{\lambda^2} + \frac{1}{4} (3\xi^2 - 4\xi^3) \right\} \frac{\lambda^2}{C_{vv}} \quad (46)$$

$$\text{and } \phi_\psi(\xi) = \frac{\cosh(\alpha\lambda\xi) - 1 + \cosh(\alpha\lambda/2) - \cosh[(1-2\xi)\alpha\lambda/2]}{\alpha\lambda \sinh(\alpha\lambda/2)}.$$

Thus, the relative maximum deflection of the beam is as follows

$$\bar{v}_{max} = \bar{v}\left(\frac{1}{2}\right) = \tilde{v}_{max} \cdot \frac{F}{E_f b h}, \quad (47)$$

where the dimensionless maximum deflection

$$\tilde{v}_{max} = (1 + C_{se}) \frac{\lambda^2}{16 C_{vv}}, \quad (48)$$

and the shear coefficient

$$C_{se} = \frac{48}{\lambda^2} \left[1 - 4 \frac{\cosh(\alpha\lambda/2) - 1}{\alpha\lambda \sinh(\alpha\lambda/2)} \right] \frac{C_{v\psi}^2}{C_{vv} C_\psi}. \quad (49)$$

The shear stresses (30) in the core with consideration of the expression (41) is in the following form

$$\tau_{xy}^{(c)}(\xi, \eta) = \bar{\tau}_{xy}^{(c)}(\xi, \eta) \cdot \frac{F}{bh}, \quad (50)$$

where the dimensionless shear stress

$$\bar{\tau}_{xy}^{(c)}(\xi, \eta) = \frac{1}{(1+\nu)\chi_c} \cdot f_c(\eta) \cdot \bar{\psi}_f(\xi). \quad (51)$$

4. SAMPLE DETAILED CALCULATIONS

Example calculations are carried out for three selected structures of sandwich beam of following data: $\lambda = 15$, $e_c = 1/20$, $\nu = 0.3$, $\chi_c = 18/20, 17/20, 16/20$. The graph of the dimensionless displacement function (42) for selected structure of sandwich beam $\chi_c = 18/20$ is shown in Fig. 6.

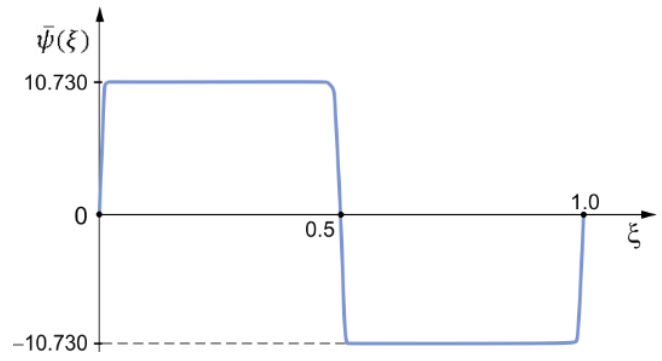


Fig. 6. The graph of the dimensionless displacement function $\bar{\psi}_f(\xi)$

The results of this calculations: values of the constant C_0 , dimensionless displacement function $\bar{\psi}_f(1/4)$, shear coefficient C_{se} , and the dimensionless maximum deflection \tilde{v}_{max} are specified in Tab. 1.

Tab. 1. The results of calculations of the selected structures of beam

| χ_c | 18/20 | 17/20 | 16/20 |
|---------------------|----------|------------|----------|
| C_0 | 0.21375 | 0.29484375 | 0.36 |
| $\bar{\psi}_f(1/4)$ | 10.730 | 10.997 | 10.915 |
| C_{se} | 0.248714 | 0.349100 | 0.433171 |
| \tilde{v}_{max} | 56.507 | 45.361 | 39.169 |

Moreover, the results of these calculations regarding the subject function (25) of variability of Young's modulus along the thickness of the core and the dimensionless shear stress (51) for $\xi = 1/4$ are presented graphically in Fig. 7 and Fig. 8.

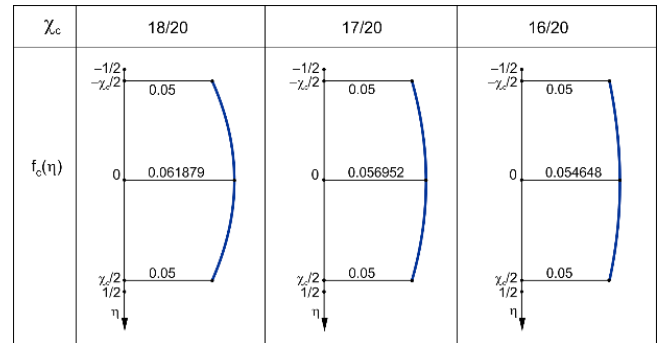


Fig. 7. Graphs of the function $f_c(\eta)$ for the selected structures of the beam

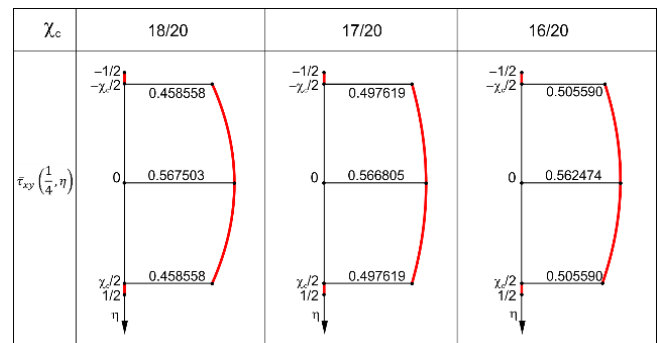


Fig. 8. Graphs of the function $\bar{\tau}_{xy}^{(c)}\left(\frac{1}{4}, \eta\right)$ for the selected structures of the beam

5. CONCLUSIONS

The research presented above, the following conclusions:

- the deformation shape of a planar cross section of a typical sandwich beam is exactly consistent with the "broken line" theory, when the Young's modulus variable along the core thickness in accordance with the function in the form (25),
- the distribution-graph of the shear stress along the core thickness is non-linear (Fig. 8).

REFERENCES

1. Carrera E. Historical review of Zig-Zag theories for multilayered plates and shells. *Applied Mechanics Reviews*. 2003;56(3):287-308.
2. Magnucka-Blandzi E, Magnucki K. Effective design of a sandwich beam with a metal foam core. *Thin-Walled Structures*. 2007;45(4):432-438.
3. Carrera E, Brischetto S. A survey with numerical assessment of classical and refined theories for the analysis of sandwich plates. *Applied Mechanics Reviews*. 2009;62(1):010803-1-17.
4. Demasi L. Partially Zig-Zag advanced higher order shear deformation theories based on the generalized unified formulation. *Composite Structures*. 2012;94:363-375.
5. Grygorowicz M, Magnucki K, Malinowski M. Elastic buckling of a sandwich beam with variable mechanical properties. *Thin-Walled Structures*. 2015;87:127-132.
6. Sayyad AS, Ghugal YM. Bending, buckling and free vibration of laminated composite and sandwich beams: A critical review of literature. *Composite Structures*. 2017;171:486-504.
7. Kędzia P, Smoczyński MJ. Homogeneity of magnetic field influence on buckling of three layer polyethylene plate. *Composite Structures*. 2018;183:331-337.
8. Paczos P, Wichniarek R, Magnucki K. Three-point bending of the sandwich beam with special structures of the core. *Composite Structures*. 2018;201:676-682.
9. Magnucka-Blandzi E. Bending and buckling of a metal seven-layer beam with crosswise corrugated main core – Comparative analysis with sandwich beam. *Composite Structures*. 2018;183:35-41.
10. Marczak J. On the correctness of results of averaged models of periodic sandwich plates depending on the set of fluctuation shape functions. *Composite Structures*. 2020;244:112269.
11. Magnucki K, Lewinski J, Magnucka-Blandzi E. A shear deformation theory of beams of bisymmetrical cross sections based on the Zhuravsky shear stress formula. *Engineering Transactions*. 2020;68(4):353-370.
12. Icardi U, Urraci A. Considerations about the choice of layerwise and through-thickness global functions of 3-D physically-based zig-zag theories. *Composite Structures*. 2020;244:112233.
13. Sharei A, Safarabadi M, Mashhadi MM, Solut RS, Haghighi-Yazdi M. Experimental and numerical investigation of low velocity impact on hybrid short-fiber reinforced foam core sandwich panel. *Journal of Composite Materials*. 2021;55(29):4375-4385.
14. Montazeri A, Safarabadi M. A comparative study on adding chopped kenaf fibers to the core of glass/epoxy laminates under quasi-static indentation: Experimental and numerical approaches. *Journal of Composite Materials*. 2022;56(25):3821-3833.
15. Magnucki K, Magnucka-Blandzi E, Wittenbeck L. Three models of a sandwich beam: Bending, buckling and free vibration. *Engineering Transactions*. 2022;70(2):97-122.
16. Magnucki K. An individual shear deformation theory of beams with consideration of the Zhuravsky shear stress formula. *Current Perspectives and New Directions in Mechanics, Modelling and Design of Structural Systems – Zingoni (ed.) - Proceedings of the 8th International Conference on Structural Engineering, Mechanics and Computation*, 2022, pp. 682–689.
17. Lewandowski R, Litewka P. Nonlinear harmonic vibrations of laminate plates with viscoelastic layers using refined zig-zag theory. Part 1–Theoretical background. *Composite Structures*. 2023;320:117200.
18. Montazeri A, Hasani A, Safarabadi M. Bending performance and failure mechanism of 3D-printed hybrid geometry honeycomb with various Poisson's ratios. *Journal of Sandwich Structures & Materials*. 2023;25(7):709-729.
19. Montazeri A, Bahmanpour E, Safarabadi M. Three-point bending behavior of foam-filled conventional and auxetic 3D-printed honeycombs. *Advanced Engineering Materials*. 2023;25(17):2300273.
20. Magnucki K, Magnucka-Blandzi E. A refined shear deformation theory of an asymmetric sandwich beam with porous core: Linear bending problem. *Applied Mathematical Modeling*. 2023;124:624-638.
21. Magnucki K, Kustos J, Goliwaj D. Effective shaping of a stepped sandwich beam with clamped ends. *Acta Mechanica et Automatica*. 2023;17(2):200-204.

Krzysztof Magnucki:  <https://orcid.org/0000-0003-2251-4697>

Ewa Magnucka-Blandzi:  <https://orcid.org/0000-0002-6349-5579>



This work is licensed under the Creative Commons BY-NC-ND 4.0 license.

AUTOMATIC DEVICE WITH SELF-BRAKING FOR FIXATION OBJECTS IN EXECUTIVE LINKS OF TECHNOLOGICAL EQUIPMENT

Borys PRYDALNYI*

*Faculty of Transport and Mechanical Engineering, Department of Applied Mechanics and Mechatronics,
Lutsk National Technical University, Lvivska Str 75, 43018 Lutsk, Ukraine

b.prydalnyi@lntu.edu.ua

received 23 January 2024, revised 25 April 2024, accepted 21 May 2024

Abstract: The main characteristics of a new automatic device for the fixation of objects in executive links of technological equipment, which determine its suitability for use, are considered. The device is based on a new structure that ensures its self-braking after the process of object fixation and increases the reliability of holding the objects, which is especially important in safety-critical applications. The proposed structure can be implemented for use in various types of executive links of technological equipment, and in the paper, it is considered the most complex application of the device—as part of a spindle assembly. For the proposed design, the method of calculating the main parameters of this type of mechanism is presented. Based on the results of the research, analytical and graphical dependencies have been obtained describing the change of the clamping force from 45 to 15 kN when increasing the spindle speed up to 10000 rpm, and the dependence of the clamping force on the torque at the input link. Based on the results of the research, a preliminary conclusion has also been drawn regarding the possibility of using electromechanical clamping mechanisms of the proposed type as a part of spindle units of machine tools, also because the rotor diameter of the mechanism is within 100 mm and the stator is within 200 mm.

Key words: spindle unit, friction locking, fixation process, clamping drive, clamping chuck

1. INTRODUCTION

The characteristics of fixing objects on the executive links of technological equipment determine the maximum values of its force interaction with tools, which limits the productivity and technological capabilities of the equipment. The characteristics of the functioning and design of automatic fixation devices determine the dynamic characteristics of the executive link on which they are located, which also affects the performance and quality of the equipment. Also, these characteristics determine the reliability of holding the fixation object, which is especially important for safety-critical applications. The simplest and most common way to automatically fix objects that are processed in technological equipment is to clamp them [1], so such fixation devices are most often called clamping mechanisms (CM). One of the features of CM of the traditional structure is the way the input energy is supplied, which is used both for the fixation process and for holding the object. This significantly reduces the reliability of object holding due to an emergency loss or uncontrolled changes in the CM power supply characteristics (pressure, voltage fluctuations, etc.). Existing CM with geometric locking does not provide a stable clamping force value for workpieces with significant diameter deviations from their nominal values.

The actuator of a CM is the main part of it and defines the performance characteristics and influences the structure of the spindle units or executive links on which it is located. The rapid introduction and widespread use of electromechanical systems in modern technological equipment are obvious. This increases and explains the need for a new type of CM with electromechanical systems not only for new machine tools being designed, but also

for the modernisation of existing units by replacing some of them in the CM, for example, the mechanical actuator of the CM with an electromechanical one. Therefore, the creation of CM with an electromechanical drive and the development of methods for their calculation determine the relevance of this area of research.

Existing studies do not evaluate automatic clamping mechanisms as separate subsystems to be developed and improved by changing their structure. In [1], the importance of measuring clamping forces in a clamping chuck and taking into account the influence of centrifugal inertia forces is highlighted. In [2], dynamic models are presented that describe the energy conversion characteristics of CMs with a rotating input link. The study of certain characteristics of backlash elimination in this type of CM to achieve the necessary settings for its functioning is revealed in [3]. At the same time, [2] and [3] did not study the characteristics of CMs built according to the proposed scheme, which determine the applicability of their use as part of the executive links of typical kinds of technological equipment and, in particular, spindle assemblies. In [4], the influence of the clamping chuck is discussed, but no information is given on the design and characteristics of the clamping mechanism drive. The possibility of controlling the clamping of thin-walled workpieces is considered in [5], however, it is not indicated how this can be used for automatic clamping mechanisms. The influence of centrifugal forces on the clamping process was evaluated in [6], but the possibilities of controlling its influence were not discussed. A scheme of the clamping mechanism for high-speed operation is presented in [7], nevertheless, no study of its characteristics determines the possibility of its use as a part of typical spindle assemblies. Issues relating to the machining of non-rigid, thin-walled workpieces are considered in [8], but no clamping mechanisms for solving the problem are given. The

control of clamping forces for clamping thin-walled workpieces was investigated in [9], although a design suitable for automatic operation at high speeds was not presented. In [10], the problems associated with the operation of a hydraulically driven chuck are investigated, and the possibility of using an electromechanical drive is not considered. Methods for calculating the required clamping forces for thin-walled workpieces are presented [11], but no mechanisms are proposed that create a clamping force with a given value. Study [12] presents conditions for increasing the stability of turning flexible workpieces at different rotation frequencies but does not present proposals for changes to the clamping mechanisms. In [13], the analysis of the stability of spindles when speed is variable is presented, which indicates the possibility of their acceleration but is not shown adapting the clamping mechanism characteristics. In [14], the possibilities of using additive composites for use in clamping and manipulation devices are disclosed, but the working characteristics of the functioning of such fixation devices are not investigated. The paper [15] indicates the possibility of improving the stability conditions of the end-turning of flexible workpieces, but no suggestions for improving the characteristics of the clamping mechanisms were provided. Work [16] analyzes the effect of cutting forces on the collet but does not indicate the impact on the power interaction of the collet and its drive. The accuracy of positioning in a new type of clamping chuck is investigated in [17], but the influence of its design on the clamping force characteristics is not indicated. The peculiarities of providing damping by collet chuck were revealed in study [18], which indicates certain advantages of using this type of chuck in CM. New approaches to the formation of workpieces with an expanded range of material and design characteristics, e.g., brittle [19] and flexible [20], create the prerequisites for an increase in the range of machined parts in mechanical engineering and, as a result, new modes of machining and clamping workpieces. This determines the need to investigate new types of CMs, in particular in terms of the possibility of adjusting the force characteristics and, in particular, the characteristics of their operation at high rotational speeds, which is necessary for efficient machining with low feeds.

2. RESEARCH METHODOLOGY TO DISCOVER THE CHARACTERISTICS OF THE PROPOSED CLAMPING MECHANISM

The purpose of the study is to determine the main characteristics of the clamping mechanism with the proposed type of electromechanical drive, which will allow a preliminary assessment of the possibility of its use in new designs and the modernisation of existing spindle assemblies to more fully utilize the potential capabilities of technological equipment. In order to achieve the objective, the following tasks are necessary:

- to develop a calculation scheme of CM including an electromechanical drive of an alternative design;
- to determine the main dependencies describing the characteristics of the output values and, in particular, the clamping forces;
- to evaluate the possibility of using the proposed drive design as part of the CM for its modernisation.

The object of the research is the automatic CM for use in executive links of technological equipment and especially spindle units that contains an electromechanical drive of a new design.

The subject of the research is the dependencies describing the main characteristics of the functioning of the automatic CM of the proposed design. The main hypothesis of the research is the compliance of the main characteristics of the CM of the proposed type with the conditions of use as a part of executive links of technological equipment, in particular, for its modernization. The assumptions made in these studies relate to the correspondence of the parameters of the structural elements (rotor, stator, helical gear, etc.) of the mechanism under study with their existing functional analogues. To simplify the study, friction is only considered in the main kinematic joints and the influence of external disturbances is not taken into account.

2.1. Features of typical and alternative structures of clamping mechanisms

The most common typical structure of a mechanical CM that provides reliable maintenance of the clamped state of the object of fixation without external energy consumption based on the principle of geometric locking of the mechanism. This is most often realized through the use of a lever mechanism and an input link containing conical and cylindrical surfaces (Fig. 1). When the point of interaction between a large arm of a lever reaches the cylindrical part of the specially-shaped link, the mechanism becomes geometrically locked. Such a structure provides a constant amount of movement of CM elements, and what is essential are the clamping elements of a chuck. As a result, the CM system's stress state values will vary if the diameter of the clamping object deviates from the nominal values for which the CM is configured.

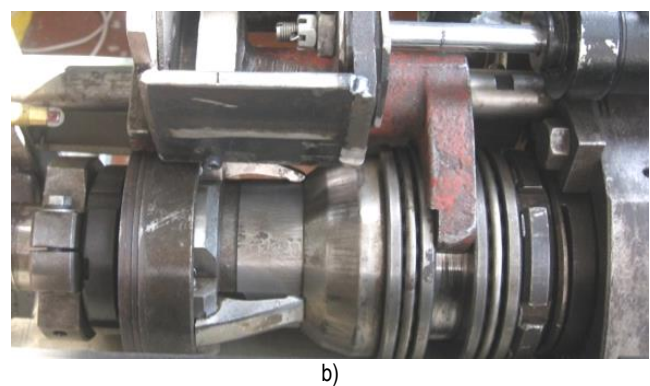
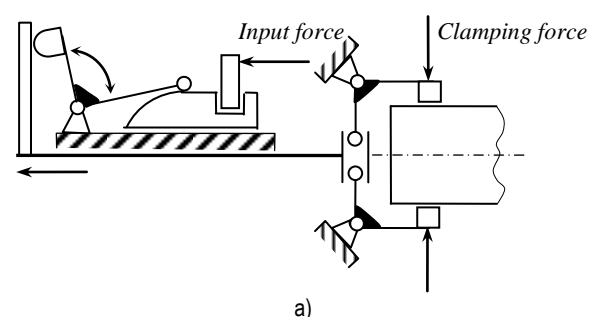


Fig. 1. Mechanical CM's actuator with geometric locking: a) functioning scheme in combination with a lever chuck (in the "clamped" state); b) general view of the mechanism (in the "unlocked" state)

This places significant limitations on the clamping of, uncalibrated objects. In addition, the presence of radially moving drive elements worsens the conditions for implementing and maintaining high-precision balancing of the spindle assembly. This disadvantage is common to all CM with geometric locking.

A new alternative structure of the electromechanical actuator of the CM has been designed based on the recommendations of previous research and structure-scheme synthesis [2]. The actuator with the new proposed structure is expected to have improved operating characteristics and is adapted to operate autonomously as well as at high rotational frequencies for use as part of a spindle assembly. The design of the proposed CM is devoid of most of the disadvantages of the hydraulic and mechanical prototypes and is protected by Patent 95323 (Ukraine). The CM drive is mounted at the rear end of spindle 1 (Fig. 2). Its body in the form of sleeve 3 is held against rotation relative to spindle 1 by key 2. Part of the external cylindrical surface of sleeve 3 is provided with an external threaded surface on which rotor 5 and nut 6 that restricts its stroke are screwed. On sleeve 3 there is also axially movable bushing 4 which has the possibility of simultaneous force interaction with cylinder 7 and rotor 5 via thrust bearings 18 (fixed with nut 19) and cylinder 17 which is rigidly connected to rotor 5. In the rear end of sleeve 3, there is installed drive bush 8 which can move in the axial direction and is capable of interacting simultaneously with nut 9 placed on drawbar 10 in the form of tube and cylinder 7 through a set of elastic elements 11. The preload of elastic elements 11 is provided by the nut 12 mounted on drive bush 8. The right end of drawbar tube 10 is connected to a clamping chuck (not shown in Fig. 2). Electric windings 13 are located on rotor 5 and can interact with electromagnetic windings 14 located on stator 15, which is rigidly connected to the spindle body 16.

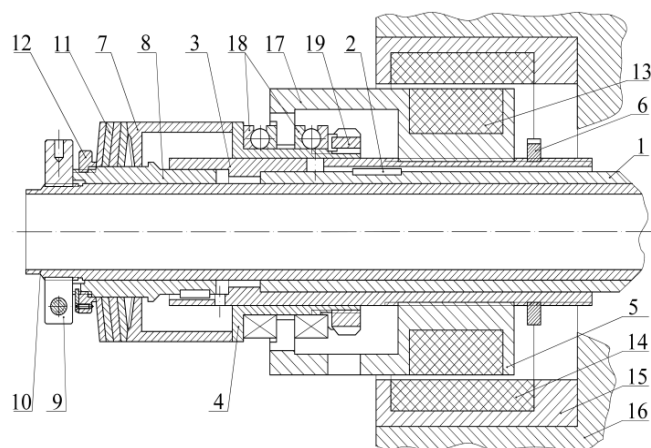


Fig. 2. Design of the new electromechanical CM actuator

The device presented (Fig. 2) works as follows. To perform the clamping operation, windings 14 of stator 15 are supplied with electricity. At the same time, a magnetic field is created around windings 14, which interacts with windings 13 of rotor 5 and gives them torque. As windings 13 are rigidly connected to rotor 5, this causes the rotational and translational movement of rotor 5 relative to body 3. The axial force from rotor 5 is transmitted through a set of structural elements to the end of drawbar 10, which is connected to the clamping chuck at the other end (not shown). The clamping process continues until the required clamping force is reached, which depends only on the parameters of the electric current supplied to stator windings 14 and is stable. This means that it does not depend on the radial dimensional deviation of the

workpiece. The rotation-translation movement of rotor 5 and the clamping process stop when the required clamping force is reached, thus increasing the force opposing the axial movement. A moment of completion of the clamping (rotor stop) is reflected in the characteristics (pattern of change) of the electric current of winding 14. At the end of the clamping operation, the electric current supplied to stator windings 14 stops and the clamping force is maintained by the self-braking of the threaded gear between rotor 5 and sleeve 3. In order to initiate the process of releasing a workpiece, a current with characteristics is supplied to windings 14, which determine the movement of rotor 5 in the opposite direction to the clamping process, until it stops at nut 6, located on body 3. The workpiece releases under the elastic forces of the collet petals (not shown).

The design of the proposed clamping mechanism possesses the following advantages: no need for mechanical contact with the elements of a spindle unit for power supply; a few movable and complex elements and no radially movable elements improves the conditions of balancing a spindle unit; an absence of subsystems for the conversion and transfer of energy to the clamping driver (electrical energy is fed directly). In order to compensate for the loss of clamping force when machining at high frequencies of rotation, the presented clamping drive allows for changing the amount of clamping force by supplying power to the stator windings with the appropriate characteristics.

2.2. Calculation of certain geometrical characteristics of the subsystems of the clamping device

For calculation parameters of the proposed CM the special calculation scheme (Fig. 3) is created.

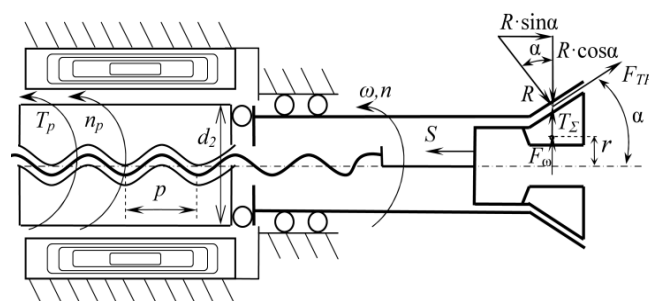


Fig. 3. The scheme for calculating CM parameters

For the calculation, the maximum output axial force that can be produced by the driver of CM is $S = 20$ kN. The thread screw transmission "rotor-spindle" is self-braking and has the diameter $d_2 = 85$ mm and the pitch $p = 2$ mm. In order to reduce wear of the thread transmission it is reasonable to choose antifriction pair materials of the inner threaded surface (in the rotor) – cast iron and the outside thread (on the spindle) – steel.

Verification of the thread diameter by wear resistance condition is done with the formula:

$$d_2 \geq \sqrt{S / (\pi \cdot \psi_H \cdot \psi_h \cdot [\sigma_{CM}])} \quad (1)$$

where $[\sigma_{CM}] = 4 \dots 6$ MPa – permissible tension values of crumpling for selected materials; $\psi_h = 0.75$ – coefficient of height of the thread; $\psi_H = 1.2$ – length coefficient of internal threaded surface of the rotor. Accordingly to (1) $85 \text{ mm} > \sqrt{20000 / (\pi \cdot 1.2 \cdot 0.75 \cdot 5)} = 38 \text{ mm}$ which means

the wear resistance is provided more than a double reserve that allows the use of less durable and lightweight materials for the inside of the threaded rotor surface.

The minimum length of the length of the threaded surface of the rotor H that is needed to provide calculated values of wear resistance, $H = \psi_H \cdot d_2 = 1.2 \cdot 38 \approx 46\text{mm}$. The value of pitch of a thread also was selected based on provided a self-braking $\psi < \phi_p$, where ψ – an angle of rise of a thread turn; ϕ_p – the angle of friction in the thread. To greased, polished and fitted surfaces threaded friction a coefficient accept is $f_p = 0.07$. The coefficient of friction f_{RP} in the screw gear takes into account the influence of an angle thread profile and is determined from the $f_{RP} = f_p / \cos \gamma_p$, where for a thrust thread $\gamma_p = 3^\circ$ – the angle of slope of the profile line of the thread. Considering the small value of the angle γ_p ($\cos \gamma_p = 0.999$) in the thrust thread, equality $f_{RP} \approx f_p$ is accepted, which defines the angle of friction $\phi_p = \arctg f \approx 4^\circ$. The helix angle of the thread $\psi = \arctg [p / (\pi \cdot d_2)] \approx 0.43^\circ$. Thus, with the selected thread pitch, a self-locking reserve ($0.43^\circ \ll 4^\circ$) is provided in the screw drive, which is necessary to prevent unscrewing in the event of alternating loads, vibrations and the occurrence of radial elastic deformations.

2.3. Calculation of the power characteristics of the clamping mechanism

Axial force S , which is transferred from the rotor through the drawbartube to the collet, is counterbalanced by reactions of the spindle and clamping forces. To calculate parameters of the screw gear, the forces acting on the surface of the thread are conditionally replaced with concentrated force that is normal to the surface of the thread profile. Taking into account the small angle of the thread profile γ_p , we count it they are coaxial with the axis of rotation and with S . Tangential force F_t which must be applied to the rotor on its radius to obtain the required amount of axial force S is determined from:

$$F_t = S \cdot \tg(\psi + \phi_p). \quad (2)$$

Torque generated by a tangential force:

$$T_p = 0.5 d_2 F_t. \quad (3)$$

From (3) $T_p = 0.5 \cdot 0.085 \cdot 20000 \cdot \tg 4.43^\circ = 66\text{Nm}$.

From expressions (1) and (2) the expression for finding the axial force S generated at the output of the actuator is obtain:

$$S = T_p / 0.5 \cdot d_2 \cdot \tg(\psi + \phi_p). \quad (4)$$

Forces in the collet clamping chuck can be calculated from the scheme (Fig. 3). In the calculation, the stiffness of the collet petals is neglected. The equation of a balance of powers which operate on the collet in conditional planes according to Fig. 3: in horizontal plane,

$$F_{TP} \cdot \cos \alpha + R \cdot \sin \alpha - S = 0; \quad (5)$$

in vertical plane,

$$F_{TP} \cdot \sin \alpha - R \cdot \cos \alpha + T_\Sigma + F_\omega = 0, \quad (6)$$

where T_Σ – total radial clamping force; R – normal reaction that acts from the spindle cone; F_{TP} – a force of friction on the cone of the collet and spindle; α – half of an angle of a cone of a collet; F_ω – centrifugal force of inertia that acts on the petals of the collet

chuck during its rotation around the axis. Taking into account $F_\omega = m \cdot \omega^2 \cdot r$; $F_{TP} = R \cdot f$ and $f = \tg \phi$ the value S can be derived from (5) and (6):

$$S = (T_\Sigma + m\omega^2 r) \cdot \tg(\alpha + \phi), \quad (7)$$

where m – the mass of the collet petals; r – the distance from the axis of rotation to the centre of weight of the collet petals; f – the coefficient of friction.

As a prototype electric motor for the drive of the proposed CM a three-phase asynchronous motor with a squirrel-cage rotor is chosen as the most common type. Initial information for the calculation includes the previously calculated torque on the rotor $T_p = 66\text{ Nm}$, which is required to produce the maximum force $S = 20\text{ kN}$, and the maximum frequency of rotation of the rotor approximately 6000 rpm. Utilizing the kinetic energy gathered by the rotor during the free run can help to produce part of the force S . The relationship between the maximal torque that can be generated by an electric motor and its nominal value is limited by its resistance to overheating (properties of insulation materials, means of cooling conditions) and displays the motor's overload capacity. The overload capacity of modern motors reaches up to three times, and there are features of the electric motor, which is part of the CM drive, that contribute to increasing the overload capacity of the motor:

- a special positive feature of the proposed design of the CM drive is the possibility of controlling its operation and, as a result, the final stage of clamping during spindle rotation, which is assumed to be 5000 rpm;
- short-term mode of operation: the motor is turned on only for the time of clamping or unclamping (about 1 sec), which, together with the continued rotation of the rotor (with the spindle during machining) after the motor is turned off, creates good conditions for its active parts cooling.

Taking everything into consideration, it was agreed that the electric motor could overload about two times. Thus, the calculation of electric motor parameters was conducted with the condition of providing a nominal torque during work in long-duration mode $M_1 = 35\text{ Nm}$.

Nominal mechanical power P_1 of electric motor is determined from:

$$P_1 = 0.1046 \cdot M_1 \cdot n_1. \quad (8)$$

For the case of the operation mode of the proposed CM, which involves its functioning (changing the value of the clamping force) during the spindle rotation, the rotational speed n_1 will be determined from $n_1 = n_p - n$ as relative frequency of rotation of the rotor, where n_p – the frequency of rotation of the rotor, n – the frequency of rotation of the spindle. According to (8), the motor power that should be used to drive the proposed CM:

$$P_1 = 0.1046 \cdot 35 \cdot (6000 - 5000) \approx 3.7\text{kW}. \quad (9)$$

Defined power is produced by the CM motor during the relatively short clamping time. After the clamping process is complete, the motor rotor rotates with the spindle due to the torque from the spindle drive. This rotation of the CM motor rotor contributes to its cooling for a period of time that is at least several times longer than the time of its operation under load. At the same time, the tension state of the system, which provides the clamping force, is ensured by self-braking. This load mode, which involves short-term operation and a long cooling period, provides improved opportunities for using motor loads above the rated values.

2.4. Determination of the general dependence of the movements of the links of the clamping mechanism in the first stage of operation

The first stage of work of the proposed CM is characterised by the action of forces of dissipative (not potential) character since no tension is created in the system. The proposed CM design can be considered a system with one degree of freedom. The position of other elements of the clamping mechanism of the proposed design depends on the angle of rotation of the rotor Ω_p , and is considered a generalised coordinate in this study. To conduct studies on the relationship between the movement of CM links in the general form is advisable to use Lagrange's Equation of second kind. With respect to the generalised coordinate Ω_p , the divergent equation of motion will be written:

$$\frac{d}{dt} \left(\frac{\partial E}{\partial \dot{\Omega}_p} \right) - \frac{\partial E}{\partial \Omega_p} = Q_r, \quad (10)$$

where E – kinetic energy of the clamping mechanism, $\dot{\Omega}_p$ – the first derivative of the angle of rotation of the rotor, which is its angular velocity, Q_r – generalised force in the form of a reduced torque is equal to the main torque of external forces relative to the rotor rotation axis, t – the time during which the action takes place.

During the operation of the SM mechanism, its kinetic energy E does not depend on the angle of rotation of the rotor Ω_p , so the partial derivative of the kinetic energy E by the angle of rotation of the rotor $\frac{\partial E}{\partial \Omega_p} = 0$, and therefore (10) takes shape:

$$\frac{d}{dt} \left(\frac{\partial E}{\partial \dot{\Omega}_p} \right) = Q_r. \quad (11)$$

The kinetic energy E of the proposed CM can be defined as the sum of the kinetic energies of its links. In general, it can be expressed as:

$$E = J_p \frac{\dot{\Omega}_p^2}{2} + m_1 \frac{V_1^2}{2} + m_2 \frac{V_2^2}{2}, \quad (12)$$

where J_p is the moment of inertia of the rotor about the axis of rotation; m_1 – total mass of elements moving in the axial direction with a speed of V_1 : masses of the rotor, draw bar (in the form of a pipe), collet and workpiece in the form of a bar (it is assumed that the bar moves with the collet at the moment of clamping); m_2 – total mass of elements moving in the radial direction (clamping elements) with a speed of V_2 .

Taking into account the characteristics of kinematic transmission, movements of links and their masses can be reduced to the rotor. The kinetic energy of the CM links is expressed through the reduced moment of inertia as:

$$E = J_r \frac{\dot{\Omega}_p^2}{2}, \quad (13)$$

where J_r – is the moment of inertia of links of the proposed CM reduced to its rotor.

The partial derivative of the expression of the kinetic energy E at the generalised velocity $\dot{\Omega}_p$ is as follows $\frac{\partial E}{\partial \dot{\Omega}_p} = \dot{\Omega}_p J_r$. When time t changes, only the angle of rotation Ω_p changes, the time derivative of the partial derivative of the previous expression will be equal to:

$$\frac{d}{dt} \left(\frac{\partial E}{\partial \dot{\Omega}_p} \right) = \ddot{\Omega}_p J_r. \quad (14)$$

Taking into account (11), expression (14) becomes:

$$\ddot{\Omega}_p J_r = Q_r. \quad (15)$$

The generalised force (torque) Q_r can be derived from the equality of the elementary work of the forces acting in CM. That is, it is necessary to consider the virtual work of active forces acting in the mechanism at small displacements Δ :

$$\Delta \Omega_p Q_r = \Delta \Omega_p T_p + \Delta \Omega_p T_s^f + \Delta x \sum_{i=1}^n F_i^T + \Delta y T_\Sigma, \quad (16)$$

where T_p – torque developed by the rotor of the CM motor during the clamping process, T_s^f – the resistance torque generated by the friction forces in the rotor screw gear, $\Delta \Omega_p$ – elementary rotor rotation angle, Δx – elementary movements in friction pairs, F_i^T – the friction force that occurs in the friction pair of the i -th link, Δy – elementary movement of the clamping elements, T_Σ – the amount of clamping force.

The motions Δx and Δy are functions of $\Delta \Omega_p$ and can be determined in accordance with the characteristics of the CM kinematic chain and in particular gear ratios for a particular mechanism. After substituting $\Delta x = f(\Omega_p)$ and $\Delta y = f(\Omega_p)$ and performing the transformations (16) can be presented in the following form:

$$Q_r = \xi_1 + \varepsilon_1 \Omega_p, \quad (17)$$

where the values ξ_1 and ε_1 does not contain variables and is a function of the geometrical parameters of the mechanism links and the forces of their interaction.

When substituting (17) into (15), the equation is formed as:

$$\ddot{\Omega}_p J_r = \xi_1 + \varepsilon_1 \Omega_p. \quad (18)$$

After the notation $\xi = \frac{\xi_1}{J_r}$ and $\varepsilon = \frac{\varepsilon_1}{J_r}$ has been introduced in (18):

$$\ddot{\Omega}_p = \xi + \varepsilon \Omega_p. \quad (19)$$

Since $\frac{d\Omega_p}{dt} = \omega_p$ as result it can be derived $\frac{d^2\Omega_p}{dt^2} = \frac{d\omega_p}{dt} = \frac{d\omega_p}{d\Omega_p} \cdot \frac{d\Omega_p}{dt} = \frac{d\omega_p}{d\Omega_p} \omega_p$. The consequence is $\frac{d\omega_p}{d\Omega_p} \omega_p = \xi + \varepsilon \Omega_p$;

$$\int \omega_p d\omega_p = \int (\xi + \varepsilon \Omega_p) d\Omega_p \text{ and } \frac{\omega_p^2}{2} = \xi \Omega_p + \varepsilon \frac{\Omega_p^2}{2} + X_1.$$

The integration constant X_1 for the initial conditions of the CM functionind is when $\Omega_p = 0$ and the rotor is motionless in relation to the spindle so their relative speed $\omega_p = 0$, value $X_1 = 0$. As a result,

$$\frac{d\Omega_p}{dt} = \sqrt{\varepsilon \Omega_p^2 + 2\xi \Omega_p} \text{ or } \int \frac{d\Omega_p}{\sqrt{\varepsilon \Omega_p^2 + 2\xi \Omega_p}} = \int dt + X_2',$$

$$\int \frac{d\Omega_p}{\sqrt{\varepsilon \Omega_p^2 + 2\xi \Omega_p}} = \frac{1}{\sqrt{\varepsilon}} \ln [2\varepsilon \Omega_p + 2\xi + 2\sqrt{2\xi \varepsilon \Omega_p + \varepsilon^2 \Omega_p^2}].$$

The solving the equation can be presented in the form,

$$\ln [2\varepsilon \Omega_p + 2\xi + 2\sqrt{2\xi \varepsilon \Omega_p + \varepsilon^2 \Omega_p^2}] = \sqrt{\varepsilon} \cdot t + X_2.$$

Under the initial conditions when $t = 0$ and $\Omega_p = 0$ the value $\ln 2\xi = X_2$, after substitution into the equation:

$$\frac{\varepsilon}{\xi} \Omega_p + \sqrt{2 \frac{\varepsilon}{\xi} \Omega_p + \frac{\varepsilon^2}{\xi^2} \Omega_p^2} = e^{\sqrt{\varepsilon} \cdot t} - 1,$$

$$\Omega_p = \frac{(e^{\sqrt{\varepsilon} \cdot t} - 1)^2}{2 \frac{\varepsilon}{\xi} e^{\sqrt{\varepsilon} \cdot t}}. \quad (20)$$

Formula (20) describes the dependence of the generalised coordinate Ω_p on time. The positive or negative values ε in (20) can indicate the type of change of Ω_p . That is, it contributes to preliminarily determine certain characteristics of the rotational motion of the CM rotor of the proposed type.

3. RESULTS OF DETERMINING THE CHARACTERISTICS OF THE CLAMPING DEVICE

As a result of substituting the expression (4) into (7) the expression for clamping force in CM propose design is obtained and expressed in the form of the graphs (Fig. 4a, Fig. 4b):

$$T_{\Sigma} = (T_p / 0.5 d_2 t g(\psi + \phi_p) t g(\alpha + \phi)) - m \omega^2 r. \quad (21)$$

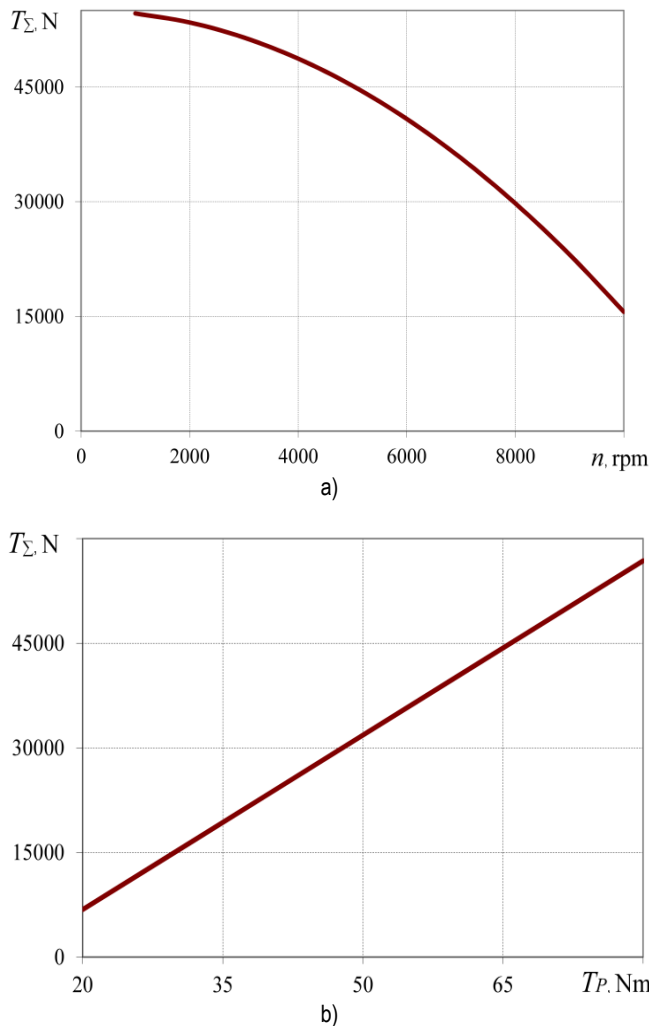


Fig. 4. Dependence of clamping force T_{Σ} in proposed CM from: a) frequency of rotation of the spindle n when the torque of the rotor of $T_p = 66$ Nm; b) torque T_p , which appears on the rotor at frequency of the spindle rotation $n = 5000$ rpm

By using the obtained formulas, the dependencies of the clamping force versus the frequency of rotation (Fig. 4a) and the rotor torque (Fig. 4b) of the proposed CM are established. For calculation the next parameters were taken: $m = 1.28$ kg; $r = 0.028 \cdot m$; $d_2 = 0.085 \cdot m$; $\varphi \approx 5^\circ$; $\phi_p \approx 4^\circ$; $\psi \approx 0.43^\circ$.

From the preliminary assessments of the asynchronous electric motor design, the approximate geometric parameters of the motor parts that can be used in the proposed clamping mechanism have been approximately determined. In order to guarantee the characteristics of the motor determined by the calculations, the values of its stator outer diameter are in the range of 180-200 mm, its rotor diameter is 90-100 mm and its rotor length is 90-100 mm. These geometric parameters are approximate as they are based on the design of typical 4A series general-purpose motors and may vary according to the current characteristics selected and, consequently, the characteristics of the power supply and control system.

In accordance with current trends in the development of electric drive designs, it is possible to reduce the above dimensions by using special technologies for the manufacture of active motor elements and their cooling systems. Taking into consideration the values of the determined geometrical parameters, a variant of the CM design with a new electromechanical drive as part of the spindle assembly of a lathe is proposed (Fig. 5)

The dependence presented in Fig. 4a shows the opposite effect of centrifugal forces acting on the clamping elements on the clamping force when clamping a 40 mm diameter rod. This indicates one of the significant obstacles to the possibility of significantly increasing the spindle speed when machining workpieces with a diameter of more than a few centimetres. This can be seen as one of the limitations to increasing productivity and surface finish quality. As a result, it can be concluded that it is advisable to further develop approaches to the creation of automatic clamping mechanisms that make it possible to change the amount of clamping force on the workpiece during spindle rotation and, in particular, as it increases.

The graph in Fig. 4b shows the need to create a relatively large torque on the rotor of the CM drive of the proposed design. This indicates the expediency of further studying the possibilities of using another type of electric motor with a design of active parts adapted to increase the torque and, in particular, the type of windings. Also, the solution to this problem may be the use of additional converters of mechanical energy characteristics in the CM structure, for example, hydraulic ones. For example, a general scheme for the implementation of this principle of energy transmission and conversion in CM is proposed (Fig. 6). The axial force S_1 from the rotor is transmitted to the hydraulic system plunger Pl_1 which has a smaller diameter. It causes a pressure of working liquid and the appearance of a greater force S_2 on the larger diameter plunger Pl_2 that is supplying the inlet of the clamping chuck. This will make it possible to transfer mechanical energy from the clamping drive to the clamping chuck without using a drawbar tube with the amplification effect. Also, one of the most promising ways to obtain high values of torque on the motor rotor is to use vector control (field-oriented control) by an electric motor. This method requires the development of a detailed mathematical model of the clamping mechanism to be used as part of the motor control system. It gives the benefit of fine-tuned motor speed and torque control.

The revealed dependence (20) makes it possible to preliminarily assess the influence of the certain parameters on the movement of its links during the first stage of operation. In particu-

lar, positive values of \mathcal{E} indicate a monotonic increase in Ω_p , which means a uniform rotational movement of the rotor. At negative values of \mathcal{E} , local decreases and increases of the Ω_p function are possible, which means rotational oscillations of the rotor.

4. DISCUSSION OF THE POSSIBILITIES OF USING THE CLAMPING DEVICE OF PROPOSED STRUCTURE

The presented design of an electromechanical drive for the clamping mechanism contributes to solving the problem of extending the range of conditions of clamping objects in the spindle units of machine tools. The proposed design provides better performance of the automatic clamping mechanism due to the contactless input power supply using electromagnetic interaction between the fixed stator and rotor located on the machine spindle unit. This

solution offers new possibilities for controlling the characteristics of the clamping mechanism, including during spindle rotation.

The geometric, power and energy parameters of the proposed design of the automatic CM (Fig. 5) determined as a result of the study indirectly indicate the possibility of using mechanisms of this type as part of the spindle units of machine tools. The problem that was identified was the need to be able to provide a torque of 70 Nm and more. To solve this problem, and if it is necessary to reduce the overall dimensions of the clamping mechanism drive (which leads to a reduction in the torque of its electric motor), a variant is proposed using a hydraulic system (Fig. 6) to increase the value of axial force. The use of a vector control system for the operation of the drive motor is also proposed as an option for improving the performance characteristics of the drive while maintaining the same overall dimensions.

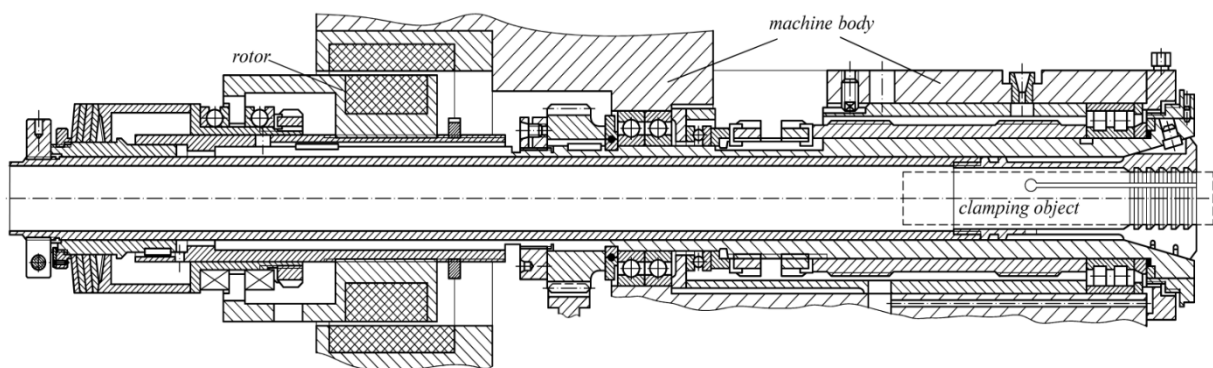


Fig. 5. Design of the proposed clamping mechanism as part of the spindle assembly

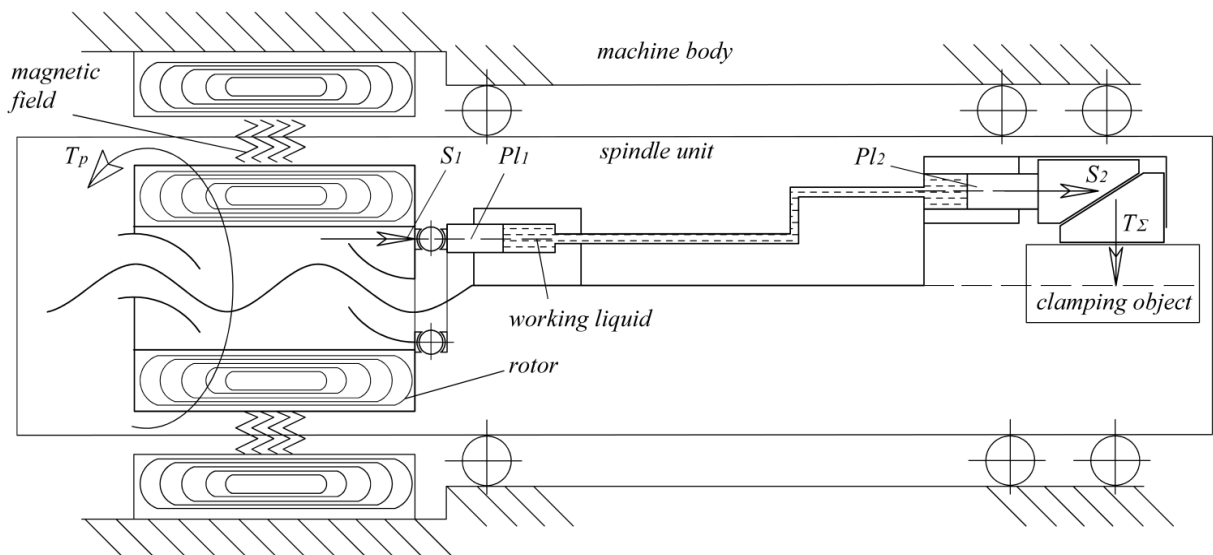


Fig. 6. Scheme of the proposed clamping mechanism with electromechanical drive and hydraulic amplification system

One of the particular advantages of the proposed clamping mechanism drive design is the improved ability to retrofit existing spindle assemblies with its use. This is due to the fact that there is no need to create complex external power and control systems, as is the case with hydraulic and mechanical analogues. The clamping mechanism drive of the proposed design is controlled by electrical and electronic sub-systems, which greatly simplifies their integration into the machine structure.

The results presented will be used to develop an effective control system for the proposed CM (Fig. 5), which will contribute

to expanding the technological capabilities of machine tools. The obtained equations (7) and (10) create conditions for the development of ways to automate the calculation of parameters of mechanisms of this type. The limitations of the results of these studies are due to the lack of data on production tests of the structural elements of the proposed CM. Also, the parameters of interaction between the CM of the proposed design and the machine control system operating in an automatic cycle have not yet been established.

The next logical stage of research will involve a more detailed

development of the elements of the proposed design and the determination of their geometric and mass parameters. It is planned to carry out theoretical studies of the process of creating a stressed state of the mechanism, which occurs after the stage of gap sampling. The research will also include the development of a control system for the presented device. Longer-term research plans envisage construction of a working prototype and experimental studies to assess the reliability of the calculated results and, consequently, the theoretical framework and assumptions used to carry them out. In general, this research should become part of a research area related to increasing the productivity and quality of machining by improving the characteristics of the spindle assembly.

5. CONCLUSIONS

As a result of determining the main characteristics of the clamping mechanism with the proposed type of clamping drive, it is possible to assume that its use as part of spindle assemblies in machine tools is possible. The design features of the clamping mechanism of the proposed structure determine the improved possibilities of their use for the modernization of existing spindle assemblies including because the rotor diameter of the mechanism is within 100 mm and the stator is within 200 mm. As a result of the research, additional opportunities arose to evaluate the effects of the design features of the new type of clamping mechanisms on their characteristics and functional capabilities. In order to achieve the desired performance characteristics, the results of the study can be used to identify more suitable design elements for the mechanism. It is proposed to use a vector control system to control the mechanism's motor, which will help to increase the accuracy of the settings and extend their range. In order to ensure the required force characteristics of the mechanism while reducing the radial dimensions of its drive, a scheme for using an additional amplifying hydraulic system is proposed. The calculation method presented can also be used as a basis for further development of such type mechanisms and for automating the calculation of their parameters.

REFERENCES

- Noske H. Monitoring of gripping force in lathe chucks. Fault Detection, Supervision and Safety for Technical Processes 1991. IFAC Symposia Series. Baden-Baden, Germany 1992;6:581-586. <https://doi.org/10.1016/B978-0-08-041275-7.50092-2>
- Prydalnyi B, Sulym H. Identification of analytical dependencies of the operational characteristics of the workpiece clamping mechanisms with the rotary movement of the input link. Acta Mechanica et Automatica. 2021;15(1):47-52. <https://doi.org/10.2478/ama-2021-0007>
- Prydalnyi B. Mathematical Model of a Backlash Elimination in the New Clamping Mechanism. Lecture Notes in Mechanical Engineering. 2022;1:109-118. https://doi.org/10.1007/978-3-030-91327-4_11
- Thorenz B, Westermann H, Kafara M, Nuetzel M, Steinhilper R. Evaluation of the influence of different clamping chuck types on energy consumption, tool wear and surface qualities in milling operations. Procedia Manufacturing. 2018;21:575-582. <https://doi.org/10.1016/j.promfg.2018.02.158>
- Yadav MH, Mohite SS. Controlling deformations of thin-walled Al6061-T6 components by adaptive clamping. Procedia Manufacturing. 2018;20:509-516. <https://doi.org/10.1016/j.promfg.2018.02.076>
- Shaoke W, Jun H, Fei D. Modelling and characteristic investigation of spindle-holder assembly under clamping and centrifugal forces. Journal of Mechanical Science and Technology. 2019;33(5):2397-2405. <https://doi.org/10.1007/s12206-019-0438-3>
- Alquraan T, Kuznetsov Yu, Tsvyd T. High-speed clamping mechanism of the CNC lathe with compensation of centrifugal forces. Procedia engineering. 2016;150:689-695. <https://doi.org/10.1016/j.proeng.2016.07.081>
- Estrems M, Carrero-Blanco J, Cumbicus W, Francisco O, Sánchez H. Contact mechanics applied to the machining of thin rings. Procedia Manufacturing. 2017;13:655-662. <https://doi.org/10.1016/j.promfg.2017.09.138>
- Gang Wang, Yansheng Cao, Yingfeng Zhang. Digital twin-driven clamping force control for thin-walled parts. Advanced Engineering Informatics. 2022;51: 1474-0346. <https://doi.org/10.1016/j.aei.2021.101468>
- Pavankumar R, Gurudath B, Virendra A, Subray R. Failure of hydraulic lathe chuck assembly. Engineering Failure Analysis. 2022;133: 106001. <https://doi.org/10.1016/j.engfailanal.2021.106001>
- Estrems M, Arizmendi M, Zabaleta A.J, Gil A. Numerical method to calculate the deformation of thin rings during turning operation and its influence on the roundness tolerance. Procedia Engineering. 2015;132:872-879. <https://doi.org/10.1016/j.proeng.2015.12.572>
- Shamei M, Tajalli SA. Stability and Bifurcation Analysis in Turning of Flexible Parts with Spindle Speed Variation Using FEM Simulation Data. International journal of structural stability and dynamics. 2023; 2450004. <https://doi.org/10.1142/s0219455424500044>
- Dong X, Shen X, & Fu Z. Stability analysis in turning with variable spindle speed based on the reconstructed semi-discretization method. International Journal of Advanced Manufacturing Technology. 2021;117:3393-3403. <https://doi.org/10.1007/s00170-021-07869-8>
- Joch R, Šajgalík M, Drbůl M, Holubjak J, Czán A, Bechný V, Matuš M. The Application of Additive Composites Technologies for Clamping and Manipulation Devices in the Production Process. Materials. 2023;16(10):3624. <https://doi.org/10.3390/ma16103624>
- Beri B, Meszaros G, Stepan G. Machining of slender workpieces subjected to time-periodic axial force: stability and chatter suppression. Journal of Sound and Vibration. 2021;504:116114. <https://doi.org/10.1016/j.jsv.2021.116114>
- Soriano-Heras E, Rubio H, Bustos A, Castejon C. Mathematical Analysis of the Process Forces Effect on Collet Chuck Holders. Mathematics. 2021;9(5):492. <https://doi.org/10.3390/math9050492>
- Liang Z, Zhao C, Zhou H, et al. Investigation on fixture design and precision stability of new-type double collect chuck for machining of long ladder shaft gear. J Mech Sci Technol. 2019;33:323-332. <https://doi.org/10.1007/s12206-018-1234-1>
- Song QH, Liu ZQ, Wan Y, Ai X. Instability of internal damping due to collet chuck holder for rotating spindle-holder-tool system. Mechanism and Machine Theory. 2016;101:95-115. <https://doi.org/10.1016/j.mechmachtheory.2016.03.007>
- Pasternak V, Samchuk L, Huliieva N, Andrushchak I, Ruban A. Investigation of the properties of powder materials using computer modelling. Materials Science Forum. 2021;1038:33-39. <https://doi.org/10.4028/www.scientific.net/MSF.1038.33>
- Li C, Zou Z, Duan W, Liu J, Gu F, Ball AD. Characterizing the Vibration Responses of Flexible Workpieces during the Turning Process for Quality Control. Applied Sciences-Basel. 2023;13(23):12611. <https://doi.org/10.3390/app132312611>

Certain approaches to the problems of this paper were improved as a result of discussions with specialists from the University of Melbourne within the framework of cooperation under the Ukraine-Australia Research Fund programme with the support of the Australian Academy of Science.

Borys Prydalnyi:  <https://orcid.org/0000-0001-8565-5986>



This work is licensed under the Creative Commons BY-NC-ND 4.0 license.

STATIC CARRYING CAPACITY OF A SINGLE-ROW BALL SLEWING BEARING TAKING INTO ACCOUNT DRIVE TRANSMISSION CONDITIONS

Szczepan ŚPIEWAK*

*Faculty Of Mechanical Engineering And Computer Science, Institute Of Mechanics And Machine Design,
Czestochowa University of Technology, Dabrowskiego Street 73, 42-201 Czestochowa, Poland

e-mail: szczepan.spiewak@pcz.pl

received 18 January 2024, revised 10 March 2024, accepted 01 April 2024

Abstract: Problems of computing a slewing bearings static carrying capacity have been presented in the paper. Particularly it was concentrated on determination of static limited load curves which include axial forces, radial forces and tilting moments. A calculation were performed on the base of single-row ball slewing bearing with four-point contact zone. In this work a procedure of determining the static limiting load curves on the basis of modeling by using the finite element method (FEM), analytic Eschmann's formulas and classical mechanics equations have been described. The structure of FEM bearings' model was considered with gear conditions between a toothed bearing's ring (rim) and a drive pinion in a power train of the excavator F250H symbol. Moreover, in the model flexibility of: the bearing rings, a contact zone ball-bearing, support structure and mutual interactions between bolts clamping the bearing rings and the support structures were taken into account. The static carrying capacity of the analyzed bearing, considered with the pinion and without was compared. Quantitative assessment of loads of the contact zones ball-raceway was achieved by using a statistic criterion.

Key words: slewing bearing, bearing capacity, bearing design, tilting moment, static limiting load curves, the toothed ring

1. INTRODUCTION

Machine rolling bearings selection is normally based on an assumed durability. Estimated external loads are initially converted to two main loads. The first load is a vector projected on rotation axis of the bearing (an axial force) and the second load is the vector (radial force) directed perpendicular to the first load. The main loads are then combined to the value of equivalent load which depends on the type of bearing rolling elements and desired durability, what allows to estimate required dynamic carrying capacity. The operating bearing conditions determine whether selection of the bearing is dependent on the value of a static or a dynamic carrying capacity. In order to minimize the bearing dimensions, the designed solutions of the bearing raceways have been shaped in such a way, in order that the given bearing adapt to one of the main loads. In practice, it can be interpreted that greater value of the main loads will determine a choice of the bearing type (in practice, it can be interpreted that greater value of the main loads, will determine a choice of the bearing type (between a radial and an axial bearing). Among the rolling bearings, slewing bearings play a more responsible role, especially when it is used in large-scale machines. In these types of rolling bearings, the external loads are combined similarly like in bearings, designed for general use. While bearing is being selected, all resultant forces may be projected into axial (axial force Q) and radial (radial force H) directions while a tilting moment M [1, 2] is a specific load of this rolling bearing type. In typical applications of slewing bearings, permissible external bearing load is dependent on static carrying capacity. The static carrying capacity of rolling bearings is determined by the deformation of the contact zone between the rolling element and raceway hence and then the so-called static carrying capacity charac-

teristic is determined for newly designed slewing bearings. The characteristic is graphically presented as dependence of the tilting moment M from the axial force Q while the system is loaded by a constant value of the radial force H [2-7]. Such way of presenting the slewing bearing serviceability results from the following designed features (specifically distinguishing the slewing bearings from bearings in general use): assembly in support structures by means of bolts, track diameters which can be in a range of several meters, bearing rings load of high axial forces, high radial forces and high tilting moment, high deformability of a contact zone rolling element-raceway, application of various materials for the production of bearing rings and rolling elements, low-speed rotation of the rings, a large number of balls and / or rollers, in some systems - toothed rim incised on circumference of the one ring. Engineers use these curves when slewing bearing is selected for load conditions of machines [3-5]. As it results from the catalog review [3, 4], static carrying capacity curves of the slewing bearings have been determined only for the zero values of radial forces H . Based on work [3], it can be stated that if the value of a radial force does not exceed 10% of the maximum permissible axial force, the course of the static carrying capacity curve will not be shifted. Another approach to the problem of taking into account the radial force was presented in Ref. [5]. The bearing manufacturer introduces the relationships used to determine the so-called equivalent tilting moment Meq and equivalent axial force Qeq . These parameters are determined on basis values of external loads M , Q , H and application coefficient, the radial force H and a safety factor. The determined values of Meq and Qeq are plotted in the catalogs of static carrying capacity curves that have been determined for zero values of a radial force. If these values are located below the curve for checked bearing then this bearing can be selected as suitable

for the rated load. A detailed reference, based on the calculation example, was presented in the paper [7]. Therefore, the identification of operating conditions of slewing bearings determination requires of the radial force share in a system of external loads. An influence of the radial forces (taking into account their sense) on the static carrying capacity of the twin slewing bearing has been demonstrated in the work [2]. The same type of slewing bearing was the subject of research of the authors of the publication [8]. The researchers using a classical model based on the static equilibrium of displacements of a rigid body and assumed durability determined the dynamic carrying capacity curves of the slewing bearing, taking into account an one radial force sense [8]. The researchers using a classical model based on the static equilibrium of displacements of a rigid body and assumed durability determined the dynamic carrying capacity curves of the slewing bearing, taking into account an one radial force sense [8].

The action of the radial force on a slewing bearing may be temporary (e.g. in an excavator with one bucket [9]) or continuous as in the case of a wind turbine [10] and a wagon tippler.

The impact of operate direction of the radial forces on the static carrying capacity of the slewing bearings was presented in Ref. [11].

It should be emphasized that the slewing bearing is the transmission element of a rotational torque between the pinion and the slewing bearing ring. There is a high probability of simultaneous operation of the external load components in one plane, which is common with the plane of the pinion symmetry at a point of teeth contact.

Continuous research and development of research methods used in slewing bearing problems analysis have great practical importance because of the fact that assembly processes of the slewing bearing are time-consuming and energy-consuming (due to size and weight). Slewing bearings in drive systems play a key role. A failure of a slewing bearing causes the machine to stop for an unpredictable period of time. Therefore, machine designers have a difficult task related to the selection of a slewing bearing in terms of its type and carrying capacity. Methods of determining static carrying capacity curves of slewing bearings are similar to each other and are widely described in publications [1, 2, 6, 10, 12, 13]. Each of the method boils down to determine the maximum force (reaction) which acts between the rolling element and the bearing raceway while components of the external loads (M , Q , and H) act on the bearing. Individual methods of determining the static carrying capacity of slewing ring bearings usually differ in the adopted range of bearings features which are included in created calculating models.

The basic features taken into account in the models of slewing bearings are: bearing clearance, initial clamp of bolts, flexibility of bearing rings, flexibility of a contact zone (raceway - rolling element), raceway hardness condition and bearing mounting structures susceptibility. The permissible load of a contact zone between the rolling element and raceway is a parameter that determines the carrying capacity of slewing bearings. Effect of technological treatments performed on the bearing raceways in reference to permissible carrying capacity of the contact area and durability tests are presented in the works [14, 15]. Evolution of a measurement technique based on the analysis of acoustic signals enables diagnostics and monitoring slewing bearings operation, what has been presented in the works [16, 19]. The descriptions of friction torque in slewing bearings are included in publications [20, 21]. Slewing bearings can also operate at elevated temperatures (e.g. in the Ljungstrom rotary air heater). Results of research on thermal

loads of the slewing bearing can be found in the publication [22]. On the basis of the distribution of loads acting in the contact zones between rolling element and raceway, which are presented in the works [1, 6, 9, 12, 23, 24], it can be concluded that these loads cause change of bearing rings' shape and deform the slewing bearing toothed ring. Simultaneously the geometrical mating conditions between the gears change.

The gear interaction, taking into account bearing ring flexibility, will undoubtedly affect a distribution of the forces loading the bearing balls. Since the force loads of the single contact zone rolling part - raceway decide about the slewing bearing static carrying capacity, however the static carrying capacity during mating the flexible toothed ring and the rigid pinion may be another. In the literature, there is a publication which concerns bearing clearance [12], preloads [25] and the stiffness of the support structures [9] in reference to courses of the static carrying capacity curves, whereas the influence of the gear condition of the toothed ring with the pinion on the course of the static carrying capacity curves, especially with the specific direction of external loads (M and H) seems to be unnoticed. Numerical studies of action gear pinion with the toothed ring of slewing bearing were carried out and based on the presented findings. The distributions of forces acting in the individual contact zones (ball - raceway) and static carrying capacity curves of the slewing bearing were determined with and without considering the conditions of the mating between the rim and the pinion.

2. A MODEL OF A POWER TRAIN WITH THE SLEWING BEARING

Acceding to formulated problem of slewing bearing load, the single-row ball slewing bearing with the four-point contact zone (made in Poland) has been considered. The choice of this bearing for study was dictated by the fact that this bearing is mounted in one-shovel tracked excavator F250H. A comprehensive model of the working structures of a body and a chassis of the F250H excavator connected with modeling the bearing was presented in work [26]. An outline of the bearing cross-section is shown in Fig. 1 and basic design parameters are listed in Tab. 1. A power train of excavator bodywork consists of a spur gear which basic parts are the pinion assembled in the bodywork and a rim made on an external slewing bearing ring. The basic parameters of the gear have been marked in Fig.2 and listed in Tab. 2. Due to required distance between centers of gears and number of tooth of the pinion, the pair of gears have been subjected to profile shift.

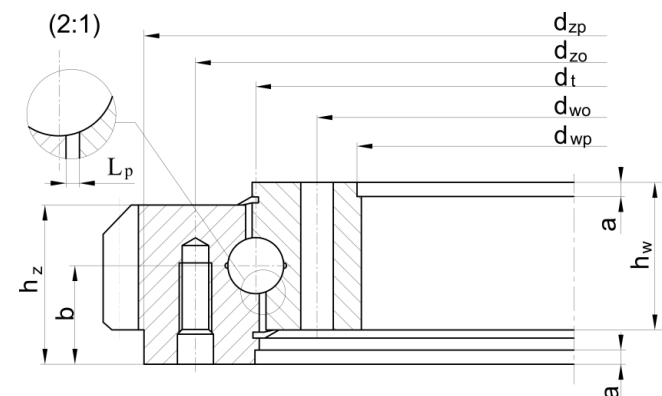


Fig. 1. Basic geometric parameters of the single-row ball slewing bearing

A sector of the profile shift was generated by using the Inventor program. Take into account complexity of the task posed, it was decided that the numerical calculations is based on the finite element method (FEM). In comparison with the analytical methods (classical) in which the main goal is idealization of the flexural-torsional stiffness of the bearing rings [6, 25] - FEM allows to take into account not only compliance of the bearing rings, but also compliance of the bearing bolts and compliance support structures.

Tab. 1. Values of basic parameters of the single-row ball slewing bearing

| Parametr of the bearing | | Value |
|-------------------------|--|----------|
| 1 | The track diameter of the bearing d_t [mm] (Fig. 1) | 1105 |
| 2 | The ball diameter d_k [mm] | 44 |
| 3 | Quotient rays of ball and reaway k_p [2, 34] | 0,96 |
| 4 | Dimension d_{zp} [mm] (Fig. 1) | 1260 |
| 5 | Dimension d_{zo} [mm] (Fig. 1) | 1200 |
| 6 | Dimension d_{wo} [mm] (Fig. 1) | 1010 |
| 7 | Dimension d_{wp} [mm] (Fig. 1) | 960 |
| 8 | High of the bering h [mm] | 137 |
| 9 | Dimension a [mm] (Fig 1) | 10 |
| 10 | Dimension b [mm] (Fig. 1) | 71 |
| 11 | Dimension h_w [mm] (Fig. 1) | 117 |
| 12 | Dimension h_z [mm] (Fig. 1) | 122 |
| 13 | Axial clearance [mm] | 0,5 |
| 14 | The clearance between the rings L_p [mm] (Fig. 1) | 7 |
| 15 | Nominal contact angle α_d [°] | 45 |
| 16 | Row fill facctor | 0,83 |
| 17 | Number of bearing balls | 64 |
| 18 | The surface balls hardness | 62HRC |
| 19 | The surface raceway hardness | 56HRC |
| 20 | Number of the bolts mounting in the internal/external ring | 42/42 |
| 21 | The size and strength class mounting bolts by [DIN] [31] | M24-12.9 |
| 22 | Mounting tension force S_w [kN] | 242 |

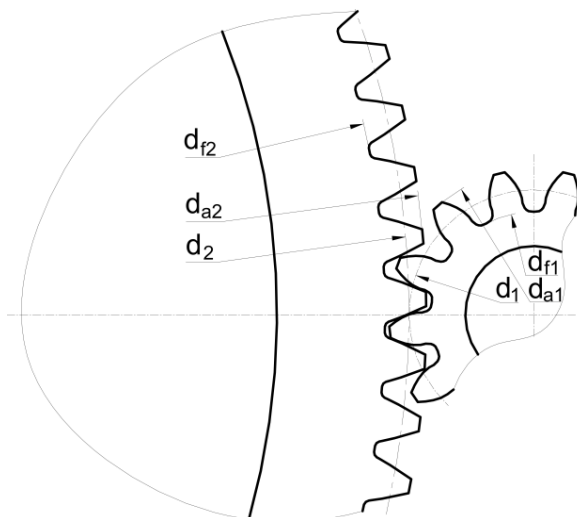


Fig. 2. The basic geometric parameter of a pinion and a toothed ring

In addition, in the case of the classical methods [6, 25], the relative displacement of the bearing rings caused by the loads have been considered as motion of a rigid body. In a slightly different way the susceptibility of the roller section- raceway contact zone have been defined.

According to above paragraph, with data contained in Tab. 1, a comprehensive model MES of single-row ball slewing bearing with the pinion in the environment of the ADINA [27, 28] have been developed, and presented as a mesh in a Fig 3.

Tab. 2. Values of gears basic parameters

| Name of parameters | | Pinion | Toothed rim |
|--------------------|---------------------------|-------------------------|-------------------|
| 1 | Reference diameter [mm] | $d_f=182$ | $d_f=1274$ |
| 2 | Tip diameter [mm] | $d_{a1}=211,763$ | $d_{a1}=1322,823$ |
| 3 | Root diameter [mm] | $d_{f1}=151,577$ | $d_{f1}=1262,637$ |
| 4 | Profile shift coefficient | $x_1=0,1135$ | $x_2=0,7942$ |
| 5 | Number of tooth | $z_1=13$ | $z_2=91$ |
| 6 | Module [mm] | $m=14$ | |
| 7 | Backlash [mm] | $j_n=0,56$ | |
| 8 | Center distance [mm] | $a_w=740$ | |
| 9 | Reference pressure angle | $\alpha_n=20^\circ$ | |
| 10 | Working pressure angle | $\alpha_w=22,414^\circ$ | |

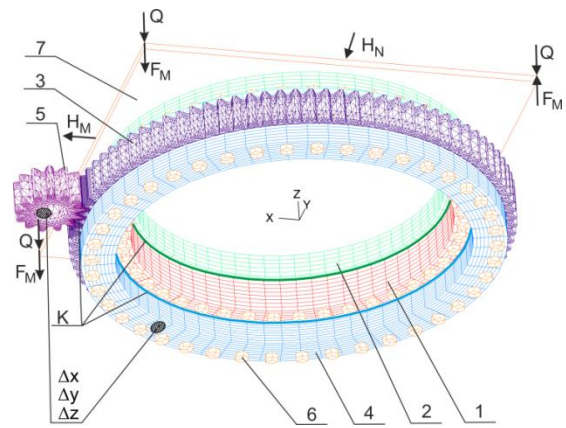


Fig. 3. A visualisation of finite elements of single-row ball slewing bearing, coupled with a drive pinion

The Fig. 3 shows: 1 - the bearing inner ring, 3 - outer ring, 2 - the upper and 4 - lower support structure, 6 - heads of the mounting bolts, and 7 - plate which have been discretized by eight-nodal finite elements type 3D-Solid [27-28], whereas 5 - the pinion and 3 - the toothed rim were discretized by twelve-nodal finite elements.

The mating conditions' model between the toothed ring and the pinion was based on the methods of tooth profile discretization presented in [29] and the issues of the teeth contact strength [30].

In order to modeling balls by using replacement elements (described below), the bearing rings were discretized by finite elements arranged in the shape of slices. Number of these slices is equal to the number of balls in the bearing. The angular scale of the slice overlaps with the angular scale of a position of the balls in the bearing. Between the upper support structure and the inner ring and between the lower support structure and the external ring conditions of contact K (including the penetration condition and friction coefficient value $\mu=0,1$ [27, 28]) were defined as well as between a contour gear of the pinion and the bearing rim. Nodes containing the flat surface of the lower cover have been taken all degrees of freedom ($\Delta x, \Delta y, \Delta z = 0$). Similarly it was done in case

of nodes describing a cylindrical pinion surface on which a drive shaft is mounted.

External load has been identified through FM, Q, HM, HN vectors. The static carrying capacity curve is determined as standard for the main system of forces M, Q, HM [11]. In the case under consideration, symmetry slewing bearing YZ plane was used to modeling the tilting moment and two opposite vectors of forces FM. The vector Q represents the axial force. Since the system of forces in the model enables consideration of radial forces, the following nomenclature is adopted: a major radial force HM and orthogonal radial force HN.

In the present task the main system of forces is contained in the pinion plane of symmetry at a point of tooth contact. The vectors of simulated loads have been hooked in the nodes one - element group of finite elements with No. 7. Group of finite elements with No. 7 was specially created as an object (plate plane) that intermediate during transmitting the load to support bearing structure (No. 2 and No.4). Nodes of group No. 2 contained in the plate plane 7 gave the conditions of displacements glue type [27]. This type boundary conditions are defined for elements of group No. 6, mapped the heads of the mounting screws and for rim coupled with outer ring. Boundary glue type conditions ensure an agreement of all displacements for all nodes which coordinates are contained in the same flat surface. The bolts have been modeled by finite elements type beam with an active bolt function [27]. The nodes of the individual beam type finite elements have been connected with finite elements of group No. 6 which represents the ends of the bolts and nuts in an assembly of the bearing and housing. Only in this way, the necessity to map the holes in the bearing rings was avoided, e.g. by defining discontinuities in the structures between the finite elements of groups no. 1, 2, 3, 4. This simplification reduces the number of finite elements and an accuracy of a calculation results in the static carrying capacity range are sufficient. An additional advantage is the shorter calculation time. Activation of the bolt function in the ADINA system enables definition of the bolt diameter, material parameters and mounting tension force [27] Sw (Tab. 1). Based on these data, the ADINA solver [27] during initial iterations calculates displacement caused by the Sw forces (according to guidelines of standard [31]) for all model nodes. In this case the slewing bearing is seated in an annular housing with the centering collar. Such a solution requires more precise shaping of the support structure, but in the system it reduces the transverse loads of bolts (reduction of shear stress). The dimensions of the support structure must ensure the appropriate system stiffness and are parametrically dependent on the bearing dimensions [3]. Those dependents was taken into account in the model during setting the dimensions of element no. 2 and 4. However, the most important simplification in the bearing model is balls replaced by an alternative finite element system called superelements [32, 33]. As it is shown in Fig.4 the superelements consisted of beam system 2 with a high stiffness combined with truss elements 1, where the end nodes are located in the curvature centers of the bearing raceways 3 (points: A, B, C, D) and the nodes of finite element meshes of the internal and external rings. The truss elements 1 have defined multilinear material characteristics. A method of determining the necessary material characteristic is described in detail in [2]. Other statistical data regarding sizes of finite elements, the number of finite elements, and the sensitivity analysis of finite elements have been included in Appendix B.

Material characteristics shall be determined on the basis of contact zone characteristics. Characteristics of the contact zone is defined as dependence the raceway deflection η caused by a

contact rolling section force F.

This dependence can be:

- defined by carrying out on the basis of experiment,
- based on average over the values of the c and w coefficients and inserted into the formula 1, which sample values are function of osculation ratio k_p to the roller bearing raceway what can be bring out from work [1]
- defined as a solution to the question of contact issue of the contact zone by using the finite element methods.

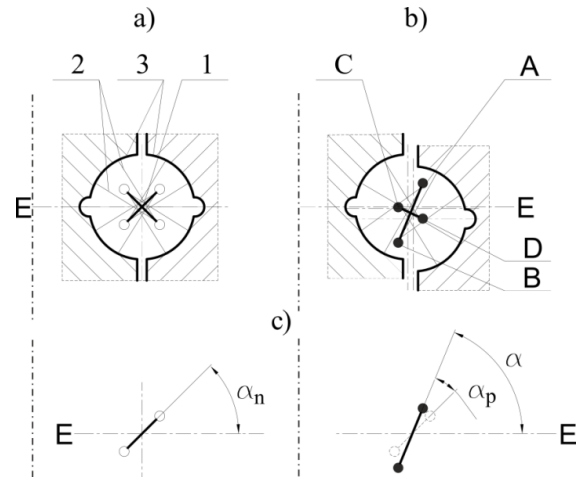


Fig. 4. Schematic position of bearing rings and replacement elements in a state before (a) and after (b) load inflicted with mapping changing of contact angle of balls in slewing bearing (c)

$$\eta = cF^w \quad (1)$$

It should be emphasized that the characteristics of rolling bearing contact zone is also shown as the dependence of the maximum normal stress at the interface between the rolling pairs in the function of the proper load of the roller part (which is the quotient of force and the square of roller part diameter) which is wider described in [9].

Use of one of the two equivalent quality descriptions of the characteristics of the contact zone can be identified with respectively two equivalent criteria for determining the load capacity of a single contact zone:

- the criterion of plastic deformation in the contact zone,
- the criterion of maximum pressure values on the surface of the contact zone.

This study was based on the criterion of the permissible plastic deformation in the contact zone which, in accordance with the assumptions [34] should not exceed 0,0002dk. Hence, the maximum force value, which is allowed for a single ball-raceway contact zone was calculated in accordance with equation 2 [34] and amount $F_{dop} = 158$ kN.

$$F_{dop} = \frac{9,9626 \cdot 10^7 \cdot d_k^2 \cdot \left(\frac{HV}{750}\right)^2}{\left(\frac{858}{a_H b_H}\right)^3 \sqrt{d_k \left(\frac{4-2k_p}{d_k} + \frac{2 \cos \alpha_0}{d_t - d_k \cos \alpha_0}\right)^2}} \quad (2)$$

The names of the formula symbols are given in the table 1. The remaining symbols represent the formula: a_H , b_H - coefficients of the elliptical contact area by [21], HV- raceway surface hardness of Vickers scale.

In contrast, the characteristic of the replacement contact zone of the bearing implemented in the model was determined according to the method described in [2] and is presented in Fig. 5. Additional information regarding, among others, the finite element mesh parameters of the contact zone model have been included in Appendix B.

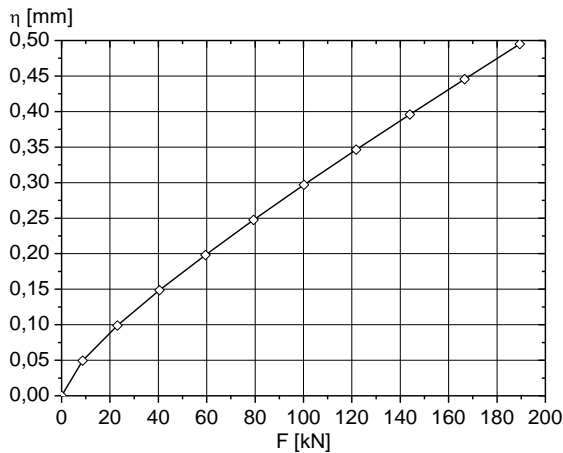


Fig. 5. Characteristic of the contact zone replacement

The system of bearing model placeholders was represented by local deformations occurring in the ball-raceway contact zone and the change of contact ball angle and consequently allows for the appointment of distributions of the reactions acting on all balls in bearing rows. Knowledge of distribution of the forces acting on each of contact zone allows to build a static carrying capacity curve, because its carrying capacity is determined by the most loaded ball, and downforce balls into the raceway is not greater than the F_{dop} .

3. STATIC CARRYING CAPACITY CURVES OF THE SLEWING BEARING

Taking into consideration the issues which have been previously identified, the impact of the radial forces and the sense of the main radial force on the slewing bearing static carrying capacity has been taken into account. Identification of force sense was associated with the sign of its value what is contractual in nature and was suggested in [11]. This work shows that sense of the main radial force have significant impact on the course of the static carrying capacity curve of the single-row ball slewing bearing. In order to make the sign of the main radial force H_M independent on an adopted local coordinate system and other directions and senses of an external loads, a definition of the main radial forces H_M directed positively was formulated. In this situation, the attention is focused on the most heavily loaded contact zone. During calculations, when increase of the main radial force cooperating with the tilting moment and the axial force causes increase load in the considered contact zone, then the main radial force is called as directed positively. Whereas, when the load of this contact zone is decreases then the sense of the main radial force is considered as negative (main radial force directed negative positively). If an orthogonal radial force H_N replaces the H_M force in the main load system, then the orthogonal radial force does not identify sense because the sense of this force has no effect on the course of the static carrying capacity curve. Points of the static carrying capacity

curves are determined an iterative manner. At the beginning of calculation in the FEM model, the individual components of the external load M , Q , H were asked incrementally (according with the individual values of time steps t). As an effect of iterations, incremental growth of the external loads generated the distribution of resultant reaction of the individual contact zones. Series of calculations were ended when one reaction acting at the point of contact ball with the raceway was equal to the force limit F_{dop} .

A full static limiting load curves of the slewing bearing have been presented in Figures A1-A4 [11] (Appendix A) but without taking into consideration the gear conditions. These charts show the influence of radial forces (specifically directed) on courses of bearing static carrying capacity curves (Q , M). A significant loss of static carrying capacity is caused by the radial forces H_N directed orthogonally and the radial forces H_M directed positively (Fig. A1). On the basis of these results (Q , M), for given radial forces H_N (Fig. A4) and H_M (positively – Fig. A2 and negatively - Fig. A3 directed), using the model presented here, comparative calculation were performed. It was concluded that plane created during the main system of forces is the plane of pinion symmetry the radial forces H_M (directed negatively) and H_N does not cause a change of the bearing static carrying capacity. A loss of the static carrying capacity occurs when the radial force H_M is directed positively. This is especially noticeable when the radial force H_M is about 15% of the maximum allowable axial force Q_{max} ($M=0$, $H_M=0$, $H_N=0$). In considered case the bearing radial force is $H_M=1,120$ [MN]. This load was implemented in the FEM slewing bearing model (Fig. 3) with taken into account gear condition. The static carrying capacity curve was determined for this load. In Fig. 6 there are shown courses of the static carrying capacity load curves of the slewing bearing with and without taken into consideration gear condition.

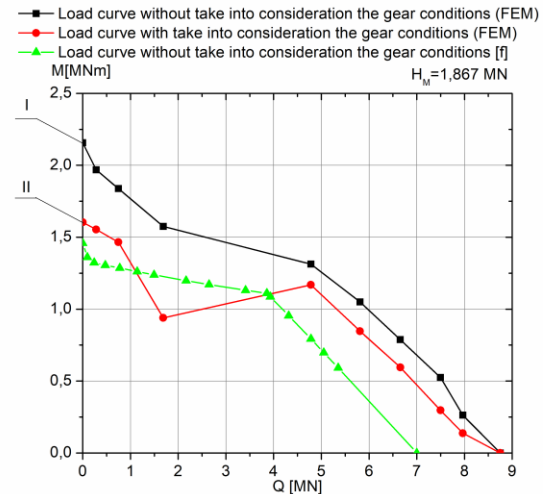


Fig. 6. Juxtaposition of static carrying capacity curves of the single-row ball slewing bearings loaded by radial forces directed positively with and without taken into consideration gear condition

In order to identify the potential causes of the presented problem, the distributions of forces acting on the individual ball - raceway contact zone of analyzed bearing for selected characteristic operation points (I and II marked in Fig. 6) have been shown in Fig. 7. The maximum allowable radial force for the assumed simulation conditions has been amounted at the level of $H_{max}=3,3$ [MN]. Whereas in case when the gear condition was omitted, a maximum value of the allowable radial force has been amounted $H_{max}=5,977$ [MN]. Decrease of H_{max} value is an effect of a distribution of the forces loading of balls. The distribution of forces acting

on the individual contact zone ball - raceway for both cases modelled bearings have been presented in Fig. 8. The elements of statistics were used for a quantitative assessment, allowing to describe the nature of load of the bearing contact zones and at the same time to determine the origin of the course of the considered static carrying capacity curve. In the presented bearing a four-point raceway-ball-raceway contact zone is identified.

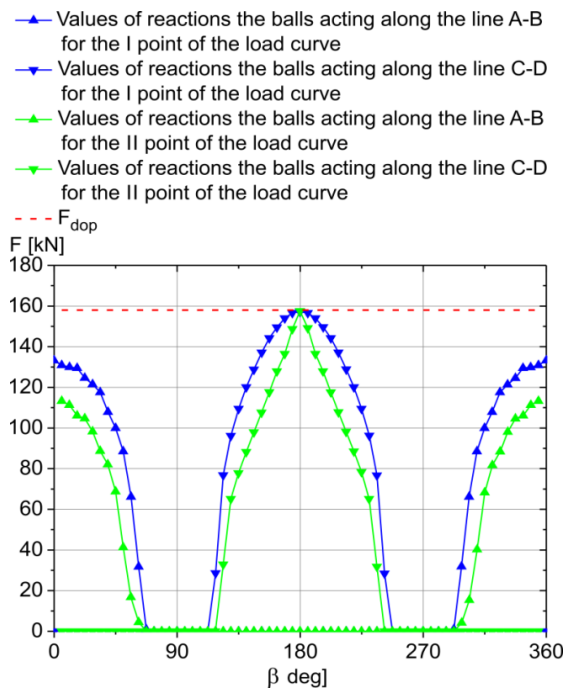


Fig. 7. Comparison of distributions of the forces acting on balls of the single-row ball slewing bearing for the points of work: I and II according to Fig. 6, β - angular coordinate

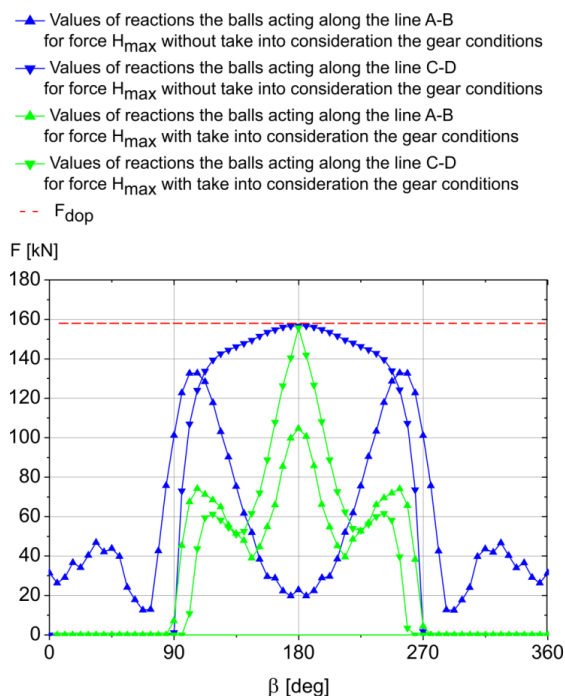


Fig. 8. Comparison of distribution of the forces acting on balls of the single-row ball slewing bearing for the maximum radial force with taken into consideration ($H_{max}=5,977$ [MN]) and without ($H_{max}=3,3$ MN) the gear condition, β - angular coordinate

During the complex state of external loads of the slewing bearing, some of contact pairs do not carry the load so zero values of forces acting on balls during the machining of the statistical distribution of balls reactions have been omitted. An arithmetic average (Eq. 3) and the standard deviation (Eq. 4) was determined on the basis of identified values (variance).

$$\bar{F} = \frac{\sum_{i=1}^n F_i}{n} \Leftrightarrow F_i > 0 \quad (3)$$

$$\Delta F = \sqrt{\frac{\sum_{i=1}^n (F_i - \bar{F})^2}{n-1}} \quad (4)$$

where: F_i [N] – forces acting on balls (balls reactions of the single-row ball slewing bearing), n – number of compressive forces of the balls (values greater than zero)

These values (for the presented in Fig. 7 and 8 of the distribution of balls reactions) have been listed in Tab. 3.

Similar FE models of slewing bearings installed in heavy-duty machines were experimentally verified by the authors of the works [35, 36, 37]. Since methodology for modelling slewing bearings presented in this article is based on the same assumptions, additional experimental verification of the model was not conducted.

It should be emphasized that formula 2 was determined based on experimental tests of the load capacity of a contact zone for the system ball-raceway.

In order to check the obtained results (similarly as in work [13]), the static carrying capacity curve of the slewing bearing was determined using a classical method called by the authors of the work [38] - the continuous loading method. Since this method does not make it possible to take into account the conditions of cooperation between a toothed bearing's ring and a drive pinion, the additional curve presented in Fig. 6 can be compared with the curve obtained based on the FEM model and described as: load curve without taking into consideration the gear conditions. This curve according to the model [38] gave an intermediate solution in the presented case.

4. SUMMARY

On the basis on performed simulation, made by developed bearing model including gear conditions, it is found that the operation of the radial forces directed to the pinion causes a decrease of the static carrying capacity of the slewing bearing. Therefore an area of work described as a course of static carrying capacity curve of the slewing bearing cooperating with a pinion and loaded by positive radial force is smaller. H_{max} force is smaller about 45%, and M_{max} value (Fig. 6) for the H_M value amounts only 15% Q_{max} is smaller about 27%.

A review of the load distribution for individual load conditions in both models allows to explain the loss of the bearing static carrying capacity.

According to statistical evaluation criterion of the strength properties of the slewing bearings (more widely presented in the work [11]) for the gear condition of the rim and the pinion, the values of arithmetic averages of ball reactions at contact points with the raceways are much smaller than in case of model without pinion. Thus, higher loads are accumulated to the smaller number of pairs of contact. According to the statistical criterion of slewing bearings, the best load conditions for the contact zones between balls and raceways occur when the mean values of the ball reaction are as high as possible, and the values of the standard deviation as low as possible.

Tab. 3. Juxtaposition of statistical parameters describing the nature of the load of ball of single-row ball slewing bearing (Fig. 8) for the selected points of work I and II (Fig. 7)

| Model of bearing | External load components | | | Number of forces | Ball reaction values F_i | |
|------------------|--------------------------|---------|-----------------|------------------|----------------------------|-------------------------|
| | Q [MN] | M [MNm] | H_M [MN] | | Arythmetic average [kN] | Standard deviation [kN] |
| Without pinion | 0 | 1,603 | 1,120 | 49 | 108,7 | 40,7 |
| With pinion | 0 | 2,156 | 1,120 | 44 | 89,5 | 38,6 |
| Without pinion | 0 | 0 | $H_{max}=3,3$ | 98 | 81,4 | 52,4 |
| With pinion | 0 | 0 | $H_{max}=5,977$ | 63 | 65,5 | 31,5 |

Limitation of the static carrying capacity also arises from the condition of contact strength of the pinion and rim and it will be the subject of another publication in this scope. During a deformation of a bearing ring the contour of the deformed toothed ring differs from a circular outline and causes that a distribution of the contact pressures along the side surface of the tooth is irregular. The distribution of displacements in the direction of the radial force H_M for operation points marked in Fig. 6 as II is shown in Fig. 9. The orthogonal projection (on the XY plane) of the deformed profile of the toothed ring has a shape which can be approximated as an ellipse. The reasons for such state are both - the condition of the external load (Q , H_M , M) and a limitation of displacements caused by the mating conditions between the toothed ring and the pinion (forces resulting from a contact of the teeth). The most loaded contact zone of the ball-raceway (Fig. 7) is located on the direction of the line connecting the rotational axes of the toothed ring and pinion.

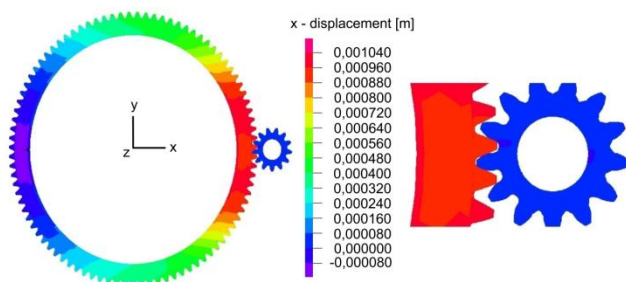


Fig. 9. The distribution of displacements in the direction of the radial force H_M for operation points marked in Fig. 6 as II

As a result of the identified deformations the working pressure angle α_w is decreased. These phenomena also has an impact on teeth strength.

The conditions of load external considered for the slewing bearing assembled in the structures of the one-shovel tracked excavator are extremely dangerous. Such a state of loads (not stipulated in the standards [3-5]) in the machine may be uncommon, but in specific operating conditions it may appear cyclically. Therefore, when the slewing bearing is selected, this issue should be taken into account. If the bearing cannot be adjusted to such extremely loads, a system should be protected against the possibility of indicated dangerous loads' cumulation.

The use of FEM for modeling a phenomena occurring in slewing bearings has many advantages over classical methods.. The most important advantage is the ability to easily increase the number of implemented parameters which changes can be analyzed, e.g. the axial clearance, the mounting tension force, selection of the number of bolts, dimensions of support structure.

The presented model of the slewing bearing complements the

missing features of the model presented by author of this work in the previous article [2]. Compared to the models of other authors (Tab. 4), the slewing bearing model was expanded to include defined conditions of cooperation between a toothed bearing's ring and a drive pinion, taking into account the contact conditions between the teeth. The characteristics of the contact zone (Fig. 5) were determined using a material model of the ball and raceway, taking into account the elastic-plastic state.

Tab. 4. Overview of features characterizing individual FE models of slewing bearings against the model presented in the article [*]

| Feature of the presented model | | Reference number |
|--------------------------------|--|---|
| 1 | The use of replacement elements for modeling rolling parts | [1], [2], [7], [9], [11], [13], [15], [18], [24], [25], [26], [32], [33], [35], [36], [37], [38],[*] |
| 2 | Taking into account the support structures in slewing bearings | [2], [7], [9], [10], [11], [25], [26], [32], [33], [35], [36], [38], [*] |
| 3 | Taking into account interactions between the bearing and bolts | [1], [2], [7], [9], [11], [13], [25], [26], [32], [33], [35], [36], [38], [*] |
| 4 | Taking into account flexible rings | [1], [2], [7], [9], [10], [11], [13], [15], [18], [24], [25], [26], [32], [33], [35], [36], [37], [38], [*] |
| 5 | Taking into account of radial forces | [1], [2], [7], [9], [10], [11], [13], [15], [18], [24], [25], [26], [32], [33], [35], [36], [38], [*] |
| 6 | Modeling of the contact zone taking into account the elastic-plastic material model | [2], [7], [11], [15], [18], [24], [26], [33], [35], [36], [*] |
| 7 | Modeling of the bearing taking into account the cooperation conditions between a toothed bearing's ring and a drive pinion | [*] |

Appendix A

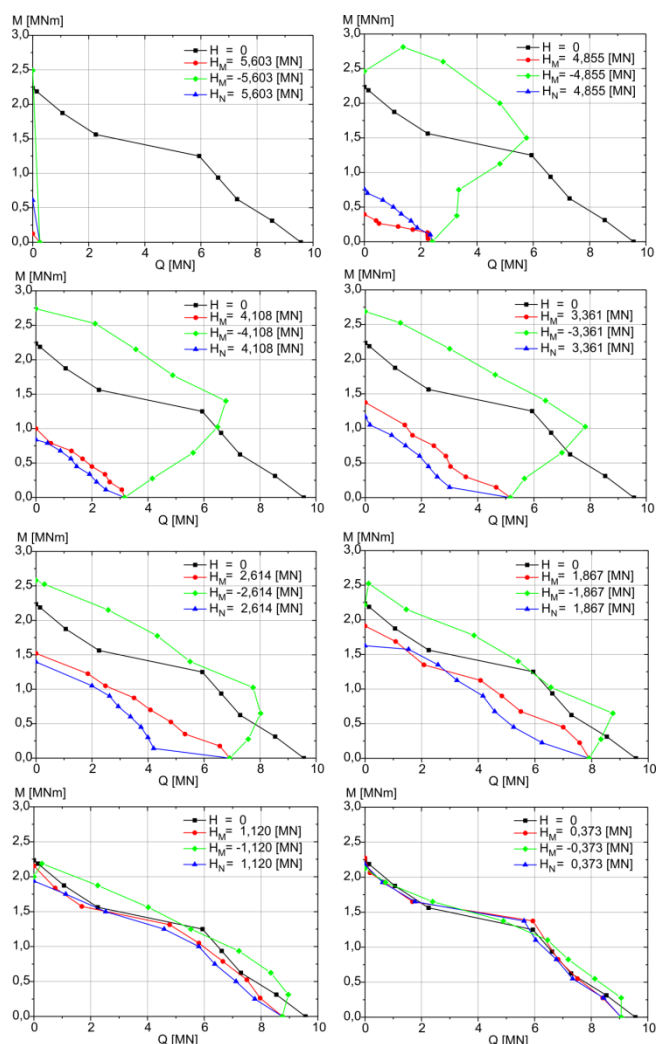


Fig. A1. Juxtaposition of static carrying capacity curves of the single-row ball slewing bearing loaded by constant values of the radial forces defined positively, negatively and orthogonally

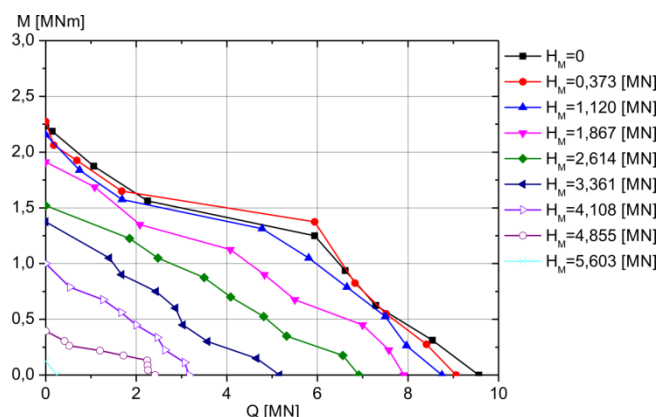


Fig. A2. Juxtaposition of static carrying capacity curves of the single-row ball slewing bearing loaded by the main radial forces H_M defined positively

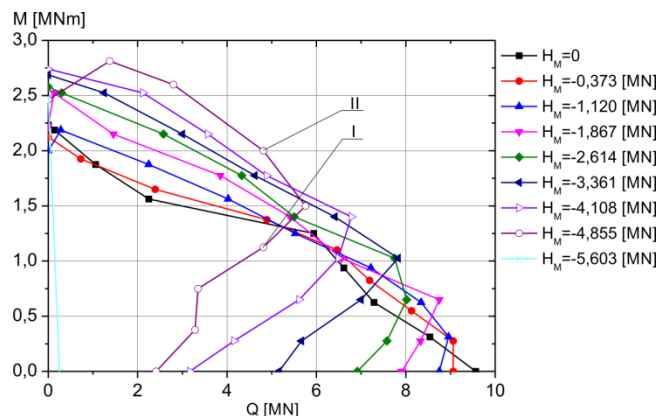


Fig. A3. Juxtaposition of static carrying capacity curves of the single-row ball slewing bearing loaded by the main radial forces H_M defined negatively

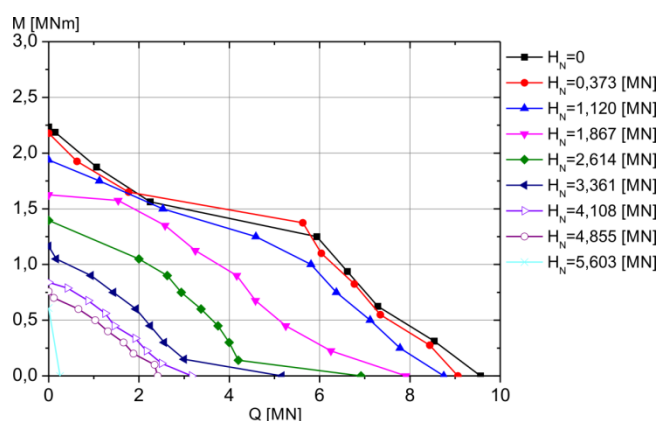


Fig. A4. Juxtaposition of static carrying capacity curves of the single-row ball slewing bearing loaded by radial forces H_N defined orthogonally

Appendix B

A specific feature of the FEM modeling method used for the presented slewing bearing is an application of two models. The first model, called the contact zone model, is used to determine replacement characteristics of the contact zone (Fig. 5). Assumptions regarding the selection of geometric and material parameters, boundary conditions and loads have been described in detail in [2]. Output data obtained from this model is then implemented (as multilinear material characteristic of the finite element type truss) to the second model, which is the slewing bearing model. This division of tasks cause that a problem of deformation of the ball and the raceway enough to solve only once, and the solution result is used to modeling all contact pairs (ball - raceway) as the replacement elements (Fig. 4). The advantage of this method is the reduction in the number of finite elements representing a curvature of the bearing raceway, which causes a reduction of calculation time of the carrying capacity. The consequence of the method used is the need to check the influence of discretization density of geometric objects of the slewing bearing on calculation results. Taking into account the example contained in [37] and a structure of the presented bearing FE model, where several types of finite elements were used, analysis of the mesh sensitivity was focused on the following structures: a contact zones ball-raceway, a bearing ring

and a gearing system. In each case, three different mesh densities were tested and described in Figures B1, B2, B3 as minimum, average and maximum density of FE mesh

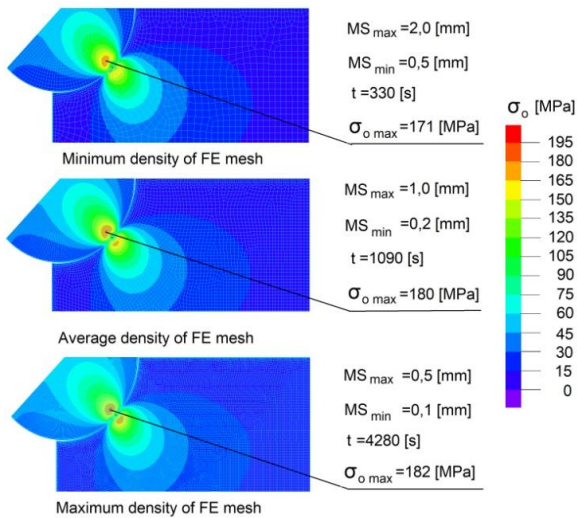


Fig. B1. Distributions of the effective stress for the tested meshes of the contact zone model

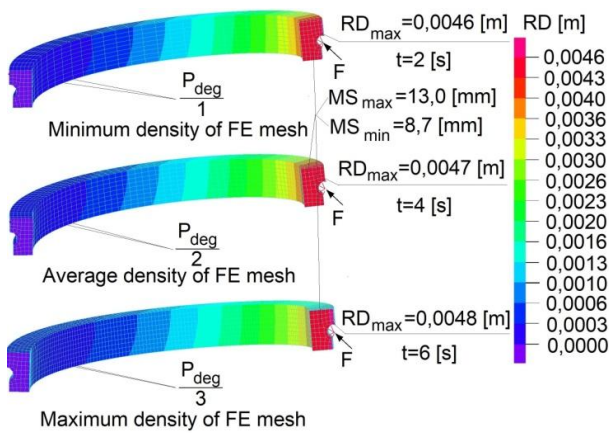


Fig. B2. Distributions of the displacements for the tested meshes of the slewing bearing ring model

The mesh size was defined by the maximum MS_{max} and minimum MS_{min} a distance between nodes of the finite element in a considered structure of an object. The calculation time, denoted by subol t in Figures B1 B2 B3, is given for all models tested. Calculations were performed using two processor cores of i5-4590, CPU 3,3 GHz and the memory of 1825 [MB]. Eight-nodal finite elements type 3D-Solid [27, 28] were used in the contact zone model. Due to the fact that in this model the contact problem is being resolved, the maximum effective stress for the permissible load of the contact zone (F_{dop}) in the direction indicated by the nominal contact angle (α_o) was adopted as a criterion for rating of convergence of the solutions. Distributions of the effective stress in the contact zone models are shown in Fig. B1. In all cases, the Bielajew zone is clearly visible, wherein the maximum effective stress $\sigma_{o max}$ were identified. Based on the formulas presented in [34], the theoretical maximum effective stress $\sigma_{o max}=185$ [MPa] was calculated.

Satisfactory convergence was obtained for the maximum density of FE mesh. This model was used to determine a characteristic of the contact zone (Fig. 5).

The slewing bearing model contains several groups of finite elements with specific properties. Due to the method of definition mutual relations between these groups a control of the mesh sensitivity carried out for a geometry of the inner ring of the slewing bearing 1 (Fig. 3) and contact pair of a toothed rim 3 and a drive pinion 5. These objects are represented using three-dimensional finite elements. It should be noted that the beam element of the superelement (Fig. 4) has a common node with the bearing ring. This node in the bearing model is a connector between elements which replace of the balls and the bearing raceways. This discretization system means that a displacement of this node caused by the point action of a load will depend on density of a mesh determined in a cross-section of the ring. The method of compensating this numerical effect is shown in [2]. Thus, discretization errors of the cross-section of the rings are reduced by modifying the characteristics of the contact zone [2]. The adopted system of connecting superelements with rings enforces angular positioning of finite elements in accordance with a pitch of the balls. Therefore, the test of mesh sensitivity concerned the circumferential arrangement of the nodes. The presented bearing model takes into account the bending and torsion of rings therefore the maximum displacement RD_{max} of the ring loaded with a constant force F through one superelement was assumed as a control criterion for testing meshes.

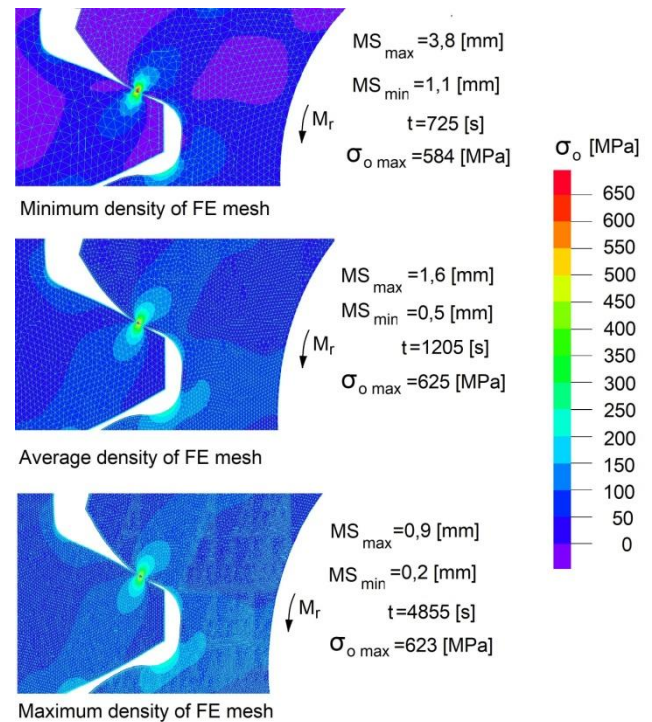


Fig. B3. Distributions of effective stress for the tested meshes of the contact zone model of a toothed rim and a drive pinion

The circumferential discretization pitch was set as a multiple of the angular pitch of the balls P_{deg} . The test calculation was performed for three different circumferential discretization pitch marked in Fig. B2. Based on the displacement distribution, it was found that a model with a minimum density of FE mesh is sufficient for bearing analysis.

Since the geometry of the gearing system is more complex than the geometry of the ring, the structure of a toothed rim and a drive pinion was modeled with twelve-nodal finite elements type

3D-Solid [27, 28]. In this model, the focus was on determining the mesh sizes for the tooth pairs in contact when bearing is loaded [30]. Permissible effective stress in the contact zone for gears was set as criterion for rating of convergence of the solution. A value of this stress for the bearing material is $\sigma_c=650$ [MPa]. Based on this value, an allowable torque $M=8717$ [Nm] was calculated. This torque was implemented in three contact zone models of a toothed rim and a drive pinion. The calculation results are presented in Fig. B3. Satisfactory convergence was obtained for the average density of FE mesh.

Based on the sensitivity analysis of the meshes, the model of slewing bearing cooperating with a drive pinion presented above was built. The statistical data of this model are summarized in Tab. B1.

Tab. B1. Statistical data of the FE model of the slewing bearing

| The modeled object | Finite element type | Number of finite elements |
|-----------------------------|---------------------|---------------------------|
| The ball as a Superelement | Truss | 128 |
| | Beam | 512 |
| Inner ring | 3D-Solid | 3584 |
| Outer ring | 3D-Solid | 3584 |
| Bolts | Beam | 84 |
| Heads of the mounting bolts | 3D-Solid | 5040 |
| Upper support structure | 3D-Solid | 3392 |
| lower support structure | 3D-Solid | 3392 |
| Płyta | 3D-Solid | 1 |
| Toothed rim | 3D-Solid | 56340 |
| Pinion | 3D-Solid | 37651 |

The calculation time necessary to determine one of the points of the static static carrying capacity curves was $t=7120$ [s].

REFERENCES

1. Aguirrebeitia J, Abasolo M, Aviles R, Bustos IF. General static load-carrying capacity for the design and selection of four contact point slewing bearings: finite element calculations and theoretical model validation. *Finite Elem. Anal. Des.* 2012; 55: 23-30. Available from: <https://doi.org/10.1016/j.finel.2012.02.002>
2. Śpiewak S. Methodology for calculating the complete static carrying capacity of twin slewing bearing. *Mechanism and Machine Theory* 2016; 101: 181–194. Available from: <https://doi.org/10.1016/j.mechmachtheory.2016.03.017>
3. Slewing Ring Turntable Bearings. Kaydon Corporation. Catalog 390, Muskegon. 2011.
4. Rothe Erde slewing berings. RotheErde GmbH. Dortmund. 2007.
5. INA Slewing rings. Catalogue 404, Schaeffler Technologies AG & Co. KG Herzogenaurach (Germany).
6. Potočník R, Göncz P, Glodež S. Static capacity of a large double row slewing ball bearing with predefined irregular geometry. *Mechanism and Machine Theory*. 2013;64:67-79. Available from: <https://doi.org/10.1016/j.mechmachtheory.2013.01.010>
7. Śpiewak S. A peculiarity of determining a static carrying capacity for the one-row ball slewing bearing loaded the large radial force. *Journal of KONES*. 2016; 3: 533 - 540.
8. Li Y, Jiang D. Dynamic carrying capacity analysis of double-row four-point contact ball slewing bearing, *Mathematical Problems in Engi-*

- neering, 2015; PT.19: 1-7. Available from: 10.1155/2015/850908
9. Smolnicki T, Derlukiewicz D, Stańco M. Evaluation of load distribution in the superstructure rotation joint of single-bucket caterpillar excavators. *Automation in Construction*. 2008;17:218–223.
10. He P, Hong R, Wang H, Lu C. Fatigue life analysis of slewing bearings in wind turbines. *International Journal of Fatigue*. 2018; 111: 233-242. Available from: <https://doi.org/10.1016/j.ijfatigue.2018.02.024>
11. Jaskot A, Śpiewak B, Śpiewak S. Influence of radial forces positively, negatively and perpendicular directed on the static carrying capacity of the one row ball slewing bearing. *Machine Dynamics Research*. 2015; 3: 33 - 47.
12. Glodež S, Potočník R, Flašker J. Computational model for calculation of static capacity and lifetime of large slewing bearing's raceway, *Mechanism and Machine Theory*. 2012;47:16-30. Available from: <https://doi.org/10.1016/j.mechmachtheory.2011.08.010>
13. Li Y, Wang R, Mao F. Calculation method for the static carrying curve of double-row different-diameter ball slewing bearings. *Science Progress*. 2023; 106(2). Available from: 10.1177/00368504231180026
14. Friederici V, Schumacher J, Clausen B. Influence of local differences in microstructure and hardness on the fatigue behaviour of a slewing bearing steel. *Procedia Structural Integrity*. 2021;31:8-14. Available from: <https://doi.org/10.1016/j.prostr.2021.03.003>
15. He P, Liu R, Hong R, Wang H, Yang G, Lu C. Hardened raceway calculation analysis of a three-row roller slewing bearing. *International Journal of Mechanical Sciences*. 2018; 137: 133-144. Available from: <https://doi.org/10.1016/j.ijmecsci.2018.01.021>.
16. Caesarendra W, Kosasih B, Tieu AK, Moodie CAS. Application of the largest Lyapunov exponent algorithm for feature extraction in low speed slewing bearing condition monitoring. *Mechanical Systems and Signal Processing*. 2015; January 50–51: 116-138. Available from: <https://doi.org/10.1016/j.ymssp.2014.05.021>
17. Caesarendra W, Kosasih B, Tieu AK, Zhu H, Moodie CAS, Zhu Q. Acoustic emission-based condition monitoring methods: Review and application for low speed slew bearing. *Mechanical Systems and Signal Processing*. 2016; 72–73: 134-159. Available from: <https://doi.org/10.1016/j.ymssp.2015.10.020>
18. Žvokelj M, Zupan S, Prebil I. EEMD-based multiscale ICA method for slewing bearing fault detection and diagnosis, *Journal of Sound and Vibration*. 2016; 26: 394-423. Available from: <https://doi.org/10.1016/j.jsv.2016.01.046>
19. Wang S, Chen J, Wang H, Zhang D. Degradation evaluation of slewing bearing using HMM and improved GRU. *Measurement*. 2019; 146: 385-395. Available from: <https://doi.org/10.1016/j.measurement.2019.06.038>
20. Heras I, Aguirrebeitia J, Abasolo M. Friction torque in four contact point slewing bearings: Effect of manufacturing errors and ring stiffness. *Mechanism and Machine Theory*. 2017; 112: 145-154. Available from: <https://doi.org/10.1016/j.mechmachtheory.2017.02.009>
21. Dindar A, Akkøk M, Çalişkan M, Experimental Determination and Analytical Model of Friction Torque of a Double Row Roller Slewing Bearing, *Journal of Tribology*. 2017; 139(2): 021503, Available from: <https://doi.org/10.1115/1.4033364>
22. Babu S, Manisekar K. Experimental Study of Heat Distribution in Polished Bearing Surfaces for Design and Development of Large Diameter Slewing Ring Bearing for FBR. *Procedia Engineering*. 2014; 86: 350-358. Available from: <https://doi.org/10.1016/j.proeng.2014.11.048>
23. Amasorraina JI, Sagartzazu X, Damián J. Load distribution in a four contact-point slewing bearing. *Mechanism and Machine Theory*. 2003; 38: 479-496. Available from: [https://doi.org/10.1016/S0094-114X\(03\)00003-X](https://doi.org/10.1016/S0094-114X(03)00003-X)
24. Göncz P, Potočník R, Glodež S. Load capacity of a three-row roller slewing bearing raceway. *Procedia Engineering*. 2011; 10: 1196-1201. Available from: <https://doi.org/10.1016/j.proeng.2011.04.199>
25. Aguirrebeitia J, Plaza J, Abasolo M, Vallejo J. Effect of the preload in the general static load-carrying capacity of four-contact-point slewing

- bearings for wind turbine generators: theoretical model and finite element calculations. *Wind Energ.* 2014; 17: 1605–1621. Available from: <https://doi.org/10.1002/we.1656>
26. Kania L, Śpiewak S. English title: Determining the reactions of balls slewing bearing mounted in working structures of the single-bucket excavator. Polish title: Wyznaczanie reakcji kulek łożyska wieńcowego osadzonego w strukturach roboczych koparki jednoznaczyniowej. *Zeszyty Naukowe Transport. Politechnika Śląska.* 2014; 83: 127-136.
 27. ADINA.Theory and Modeling Guide. Vol. 1: ADINA Solids & Structures. ADINA R&D Inc. Watertown. 2012.
 28. Bathe KJ, Finite Element Procedures. Prentice-Hall. Inc. Simon & Schuster/A Viacom Company Upper Saddle River. New Jersey. 1996.
 29. Hwang SC, Lee JH, Lee DH, Han SH, Lee KH. Contact stress analysis for a pair of mating gears. *Mathematical and Computer Modelling.* 2013; 57:40-49. Available from: <https://doi.org/10.1016/j.mcm.2011.06.055>
 30. Li S. Effect of addendum on contact strength, bending strength and basic performance parameters of a pair of spur gears. *Mechanism and Machine Theory.* 2008; 43: 1557–1584.
 31. DIN/ISO – 898.
 32. Smolnicki T, Rusiński E. Superelement-based modeling of load distribution in large-size slewing bearings. *Journal of Mechanical Design.* 2007; 129: 459-463.
 33. Kania L., Śpiewak S. Współczynnik krotności łożysk wieńcowych podwójnych. *Acta Mechanica et Automatica.* 2009;3(1): 65-67.
 34. Brändlein J, Eschmann P, Hasbargen L, Weigand K, Die Wälzlagerpraxis. Vereinigte Fachverlag GmbH. 1998. Mainz.
 35. Smolnicki T., Modelling, computing, and analyzing large-size rotary joints; In: Sokolski, M. (eds) *Mining Machines and Earth-Moving Equipment.* Springer. 2020. Cham. Available from: https://doi.org/10.1007/978-3-030-25478-0_3
 36. Sokolski P, Smolnicki T. A method for monitoring the technical condition of large-scale bearing nodes in the bodies of machines operating for extended periods of time. *Energies.* 2021;14:6637. Available from: <https://doi.org/10.3390/en14206637>
 37. He P, Qian Q, Wang Y, Liu H, Guo E, Wang H. Influence of finite element mesh size on the carrying capacity analysis of single-row ball slewing bearing. *Advances in Mechanical Engineering.* 2021; 13: 1–12.
 38. Kania L, Krynke M, Mazanek E. A catalogue capacity of slewing bearings. *Mechanism and Machine Theory.* 2012; 58: 29–45. Available from: <https://doi.org/10.1016/j.mechmachtheory.2012.07.012>

Szczepan Śpiewak:  <https://orcid.org/0000-0002-7057-8356>



This work is licensed under the Creative Commons BY-NC-ND 4.0 license.

A CONCEPT OF A MICRO-POLYGENERATION SYSTEM FOR ZERO-ENERGY BUILDING

Paula KRAJEWSKA*, Bartosz DAWIDOWICZ*, Janusz T. CIEŚLIŃSKI*

*Faculty of Mechanical Engineering and Ship Technology, Institute of Energy, Gdańsk University of Technology,
Narutowicza 11/12, 80-233 Gdańsk, Poland

paulakrajewska98@gmail.com, bardawid@pg.edu.pl, jcieslin@pg.edu.pl

received 10 November 2022, revised 27 May 2024, accepted 29 May 2024

Abstract: This paper presents a concept of a zero-energy system for powering a single-family house based on a PV system, an electrolyser, a hydrogen gas storage, a fuel cell and a heat pump. Estimated is the demand for electricity and thermal energy consumed in a house inhabited by 3 people and a usable area of 80 m². The investment costs of the installation were estimated based on the commercially available offer.

Keywords: hydrogen; hydrogen storage; power-to-gas; fuel cell; photovoltaics

1. INTRODUCTION

Popularization and increasing use of renewable power sources for distributed generation and increasing energy price, encourage to the production of electricity for private use. On the other hand, energy production with renewable energy sources depends on weather conditions. Photovoltaic and other solar systems depend on solar radiation and ambient temperature. Therefore, the same amount of energy cannot be provided at the all-time and other sources need to be found to provide electrical energy at the time when production with renewable energy is not possible, has made it the application of storage systems a necessity to ensure the continuous supply. In the building sector, this has led to growing interest in energy self-sufficient buildings that feature battery and other energy storage. Different techniques are today used to store both electric and thermal energy, making use of mechanical, electric, chemical, thermal and biological systems, the most widespread and versatile of which are presently batteries. Battery-electric systems are widely installed in residential buildings in order to increase self-consumption from PV. Advancements in battery technology seek to lower capacity costs and reduce environmental impacts. Another approach is to store energy in the form of hydrogen. Hydrogen is important as a large-quantity, long-term energy storage. Hydrogen storage has a very low rate of self-discharge and high energy density. Hydrogen is considered an excellent clean fuel with potential applications in many fields thus the hybridization of hydrogen and solar energy technologies is an interesting option to satisfy power in locations that are isolated from the electric grid as well as households. Hybrid system (photovoltaic-hydrogen) makes it possible of power hydrogen storage by means of an electrolyzer in pressurized tanks which and then converted into electricity in fuel cells when needed. Thus, electrolysis and hydrogen storage have been highly recommended for long-term alternatives for electricity storage [6]. A self-sufficient energy supply with hydrogen storage has already been realized for single- and multi-family dwellings, as

well as for residential districts, and there are commercial suppliers that offer all-in-one hydrogen solutions for residential storage. Numerous hybrid systems based on renewable energy and H₂ for building have been discussed in [2,3,5]. A combination of photovoltaic systems and hydrogen fuel cells is shown to be able to provide complete self-sufficiency in electrical energy [4,5]. Paper [3] presents an analysis of energy production in a pilot building located in Slovenia, which is a typical residential house with an installed photovoltaic system and battery system for storage electricity. This study shows that complete self-sufficiency can be achieved by supplementing photovoltaic systems with hydrogen fuel cells. Whereas in paper [4] the comprehensive thermo-economic analysis is presented for a novel integrated solar hydrogen energy system for standalone operation. Authors in the work [1] described a methodology to design PV-H₂ hybrid systems that considers the weather data and the electrical variables of the components to perform energy balances and to assess the system in terms of the load requirements, the levels of energy stored and the resulting costs. The work [6] presents the results of simulation of battery and hydrogen technologies for renewable energy management, load-levelling and peak-shaving in a single grid-connected house in Nottingham (United Kingdom) where three people live. A 10 kWh lead-acid battery and a 1 kW fuel cell together, with a 600 l hydrogen storage tank at 15 bar are used for these simulations for short (daily cycles) and mid-term (3-day cycles) storage, respectively. Showed that the battery increases the local use of PV energy generated on-site by 171%, while the hydrogen increases it by 159%. In the paper [7] shows a demonstration installation of the Hydro Q-BiC®, consisting of 64.75 kW photovoltaic (PV) panels, a 5 Nm³/h water electrolyzer, 40 Nm³ of metal hydride hydrogen storage, 14 kW fuel cells and 20 kWh Li-ion batteries, is discussed here. In all cases, the CO₂ reduction capability is shown to be better than that of the PV-only system. Simulating annual CO₂ emissions indicates that the Hydro Q-BiC® can reduce emissions by more than 50%.

We can safely say that a synergy between photovoltaic system and hydrogen fuel cells is a step forward to complete self-

sufficiency with renewable energy sources, were by introducing fuel cells, electrical energy can be provided independently of the seasons and weather conditions.

2. A MICRO-POLIGENERATION SYSTEM FOR ZERO-ENERGY BUILDING

The polygeneration system is considered for a single-family house located in Gdańsk with an area of 80 m², inhabited by 3 people with roof of the facing south. It was assumed that utility water and the house will be electrically heated.

The installation scheme and its components for the considered house is shown in Fig. 1. The installation consists of an electric power generation system endowed with photovoltaic panels, a charge regulator, an inverter, a battery pack, an electrolyzer for hydrogen production, a hydrogen compressor, hydrogen storage tanks, a fuel cell for production of electricity and a heat pump. An air heat pump was used to reduce electricity consumption for heating the house and domestic water.

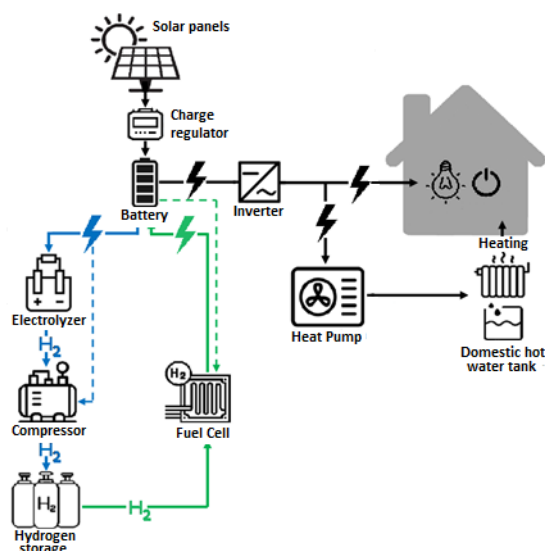


Fig. 1. Scheme of a self-sufficient residential energy system

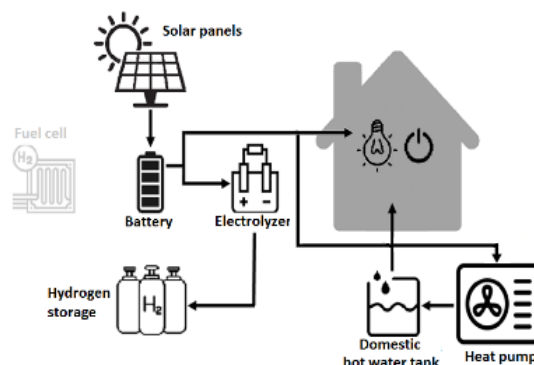
The photovoltaic system consists of 26 monocrystalline photovoltaic panels with a power of 390 W and an efficiency of 20.6% each. The total power of photovoltaic panels is 10.14 kWp. For the generated power, an inverter from VOLT POLSKA was selected, which converts 24 V DC into 230 V and 50 Hz alternating current with 95% efficiency. An AGM battery with a capacity of 43 kWh and a voltage of 24 V was used to store electricity. The battery has 1800 charging cycles. To safely charge the battery, a Lumiax voltage regulator is used, which ensures the correct charging current and protects the battery against overcharging. The excess of electric current generated by photovoltaic panels is directed to the PEM electrolyzer manufactured by McPhy to convert electric energy into hydrogen chemical energy. The capacity of the electrolyzer is 1 - 1.6 Nm³/h, and the power is 6 - 9 kW. It is an electrolyzer that works well in small home hydrogen power plants. The hydrogen produced in the electrolyzer is compressed in a compressor to a pressure of 350 bar. Then, the compressed hydrogen is stored in 18 tanks manufactured by MAHYTEC with a capacity of 0.25 m³ at the pressure of 350 bar. In order to recover electricity from hydrogen, a Horizon PEM fuel cell with a power of 5 kW

and an efficiency of 60% was used. In order to reduce electricity consumption for heating the building and domestic hot water, an air heat pump was used with the power of 4.6 kW with a COP 3.26 coefficient.

The system works in two modes, spring - summer and autumn - winter depending on the intensity of solar radiation.

First mode - short-term energy storage (spring-summer period). When the solar irradiation is higher than the electricity requirement of the house, excess electric power goes to the battery and electrolyzer, which generates hydrogen which after compressed goes to the storage tanks. When the solar irradiation is lower than the electricity requirement of the house or it is nighttime, the energy is drawn from the batteries. Thus, the batteries must have a capacity to meet the demand for electricity not only at night but also on a sunless day. Short-term energy storage for about 1 to 2 days can be most efficiently achieved with batteries with high energy conversion efficiency. Efficiency of storage and recovery energy for batteries is 85%. The diagram of the system operation in the spring-summer period is shown in Fig. 2.

a)



b)

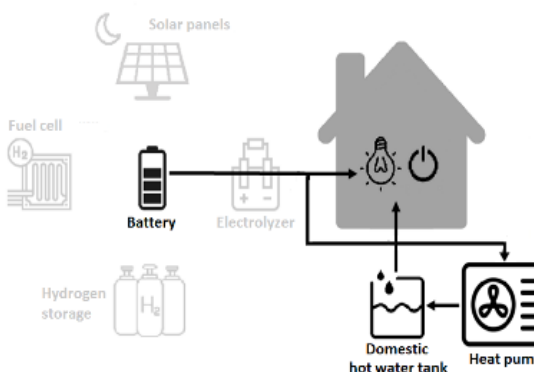


Fig. 2. System operation in the spring-summer period: a) during the day, b) after sunset

Second mode - long-term energy storage (autumn-winter period). When the solar irradiation is permanently lower than the electricity requirement of the house, both during the day and at night the energy is simultaneously drawn from the batteries and the fuel cell which consumes previously stored hydrogen. The hydrogen storage should be large enough to provide energy for the entire autumn and winter period. Efficiency of storage and recovery energy for hydrogen is 35% (it is a total efficiency of energy conversion for an electrolyzer, a compressor and a fuel cell). The diagram of the system operation in the autumn-winter period is shown in Fig. 3.

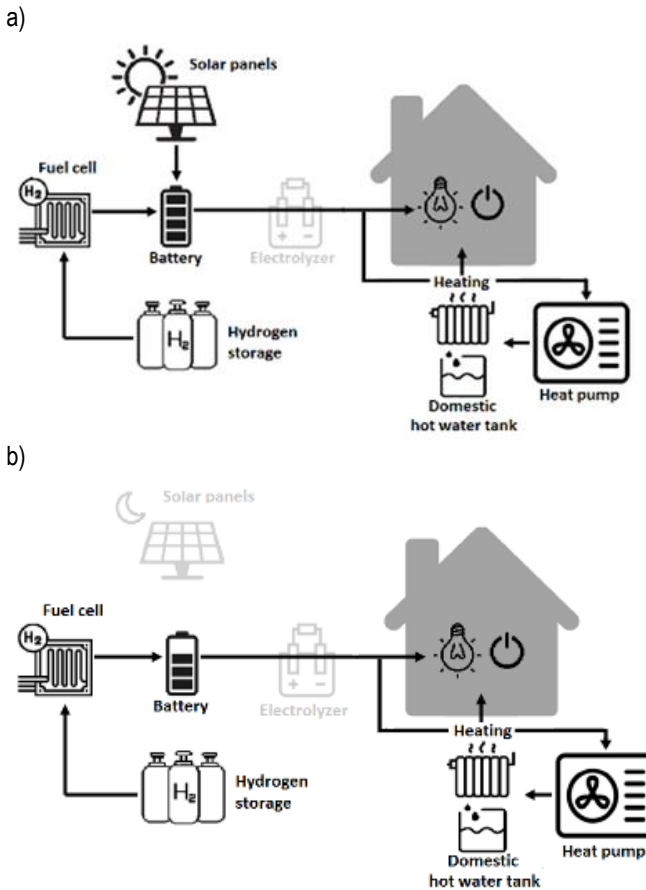


Fig. 3. System operation in the autumn-winter period: a) during the day, b) after sunset

Tab. 1 shows the efficiency and lifetime of the components of the polygeneration system.

Tab 1. Efficiency and lifetime for the components

| Component | Efficiency [%] | Lifetime [year] | Source |
|---------------------|------------------|-----------------|-----------------|
| Photovoltaic panels | η_{el} 20.6 | 20 | [2,9] |
| Charge regulator | η_{el} 97 | 15 | own assumptions |
| Inverter | η_{el} 95 | 15 | [2] |
| Battery | η_{el} 92 | 15 | [9] |
| Electrolyzer | η_{el} 75 | 15 | [2] |
| Hydrogen compressor | η_{el} 87 | 20 | [2] |
| Fuel cell | η_{el} 60 | 15 | [2,10] |
| Heat pump | SCOP 3.26 | 20 | [10] |

3. CALCULATION AND RESULTS

Calculations for the energy demand of the house were made on the basis of our own energy measurements, the currently applicable standards and regulations as well as official statistical data from the Statistics Poland (GUS). Additionally, a PVGIS calculator was used to calculate and simulate photovoltaic energy (for Europe, Asia, Africa and South and North America). This

application allows you to calculate the monthly and yearly potential electricity production of a PV system with a defined slope and orientation of the modules.

3.1. Household's electricity demand

The demand for electricity was estimated on the basis of own measurements and data from the Statistics Poland (GUS). The average consumption of electricity in a household with an area of approximately 100 m² is 2375 kWh per year, and is similar to the values obtained from own measurements where it was 2400 kWh per year.

3.2. Household's energy demand for heating domestic hot water

The annual energy demand for heating domestic hot water was calculated in two ways, according to the method contained in the regulation of the Minister of Infrastructure of November 6, 2008 (equation 1).

$$Q_{W,Nd1} = \frac{V_{CW,i} \cdot L_i \cdot c_w \cdot \rho_w \cdot (\theta_w - \theta_o) \cdot k_t \cdot t_{uz}}{3600} \quad (1)$$

where: $Q_{W,Nd1}$ - annual utility energy demand for domestic hot water preparation [kWh], $V_{CW,i}$ - daily unit consumption of hot water at 55 °C depending on the type of building [dm³/(units per day)], L_i - number of reference units - number of people living in the building [-], c_w - specific heat of water [kJ/(kg K)], ρ_w - water density [kg/dm³], θ_w - hot water temperature in the tap [°C], θ_o - cold water temperature [°C], k_t - correction factor [-], t_{uz} - time of use, less holiday breaks, on average during the year by 10% [days], and according to the method described in the regulation of the Minister of Infrastructure of June 3, 2014 (equation 2).

$$Q_{W,Nd2} = \frac{V_{W,i} \cdot A_f \cdot c_w \cdot \rho_w \cdot (\theta_w - \theta_o) \cdot k_R \cdot t_R}{3600} \quad (2)$$

where: $Q_{W,Nd2}$ - annual utility energy demand for domestic hot water preparation [kWh], $V_{W,i}$ - daily unit demand for domestic hot water [dm³/(m² day)], A_f - area of rooms with regulated air temperature [m²], c_w - specific heat of water [kJ/(kg K)], ρ_w - water density [kg/dm³], θ_w - hot water temperature in the tap [°C], θ_o - cold water temperature [°C], k_R - correction factor for interruptions in the use of domestic hot water [-], t_R - usage time [days].

Thus, the demand for thermal energy to heat domestic hot water for a family of three living in a single-family building according to the Regulation of the Minister of Infrastructure of November 6, 2008 (equation 5.1), amounted to 1806.545 kWh per year, while according to the Ordinance of the Minister of Infrastructure of June 3, 2014 (equation 5.2), the following was obtained 2141.09 kWh per year. For further calculations, the value obtained from equation 5.1 was adopted, which is close to the actual values resulting from own operational measurements at home.

3.3. Household's energy demand for heating house

The annual demand for thermal energy in the house results from the adopted rules (Standard WT 2021) that in newly con-

structed single-family houses, the value of the primary energy index should be no more than 70 kWh /m² per year. Thus, the annual total energy requirement for the proposed house is 5600 kWh per year.

3.4. Household's total energy demand

The annual total energy demand for a single-family energy-saving house with an area of 80 m² was calculated from the dependence 3 and is:

$$Q_c = Q_{CO} + Q_{CWU} + Q_{el} = 9806.545 \frac{kWh}{year} \quad (3)$$

where: Q_c - annual total energy demand of the building [kWh/year], Q_{CO} - annual energy demand to heat the building [kWh/year], Q_{CWU} - annual energy demand for heating domestic hot water [kWh/year], Q_{el} - annual electricity demand [kWh/year].

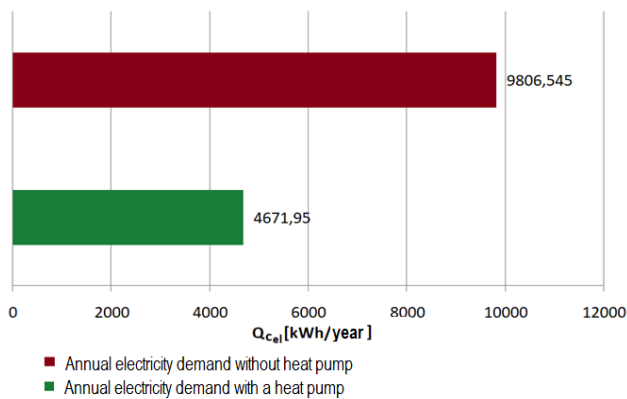


Fig. 4. Annual electricity demand for a power system with and without a heat pump

Tab. 2. Electricity demand depending on the month

| Month | Electricity demand for heating the building | Demand for electricity to heat domestic hot water | Electricity demand for other needs | Total electricity |
|-------|---|---|------------------------------------|-------------------|
| | [kWh] | [kWh] | [kWh] | [kWh] |
| Jan | 343.56 | 46.181 | 220 | 609.739 |
| Feb | 319.51 | 46.181 | 220 | 585.69 |
| Mar | 240.49 | 46.181 | 220 | 506.672 |
| Apr | 132.27 | 46.181 | 180 | 358.451 |
| May | 22.33 | 46.181 | 180 | 248.512 |
| Jun | 0 | 46.181 | 180 | 226.181 |
| Jul | 0 | 46.181 | 180 | 226.181 |
| Aug | 0 | 46.181 | 180 | 226.181 |
| Sep | 22.33 | 46.181 | 180 | 248.512 |
| Oct | 123.68 | 46.181 | 220 | 389.862 |
| Nov | 218.16 | 46.181 | 220 | 484.34 |
| Dec | 295.46 | 46.181 | 220 | 561.641 |

The use of a heat pump with a SCOP coefficient of 3.26 allows to reduce the demand for electricity for heating the building and domestic hot water to 1717.79 kWh (30.7% less energy in comparison to heating without heat pump) per year and 554.15 kWh (30.7% less energy in comparison to heating without heat pump) per year, respectively. Fig. 4 shows comparing annual electricity demand in cases where the heating of the building and domestic hot water is provided by an electrical installation or a heat pump.

In order to properly distribute energy, it was necessary to estimate the monthly energy demand for the house. Tab. 2 shows the monthly demand for thermal energy for house in Gdańsk and electricity for heat domestic water and other needs. To simplify the calculations, a constant monthly demand for electricity for water heating was assumed.

3.5. Photovoltaic installation

Based on the calculated demand for electricity, the power of the photovoltaic installation was estimated, taking into account the losses resulting from the aging of photovoltaic cells and energy conversion losses in the production and storage of hydrogen as well as loss related to the conversion of hydrogen to electricity in the fuel cell. In order for the designed system to meet certain assumptions, the total power of the modules should be 10.14 kWp. On this basis, a simulation was carried out in the PVGIS calculator, which determines the monthly production of electricity from the photovoltaic system located in Gdańsk. The results obtained for the photovoltaic installation are shown in Fig. 5.

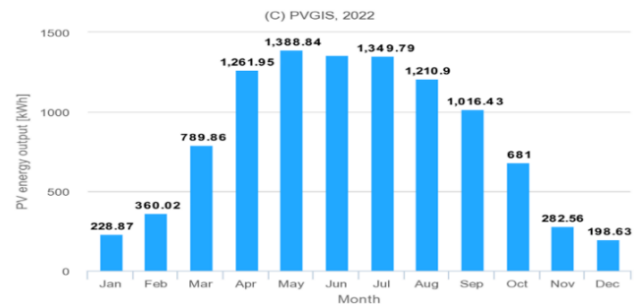


Fig. 5. Monthly energy production from a photovoltaic system with a capacity of 10.14 kWp

Based on a simulation of a photovoltaic installation, knowing the monthly electricity demand of a household, it was determined that from March to October, the photovoltaic system produces more electricity than the recipients' demand. In March, the system starts the process of producing and storing hydrogen. All electricity from the photovoltaic system is directed via the charge regulator to the battery. However, in January, February, November and December, the electricity from the photovoltaic system does not cover the household's electricity needs, so during this time the photovoltaic installation is supported by the hydrogen system. Tab. 3 presents the calculations of energy conversion at individual stages of the system.

Tab. 3. Results of calculations of energy conversion for a 10.14 kWp photovoltaic installation after 25 years of use for individual months

| Month | Jan | Feb | Mar | Apr | May | Jun | Jul | Aug | Sep | Oct | Nov | Dec |
|--|-------|-------|-------|--------|--------|--------|--------|--------|--------|--------|--------|--------|
| Total electricity requirement [kWh] | 609.7 | 585.7 | 506.7 | 358.5 | 248.5 | 226.2 | 226.2 | 226.2 | 248.5 | 389.9 | 484.3 | 561.6 |
| Electricity from a photovoltaic panels [kWh] | 196.8 | 309.6 | 679.3 | 1085.3 | 1194.4 | 1167.1 | 1160.8 | 1041.4 | 874.1 | 585.7 | 243.0 | 170.8 |
| Electricity output from the charge regulator [kWh] | 190.9 | 300.3 | 658.9 | 1052.7 | 1158.6 | 1132.1 | 1126.0 | 1010.1 | 847.9 | 568.1 | 235.7 | 165.7 |
| Electricity output from the battery [kWh] | 175.6 | 276.3 | 606.2 | 968.5 | 1065.9 | 1041.6 | 1035.9 | 929.3 | 780.1 | 522.6 | 216.8 | 152.4 |
| Electricity drawn from the battery [kWh] | 175.6 | 276.3 | 533.3 | 377.3 | 261.6 | 238.1 | 238.1 | 238.1 | 261.6 | 410.4 | 216.8 | 152.4 |
| Electricity supplied to consumers [kWh] | 166.9 | 262.5 | 506.7 | 358.5 | 248.5 | 226.2 | 226.2 | 226.2 | 248.5 | 389.9 | 206.0 | 144.8 |
| Electricity output from the battery supplied to the electrolyzer [kWh] | 0.0 | 0.0 | 72.9 | 591.2 | 804.3 | 803.5 | 797.8 | 691.2 | 518.5 | 112.3 | 0.0 | 0.0 |
| Energy contained in hydrogen after the electrolysis process [kWh] | 0 | 0 | 54.64 | 443.3 | 603.2 | 602.6 | 598.3 | 518.4 | 388.8 | 84.19 | 0 | 0 |
| Energy stored in hydrogen in the tank [kWh] | 619.2 | 2.9 | 47.5 | 433.3 | 958.1 | 1482.4 | 2002.9 | 2454.0 | 2792.3 | 2865.5 | 2304.2 | 1463.7 |
| The sum of the accumulated amount of hydrogen in the tank [kg] | 18.6 | 0.1 | 1.4 | 13.0 | 28.7 | 44.5 | 60.1 | 73.6 | 83.8 | 86.0 | 69.1 | 43.9 |

An example of the system operation in January is presented in Fig. 6.

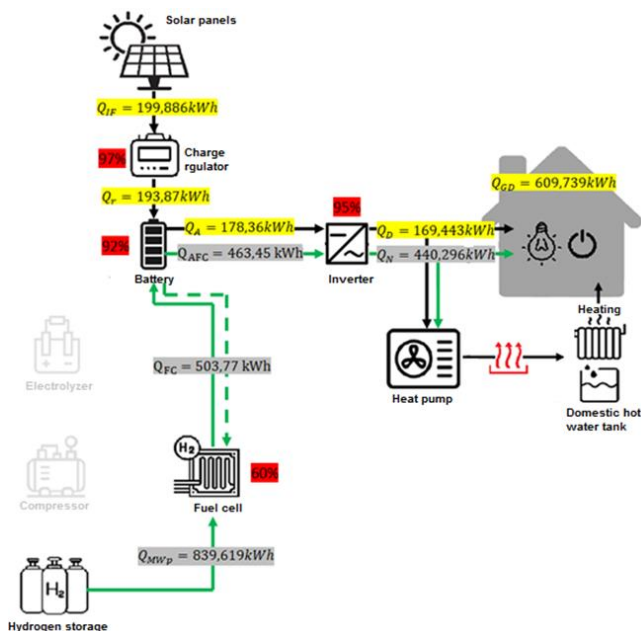


Fig. 6. The example of the system operation in the month of January

Was calculate that the average electricity demand is 2400 kWh per year, the energy for domestic hot water is 1806 kWh per year and the energy for heating the building is 5600 kWh per year.

The total energy demand for the house is 9806 kWh/year. The use of a heat pump reduces the energy requirement to 4672 kWh/year. Therefore to ensure the energy self-sufficiency of the building (both direct energy consumption and storage in the form of hydrogen), the power of photovoltaic panels should be 10.14 kWp. For solar energy available in Gdańsk, from the excess electricity of the PV system over 108 kgH₂/year may be produced. The excess electricity from photovoltaics lasts from March, peaking in May, through October. The electrical energy efficiency of the hydrogen system equals 35.33%. Whereas, the electrical energy efficiency of the battery system equals 85%.

4. INVESTMENT COSTS

The investment costs of the devices included in the installation were estimated on the basis of the offer available on the market from January 2022 – Tab. 4. In addition, the amount obtained should include assembly costs, the cost of safety installations, fire and explosion-proof installations and elements such as cables, surge arresters, connectors and others. Using the literature [11], it was found that the cost of the system, taking into account the expenses for additional installations and elements, will increase by about 36.5%. Thus, the total value of the energy self-sufficient system is estimated at 300000 PLN. It is a preliminary concept, the assumption of which was to estimate the possibility of proposing such a system and the approximate investment costs.

Tab. 4. Cost of devices used in the designed system (price from January 2022)

| Device | Producer | Price per piece [PLN] | Quantity [pcs] | Gross price [PLN] |
|----------------------------------|---------------|-----------------------|----------------|-------------------|
| Solar panel Q.PEAK DUO ML-G9 390 | Q.CELLS | 873.30 | 26 | 22 705.80 |
| Charge regulator MT2075 | Lumiax | 319.00 | 1 | 319.00 |
| Battery 2000RE-24 | Outback Power | 62 004 .07 | 1 | 62 004.07 |
| Inverter SINUSPRO-2000S | VOLT POLSKA | 1 264.00 | 1 | 1 264.00 |
| Heat pump 04S23D6V | DAIKIN | 22 580 .00 | 1 | 22 580.00 |
| Electrolyzer Piel P | McPhy | 19 937 .00 | 1 | 19 937.00 |
| Compressor WW-0.1/0.1-300 | AOT | 25 080 .75 | 1 | 25 080.75 |
| Hydrogen tank 250l | MAHYTEC | 3 210.43 | 18 | 57 787.74 |
| Fuel cell FCS-C5000 | Horizon | 106 86 2.32 | 1 | 106 862.32 |
| Total cost | | | | 215 467.14 |

5. CONCLUSIONS

A solar hydrogen and electricity producing system along with their storage facilities are developed and investigated parametrically for residential use. Preliminary calculations of an integrated power generation system consisting of the PV modules, electrolyzer, compressor, hydrogen tanks, fuel cell, and battery and heat pump was conducted. In the proposed system, energy can be stored and consumed at required times from the battery and/or hydrogen storage tank. An important issue in the proposed system is the estimation of the daily and annual power demand for the building. For the solar energy available in Gdańsk, the excess electricity of the PV system produces over 108 kg hydrogen over one year. The electrical energy efficiency of the hydrogen system equals 35.33%. Whereas, the electrical energy efficiency of the battery system equals 85%. A hybrid system with photovoltaic system and hydrogen fuel cells can be a solution for complete self-sufficiency. Low-temperature PEM fuel cells are highly efficient energy conversion systems, as they convert the hydrogen energy directly into electricity without being subjected to the limitation of Carnot efficiency. The main advantages of using PEMFCs are their fast response to variable loads, rapid start-up, low operating temperature (60-100°C), high power density [8]. The investment is relatively expensive, because of the high cost of the electrolyzer, hydrogen compressor, hydrogen storage tank and fuel cell and other component.

REFERENCES

- Gutiérrez-Martín F, Calcerrada AB, de Lucas-Consuegra A, Dorado F. Hydrogen storage for off-grid power supply based on solar PV and electrochemical reforming of ethanol-water solutions. *Renewable Energy*. 2020;147:639-649. <https://doi.org/10.1016/j.renene.2019.09.034>
- Knosala K, Kotzur L, Röben FTC, Stenzel P, Blum L, Robinius M, Stolten D. Hybrid Hydrogen Home Storage for Decentralized Energy Autonomy. *International Journal of Hydrogen Energy*. 2021;46:21748-21763. <https://doi.org/10.1016/j.ijhydene.2021.04.036>
- Lokar J, Viti P. The potential for integration of hydrogen for complete energy self-sufficiency in residential buildings with photovoltaic and battery storage systems. *International Journal of Hydrogen Energy*. 2020;45:34566-34578. <https://doi.org/10.1016/j.ijhydene.2020.04.170>
- Jafari M, Armaghan D, Seyed Mahmoudi SM, Chitsaz A. Thermoeconomic analysis of a standalone solar hydrogen system with hybrid energy storage. *International Journal of Hydrogen Energy*. 2019;44:19614-19627. <https://doi.org/10.1016/j.ijhydene.2019.05.195>
- Marino C, Nucara A, Panzera MF, Pietrafesa M, Varano V. Energetic and economic analysis of a stand alone photovoltaic system with hydrogen storage. *Renewable Energy*. 2019;142:316-329. <https://doi.org/10.1016/j.renene.2019.04.079>
- Parra D, Walker GS, Gillott M. Modeling of PV generation, battery and hydrogen storage to investigate the benefits of energy storage for single dwelling. *Sustainable Cities and Society*. 2014;10:1-10. <https://doi.org/10.1016/j.scs.2013.04.006>
- Segawa Y, Endo N, Shimoda E, Maeda T. Pilot-scale hydrogen energy utilization system demonstration: A commercial building case study on on-site green hydrogen production and use. *International Journal of Hydrogen Energy*. 2022;47:15982-15991. <https://doi.org/10.1016/j.ijhydene.2022.03.073>
- Cieśliński JT, Kaczmarczyk TZ, Dawidowicz B. Dynamic characteristics of the proton exchange membrane fuel cell module. *Archives of Thermodynamics*. 2018;39(4):125-140. <https://doi.org/10.1515/aoter-2018-0033>
- Eigenversorgung aus Solaranlagen. Das Potenzial für Photovoltaik-Speicher-Systeme in Ein- und Zweifamilienhäusern, Landwirtschaft sowie im Lebensmittelhandel. Analyse im Auftrag von Agora Energiewende. Prognos. 2016;19-20. <https://www.agora-energiewende.de/publikationen/eigenversorgung-aus-solaranlagen>
- Murray P, Orehounig K, Grosspietsch D, Carmeliet J. A comparison of storage systems in neighbourhood decentralized energy system applications from 2015 to 2050. *Applied Energy*. 2018;231:1285-1306. <https://doi.org/10.1016/j.apenergy.2018.08.106>
- Manufacturing Cost Analysis of 100 and 250 kW Fuel Cell Systems for Primary Power and Combined Heat and Power Applications. Battelle Memorial Institute. Battelle. 2017. <https://www.energy.gov/eere/fuelcells/articles/manufacturing-cost-analysis-100-and-250-kw-fuel-cell-systems-primary-power>

Bartosz Dawidowicz:  <https://orcid.org/0000-0002-5592-1785>

Janusz T. Cieśliński:  <https://orcid.org/0000-0002-8919-984X>



This work is licensed under the Creative Commons BY-NC-ND 4.0 license.

DUAL THERMAL ANALYSIS OF FRACTIONAL CONVECTIVE FLOW THROUGH ALUMINUM OXIDE AND TITANIUM DIOXIDE NANOPARTICLES

Qasim ALI^{*}, Rajai S. ALASSAR^{**}, Irfan. A. ABRO^{***}, Kashif. A. ABRO^{****}

^{*}Faculty of Natural Sciences, Department of Mathematics, University of Chakwal, Chakwal 48800, Pakistan

^{**}Faculty of Computing and Mathematics, Department of Mathematics, Interdisciplinary Research Center for Sustainable Energy Systems, King Fahd University of Petroleum & Minerals, Dhahran 31261, Saudi Arabia

^{***}School of Materials Science and Engineering, Beijing Institute of Technology, Beijing 100081, China

^{****}Faculty of Sciences, Technology and Humanities, Department of Basic Sciences and Related Studies, Mehran University of Engineering and Technology, Jamshoro, Pakistan

aliqasim829@gmail.com, rajaiassar@gmail.com, Irfan.abro@bit.edu.cn, kashif.abro@faculty.muett.edu.pk

received 05 January 2024, revised 04 March 2024, accepted 11 March 2024

Abstract: Dual assessing for thermal analysis via nanoparticles (aluminium oxide and titanium dioxide) and base fluids (water and blood) for mixed convection flows over an inclined plate is studied. The governing equations have been developed through fractional formats by exploiting modern definitions of CF (based on exponential function having no singularity) and AB (having non-singular and non-local kernel) fractional derivatives. This is an important theoretical and practical research that models the movement of heat in materials of various scales and heterogeneous media. The solution to the problem is achieved through Laplace transform with slip boundary and magnetic field. To explain the physical perception of fractional models, the dual fractional solutions of velocity field and temperature distribution are derived by comparing non-singularity and non-locality. The fractional solutions through numerical methods namely Stehfest and Tzou's have been invoked. The embedded thermo-dynamical fluctuating parameters have been traced out for the better performance of heat transfer. The results of temperature as well as velocity suggested decaying trends in characterization with rapid thermal analysis.

Keywords: Non-singularized derivative, Mixed convection flow with nanoparticles, Heat transfer of inclined plate, Integral transforms

1. INTRODUCTION

The applications of free convection flow are perceived in many fields of engineering and science such as heat exchangers, solar energy, drying processes, electric components of communication lines, and thermal storage systems. Several of its applications are also found in conservation, ventilation systems, dehydration, concentration, etc. These forms of flow are frequently inspected with a vertical plate in various manufacturing developments i.e., petroleum industry, geothermal phenomena, thermal insulation, etc. The free convection MHD flow with permeable plate by the AB derivatives along with integral transform is studied in [1]. In [2], free convection with NF in the presence of a magnetic field is deliberated by utilizing a fractional approach. A mathematical study with NFs with radiation impact is studied in [3]. A natural convection fluid flow with a long and vertical cylinder is considered in [4]. They studied the impacts of energy as well as mass transfer with time. Different investigators applied various techniques to study convection fluid flow with diverse structures [5-11].

Firstly, Choi presented NFs comprising nanoparticles in 1995. There are numerous uses of NFs in many fields for example fluid dynamics, in many engineering branches, and biomedical fields. NFs are considered the most excellent alternate ways to usual fluids [12-14]. The small particles in the base fluid which progress the competency of the characteristics of NFs for minimizing the system are known as nanoparticles and the key purpose of NFs is to realize the extreme possible heat conduction at a short nanoparticle concentration. The main conclusions have been distinguished because of the chemical configuration of the nanoparticles when are jumped in the base liquid i.e., reduced possibilities of erosion, thermal

transmission, and solidity of the combination. These features play an exceptional part in increasing thermal transmission and energy proficiency in several fields i.e. biomedical instruments, microelectronics, and power generation [15]. Mud nanoparticles consume many practical uses in the penetrating of gasses and oil liquids because of their thermal conduction expressively. The growth of nanoparticles increases the thermal conduction and viscosity of NFs that oppose the intensifying temperature. Currently, because of their extensive uses in many branches of science and technology, NFs are now a fascinating and dominant field for research in fluid mechanics. The impacts of volume fraction and natural convection flow with NFs along with fractional calculus are studied in [16]. A viscous flow with NF (Titania-sodium cellulose) was discussed in [17]. To inspect and enhance the performance of solar accumulators exploited the NFs were studied by Farhana et al. [18]. Jamshed et al. [19-24] applied different techniques to study Eyring NF, Casson NF, second-grade NF, Williamson hybrid NF and tetra hybrid binary NF in different channels. Many researchers applied various methods to study NF flow models with diverse constructions [25-31].

In 1695 [32], firstly, the concept of fractional derivative was given by Leibnitz and L'Hospital which is a proficient tool related to memory facts. Memory function narrates to the kernel of the time-fractional derivative that has not simulated a physical development. Fractional calculus deals with non-local differentiation and integration [33]. The numerical solution of a fractional Oldroyd B-fluid is achieved by the modified Bessel equation as well as the Laplace method [34]. They showed that shear stress is improved as dynamic viscosity is increased. Fractional derivatives are most suitable to the problems of physical nature i.e., earth quick vibrations,

polymers, viscoelasticity, heat transfer problems, fluid flows, etc. Over time, various algorithms and definitions were determined by different mathematicians. To find the solution to various mathematical models, the researchers used different fractional derivatives i.e., Riemann-Liouville, Caputo, CF, and AB derivatives. Fractional models can define more proficiently the consequences of the real nature of world problems such as electromagnetic theory, diffusive transfer, electrical networks, fluid flows, rheology, and viscoelastic materials. Then due to a few complications and limitations, Caputo and Fabrizio proposed the latest non-integer order model named CF fractional derivative along with an exponential and non-singular kernel [35-39].

According to the author's knowledge, there is no investigation on the study of mixed convection flow with Al_2O_3 and TiO_2 nanoparticles with water and blood-based NF in several situations which is a significant theoretical and practical study for the solution of important problems based on the fractional derivative. By getting motivation from these facts, our main purpose is to study a mixed convection flow with Al_2O_3 and TiO_2 nanoparticles with water and blood-based NF along with new definitions of fractional derivatives i.e., AB and CF fractional operators. A semi-analytical approach for AB and CF-based fractional models is applied by the Laplace transform technique along with Stehfest and Tzou's numerical schemes. To improve the novelty of the recent work some particular cases of velocity profile are also deliberated whose physical importance is prominent in the literature. The graphical illustration for the under-discussed mathematical problem by changing diverse flow parameters is underlined.

2. CHAPTER TITLE

We assume that a mixed convection fluid flow with Al_2O_3 and TiO_2 nanoparticles are flowing over an inclined plate with an inclination angle δ with the x -axis. Initially, when $t = 0$, the plate, as well as the fluid, is at rest and ambient medium temperature T_∞ . When $t = 0^+$, the plate moves by a constant value of velocity $\frac{g(t)}{\mu}$ where $g(0) = 0$, and temperature increases from T_∞ to T_w . By this motion of the plate, the fluid begins to move over the plate. Along with all these conditions, it is also supposed the slip impacts the boundaries of the plate. A magnetic field with an angle, θ is also utilized upon the plate as revealed in Fig 1.

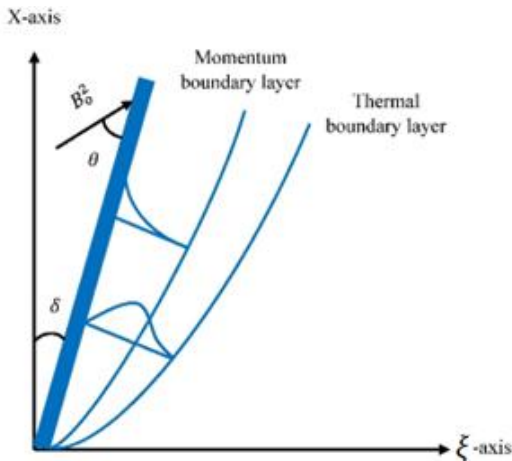


Fig 1. Geometry of the problem

We suppose the characteristics of the physical nanoparticles are from Table 1. The fluid velocity as well as the temperature depends on ξ and t . With Boussinesq's approximation and in the absence of pressure gradient [7, 45], the governing equations are:

Momentum Equation:

$$\rho_{nf} \frac{\partial w(\xi, t)}{\partial t} = \mu_{nf} \left(1 + \alpha_1 \frac{\partial}{\partial t} \right) \frac{\partial^2 w(\xi, t)}{\partial \xi^2} + g(\rho\beta_T)_{nf} [T(\xi, t) - T_\infty] \cos\delta - \sigma_{nf} B_0^2 \sin\theta w(\xi, t); \quad \xi, t > 0. \quad (1)$$

The thermal balance Equation:

$$(\rho C_p)_{nf} \frac{\partial T(\xi, t)}{\partial t} = - \frac{\partial q_1}{\partial \xi}; \quad \xi, t > 0. \quad (2)$$

Fourier law [9]:

$$q_1(\xi, t) = -k_{nf} \frac{\partial T(\xi, t)}{\partial \xi} \quad (3)$$

with the appropriate initial and boundary conditions

$$w(\xi, 0) = 0, \quad T(\xi, 0) = T_\infty; \quad \xi > 0, \quad (4)$$

$$w(0, t) - b \frac{\partial w(\xi, t)}{\partial \xi} \Big|_{\xi=0} = \frac{g(t)}{\mu}, \quad T(0, t) = T_w; \quad t > 0 \quad (5)$$

$$w(\xi, t) \rightarrow 0, \quad T(\xi, t) \rightarrow T_\infty; \quad \xi \rightarrow \infty, \quad t > 0 \quad (6)$$

The appropriate non-dimensional parameters are taken as

$$\xi^* = \frac{\xi v_o}{v_f}, \quad w^* = \frac{w}{U_o}, \quad t^* = \frac{v_o^2 t}{v_f}, \quad \vartheta^* = \frac{T - T_\infty}{T_w - T_\infty},$$

$$b^* = \frac{h}{k} b, \quad q^* = \frac{q}{q_o}, \quad q_o = \frac{k_{nf}(T_w - T_\infty)v_o}{v_f}, \quad g^*(t^*) =$$

$$\frac{1}{\mu} \sqrt{\frac{t_o}{v}} f(t_o t^*). \quad (7)$$

By using the above non-dimensional parameters in Eq. (7), the governing Eqs. (1)-(3) and equivalent conditions (4)-(6) take the form as

$$\frac{\partial w(\xi, t)}{\partial t} = \frac{1}{\Lambda_o \Lambda_1} \left(1 + \beta_1 \frac{\partial}{\partial t} \right) \frac{\partial^2 w(\xi, t)}{\partial \xi^2} + \frac{\Lambda_2}{\Lambda_o} Gr \vartheta(\xi, t) \cos\delta - \frac{1}{\Lambda_o} M \sin\theta w(\xi, t), \quad (8)$$

$$\Lambda_3 Pr \frac{\partial \vartheta(\xi, t)}{\partial t} = - \frac{\partial q(\xi, t)}{\partial \xi}; \quad \xi, t > 0, \quad (9)$$

$$q(\xi, t) = -\Lambda_4 \frac{\partial \vartheta(\xi, t)}{\partial \xi}, \quad (10)$$

along with corresponding conditions

$$w(\xi, 0) = 0, \quad \vartheta(\xi, 0) = 0; \quad \xi > 0 \quad (11)$$

$$w(0, t) - b \frac{\partial w(\xi, t)}{\partial \xi} \Big|_{\xi=0} = g(t), \quad \vartheta(0, t) = 1; \quad t > 0, \quad (12)$$

$$w(\xi, t) \rightarrow 0, \quad \vartheta(\xi, t) \rightarrow 0; \quad \xi \rightarrow \infty, \quad t > 0 \quad (13)$$

where:

$$\rho_{nf} = (1 - \varphi)\rho_f + \varphi\rho_s, \quad \mu_{nf} = \frac{\mu_f}{(1 - \varphi)^{2.5}},$$

$$(\rho\beta)_{nf} = (1 - \varphi)(\rho\beta)_f + \varphi(\rho\beta)_s, \quad (\rho C_p)_{nf} =$$

$$(1 - \varphi)(\rho C_p)_f + \varphi(\rho C_p)_s,$$

$$\frac{k_{nf}}{k_f} = \frac{k_s + 2k_f - 2\varphi(k_f - k_s)}{k_s + 2k_f + 2\varphi(k_f - k_s)}, \quad \frac{\sigma_{nf}}{\sigma_f} = 1 + \left\{ 3 \left(\frac{\sigma_s}{\sigma_f} - 1 \right) \varphi \right\} \left\{ \left(\frac{\sigma_s}{\sigma_f} + 2 \right) - \left(\frac{\sigma_s}{\sigma_f} - 1 \right) \varphi \right\}^{-1},$$

$$\Lambda_o = (1 - \varphi) + \varphi \frac{\rho_s}{\rho_f}, \quad \Lambda_1 = \frac{1}{(1 - \varphi)^{2.5}}, \quad \Lambda_2 = (1 - \varphi) + \varphi \frac{(\rho\beta_T)_s}{(\rho\beta_T)_f},$$

$$\Lambda_3 = (1 - \varphi) + \varphi \frac{(\rho c_p)_s}{(\rho c_p)_f}, \quad \Lambda_4 = \frac{k_{nf}}{k_f}, \quad Pr = \frac{(\mu c_p)_f}{k_f},$$

$$Gr = \frac{g(\beta\nu)_f(T_w - T_\infty)}{U_o^3}, \quad M = \left(\frac{\nu_f}{\nu_o} \right)^2 \frac{\sigma_{nf} B_o^2}{\rho_f \nu_f}, \quad \beta_1 = \alpha_1 \nu_f \left(\frac{\nu_f}{\nu_o} \right)^2.$$

Tab. 1. Thermophysical characteristics of base fluids (water and blood) and nanoparticles [6,38].

| Material | H ₂ O | Blood | Al ₂ O ₃ | TiO ₂ |
|------------------------------|------------------|-------|--------------------------------|------------------|
| $\rho(kgm^{-3})$ | 997.1 | 1053 | 1600 | 4250 |
| $C_p(kg^{-1}k^{-1})$ | 0.4179 | 3594 | 796 | 686.2 |
| $K(Wm^{-1}k^{-1})$ | 0.613 | 0.492 | 3000 | 8.9528 |
| $B_T \times 10^{-5}(k^{-1})$ | 21 | 0.18 | 44 | 0.90 |

2.1. Formulation of governing equations by using non-singular kernels

To formulate the fractional model recent proposed definitions of fractional derivatives i.e., AB and CF derivatives. The AB derivative of order $0 < \beta < 1$ is defined as [41]

$${}^{AB}\mathcal{D}_t^\beta h(t) = \frac{1}{\Gamma(1-\beta)} \int_0^t E_\beta \left(\frac{\beta(t-\varepsilon)^\beta}{(t-\varepsilon)} \right) h'(\varepsilon) d\varepsilon; \quad 0 < \beta < 1$$

(14)

and $E_\beta(z)$ is a Mittag-Leffler function defined by

$$E_\beta(z) = \sum_{r=0}^{\infty} \frac{z^\beta}{\Gamma(r\beta+1)}; \quad 0 < \beta < 1, \quad z \in \mathbb{C}.$$

The Laplace transform for the AB derivative is [42]

$$\mathcal{L}\left\{{}^{AB}\mathcal{D}_t^\beta g(\xi, t)\right\} = \frac{q^\beta \mathcal{L}[g(\xi, t)] - q^{\beta-1} g(\xi, 0)}{(1-\beta)q^\beta + \beta} \quad (15)$$

with

$$\lim_{\beta \rightarrow 1} {}^{AB}\mathcal{D}_t^\beta g(\xi, t) = \frac{\partial g(\xi, t)}{\partial t}.$$

The CF derivative of order $0 < \alpha < 1$ is defined as [37,43]

$${}^{CF}\mathcal{D}_t^\alpha h(t) = \frac{1}{\Gamma(1-\alpha)} \int_0^t \text{Exp} \left(\frac{\beta(t-\varepsilon)^\beta}{(t-\varepsilon)} \right) h'(\varepsilon) d\varepsilon, \quad 0 < \alpha < 1, \quad (16)$$

The Laplace transform for the CF derivative is [27,38]

$$\mathcal{L}\{{}^{CF}\mathcal{D}_t^\alpha g(\xi, t)\} = \frac{q^\alpha \mathcal{L}[g(\xi, t)] - g(\xi, 0)}{(1-\alpha)q + \alpha} \quad (17)$$

with

$$\lim_{\alpha \rightarrow 1} {}^{CF}\mathcal{D}_t^\alpha g(\xi, t) = \frac{\partial g(\xi, t)}{\partial t}.$$

It is important to note that AB and CF fractional operators can also be extended significantly by letting $\beta = 1$ in Eq. (14) and $\alpha = 1$ in Eq. (16) respectively.

The limitation of fractional parameters in derivatives, such as the AB and CF derivatives, to the interval (0,1) derives from their interpretation and physical significance of these values. This range permits for a smooth transition across integer-order derivatives, recording abnormalities as well as long-memory effects in processes, making it ideal for modelling phenomena using sub-diffusive behaviour as well as memory-dependent dynamics in fields such as time series analysis, signal processing, and anomalous diffusion.

3. MODEL OF NANOFLUID WITH AB DERIVATIVE

The model to the problem with AB derivative can be expressed by substituting the ordinary derivative with AB derivative operator in Eqs. (8)-(10), we get

$${}^{AB}\mathcal{D}_t^\beta w(\xi, t) = \frac{1}{\Lambda_o \Lambda_1} \left(1 + \beta_1 {}^{AB}\mathcal{D}_t^\beta \right) \frac{\partial^2 w(\xi, t)}{\partial \xi^2} + \frac{\Lambda_2}{\Lambda_o} Gr \vartheta(\xi, t) \cos \delta - \frac{1}{\Lambda_o} M \sin \theta w(\xi, t), \quad (18)$$

$$\Lambda_3 Pr {}^{AB}\mathcal{D}_t^\beta \vartheta(\xi, t) = - \frac{\partial q(\xi, t)}{\partial \xi}; \quad \xi, t > 0, \quad (19)$$

$$q(\xi, t) = -\Lambda_4 \frac{\partial \vartheta(\xi, t)}{\partial \xi}. \quad (20)$$

3.1. Temperature with ab derivative

By employing the Laplace transform on Eqs. (19) and (20), we get

$$\frac{\partial^2 \bar{\vartheta}(\xi, q)}{\partial \xi^2} - \frac{\Lambda_3 Pr}{\Lambda_4} \left(\frac{q^\beta}{(1-\beta)q^\beta + \beta} \right) \bar{\vartheta}(\xi, q) = 0, \quad (21)$$

where $\bar{\vartheta}(\xi, q)$ is the Laplace transform for $\vartheta(\xi, t)$, and the transformed conditions after Laplace transform are as follows

$$\bar{\vartheta}(\xi, q) = \frac{1}{q} \quad \text{and} \quad \bar{\vartheta}(\xi, q) \rightarrow 0 \quad \text{as} \quad \xi \rightarrow \infty. \quad (22)$$

With the above conditions of Eq. (22), we get the temperature as

$$\bar{\vartheta}(\xi, q) = \frac{1}{q} e^{-\xi \sqrt{\frac{\Lambda_3 Pr}{\Lambda_4} \left(\frac{q^\beta}{(1-\beta)q^\beta + \beta} \right)}}. \quad (23)$$

Eq (23) can be written as

$$\bar{\vartheta}(\xi, q) = \frac{1}{q} e^{-\xi \sqrt{\frac{c_1 q^\gamma}{q^\gamma + c_2}}} \quad (24)$$

where:

$$c_1 = \frac{\Lambda_3 Pr \gamma}{\Lambda_4}, \quad c_2 = \beta \gamma, \quad \gamma = \frac{1}{1-\beta}.$$

Eq (24) can also be written in summation form as

$$\bar{\vartheta}(\xi, q) = \frac{1}{q} + \sum_{a_1=1}^{\infty} \sum_{a_2=0}^{\infty} \frac{(-\xi \sqrt{c_1})^{a_1}}{a_1!} \frac{(-c_2)^{a_2}}{q^{1+a_2} \beta} \frac{\Gamma(\frac{a_1}{2} + a_2)}{\Gamma(\frac{a_1}{2}) \Gamma(a_2 + 1)} \quad (25)$$

By taking the Laplace inverse of Eq. (25), we have

$$\vartheta(\xi, t) = 1 + \sum_{a_1=1}^{\infty} \sum_{a_2=0}^{\infty} \frac{(-\xi \sqrt{c_1})^{a_1}}{a_1!} \frac{\Gamma(\frac{a_1}{2} + a_2)}{\Gamma(\frac{a_1}{2}) \Gamma(a_2 + 1)} \frac{(-c_2)^{a_2} t^{a_2} \beta}{\Gamma(1 + a_2 \beta)} \quad (26)$$

When $\beta \rightarrow 1$, Eq. (26) becomes

$$\vartheta(\xi, t) = \frac{\xi \left(1 - \operatorname{erf} \left(\frac{|\xi| \sqrt{\Lambda_3 Pr}}{2 \sqrt{\Lambda_4 t}} \right) \right)}{|\xi|}; \quad \xi, \sqrt{\frac{\Lambda_3 Pr}{\Lambda_4}} > 0. \quad (27)$$

3.2. Velocity with ab derivative

By using the Laplace transform on Eq. (18), we get

$$\left(\frac{q^\beta}{(1-\beta)q^\beta + \beta} \right) \bar{w}(\xi, q) = \frac{1}{\Lambda_0 \Lambda_1} \left(1 + \beta_1 \frac{q^\beta}{(1-\beta)q^\beta + \beta} \right) \frac{\partial^2 \bar{w}(\xi, q)}{\partial \xi^2} + \frac{\Lambda_2}{\Lambda_0} Gr \cos \delta \bar{\vartheta}(\xi, q) - \frac{1}{\Lambda_0} M \sin \theta \bar{w}(\xi, q) \quad (28)$$

with the corresponding conditions

$$\bar{w}(0, q) - b \frac{\partial \bar{w}(\xi, q)}{\partial \xi} \Big|_{\xi=0} = G(q)$$

and

$$\bar{w}(\xi, q) \rightarrow 0 \quad \text{as} \quad \xi \rightarrow \infty. \quad (29)$$

Eq (28) is solved by utilizing Eq. (29) and we get

$$\bar{w}(\xi, q) = \frac{1}{1+b \sqrt{\frac{\Lambda_0 \Lambda_1 \gamma q^\beta + (q^\beta + \beta \gamma) \Lambda_1 M \sin \theta}{q^\beta + \beta \gamma + \beta_1 q^\beta \gamma}}} \left(\frac{\Lambda_2 Gr \cos \delta}{\Lambda_0 q} \frac{1}{\frac{\Lambda_3 Pr}{\Lambda_4} \left(\frac{q^\beta \gamma}{q^\beta + \beta \gamma} \right) - \frac{\Lambda_0 \Lambda_1 \gamma q^\beta + (q^\beta + \beta \gamma) \Lambda_1 M \sin \theta}{q^\beta + \beta \gamma + \beta_1 q^\beta \gamma}} \left(1 + b \sqrt{\frac{\Lambda_3 Pr}{\Lambda_4} \left(\frac{q^\beta \gamma}{q^\beta + \beta \gamma} \right)} + G(q) \right) e^{-\xi \sqrt{\frac{\Lambda_0 \Lambda_1 \gamma q^\beta + (q^\beta + \beta \gamma) \Lambda_1 M \sin \theta}{q^\beta + \beta \gamma + \beta_1 q^\beta \gamma}}} \right)$$

$$- \frac{\Lambda_2 Gr \cos \delta}{\Lambda_0 q} \frac{1}{\frac{\Lambda_3 Pr}{\Lambda_4} \left(\frac{q^\beta \gamma}{q^\beta + \beta \gamma} \right) - \frac{\Lambda_0 \Lambda_1 \gamma q^\beta + (q^\beta + \beta \gamma) \Lambda_1 M \sin \theta}{q^\beta + \beta \gamma + \beta_1 q^\beta \gamma}} e^{-\xi \sqrt{\frac{\Lambda_3 Pr}{\Lambda_4} \left(\frac{q^\beta \gamma}{q^\beta + \beta \gamma} \right)}}. \quad (30)$$

When $\beta \rightarrow 1$, Eq. (30) becomes

$$\bar{w}(\xi, q) = \frac{1}{1+b \sqrt{\frac{\Lambda_0 \Lambda_1 q + \Lambda_1 M \sin \theta}{1+\beta_1 q}}} \left(\frac{\Lambda_2 Gr \cos \delta}{\Lambda_0 q} \frac{1}{\frac{\Lambda_3 Pr}{\Lambda_4} q - \frac{\Lambda_0 \Lambda_1 q + \Lambda_1 M \sin \theta}{1+\beta_1 q}} \left(1 + b \sqrt{\frac{\Lambda_3 Pr}{\Lambda_4} q} + G(q) \right) e^{-\xi \sqrt{\frac{\Lambda_0 \Lambda_1 q + \Lambda_1 M \sin \theta}{1+\beta_1 q}}} - \frac{\Lambda_2 Gr \cos \delta}{\Lambda_0 q} \frac{1}{\frac{\Lambda_3 Pr}{\Lambda_4} q - \frac{\Lambda_0 \Lambda_1 q + \Lambda_1 M \sin \theta}{1+\beta_1 q}} e^{-\xi \sqrt{\frac{\Lambda_3 Pr}{\Lambda_4} q}} \right) \quad (31)$$

The Laplace inverse of these solutions is determined numerically through Stehfest as well as Tzou's approaches as in Tables 2-3.

4. MODEL OF NANOFLUID WITH CF DERIVATIVE

In the above section, the temperature, as well as velocity, is determined by using the AB-fractional derivative, now the modelling of governing equations by CF-fractional derivative may be expressed by replacing the ordinary derivative with CF-fractional derivative operative ${}^{CF}\mathcal{D}_t^\alpha$, the governing equations for the CF-fractional derivative model are attained as

$${}^{CF}\mathcal{D}_t^\alpha w(\xi, t) = \frac{1}{\Lambda_0 \Lambda_1} (1 + \beta_1 {}^{CF}\mathcal{D}_t^\alpha) \frac{\partial^2 w(\xi, t)}{\partial \xi^2} + \frac{\Lambda_2}{\Lambda_0} Gr \vartheta(\xi, t) \cos \delta - \frac{1}{\Lambda_0} M \sin \theta w(\xi, t), \quad (32)$$

$$\Lambda_3 Pr {}^{CF}\mathcal{D}_t^\alpha \vartheta(\xi, t) = - \frac{\partial q(\xi, t)}{\partial \xi}; \quad \xi, t > 0, \quad (33)$$

$$q(\xi, t) = -\Lambda_4 \frac{\partial \vartheta(\xi, t)}{\partial \xi}. \quad (34)$$

4.1. Temperature with cf derivative

By taking Laplace transform on Eqs. (33), and (34), we get

$$\frac{\partial^2 \bar{\vartheta}(\xi, q)}{\partial \xi^2} - \frac{\Lambda_3 Pr}{\Lambda_4} \left(\frac{q}{(1-\alpha)q + \alpha} \right) \bar{\vartheta}(\xi, q) = 0. \quad (35)$$

By using the corresponding conditions of Eq. (22), the solution of Eq. (35) is

$$\bar{\vartheta}(\xi, q) = \frac{1}{q} e^{-\xi \sqrt{\frac{\Lambda_3 Pr}{\Lambda_4} \left(\frac{q}{(1-\alpha)q + \alpha} \right)}}. \quad (36)$$

Eq (36) can be written as

$$\bar{\vartheta}(\xi, q) = \frac{1}{q} e^{-\xi \sqrt{\frac{d_1 q}{q + d_2}}} \quad (37)$$

Where

$$d_1 = \frac{\Lambda_3 Pr \gamma}{\Lambda_4}, \quad d_2 = \alpha \gamma, \quad \gamma = \frac{1}{1-\alpha}$$

Eq (37) may be written in summation form as

$$\bar{\vartheta}(\xi, q) = \frac{1}{q} + \sum_{a_1=1}^{\infty} \sum_{a_2=0}^{\infty} \frac{(-\xi \sqrt{d_1})^{a_1}}{a_1!} \frac{(-d_2)^{a_2}}{q^{1+a_2}} \frac{\Gamma(\frac{a_1}{2} + a_2)}{\Gamma(\frac{a_1}{2}) \Gamma(a_2 + 1)} \quad (38)$$

By utilizing the Laplace inverse of Eq. (38), we have

$$\vartheta(\xi, t) = 1 + \sum_{a_1=1}^{\infty} \sum_{a_2=0}^{\infty} \frac{(-\xi \sqrt{d_1})^{a_1}}{a_1!} \frac{(-d_2)^{a_2}}{\Gamma(a_2 + 1)} \frac{t^{a_2}}{\Gamma(\frac{a_1}{2}) \Gamma(a_2 + 1)} \quad (39)$$

For the special case for ordinary solution replace $\alpha \rightarrow 1$ in Eq (39), and then the solution will be

$$\vartheta(\xi, t) = \frac{\xi \left(1 - \operatorname{erf} \left(\frac{|\xi| \sqrt{\Lambda_3 Pr}}{2 \sqrt{\Lambda_4 t}} \right) \right)}{|\xi|}; \quad \xi, \sqrt{\frac{\Lambda_3 Pr}{\Lambda_4}} > 0. \quad (40)$$

4.2. Velocity with cf derivative

By using the Laplace transform on Eqs. (32), we get

$$\left(\frac{s}{(1-\alpha)s + \alpha} \right) \bar{w}(\xi, s) = \frac{1}{\Lambda_0 \Lambda_1} \left(1 + \beta_1 \left(\frac{s}{(1-\alpha)s + \alpha} \right) \right) \frac{\partial^2 \bar{w}(\xi, s)}{\partial \xi^2} + \frac{\Lambda_2}{\Lambda_0} Gr \bar{\vartheta}(\xi, s) \cos \delta - \frac{1}{\Lambda_0} M \sin \theta \bar{w}(\xi, s). \quad (41)$$

By solving Eq (41) with the corresponding conditions in Eq. (29), we get

$$\bar{w}(\xi, q) = \frac{1}{1 + b \sqrt{\frac{\Lambda_0 \Lambda_1 \gamma q + (q + \alpha \gamma) \Lambda_1 M \sin \theta}{q + \alpha \gamma + \beta_1 q \gamma}}} \left(\frac{\Lambda_2 Gr \cos \delta}{\Lambda_0 s} \frac{1}{\frac{\Lambda_3 Pr}{\Lambda_4} \left(\frac{q \gamma}{q + \alpha \gamma} \right) - \frac{\Lambda_0 \Lambda_1 \gamma q + (q + \alpha \gamma) \Lambda_1 M \sin \theta}{q + \alpha \gamma + \beta_1 q \gamma}} \left(1 + b \sqrt{\frac{\Lambda_3 Pr}{\Lambda_4} \left(\frac{q \gamma}{q + \alpha \gamma} \right)} \right) + G(q) \right) e^{-\xi \sqrt{\frac{\Lambda_0 \Lambda_1 \gamma q + (q + \alpha \gamma) \Lambda_1 M \sin \theta}{q + \alpha \gamma + \beta_1 q \gamma}}} - \frac{\Lambda_2 Gr \cos \delta}{\Lambda_0 q} \frac{1}{\frac{\Lambda_3 Pr}{\Lambda_4} \left(\frac{q \gamma}{q + \alpha \gamma} \right) - \frac{\Lambda_0 \Lambda_1 \gamma q + (q + \alpha \gamma) \Lambda_1 M \sin \theta}{q + \alpha \gamma + \beta_1 q \gamma}} e^{-\xi \sqrt{\frac{\Lambda_3 Pr}{\Lambda_4} \left(\frac{q \gamma}{q + \alpha \gamma} \right)}}. \quad (42)$$

When $\alpha \rightarrow 1$, Eq. (42) becomes

$$\bar{w}(\xi, q) = \frac{1}{1 + b \sqrt{\frac{\Lambda_0 \Lambda_1 q + \Lambda_1 M \sin \theta}{1 + \beta_1 q}}} \left(\frac{\Lambda_2 Gr \cos \delta}{\Lambda_0 q} \frac{1}{\frac{\Lambda_3 Pr}{\Lambda_4} q - \frac{\Lambda_0 \Lambda_1 q + \Lambda_1 M \sin \theta}{1 + \beta_1 q}} \left(1 + b \sqrt{\frac{\Lambda_3 Pr}{\Lambda_4} q} \right) + G(q) \right) e^{-\xi \sqrt{\frac{\Lambda_0 \Lambda_1 q + \Lambda_1 M \sin \theta}{1 + \beta_1 q}}} - \frac{\Lambda_2 Gr \cos \delta}{\Lambda_0 q} \frac{1}{\frac{\Lambda_3 Pr}{\Lambda_4} q - \frac{\Lambda_0 \Lambda_1 q + \Lambda_1 M \sin \theta}{1 + \beta_1 q}} e^{-\xi \sqrt{\frac{\Lambda_3 Pr}{\Lambda_4} q}}. \quad (43)$$

$$\left(b \sqrt{\frac{\Lambda_3 Pr}{\Lambda_4} q} + G(q) \right) e^{-\xi \sqrt{\frac{\Lambda_0 \Lambda_1 q + \Lambda_1 M \sin \theta}{1 + \beta_1 q}}} - \frac{\Lambda_2 Gr \cos \delta}{\Lambda_0 q} \frac{1}{\frac{\Lambda_3 Pr}{\Lambda_4} q - \frac{\Lambda_0 \Lambda_1 q + \Lambda_1 M \sin \theta}{1 + \beta_1 q}} e^{-\xi \sqrt{\frac{\Lambda_3 Pr}{\Lambda_4} q}}. \quad (43)$$

To find out the Laplace inverse, various researchers applied different numerical approaches to find the solution of diverse differential fractional models as in [44-47]. Consequently, here we will also utilize the Stehfest scheme to find the numerical solution of temperature as well as velocity numerically. Grave Stehfest scheme [48] can be expressed as

$$w(\xi, t) = \frac{\ln(2)}{t} \sum_{n=1}^M v_n \bar{w} \left(\xi, n \frac{\ln(2)}{t} \right) \quad (44)$$

where M be a non-negative integer, and

$$v_n = (-1)^{n+\frac{M}{2}} \sum_{p=\lfloor \frac{q+1}{2} \rfloor}^{\min(q, \frac{M}{2})} \frac{p^{\frac{M}{2}} (2p)!}{(\frac{M}{2}-p)! p! (p-1)! (q-p)! (2p-q)!} \quad (45)$$

However, we also applied another estimation for temperature as well as velocity solutions, Tzou's method for the comparison and validation of our numerical findings with the Stehfest [48] scheme. Tzou's scheme [49] has the form as

$$w(\xi, t) = \frac{e^{4.7}}{t} \left[\frac{1}{2} \bar{w} \left(r, \frac{4.7}{t} \right) + \operatorname{Re} \left\{ \sum_{j=1}^N (-1)^k \bar{w} \left(r, \frac{4.7 + k \pi i}{t} \right) \right\} \right] \quad (46)$$

where i and $\operatorname{Re}(\cdot)$ are imaginary units and real portions and $N > 1$ is a natural number.

5. PARTICULAR CASES

As the solution of the velocity field with AB and CF derivative in Eq. (30) and (42) correspondingly, is in a more general form. Consequently, to demonstrate some more physical perception of the problem, we will deliberate some particular cases for the function $g(t)$ for the velocity whose physical explanation is prominent in the literature.

Case 1: $g(t) = t$

In this case, we take $g(t) = t$ then the expressions of velocity with AB and CF derivative along with Eqs. (30) and (42) respectively will take the form as

$$\bar{w}(\xi, q) = \frac{1}{1 + b \sqrt{\frac{\Lambda_0 \Lambda_1 \gamma q^\beta + (q^\beta + \beta \gamma) \Lambda_1 M \sin \theta}{q^\beta + \beta \gamma + \beta_1 q^\beta \gamma}}} \left(\frac{\Lambda_2 Gr \cos \delta}{\Lambda_0 q} \frac{1}{\frac{\Lambda_3 Pr}{\Lambda_4} \left(\frac{q^\beta \gamma}{q^\beta + \beta \gamma} \right) - \frac{\Lambda_0 \Lambda_1 \gamma q^\beta + (q^\beta + \beta \gamma) \Lambda_1 M \sin \theta}{q^\beta + \beta \gamma + \beta_1 q^\beta \gamma}} \left(1 + b \sqrt{\frac{\Lambda_3 Pr}{\Lambda_4} \left(\frac{q^\beta \gamma}{q^\beta + \beta \gamma} \right)} \right) + \frac{1}{q^2} \right) e^{-\xi \sqrt{\frac{\Lambda_0 \Lambda_1 \gamma q^\beta + (q^\beta + \beta \gamma) \Lambda_1 M \sin \theta}{q^\beta + \beta \gamma + \beta_1 q^\beta \gamma}}} - \frac{\Lambda_2 Gr \cos \delta}{\Lambda_0 q} \frac{1}{\frac{\Lambda_3 Pr}{\Lambda_4} \left(\frac{q^\beta \gamma}{q^\beta + \beta \gamma} \right) - \frac{\Lambda_0 \Lambda_1 \gamma q^\beta + (q^\beta + \beta \gamma) \Lambda_1 M \sin \theta}{q^\beta + \beta \gamma + \beta_1 q^\beta \gamma}} e^{-\xi \sqrt{\frac{\Lambda_3 Pr}{\Lambda_4} \left(\frac{q^\beta \gamma}{q^\beta + \beta \gamma} \right)}}. \quad (47)$$

$$\text{and } \bar{w}(\xi, q) = \frac{1}{1+b \sqrt{\frac{\Lambda_0 \Lambda_1 \gamma q + (q+\alpha\gamma) \Lambda_1 M \sin \theta}{q+\alpha\gamma+\beta_1 q\gamma}}} \left(\frac{\Lambda_2 Gr \cos \delta}{\Lambda_0 q} \frac{1}{\frac{\Lambda_3 Pr \left(\frac{q\gamma}{q+\alpha\gamma} \right) - \frac{\Lambda_0 \Lambda_1 \gamma q + (q+\alpha\gamma) \Lambda_1 M \sin \theta}{q+\alpha\gamma+\beta_1 q\gamma}} \left(1 + b \sqrt{\frac{\Lambda_3 Pr \left(\frac{q\gamma}{q+\alpha\gamma} \right)}{\Lambda_4}} + \frac{1}{q^2} \right) e^{-\xi \sqrt{\frac{\Lambda_0 \Lambda_1 \gamma q + (q+\alpha\gamma) \Lambda_1 M \sin \theta}{q+\alpha\gamma+\beta_1 q\gamma}}} - \frac{\Lambda_2 Gr \cos \delta}{\Lambda_0 s} \frac{1}{\frac{\Lambda_3 Pr \left(\frac{q\gamma}{q+\alpha\gamma} \right) - \frac{\Lambda_0 \Lambda_1 \gamma q + (q+\alpha\gamma) \Lambda_1 M \sin \theta}{q+\alpha\gamma+\beta_1 q\gamma}} e^{-\xi \sqrt{\frac{\Lambda_3 Pr \left(\frac{q\gamma}{q+\alpha\gamma} \right)}{\Lambda_4}}} \right). \quad (48)$$

Case 2: $g(t) = \sin(\omega t)$

In this case, we take $g(t) = \sin(\omega t)$ where ω denotes the intensity of the shear stress, then the expressions for velocity with AB and CF derivative with Eqs. (30) and (42) correspondingly will take the form as

$$\bar{w}(\xi, q) = \frac{1}{1+b \sqrt{\frac{\Lambda_0 \Lambda_1 \gamma q^\beta + (q^\beta + \beta\gamma) \Lambda_1 M \sin \theta}{q^\beta + \beta\gamma + \beta_1 q^\beta \gamma}}} \left(\frac{\Lambda_2 Gr \cos \delta}{\Lambda_0 q} \frac{1}{\frac{\Lambda_3 Pr \left(\frac{q^\beta \gamma}{q^\beta + \beta\gamma} \right) - \frac{\Lambda_0 \Lambda_1 \gamma q^\beta + (q^\beta + \beta\gamma) \Lambda_1 M \sin \theta}{q^\beta + \beta\gamma + \beta_1 q^\beta \gamma}} \left(1 + b \sqrt{\frac{\Lambda_3 Pr \left(\frac{q^\beta \gamma}{q^\beta + \beta\gamma} \right)}{\Lambda_4}} + \frac{\omega}{\omega^2 + q^2} \right) e^{-\xi \sqrt{\frac{\Lambda_0 \Lambda_1 \gamma q^\beta + (q^\beta + \beta\gamma) \Lambda_1 M \sin \theta}{q^\beta + \beta\gamma + \beta_1 q^\beta \gamma}}} - \frac{\Lambda_2 Gr \cos \delta}{\Lambda_0 q} \frac{1}{\frac{\Lambda_3 Pr \left(\frac{q^\beta \gamma}{q^\beta + \beta\gamma} \right) - \frac{\Lambda_0 \Lambda_1 \gamma q^\beta + (q^\beta + \beta\gamma) \Lambda_1 M \sin \theta}{q^\beta + \beta\gamma + \beta_1 q^\beta \gamma}} e^{-\xi \sqrt{\frac{\Lambda_3 Pr \left(\frac{q^\beta \gamma}{q^\beta + \beta\gamma} \right)}{\Lambda_4}}} \right) \quad (49)$$

and

$$\bar{w}(\xi, q) = \frac{1}{1+b \sqrt{\frac{\Lambda_0 \Lambda_1 \gamma q + (q+\alpha\gamma) \Lambda_1 M \sin \theta}{q+\alpha\gamma+\beta_1 q\gamma}}} \left(\frac{\Lambda_2 Gr \cos \delta}{\Lambda_0 q} \frac{1}{\frac{\Lambda_3 Pr \left(\frac{q\gamma}{q+\alpha\gamma} \right) - \frac{\Lambda_0 \Lambda_1 \gamma q + (q+\alpha\gamma) \Lambda_1 M \sin \theta}{q+\alpha\gamma+\beta_1 q\gamma}} \left(1 + b \sqrt{\frac{\Lambda_3 Pr \left(\frac{q\gamma}{q+\alpha\gamma} \right)}{\Lambda_4}} + \frac{\omega}{\omega^2 + q^2} \right) e^{-\xi \sqrt{\frac{\Lambda_0 \Lambda_1 \gamma q + (q+\alpha\gamma) \Lambda_1 M \sin \theta}{q+\alpha\gamma+\beta_1 q\gamma}}} - \frac{\Lambda_2 G \cos \delta}{\Lambda_0 q} \frac{1}{\frac{\Lambda_3 Pr \left(\frac{q\gamma}{q+\alpha\gamma} \right) - \frac{\Lambda_0 \Lambda_1 \gamma q + (q+\alpha\gamma) \Lambda_1 M \sin \theta}{q+\alpha\gamma+\beta_1 q\gamma}} e^{-\xi \sqrt{\frac{\Lambda_3 Pr \left(\frac{q\gamma}{q+\alpha\gamma} \right)}{\Lambda_4}}} \right) \quad (50)$$

Case 3: $g(t) = t \cos(t)$

In this case, we take $g(t) = t \cos t$ with its Laplace $G(q) = \frac{q^2-1}{(q^2+1)^2}$, then the expressions of velocity through AB and CF derivative along with Eqs. (30) and (42) correspondingly will take the form as

$$\bar{w}(\xi, q) = \frac{1}{1+b \sqrt{\frac{\Lambda_0 \Lambda_1 \gamma q^\beta + (q^\beta + \beta\gamma) \Lambda_1 M \sin \theta}{q^\beta + \beta\gamma + \beta_1 q^\beta \gamma}}}$$

$$\left(\frac{\Lambda_2 Gr \cos \delta}{\Lambda_0 q} \frac{1}{\frac{\Lambda_3 Pr \left(\frac{q^\beta \gamma}{q^\beta + \beta\gamma} \right) - \frac{\Lambda_0 \Lambda_1 \gamma q^\beta + (q^\beta + \beta\gamma) \Lambda_1 M \sin \theta}{q^\beta + \beta\gamma + \beta_1 q^\beta \gamma}} \left(1 + b \sqrt{\frac{\Lambda_3 Pr \left(\frac{q^\beta \gamma}{q^\beta + \beta\gamma} \right)}{\Lambda_4}} + \frac{q^2-1}{(1+q^2)^2} \right) e^{-\xi \sqrt{\frac{\Lambda_0 \Lambda_1 \gamma q^\beta + (q^\beta + \beta\gamma) \Lambda_1 M \sin \theta}{q^\beta + \beta\gamma + \beta_1 q^\beta \gamma}}} - \frac{\Lambda_2 Gr \cos \delta}{\Lambda_0 q} \frac{1}{\frac{\Lambda_3 Pr \left(\frac{q^\beta \gamma}{q^\beta + \beta\gamma} \right) - \frac{\Lambda_0 \Lambda_1 \gamma q^\beta + (q^\beta + \beta\gamma) \Lambda_1 M \sin \theta}{q^\beta + \beta\gamma + \beta_1 q^\beta \gamma}} e^{-\xi \sqrt{\frac{\Lambda_3 Pr \left(\frac{q^\beta \gamma}{q^\beta + \beta\gamma} \right)}{\Lambda_4}}} \right) \quad (51)$$

and

$$\bar{w}(\xi, q) = \frac{1}{1+b \sqrt{\frac{\Lambda_0 \Lambda_1 \gamma q + (q+\alpha\gamma) \Lambda_1 M \sin \theta}{q+\alpha\gamma+\beta_1 q\gamma}}} \left(\frac{\Lambda_2 Gr \cos \delta}{\Lambda_0 q} \frac{1}{\frac{\Lambda_3 Pr \left(\frac{q\gamma}{q+\alpha\gamma} \right) - \frac{\Lambda_0 \Lambda_1 \gamma q + (q+\alpha\gamma) \Lambda_1 M \sin \theta}{q+\alpha\gamma+\beta_1 q\gamma}} \left(1 + b \sqrt{\frac{\Lambda_3 Pr \left(\frac{q\gamma}{q+\alpha\gamma} \right)}{\Lambda_4}} + \frac{q^2-1}{(1+q^2)^2} \right) e^{-\xi \sqrt{\frac{\Lambda_0 \Lambda_1 \gamma q + (q+\alpha\gamma) \Lambda_1 M \sin \theta}{q+\alpha\gamma+\beta_1 q\gamma}}} - \frac{\Lambda_2 Gr \cos \delta}{\Lambda_0 q} \frac{1}{\frac{\Lambda_3 Pr \left(\frac{q\gamma}{q+\alpha\gamma} \right) - \frac{\Lambda_0 \Lambda_1 \gamma q + (q+\alpha\gamma) \Lambda_1 M \sin \theta}{q+\alpha\gamma+\beta_1 q\gamma}} e^{-\xi \sqrt{\frac{\Lambda_3 Pr \left(\frac{q\gamma}{q+\alpha\gamma} \right)}{\Lambda_4}}} \right). \quad (52)$$

Case 4: $g(t) = t e^t$

In the final case, we take $g(t) = t e^t$ with its Laplace $G(q) = \frac{1}{(q-1)^2}$, then the expressions of velocity through AB and CF derivative along with Eqs. (30), and (42) correspondingly will take the form as

$$\bar{w}(\xi, q) = \frac{1}{1+b \sqrt{\frac{\Lambda_0 \Lambda_1 \gamma q^\beta + (q^\beta + \beta\gamma) \Lambda_1 M \sin \theta}{q^\beta + \beta\gamma + \beta_1 q^\beta \gamma}}} \left(\frac{\Lambda_2 Gr \cos \delta}{\Lambda_0 q} \frac{1}{\frac{\Lambda_3 Pr \left(\frac{q^\beta \gamma}{q^\beta + \beta\gamma} \right) - \frac{\Lambda_0 \Lambda_1 \gamma q^\beta + (q^\beta + \beta\gamma) \Lambda_1 M \sin \theta}{q^\beta + \beta\gamma + \beta_1 q^\beta \gamma}} \left(1 + b \sqrt{\frac{\Lambda_3 Pr \left(\frac{q^\beta \gamma}{q^\beta + \beta\gamma} \right)}{\Lambda_4}} + \frac{1}{(q-1)^2} \right) e^{-\xi \sqrt{\frac{\Lambda_0 \Lambda_1 \gamma q^\beta + (q^\beta + \beta\gamma) \Lambda_1 M \sin \theta}{q^\beta + \beta\gamma + \beta_1 q^\beta \gamma}}} - \frac{\Lambda_2 Gr \cos \delta}{\Lambda_0 q} \frac{1}{\frac{\Lambda_3 Pr \left(\frac{q^\beta \gamma}{q^\beta + \beta\gamma} \right) - \frac{\Lambda_0 \Lambda_1 \gamma q^\beta + (q^\beta + \beta\gamma) \Lambda_1 M \sin \theta}{q^\beta + \beta\gamma + \beta_1 q^\beta \gamma}} e^{-\xi \sqrt{\frac{\Lambda_3 Pr \left(\frac{q^\beta \gamma}{q^\beta + \beta\gamma} \right)}{\Lambda_4}}} \right) \quad (53)$$

$$\text{and } \bar{w}(\xi, q) = \frac{1}{1+b \sqrt{\frac{\Lambda_0 \Lambda_1 \gamma q + (q+\alpha\gamma) \Lambda_1 M \sin \theta}{q+\alpha\gamma+\beta_1 q\gamma}}} \left(\frac{\Lambda_2 Gr \cos \delta}{\Lambda_0 q} \frac{1}{\frac{\Lambda_3 Pr (q\gamma)}{\Lambda_4 (q+\alpha\gamma)} - \frac{\Lambda_0 \Lambda_1 \gamma q + (q+\alpha\gamma) \Lambda_1 M \sin \theta}{q+\alpha\gamma+\beta_1 q\gamma}} \left(1 + b \sqrt{\frac{\Lambda_3 Pr (q\gamma)}{\Lambda_4 (q+\alpha\gamma)}} + \frac{1}{(q-1)^2} \right) e^{-\xi \sqrt{\frac{\Lambda_0 \Lambda_1 \gamma q + (q+\alpha\gamma) \Lambda_1 M \sin \theta}{q+\alpha\gamma+\beta_1 q\gamma}}} - \frac{\Lambda_2 Gr \cos \delta}{\Lambda_0 q} \frac{1}{\frac{\Lambda_3 Pr (q\gamma)}{\Lambda_4 (q+\alpha\gamma)} - \frac{\Lambda_0 \Lambda_1 \gamma q + (q+\alpha\gamma) \Lambda_1 M \sin \theta}{q+\alpha\gamma+\beta_1 q\gamma}} e^{-\xi \sqrt{\frac{\Lambda_3 Pr (q\gamma)}{\Lambda_4 (q+\alpha\gamma)}}} \right) \quad (54)$$

6. RESULTS AND DISCUSSION

The mixed convection fluid flow with Al_2O_3 and TiO_2 nanoparticles with water and blood as base fluids are investigated with a slip effect at the boundaries on an inclined plane under the magnetic field by using AB and CF derivative schemes. The solution for the considered problem is explored with the Laplace scheme and numerical approaches i.e., Stehfest and Tzou for the inversion phenomenon of the Laplace transform. To obtain some physical features of velocity attained with AB and CF derivatives, some particular cases are also discussed. For studying the impacts of diverse flow parameters i.e., fractional parameters (α, β) , angle of inclination, magnetic parameter, volume fraction, Pr , and Grashof number, graphical diagrams are presented in Figs 2-9 through Mathematica.

The impact of fractional parameters (α, β) , on temperature is shown in Figs. 2(a, b). By raising the estimations of α, β , the temperature illustrates decaying behaviour (at a small time) and an increasing trend at a large time, consequently, we see that the fractional parameters have dual behaviour (for small and large time) for temperature. This specifies the consequence of the CF and AB fractional operators that promise to illustrate the generalized memory and hereditary features. This is due to the different properties of CF (based on exponential function having no singularity) and AB (having non-singular and non-local kernel) fractional operators. From Fig. 3a, as improvement in the estimations of Pr shows that development in the viscosity of liquid declines the difference among thermal boundary layers of the liquid, so the temperature profile declines because of the rises in the estimations of Pr and in the same way, the comparison of two nanofluids is shown in Fig. 3b by considering other parameters constant and changing the fractional parameters α, β . We see that the temperature of the blood-based NF is smaller than the water-based nanofluid, which is due to the physical characteristics of certain nanoparticles.

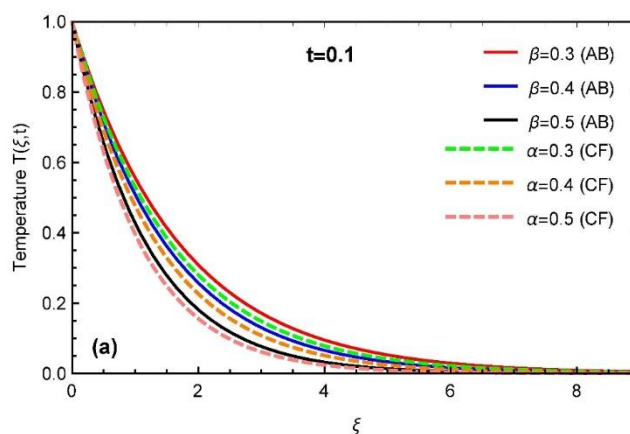
From Figs. 4a and 4b, we see that the velocity of fluid also decelerates by enhancing the estimation of α, β for a small time but speeds up at a large time. This is also due to the diverse properties of CF (based on exponential function having no singularity) and AB (having non-singular and non-local kernel) fractional operators. The fluid velocity is increased as Gr grows as shown in 5a. The velocity increases because of enhancing the values Gr . The relative impact of the heat buoyant behaviour on the viscous force is investigated using Gr . Such effects happen because of the existence of buoyant forces. An enhancement in the Pr declines the fluid velocity due to

development in the fluid viscosity as in 5b Pr is inversely related to thermal diffusivity, resulting in declining heat transmission. The effect of volume fraction (φ) on velocity is illustrated in Fig 6a with the variation in time. The increase in volume fraction enhances the viscous impact of fluid flow which slows down the velocity of the fluid.

In Figs. 7a and 7b, growing the estimation of the magnetic parameter slows down the fluid velocity. Larger estimates of M lead to decreased velocity. Physical applications for such observations are because of the Lorentz force which produces a resistance in the flow. Similarly, the behaviour of the inclination angle of the magnetic field is shown in Fig 7b. The growth in the inclination angle declines the influence of the magnetic field which conveys off the Lorentz force effect, so by growing the estimation of the inclination angle, the fluid velocity again decreases. For $\theta = \pi/2$ (normal magnetic field), the velocity is maximum declined, such observations are because of the Lorentz force which produces resistance in the flow. The Lorentz force has the greatest influence on velocity, decreasing velocity.

The comparison of ordinary and fractional fluid velocity is illustrated in Fig. 8a and 8b for diverse values of fractional parameters. We observe that when the fractional parameter i.e., $\alpha, \beta \rightarrow 1$, the fractional fluid velocity almost overlaps with ordinary velocity, which represents the convergence of our obtained numerical solutions of the velocity profile. From the graphical illustration, we see that the results attained by the AB-fractional derivative show more growing behaviour than the CF-fractional derivative. This is also due to the different properties of CF- (based on exponential function having no singularity) and AB (having non-singular and non-local kernel) fractional operators.

The comparison of different nanofluids for velocity field is shown in Fig. 9a. We see that the enhancement in velocity, due to $(H_2O-Al_2O_3)$ and $(\text{Blood}-Al_2O_3)$ is more advanced, than (H_2O-TiO_2) and $(\text{Blood}-TiO_2)$ based NFs but $(H_2O-Al_2O_3)$ based NF has a higher velocity than $(\text{Blood}-Al_2O_3)$ based NF, all this behaviour is due to the physical characteristics of certain nanoparticles. The comparison of numerical methods specifically Grave Stehfest as well as Tzou's is considered in Fig. 9b. The curves of the Stehfests, as well as Tzou's scheme, overlap each other in both cases, which also validates our present results. Furthermore, to make the validity of our attained solutions, the numerical comparison of temperature as well as velocity field through Stehfest and Tzou's with Nusselt number as well as skin friction, are presented in Tables 2-3.



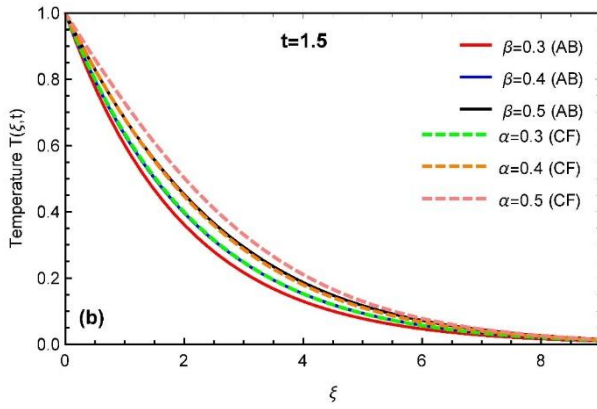


Fig. 2. Plot of temperature field for both fractional models when $Pr = 0.3, \varphi = 0.01$ with (a): $t = 0.1$ and (b): $t = 1.5$

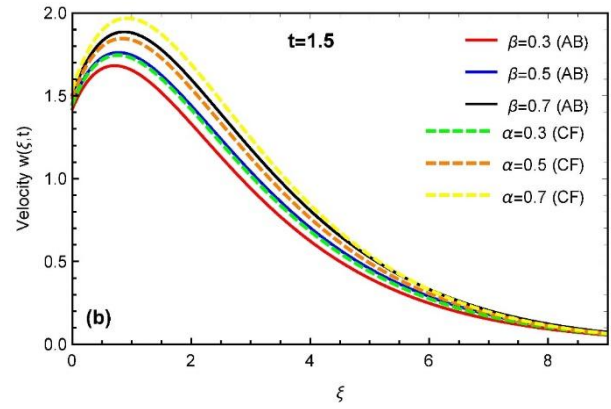


Fig. 4. Effect of (α, β) on velocity for $Pr = 0.3, M = 0.5, Gr = 4, \theta = \frac{\pi}{4}, w = 0.9, b = 0.5, \delta = \frac{\pi}{4}$ and (a): $t = 0.1$ (b): $t = 1.5$

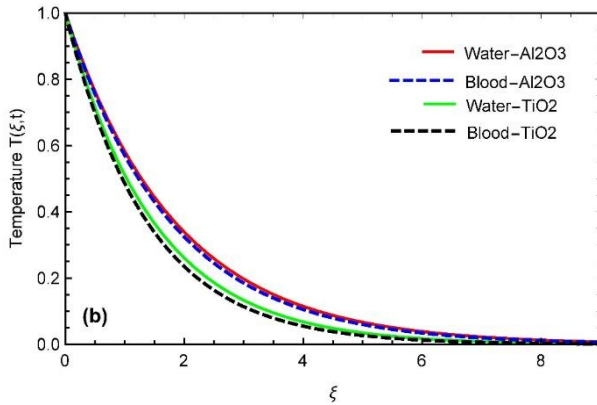
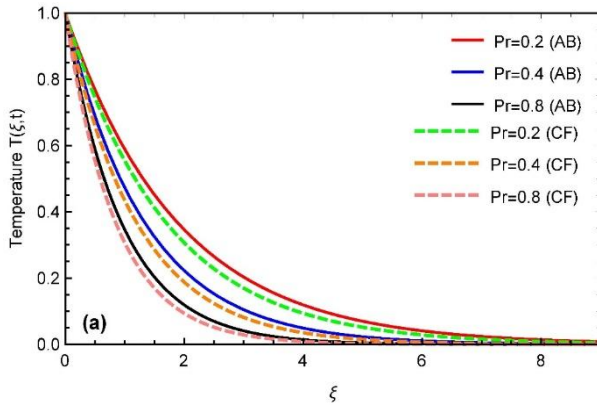


Fig. 3. Temperature field for diverse values of (a): Prandtl number and (b): nanofluid with $\alpha, \beta = 0.5, \varphi = 0.01$, and $t = 0.1$

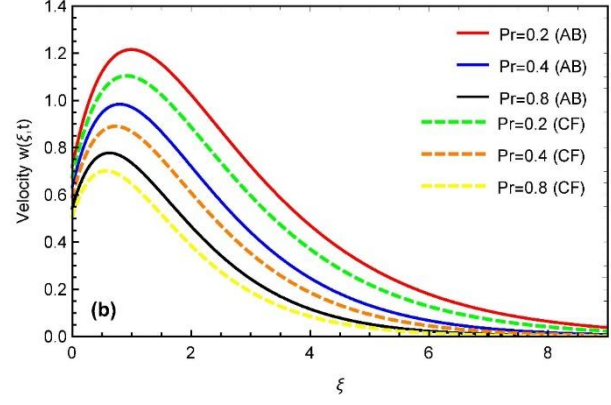
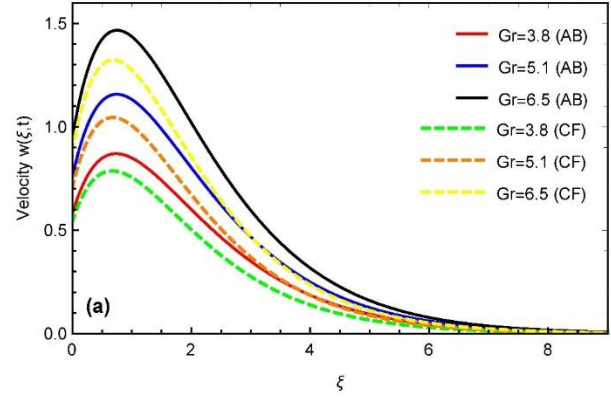


Fig. 5. The effect of (a): Grashof number (b): Pr on velocity when $\alpha, \beta = 0.5, M = 0.5, \theta = \frac{\pi}{4}, w = 0.9, b = 0.5, \delta = \frac{\pi}{4}, t = 0.1$

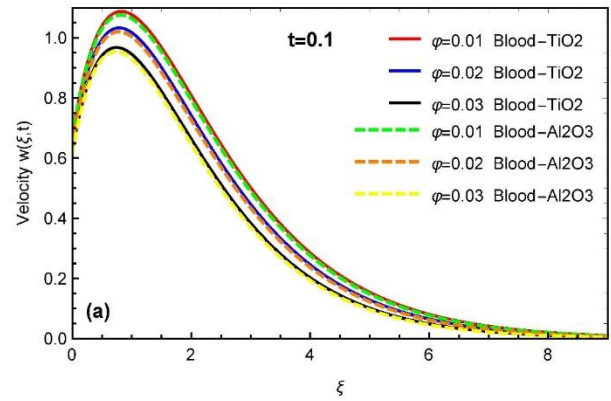
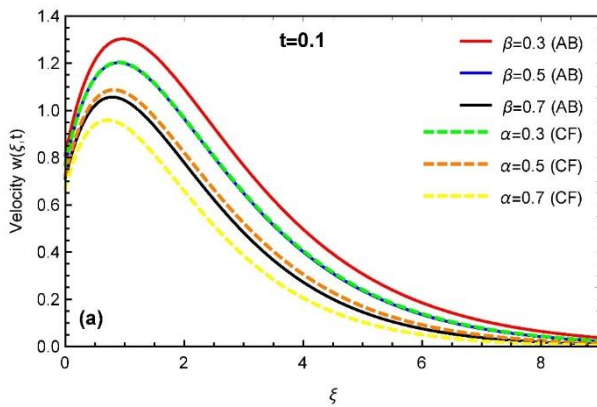


Fig. 6. Effect of volume fraction φ on velocity for $\alpha, \beta = 0.5, Pr = 0.3, M = 0.5, Gr = 4, \theta = \frac{\pi}{4}, w = 0.9, b = 0.5, \delta = \frac{\pi}{4}$

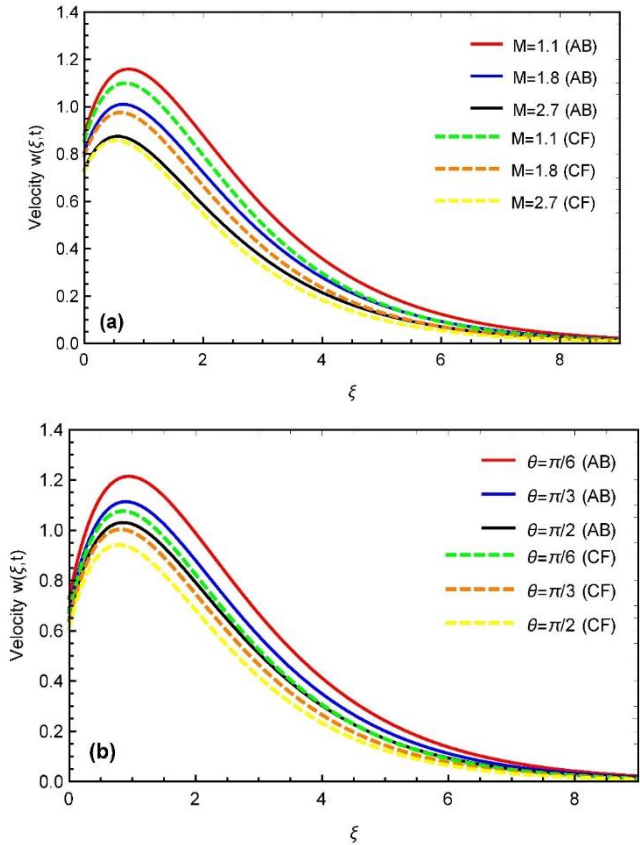


Fig. 7. Variation in (a): magnetic parameter and (b): the inclination of magnetic field for velocity field with $\alpha, \beta = 0.5$, $Pr = 0.3$, $Gr = 4$, $w = 0.9$, $b = 0.5$, $\delta = \frac{\pi}{4}$, $t = 0.1$

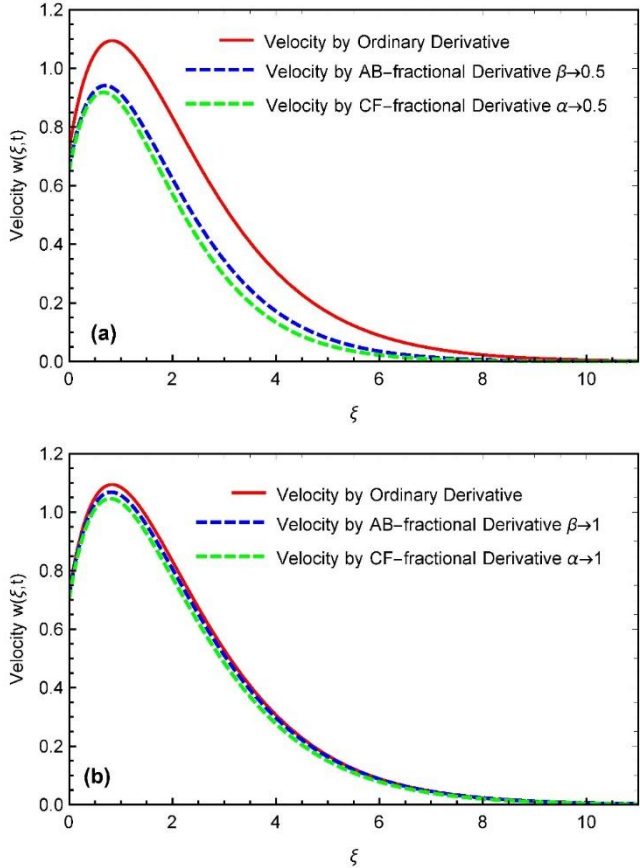


Fig. 8. Comparison of ordinary and fractional velocity when (a): $\alpha, \beta \rightarrow 0.5$ and (b): $\alpha, \beta \rightarrow 1$

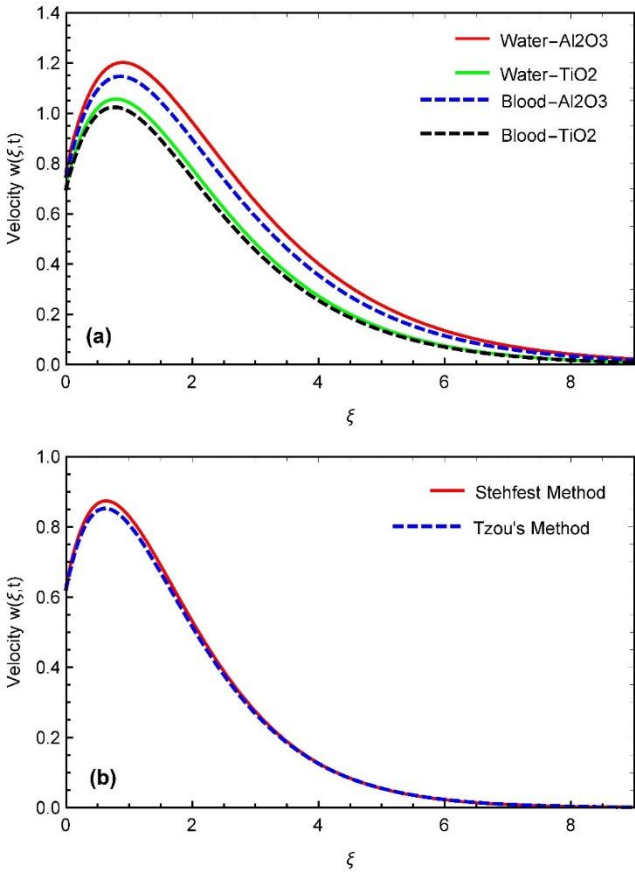


Fig. 9. Comparison of (a): nanofluids and (b): numerical techniques for the velocity field

Tab. 2. A comparison of solutions with two diverse approaches

| ξ | Temperature by Stehfest | Temperature by Tzou | Velocity by Stehfest | Velocity by Tzou |
|-------|-------------------------|---------------------|----------------------|------------------|
| 0.1 | 0.9471 | 0.9471 | 0.7001 | 0.6999 |
| 0.2 | 0.8971 | 0.8971 | 0.7856 | 0.7854 |
| 0.3 | 0.8496 | 0.8496 | 0.8532 | 0.8530 |
| 0.4 | 0.8046 | 0.8046 | 0.9053 | 0.9051 |
| 0.5 | 0.7619 | 0.7619 | 0.9438 | 0.9436 |
| 0.6 | 0.7215 | 0.7215 | 0.9707 | 0.9705 |
| 0.7 | 0.6831 | 0.6831 | 0.9875 | 0.9872 |
| 0.8 | 0.6468 | 0.6468 | 0.9956 | 0.9954 |
| 0.9 | 0.6123 | 0.6123 | 0.9964 | 0.9961 |

Tab. 3. Numerical analysis of Nusselt number as well as skin friction for CF and AB derivatives

| α, β | Nu by CF | Nu by AB | C_f by AB | C_f by CF |
|-----------------|------------|------------|-------------|-------------|
| 0.1 | 0.5352 | 0.5309 | 0.1836 | 0.1824 |
| 0.2 | 0.5276 | 0.5204 | 0.1751 | 0.1553 |
| 0.3 | 0.5151 | 0.5053 | 0.1611 | 0.1335 |
| 0.4 | 0.4972 | 0.4842 | 0.1423 | 0.1127 |
| 0.5 | 0.4730 | 0.4558 | 0.1203 | 0.0934 |
| 0.6 | 0.4411 | 0.4193 | 0.0965 | 0.0777 |
| 0.7 | 0.4000 | 0.3761 | 0.0728 | 0.0677 |
| 0.8 | 0.3502 | 0.3326 | 0.0513 | 0.0637 |
| 0.9 | 0.2965 | 0.2996 | 0.0359 | 0.0654 |

7. CONCLUSIONS

We study mixed convection flows over an inclined plate with Al_2O_3 and TiO_2 nanoparticles with water and blood-based fluids along with new definitions of CF (based on exponential function having no singularity) and AB (having non-singular and non-local kernel) fractional operators in several circumstances which is a significant theoretical and practical study for the solution of important problems. A semi-analytical approach for AB and CF-based models is applied by the Laplace transform technique along with Stehfest and Tzou's numerical schemes.

- The temperature shows dual behaviour with different estimations of fractional parameters with diverse estimations (small and large) of the time.
- The temperature displays decaying behaviour for large estimations of the Pr .
- The velocity slows down by growing the estimation of M .
- The velocity profile speeds up as increasing the estimations of Gr and declines for increasing values of volume fraction φ .
- The enhancement in velocity, due to $(H_2O-Al_2O_3)$ and (Blood- Al_2O_3) is more advanced, than (H_2O-TiO_2) and (Blood- TiO_2) based NFs.
- Our obtained solutions through different numerical methods specifically Stehfest and Tzou's are alike.

Consequently, our claimed results offer significant insights into industrial and engineering systems. These findings guide the development of thermal transfer technologies, assisting in the optimization of processes for better efficiency in applications such as cooling mechanisms and power generation. The research advances heat transfer processes, increasing the overall efficiency of industrial systems.

Nomenclature:

| Symbol | Quantity | Unit |
|------------|------------------------------------|--------------|
| w | Velocity | (m/s) |
| t | Time | (s) |
| T | Temperature | (K) |
| k_{nf} | Thermal conductivity of nanofluid | (W/mk) |
| T | Temperature | (K) |
| T_∞ | Ambient temperature | (K) |
| Gr | Grashof number | ($-$) |
| M | Dimensionless magnetic parameter | ($-$) |
| Pr | Prandtl number | ($-$) |
| q | Laplace transform variable | ($-$) |
| B_o | Strength of magnetic field | (kg/s^2) |
| C_p | Specific heat at constant pressure | (J/kgK) |
| b | Slip parameter | ($-$) |
| C_f | Skin friction | ($-$) |
| Nu | Nusselt number | ($-$) |

Greek Letters:

| | | |
|-----------------|--------------------------------------|------------------|
| μ_{nf} | Dynamic viscosity | ($Pa \cdot s$) |
| α, β | Fractional parameters | ($-$) |
| α_1 | Second-grade parameter | ($-$) |
| β_T | Volumetric coefficient of expansion | ($-$) |
| ρ_{nf} | Density of nanofluid | (kg/m^3) |
| θ | The angle of magnetic inclination | ($-$) |
| δ | The inclination angle of the plate | (mol/m^3) |
| β_T | Volumetric coefficient of expansion | ($-$) |
| σ_{nf} | Electrical conductivity of nanofluid | ($-$) |
| ρ_f | Density of fluid | (kg/m^3) |
| ρ_s | Density of solid | (kg/m^3) |
| φ | The volume fraction of nanofluid | ($-$) |

Note: This ($-$) signifies the dimensionless quantity.

Abbreviations:

| | |
|-----|---|
| AB | Atangana Baleanu time fractional derivative |
| NF | Nanofluid |
| CF | Caputo-Fabrizio time fractional derivative |
| MHD | Magnetohydrodynamics |

REFERENCES

1. Aman S, Abdeljawad T, Al-Mdallal Q. Natural convection flow of a fluid using Atangana and Baleanu fractional model. *Advances in Difference Equations*. 2020;(1):305.
2. Ali FH, Hamzah HK, Egab K, Arıcı M, Shahsavari A. Non-Newtonian nanofluid natural convection in a U-shaped cavity under magnetic field. *International Journal of Mechanical Sciences*. 2020;186:105887.
3. Tayebi T, Öztürk HF, Chamkha AJ. Natural convection and entropy production in hybrid nanofluid filled-annular elliptical cavity with internal heat generation or absorption. *Thermal Science and Engineering Progress*. 2020;19:100605.
4. Paul A, Deka RK. Unsteady natural convection flow past an infinite cylinder with thermal and mass stratification. *International Journal of Engineering Mathematics*. 2017(1):8410691.
5. Shaikh TS, Akgül A, Rehman MA, Ahmed N, Iqbal MS, Shahid N, Rafiq M, De la Sen M. A nonlinear structure of a chemical reaction model and numerical modeling with the new aspect of existence and uniqueness. *Mathematics*. 2022;11(1):37.
6. Amir M, Ali Q, Raza A, Almusawa MY, Hamali W, Ali AH. Computational results of convective heat transfer for fractionalized Brinkman type tri-hybrid nanofluid with ramped temperature and non-local kernel. *Ain Shams Engineering Journal*. 2024;15(3):102576.
7. Ali Q, Riaz S, Memon IQ, Chandio IA, Amir M, Sarris IE, Abro KA. Investigation of magnetized convection for second-grade nanofluids via Prabhakar differentiation. *Nonlinear Engineering*. 2023;12(1):20220286.
8. Yasin MW, Ahmed N, Iqbal MS, Rafiq M, Raza A, Akgül A. Reliable numerical analysis for stochastic reaction-diffusion system. *Physica Scripta*. 2022;98(1):015209.
9. Awan AU, Ali Q, Riaz S, Shah NA, Chung JD. A thermal optimization through an innovative mechanism of free convection flow of Jeffrey fluid using non-local kernel. *Case Studies in Thermal Engineering*. 2021;24:100851.
10. Riaz S, Sattar M, Abro KA, Ali Q. Thermo-dynamical investigation of constitutive equation for rate type fluid: a semi-analytical approach. *International Journal of Modelling and Simulation*. 2023;43(3):123-34.
11. Ali Q, Riaz S, Awan AU, Abro KA. A mathematical model for thermography on viscous fluid based on damped thermal flux. *Zeitschrift für Naturforschung A*. 2021;76(3):285-94.
12. Ajeel RK, Salim WI, Hasnan K. Design characteristics of symmetrical semicircle-corrugated channel on heat transfer enhancement with nanofluid. *International Journal of Mechanical Sciences*. 2019;151:236-50.
13. Abro KA, Atangana A, Gomez-Aguilar JF. An analytic study of bioheat transfer Pennes model via modern non-integers differential techniques. *The European Physical Journal Plus*. 2021;136:1-1.
14. Abro KA, Abdou A. A computational technique for thermal analysis in coaxial cylinder of one-dimensional flow of fractional Oldroyd-B nanofluid. *International Journal of Ambient Energy*. 2022;43(1):5357-65.
15. Ganvir RB, Walke PV, Kriplani VM. Heat transfer characteristics in nanofluid—A review. *Renewable and sustainable energy reviews*. 2017;75:451-60.
16. Aman S, Khan I, Ismail Z, Salleh MZ. Applications of fractional derivatives to nanofluids: exact and numerical solutions. *Mathematical Modelling of Natural Phenomena*. 2018;13(1):2.
17. Hussanan A, Trung NT. Heat transfer analysis of sodium carboxymethyl cellulose based nanofluid with titania nanoparticles. *Journal of Advanced Research in Fluid Mechanics and Thermal Sciences*. 2019;56(2):248-56.
18. Farhana K, Kadrigama K, Noor MM, Rahman MM, Ramasamy D, Mahamude AS. CFD modelling of different properties of nanofluids in header and riser tube of flat plate solar collector. *InOP Conference Series: Materials Science and Engineering* 2019, 469: 012041.
19. Jamshed W, Aziz A. A comparative entropy based analysis of Cu and Fe₃O₄/methanol Powell-Eyring nanofluid in solar thermal collectors subjected to thermal radiation, variable thermal conductivity and impact of different nanoparticles shape. *Results in physics*. 2018; 9:195-205.
20. Jamshed W, Goodarzi M, Prakash M, Nisar KS, Zakarya M, Abdel-Aty AH. Evaluating the unsteady Casson nanofluid over a stretching sheet with solar thermal radiation: An optimal case study. *Case Studies in Thermal Engineering*. 2021; 26:101160.
21. Jamshed W, Nisar KS, Gowda RP, Kumar RN, Prasannakumara BC. Radiative heat transfer of second grade nanofluid flow past a porous flat surface: a single-phase mathematical model. *Physica Scripta*. 2021;96(6):064006.
22. Jamshed W, Nisar KS, Ibrahim RW, Mukhtar T, Vijayakumar V, Ahmad F. Computational frame work of Cattaneo-Christov heat flux effects on Engine Oil based Williamson hybrid nanofluids: A thermal case study. *Case Studies in Thermal Engineering*. 2021; 26:101179.
23. Jamshed W, Devi SU, Nisar KS. Single phase based study of Ag-Cu/EO Williamson hybrid nanofluid flow over a stretching surface with shape factor. *Physica Scripta*. 2021;96(6):065202.
24. Jamshed W, Eid MR, Rehman S, Mohamed Isa SS, Abd-Elmonem A, Alanzi AM, Farooq S. Numerical heat and solutal transfer simulation of fluid flowing via absorptive shrinkable sheet with Ohmic heat resistance. *Numerical Heat Transfer, Part A: Applications*. 2024;85(10):1552-68.
25. Aziz A, Jamshed W, Aziz T, Bahaidarah HM, Ur Rehman K. Entropy analysis of Powell-Eyring hybrid nanofluid including effect of linear thermal radiation and viscous dissipation. *Journal of Thermal Analysis and Calorimetry*. 2021;143(2):1331-43.
26. Sajid T, Gari AA, Jamshed W, Eid MR, Islam N, Irshad K, Altamirano GC, El Din SM. Case study of autocatalysis reactions on tetra hybrid binary nanofluid flow via Riga wedge: Biofuel thermal application. *Case Studies in Thermal Engineering*. 2023; 47:103058.
27. Kai Y, Ali K, Ahmad S, Ahmad S, Jamshed W, Raizah Z, El Din SM. A case study of different magnetic strength fields and thermal energy effects in vortex generation of Ag-TiO₂ hybrid nanofluid flow. *Case Studies in Thermal Engineering*. 2023; 47:103115.
28. Hanif H, Jamshed W, Eid MR, Ibrahim RW, Shafie S, Raedah AA, El Din SM. Numerical Crank-Nicolson methodology analysis for hybridized aluminium alloy nanofluid flowing based-water via stretchable horizontal plate with thermal resistive effect. *Case Studies in Thermal Engineering*. 2023; 42:102707.
29. Kai Y, Ahmad S, Takana H, Ali K, Jamshed W, Eid MR, Abd-Elmonem A, El Din SM. Thermal case study and generated vortices by dipole magnetic field in hybridized nanofluid flowing: Alternating direction implicit solution. *Results in Physics*. 2023; 49:106464.
30. Ullah I, Ali F, Isa SM, Murtaza S, Jamshed W, Eid MR, Amjad A, Guedri K, Khalifa HA, El Din SM. Electro-magnetic radiative flowing of Williamson-dusty nanofluid along elongating sheet: Nanotechnology application. *Arabian Journal of Chemistry*. 2023;16(5):104698.
31. Zhang X, Yang D, Katbar NM, Jamshed W, Ullah I, Eid MR, Raizah Z, Ibrahim RW, Khalifa HA, El Din SM. Entropy and thermal case description of monophasic magneto nanofluid with thermal jump and Ohmic heating employing finite element methodology. *Case Studies in Thermal Engineering*. 2023;45:102919.
32. Podlubny I. Fractional differential equations: an introduction to fractional derivatives, fractional differential equations, to methods of their solution and some of their applications. *elsevier*; 1998, 198:1-340.
33. Baleanu D, Fernandez A. On fractional operators and their classifications. *Mathematics*. 2019;7(9):830.
34. Wang BO, Tahir M, Imran M, Javaid M, Jung CY. Semi analytical solutions for fractional Oldroyd-B fluid through rotating annulus. *IEEE Access*. 2019; 7:72482-91.
35. Ullah Z, Abbas A, El-Zahar ER, Seddek LF, Akgul A, Hassan AM. Significance of thermal density and viscous dissipation on heat and mass transfer of chemically reactive nanofluid flow along stretching sheet under magnetic field. *Results in Engineering*. 2023; 20:101413.
36. Ahmed N, Baber MZ, Iqbal MS, Annum A, Ali SM, Ali M, Akgül A, El Din SM. Analytical study of reaction diffusion Lengyel-Epstein system by generalized Riccati equation mapping method. *Scientific Reports*.

- 2023;13(1):20033.
37. Caputo M, Fabrizio M. A new definition of fractional derivative without singular kernel. *Progress in Fractional Differentiation & Applications*. 2015;1(2):73-85.
 38. Qayyum M, Afzal S, Saeed ST, Akgül A, Riaz MB. Unsteady hybrid nanofluid (Cu-UO₂/blood) with chemical reaction and non-linear thermal radiation through convective boundaries: An application to bio-medicine. *Heliyon*. 2023;9(6):e16578.
 39. Ahmad B, Ahmad MO, Farman M, Akgül A, Riaz MB. A significance of multi slip condition for inclined MHD nano-fluid flow with non linear thermal radiations, Dufour and Sorrot, and chemically reactive bio-convection effect. *South African Journal of Chemical Engineering*. 2023;43:135-45.
 40. Riaz S, Sattar M, Abro KA, Ali Q. Thermo-dynamical investigation of constitutive equation for rate type fluid: a semi-analytical approach. *International Journal of Modelling and Simulation*. 2023;43(3):123-34.
 41. Atangana A, Baleanu D. New fractional derivatives with nonlocal and non-singular kernel: theory and application to heat transfer model. *arXiv preprint arXiv:1602.03408*. 2016.
 42. Riaz MB, Iftikhar N. A comparative study of heat transfer analysis of MHD Maxwell fluid in view of local and nonlocal differential operators. *Chaos, Solitons & Fractals*. 2020;132:109556.
 43. Atangana A. On the new fractional derivative and application to non-linear Fisher's reaction-diffusion equation. *Applied Mathematics and computation*. 2016;273:948-56.
 44. Riaz S, Ali Q, Khanam Z, Rezazadeh H, Esfandian H. Modeling and computation of nanofluid for thermo-dynamical analysis between vertical plates. *Proceedings of the Institution of Mechanical Engineers, Part E: Journal of Process Mechanical Engineering*. 2023;237(5):1750-60.
 45. Riaz S, Amir M, Memon IQ, Ali Q, Abro KA. A comparative study for solidification of nanoparticles suspended in nanofluids through non-local kernel approach. *Arabian Journal for Science and Engineering*. 2023;48(9):11645-63.
 46. Riaz S, Ali S, Ali Q, Khan SU, Amir M. Fractional simulations for mixed convection flow of hybrid nanofluids due to inclined channel with chemical reaction and external heat source features. *Waves in Random and Complex Media*. 2023;1-9.
 47. Ali Q, Yassen MF, Asiri SA, Pasha AA, Abro KA. Role of viscoelasticity on thermoelectromechanical system subjected to annular regions of cylinders in the existence of a uniform inclined magnetic field. *The European Physical Journal Plus*. 2022;137(7):1-0.
 48. Stehfest H. Algorithm 368: Numerical inversion of Laplace transforms [D5]. *Communications of the ACM*. 1970;13(1):47-9.
 49. Tzou DY. *Macro-to microscale heat transfer: the lagging behavior*. John Wiley & Sons; 2014.

Dr. Kashif Ali Abro is thankful to Mehran University of Engineering and Technology, Jamshoro, Pakistan, for the generous support and facilities of this research work.

Qasim Ali:  <https://orcid.org/0000-0003-4118-4515>

Rajai S. Alassar:  <https://orcid.org/0000-0003-3084-7782>

Irfan. A. Abro:  <https://orcid.org/0000-0001-9350-0407>

Kashif. A. Abro:  <https://orcid.org/0000-0003-0867-642X>



This work is licensed under the Creative Commons BY-NC-ND 4.0 license.

THE INFLUENCE OF SOIL STRUCTURE INTERACTION ON THE PLACEMENT OF ACTIVE CONTROL SYSTEMS IN STRUCTURES

RETERI Khadidja*, MEGNOUNIF Abdellatif*

*Faculty of technology, RISAM Laboratory, Department of Civil Engineering, University Abou Bekr Belkaid of Tlemcen, Algeria

khadidjareteri@yahoo.fr, abdellatif_megnounif@yahoo.fr

received 10 November 2023, revised 27 May 2024, accepted 18 June 2024

Abstract: This article begins by outlining the developed program and subsequently applies it to typical structures to emphasize the importance of active control and SSI. The study involves a comparison of dynamic response and control force results to determine the optimal controller position for a column-beam type structure, with and without considering SSI. The central question addressed is whether the influence of soil-structure interaction can be disregarded in selecting the optimal controller position. To address this, a digital simulation is conducted on a simple three-story structure within this document.

Key words: control, position, soil-structure interaction, beam-column, simulation.

1. INTRODUCTION

Numerous engineering systems experience unwanted vibrations. Managing these vibrations in mechanical systems poses significant challenges, requiring methods to either eliminate or reduce them. In the field of civil engineering, structures were traditionally designed without considering the impact of soil-structure interaction (SSI), assuming it to be negligible. However, it has been demonstrated that various factors influence the SSI phenomenon's outcomes. Various approaches exist to address the SSI effect, one of which involves utilizing the substructure method. This technique relies on superimposing two substructures (soil and structure), assuming a rigid interface between them.

Control is the name given to the task to arrive to a desired result. It is applied to structures of civil engineer offer a protection against the harmful effects of the destructive seismic force or discomfort of the man on the movement structural induced by the strong wind and other types of vibrations. Structural control is defined like a mechanical system installed in a structure to reduce the structural vibrations during the loadings such as the winds, earthquakes...etc. It is developed by Yao 1972, Soong 1990, Housner et al. 1997, Spencer and Nagarajaiah 2003.

Into paraseismic structural control is defined like a new fashion of protection [1], which this time does not propose any more to absorb the energy of an earthquake by a reinforcement of the structure itself, in order to make it resistant, but by the addition of special devices aiming to contain or control the answer of the structure at the time of the arrival of a seismic wave by the soil. Also let us note that some of these monitoring systems of the answer, are used to protect from the structure against of another risks that the seismic risk, such as the wind, of the risks of to special equipment.

Several studies ignore the effect of soil-structure interaction (SSI) in the study of reliability and effectiveness of control on seismic response. To verify the effect of SSI on the efficiency and reliability of soil control, Wang et al treat the effect of passive TMD

on the simic response of a long building with soil-structure interaction, the results show that the passive TMD will become poorly tuned when the SSI effect is introduced with different ground models [2]. To solve the problem, a adaptive-passive eddy current pendulum Tuned Mass Damper (APEC-PTMD) was developed [3-4], an APEC-PTMD is applied to a 40-story building including SSI, and four different soil conditions are considered, the results show that the APEC-PTMD gives better seismic protection than the passive TMD in the case of a structure with the SSI [2]. Which concludes that we must take into consideration the effect of the ISS on the effect of the control on the seismic response of the structures. This structural monitoring system can be divided into two parts, a part relates to the algorithms of control [5-6]. In this article one with used active control and algorithm GOAC. Our second objective in this study is to introduce the effect of the soil-structure interaction by the substructure method cited in [5].

2. CONTROL STRUCTURAL

In recent years, increased attention has been paid to the in-depth study of various types of control systems, with the aim of improving their effectiveness and resilience to natural hazards such as earthquakes and hurricanes. Depending on the energy and performance levels required, these systems can be classified into four distinct categories: passive, active, semi-active and hybrid control systems [7].

A passive control system is a system in which structural vibrations are reduced by a device, which gives force to the structure in response to its movement. Passive monitoring has certain advantages. First, it does not require an external power source for its operation, which makes it more economical than other systems. In addition, it is smaller in size requiring less space for its installation. Finally, due to its simplicity, this type of control has received a lot of attention from researchers, making it more reliable to use. The principle of this system is the integration of materials or systems,

possessing damping properties, and therefore the structural vibration dampened passively [8-9].

The most common in this type are seismic isolation and tuned mass damper (TMD) [10-11]. Seismic isolation is a seismic design approach that relies on decoupling ground motion from that of the structure, resulting in a reduction in the forces applied to the structure during an earthquake. The first experiments with the principle of seismic isolation date back to the beginning of the 20th century, and the first application of modern seismic isolation technology was carried out in 1969 [12].

A tuned mass damper (TMD) is a device consisting of a mass, a spring, and a damper that is attached to a structure in order to reduce its dynamic response. The frequency of the damper is tuned to a particular structural frequency so that when that frequency is excited, the damper will resonate out of phase with the structural movement. When it is poorly tuned, the effectiveness of the control will be rapidly diminished [13-14]. An active control system is a system that is fully adaptive and uses an external power supply to produce the required control force to decrease structural response [8]. The advantage of an active control system is that the system achieves an excellent control result. However, there are downsides. It is an expensive system to design and expensive to use because of its high power requirement. In addition, it tends to take up more space than passive controls [8].

In the semi-active control system, mechanisms are employed to control or assist a passive control device. The inherent advantage of a semi-active control device is that the mechanism used does not require a large amount of external power. Many semi-active devices can be powered by batteries protecting them against sudden loss of power during earthquakes. In addition, semi-active control devices are mechanically less complex than active devices. Semi-active systems are more aggressive than passive systems and usually obtain control results close to that of an active control system [8].

The semi-active control strategy is similar to the active control strategy [15]. Only here, the control system does not add energy to the structure. Several research studies have carried out on the effect of semi-active control on the attenuation of the seismic response [16-17, 13, 1, 10-11].

Semi-active devices require much less power than active devices; and energy can often be stored locally, in a battery, thus making the unit type semi active independent of any external power supply. Another critical theme with active control is stability robustness with respect to sensor failure; this problem is particularly difficult when centralized controllers are employed [18].

There are many semi-active systems that can be fitted to structures of any type. They are also used to meet needs other than response control in the field of earthquake architecture [5].

The most common in semi-active systems are magneto-rheological fluid dampers [19], these are dissipative non-linear components, used in semi-active suspension control, where the damping coefficient varies according to the electric current. The hardness of this type of shock absorber depends on the viscosity of the fluid, which is controlled by the magnetic field. This system with a Magneto-rheological fluid inside, is a silicone oil containing ferro-magnetic particles of micrometric size forming aggregated structures under the action of a magnetic field [20]. Wall et al. [16] suggest the integration of a semi-active tuned mass damper (STMD) to enhance the seismic resilience of base-isolated structures. They concluded that the STMD significantly improves the displacement and acceleration capabilities of these structures, irrespective of their linearity.

Hybrid control strategies have been studied by many researchers to exploit their potential to increase the reliability and overall efficiency of the actively controlled structure [21]. These hybrid control systems have received a lot of attention since the 1990s [22]. A hybrid control system generally refers to a combined passive and active control system, which increases the reliability and overall efficiency of the potentially controlled structure [23]. So this system wins the advantages of both techniques. This makes this system capable of halving the amplitude of movement of constructions [5]. An example of a hybrid system, a Hybrid Mass Damper (HMD) is a system proposed to suppress the response of a large building against strong winds and moderate seismic loads to meet the requirement on the vibration level for comfort [24].

3. SOIL STRUCTURE INTERACTION

Soil structure interaction is often neglected by engineers when analyzing and designing a structure, although this phenomenon has a great effect on the behavior of structures, which depends on the characteristics of the soil and structure. herself. For this reason, several researches have been done in this area. We will briefly cite a few:

In 1996, Steven L Kramer [25] presented in "Geotechnical EQ Engineering" the effects of the soil structure interaction phenomenon, and gave different methods to take into account the SSI effect. The SSI problem was treated in 2000 in the context of multi-support structures, such as the bridge, by Clough & Penzien in their work "Dynamics of structures".

A modeling is made in finite elements (2D) of the dynamic soil-structure interaction of a building by the substructure method, in 2000 by M. Kutanis & M. Elmas [26]. Several comparisons were carried out:

- A comparison between three types of analyses: a linear and non-linear analysis of the dynamic SSI compared with the case of embedding of the same structure.
- A comparison of the analyzes carried out for three seismic records having three different PGA values (0.15 g, 0.3 g and 0.45 g) chosen to request the model.
- Finally, to show the influence of soil characteristics on the effect of SSI, three types of soil were chosen characterized by shear wave propagation speeds of 200s/300 and 500s.

In 2004, John P. Wolf & Andrew J. Deeks [27] developed the theory of cones (conical column-beams), who applied it to foundation vibration analyses. This work shows the influence of soil characteristics on the movement of the structure.

Also in 2004, H. Shakibet and A. Fuladgar [28] formulated an approach in the temporal domain for the 3D linear analysis of the ground-structure interaction of a building with an anti-symmetrical shape, for the evaluation of the seismic response of the structure. The contact between the foundation and the ground is modeled by linear plane interface elements of zero thickness.

In 2005, M. Oudjene et al [29] demonstrated that the modification of the seismic action of high frequencies is not taken into account by the shape of the different response spectra thus proposed in the high frequency range. Then, they discussed the current state of these computational spectra and suggested that the lengthening of the fundamental period does not systematically imply the decrease of the spectral acceleration.

In the seismic calculation of structures, the excitation is de-

finied by one or more acceleration recordings often measured at the ground surface in the absence of any construction. These recordings give the free-field accelerograms. In the presence of a building or any other construction, the movements in the vicinity of the foundations may differ from those existing in the open field. Indeed, the forces in contact between the structure and its foundation disrupt the movement of the ground, and the moment of embedding at the base causes its rotation. This phenomenon is referred to as "Soil Structure Interaction" or "SSI" [30].

There are many methods to take into account the effect of soil structure interaction. Many studies have been conducted to demonstrate a detailed comparison between approaches to soil-structure interaction (SSI) analysis, such as direct and indirect methods (substructure), etc. [31-35]. The direct method is considered the most rigorous approach for solving SSI problems for complex structural geometries and the nonlinearity of soil; in this approach, the structure and soil are modeled as a single system [36].

While this strategy is highly effective for solving simple linear and difficult nonlinear problems, it is also complicated, inefficient, and expensive, making it an illogical way to design typical structures [37]. The substructure method is widely used in current SSI analysis practice due to its simplicity and computational efficiency [31, 35]; many researchers have adopted this approach for soil-structure interaction analysis [32-34]. However, researchers have discussed the limitations of this approach. Therefore, Taha A. et al [31] suggest future research to develop this approach to enhance the accuracy of substructure approach simulation.

We will use the substructure method. This method is based on the principle of the superposition of two substructures (soil and structure), such that the soil-structure interface is assumed to be rigid (see Fig. 1).

The loads can be applied to the structure, or through the soil by seismic excitation which propagates vertically in the form of waves, applied to the soil structure interface [38].

The node at the center of the soil-structure interface is designated by 0, and the other nodes of the structure are designated by S.

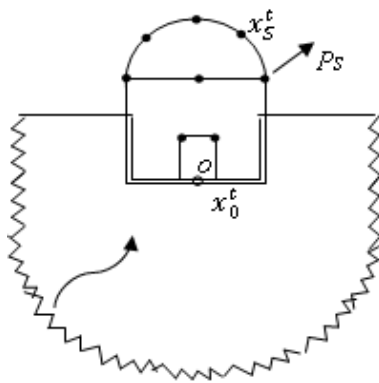


Fig. 1. The two substructures : soil and rigid structure with soil-structure interface [38]

The equation of motion in the time domain expresses the system equilibrium, which gives :

$$[M]\{\ddot{X}^t(t)\} + [C]\{\dot{X}^t(t)\} + [K]\{X^t(t)\} = \{P(t)\} \quad (1)$$

In the complex domain we have :

$$\{X^t(t)\} = \{X^t(w)\} e^{iwt} \quad (2)$$

$$\{P(t)\} = \{P(w)\} e^{iwt} \quad (3)$$

Equation (1) in the complex domain becomes :

$$\{P(w)\} = (-w^2[M] + iw[C] + [K])\{X^t(w)\} \quad (4)$$

We can write equation (4) in the form :

$$\{P(w)\} = [S(w)]\{X^t(w)\} \quad (5)$$

The dynamic stiffness matrix $[S(w)]$ is

$$[S(w)] = -w^2[M] + iw[C] + [K] \quad (6)$$

$[M]$, $[C]$ et $[K]$: are the mass, damping and stiffness matrices of the complete system.

$\{X^t(w)\}$: represents the total displacement.

$\{P(w)\}$: The vector of the amplitudes of the loads acting on the structure.

Equation (5) becomes :

$$\{X^t(w)\} = [S(w)]^{-1}\{P(w)\} = [G(w)]\{P(w)\} \quad (7)$$

Such that $[G(w)]$ is the dynamic flexibility matrix of the system.

The equation of motion (5) of the structure is formulated as follows [38] :

$$\begin{bmatrix} [S_{SS}(w)] & [S_{S0}(w)] \\ [S_{0S}(w)] & [S_{00}^g(w)] \end{bmatrix} \begin{Bmatrix} \{x_S^t(w)\} \\ \{x_0^t(w)\} \end{Bmatrix} = \begin{Bmatrix} \{P_S(w)\} \\ \{-P_0(w)\} \end{Bmatrix} \quad (8)$$

$\{x_S^t(w)\}$ and $\{x_0^t(w)\}$ concern the structure.

$\{x_0^t(w)\}$ and $\{P_0(w)\}$ concern the soil-structure interface.

The substructure of the unbounded ground system, with a rigid and massless ground-structure interface is discussed, to express $\{P_0(w)\}$, this system is illustrated in Fig. 2 [38].

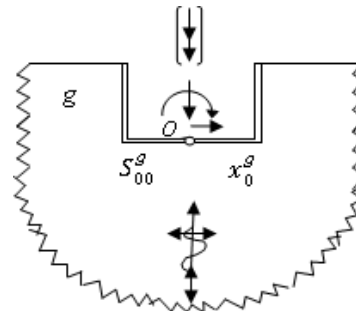


Fig. 2. Substructures: unbounded soil

As $[S_{00}^g(w)]$ denotes the dynamic stiffness matrix, and $\{x_0^g(w)\}$ represents the displacement amplitudes of the soil system mass caused by seismic excitation [38].

For P-waves to propagate vertically, the free-field displacement is also vertical, and the effective base input motion consists of a vertical component, which could result in free-field displacement in the fixed zone. Conversely, for S-waves, the free-field displacement is horizontal, and the base input motion consists of a horizontal component, leading to an average free-field displacement and rotation in the fixed zone. For the motion $\{x_0^g(w)\}$, the interaction forces acting on node 0 vanish,

because for this loading condition, the soil-structure interface is a free surface. This implies that the soil interaction forces depend on the position relative to the effective base input motion $\{x_0^g(w)\}$, and their amplitudes can be expressed as follows [38]:

$$\{P_0(w)\} = [S_{00}^g(w)](\{x_0^t(w)\} - \{x_0^g(w)\}) \quad (9)$$

Tel que : $\{x_0^g(w)\}$: caractérise l'excitation sismique.

Such as : $\{x_0^g(w)\}$: characterizes the seismic excitation

From equation (9), equation (8) can be reformulated as follows

$$\begin{bmatrix} [S_{SS}(w)] & [S_{S0}(w)] \\ [S_{0S}(w)] & [S_{00}^g(w)] + [S_{00}^g(w)] \end{bmatrix} \begin{Bmatrix} \{x_s^t(w)\} \\ \{x_0^t(w)\} \end{Bmatrix} = \begin{Bmatrix} \{P_s(w)\} \\ [S_{00}^g(w)](\{x_0^g(w)\}) \end{Bmatrix} \quad (10)$$

Equation (10) represents the motion equation of the soil-structure system with a rigid soil-structure interface expressed in terms of total displacement amplitudes [38].

4. EQUATION OF STATE OF A STRUCTURE OF TYPE BEAM-COLUMN WITH AND WITHOUT INTERACTION CONTROLLED BY AN ACTIVE TENDON

4.1. With SSI

For the development of the equation of motion, one considers a structure beam-column in "NO" floors controlled actively by active tendons (Fig. 3). To take account of the soil-structure interaction, it is supposed that the structure rests on a flexible foundation built-in a soil with several in depth layers whose characteristics can vary from a layer with another but remain constant along the layer considered. In this case the effect of the soil will be represented by forces of interactions noted $R_0(t)$.

$$[M]\{\ddot{X}^{tg}(n)\} + [C]\{\dot{X}^{tg}(n)\} + [K]\{X^{tg}(n)\} = \begin{Bmatrix} 0 \\ -R_0(n) \end{Bmatrix} \quad (11)$$

By separating the degrees of freedom from the structure and those of the foundation, the equation (11) will be written [39]:

$$\begin{bmatrix} [M_{SS}]_{NO \times NO} & [M_{S0}]_{NO \times 2} \\ [M_{0S}]_{2 \times NO} & [M_{00}]_{2 \times 2} \end{bmatrix} \begin{Bmatrix} \ddot{x}_s^{tg}(n) \\ \ddot{x}_0^{tg}(n) \end{Bmatrix} + \begin{bmatrix} [C_{SS}]_{NO \times NO} & [C_{S0}]_{NO \times 2} \\ [C_{0S}]_{2 \times NO} & [C_{00}]_{2 \times 2} \end{bmatrix} \begin{Bmatrix} \dot{x}_s^{tg}(n) \\ \dot{x}_0^{tg}(n) \end{Bmatrix} + \begin{bmatrix} [K_{SS}]_{NO \times NO} & [K_{S0}]_{NO \times 2} \\ [K_{0S}]_{2 \times NO} & [K_{00}]_{2 \times 2} + [\tilde{K}_{00}]_{2 \times 2} \end{bmatrix} \begin{Bmatrix} x_s^{tg}(n) \\ x_0^{tg}(n) \end{Bmatrix} = \begin{Bmatrix} \delta_s \\ \delta_0 \end{Bmatrix} \ddot{x}_0^g(n) + \begin{bmatrix} [\gamma_S]_{NO \times NCR} \\ [\gamma_0]_{2 \times NCR} \end{bmatrix} \{\ddot{U}(n)\} + \begin{Bmatrix} 0 \\ -R_0(n) \end{Bmatrix} \quad (12)$$

Where the matrices $[M_{SS}]$, $[C_{SS}]$ and $[K_{SS}]$ represent the respective diagonal masses of the floors, the proportional damping matrix, and the stiffness of the symmetric columns of the structure. The matrices $[M_{S0}]$, $[C_{S0}]$ and $[K_{S0}]$, as well as the matrices $[M_{0S}]$, $[C_{0S}]$ and $[K_{0S}]$, respectively, denote the mass, stiffness, and damping matrices associated with the superstructure and the rigid foundation. The matrices $[M_{00}]$, $[C_{00}]$ and

$[K_{00}]$ respectively represent the mass, stiffness, and damping associated with the rigid foundation.

The vector $\{\delta_s\}$ represents the vector of horizontal acceleration coefficients of the soil for the superstructure. The vector $\{\delta_0\}$ represents the vector of horizontal acceleration coefficients of the soil for the foundation.

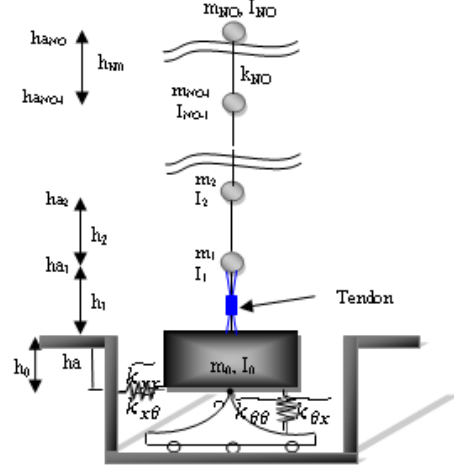


Fig. 3. Model of a structure equipped with active tendons and with SSI

The matrices $[\gamma_S]$ and $[\gamma_0]$ represent the localization matrices of the controllers for the superstructure and the foundation, where NCR is the number of active controllers.

$\{X_s^{tg}(n)\}$, with dimensions $(NO \times 1)$, represents the vector of floor displacements $(x_{NO}^{tg} x_{NO-1}^{tg} \dots x_1^{tg} \dots x_2^{tg} x_1^{tg})^T$ and $\{X_0^{tg}(n)\}$, with dimensions (2×1) , is the vector of displacement and rotation of the foundation at point "O" $(x_0^{tg}, \theta_0^{tg})^T$.

The vector $\{R_0(n)\} = [R_x(n) \ R_\theta(n)]^T$, with dimensions (2×1) , where $R_x(n)$ is the horizontal interaction force and $R_\theta(t)$ is the interaction moment at point O.

To solve this system, it is assumed that the state vector $Z^{tg}(n)$, with dimensions $(2(NO+2) \times 1)$ [1]:

$$Z^{tg}(n) = \begin{Bmatrix} \{x_s^{tg}(n)\} \\ \{x_0^{tg}(n)\} \\ \{\dot{x}_s^{tg}(n)\} \\ \{\dot{x}_0^{tg}(n)\} \end{Bmatrix} \quad (13)$$

In replacing equation (13) into (12), we obtain the following state equation [39]:

$$\{\dot{Z}^{tg}(n)\} = [A]\{Z^{tg}(n)\} + [B]\{\ddot{U}(n)\} + \{E(n)\} \quad (14)$$

We can express equation (14) in the following form :

$$\{\dot{Z}^{tg}(n)\} = [D]\{Z^{tg}(n)\} + \{E(n)\} \quad (15)$$

Where $[D]$ is the time-independent 'plant' matrix, with dimensions of $(2(NO+2) \times 2(NO+2))$:

$$[D] = [A] + [B][G^{ISS}] \quad (16)$$

With: $[G^{ISS}]$ The control gain matrix, computed in this work using the Generalized Optimal Active Control (GOAC) algorithm (section 4.1.1) [40].

$[A]$ is the characteristic matrix of the controlled system, with

dimensions of $(2(\text{NO}+2) \times 2(\text{NO}+2))$:

$$[A] = \begin{bmatrix} [0] & [I] \\ -[M]^{-1}[K] & -[M]^{-1}[C] \end{bmatrix} \quad (17)$$

$[B]$ is the actuator placement matrix, with dimensions of $(2(\text{NO}+2) \times \text{NCR})$

$$[B] = \begin{bmatrix} [0] \\ [M]^{-1} [Y] \end{bmatrix} \quad (18)$$

$\{E\}$ is the vector of external disturbances, with dimensions of $(2(\text{NO}+2) \times 1)$, $\{C\}$ is the vector related to the base acceleration of the structure, with dimensions of $(2(\text{NO}+2) \times 1)$, $\{\tilde{R}_0(n)\}$ is the vector of accelerations, with dimensions of $(2(\text{NO}+2) \times 1)$, and $\{\tilde{R}_0\}$ is the dynamic vector of equivalent forces.

The vectors $\{x_0^{\text{tg}}(t)\}$ and $\{R_0(t)\}$ at time t are related by the system's ground flexibility matrix through the following convolution integral [40] :

$$\{x_0^{\text{tg}}(t)\} = \int_0^{\infty} [F_{00}^g(\tau)] \{R_0(t - \tau)\} d\tau \quad (19)$$

With: $[F_{00}^g(\tau)]$ is the dynamic soil flexibility matrix.

Where $[F_{00}^g(w)] = [S_{00}^g(w)]^{-1}$, where $[S_{00}^g(w)]$ is the dynamic soil stiffness matrix

4.2. Generalized Optimal Active Control (GOAC) algorithm

Research efforts in active structural control have focused on various control algorithms based on multiple control design criteria. These active control algorithms are used to determine the control force of the measured structural response, providing a control law and a mathematical model of the controller for an active control system [39]. Some are considered classical as they are direct applications of modern control theory [41]. Examples include the Riccati Optimal Active Control (ROAC) based on integrated performance over the entire duration of seismic excitation, and the classic pole placement algorithm, showing promising application in civil engineering smart structures [39]. These classical algorithms, however, are not truly optimal as they ignore the excitation term in their calculation [41]. Recognizing that at any particular time t , knowledge of the external excitation may be available, this knowledge can be used to develop improved control algorithms [41]. This led to the development of the Instantaneous Optimal Active Control (IOAC) algorithm, which differs from ROAC in that its performance index depends on time [39]. However, IOAC's control force is proportional to the time increment, resulting in non-uniform control forces for structures subjected to different seismic loadings over time [39]. To address these limitations, Japanese researchers Cheng and Tian developed the Generalized Optimal Active Control (GOAC) algorithm, which can adjust the feedback gain matrix to achieve better controllability [39-40].

The following equation is the simplest notation of equation (14) :

$$\{\dot{Z}(t)\} = [A]\{Z(t)\} + [B]\{\vec{U}(t)\} + \{E(t)\} \quad (20)$$

All parameters in the following algorithms pertain to a building taking into account the effect of soil-structure interaction. In this section, we will examine in detail the GOAC algorithm for closed-loop structural control [39].

– The transversality conditions:

Let's consider a system governed by free-end boundary conditions with equation (20) given by [40] :

$$\begin{cases} t_{i-1} = t_0 + (i-1)\Delta t \\ \{Z(t_{i-1})\} = \{Z_{i-1}\} \\ t_i = t_0 + (i)\Delta t \end{cases} \quad (21)$$

Such as :

$$\Delta t = \frac{1}{N}(t_f - t_0); \quad i = 1, 2, \dots, N$$

$\{Z_{i-1}\}$: is the value of $\{Z(t)\}$ at t_{i-1} , vector of dimension $(2(\text{NO}+2) \times 2(\text{NO}+2))$

Equation (21) can be written in the following vector form :

$$\{\Omega\} = \begin{Bmatrix} \Omega_1 \\ \Omega_2 \\ \Omega_3 \end{Bmatrix} = \begin{Bmatrix} (t_{i-1} - t_0) - (i-1)\Delta t \\ \{Z(t_{i-1})\} - \{Z_{i-1}\} \\ (t_i - t_0) - (i)\Delta t \end{Bmatrix} = \{0\} \quad (22)$$

By introducing multipliers $\{\mu\}$ and $\{\lambda(t)\}$ and forming :

$$G = g(\{Z(t_i)\}) + \{\mu\}^T \{\Omega\} \quad (23)$$

$$F = \bar{f}(t) - \{\lambda(t)\}^T \{f(t)\} \quad (24)$$

Such as :

$$g(\{Z(t_i)\}) = \frac{1}{2} \{Z(t_i)\}^T [S] \{Z(t_i)\} \quad (25)$$

$$\bar{f}(t) = \{Z(t)\}^T [Q] \{Z(t)\} + \{U(t)\}^T [R] \{U(t)\} \quad (26)$$

$$\{f(t)\} = \frac{1}{2} ([A]\{Z(t)\} + [B]\{U(t)\} + \{E(t)\} - \{\dot{Z}(t)\}) \quad (27)$$

Then the transversality condition can be expressed as follows :

$$dG - \left[\left(\left\{ \frac{\partial F}{\partial \{Z(t)\}} \right\}^T \{\dot{Z}(t)\} - F \right) dt \right]_{t_{i-1}}^{t_i} + \left[\left\{ \frac{\partial F}{\partial \{Z(t)\}} \right\}^T d\{Z(t)\} \right]_{t_{i-1}}^{t_i} = 0 \quad (28)$$

Applying equation (28) to equation (23) and (24), we obtain :

$$[S]\{Z(t_i)\} - \{\lambda(t_i)\} = \{0\} \quad (29)$$

Where: $g(\{Z(t_i)\})$ is an optimization function of boundary conditions at each end time t_i .

$[S]$ and $[Q]$ are positive semi-definite matrices, both of dimension $(2(\text{NO}+2) \times 2(\text{NO}+2))$. $[R]$ is a positive definite matrix of dimension $(\text{NCR} \times \text{NCR})$.

– Generalized performance index:

In this algorithm, the control time interval $[t_0, t_f]$ is divided into N segments in the calculation of the performance index J , which is defined and minimized to obtain an optimal solution for the state vector $\{Z(t)\}$ and the control force vector $\{U(t)\}$ [1].

$$J = \sum_{i=1}^N \frac{1}{2} \int_{t_{i-1}}^{t_i} (\{Z(t)\}^T [Q] \{Z(t)\} + \{U(t)\}^T [R] \{U(t)\}) dt \quad (30)$$

The boundary conditions in the performance index equation in the Riccati algorithm are as follows :

$$\begin{cases} \{Z(t_0)\} = \{Z(t_f)\} = \{0\} \\ \{U(t_0)\} = \{U(t_f)\} = \{0\} \end{cases} \quad (31)$$

The performance index J will be integrated step by step. At

each integration step of $[t_{i-1}, t_i]$ such that ($i = 1, 2, \dots, N$), at least one of the two limit values of the state vector is unknown. The values of the state vector $\{Z(t)\}$ is specified at t_{i-1} , and unspecified and mobile at time t_i .

We have already said that the state vector $\{Z(t_i)\}$ is unknown, it must be reduced to a minimum to include it in the performance index equation. By introducing the transverse conditions at time t_f , the performance index is expressed as follows:

$$J_i = g(\{Z(t_i)\}) + \frac{1}{2} \int_{t_{i-1}}^{t_i} (\{Z(t)\}^T [Q] \{Z(t)\} + \{U(t)\}^T [R] \{U(t)\}) dt \quad (32)$$

Thus :

$$J_i = g(\{Z(t_i)\}) + \frac{1}{2} \int_{t_{i-1}}^{t_i} \bar{f}(t) dt \quad (33)$$

– The feedback gain matrix and the control force.

The Euler equations :

$$\begin{cases} \frac{\partial F(t)}{\partial \{Z(t)\}} - \frac{d}{dt} \left(\frac{\partial F(t)}{\partial \{\dot{Z}(t)\}} \right) = \{0\} \\ \frac{\partial F(t)}{\partial \{U(t)\}} - \frac{d}{dt} \left(\frac{\partial F(t)}{\partial \{\dot{U}(t)\}} \right) = \{0\} \end{cases} \quad (34)$$

Replacing equation (24) into equation (34), we will have :

$$\begin{cases} \frac{\partial}{\partial \{Z(t)\}} \left[\frac{1}{2} \{Z(t)\}^T [Q] \{Z(t)\} \right] = [Q] \{Z(t)\} \\ \frac{\partial}{\partial \{\dot{Z}(t)\}} [\{\lambda(t)\}^T [A] \{Z(t)\}] = [A]^T \{\lambda(t)\} \\ \frac{d}{dt} \left[\frac{\partial}{\partial \{\dot{Z}(t)\}} (-\{\lambda(t)\}^T \{\dot{Z}(t)\}) \right] = -\{\lambda(t)\} \\ \frac{\partial}{\partial \{U(t)\}} (\{U(t)\}^T [R] \{U(t)\}) = [R] \{U(t)\} \\ \frac{\partial}{\partial \{\dot{U}(t)\}} (\{\lambda(t)\}^T [B] \{U(t)\}) = [B]^T \{\lambda(t)\} \end{cases} \quad (35)$$

So equation (34) becomes :

$$\begin{cases} [Q] \{Z(t)\} + [A]^T \{\lambda(t)\} + \{\dot{\lambda}(t)\} = \{0\} \\ [R] \{U(t)\} + [B]^T \{\lambda(t)\} = \{0\} \end{cases} \quad (36)$$

By replacing equations (25) and (22) into equation (23), we find the function G :

$$G = \frac{1}{2} \{Z(t_i)\}^T [S] \{Z(t_i)\} + \mu_1 [(t_{i-1} - t_0) - (i-1)\Delta t] + \{\mu_2\}^T [\{Z(t_{i-1})\} - \{Z_{i-1}\}] + \mu_3 [(t_i - t_0) - (i)\Delta t] \quad (37)$$

Where G is the augmented function of the function g .

As the multiplier $\{\mu\}^T = [\mu_1, \{\mu_2\}^T, \mu_3]$

With:

$$\begin{cases} \frac{\partial G}{\partial t_{i-1}} = \mu_1 \\ \frac{\partial G}{\partial \{Z(t_{i-1})\}} = \{\mu_2\} \\ \frac{\partial G}{\partial t_i} = \mu_3 \\ \left\{ \frac{\partial G}{\partial \{Z(t_i)\}} \right\} = [S] \{Z(t_i)\} \end{cases} \quad (38)$$

From the second equation of equation (36), we have the equation of the control force :

$$\{U(t)\} = -[R]^{-1} [B]^T \{\lambda(t)\} \quad (39)$$

\Rightarrow

$$\{U(t)\} = -[R]^{-1} [B]^T [S] \{Z(t)\} \quad (40)$$

$$\{U(t)\} = [G^{ISS}] \{Z(t)\} \quad (41)$$

So :

$$[G^{ISS}] = -[R]^{-1} [B]^T [S] \quad (42)$$

So, where $[G]$ is the feedback gain matrix, this matrix represents an optimal control law. It is of dimension $(NCR \times 2(NO+2))$. It is independent of time t , where $t \in [t_{i-1}, t_i]$ and of the time increment Δt .

From equation (42), we notice that if we choose the matrix $[S] = [P]$, where $[P]$ is the Riccati matrix, we obtain the same equation for the feedback gain matrix found in the Riccati algorithm. This means that the Riccati algorithm is a case of the GOAC algorithm, which is why the algorithm is called the generalized GOAC algorithm. This gain matrix $[G^{ISS}]$ is obtained from the state equation (20), which can be solved using the diagram in the following figure.

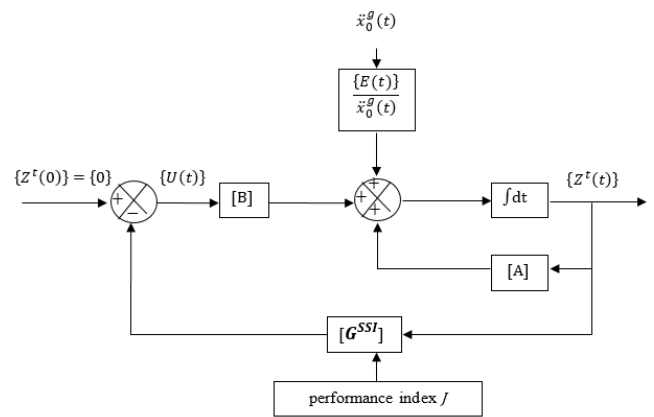


Fig. 4. Flowchart of solving the state equation with active control [18]

In the case of SSI, the matrices $[S]$ and $[Q]$ are of dimension $(2(NO+2) \times 2(NO+2))$. The matrix $[R]$ is of dimension $(NCR \times NCR)$. They are defined as follows :

$$[Q] = \begin{bmatrix} [K_{ss}] & [K_{s0}] & [0] & [0] \\ [K_{s0}]^T & [\tilde{K}_{00}] & [0] & [0] \\ [0] & [0] & [M_{ss}] & [0] \\ [0] & [0] & [0] & [M_{00}] \end{bmatrix} \quad (43)$$

And

$$[R] = \begin{bmatrix} [\gamma_s] \\ [\gamma_0] \end{bmatrix}^T \begin{bmatrix} [K_{ss}] & [K_{s0}] \\ [K_{s0}]^T & [\tilde{K}_{00}] \end{bmatrix}^{-1} \begin{bmatrix} [\gamma_s] \\ [\gamma_0] \end{bmatrix} \quad (44)$$

With:

$$[\tilde{K}_{00}] = \begin{bmatrix} k_1 + \tilde{K}_{xx} & -h_{a1} k_1 + \tilde{K}_{x\theta} \\ -h_{a1} k_1 + \tilde{K}_{\theta x} & h_{a1}^2 k_1 + \tilde{K}_{\theta\theta} \end{bmatrix}^{-1} \quad (45)$$

The matrix $[S]$ is chosen as an arbitrary row matrix :

$$[S] = \begin{bmatrix} [0] & [0] \\ [S_D] & [S_V] \end{bmatrix} \quad (46)$$

To ensure a semi-definite positive state of the matrix $[S]$, the symmetric matrix can be chosen as follows:

$$[S] = \gamma_D \begin{bmatrix} \Omega_V^{-1} [\tilde{K}] & [\tilde{K}] \\ [\tilde{K}] & \Omega_V [\tilde{K}] \end{bmatrix} \quad (47)$$

With :

$$[\tilde{K}] = \begin{bmatrix} [K_{ss}] & [K_{s0}] \\ [K_{s0}]^T & [\tilde{K}_{00}] \end{bmatrix} \quad (48)$$

Where γ_D is the stiffness scale factor, and Ω_V is the damping scale factor.

We can write equation (14) as follows:

$$\{\dot{Z}^{tg}(t)\} = [D]\{Z^{tg}(t)\} + \{E(t)\} \quad (49)$$

Where $[D]$ is the matrix of the horizontal component of the damping force, and it is of dimension $(2(NO+2) \times 2(NO+2))$:

$$[D] = [A] + [B][G^{ISS}] \quad (50)$$

$\{E\}$ is the vector of external disturbances, it has dimension $(2(NO+2) \times 1)$

$$\{E(t)\} = \{C\}\ddot{x}_0^g(t) + \{-\tilde{R}_0(t - \Delta t)\} \quad (51)$$

The influence of S_D , S_V , γ_D and Ω_V on the overall system can be studied by substituting the equation for the gain matrix from equation (42) into the equation for the matrix of the horizontal component of the damping force (50), yielding:

$$[D] = [A] - \frac{1}{R} [B][B]^T [S] \quad (52)$$

The technical solution:

$$[\vec{U}(t)] = [G^{SSI}]\{Z^t(t)\} \quad (53)$$

$[G^{SSI}]$ is the feedback gain matrix, it is time-independent, and it has dimensions of $(NCR \times 2(NO+2))$.

The simplification of equation (20) is as follows :

$$\{\dot{Z}(t)\} = [D]\{Z(t)\} + \{E(t)\} \quad (54)$$

$$[T] = [\{a_1\}\{b_1\}; \dots; \{a_i\}\{b_i\}; \dots; \{a_{NO+2}\}\{b_{NO+2}\}] \quad (55)$$

The transformation matrix $[T]$ is constructed from the eigenvectors of the matrix $[A]$. It is necessary to transform the equation of state into canonical form. In which $\{a_i\}$ and $\{b_i\}$ are respectively the real and imaginary parts of the eigenvector i of the matrix $[A]$, and they have dimensions $(2(NO+2) \times 1)$. So the transformation matrix $[T]$ has dimension $(2(NO+2) \times 2(NO+2))$.

$$[\Lambda] = [T]^{-1}[D][T] \quad (56)$$

$[\Lambda]$ is a real matrix, it has dimension $(2(NO+2) \times 2(NO+2))$, and it has the following form :

$$[\Lambda] = \begin{bmatrix} [\Lambda_1] & \dots & [0] & \dots & [0] \\ \vdots & \ddots & \vdots & \ddots & \vdots \\ [0] & \vdots & [\Lambda_i] & \dots & [0] \\ \vdots & \vdots & \vdots & \ddots & \vdots \\ [0] & \vdots & [0] & \vdots & [\Lambda_{NO+2}] \end{bmatrix} \quad (57)$$

With :

$$[\Lambda_i] = \begin{bmatrix} \mu_i & \nu_i \\ -\nu_i & \mu_i \end{bmatrix} \quad (58)$$

The solution to equation (54) is expressed as follows:

$$\{Z(t)\} = [T]\{\Phi(t)\} \quad (59)$$

Substituting equations (56) and (59) into (54), we obtain:

$$[T]\{\dot{\Phi}(t)\} = [D][T]\{\Phi(t)\} + \{E(t)\} \quad (60)$$

$$\{\dot{\Phi}(t)\} = [T]^{-1}[D][T]\{\Phi(t)\} + [T]^{-1}\{E(t)\} \quad (61)$$

$$\{\dot{\Phi}(t)\} = [\Lambda]\{\Phi(t)\} + \{\Gamma(t)\} \quad (62)$$

With :

$$\{\Gamma(t)\} = [T]^{-1}\{E(t)\} \quad (63)$$

$$\{Z(0)\} = \{0\} \Rightarrow \{\Phi(0)\} = 0 \quad (64)$$

$$\ddot{x}_0^g(0) = 0, \{R_0(0)\} = \{0\} \quad (65)$$

$$\{\Gamma(0)\} = \{0\} \quad (66)$$

$$\{\dot{\Phi}(t)\} - [\Lambda]\{\Phi(t)\} = \{\Gamma(t)\} \quad (67)$$

$$\{\Phi(t)\} = [\exp([\Lambda]t)]\{\Phi(0)\} + [\exp([\Lambda]t)] \int_0^t [\exp(-[\Lambda]\tau)] \{\Gamma(\tau)\} d\tau \quad (68)$$

$$\{\Phi(t)\} = [\exp([\Lambda]t)]\{\Phi(0)\} + \int_0^t [\exp([\Lambda](t - \tau))] \{\Gamma(\tau)\} d\tau \quad (69)$$

$$[\exp([\Lambda]t)] = \begin{bmatrix} [\exp([\Lambda_1]t)] & [0] & [0] \\ [0] & [\exp([\Lambda_i]t)] & [0] \\ [0] & [0] & [\exp([\Lambda_{NO+2}]t)] \end{bmatrix} \quad (70)$$

With :

$$[\exp([\Lambda_i]t)] = \exp(\mu_i t) \begin{bmatrix} \cos(\nu_i t) & \sin(\nu_i t) \\ -\sin(\nu_i t) & \cos(\nu_i t) \end{bmatrix} \quad (71)$$

$$\{\Phi(n\Delta t)\} = [\exp([\Lambda]n\Delta t)]\{\Phi(0)\} + \frac{\Delta t}{2} [\exp([\Lambda]n\Delta t)]\{\Gamma(0)\} + \Delta t \sum_{m=1}^{n-1} [\exp([\Lambda](n - m)\Delta t)]\{\Gamma(m\Delta t)\} + \frac{\Delta t}{2} \{\Gamma(n\Delta t)\} \quad (72)$$

$$\{\Phi(n\Delta t)\} = \Delta t \sum_{m=1}^{n-1} [\exp([\Lambda](n - m)\Delta t)]\{\Gamma(m\Delta t)\} + \frac{\Delta t}{2} \{\Gamma(n\Delta t)\} \quad (73)$$

$$\{\Phi(n\Delta t)\} = \{\Pi((n - 1)\Delta t)\} + \frac{\Delta t}{2} \{\Gamma(n\Delta t)\} \quad (74)$$

$$\{\Pi((n - 1)\Delta t)\} = \Delta t \sum_{m=1}^{n-1} [\exp([\Lambda](n - m)\Delta t)]\{\Gamma(m\Delta t)\} \quad (75)$$

$$\{\Pi((n - 1)\Delta t)\} = [\exp([\Lambda]\Delta t)]\{\Pi((n - 2)\Delta t)\} + \Delta t \{\Gamma((n - 1)\Delta t)\} \quad (76)$$

The solution of the state equation (20) is also used for the case without control by setting the control term $[B]$ to zero, yielding

$$\{\dot{Z}^{tg}(t)\} = [A]\{Z^{tg}(t)\} + \{E(t)\} \quad (77)$$

4.3. Without SSI

The motion equation of a fixed-end post-beam type structure is [39] :

$$[M_{ss}]\{\ddot{X}^{tg}(n)\} + [C_{ss}]\{\dot{X}^{tg}(n)\} + [K_{ss}]\{X^{tg}(n)\} = \{\delta_s\}\ddot{x}_0^g(n) + [\gamma_s]\{\vec{U}(n)\} \quad (78)$$

5. SIMULATION NUMERIQUE

This section aims to demonstrate the influence, importance, and position of control on the structure, taking into account the effect of SSI by comparing it with the case of embedding. For this purpose and for numerical application, the dynamic loading used for exciting structures (buildings) is the 1940 El Centro earthquake with North-South components (Fig. 5.)

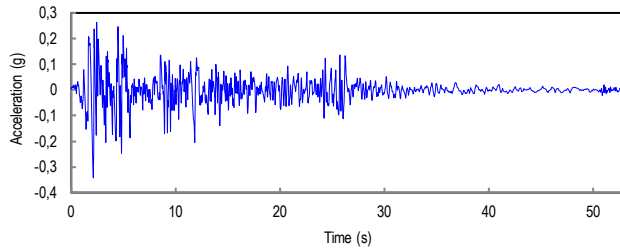


Fig. 5. El-centro 1940 of the N-S Components

The structure used for numerical applications is a three-story structure, and the data is as follows:

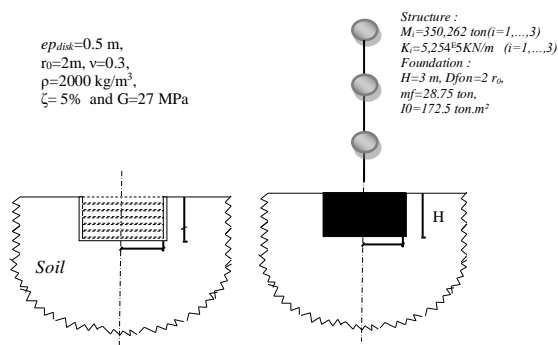


Fig. 6. The data of the studied model

The obtained result for the stiffness matrix of the studied soil

$$[\tilde{K}_{00}] = \begin{bmatrix} 827261,766 & -7243805,42 \\ -7243805,42 & 144541041 \end{bmatrix}$$

The Table 1 presents the natural frequencies of the first three modes for both cases, with and without SSI. It is noteworthy that the natural frequencies in the fixed case are higher than those in the SSI case.

Tab. 1. The natural frequencies of the studied model with and without SSI (rad/s)

| Floor | SSI | Fixed |
|-------|--------|--------|
| 1 | 14,514 | 17,236 |
| 2 | 43,162 | 48,295 |
| 3 | 68,091 | 69,789 |

The following figure provides the displacement, velocity and acceleration history of the last floor of the model with SSI, which is compared to that of the fixed case.

Now, let's assume that the model is controlled by an active tendon system placed on the first floor for the case with ISS, and on the last floor for the case without ISS. The algorithm used is the GOAC algorithm. We will employ various values of the S/R ratios to determine the optimal S/R ratio. The results are plotted in the following figure.

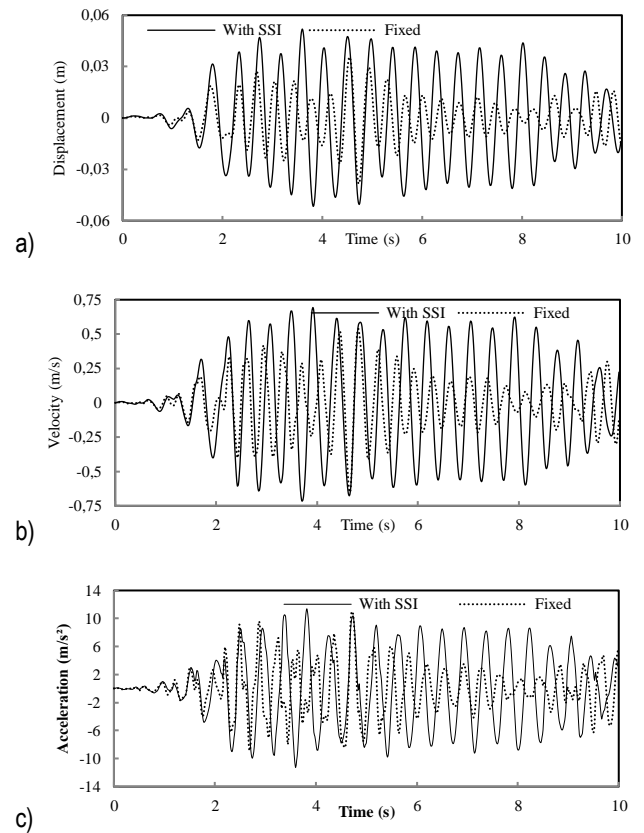


Fig. 7. The displacement, b) the velocity, and c) the acceleration of the final floor of the studied model, considering the effect of SSI, compared with the fixed case without control

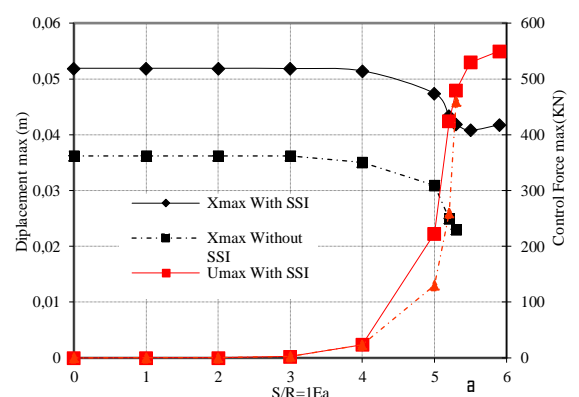


Fig. 8. Variation of maximum displacement at the last floor and maximum control force as a function of S/R ratios

According to Fig. 8, the chosen value is $S/R=2E5$ for the case with ISS, and $S/R=2.7E5$ for the case without SSI.

According to Fig. 9, we observe that the displacement decreases in the presence of control for both cases, with and without SSI. Additionally, the controller position has an influence on the control effect. In this model, the optimal positions are at the last

floor for the case without SSI, and at the first floor for the case with SSI.

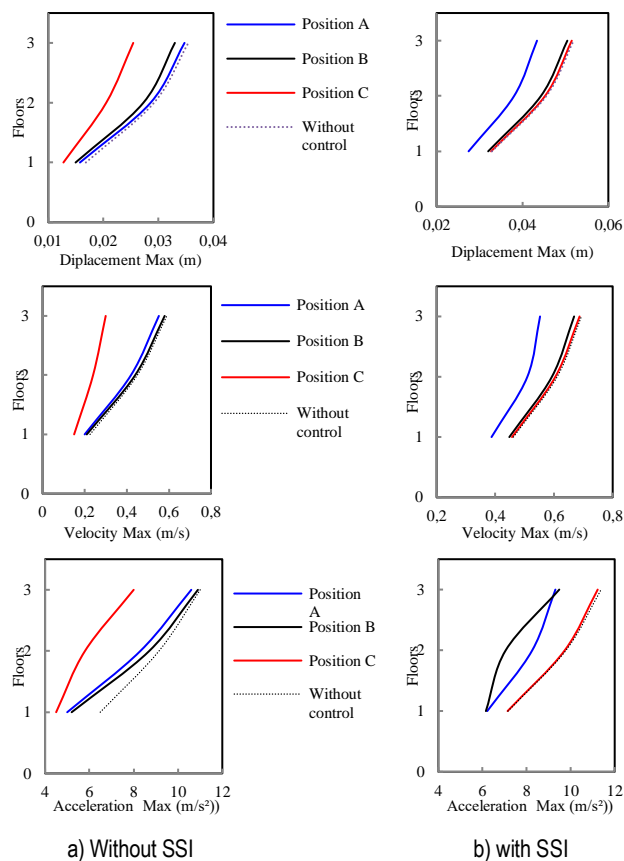


Fig. 9. Maximum displacements, velocities, and accelerations a) without and b) with ISS for the three controller positions compared to the case without control

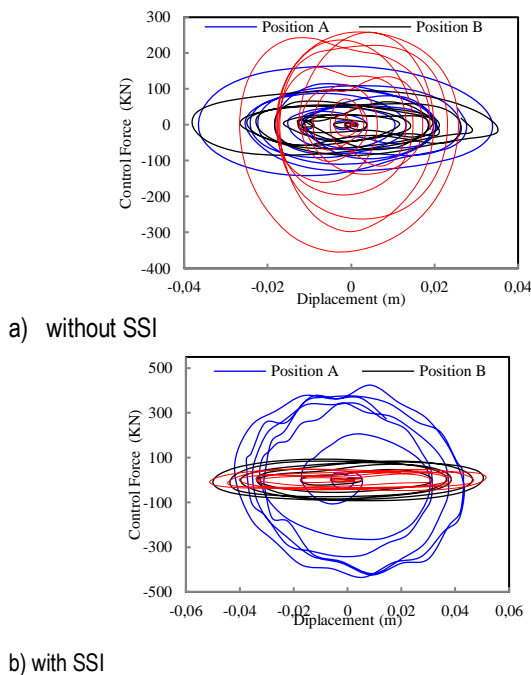


Fig. 10. The control force-displacement relationship at the last floor of the studied model a) without SSI and b) with SSI for the three controller positions compared to the case without control

6. CONCLUSION

In civil engineering, modern structures are becoming increasingly complex, necessitating advanced techniques for understanding and controlling their behavior. When subjected to dynamic loads such as earthquakes or strong winds, these structures can experience significant vibrations, often leading to their failure. Despite numerous efforts to design structures capable of withstanding such loads, as evidenced by the many codes developed in this field, these structures remain highly vulnerable, with limited capacity to resist and dissipate energy. This behavior becomes even more intricate when considering that structures are founded on soils through which applied loads are transmitted, taking into account the operation of the entire soil-structure system. This phenomenon is referred to as Soil-Structure Interaction (SSI).

The most noteworthy conclusions drawn from the findings are as follows :

- Based on the obtained results, it has been demonstrated that active control has a significant impact on the structural response, whether with or without Soil-Structure Interaction (SSI). The displacement due to dynamic loads is generally greatly reduced.
- In the presence of control, the S/R ratio has a significant influence on the effectiveness of the control. Both the maximum structural displacement and control force depend on it.
- The phenomenon of SSI directly affects the maximum structural displacement and subsequently the control force. Displacements generally increase compared to the case of perfect embedding.
- The position of the tendon has a major influence on structural displacements. For a single tendon, positioning it closer to the top is much more beneficial for structures without SSI, whereas positioning it lower is more advantageous in cases with SSI.

Overall, the study underscores the critical importance of active control strategies in mitigating dynamic responses of complex structures. Additionally, it highlights the need for careful consideration of Soil-Structure Interaction effects and optimal positioning of control elements for effective structural performance.

REFERENCES

1. Wang L et al. Seismic control of a smart structure with semi-active tuned mass damper and adaptive stiffness property. *Earthquake Engineering and Resilience*. 2023;2(1): 74-93. DOI:10.1002/eer.2.38
2. Wang L et al. Adaptive-passive tuned mass damper for structural aseismic protection including soil-structure interaction. *Soil Dynamics and Earthquake Engineering*. 2022; 158: 107298. DOI:10.1016/j.soildyn.2022.107298
3. Wang L et al. Study on adaptive-passive eddy current pendulum tuned mass damper for wind-induced vibration control. *The Structural Design of Tall and Special Buildings*. 2020; 29(15): e1793. DOI:10.1002/tal.1793
4. Wang L et al, Zhou Y. An adaptive-passive retuning device for a pendulum tuned mass damper considering mass uncertainty and optimum frequency. *Structural Control and Health Monitoring*. 2019;26(7): e2377. DOI:10.1002/stc.2377
5. Reteri K. Comportement dynamiques des structures intelligentes Poteau-poutre en tenant compte de l'effet de l'interaction sol-structure, Mémoire de Magister, option génie parasismique, université A.B.B. Tlemce., 2013. <http://dspace1.univ-tlemcen.dz/handle/112/4499>

6. Zhang H et al. Seismic control of adaptive variable stiffness intelligent structures using fuzzy control strategy combined with LSTM. *Journal of Building Engineering*. 2023; 78:107549. DOI:10.1016/j.jobe.2023.107549
7. Soong T, Spencer B Jr. Supplemental energy dissipation: state-of-the-art and state-of-the-practice. *Engineering Structures*. 2002; 24(3):243–259 DOI: 10.1016/S0141-0296(01)00092-X
8. Lynch JP. Active Structural Control Research at Kajima Corporation (The National Science Foundation's Summer Institute in Japan Program). 1998. Ph.D. Candidate (jplynch@stanford.edu) Department of Civil and Environmental Engineering Stanford University.
9. Trindade MA. Contrôle hybride actif- passif des vibrations de structures par des matériaux Piézoélectriques et viscoélastiques: Poutres sandwich/multicouches intelligentes 2000.
10. Wang L et al. Study on self-adjustable variable pendulum tuned mass damper. *The Structural Design of Tall and Special Buildings* 2018; 28(1): e1561. DOI:10.1002/tal.1561
11. Wang L et al. Semi-active eddy current pendulum tuned mass damper with variable frequency and damping. *Smart Structures and Systems*. 2020; 25(1): 65-80. DOI:10.12989/sss.2020.25.1.065
12. Mekki BO. Amortissement semi-actif des structures flexibles: présentée à L'Université à degli Studi di Roma "Tor Vergata" et du diplôme de docteur de l'école nationale des ponts et chaussées. 2006.
13. Wang L et al. Bi-directional semi-active tuned mass damper for torsional asymmetric structural seismic response control. *Engineering Structures*. 2023; 294: 116744. DOI:10.1016/j.engstruct.2023.116744
14. Wang L et al. An adaptive-passive retuning device for a pendulum tuned mass damper considering mass uncertainty and optimum frequency. *Structural Control and Health Monitoring*. 2019; 26(7): e2377. DOI:10.1002/stc.2377
15. Richard E, Christenson BS. Semi-active Control Of Civil Structures For Natural Hazard Mitigation: Analytical And Experimental Studies A Dissertation Submitted to the Graduate School of the University of Notre Dame in Partial Fulfillment of the Requirements for the Degree of Doctor of Philosophy by Department of Civil Engineering and Geological Sciences Notre Dame. 2001. Indiana.
16. Wang L et al. Seismic performance improvement of base-isolated structures using a semi-active tuned mass damper, *Engineering Structures*. 2022;271:114963. DOI:10.1016/j.engstruct.2022.114963
17. Wang L et al. Seismic Response Control of a Nonlinear Tall Building Under Mainshock-Aftershock Sequences Using Semi-Active Tuned Mass Damper. *International Journal of Structural Stability and Dynamics*. 2023; 23(16-18): 2340027. DOI:10.1142/S0219455423400278
18. Preumont A. *Vibration Control of Active Structures: An Introduction* Third Edition. 2011(179). ISBN : 978-94-007-2032-9
19. Julliere B. Contrôle actif à l'aide de piézo-composites des déformations induites thermiquement dans les matériaux composites: Mémoire présenté à la Faculté des études supérieures de l'Université Laval dans le cadre du programme de maîtrise en génie mécanique pour l'obtention du grade de maîtresses sciences (M.Sc.). 2006.
20. Jean P. Isolation vibratoire par contrôle semi-actif d'amortisseurs magnéto-rhéologiques pour l'interface lanceur/charge utile (Thèse de doctorat du Conservatoire National des Arts et Métiers (Spécialité Mécanique). 2006.
21. Ho Chey M. Passive And Semi-Active Tuned Mass Damper Building Systems. These de doctorat. 2007. University of Canterbury. Christchurch. New Zealand.
22. Cheng FY et al. *Smart structures Innovative systems for Seismic Response control*. Taylor and Francis group. 2008.
23. Spencer BF. *Structural Control in Honor of Takuji Kotori: The 14th World Conference on Earthquake Engineering* October 12-17. 2008. Beijing. China.
24. Maebayashi K, Shiba K, Mita A, Inada Y. Hybrid mass damper system for response control of building. 1992.
25. Steven L Kramer. *Geotechnical Earthquake Engineering*. Prentice Hall. New Jersey. 1996.
26. Kutanis M, Elmas M. Non-linear Seismic Soil-Structure Interaction Analysis Based on the Substructure Method in the Time Domain. *Journal of Structural Engineering*. 2001(25): 617-626.
27. Wolf JP, Deeks AJ. *Foundation Vibration Analysis: A Strength-of-Materials Approach* (ISBN 0 7506 6164 X). Printed and bound in Great Britain by Biddles. 2004. Kings Lynn (Designs and Patents Act 1988).
28. Shakibet H, Fuladgar A. Dynamic soil-structure interaction effects on the seismic response of asymmetric buildings. 2004.
29. Oudjene M et al. Influence de la catégorie de site sur le comportement sismique des structures rigides. 2005. Application des règles parasismiques algériennes 99 (RPA99).
30. Seghir A. Contribution à la modélisation numérique de la réponse sismique des ouvrages avec interaction sol-structure et interaction fluide-structure: Application à l'étude des barrages poids en béton. Thèse de doctorat. 2011.
31. Taha A et al. Time-Domain Analysis Approaches of Soil-Structure Interaction: A Comparative Study, *Engineering and Technology International Journal of Structural and Construction Engineering*. 2022; 16(12). <https://www.researchgate.net/publication/366701958>
32. Hassani N et al. Effect of soil-structure interaction on inelastic displacement ratios of degrading structures. *Soil Dyn. Earthq. Eng.* 2018; 104: 75–87. DOI:10.1016/j.soildyn.2017.10.0040
33. Mercado J et al. Evaluation of substructure and direct modeling approaches in the seismic response of tall buildings *Geo-Congress* 2020; 30-40. doi:10.1061/9780784482810.004
34. Oz I et al. Effect of soil-structure interaction on the seismic response of existing low and mid-rise RC buildings. *Appl. Sci.* 2020;10(23):8357. DOI:10.3390/app10238357
35. Bapir B et al. Soil-structure interaction: A state-of-the-art review of modeling techniques and studies on seismic response of building structures, *Frontiers in Built Environment*. 2023;9:1120351 doi: 10.3389/fbuil.2023.1120351
36. Ragi K et al. The Effect of Soil-Structure Interaction (SSI) on Structural Stability and Sustainability of RC Structures, *Civil and Environmental Engineering Reports*. 2024; 34(1). doi :10.59440/ceer/184254
37. Jabini A et al. Comparing the performance of substructure and direct methods to estimate the effect of SSI on seismic response of mid-rise structures," *International Journal of Geotechnical Engineering*. 2021; 15 (1): 81–94. DOI: 10.1080/19386362.2019.1597560
38. Wolf JP, Deeks AJ. *Foundation Vibration Analysis: A Strength-of-Materials Approach* (ISBN 0 7506 6164 X). Printed and bound in Great Britain by Biddles. 2004. Kings Lynn (Designs and Patents Act 1988).
39. Cheng FY et al. *Smart structures Innovative systems for Seismic Response control*, Taylor and Francis group. 2008.
40. Cheng FY et al. Generalized Optimal Active Control Algorithm Of Seismic Structures And Related Soil-Structure Formulation in Computational mechanics in structural engineering recent developments and future trends: Cheng FY and Fu ZZ (eds). Elsevier Applied Science. London. 1991.
41. Soong TT. *Active Structural Control: Theory and Practice*. 1st edn. Longman Scientific&Technical. UK and John Wiley & Sons. 1990. New York. ISBN 0-470-21670-0.

Reteri Khadidja:  <https://orcid.org/0000-0001-5212-9437>

Megnounif Abdellatif:  <https://orcid.org/0000-0001-7181-2928>



This work is licensed under the Creative Commons BY-NC-ND 4.0 license.

TYPE-APPROVAL AND QUALIFICATION TESTING OF AIR BRAKING SYSTEMS OF AGRICULTURAL TRAILERS UNDER STATIONARY CONDITIONS

Zbigniew KAMIŃSKI^{*}, Jarosław CZABAN^{*}

^{*}Faculty of Mechanical Engineering, Białystok University of Technology, Wiejska 45C, 15-351 Białystok, Poland

z.kaminski@pb.edu.pl, j.czaban@pb.edu.pl

received 10 October 2023, revised 05 September 2024, accepted 10 September 2024

Abstract: For road safety reasons, agricultural vehicle braking systems must comply with the approval requirements of EU Delegated Regulation 2015/68, which are evaluated during stationary and road testing conditions. For the stationary tests, an algorithm and procedures are developed to test the air braking systems of towed vehicles, including checking for tightness, pushrod strokes of brake chambers (adjustment), response times and the capacity of the compressed air reservoirs. Testing of a single-axle trailer braking system was carried out using a computer-controlled diagnostic device incorporating a simulator of the tractor's braking system developed by the authors. The trailer test results obtained confirmed the usefulness of the methodology developed and showed high accuracy and repeatability of measurements. The results of this work can be used not only by type-approval bodies, but also by manufacturers of trailers and towed agricultural machinery for quality control or product qualification tests.

Key words: agricultural trailer, pneumatics, braking system, type-approval test, stationary test, simulator

1. INTRODUCTION

The braking system controlling the stopping function of a vehicle is one of the most important structural components with a decisive impact on the level of active safety [1]. Therefore, newly manufactured agricultural vehicles are subject to various type-approval tests [25], including braking and confirming the vehicle's ability to function on the road, in accordance with the regulations and technical requirements for the vehicle category in question. Vehicle braking systems are also subject to inspection on production lines, as part of qualification testing and product quality control. The results of these tests may be used as the basis for the evaluation of the Conformity of Production (CoP), as a means of evidencing the ability to produce a series of products [29] that exactly match the specification, performance and marking requirements outlined in the type approval documentation. The technical condition of the brakes of in-service vehicles is also checked periodically during mandatory periodic technical inspections [23], [27].

In view of road safety, the braking systems of agricultural vehicles must meet a number of requirements for, among other things, braking efficiency, the follow-up action during slow braking, and a high speed of action during sudden braking [11]. A completely new set of requirements for the braking systems of agricultural vehicles (formulated in the Delegated Regulation (EU) 2015/68 [6]) was set in 2015, based on the commercial truck and trailers requirements in UN/ECE Regulation 13 [24]. It sets the same level of performance for both pneumatic and hydraulic braking systems (minimum 50% braking efficiency for vehicles operating above 30 km/h). In addition, for agricultural trailers with a gross mass of more than 3,500 kg (categories R3 and R4) and travelling at a speed of more than 40 km/h, a specific distribution of braking forces between the vehicle axles is required, as well as

ensuring synchronisation of tractor and trailer braking [6]. The last requirement is deemed to be met if the waveform of the braking rate as a function of control pressure at the coupling head falls within prescribed tolerance zones, referred to as 'compliance bands' or 'compatibility corridors', for the towing and towed vehicle in both the laden and unladen states.

For the type-approval of any agricultural vehicle, the braking performance is measured during road tests [2], [13]. The performance of service and emergency braking systems of trailers is expressed in terms of a braking rate calculated as the percentage of mean fully developed deceleration (MFDD) to the gravitational acceleration constant. MFDD means the average deceleration calculated on the basis of the measured distance recorded when decelerating a vehicle between two specified speeds (80% and 10% of the start speed) [30]. The braking rate determined for a tractor-trailer unit is then converted to the braking rate of the trailer alone, taking into account the force in the coupling or the tractor and trailer masses (when only the trailer brakes), depending on the measurement method [6]. The performance of parking braking systems is based on the ability to hold the laden trailer stationary, facing up and down slopes. Road tests are costly and not always feasible, due to weather conditions, and so, for qualification tests, manufacturers check the braking performance of trailers on roller brake testers [19].

Despite the disadvantages of air braking systems, they are technologically refined [33] and implemented on newly manufactured trailers and towed agricultural machinery in many EU countries. Before the dynamic testing of trailers equipped with air braking systems can be performed, stationary tests should be carried out. In the case of qualification tests, the brake pushrod stroke should be checked and adjustments made if necessary; the air system should be checked for leaks. In the case of the approval and conformity of production tests, the response time of the braking system must also be measured and the capacity of the

trailer's compressed-air reservoir checked [32].

The response time for the service braking system of towed vehicles is determined while the vehicle is stationary (without the tractor), using a special simulator, to which the coupling heads of the supply and control line are connected. The conceptual scheme and guidelines for the design of a pneumatic simulator, providing a standard and repeatable build-up of air pressure in the control line, are described in the relevant regulations [6], [24].

Commercially available simulators are usually suitcase-type devices [32], [28] that allow response time measurement and checking of the air reservoir capacity. However, these devices are of little use for testing air brake systems under industrial conditions on production lines. Therefore, the authors developed a device for the comprehensive diagnosis of both single and dual-line air brake systems of towed agricultural vehicles [14], even before the introduction of the new regulations [6]. One prototype version of such a device was made in collaboration with Metal-Fach, as part of an EU-funded project [15]. This paper presents a methodology for stationary testing of air brake systems using a device for dual-line brakes, as only such can be used on agricultural vehicles after 2022. The device (tractor simulator) developed by the authors is computer-controlled, which enables automatic control of the diagnostic session and generation of a test report. The advantage of the device is that it can co-operate with roller dynamometers to check the braking efficiency and to produce the braking characteristics of the towed vehicle [26]. This can be done by successively applying the brakes of all axles of the towed vehicle at predetermined control pressures generated by the device [4].

The remainder of the paper is organised as follows. Section 2 describes the programme of stationary approval and qualification testing of the air braking systems of trailers and towed agricultural machinery, as well as the requirements and conditions for the individual tests. Section 3 describes the construction and operation of the testing equipment. The results of example tests on an agricultural trailer are discussed in Section 4. Finally, a summary and the conclusions are presented in Section 5.

The results of this work may be useful for institutions involved in vehicle type approval testing and, above all, for companies manufacturing trailers and towed agricultural machinery, the production of which requires components and parts from various domestic and foreign suppliers. Guaranteeing the desired quality of the final product requires the use of appropriate procedures and equipment on production lines for the diagnosis of individual systems and assemblies during product qualification tests. By applying the developed device to the production line of trailers and towed agricultural machinery, it is possible not only to achieve better product quality, but also to ensure the continuity of quality control processes, reduce errors and detect defects more quickly. Well-planned quality control ensures that the finished product meets strict quality standards and builds a positive brand image and customer confidence. Minimising the number of defective products also has a significant impact on reducing the cost of warranty service. The use of modern methods and diagnostic equipment enables the improvement of the achieved results of production activities, the effective use of the company's resources, as well as the involvement of all employees in the process of creating quality.

2. TESTING PROGRAM, REQUIREMENTS AND CONDITIONS

A testing programme was adopted on the basis of an analysis of the requirements, standards and regulations [6], [24], [3], [22] and included:

- checking the tightness of the trailer's pneumatic braking system,
- checking the working stroke of the brake, brake chambers or cylinders,
- checking the response time of the braking system, and
- checking the capacity of the compressed air reservoir.

The first two tests for checking the quality of the installation and adjustment of important components of the pneumatic braking system (actuators, braking valves and force regulators) are used in basic qualification tests and in the preparation of vehicles for approval tests. The latter two tests are the basis for assessing the correctness of operation and component selection in approval tests, according to the requirements of Delegated Regulation 2015/68 [6]. However, trailer manufacturers often conduct them as part of their qualification testing.

2.1. Checking tightness of a braking system

Requirements: According to the Polish standard PN-90/R-36123 [22] and the industry standard BN-86/3611-03 [3], the tightness of an air-braking system should be such that, after disconnecting the supply line from the simulator (within 10 min), the pressure drop measured in the reservoir or the brake chamber is no greater than 2% of the initial pressure.

Test conditions:

- before disconnection, the pressure in the supply line should be 6.5 ± 0.15 bar,
- the supply line should be disconnected for automatic trailer braking,
- the brake force regulator should be set to the position corresponding to the maximum load of the trailer, and
- ambient temperature should be about 20°C.

Due to the relatively long measurement times, faster and less restrictive tests are usually used in industrial settings. For example, according to Wabco, a braking system is considered to have no leaks if the pressure does not drop by more than 0.2 bar within 5 min [31]. 6.5 bar can be taken as the initial pressure.

2.2. Checking the stroke of the brake actuator

Requirements: According to Wabco [31], when the brakes are fully applied, the stroke of the brake actuators should be between 1/2 and 2/3 of the rated stroke. In this regard, more precise regulations are used in North America [21], where the brake adjustment limit of the stroke is given for brake chambers of various types and sizes, including long stroke chambers [20]. These range from about 77-80% of the rated stroke.

Test conditions [31]:

- After applying the brakes, the stroke of the actuator should be measured (e.g. using a cable encoder) and the pressure measured in the brake chamber should be greater than 6 bar,
- the initial pressure in the supply line should be between 7.0-8.1 bar, and

- the initial pressure in the control line should be between 7.0-8.0 bar.

For the sake of simplicity, equal initial pressure settings can be assumed for both lines, e.g. 7+0.15 bar.

2.3. Response time checking

Requirements: During braking, the time elapsing between the moment when the pressure produced in the control line by the simulator reaches 0.65 bar (10% of 6.5 bar) and the moment when the pressure in the brake actuator of the towed vehicle reaches 75% of its asymptotic value, shall not exceed 0.4 s.

The response time determined during testing is rounded to the nearest tenth of a second. If the number representing hundredths of a second is 5 or more, the reaction time is rounded to the next larger tenth. Thus, the allowed maximum value of reaction time is 0.449 seconds.

Test conditions:

- During the test, the strokes of the brake actuators of all axles should be adjusted to correspond as closely as possible to the required values,
- the pressure in the supply line before the test should be 6.5+0.15 bar,
- the brake force regulator should be set in a position corresponding to the maximum load capacity of the trailer,
- the place of measuring the pressure in the trailer is the actuator furthest from the trailer emergency brake valve,
- the control line is connected to a simulator that reproduces the reference pressure waveform during braking (the calibration of the simulator is described in the next section).

In some countries, additional requirements are placed on the speed of air-braking systems. For example, in New Zealand, the trailer release time and the response time on the control line for braking of the next trailer are also checked [17]. The equipment developed by the authors also takes these options into account.

2.4. Checking the capacity of the trailer tank

Requirements: Air reservoirs (energy reservoirs) installed on towed vehicles should be such that, after eight full-stroke actuations of the tractor's service braking system (simulator), the pressure supplied to the actuators using it does not fall below a level equivalent to one-half of the figure obtained at the first brake application and without actuating either the automatic or the parking braking system of the towed vehicle.

Test conditions:

- The pressure in the reservoirs at the beginning of the test should be 8.5 bar,
- the supply line should be closed (preferably disconnected) so that the reservoirs shall not be replenished during the test; in addition, all energy storage devices for auxiliary equipment should be shut off,
- at each brake application, the pressure in the control line shall be 7.5 bar,
- brakes should be adjusted as accurately as possible during the test.

3. DESIGN AND OPERATION OF THE DIAGNOSTIC DEVICE

In developing the concept of the device, the following design assumptions and requirements were applied:

- installation of a pneumatic system, electrical system, computer and measuring apparatus in the control cabinet,
- supplying the simulator with compressed air from an external air preparation station with an operating pressure of more than 9 bar,
- the supply voltage of electrical and electronic components is 24 V,
- automatic control of parameters and the course of the diagnostic session of trailer braking systems, by opening or closing the appropriate solenoid valves in accordance with the algorithms in the computer program,
- use of a measurement card for recording diagnostic parameters and actuation of electromagnetic valves by means of digital outputs (TTL) and voltage-current amplifiers,
- the ability to generate and print the test report,
- integration of the simulator software with other diagnostic equipment, including a roller dynamometer and also an instrument for testing the electrical system of a trailer.

A block diagram of the device, which includes the pneumatic scheme of the simulator together with the dual-line braking system of the trailer under test, is shown in Fig. 1. The device's design guidelines in Regulation 68/2015 [6] were used in its development.

The device consists of three basic modules:

1. a tractor braking system simulator to supply and control the braking system of the trailer under test,
2. a measurement and diagnostic system, including:
 - apparatus for measuring and recording the time waveforms of pressure in selected elements of the simulator and the trailer braking system, as well as measuring the displacement of the brake actuator piston (computer, control device with measurement card, PT pressure transducers, DL displacement transducer), and
 - a computer program for measurement acquisition, graphical presentation of results, system diagnosis and printing of test protocol,
3. input-output adapter for powering the pressure transducers and converting voltage signals from the transducers to the measurement card.

The simulator is supplied from the APS air preparation station through the SOV shut-off valve. A pressure reducing valve PRV is used to preset the pressure value in the simulator system (above 9 bar). Accurately setting the pressure in compressed air reservoir R, with a capacity of 30 l, measured by sensor M and pressure transducer PT1, is achieved by opening the inlet or outlet of the reservoir via two-way two-position solenoid valves SV1 and SV2, which are normally closed (NZ). A two-way two-position solenoid valve, SV3, is normally closed (NZ) and is used to supply compressed air to the trailer under test. A direct-acting, normally closed (NZ) three-way two-position solenoid valve, SV4, is used to apply the trailer's brakes during the response time test. The throughput of the O orifice determining the speed of the pressure signal from the simulator controlling the trailer brakes should be selected experimentally in the calibration process, using calibration reservoirs CR1 and CR2 with capacities of $385 \pm 5 \text{ cm}^3$ and $1155 \pm 15 \text{ cm}^3$, respectively. During the diagnostic session, the CU

control device manages the actuation of the solenoid valves based on the signals generated from the digital outputs of the measurement card after amplification.

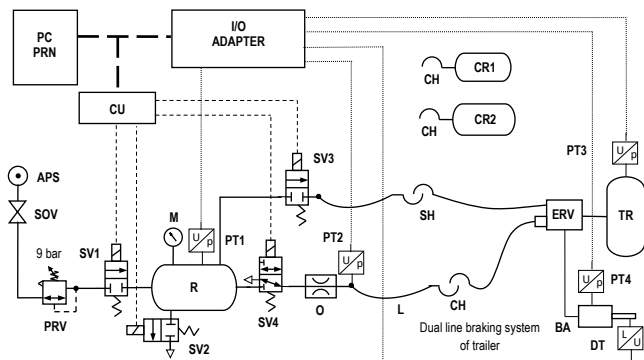


Fig. 1. Diagram of the device for diagnosing two-line air brake systems of agricultural trailers and towed machines: APS - air preparation station; BA - brake actuator; CH - control coupling head; CR1 and CR2 - calibration reservoirs with volumes of $385 \pm 5 \text{ cm}^3$ and $1155 \pm 15 \text{ cm}^3$, respectively (including its coupling head); CU - control unit; DT - displacement transducer (cable encoder); ERV - emergency relay valve; I/O Adapter - input-output adapter; L - line from orifice O up to and including its coupling head CH (having an inner volume of $385 \pm 5 \text{ cm}^3$ under a pressure of 6.5 bar); M - manometer; O - calibrated orifice; PC - computer; PRN - printer; PRV - pressure reducing valve; PT_i - ith pressure transducer; R - compressed air tank with a capacity of 30 litres; SH - supply coupling head; SOV - shut-off valve; SV1, SV2, and SV3 - 2/2 electrovalves (NC); SV4 - direct-acting 3/2 electrovalve (NC); and TR - trailer reservoir

Before measuring the response time, the device should be calibrated. The simulator should be adjusted by selecting nozzle O so that when a $385 \pm 5 \text{ cm}^3$ CR1 reservoir is connected to it, the time required for the pressure to rise from 0.65 bar to 4.9 bar (10% and 75% of the rated pressure of 6.5 bar, respectively) is $0.2 \pm 0.01 \text{ s}$. If a $1155 \pm 15 \text{ cm}^3$ CR2 reservoir is inserted instead of the aforementioned tray, the time for the pressure to rise from 0.65 bar to 4.9 bar without further adjustment should be $0.38 \pm 0.02 \text{ s}$. Between these two values, the pressure should increase approximately linearly.

An integral part of the device's measurement and diagnostic system is the Windows-based computer programme 'Simulator'. This programme allows the management of the diagnostic session, the acquisition of measurement data and the printing of the test protocol. Either the mouse or the keyboard can be used to operate the programme's menus. The measurement system is based on voltage pressure and displacement transducers (0-10 V output voltage) and Advantech's PCI 1710L measurement card.

The general algorithm of the program for the adopted test methodology is shown in Fig. 2. For each test, the control logic of individual solenoid valves in the simulator was analysed to achieve the required pressure in the air reservoir of the simulator and the braking system under test, as well as the control of the trailer braking system. Therefore, before the trailer braking system leakage test, valve SV1 and valve SV3 are opened, in order to fill the compressed air reservoirs (R of the simulator and TR of the trailer) to the required pressure level. The required value of the pressure in the R tank, measured by the PT1 transducer, is determined by opening or closing valves SV1 and SV2. Valve SV3 is

then closed and, after the trailer is disconnected from the simulator, the pressure drop in the trailer tank (pressure transducer PT3) is recorded over the accepted time interval. The desired initial pressure level, the time of measurement, and the permissible value of the pressure drop, are then specified in the settings of the computer program, according to the adopted testing methodology.

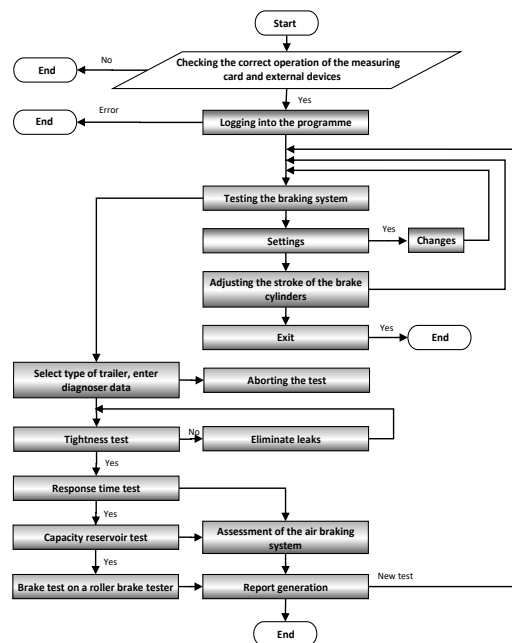


Fig. 2. General algorithm of a computer programme for the diagnosis of braking systems of agricultural machinery and trailers

The view of the 'Measurement' window of the 'Simulator' programme, for managing the course of the diagnostic session, is shown in Fig. 3.

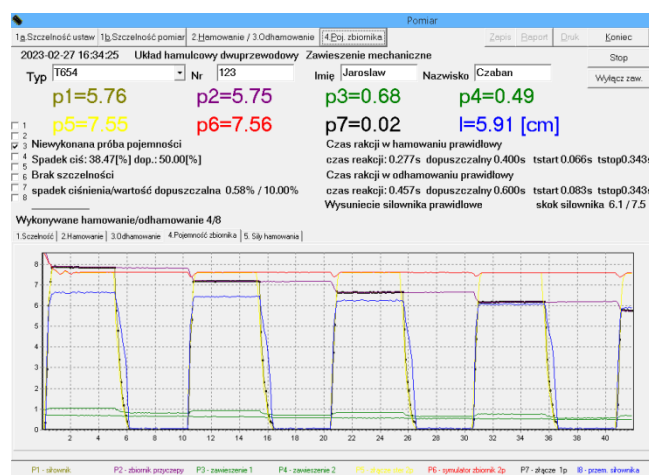


Fig. 3. 'Measurement' window of the 'Simulator' program when checking air tank capacity (in Polish)

4. SAMPLE TEST RESULTS

The tests were carried out under laboratory conditions at the Vehicle Pneumatic Systems Research Laboratory of the Faculty of Mechanical Engineering of Białystok University of Technology.

A model of a dual-line braking system, built from components from a T-654 single-axe trailer from Pronar [12], was used for the tests. The pneumatic circuit and a view of the trailer's braking system connected to the diagnostic device are shown in Fig. 4. The tests included tightness checking, measuring response time and checking the capacity of the trailer's air reservoir after adjusting the stroke of the brake actuator. A device on the laboratory equipment was used for the tests. In addition, comparative response time tests were carried out using a device operating on the production line of one of the domestic manufacturers of agricultural trailers. Their purpose was to evaluate the repeatability and comparability of response time measurements made on different devices but for the same braking system.

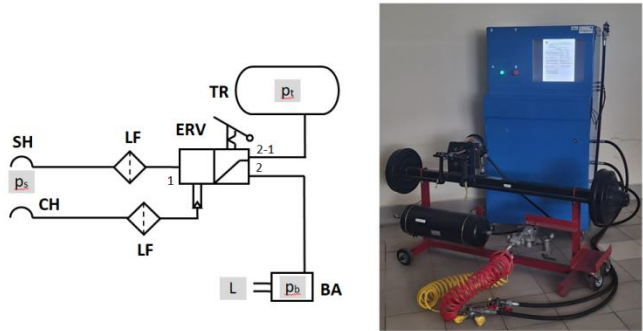


Fig. 4. Diagram and view of the dual-line trailer pneumatic system: SH - supply coupling head; CH - control coupling head; LF - line filter; ERV - emergency relay valve combined with a manual brake force regulator; TR - 20 dm³ air reservoir; BA - type 20LS brake chamber

The results of the tightness test are shown in Fig. 5. The recorded pressure drop p_t of 0.051 bar in the trailer reservoir over a period of 10 min is within the permissible limits (dashed lines), which proves that the tested braking system is sufficiently tight. Wabco's requirements are also met, as the drop over 5 minutes was 0.041 bar and did not exceed the permissible value of 0.2 bar [31]

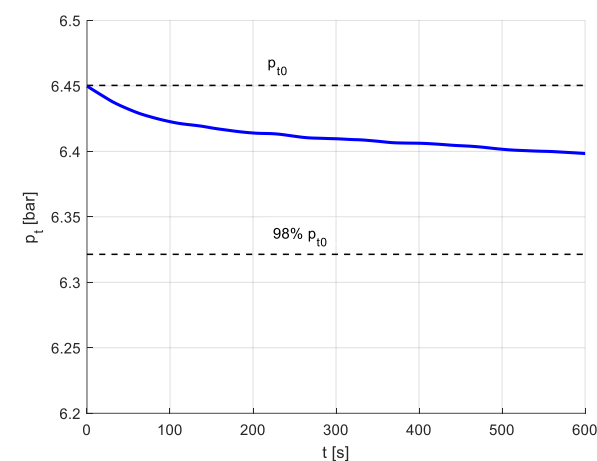


Fig. 5. The course of the pressure p_t in the trailer reservoir during the tightness test of the braking system

Examples of the time waveforms of control pressure p_c in the simulator, pressure p_s in the simulator reservoir, pressure p_t in the trailer reservoir, pressure p_a in the brake chamber and the stroke L of the actuator rod during the checking of braking system speed operations are shown in Fig. 6.

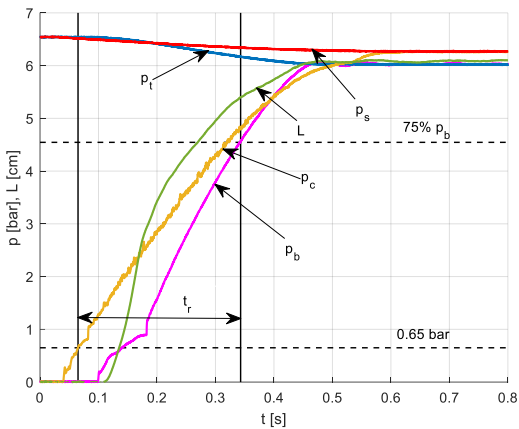


Fig. 6. The course of measured quantities during the response time test: p_c - pressure of the simulator control; p_s - pressure in the simulator reservoir; p_t - pressure in the trailer reservoir; p_a - pressure in the brake chamber; L - stroke of the actuator

The results of 15 test trailer response time measurements, determined using two simulators, are summarised in Table 1.

Tab. 1. Results of response time t_r [s] of the braking system of the tested trailer

| No. | Bialystok University of Technology simulator | Industrial simulator |
|----------------------------------|--|----------------------|
| 1 | 0.282 | 0.282 |
| 2 | 0.281 | 0.280 |
| 3 | 0.280 | 0.281 |
| 4 | 0.281 | 0.280 |
| 5 | 0.280 | 0.280 |
| 6 | 0.279 | 0.280 |
| 7 | 0.280 | 0.280 |
| 8 | 0.279 | 0.280 |
| 9 | 0.279 | 0.281 |
| 10 | 0.282 | 0.281 |
| 11 | 0.280 | 0.281 |
| 12 | 0.279 | 0.280 |
| 13 | 0.280 | 0.281 |
| 14 | 0.280 | 0.282 |
| 15 | 0.281 | 0.280 |
| Mean | 0.2802±0.0008 | 0.2806±0.0006 |
| Test name | | |
| SDA | H0/ 0.3756 | H0/0.1406 |
| DLM | H0/0.5722/0.8409 | H0/0.0650/0.2546 |
| DH | H0/0.5855 | H0/0.1037 |
| G | H0/0.7342 | H0/0.0648 |
| Result of the test Welch/p-value | H0/0.2278 | |
| Result of the test MWW/p-value | H0/0.2065 | |
| Response time [6] | 0.3 | 0.3 |

The normality of the distribution at the significance level $\alpha=0.01$ was checked using tests applied to small sample sizes:

the D'Agostino SDA skewness test ($n > 8$) [8], the Desgagné and Lafaye de Micheaux DLM test ($n > 9$) [9], the Doornik-Hansen DH test ($n > 7$) [10], and the Geary G test ($n > 11$) [7]. The probability values p associated with the distributions of the individual test results are summarised in Table 1. All of the tests confirmed the assumption of a normal distribution for both measured response times ($p > \alpha$).

Both the Welch's t-test (for populations with a normal distribution and unknown variances) [34], [16] and the non-parametric Mann Whitney U-test, also known as the Mann-Whitney-Wilcoxon (MWW) test [16], [18], were used to test the statistical significance of the differences in the mean response time values measured on the two simulators. For both tests, the values of the test statistics (t and U), their critical values, and associated probability p -values were determined and then compared with a significance level of $\alpha = 0.01$. If $p > \alpha$, it was assumed that there was no reason to reject the zero hypothesis H_0 about the equality of means. If $p \leq \alpha$, the alternative hypothesis H_1 about the significance of differences between the means of the response times was accepted. Table 1 shows the results of the p -values and test results. Statistical calculations were performed in the Matlab programming environment and a ready-made m-file `mwwtest` [5] was used to calculate the MWW test.

The difference between the mean response time values measured by the two different devices, built upon the same concept, using the same critical components (valves), and was only 0.0004 s. In practice, this means that the response time of the air braking system of a given trailer, as measured by these devices, can be considered to be almost identical.

Examples of the time waveforms of the control pressure p_c of the simulator, the pressure p_s in the simulator reservoir, the pressure p_t in the trailer reservoir, and the stroke L of the actuator, when checking the capacity of the trailer reservoir, are shown in Fig. 7.

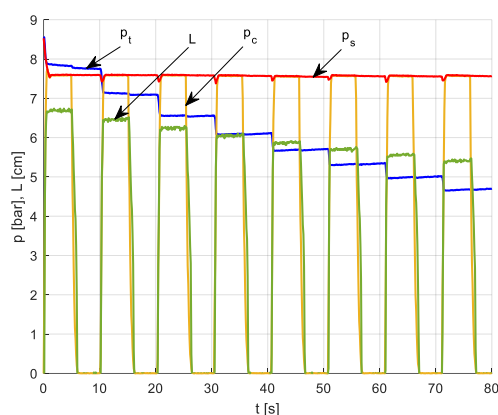


Fig. 7. The course of measured quantities during checking of the capacity of the air reservoir: p_c - control pressure of the simulator; p_s - pressures in the simulator reservoir; p_t - pressures in the trailer reservoir; and L - stroke of the actuator

Based on the recorded pressure p_t in the trailer reservoir, the pressure $p_{t1} = 7.76$ bar after the first braking and pressure $p_{t8} = 4.09$ bar after the eighth braking, were determined. The test results prove the correctness of the selection of the trailer's compressed air reservoir capacity ($p_{t8} > 0.5p_{t1}$).

5. SUMMARY AND CONCLUSIONS

The programme of stationary air brake system testing described in this paper covers the most important aspects of diagnosing trailers and towed agricultural machinery for approval testing. The adopted procedures for individual diagnostic tests (requirements and test conditions) are in accordance with the requirements for testing the brakes of agricultural vehicles given in Delegated Regulation 2015/68 [6].

The methodology presented for diagnosing the braking system can be used, in whole or in part, for production conformity assessment, qualification testing and the quality control of trailers and other towed agricultural machinery on production lines.

The device developed by the authors to perform stationary tests (leakage, response time and air reservoir capacity) has the ability to operate automatically and generate test reports. This reduces the number of errors resulting from manual testing and increases the efficiency of the testing process. Another advantage is the possibility of co-operating with the roller tester in order to check the braking efficiency and to draw up the braking characteristics of a towed vehicle.

Based on the testing of the braking system of a single-axle trailer, the following conclusions can be made:

1) The measured pressure drop in the reservoir of 0.051 bar in 10 min did not exceed 2% of the initial pressure value of 6.45 bar; the pressure drop of 0.041 bar in 5 min did not exceed the value of 0.2 bar allowed by Wabco [31], which indicates that the system is sufficiently tight.

2) The response time of the trailer braking system of 0.3 s, after rounding, was less than the 0.4 s allowed.

3) The drop in trailer reservoir pressure after the eighth braking of 4.09 bar was greater than half the pressure value after the first braking of 3.88 bar, indicating sufficient trailer reservoir capacity.

4) The average response time of the braking system of the tested trailer, determined from 15 measurements using two simulators, differed by only 0.0004 s.

5) The results of Welch's t-test and the Mann-Whitney-Wilcoxon test showed that there was no basis for rejecting the null hypothesis H_0 for the equality of the mean reaction time values measured on the two simulators.

Therefore, the tested trailer meets the requirements of Regulation 2015/68 [6] and other regulations and recommendations. Positive test results help to build manufacturer and users confidence in the safety and performance of the braking system, demonstrate high manufacturing standards, enhance the company's image and reputation with contractors and users.

The simulators used for the study, built according to the same concept and using the same key components (valves), are characterized by high accuracy and repeatability of measurements. The test results confirmed the suitability of the developed methodology for type approval testing and quality control of air brake systems of trailers and towed agricultural machinery.

REFERENCES

1. Aleksandrowicz P. The impact of a vehicle braking system state on safe driving. Part two. AIP Conf. Proc. 21 February 2019; 2077 (1): 020001. <https://doi.org/10.1063/1.5091862>

2. Borawska E, Borawski A. Influence of the initial speed of the agricultural tractor on the brakes heating process during emergency braking. *Heat Transfer Research*. 2020; 51(10): 967-974. <https://doi.org/10.1615/HEATTRANSRES.2020032024>
3. BN-86/3611-03. Pojazdy samochodowe i przyczepy. Hamulce. Ogólne zasady budowy powietrznych układów przenoszących.
4. Caban A, Kidawski A, Włodarczyk A. Synchronization of the braking of heavy tractor-trailer and tractor-semitrailer units: operational problems. *The Archives of Automotive Engineering – Archiwum Motoryzacji*. 2017; 77(3), 17-29. <https://doi.org/10.14669/AM.VOL.77.ART2>
5. Cardillo G. MWWtest: Mann-Whitney-Wilcoxon non parametric test for two unpaired samples. 2009. <http://www.mathworks.com/matlabcentral/fileexchange/25830>
6. Commission Delegated Regulation (EU) 2015/68 of 15 October 2014 supplementing Regulation (EU) No 167/2013 of the European Parliament and of the Council with regard to vehicle braking requirements for the approval of agricultural and forestry vehicles Text with EEA relevance. <https://eurlex.europa.eu/legalcontent/EN/TXT/?uri=CELEX%3A32015R0068>
7. D'Agostino RB. Simple compact portable test of normality: Geary's test revisited. *Psychological Bulletin*. 1970; 74(2): 138-140. <https://doi.org/10.1037/h0029499>
8. D'Agostino RB, Belanger A, D'Agostino Jr. RB. A suggestion for using powerful and informative tests of normality. *American Statistician*. 1990; 44(4): 316-321. <https://doi.org/10.1080/00031305.1990.10475751>
9. Desgagné A, Lafaye de Micheaux P. A powerful and interpretable alternative to the Jarque-Bera test of normality based on 2nd-power skewness and kurtosis, using the Rao's score test on the APD family. *Journal of Applied Statistics*. 2018; 45(13): 2307-2327. <https://doi.org/10.1080/02664763.2017.1415311>
10. Doornik JA, Hansen H. An omnibus test for univariate and multivariate normality. *Oxford Bulletin of Economics and Statistics*. 2008; 70(1): 927-939. <https://doi.org/10.1111/j.1468-0084.2008.00537.x>
11. Glišović J, Lukić J, Šušteršič V, Čatić D. Development of tractors and trailers in accordance with the requirements of legal regulations. In: *Proc. of 9th International Quality Conference*. Kragujevac. Serbia 2015; 193-202.
12. Instrukcja obsługi. Przyczepa rolnicza Pronar t654 Pronar t654/1. http://pronar.pl/pdf/instrukcje/T654%20T654_1_PL.pdf
13. Kamiński Z, Czaban J. Diagnosing the agricultural tractor braking system within approval tests. *Eksplotacja i Niezawodność – Maintenance and Reliability*. 2012; 14 (4): 319-326.
14. Kamiński Z, Czaban J. Urządzenie do diagnostyki powietrznego układu hamulcowego (Device for diagnosing air braking system). Patent PL 225 170 B1.
15. Kamiński Z, Czaban J, Sokolowski R. Integrated system for agricultural machinery and trailers on the production line. Project entitled "Technology transfer to industry" implemented under Sub-measure 8.2.1 of the Human Capital Operational Programme 2013.
16. Kanji GK. 100 Statistical Tests. Sage Publications Ltd. London 2006.
17. Land Transport Rule. Heavy-vehicle Brakes. Rule 32015, New Zealand 2006. <https://www.nzta.govt.nz/assets/resources/rules/docs/heavy-vehicle-brakes-2006.pdf>
18. Marx A, Backes C, Meese E, Lenhof HP, Keller A. EDISON-WMW: Exact Dynamic Programming Solution of the Wilcoxon-Mann-Whitney Test. *Genomics, Proteomics and Bioinformatics*. 2016; 14(1): 55-61. <https://doi.org/10.1016/j.gpb.2015.11.004>
19. Nordstrom O. Feasibility of using roller brake testers instead of road tests for heavy vehicles. Summary report of investigations carried out by VTI and A88 sponsored by the Swedish National Road Administration, 1998. <https://www.diva-portal.org/smash/get/diva2:669831/FULLTEXT01.pdf>
20. North American Standard Out-Of-Service Criteria. Commercial Vehicle Safety Alliance. 2014. https://gacc.nifc.gov/rmcc/documents/engine_academy/ooscriteria.pdf
21. North American Standard Out-Of-Service Criteria. Handbook edition, 2020. <https://exams.sfdtraining.com/engineer/2021/res/driveroperator/main/North%20American%20Standard%20Out-Of-Service%20Criteria%202020.pdf>
22. PN-90/R-36123. Ciągniki. Przyczepy i przyczepiane maszyny rolnicze. Powietrzny jednoprzewodowy układ przenoszący hamulców. Wymagania i badania.
23. Recommendation N° 8 "Brake testing in periodic technical inspection". CITA/WG1-09-2017-110 2018. https://citainsp.org/wp-content/uploads/2017/10/CITA_Recommendation_8_brakes.pdf
24. Regulation No 13 of the Economic Commission for Europe of the United Nations (UN/ECE): Uniform provisions concerning the approval of vehicles of categories M, N and O with regard to braking [2016/194]. <https://eur-lex.europa.eu/legal-content/EN/TXT/?uri=CELEX%3A42016X0218%2801%29>
25. Robinson BJ, Scarlett AJ, Seidl M. Development of technical requirements/performance specifications for functional and occupational safety topics of agricultural and forestry vehicles - Final Report. Transport Research Laboratory, 2013.
26. Saffholland. Test sheet for synchronization of braking forces for semi-tractor/trailer combinations. https://saffholland.com/dk/en/download-center/document/resource/environment/project1_p/documents/documentationP/Before%2520Empolis%2520Box%2520update/pLiterature/BrakeTech_Test_sheet_for_synchronization_en-DE.pdf
27. Tarancón-Andrés E, Santamaría-Peña J, Arancón-Pérez D, Martínez-Cámara E, Blanco-Fernández J. Technical Inspections of Agricultural Machinery and Their Influence on Environmental Impact. *Agronomy*. 2022; 12(4): 907-1010. <https://doi.org/10.3390/agronomy12040907>
28. Tietjen. Air brake systems for trailers. Available from: <https://www.tietjengmbh.de/en/products/air-brake-systems-for-trailers>
29. Urdhwaresh HP. Risk Assessment in Conformity of Production (COP) Tests. SAE Technical Paper 2017-26-0130. 2017. <https://doi.org/10.4271/2017-26-0130>
30. Vrabel J, Jagelčák J, Rievaj V, Caban J. The quality of the brake components and its impact on the basic parameters of braking. *Machines. Technologies. Materials*. 2014; 8(6): 6-8.
31. Wabco. Air brake system agriculture and forestry. Maintenance, testing & fault-finding. <https://www.wabco-customercentre.com/catalog/docs/8150100833.pdf>
32. Wabco. Conformity test unit. System description. Edition 3. 815 010 190 3 (en). <https://www.wabco.info/i/142>
33. Wabco. Pneumatic braking system agriculture and forestry. Product catalogue. <https://www.wabco-customercentre.com/catalog/docs/8150100823.pdf>
34. Welch BL. The generalisation of students' problems when several different population variances are involved. *Biometrika*. 1947; 34(1-2): 28-35. <https://doi.org/10.1093/biomet/34.1-2.28>

This research was funded through a subsidy from the Ministry of Science and Higher Education of Poland, for the discipline of mechanical engineering at the Faculty of Mechanical Engineering at Białystok University of Technology (WZ/WM-IIM/5/2023).

Zbigniew Kamiński:  <https://orcid.org/0000-0003-2693-5077>

Jarosław Czaban:  <https://orcid.org/0000-0002-0677-7342>



This work is licensed under the Creative Commons BY-NC-ND 4.0 license.

THE INFLUENCE OF SELECTED BRUSHING PROCESS PARAMETERS ON THE TOOL'S OPERATING TIME

Karol FALANDYS^{*/***}, Tomasz ZYMRÓZ^{*}, Krzysztof KURC^{**}

^{*}Safran Aircraft Engines Poland, Południowa 23, 39-120 Sędziszów Małopolski, Poland

^{**}Rzeszów University of Technology, Faculty of Mechanical Engineering and Aeronautics,
Department of Applied Mechanics and Robotics, al. Powstańców Warszawy 12, 35-959 Rzeszów, Poland

^{***}Rzeszów University of Technology, Faculty of Mechanical Engineering and Aeronautics,
Department of Aerospace Engineering, al. Powstańców Warszawy 12, 35-959 Rzeszów, Poland

karol.falandys@safranngroup.com, tomasz.zymroz@safranngroup.com, kkurc@prz.edu.pl

received 27 March 2024, revised 09 October 2024, accepted 10 October 2024

Abstract: The article concerns the possibility of carrying out an optimization process of the extending the life of a brush tool which is use during the process of removing burrs and rounding edges. The work focused on the influence of selected parameters on the wear time of tools. A number of tests were carried out to optimize the selection of parameters in terms of tool life, while maintaining the proper quality of the manufactured products, which translates into their reliability. As part of the work carried out, an optimal set of parameters was prepared to extend the tool's operational time. These parameters are the rotational speed of 1400 rpm and the external diameter of the tool of 200 mm. Thanks to the use of new parameters of the brushing process, the tool's operational time was extended by about 67%. The work carried out, after verification as part of large-scale production, led to a reduction in the consumption of tools, which had a positive impact on the improvement of the company's financial result (reduction of cost per part) and also contributed to the reduction of the carbon footprint. The work indicates further areas for development.

Key words: edge deburring, optimization, processing, measurement, operation, automation

1. INTRODUCTION

Manufacturing companies, especially those operating in the aviation industry, aim to ensure the proper quality of their products, which then translated into the reliability of the manufactured devices. These requirements have a direct impact on the performance, safety and operational life of the aircraft. Due to the increased performance of currently produced engines, compared to the designs from the last century, with simultaneous actions aimed at reducing the weight of all aircraft components, the requirements related to guaranteeing appropriate material and drawing properties, were increased [1-5].

The second, equally important goal is to strive to maximize profits by reducing all types of costs related to the production of parts. Taking into account the economic situation and economic conditions ("Ready for 55"), companies operating in the aviation industry set one of their main goals to reduce unit costs to increase competitiveness compared to other manufacturers operating in a similar production area. This goal is achieved by reducing the demand for electricity, reducing tools used in the production process, and reducing the number of man-hours devoted to the production of components. One of the possibilities to improve financial results by reducing production costs, as well as ensuring appropriate technological possibilities and repeatability, is the automation of individual production stages [6-14].

One of the possibilities to improve the economic results of the plant by reducing unit costs directly related to production, as well as ensuring appropriate technological capabilities and repeatability, is the automation of individual stages of production processes.

The introduction of robotization and automation of individual production operations, further enables objective optimization of individual production operations by eliminating the subjective feelings of individual operators from the optimization procedures. The introduction of automation and robotization also improves working conditions by eliminating the risk of injuries to employees as well as limiting the impact of harmful factors such as noise and dust on employees [15-19]. In a broader perspective, it also enables the impartial conduct of research plans aimed at establishing a set of technological parameters ensuring, on the one hand, minimization of costs (minimization of tool wear), as well as sustaining the level of quality of manufactured products necessary for the aviation industry. Therefore, before starting the work described in this publication, a fully automated workstation was introduced, enabling the brushing process to be carried out in fully repeatable conditions.

In line with the above trend, research work was undertaken to optimize the brushing process by modifying selected parameters of the production process in order to reduce tool wear (extend tool life). The above-mentioned works are of key importance due to the company's goals, because while maintaining the current quality standard, they will allow for reducing operating costs and, as a result, reduce the carbon footprint. In the work carried out so far [20] related to the brushing process, it was observed that changing the parameters of the technological process, such as rotational speed or engagement depth, translates directly into the level of mutual interaction moments between the tool and the processed detail. Due to the complexity of the deburring process and the need to find an optimum guaranteeing the most effective use of

the tool, it was decided to carry out a number of experiments aimed at determining the local minimum in relation to the "consumption" of the tool during the process. For this purpose, it was decided to carry out a number of experiments based on a two-level static determined plan. This means that the selected process parameters will be set on two extreme positions corresponding to the minimum and maximum values of the selected parameter. The planned research aims to determine the impact of individual brushing parameters on the final thickness of the bristles from which the tool is made. The final result of the experiment will be an equation describing the degree of tool wear depending on the selected values of individual parameters, which will make it possible, using analytical methods, to determine the local minimum corresponding to the longest operating time of the brush used for deburring. Then, the set of technological parameters prepared in this way will be tested in large-scale production to confirm the correctness of the work carried out.

2. DESCRIPTION OF THE PROBLEM

The proper implementation of the brushing process of the device's components is directly related to the quality of the finished product and safety during assembly. The basic purpose of the brushing process is to remove all types of burrs created at earlier stages of the production process [21-24]. This will enable the proper assembly of individual engine components and will also contribute to reducing the risks faced by the employee during the assembly process. From the point of view of the reliability and durability of the components of a modern jet engine, the key factor is the requirement to ensure the desired value of the edge radius. This radius is directly related to the local stress level, which translates into the life of the parts and the entire device (engine, aircraft).

With reference to the work related to the introduction of industrial robots to machining operations, many research works have been created [25-32]. These studies indicate many advantages of introducing robotization in the form of increased repeatability and contributing to the reduction of product manufacturing costs. Industrial robots are successfully used for deburring, milling, deburring of thin-walled elements, grinding and polishing, and in measurement control of required places [33-39].

Thanks to the automation of the brushing process, the repeatability of the process was increased, it was possible to control the mutual impact of the processed detail and the tool, and it also led to a significant improvement in working conditions by reducing exposure to noise, dust and other harmful factors [20, 40, 41].

3. PROPOSED SOLUTION

In order to obtain unequivocal and objective optimization results, it was decided to carry out a number of tests. The purpose of the tests is to obtain a mathematical description of the rate of brush wear (bristle abrasion) depending on the selected process parameters. Such action will make it possible, using mathematical analysis methods, to find local minimums allowing for a reduction in the number of tools used and, consequently, will reduce the unit cost of manufactured components. Before carrying out the tests, it was decided to analyze possible process parameters that impact on the level of interaction between the tool (brush) and the detail.

The influence of the rotational speed and the depth of penetration of the workpiece into the tool was examined in [20].

Performed research clearly shows that:

- A double increase in the brush rotation speed translates into a linear increase in torque. The obtained results confirm that the above relationship is correct for various rotational speeds;
- The increase in the depth of the detail in relation to the disc translates into a non-linear increase in torque. The observed effect is much smaller for higher rotational speeds.

Therefore, it was decided that the rotational speed and the depth of engagement of the detail to the tool would be used in further work.

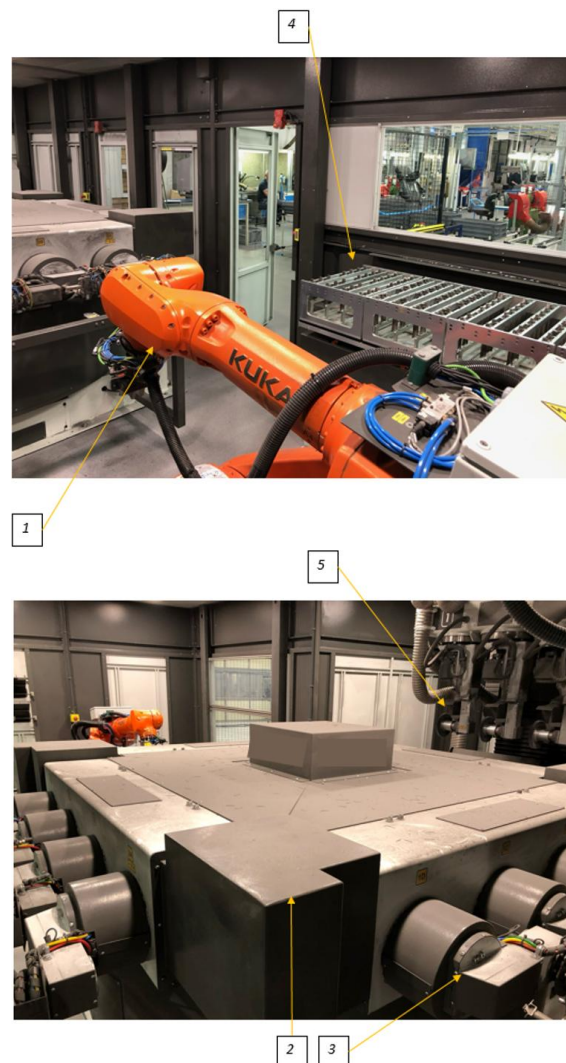


Fig. 1. Work station (1 - industrial manipulator, 2 - rotary table, 3 - workpiece gripper, 4 - workpiece magazine, 5 - tool holder)

The workstation used for the edge deburring process is shown schematically (Fig. 1). The station includes an industrial manipulator used to fasten processed details on a rotary table, after previously taking parts from the warehouse. In order to improve the operation of the station, it was equipped with a gripper warehouse. The last components of the workstation are the columns serving as handles and drives for the brushes used in the process. The entire area of the workstation is fenced with special barriers designed to ensure an appropriate level of safety for employees. Due to the assumed capacity of the workstation, it

was decided not to consider the possibility of modifying the operating time allocated to the deburring procedure. From the point of view of cost reduction, extending the operation time would not have a beneficial effect on reducing the overall process costs. On the other hand, the time allocated for the analyzed operation has been optimized in terms of production cycle and does not require any further modifications from the company point of view.

One of the parameters of the technological process may also be the resistive moment of the tool generated during operation (due to the friction occurring between the rotating tool brought into contact with the workpiece). For the workstation presented (Fig. 1), the resistive torque is determined based on the current consumption of individual servo drives. It was considered to link the above-mentioned brush resistance torque with the bristle abrasion rate. In large-scale production conditions, a number of different parts are brushed at the workstation, which differ in size and thus affect the analyzed parameter. Therefore, it was decided to eliminate this parameter in further considerations. Also, the variation associated with the different number of burrs to be removed on individual parts affects the variability of the resistive torque. As a consequence, this makes it impossible to optimize tool consumption depending on the parameter in question. In order to illustrate the presented situation, the results of the registered resistance torque for individual production pieces are presented.

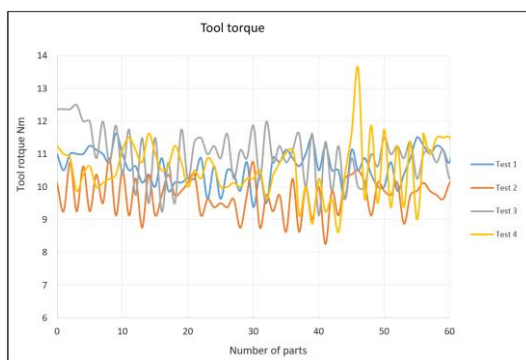


Fig. 2. Tool torque in relations with numer of brushed parts

In order to confirm the observations, it was decided to carry out four tests. Based on the graphical presentation of the results (Fig. 2), it was concluded that the resistive torque changes chaotically, regardless of tool wear.

Based on experience related to large-scale production, it was decided to use a brush-type tool in all optimization works (Fig. 3).



Fig. 3. A brush-type tool used in the production process

The basic technical parameters of the tool (Fig. 3) include an external diameter of 200 mm, a bristle length of 35 mm (measured along the radius) and a bristle thickness of approximately 1.1 mm. The material from which the bristles are made is silicon carbide (SiC), known under the trade name ABRALON612. The brush disc is made of structural steel.

In order to obtain an equation characterizing the tool wear process, it was decided to conduct an experiment based on a two-level static determined plan (Fig. 4).

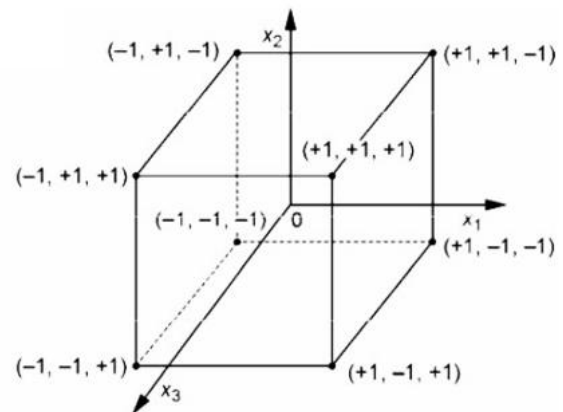


Fig. 4. Implementation scheme of experiment (3 input factors on 2 levels) [42]

A test plan was used without taking into account the effects of interactions between the analyzed parameters. To systematize the tests, a planning matrix was prepared in Table 1. Due to the complexity of the movements of the tool and the processed detail, it was impossible to present a single value defining the depth of penetration of the detail into the tool. Initially, this value was selected empirically based on the obtained process results (the value of the edge radius and the quantity of burr removal, average depth of approximately 4 mm, maximum of approximately 10 mm).

Therefore, it was decided to control the brush diameter parameter, which translated into shifting each point from the trajectory of mutual movements by a specific value. Therefore, the value of 198 mm from Table 1 should be interpreted as an increase in the engagement by 1 mm.

Tab. 1. Test matrix, columns X1, X2, X3 define the top level ("+") and bottom level ("-") of selected process parameters

| Test number | X1 | X2 | X3 | Rotation i speed rpm | Engagement as brush diameter mm | Number of brushed parts |
|-------------|----|----|----|----------------------|---------------------------------|-------------------------|
| 1 | + | + | + | 2000 | 200 | 60 |
| 2 | + | + | - | 2000 | 200 | 30 |
| 3 | + | - | + | 2000 | 198 | 60 |
| 4 | + | - | - | 2000 | 198 | 30 |
| 5 | - | + | + | 1400 | 200 | 60 |
| 6 | - | + | - | 1400 | 200 | 30 |
| 7 | - | - | + | 1400 | 198 | 60 |
| 8 | - | - | - | 1400 | 198 | 30 |

Planned test in the test matrix were performed randomly. The capacity of the test stand made it possible to conduct a test con-

sisting of 12 repetitions at the same time to eliminate the influence of randomness.

4. TEST RESULTS

Analysis of the tool wear in large-scale production conditions, it was observed that the bristles wear out at a maximum distance of approximately 8 mm, measured from the outer edge of the brush (Fig. 5). It was observed that the bristles were worn – a reduction in thickness in the circumferential direction of the brush. No wear of the bristles was observed in the axial direction of the tool.

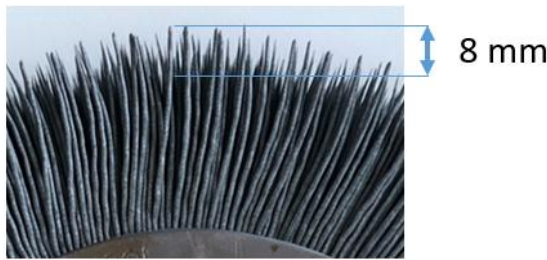


Fig. 5. The depth to which the brush tool was wear

It was decided to adopt the assumption of measuring the bristle thickness at a distance of approximately 4 mm from the maximum diameter of the brush (Fig. 6). Measurements were taken using a caliper.



Fig. 6. Place of measurement of bristle thickness after the test

The results of the measured bristle thickness according to the presented schema are presented in Table 2.

Tab. 2. Test results – measured bristle thickness

| Test number | y_1 | y_2 | y_3 | y_4 | y_5 | y_6 | y_7 | y_8 | y_9 | y_{10} | y_{11} | y_{12} | \bar{y} |
|-------------|-------|-------|-------|-------|-------|-------|-------|-------|-------|----------|----------|----------|-----------|
| 1 | 0.64 | 0.55 | 0.55 | 0.63 | 0.73 | 0.64 | 0.59 | 0.51 | 0.41 | 0.41 | 0.55 | 0.56 | 0.56 |
| 2 | 0.9 | 0.6 | 0.83 | 0.48 | 0.66 | 0.74 | 0.73 | 0.64 | 0.43 | 0.95 | 0.86 | 0.86 | 0.72 |
| 3 | 0.6 | 0.52 | 0.62 | 0.53 | 0.53 | 0.54 | 0.53 | 0.58 | 0.55 | 0.55 | 0.6 | 0.54 | 0.56 |
| 4 | 0.57 | 0.48 | 0.46 | 0.75 | 0.6 | 0.55 | 0.61 | 0.69 | 0.66 | 0.55 | 0.62 | 0.7 | 0.60 |
| 5 | 0.4 | 0.54 | 0.42 | 0.64 | 0.64 | 0.69 | 0.76 | 0.8 | 0.7 | 0.82 | 0.74 | 0.85 | 0.67 |
| 6 | 0.8 | 0.92 | 0.75 | 0.69 | 0.83 | 0.8 | 0.62 | 0.5 | 0.62 | 0.45 | 0.7 | 0.65 | 0.69 |
| 7 | 0.47 | 0.67 | 0.3 | 0.45 | 0.46 | 0.4 | 0.36 | 0.4 | 0.38 | 0.35 | 0.56 | 0.5 | 0.44 |
| 8 | 0.3 | 0.4 | 0.55 | 0.59 | 0.3 | 0.63 | 0.53 | 0.56 | 0.64 | 0.77 | 0.89 | 0.49 | 0.55 |

where: y_n – bristle thickness in the n-th measurement,
 \bar{y} – average value

In order to obtain mathematical equation following calculations have to be made:

Calculation of the unit of variability:

– For rotational speed:

$$\Delta x_1 = \frac{r_{max} - r_{min}}{2} = \frac{2000 - 1400}{2} = 300 \text{ rpm} \quad (1)$$

– For brush diameter:

$$\Delta x_2 = \frac{d_{max} - d_{min}}{2} = \frac{200 - 198}{2} = 1 \text{ mm} \quad (2)$$

– For number of brushed parts:

$$\Delta x_3 = \frac{q_{max} - q_{min}}{2} = \frac{60 - 30}{2} = 15 \text{ pcs} \quad (3)$$

Calculations of the central values for inputs:

– For rotational speed:

$$x_{10} = \frac{r_{max} + r_{min}}{2} = \frac{2000 + 1400}{2} = 1700 \text{ rpm} \quad (4)$$

– For brush diameter:

$$x_{20} = \frac{d_{max} + d_{min}}{2} = \frac{200 + 198}{2} = 199 \text{ mm} \quad (5)$$

– For number of brushed parts:

$$x_{30} = \frac{q_{max} + q_{min}}{2} = \frac{60 + 30}{2} = 45 \text{ pcs} \quad (6)$$

Coding of inputs:

– For rotational speed:

$$x_1 = \frac{\hat{x}_1 - \hat{x}_{10}}{\Delta \hat{x}_1} = \frac{r - 1700}{300} \quad (7)$$

– For brush diameter:

$$x_2 = \frac{\hat{x}_2 - \hat{x}_{20}}{\Delta \hat{x}_2} = \frac{d - 199}{1} \quad (8)$$

– For number of brushed parts:

$$x_3 = \frac{\hat{x}_3 - \hat{x}_{30}}{\Delta \hat{x}_3} = \frac{q - 45}{15} \quad (9)$$

Calculation of the coefficients of the regression equation:

The variance of the measurement error was calculated based on the following formula:

$$S^2(y)_i = \frac{\sum_{i=1}^j (y_{ui} - \bar{y}_i)^2}{j-1} \quad (10)$$

Values for performed tests are presented in Table 3.

Tab. 3. Error variance for individual trials

| Test number | S2 |
|-------------|--------|
| 1 | 0.0079 |
| 2 | 0.0253 |
| 3 | 0.0010 |
| 4 | 0.0070 |
| 5 | 0.0200 |
| 6 | 0.0171 |
| 7 | 0.0094 |
| 8 | 0.0276 |

The coefficients of the regression equation are as follows:

$$b_0 = \frac{1}{N} \sum_{i=1}^j x_{0i} y_i^2 = 0.600 \quad (11)$$

$$b_1 = \frac{1}{N} \sum_{i=1}^j x_{1i} y_i^2 = 0.011 \quad (12)$$

$$b_2 = \frac{1}{N} \sum_{i=1}^j x_{2i} y_i^2 = 0.061 \quad (13)$$

$$b_3 = \frac{1}{N} \sum_{i=1}^j x_{3i} y_i^2 = -0.043 \quad (14)$$

Assessment of the repeatability of the experiment conditions:

– Calculation of the G coefficient value:

$$G = \frac{S^2(y)_{i \max}}{\sum_{i=1}^n S^2(y)_i} = 0.151 \quad (15)$$

– Calculation of the number of degrees of freedom:

$$f_1 = N = 8 \quad (16)$$

$$f_2 = r - 1 = 11 \quad (17)$$

– Determination of the critical value of the G coefficient of the Cochran statistic:

Critical values of the Cochran G statistic ($\alpha=0.05$). Values read from position [42].

$$G_{kr} = G_{(\alpha; f_1; f_2)} = 0.2364 \quad (18)$$

Because the following condition is met:

$$G < G_{kr} \quad (19)$$

The experiments were conducted with satisfactory repeatability.

Checking the significance of regression coefficients:

– Calculation of variations in measurement errors:

$$S^2(y) = \frac{1}{N} \sum_{i=1}^N S^2(y)_i = 0.014 \quad (20)$$

– Determining the number of degrees of freedom:

$$f = N(r - 1) = 88 \quad (21)$$

Determination of the critical value of the t coefficient. Value read from position [42].

$$t_{kr} = t_{(\alpha; f)} = 1.99 \quad (22)$$

$$b_{kr} = t_{(\alpha; f)} \sqrt{\frac{S^2(y)}{Nr}} = 0.024 \quad (23)$$

Hence:

$$|b_0| > b_{kr} \text{ so the coefficient is considered as significant} \quad (24)$$

$$|b_1| < b_{kr} \text{ so the coefficient is considered as not significant} \quad (25)$$

$$|b_2| > b_{kr} \text{ so the coefficient is considered as significant} \quad (26)$$

$$|b_3| > b_{kr} \text{ so the coefficient is considered as significant} \quad (27)$$

After eliminating the insignificant term, the regression equation takes the following form:

$$y = 0.600 + 0.061x_2 - 0.043x_3 \quad (28)$$

Assessment of the adequacy of the regression equation:

– Calculation of adequacy variance:

$$S_{ad}^2(y) = \frac{r \sum_{i=1}^N (\hat{y}_i - \bar{y})^2}{N - k - 1} = 0.033 \quad (29)$$

– Determination of calculation value for F coefficient:

$$F = \frac{S_{ad}^2(y)}{S^2(y)} = 2.278 \quad (30)$$

– Calculation of number of degrees of freedom for numerator:

$$f_1 = N - k - 1 = 5 \quad (31)$$

– Calculation of number of degrees of freedom for denominator:

$$f_m = f_2 = N(r - 1) = 88 \quad (32)$$

Critical values of F test Fischera-Snedecora ($\alpha=0.05$). Values read from position [42].

– Calculation of critical value of F test coefficient:

$$F_{kr} = F_{(\alpha; f_1; f_m)} = 2.33 \quad (33)$$

Since the relationship $F < F_{kr}$ is met, the obtained regression equation is considered adequate.

Decoding the regression equation by substituting equations (8) and (9) into formula (28):

$$y = 0.061458 d - 0.00288 q - 11.5 \quad (34)$$

where: y – bristle thickness, d – brush outer diameter, q – quantity of brushed parts.

In order to maintain the appropriate quality of the manufactured products, it was decided to control the results of the brushing process both visually (visual inspection of the absence of burrs after brushing). The results, such as the removal of all burrs, prove that the process was carried out correctly. The condition of the parts before and after the brushing process is shown in Fig. 7.

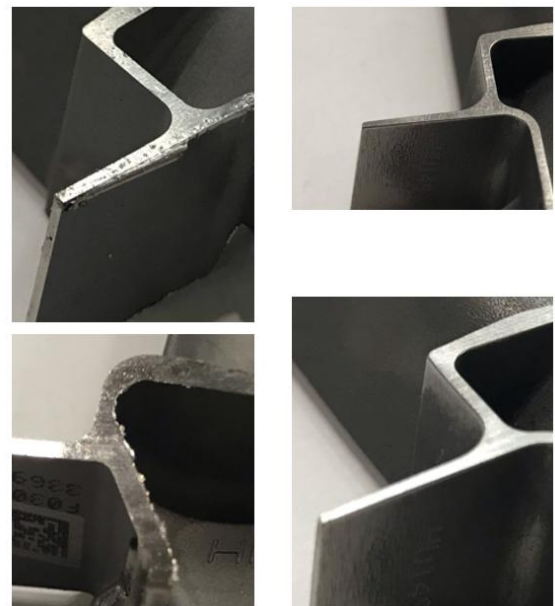


Fig. 7. Typical parts condition before (left side) and after (right side) of brushing process

The second control parameter analyzed to determine the correctness of the brushing process is the edge radius. A profilograph is used to measure the mentioned radius. For all tests with different process parameters, selected edges were measured (the measurement points were selected based on experience). The location of measurement points in the area of the blade lock is shown schematically in Fig. 8.

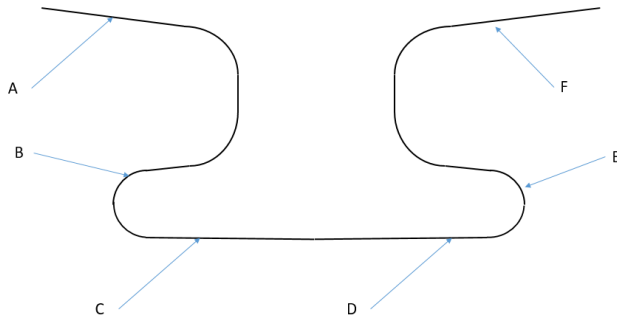


Fig. 8. Location of control points – blade lock

The values of the edge break radius, measured for all tests, are in Table 4.

Tab. 4. Results of the tests - the radius of edge break in chosen locations of the detail

| Test number | Measured value of Edge break, mm | | | | | |
|-------------|----------------------------------|------|------|------|------|------|
| - | A | B | C | D | E | F |
| 1 | 0.16 | 0.11 | 0.17 | 0.16 | 0.31 | 0.29 |
| 2 | 0.15 | 0.10 | 0.13 | 0.15 | 0.34 | 0.36 |
| 3 | 0.18 | 0.19 | 0.17 | 0.14 | 0.25 | 0.27 |
| 4 | 0.27 | 0.16 | 0.19 | 0.19 | 0.33 | 0.3 |
| 5 | 0.17 | 0.12 | 0.18 | 0.14 | 0.24 | 0.27 |
| 6 | 0.13 | 0.11 | 0.13 | 0.13 | 0.29 | 0.25 |
| 7 | 0.13 | 0.12 | 0.15 | 0.13 | 0.30 | 0.30 |
| 8 | 0.14 | 0.10 | 0.20 | 0.13 | 0.32 | 0.35 |

The test results are presented in Fig. 9 in the form of a histogram.

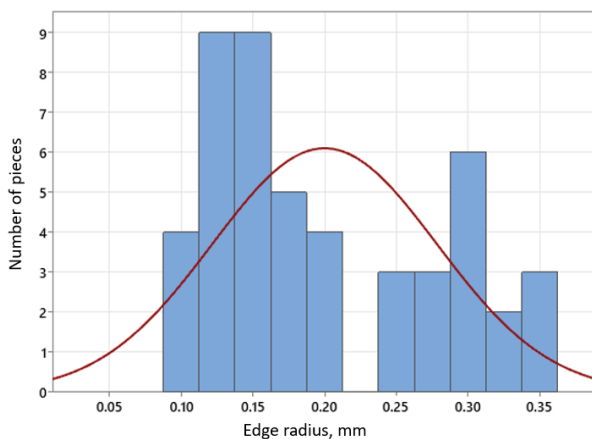


Fig. 9. Results of test- histogram

The break radius values obtained in the tests, ranging from 0.10 to 0.40 mm, are considered as satisfactory from the point of view of the operational requirements of brushed details. In order to confirm the obtained mathematical model, it was decided to

carry out large-series tests. The tests used process parameters prepared based on the obtained mathematical model of the tool wear rate.

5. DISCUSSION OF THE RESULTS

The carried out optimization procedure made it possible to mathematically describe the nature of brush wear depending on the selected parameters of the brushing process. As a result of the mathematical operations performed, information was obtained about which of the selected process parameters significantly affect the wear time of the tools life (outer diameter of the brush, number of processed details), and which of them can be neglected (rotational speed). Importantly, from the point of view of the quality of the manufactured parts, in the entire analyzed range of selected process parameters, i.e. for brush diameters in the range of 198 to 200 mm, rotational speeds of 1,400 to 2,000 rpm, the brushing process fully guaranteed the correct removal of burrs and proper edge break radius.

In order to visualize the data collected during all test trials, it was decided to prepare a chart (Fig. 10) illustrating the rate of tool wear depending on the rotational speed and feed (brush diameter).

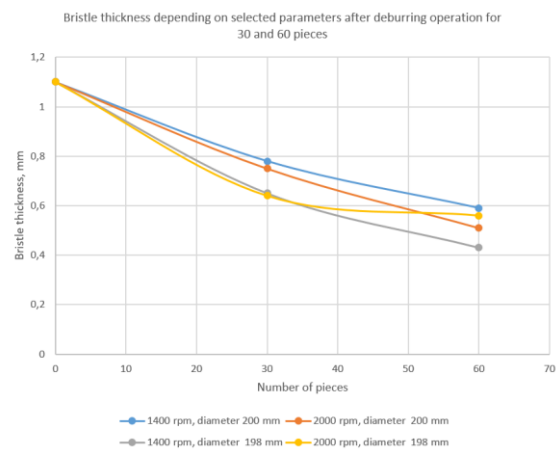


Fig. 10. Bristle thickness depending on selected parameters after deburring operation for 30 and 60 pieces

The graph clearly shows that the bristles were worn out the least, both after 30 and 60 pieces, in the case of the following combination of parameters: rotational speed of 1400 rpm and brush diameter of 200 mm. From the other hand, the worst values were achieved for the following combination of analyzed parameters: rotational speed 1400 rpm, brush diameter 198 mm.

In turn, the graphical representation in Fig. 11 of the obtained equation is as follows:

$$t = 0.061458 \times d - 0.00288 \times q - 11.5 \quad (35)$$

Based on the prepared charts and analysis of data collected during experiments, it was decided to recommend the following combination of process parameters for further testing:

- tool rotation speed 1400 rpm;
- external diameter of the tool 200 mm.

The estimated life of the brush has been extended, from the initial value of approximately 60 pieces to a value of 120 pieces (an increase of 100%).

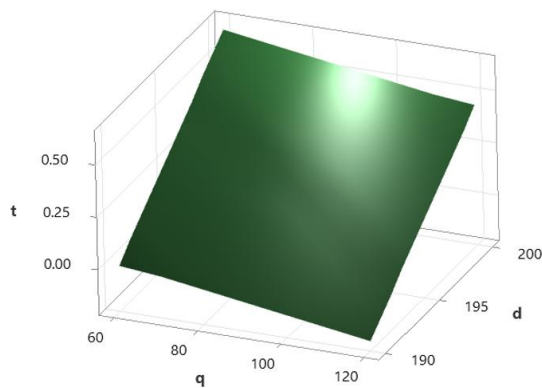


Fig. 11. Graphical presentation of equation (35) (t – bristle thickness mm, d – brush diameter mm, q – number of processed parts)

Based on the test results in large-scale production, it was confirmed that the prepared set of parameters allowed for a significant extension of the tool's use time. It turned out that after tests lasting several days, the actual life of the brush is not 120, as the analysis might suggest, but 100 pieces. The difference between the theoretical and actual life expectancy of the brush (expressed in the number of pieces successfully processed) can be explained by the different amount of burr to be removed between individual pieces (natural variation in the production process), as well as the difference in the component on which the tests were carried out (tests used for developing a mathematical description of the brush wear rate was carried out using one type of part, while tests confirming the effectiveness of the introduced changes were carried out in production conditions, where individual components differed in size). The increase in the life expectancy of the brush from the initial value of 60 pieces to 100 pieces per tool should be considered a satisfactory value.

There are a number of studies in which the authors dealt with the selection of optimal parameters of the technological process for the simultaneous extension of the tool operating time and the quality of the obtained details. The authors of the study [43] worked on extending the tool operating time depending on the input parameters. Modification of a number of parameters had a different impact on the length of tool use. Some of the parameters were characterized by a linear translation, and some by a non-linear translation on the length of tool use. The result itself in the form of the number of minutes varied from about 90 to over 670 minutes, depending on the selected set of parameters. In turn, in the study [44], the author selects the parameters of the technological process in order to both extend the tool life and reduce the consumption of electric energy. Similarly to the authors of the study [43], he obtains both linear and non-linear relationships between the parameters of the technological process and the tool life. The final set of proposed parameters translates into an extension of the tool life by about 20%. As can be seen in the cited studies, different researchers dealt with similar topics and obtained similar results, i.e. their nature and results do not differ significantly from the observed regularities for the case under consideration.

6. CONCLUSIONS

Based on the experiments carried out to define the mathematical description of the tool wear rate, the following conclusions can be drawn:

- the rotational speed of the brush is a parameter irrelevant from the point of view of the abrasion rate of the brush bristles;
- the values of the tool diameter and the number of processed pieces have a significant impact on the rate of bristle abrasion;
- for the analyzed process and the associated pair of materials (both the tool and the workpiece), the brush wear process can be described by the following equation (35);
- all configurations of modified parameters enabled the deburring process to be carried out correctly, i.e. by removing all the burr present on the parts and guaranteeing the edge deburring radius in the range from 0.10 to 0.36 mm, which should be considered a correct value from the point of view of strength;
- modification of technological process parameters made it possible to extend the tool life by approximately 67%, which allowed to reduce the unit cost of manufactured details by PLN 0.75/piece in large-scale production conditions;
- the work carried out to optimize the parameters of the deburring process, thanks to reducing the number of tools used, also led to a reduction of the carbon footprint left by the production plant.

The work carried out on the optimization of the brushing process sheds new light on the approach to cost optimization, especially in large-scale production. It turns out that a small change in the parameters of the technological process leads to significant savings and has a positive impact on the natural environment. Optimization of production processes not only through robotization and automation, but also in the form of selecting technological parameters leading to the extension of the operational time of tools (while maintaining an appropriate level of quality) should be a natural stage in the maturation of production processes.

As part of further work aimed at optimizing the brushing process, attention can be paid to verifying the selected brush material. So far, this area has not been verified empirically. Also, experiments related to bristle thickness may lead to a reduction in unit costs.

REFERENCES

1. Balon P, Świątoniowski A, Rejman E, Kielbasa B, Smusz R, Szostak J, Cieślak J. Zastosowanie cienkościennych konstrukcji integralnych w lotnictwie na przykładzie projektu SAT-AM. Zeszyty Naukowe Politechniki Rzeszowskiej. Mechanika. 2020;92(300): 5–17. <https://doi.org/10.7862/rm.2020.01>
2. Wen-Hsien T, Yao-Chung Ch, Sin-Jin L, Hui-Chiao Ch, Po-Yuan Ch. A green approach to the weight reduction of aircraft cabins. Journal of Air Transport Management. 2014;40: 65–77. <https://doi.org/10.1016/j.jairtraman.2014.06.004>
3. da Silva A, Jorge M, Ogashawara O. Weight reduction of amorphous alloy core electrical transformers for aircraft applications. In 2016 International Conference on Electrical Systems for Aircraft, Railway, Ship Propulsion and Road Vehicles & International Transportation Electrification Conference (ESARS-ITEC); 1–4: IEEE. <https://doi.org/10.1109/ESARS-ITEC.2016.7841347>
4. Zeng Y, Li J, Lin S, He X, Li B, Deng T. Comparison of Manual Setting Weight Reduction and Topology Optimization of the Wing Tips of Electric Vertical Take-Off and Landing Aircraft. Applied Sciences. 2022;12(11): 5548. <https://doi.org/10.3390/app12115548>
5. Yang S, Ordóñez J. C. Aircraft Weight Reduction and Onboard Combined Power Cycle Efficiency Improvement-An Integrative Approach. In AIAA Aviation 2019 Forum 3470: Published Online 14 Jun 2019. <https://doi.org/10.2514/6.2019-3470>

6. Uliasz M, Ornat A, Burghardt A, Muszyńska M, Szybicki D, Kurc K. Automatic Evaluation of the Robotic Production Process for an Aircraft Jet Engine Casing. *Applied Sciences*. 2022;12(13):6443. <https://doi.org/10.3390/app12136443>
7. Ornat A, Uliasz M, Bomba G, Burghardt A, Kurc K, Szybicki D. Robotised Geometric Inspection of Thin-Walled Aerospace Casings. *Sensors*. 2022;22(9): 3457. <https://doi.org/10.3390/s22093457>
8. Kurc K, Burghardt A, Gierlak P, Muszyńska M, Szybicki D, Ornat A, Uliasz M. Application of a 3D Scanner in Robotic Measurement of Aviation Components. *Electronics*. 2022;11(19): 3216. <https://doi.org/10.3390/electronics11193216>
9. Glukhov G.E, Chernikov P.E, Karapetyan A.G, Konkov A.Y, Sharypov A.N. Automated management system of technological and production processes of the civil aviation air enterprise known as 'the custom module' the operator. In *Proceedings of the 34th International Business Information Management Association Conference-Vision 2020: Sustainable Economic Development and Application of Innovation Management from Regional expansion to Global Growth*: 7297–7309.
10. Szybicki D, Burghardt A, Kurc K, Gierlak P. Device for Contact Measurement of Turbine Blade Geometry in Robotic Grinding Process. *Sensors*. 2020;20(24): 7053. <https://doi.org/10.3390/s20247053>
11. Burghardt A, Kurc K, Szybicki D, Muszyńska M, Nawrocki J. Robot-operated quality control station based on the UTT method. *Open Engineering*. 2017;7(1): 37–42. <https://doi.org/10.1515/eng-2017-0008>
12. Burghardt A, Szybicki D, Gierlak P, Kurc K, Muszyńska M. Robotic Grinding Process of Turboprop Engine Compressor Blades with Active Selection of Contact Force. *Tehnički vjesnik*. 2022;29(1): 15–22. <https://doi.org/10.17559/TV-20190710141137>
13. Sha J, Wang J, Hu H, Ye Y, Xu G. Development of an Accurate and Automated Quality Inspection System for Solder Joints on Aviation Plugs Using Fine-Tuned YOLOv5 Models. *Applied Sciences*. 2023;13(9): 5290. <https://doi.org/10.3390/app13095290>
14. Bernabei M, Eugeni M, Gaudenzi P, Costantino F. Assessment of Smart Transformation in the Manufacturing Process of Aerospace Components Through a Data-Driven Approach. *Glob J Flex Syst Manag*. 2023;24: 67–86. <https://doi.org/10.1007/s40171-022-00328-7>
15. Vasic M, Billard A. Safety issues in human-robot interactions. In *2013 IEEE International Conference on Robotics and Automation*: 197–204. <https://doi.org/10.1109/ICRA.2013.6630576>
16. Chinniah Y. (2016). Robot safety: overview of risk assessment and reduction. *Advances in Robotics & Automation*. 2016;5(01): 1–5. <https://doi.org/10.4172/2168-9695.1000139>
17. Alvarado M.L. A risk assessment of human-robot interface operations to control the potential of injuries/losses at XYZ manufacturing company. 2002.
18. Siying Yang, Yifan Zhong, Dawei Feng, Rita Yi Man Li, Xue-Feng Shao, Wei Liu. Robot application and occupational injuries: Are robots necessarily safer?. *Safety Science*. 2022;147: 105623. <https://doi.org/10.1016/j.ssci.2021.105623>
19. Dhillon B.S, Anude O.C. Robot safety and reliability: A review, *Microelectronics Reliability*. 1993;33(3): 413–429. [https://doi.org/10.1016/0026-2714\(93\)90030-3](https://doi.org/10.1016/0026-2714(93)90030-3)
20. Falandys K, Kurc K, Burghardt A, Szybicki D. Automation of the Edge Deburring Process and Analysis of the Impact of Selected Parameters on Forces and Moments Induced during the Process. *Applied Sciences*. 2023;13(17): 9646. <https://doi.org/10.3390/app13179646>
21. Gusri A.I, Yanuar B, Yasir M.A. (2020). Burr Formation Analysis When Micro Milling Ti-6Al-4v Eli Using End Mill Carbide Insert. *PalArch's Journal of Archaeology of Egypt/Egyptology*. 2020;17(9): 4061–4067.
22. Matuszak J, Zaleski K. Warunki technologiczne procesu usuwania zadziórów z przedmiotów wykonanych ze stopów aluminium. *Przegląd Mechaniczny*. 2016;12: 29–32. <https://doi.org/10.15199/148.2016.12.5>
23. Kurniawan R, Kumaran S.T, Prabu V.A, Zhen Y, Park K.M, Kwak Y.I, Ko T.J. Measurement of burr removal rate and analysis of machining parameters in ultrasonic assisted dry EDM (US-EDM) for deburring drilled holes in CFRP composite. *Measurement*. 2017;110: 98–115. <https://doi.org/10.1016/j.measurement.2017.06.008>
24. Kim Y.G, Kim K.J, Kim K.H. Efficient Removal of Milling Burrs by Abrasive Flow. *International Journal of Precision Engineering and Manufacturing*. 2021;22: 441–451. <https://doi.org/10.1007/s12541-020-00455-0>
25. Makulavičius M, Petkevičius S, Rožėnė J, Dziedzickis A, Bučinskas V. Industrial Robots in Mechanical Machining: Perspectives and Limitations. *Robotics*. 2023;12(6): 160. <https://doi.org/10.3390/robotics12060160>
26. Iglesias I, Sebastián M.A, Ares J.E. Overview of the State of Robotic Machining: Current Situation and Future Potential. *Procedia Engineering*. 2015;132: 911–917. <https://doi.org/10.1016/j.proeng.2015.12.577>
27. Pandremenos J, Doukas C, Stavropoulos P, Chtabolouris G. Machining with robots: a critical review. *Proceedings of DET2011*. 1–9.
28. Denkena B, Bergmann B, Lepper T. Design and optimization of a machining robot. *Procedia Manufacturing*. 2017;14: 89–96. <https://doi.org/10.1016/j.promfg.2017.11.010>
29. Klimchik A, Ambiehl A, Garnier S, Furet B, Pashkevich A. Efficiency evaluation of robots in machining applications using industrial performance measure. *Robotics and Computer-Integrated Manufacturing*. 2017;48: 12–29. <https://doi.org/10.1016/j.rcim.2016.12.005>
30. Pan Z, Zhang H, Zhu Z, Wang J. Chatter analysis of robotic machining process. *Journal of Materials Processing Technology*. 2006;173(3): 301–309. <https://doi.org/10.1016/j.jmatprotec.2005.11.033>
31. Schnoes F, Zaeh M.F. Model-based planning of machining operations for industrial robots. *Procedia CIRP*. 2019;82: 497–502. <https://doi.org/10.1016/j.procir.2019.04.331>
32. Kim S.H, Nam E, Ha T.I, Hwang S.H, Lee J.H, Park S.H, Min B.K. Robotic machining: A review of recent progress. *International Journal of Precision Engineering and Manufacturing*. 2019;20: 1629–1642. <https://doi.org/10.1007/s12541-019-00187-w>
33. Burghardt A, Kurc K, Szybicki D, Muszyńska M, Szczęch T. Monitoring the parameters of the robot-operated quality control process. *Advances in Science and Technology. Research Journal*. 2017;11(1): 232–236. <https://doi.org/10.12913/22998624/68466>
34. Onstein I.F, Semeniuta O, Bjerkeng M. Deburring using robot manipulators: A review. In *2020 3rd international symposium on small-scale intelligent manufacturing systems (SIMS)*: 1–7. IEEE. <https://doi.org/10.1109/SIMS49386.2020.9121490>
35. Posada J.R.D, Kumar S, Kuss A, Schneider U, Drust M, Dietz T, Verl A. Automatic programming and control for robotic deburring. In *Proceedings of ISR 2016: 47st International Symposium on Robotics*: 1–8. VDE.
36. Hu J, Kabir A.M, Hartford S.M, Gupta S.K, Pagilla P.R. Robotic deburring and chamfering of complex geometries in high-mix/low-volume production applications. In *2020 IEEE 16th international conference on automation science and engineering (CASE)*: 1155–1160. IEEE.
37. Bottin M, Cocuzza S, Massaro M. Variable Stiffness Mechanism for the Reduction of Cutting Forces in Robotic Deburring. *Applied Sciences*. 2021;11(6): 2883. <https://doi.org/10.3390/app11062883>
38. Wang Q, Wang W, Zheng L, Yun C. Force control-based vibration suppression in robotic grinding of large thin-wall shells. *Robotics and Computer-Integrated Manufacturing*. 2021;67: 102031. <https://doi.org/10.1016/j.rcim.2020.102031>
39. Zhu D, Feng X, Xu X, Yang Z, Li W, Yan S, Ding H. Robotic grinding of complex components: a step towards efficient and intelligent machining—challenges, solutions, and applications. *Robotics and Computer-Integrated Manufacturing*. 2020;65: 101908. <https://doi.org/10.1016/j.rcim.2019.101908>
40. Matuszak J, Klonica M, Zagórski I. Effect of brushing conditions on axial forces in ceramic brush surface treatment. In *2019 IEEE 5th International Workshop on Metrology for AeroSpace (MetroAeroSpace)*: 644–648: IEEE.

- <https://doi.org/10.1109/MetroAeroSpace.2019.8869605>
41. Onstein I.F, Semeniuta O, Bjerkeng M. Deburring using robot manipulators: A review. In 2020 3rd international symposium on small-scale intelligent manufacturing systems (SIMS): 1–7. IEEE. <https://doi.org/10.1109/SIMS49386.2020.9121490>
 42. Korzyński M. Metodyka eksperymentu. Planowanie, realizacja i statystyczne operacowanie wyników eksperymentów technologicznych. Wydanie II. Wydawnictwa Naukowo-Techniczne; 2017.
 43. Chomsamutr K, Jongprasithporn S. Optimization parameters of tool life model using the Taguchi approach and response surface methodology. International Journal of Computer Science Issues (IJCSI). 2012;9(1):120.
 44. Bhushan R. K. Optimization of cutting parameters for minimizing power consumption and maximizing tool life during machining of Al alloy SiC particle composites. Journal of cleaner production. 2013;39: 242-254. <https://doi.org/10.1016/j.jclepro.2012.08.008>

Karol Falandys:  <https://orcid.org/0009-0009-7034-7978>

Tomasz Zymróz:  <https://orcid.org/0009-0009-0308-0820>

Krzysztof Kurc:  <https://orcid.org/0000-0002-1765-2430>



This work is licensed under the Creative Commons BY-NC-ND 4.0 license.

SIMULATION ON THE YARN-LEVEL AND EXPERIMENTAL VALIDATION OF SPACER FABRICS COMPRESSION BY A RIGID PUNCH. INFLUENCE OF SEAMS IN THE SPACER FABRIC

Maxime KRIER*, Julia ORLIK*, Kathrin PIETSCH**

*Fraunhofer ITWM, Fraunhofer-Platz 1, D-67663 Kaiserslautern, Germany

**Institute of textile Machinery and High Performance Material Technology, D-01062 Dresden, Germany

maxime.krier@itwm.fraunhofer.de, julia.orlik@fraunhofer.de, kathrin.pietsch@tu-dresden.de

received 13 April 2024, revised 02 July 2024, accepted 08 August 2024

Abstract: Spacer fabrics are 3D technical textiles, consisting of two parallel textile layers, which are connected by a series of monofilaments. In many industrial applications, such as the deployment as a distance holder, the compression properties of spacer fabrics play a crucial role. The article experimentally investigates the potential of influencing these compression properties by the incorporation of parallel seams into the fabric. Moreover, an efficient simulation-based finite-element approach is presented, that allows the a-priori estimation of effective compression resistance. For this purpose, a dimension reduction approach is employed, that reduces the arising highly complex multi-contact problems to simulations on the yarn and monofil centerlines. Input for the simulation are known mechanical properties of the yarns and the general lapping plan of the spacer fabric. The proposed model is applicable to the linear compression regime, i.e., before buckling and large bending arises. As a proof-of-concept, the compression experiment for a plane, circular punch on the spacer fabric with and without added seams is simulated and afterwards validated by experiments. The good agreement of the attained compression curves demonstrates the applicability of the numerical approach

Key words: spacer fabrics, seams, contact problems, dimension reduction

1. INTRODUCTION

Spacer fabrics offer a unique combination of properties suitable for various applications. They are typically composed of three layers (Figure 1a): the front layer and back layer (Fig. 1, b) and the spacer area (Fig 1, c). The top and bottom layers are warp knitted (refer to [18-20]). The spacer area comprises a series of monofilaments, which can be integrated in different ways, allowing for a shift between the meshes of the top and bottom layers. Due to their versatility, there is a high interest in experimental research concerning the mechanical properties of spacer fabrics, see e.g. [2], [9]-[11].

In particular, the compression resistance of spacer fabrics finds utility in diverse applications such as in shoes, car seats, furniture, and others [1]. In recent years, researchers have delved into producing weft knitted spacer fabrics and into investigating their properties, as discussed in [2], showcasing potential for shaping in three dimensions.

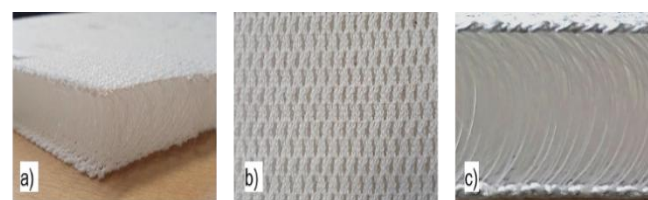


Fig. 1. Principal construction of spacer fabrics – a) 3D-structure, b) front and back side, c) spacer area

This paper first experimentally and numerically investigates the compression resistance of spacer fabrics. In a second step, parallel seams are added perpendicular to the front and back layer. This leads to local sections in the spacer fabric and the fabric becomes with the variable thickness. A range of sewing parameters, such as the seam placement, stitch length, distances in-between adjacent stitches and the stitch-yarn pre-stress are investigated. A numerical simulation approach is proposed to investigate the influence of these parameters on the compressional behavior. Related numerical investigations for the compressional behavior of warp knitted fabrics can be found in [3]-[12].

The numerical computations in this paper are based on the following input: the spacer fabrics scheme, also used by the producing machine (see [1]) and the yarn's elastic and contact properties. Due to the employment of an efficient one-dimensional model based on asymptotic methods (see [13]-[17], [21]-[27]), the computations can be performed fast. The resulting meso-scale model represents an idealized textile structure, neglecting stochastic effects in manufacturing such as variations in the yarn cross sections along the yarn length. A potential remedy is the structure generation based on CT-scans, which leads to a high accuracy in the textile representation as demonstrated in [7], at the cost of an expensive data acquisition method.

First, the effective compression behavior of a spacer fabric without seams is modeled on the yarn level and homogenized and then the influence of seams is modeled. Such multi-scale models simplify the optimization procedure of the design of seam-placing, e.g., to reach desired compressional fabric properties. The inves-

tigations provide a fundamental basis for engineering designs of such products in the future. This is the novelty of the approach for the application.

- Another novelty of the paper is the numerical approach for the evolutionary contact search for yarn-made materials, presented in Section 3 and Appendix, which is a research novelty in the field of the applied- problem simulation. The simulations allow to reduce the number of time-expensive experiments for spacer fabrics with and without seams.
- The next novelty of the paper is a discussion of a possible multi-linear behavior of the spacer fabric under the compression and the explanation of bounds and the phenomenology of its behavior from the structural large rotation, or buckling effects on the yarn level, as well as due to the changing number of the contact points between monofilaments on the large compression strains.

For the experimental investigation, calibration and validation of the numerical models, compression tests according to the test standard DIN EN ISO 3386-1 are performed. The compression forces dependent on the compression distance are measured. The experimental results are analyzed and investigated in terms of the influence of the variation of the seam distance.

The simulation of the spacer fabric on the yarn level with TexMath, [16], requires all structural details about the composition of the spacer fabric, as well as the force-strain measurements of each yarn's properties and the frictional coefficients between the yarn pairs.

First, a model of the spacer fabric without seams is developed. The experimental compression test is recreated in the simulation. With this, the friction coefficients between yarns can be calibrated. The size of the specimen (height) is the same as in the experimental part. After the material model is calibrated, the same material model is used for the following simulation models of the spacer fabrics with seams. All contacts with the seam yarns will be found, the seam yarn will be pre-stressed and the whole fabric relaxed, which leads to its local and particularly global compression. In the last step, the compression test with a rigid punch and this fabric is repeated. Dynamical contacts, see Appendix, will be found.

2. DESCRIPTION OF THE COMPRESSION TEST WITH A RIGID PUNCH ON THE SPACER FABRIC AND THEN ON A ROUGH FABRIC LAYER WITH SEAMS

2.1. Material

Four different spacer fabric variation have been produced, tested and modelled. All spacer fabrics are manufactured by Essedea GmbH/D. All specimens' initial state is the spacer fabric without seams, seen in Fig.2 a – bottom/ Fig. 2, b – top/left.

To the three other specimen seams in various distances have been inserted. The seams have been inserted with a Dürkopp Adler sewing machine Delta "M-Type". The seam distances are constant for each specimen and have average seam distances of 18 mm, 24 mm and 43 mm. Within the sections between the seams a cushion area occurs, whose overall shape significantly differs between the considered seam distances. The measurement of the seam distance and cushion height can be seen in Fig. 2. A summary of the material data is listed in Tab. 1.



Fig. 2 Spacer fabric variations for experimental testing: (a) cross view, (b) top view; h cushion height, d seam distance

Tab. 1. Technical data of the spacer fabric specimen

| Spacer fabric variation | Parameter | Value |
|-------------------------|-----------------------------|---|
| Initial spacer fabric | Manufacturer | Essedea GmbH/D |
| | Density | 2.349 g/mm ³ |
| | Material (knitting threads) | Top/Back side: PES-multifilament |
| | | Space: PES monofilaments |
| All sewn specimen | Sewing machine | Delta Machine "M-Type" (Dürkopp Adler, D) |
| | Stitch | Double lock stitch 301 |
| | Stitch length | 4 mm |
| | Tension needle thread | 40 % |
| | Foot stroke | 9 mm |
| | Sewing foot pressure | 1 (intern machine parameter without unit) |
| | Sewing threads | Amann Rasant Nm75 (PES) /D |
| Spacer fabric 18 | Seam distance d | 18 mm |
| Spacer fabric 24 | | 24 mm |
| Spacer fabric 43 | | 43 mm |
| Without seams | Cushion height h | 20 mm (overall height/thickness) |
| Spacer fabric 18 | | 8 mm |
| Spacer fabric 24 | | 15 mm |
| Spacer fabric 43 | | 20 mm |

2.2. Experimental test set up to test the compression behaviour of spacer fabrics

To test the compression behaviour of various spacer fabrics, each specimen is tested according to DIN standard 3386. The specimen properties can be seen in Table 1.

The compression tests were performed at a Zwick Z 2,5 (Zwick GmbH, D). A force sensor of 500 N and pressing plates with an area of 121 cm² (perforated) were used. The speed was 100 mm/min. In Fig. 3 the experimental compression test of the spacer fabric without seams (a), with seams (b) and of the edge-force-test (c) can be seen.

Mathematical formulas should be type written in mathematical style, aligned to left and numbered irrespective of chapter numbering.

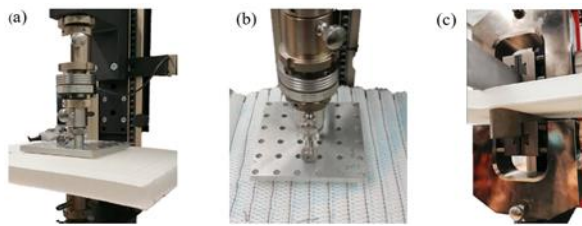


Fig. 3. Test setup for various compression tests (a) spacer fabric without seams, (b) spacer fabric with seams, (c) Edge-force-test to a spacer fabric without seams

2.3. Experimental test set up to test the compression behaviour of spacer fabrics

In Fig. 4 experimental results of the compression tests with sectioned spacer fabrics with seams are presented. Because the initial heights of all tested specimens are different due to the seam placement, the curves are visualised as if the compression plates start at the same plate distance of 20 mm. This means, that for the specimen with a seam distance of 18 mm and an average cushion height of 12 mm, the force measurement starts between 8 - 12 mm.

It can be observed that all curves can be sectioned into three main areas. A first section, where the force increases slightly over the compression distance. A second section, where except for the spacer fabric without seams, a higher, nearly constant increase of the force over the distance can be seen. And a third section, where the material is stiffened up even more compared to section two.

In the first section it can be seen that the more seams are inserted, the longer the section of the low force/compression magnitude exists. The result is to be expected, since the more seams are inserted, the more the spacer threads are bent, reducing their capability to absorb forces. Another reason is that the heights of the sectioned areas of the spacer fabric differ more. This can be seen in Fig.4. The deviation from the average height of the specimen with a higher seam number is higher. Thus, not all sections absorb forces at the same time. The compression plate is getting in contact with one cushion after another and not with all cushions at the same time. This leads to a lower compression force increase. This assumption is supported by investigating the compression force – compression distance – curve of the spacer fabric without seams (Fig.4., red curve), which has a nearly constant height and thus the contact with the compression plate is at the same time at every point of the spacer fabrics surface. This results in a direct increase in force.

In the next graph section, the fabrics are stiffened up by the reduced thickness and the increased fibre density.

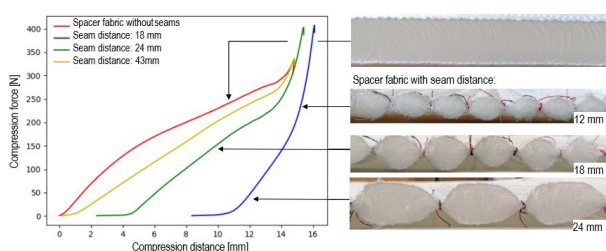


Fig. 4 Experimental results of compression tests of spacer fabrics with various seam distances

In conclusion a spacer fabric with more seams can absorb less compression forces due it previously inserted compression force through the seams. But the more seams are inserted, the stiffer the spacer fabric gets due to its structural change and locking of movements of the pile threads.

3. DESCRIPTION OF THE COMPRESSION TEST WITH A RIGID PUNCH ON THE SPACER FABRIC AND THEN ON A ROUGH FABRIC LAYER WITH SEAMS

This section is devoted to the simulation of the described above experiment with the chosen spacer fabric on the yarn level. First, the effective behavior in the elastic deformation range (before the monofil buckling) is computed. Afterwards, seams are virtually placed and the evolutionary contact of a punch with the spacer fabric with and without seams is simulated.

In the first simulation setup, the spacer fabric is resolved on the yarn level in the software package TexMath [16]. The virtual yarn structures are created based on the available pattern data and in visual comparison to the physical samples. The analyzed virtual structures are assumed to be deterministic and of periodic nature which minimizes computational effort. These assumptions are not too restrictive, since deviations from the deterministic structure are small in the machine produced fabrics.

For the simulations, an elastic frame-description of the structure is chosen: In our model, each yarn is individually parametrizable by its cross-sectional shape as well as its linear material properties, i.e., its Young's modulus as well as its Poisson's ratio. In accordance with the physical sample, we differentiate between three different sets of yarns for the spacer fabric itself, see Fig. 5, as well as an additional yarn type for the seam. Their respective material parameters are determined experimentally by standard tensile tests, see Fig. 6, but one might alternatively consider literature values if the material itself is known a priori.

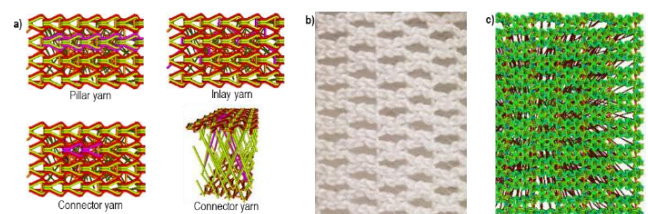


Fig. 5. (a) Individual yarn types highlighted in purple, (b) + (c) the virtual spacer fabric sample on the right, compared to the physical sample in the middle

For simulations of elasticity problems such as the compression of the spacer fabric as well as the seaming process, a beam FE formulation with additional contact conditions in-between yarns as well as in-between textile structure and pressing plates is considered, see e.g. [14] for further details. The presented models were already successfully employed for the simulative prediction of the effective mechanical properties of spacer fabrics as well as their air- permeability in [15].

After creation of the virtual spacer fabric sample, an optional additional simulative step is performed in which the seams are added. A schematic illustration of the employed double lock stitch is shown in Fig. 6. The double lock stitches are included in the structure as highlighted in purple for a cross section in Fig. 7

based on the chosen seam distance as well as the stitch distance. As can be seen, the stitch yarn is initially perpendicular to the knitted layers of the fabric but modelled with an effective pre-stress resulting from the machine's needle tension, which causes local compression as depicted in Fig. 8. In order to achieve the experimentally attained compression profile along the fabric, it is vital to resolve all contact points between the yarns in the spacer fabric and the stitch yarn.

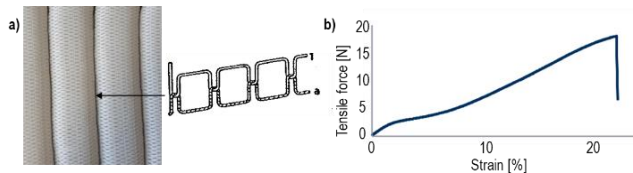


Fig. 6. (a) Schematic representation of the double lock stitch, (b) measured force-strain curve for the yarn material

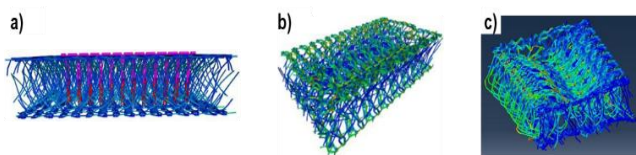


Fig. 7. Axial stresses in the pre-stressed seams and yarns of the spacer fabric simulated with (a) + (b) TexMath- tool and (c) Abaqus - Colours indicate local stresses.

The simulatively attained compression profile for the sewing distance of 43 mm is presented in Fig. 8 on the left. In order to ensure efficient computations, periodicity in the viewing direction was exploited with corresponding boundary conditions. The cushion height of the physical sample is closely met with 20.3 mm. For the other sewing distances, the model predicts the values 10.23 mm and 14.33 mm. Their profiles are shown on the right of Figure 8. For better visualization of the contracted lock stitch, we only visualize pillar and inlay yarns.

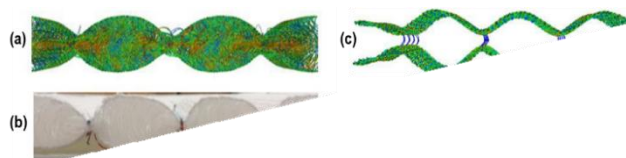


Fig. 8. Visual comparison of the spacer fabric with 43 mm seam distance (a) simulated and (b) experimental manufactured and simulated spacer fabrics with (c) 24 mm seam distance and (d) 18 mm seam distance

An intuitive model parameter that can be analyzed and optimized is the stitch yarn's pre-stress. Fig. 9 shows the simulation result for the seam distance of 43 mm but with only a 15 % relative strain. As can be seen, this value is not large enough to overcome the rigidity of connector yarns, leading to a drastically differing compression profile.

Finally, the compression experiments described in the previous section are performed on the virtual samples. For the simulations, dynamic contact conditions are prescribed in-between the compression plates and the fabric. The applied load is assumed to be uniformly distributed across the top plate, while the bottom plate is assumed to be stationary. The simulation predicts the state in which the compressive stiffness of the analyzed sample

and the applied compressive stresses are balanced. A qualitative demonstration of the predicted compression profiles for the unstitched spacer fabric sample are demonstrated in Fig. 10 for an increasing value of applied compressive force. The details of the algorithm can be found in Appendix. For better visualization, only the pillar and inlay yarns are shown.

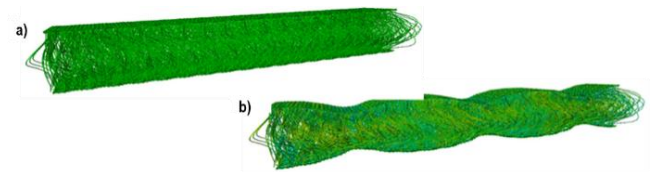


Fig. 9. Spacer fabric with seam distance of 43 mm before and after applying the pre-stress to the stitch yarn

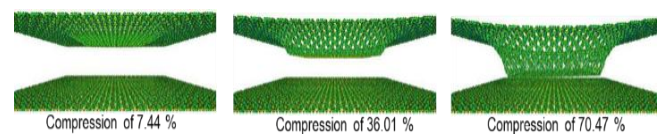


Fig. 10. Qualitative comparison of compression profiles at increasing compression levels for unstitched spacer fabric sample

The simulatively attained compression values for the unstitched sample as well as for the sample with stitch distance of 24 mm are presented in Fig. 11. By comparison with the experimental values, a good agreement of the model prediction till 30% compression can be observed. For larger compression values, it should be accounted for further changing parameters. First, the large deformations should be accounted for, i.e., the inextensible monofilaments preserve their length, whose curve would be arcs, parts of circles under compression, if they were not in a contact with each other. Furthermore, large bending leads to the increment of the contact point number between monofilaments, which changes the linear compression behavior of the fabric. It is possible to account for this, but it is out of the scope in this work.

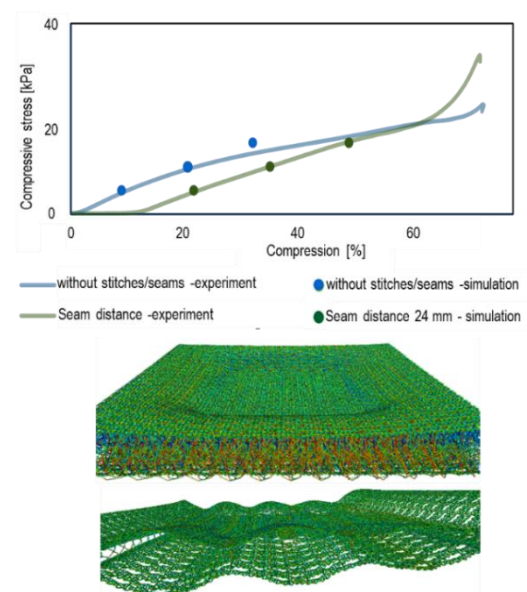


Fig. 11. Simulative and experimentally attained compression values for unstitched spacer fabric and sample with seam distance of 24 mm. Visualization of compressed samples below

Fig. 11 demonstrates that in case of the seams, the non-linearity occurs due to the evolutionary contact, involving different and increasing sets of contact points with the plane punch in each evolutionary step.

4. CONCLUSION AND DISCUSSION

This paper presents an experimental and numerical analysis of the compressive behaviour of spacer fabrics and modified spacer fabrics with seams. Four different specimen have been tested and modelled. Three specimens have been local sectioned by seams. One specimen was a spacer fabric without seams and functioned as a reference. A two-step simulation has been performed. Firstly the spacer fabric structures with seams have been recreated virtually and then the compression test as in the experimental set up has been performed. The shape deformation and compression force – compression distance curve of the experimental and modelling results have been analyzed and compared.

The model limitations are large rotations on the yarn level (starting after 25-30% of the compression for the non-stitched fabric), leading to the non-linear effective compression behavior and changing number of the contact points. Increased number of monofil contacts leads to a “solidification” of the spacer fabric.

We conclude that spacer fabrics with a higher number of seams become stiffer for the compression because of their increasing density. Additionally, many new contacts lead to a stabilization of the fabric for the compression, what leads to almost linear stiffened behaviour at the last part of the curve in the mechanical experiments.

The attained shape of the sectioned areas in the virtual spacer fabrics and the height match with the manufactured samples. Additionally, the virtually performed compression tests show a satisfactory alliance of numerical and experimental compression curves.

Numerical simulations are cheap in the sense of the computation time. Each contact iteration is in the range of seconds. This is possible thanks to one-dimensional models, obtained in advance by an asymptotic dimension reduction for contact problems between continuous fibres or long and thin cylinders. A contact search approach was suggested in this paper and is presented in the Annex.

Appendix. Numerical algorithm for the contact search

The used computational tool in this section is TexMath, which is based on the finite element method for frames of beams, extended to contact conditions between one dimensional objects, [21]-[27]. The dimension reduction of the contact conditions between yarns is based on asymptotic analysis and dimension reduction [22]-[24], [26]. Detecting contacts in-between individual yarns requires a delicate contact search. Moreover, during the compression process new contacts between textile and compression plates have to be resolved, depending on the compressive state. In [28]-[32], comparable contact problems with rough surfaces and layers are considered and problems related to topological and scaling issues are addressed. The search of the contact node sets should be automatized here.

We start with shifting down the punch or the plate, which meets parts of the upper layer of the spacer fabric, see Fig. 12.

The process is performed iteratively. After each computational step, we need the total displacement vector u , global contact stiffness matrix $GSM_{contact}$ and the right-hand side vector given by contacts $RHS_{contact}$.



Fig. 12. Critical area of contact search for the compression of stitched spacer fabric samples

Initially, we set the contact conditions on all the surface nodes. In the model, a contact induces a right-hand side force on nodes in the finite element mesh according to the formulas presented on the bottom. The absolute value of this force is controlled by a contact parameter γ , which penalizes deviations of the current node distance from the smallest possible distance given by the sum of involved yarn radii. Due to the linear nature of these forces, a contact between two nodes can either act attracting or repulsing, see Fig. 13. An attracting contact is generally undesired, as it potentially increases the amount of computed compression. The repulsing contacts on the other hand are vital, as they stop the unphysical penetration of the two involved yarns. The two types can be differentiated by the respective sign or direction of the contact force.

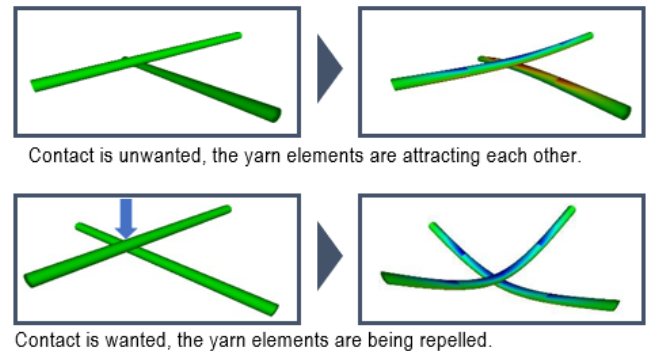


Fig. 13. Visualization of attracting (top) and repulsing (bottom) contacts. The simulation setup is the same, apart from an additional right-hand side force applied on the crossing centre at the bottom, indicated by the blue arrow

In more detail, let $RHS_{contact}$ be the right-hand side vector whose node entries are zero for non-contact nodes and for each contact node pair (n_1, n_2) let

$$RHS_{contact}|_{n_1} = -\frac{n_1 - n_2}{|n_1 - n_2|} \frac{1}{\gamma} ((r_1 + r_2) - |n_1 - n_2|),$$

$$RHS_{contact}|_{n_2} = +\frac{n_1 - n_2}{|n_1 - n_2|} \frac{1}{\gamma} ((r_1 + r_2) - |n_1 - n_2|).$$

The total discrete right-hand side force acting on the textile can be decomposed into an external force f_{ext} , containing e.g., the discrete compressive forces, and the forces arising due to the set contacts $f_{contact}$ with

$$f_{contact} = GSM_{contact} * u + RHS_{contact}.$$

Here, u is the prediction of the discrete total displacement field in steady state for the currently set contacts.

An iterative approach can be employed, which first predicts the equilibrium state of the compressed fabric by solving the underlying elasticity equations for a given set of contacts. Afterwards, the discrete right-hand side force that was exerted from each contact is computed and contacts which show attracting behavior are removed. The number of contacts that are removed in one iteration can be chosen smaller than the total number of found attracting contacts. This is to relax the iterative approach and evades under-prediction of the compression by removing too many contacts. Removing 25% of found contacts in one iteration generally led to satisfactory results in the considered simulation settings. Starting with a finite (but potentially large) number of initial contacts, the algorithm is guaranteed to converge to a steady state, since it will stop at latest when the entirety of all initially set contacts was removed.

As an example, Fig. 14 demonstrates the found contacts in the final iteration of the algorithm for an applied compressive stress of 10 kPa. They are displayed as blue elements in-between nodes and are located at sensible positions.

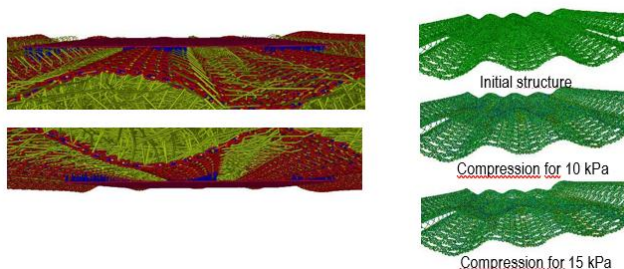


Fig. 14. Found contacts after the final iteration of the removal algorithm and stitched fabric under different compressive loads


REFERENCES

- Helbig FU. Druckelastische 3D-Gewirke: Gestaltungsmerkmale und mechanische Eigenschaften druckelastischer Abstandsgewirke. Saarbrücken: Südwestdeutscher Verlag für Hochschulschriften. 2011.
- Chen F, Wang J, Gao, S, Ning, X, Yan P, Tian M. An experimental study on the vibration behavior and the physical properties of weft-knitted spacer fabrics manufactured using flat knitting technology. Text Res J. 2022;004051752211249. Available from: <https://doi.org/10.1177/00405175221124929>
- Yu S, Liu H, Wu S, Ma P. Numerical characterizations for compressive behaviors of warp-knitted spacer fabrics with multi-layers from simplified finite element model. J. Ind. Text. 2022;52:1-22. Available from: <https://doi.org/10.1177/1528083722112402>
- Yu L et al. Finite element simulation and experimental verification of quasi-static compression properties for 3D spacer fabric/hollow microspheres reinforced three phase composites. Mater Res Express. 2021;8(5): 55305. Available from: <https://stats.iop.org/article/10.1088/2053-1591/ac0265>.
- Hou X, Hu H, Liu Y, Silberschmidt V. Nonlinear Compression Behavior of Warp-Knitted Spacer Fabric: Effect of Sandwich Structure. Comput. Mater. Contin. 2011;23(2):119–134. Available from: <https://doi.org/10.3970/cm.2011.023.119>
- Datta MK, Behera BK, Goyal A. Prediction and analysis of compression behaviour of warp-knitted spacer fabric with cylindrical surface. J. Ind. Text. 2019;48(9):1489–1504. Available from: <https://doi.org/10.1177/1528083718769936>
- Liu Y, Hu H. Finite element analysis of compression behaviour of 3D spacer fabric structure. Int. J. Mech. Sci. 2015;94-95:244–259. Available from: <https://doi.org/10.1016/j.jmecs.2015.02.020>
- Liu H, Jiang G, Dong Z. Lapping modeling of looped warp knitted jacquard fabrics based on web. J. Eng. Fibers Fabr. 2020;15. Available from: <https://doi.org/10.1177/1558925020979300>
- Liu Y, Hu H. Compression property and air permeability of weft-knitted spacer fabrics. J. Text. Inst. 2011;102(4):366–372. Available from: <https://doi.org/10.1080/00405001003771200>
- Liu Y, Hu H, Zhao L, Long H. Compression behavior of warp-knitted spacer fabrics for cushioning applications. Text Res J. 2012;82(1):11-20. Available from: <https://doi.org/10.1177/00405175111416>
- Liu Y, Hu H. An experimental study of compression behavior of warp-knitted spacer fabric. JEFF. 2014;9(2). Available from: <https://doi.org/10.1177/155892501400900207>
- Vassiliadis S, Kallivretaki A, Psilla N, Provatis Ch, Mecit D, Roye A. Numerical Modelling of the Compressional Behaviour of Warp-knitted Spacer Fabrics. Fibres Text. East. Eur. 2009;76(5):56–61. Available from: https://www.openarchives.gr/aggregator-openarchives/edm/ntua/000011-123456789_28784
- Griso G, Khilkova L, Orlik J. Asymptotic Behavior of Unstable Structures Made of Beams. J Elast. 2022;150:7–76. Available from: <https://doi.org/10.1007/s10659-022-09892-6>
- Orlik J, Krier, M, Neusius D, Pietsch K, Sivak O, Steiner K. Recent efforts in modeling and simulation of textiles. Textiles. 2021;1(2):322–336. Available from: <https://doi.org/10.3390/textiles1020016>.
- Orlik J, Pietsch K, Fassbender A, Sivak O, Steiner K. Simulation and Experimental Validation of Spacer Fabrics Based on their Structure and Yarn's Properties. Appl. Compos. Mater. 2018;25:709-724. Available from: <https://doi.org/10.1007/s10443-018-9726-9>.
- TexMath Software Tool for Simulation of Textiles. itwm.fraunhofer.de/TexMath (accesses on 28.06.2023).
- Orlik J, Neusius D, Steiner K., Krier M. On the ultimate strength of heterogeneous slender structures based on multi-scale stress decomposition. Int. J. Eng. Sci. 2024;195: 104010. Available from: <https://doi.org/10.1016/j.ijengsci.2023.104010>.
- Yu S, Dong M, Jiang G, Ma P. Compressive characteristics of warp-knitted spacer fabrics with multi-layers. Compos Struct. 2021;256:113016. Available from: <https://doi.org/10.1016/j.compstruct.2020.113016>
- Schwager C, Peiner C, Bettermann I, Gries T. Development and standardization of testing equipment and methods for spacer fabrics. Appl. Compos. Mater. 2022;29(1):325-341. Available from: <https://doi.org/10.1007/s10443-021-09959-y>
- Yu A, Sukigara S, Takeuchi S. Effect of inlaid elastic yarns and inlay pattern on physical properties and compression behaviour of weft-knitted spacer fabric. J Ind Text. 2022;51(2):2688S-2708S. Available from: <https://doi.org/10.1177/1528083720947740>
- Orlik J, Panasenko G, Shiryayev V. Optimization of textile-like materials via homogenization and beam approximations. Model Simul. 2016;14(2): 637-667. Available from: <https://doi.org/10.1137/15M1017193>
- Shiryayev V, Orlik J. A one-dimensional computational model for hyperelastic string structures with Coulomb friction. Math. Methods Appl. Sci. 2017;40(3):741-756. Available from: <https://doi.org/10.1002/mma.4005>
- Bare DZ, Orlik, J., Panasenko, G. Asymptotic dimension reduction of a Robin-type elasticity boundary value problem in thin beams. Appl Anal. 2014;93(6):1217-1238. Available from: <https://doi.org/10.1080/00036811.2013.823481>
- Bare Z, Orlik J, Panasenko G. Non homogeneous Dirichlet conditions for an elastic beam: an asymptotic analysis. Appl Anal. 2016;95(12):2625-2636. Available from: <https://doi.org/10.1080/00036811.2015.1105960>
- Orlik J, Andrä H, Argatov I, Staub S. Does the weaving and knitting pattern of a fabric determine its relaxation time. QJMAM. 2017;70(4):337-361. Available from: <https://doi.org/10.1093/qjmam/hbx011>
- Griso G, Orlik J, Wackerle S. Asymptotic behavior for textiles. SIAM. 2020;52(2):1639-1689. Available from: <https://doi.org/10.1137/19M1288693>

London). 2015. ISSN 1869-8433.

27. Orlik J, Falconi R, Griso G, Wackerle S. Asymptotic behavior for textiles with loose contact.
28. Math. Methods Appl. Sci. 2023;46(16):17082-17127. Available from: <https://doi.org/10.1002/mma.9490>
29. Orlik J, Zhurov A, Middleton J. On the secondary stability of coated cementless hip replacement: parameters that affected interface strength. Med Eng Phys. 2003;25(10):825-831. Available from: [https://doi.org/10.1016/S1350-4533\(03\)00099-7](https://doi.org/10.1016/S1350-4533(03)00099-7)
30. Andrä H, Battiato S, Bilotta G, Farinella GM, Impoco G, Orlik J., Russo G, Zemitis A. Structural simulation of a bone-prosthesis system of the knee joint. Sensors. 2008; 8(9):5897-5926. DOI: 10.3390/s8095897. Available from: <https://doi.org/10.3390/s8095897>
31. Orlik J, Zhurov A. Homogenization for contact problems with known microroughness of the contacting surfaces. J. mech. behav. mater. 2009;19(2-3):143-150. Available from: <https://doi.org/10.1515/JMBM.2009.19.2-3.143>
32. Argatov II, Borodich FM, Popov VL. JKR adhesive contact for a transversely isotropic layer of finite thickness. J Phys D. 2015;49(4):045307. DOI 10.1088/0022-3727/49/4/045307. Available from: <https://orca.cardiff.ac.uk/id/eprint/90101>
33. Argatov I, Mishuris G. Contact mechanics of articular cartilage layers. Asymptotic models. Springer (Cham Heidelberg New York Dordrecht

The research is funded by DFG, German Research Foundation, project numbers ROE 1303/20-1, PI 1251/1-3 and OR 190/6-3.

Maxim Krier:  <https://orcid.org/0009-0005-5917-0367>

Julia Orlik:  <https://orcid.org/0000-0002-0450-8034>

Kathrin Pietsch:  <https://orcid.org/0000-0003-1976-7749>



This work is licensed under the Creative Commons BY-NC-ND 4.0 license.

A SMALL-SIZED ROBOT PROTOTYPE DEVELOPMENT USING 3D PRINTING

Igor NEVLIUDOV*, Vladyslav YEVSIEIEV*, Svitlana MAKSYMOMA*, Olena CHALA*

* Faculty of Automatics and Computerized Technologies, Department of Computer-Integrated Technologies, Automation and Robotics, Ukraine, Kharkiv National University of Radioelectronics, Nauky ave. 14, Kharkiv, Ukraine

igor.nevliudov@nure.ua, vladyslav.yevsieiev@nure.ua, svitlana.milyutina@nure.ua, olena.chala@nure.ua

received 26 January 2024, revised 25 October 2024, accepted 30 October 2024

Abstract: Our article is devoted to the development of a small robot prototype using 3D printing technology. Particular attention is paid to its use in conditions associated with the destruction of reinforced concrete panel buildings, which becomes especially relevant in connection with man-made destruction as a result of military operations in Ukraine. The robot is an innovative technology solution designed to improve rescue, recovery and safety operations in environments where traditional methods may not be effective. In this article, we will look at the development process and functional features of this mobile robot, and also discuss the prospects for its use in complex and emergency situations.

Key words: 3D Printing, mobile robot, small-sized robot, prototype, assembly

1. INTRODUCTION

In modern conditions of destructive man-made disasters and military events that can cover various regions of the world, issues of safety and efficiency of restoration are becoming increasingly relevant. One of the important accents when studying damaged buildings built on the principle of reinforced concrete panel structures is its fragility, unpredictability of behavior, as well as minimal working spaces inside or between the slabs. This complicates search and rescue operations and structural analysis of the strength of damaged buildings. An example of such destroyed buildings in the city of Kharkov, Ukraine, as a result of the military aggression of the Russian Federation is shown in Fig. 1.



Fig. 1. Example of destroyed panel houses in Kharkov due to the war

Taking into account the peculiarities of structural damage to reinforced concrete panel buildings when hit by a shell or missile, they can be as follows:

- punching and penetration. A projectile or missile can cause penetration through the surface layers of reinforced concrete. This can create holes, cause panel deformation and lead to

structural collapse in the form of panels collapsing or partial destruction;

- formation of cracks and shedding. A projectile hit can cause cracks in the concrete structure. This can lead to shedding of surface layers and, possibly, further destruction of the structure;
- compression and deformation. Impact impacts can cause compression and deformation of reinforced concrete panels. This can lead to a loss of strength and a change in the shape of the structure, partial collapse of the building's structural elements;
- general destruction and collapse. Once hit by a projectile, general destruction and even collapse of parts or the entire building may occur, especially if structural elements are significantly damaged.

It can be seen that the use of classical mobile robots for conducting research in damaged buildings is not advisable due to the minimally limited working space. Such conditions arise when building panel structures are assembled. Due to the large dimensions of such robots, the likelihood of a mobile robot falling into rubble increases. It becomes possible to lose it completely. This can lead to high costs due to the high cost of the robot itself, which can reach ~\$5,000-15,000 or more. Examples of such mobile robots are shown in Fig. 2.

Therefore, the development of small-sized robots is relevant. Of particular interest is the use of additive 3D printing technologies to produce most of the parts of these robots. Plenty of authors use such a technology for soft robotics [4]-[6], but we propose to use it for our small robots. They will be able to quickly and effectively interact inside destroyed reinforced concrete panel structures in a limited working space. This represents an important step in ensuring safety and rapid investigation of damage sites to make appropriate decisions regarding the condition of the building. It should be noted separately here that such a solution is cheap.



a)



b)



c)

Fig. 2. Classic mobile robots for conducting research in damaged buildings

2. DESIGN OF A MOBILE ROBOT

Robots for working in man-made disaster zones, especially in areas with limited work space, must be designed taking into account the specifics of their operation. As part of these studies, we will introduce the following requirements for the mobile robot design being developed:

- compact size and maneuverability: the robot must be compact in order to easily penetrate limited and hard-to-reach places, such as between reinforced concrete structures;
- intelligent navigation system: development of intelligent navigation algorithms that allow robot to avoid obstacles and correctly route in difficult conditions;
- cameras and sensors: using cameras, laser sensors and other sensors to navigate and search for problem areas in structures;

- stability and distance control: robots must be stable and able to withstand uneven surfaces and be capable of distance control to avoid risks to the operator;
- protection from external factors: the design must be protected from dust to ensure reliable operation in contaminated environments.
- safety: the use of safe materials and additional safety measures to avoid emergency situations, especially in conditions of collapses or hazardous areas.
- range and duration of operation: Ensuring sufficient range and duration of operation in one cycle to effectively perform tasks in limited access conditions.

Based on the requirements stated above, there was developed a design concept for a small-sized mobile robot, a sketch of which is presented in Fig. 3.

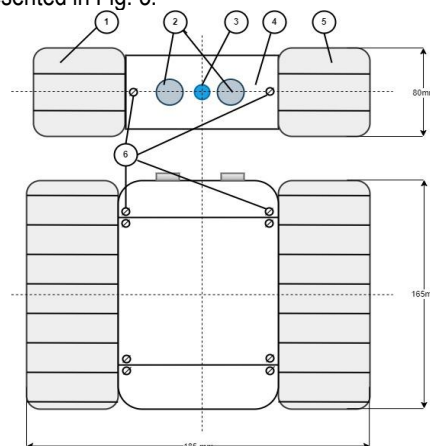


Fig. 3. A small-sized mobile robot design sketch

Let us describe the designation of the main elements that are indicated on a small-sized mobile robot design sketch (Fig. 3). 1,5 – caterpillars; 2 – ultrasonic sensor HC-SR04; 3 – camera OV2640; 4 – a mobile robot housing obtained using 3D printing; 6 – hardware for fastening housing elements.

The next stage is the development of a small-sized mobile robot detailed 3D model. The choice of the SolidWorks CAD system for developing a mobile robot 3D model was justified by its wide capabilities in the field of mechanical design and many years of success in the engineering field. SolidWorks provides an intuitive interface and powerful tools, allowing you to create complex mechanical designs with high precision. Its integration with CAM systems provides efficient preparation for 3D printing, making SolidWorks the optimal choice for developing innovative and technically complex projects, such as mobile robots. Based on the SolidWorks CAD system, a detailed assembly of a small-sized mobile robot was designed; the “explosive” model is shown in Figure 4.

To print the designed parts, we will use an Anet 8a Plus 3D printer with the following printing parameters: plastic – PLA; printing characteristics: extruder temperature 200 °C, table 56 °C; extruder diameter – 0.2 mm; layer height – 0.2 mm; line width – 0.3 mm. To prepare stl files for printing, the Ultimaker Cura 5.2.2 slicer was used. The obtained 3D printing results are presented in Table 1.

To print the designed parts, we will use an Anet 8a Plus 3D printer with the following printing parameters: plastic – PLA; printing characteristics: extruder temperature 200°C, table 56°C; extruder diameter – 0.2 mm; layer height – 0.2 mm; line width –

0.3 mm. To prepare stl files for printing, the Ultimaker Cura 5.2.2 slicer was used. The obtained 3D printing results are presented in Table 1.

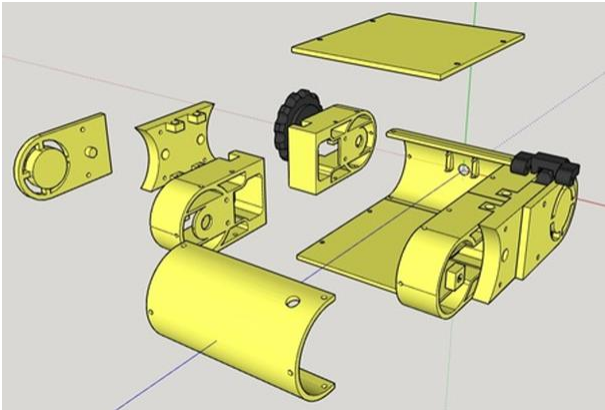
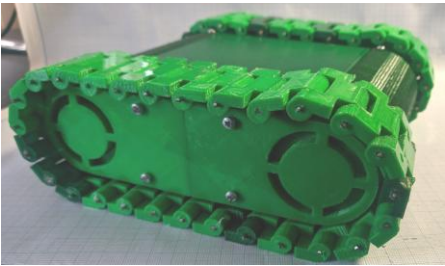


Fig. 4. Classic mobile robots for conducting research in damaged buildings

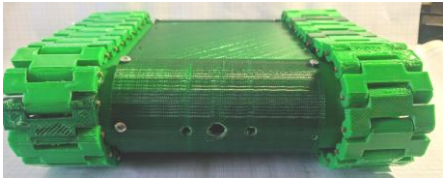
Tab. 1. Obtained 3D printing results

| 3D model in SolidWorks | Physical design in assembly |
|------------------------|-----------------------------|
| | |
| | |
| | |
| | |
| | |

The assembled housing design of a small-sized mobile robot for research in the zone of man-made disasters, obtained on the basis of 3D printing, is shown in Fig. 5.



a)



b)

Fig. 5. Assembled housing design of a small-sized mobile robot a) side view; b) front view

3. A MOBILE ROBOT CONTROL SYSTEM DEVELOPMENT

Considering the small overall dimensions of a compact mobile robot, to develop a control system it is necessary to select microcontroller modules that provide the following requirements: small overall dimensions, support for wireless information networks (Wi-Fi), the ability to create an access point with support for the HTTP protocol (HTTPS) and connection support cameras for computer vision system. Based on these requirements, the following microcontroller modules were analyzed, which are presented in Fig. 6.



a)



b)



c)

Fig. 6. Microcontroller modules a) ESP32-CAM [7], b) OpenMV Cam H7 R2 [8], c) Raspberry Pi Zero W [9]

Each analyzed module supports hardware connections of different video cameras models with the ability to support transmitted image quality UXGA 1600x1200 (15 fps) / SVGA 800x600 (30 fps). But at the same time they have fundamental differences, for example, Raspberry Pi Zero W+Cam allows you to deploy Raspberry OS/OS Android on it with support for C++ and Python languages, OpenMV Cam H7 R2 is designed for programming in the MicroPython language. At the same time, the basic operating principle is similar to the ESP32-CAM, which is programmed through the Arduino IDE (in a C-like language). Considering that the main task assigned to the mobile robot control system is to control movement and transmit the video stream to the operator, the main selection criteria will be the following parameters: power supply features, overall dimensions of the hardware module, weight and price.

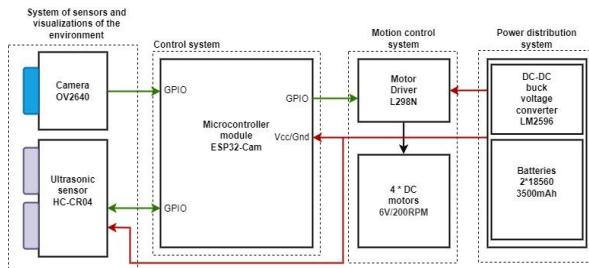


Fig. 7. A small-sized mobile robot control block diagram

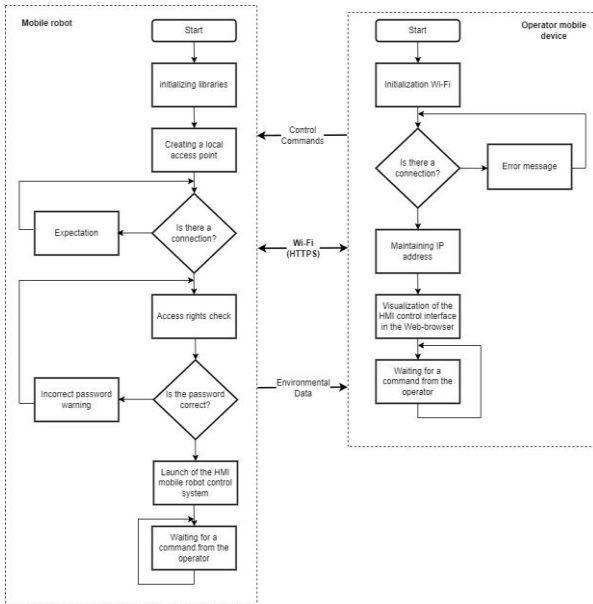


Fig. 8. Generalized control algorithm for a small-sized mobile robot

Based on own experience [7, 10, 11] with these hardware modules, the authors consider it inappropriate to use the Raspberry Pi Zero W, since for its stable operation it is necessary to provide it with 5V 2.5A power. If these recommendations are not followed, the Raspberry Pi Zero W may freeze and reboot. This module also has large overall dimensions. The ESP32-CAM module and OpenMV Cam H7 R2 operate stably with a power supply of 5V 1A. At the same time, they have approximately the same overall dimensions. They also have different price criteria, ESP32-CAM is about 6 times cheaper than OpenMV Cam H7 R2. As a result, to develop an experimental mobile robot prototype on omnidirectional wheels,

ESP32-CAM will be used for a control system. Based on the selected microcontroller module, we will develop a control block diagram (Fig. 7).

A general algorithm for controlling a small-sized mobile robot using wireless data transmission technologies is presented in Fig. 8.

4. EXPERIMENTAL RESEARCH AND ANALYSIS OF THE RESULTS OBTAINED

To conduct research, an experimental small-sized mobile robot prototype was assembled to work in areas of man-made disasters such as destruction or partial destruction of reinforced concrete panel houses and buildings. A general view of the assembled prototype during field testing is shown in Fig. 9.



Fig. 9. Assembled small-sized mobile robot prototype general view

The purpose of the first experiment was to test the operating time of a mobile robot and find the distance of a stable control signal with the streaming video transmission. To conduct the experiment, a location was chosen that contained small fragments of concrete and graphite, as well as complex terrain. The results obtained are presented in Table 2.

Tab. 1. Results of testing the operating time of a mobile robot and finding the distance of a stable control signal with streaming video transmission

| Parameters | Value |
|---|------------------|
| Test results (without additional antenna) | |
| Continuous operation time | ~ 15 hours |
| Video stream transmission (open area) | ~ 50-70 meters |
| Video stream transmission (reinforced concrete structure) | ~ 35-55 meters |
| Test results (with additional antenna) | |
| Continuous operation time | ~ 15 hours |
| Video stream transmission (open area) | ~ 170-200 meters |
| Video stream transmission (reinforced concrete structure) | ~ 100-150 meters |

As can be seen from the obtained experimental values, the developed mobile robot for working in areas of man-made disasters makes it possible to confidently receive a video stream about the surrounding space, as a result of which to conduct research and analysis of the degree of damage to reinforced concrete structures at distances of 100-150 meters using an additional antenna that is installed to the ESP32-Cam module. The cost of the developed mobile robot housing was less than \$10. At the same time, the total price of the developed mobile robot does not exceed \$300-350, taking into account the cost of PLA plastic, and the printing time with the above slicer parameters was ~ 72 hours.

5. CONCLUSIONS

The article proposes the development of a small-sized mobile robot, the body of which is created using 3D printing technology. Currently, in conditions of war, destruction of panel buildings has become extremely common. It is advisable to use mobile robots to study them. Moreover, such robots had to be small to provide access to the cracks formed by the folded panels. Moreover, the risk of loss or destruction of such robots is high, so the cost should be as low as possible.

The development of just such a robot is proposed in this article. Studies have shown that the developed robot can work without recharging the batteries for up to 15 hours. Without an antenna, Video stream transmission (open area) ranged from 50 to 70 meters depending on the direction of signal transmission, Video stream transmission (reinforced concrete structure) ranged from 35 to 55 meters depending on the thickness and number of reinforced concrete structures. With an antenna, video stream transmission (open area) was from 170 to 200 meters, and Video stream transmission (reinforced concrete structure) was from 100 to 150 meters. Remote control will be possible from any mobile device: phone, tablet, etc. This robot is under development. In the future, it is planned to improve the model for greater impact resistance.

REFERENCES

1. Massy-Beresford, H. Robot rescuers to help save lives after disasters. Horizon Magazine. Available from: <https://horizon-magazine.eu>. <https://ec.europa.eu/research-and-innovation/en/horizon-magazine/robot-rescuers-help-save-lives-after-disasters>. 2023.
2. Autonomous Systems and Biomechatronics Lab. Robot-Assisted Emergency Response. Available from: <http://asblab.mie.utoronto.ca/research-areas/robot-assisted-emergency-response>. 2023.
3. Tohoku University. Feature Highlights Robo Rescue! Available from: https://www.tohoku.ac.jp/en/research/research_highlights/research_highlight_14.html. 2023.
4. Yap YL, Sing SL, Yeong WY. A review of 3D printing processes and materials for soft robotics. *Rapid Prototyping Journal*. 2020;26(8):1345-1361.
5. Sachyani Keneth E, Kamyshny A, Totaro M, Beccai L, Magdassi S. 3D printing materials for soft robotics. *Advanced Materials*. 2021;33(19): 2003387.
6. Tiryaki ME, Zhang X, Pham QC. Printing-while-moving: a new paradigm for large-scale robotic 3D Printing. In 2019 IEEE/RSJ International Conference on Intelligent Robots and Systems (IROS) IEEE. 2019;2286-2291.
7. Yevsieiev V, Maksymova S, Starodubcev N. Software Implementation Concept Development for the Mobile Robot Control System on ESP-32CAM. In Current issues of science, prospects and challenges: collection of scientific papers «SCIENTIA» with Proceedings of the II International Scientific and Theoretical Conference. Sydney Australia: European Scientific Platform. 2022;254-256.
8. Mikronika. OpenMV Cam H7 R2 Камера машинного зору. Available from: <https://mikronika.net/product/openmv-cam-h7-r2>. 2023
9. uAmper.com. Raspberry Pi Zero W. Available from: https://uamper.com/index.php?route=product/product&path=84&product_id=1156&ad_source=1&gclid=CjwKCAiApaarBhB7EiwAYiMwqqaGRQTR9GLRbQ_VoJMUyvk4m8yDhCPbeCRVvWj2LB7yEogaA-BsoxoCI3gQAvD_BwE. 2023
10. Yevsieiev V, Maksymova S, Starodubcev N. Development of an Algorithm for ESP32-Cam Operation in HTTP Server Mode for Streaming Video. In Collection of scientific papers «ΛΟΓΟΣ». Paris France. 2022;177-179.
11. Nevliudov I, Yevsieiev V, Maksymova S, Demska N, Kolesnyk K, Miliutina, O. Mobile Robot Navigation System Based on Ultrasonic Sensors. In IEEE XXVIII International Seminar/Workshop on Direct and Inverse Problems of Electromagnetic and Acoustic Wave Theory (DIPED). 2023;1:247-251.

Igor Nevliudov:  <https://orcid.org/0000-0002-9837-2309/>

Vladyslav Yevsieiev:  <https://orcid.org/0000-0002-2590-7085>

Svitlana Maksymova:  <https://orcid.org/0000-0002-1375-9337>

Olena Chala:  <https://orcid.org/0000-0003-2454-3774>



This work is licensed under the Creative Commons BY-NC-ND 4.0 license.

SYSTEM FOR AUTOMATED DESIGN BY PHYSICAL PROCESSES OF 3D MODELS IN A DRYING CHAMBER FOR HYGROSCOPIC MATERIALS

Yaroslav SOKOLOVSKYY*, Oleksiy SINKEVYCH**

*Department of Computer-Aided Design Systems, Lviv Polytechnic National University,
79058, Ukraine, Lviv, str. Mytropolyta Andriya, 3

**Department of Computer Science, Ukrainian National Forestry University,
79058, Ukraine, Lviv, str. Gen. Chuprynky, 103

yaroslav.i.sokolovskyy@lpnu.ua, oleksiy1694@gmail.com

received 18 January 2024, revised 27 November 2024, accepted 28 December 2024

Abstract: Designing 3D models of drying chambers, especially of a new type, is a long and complex process. Nevertheless, the availability of 3D models of drying chambers allows for the necessary research before their actual design. In this paper, a software for the automated design of a 3D model of a drying chamber was developed to save time and material resources. To simulate the drying process of hygroscopic materials in this 3D model, an asynchronous cellular automaton model was developed. The software is the result of the programming implementation of several algorithms, including: an algorithm for automated design of a 3D model of a drying chamber using SolidWorks API tools; an algorithm for representing the 3D model under study as a cellular automaton field; an algorithm for calculating input data for simulation; an algorithm that uses transition rules for the asynchronous cellular automaton model; an algorithm for saving and displaying simulation results; and an algorithm for comparing simulation results. The software was verified and the mathematical models were validated using experimental data. The input data for the simulation were obtained from real technological conditions implemented in real drying chambers. The modeling results were used to obtain graphical dependencies of the desired material and drying agent parameters over time. The analysis of the results included their comparison with the data obtained by sensors in a real drying chamber. The relative error was determined, the average values of which did not exceed 13%, which confirms the accuracy of the results. In the long-term, the developed software has the potential to become a valuable tool in the design of new and more efficient drying chambers, offering opportunities for designing, modeling, and analyzing research results.

Key words: software, hygroscopic materials, cellular automaton field, SolidWorks API, modeling process

1. INTRODUCTION

In the rapidly advancing world of technology, it is essential not only to keep pace with changes but also to actively leverage cutting-edge information technologies to enhance traditional industries. This is particularly relevant to the modeling of the drying process of hygroscopic materials, such as wood, which has played a crucial role in the production of high-quality wooden products and materials for decades. This process also affects sectors such as construction, furniture manufacturing, and the packaging industry. In particular, the development of software for the computer-aided design of 3D models of drying chambers and the simulation of drying processes in them offers significant potential for increasing efficiency in these sectors.

Over the past decades, many efforts have been made to improve the design of drying chambers and increase their efficiency. Researches such as [1] and [2] emphasize the advantages of automating the design of drying chambers using modern software interfaces, in particular the SolidWorks API. In turn, research [2] focuses on the creation of simplified, operator-usable 3D models of drying chambers, while in [3], complex mathematical models developed to simulate heat and moisture exchange processes in such chambers. In addition, studies such as [4] address the problems of high-temperature drying, propose advanced mathematical

approaches, including the Navier-Stokes equation, to model the related heat, and mass transfer processes.

Despite these advances, traditional modeling methods remain computationally intensive, requiring significant time and computing resources. Nevertheless, recent studies [5] and [6] show that the cellular automata method can serve as a promising alternative, offering faster modeling without compromising accuracy. For example, in [5], finite element methods are compared with cellular automata for modeling wood drying, demonstrating comparable accuracy in a two-dimensional scenario, but with reduced computational expense. Similarly, in [6], asynchronous cellular automata were successfully applied to heat conduction problems, emphasizing their potential for high-speed computing in complex systems.

Even though cellular automata demonstrate high efficiency in modeling, the possibility of integrating them with 3D models of drying chambers is still insufficiently studied. This unsolved problem emphasizes the need for further research to develop innovative solutions. These solutions can improve the efficiency and accuracy of not only the computer-aided design of 3D models of new and potentially more efficient drying chambers, but also the simulation of the drying process in them.

The object of research in this work is the process of drying hygroscopic materials in drying chambers.

The subject of the study is a cellular automata model for simulating the drying process of hygroscopic materials in drying cham-

bers, for example wood.

The purpose of the research is the development and software implementation of a cellular automata model for simulating the drying process of hygroscopic materials, which includes a cellular automata field and corresponding rules of transitions. To achieve the set goal, the following main tasks are defined:

- Automated design of a 3D model of a drying chamber in the SolidWorks environment by using the SolidWorks API;
 - Development and software implementation of algorithms for presenting this 3D model in the form of a cellular automata field;
 - Analysis of mathematical models of heat and moisture transfer processes in drying chambers;
 - Based on the conducted analysis, development of transition rules for the cellular automata model;
 - Development of a database for saving input data, intermediate data, as well as results for each of the cells on the field;
 - Modeling of drying processes of hygroscopic materials in a drying chamber by using a cellular automata model;
 - Analysis and verification of obtained simulation results with real experimental data.
 - The scientific novelty is as follows:
 - A new model of cellular automata was developed to determine changes in the main parameters of hygroscopic material and its drying agent;
 - The structure of the cellular automaton field was improved, which, in contrast to the existing ones, allows taking into account the physical and geometric characteristics of the 3D model of the drying chamber;
 - algorithms for parameterization and CAD design of the 3D model of the drying chamber and its main components were developed, which makes it possible to effectively change their characteristics to specific process conditions.
- The practical significance of the research is as follows:
- Saving time and material resources due to the rapid change of geometric characteristics of the 3D model of the drying chamber or its components, without the need to recreate them;
 - Minimal user intervention in the process of creating a field of cellular automata with different types of cells, by developing and programmatically implementing the appropriate algorithm;
 - Increasing the speed of modeling compared to the finite difference method by developing a scheme of relationships between adjacent and tangential cells and using it in conjunction with transition rules.

In this work, the 3D design method was used to create a 3D model of the drying chamber, the cellular automata method was used for modeling, and the method for determining the relative error was used to compare the simulation results.

2. AUTOMATED DESIGN OF THE 3D MODEL OF THE DRYING CHAMBER

A drying chamber comprises numerous components, and designing each of them can be a time-consuming and resource-intensive task. Especially when these components are not always considered in the modeling of various physical processes, notably the drying process. To streamline the design process, it is practical to simplify by focusing on the main components, such as walls, doors, ceilings, roofs, stacks of drying material, heaters, nozzles, and fans. Each of

these components serves crucial functions, including delineating the study area (doors, walls, roof, ceiling), defining the study area (stacks of drying materials), heating the drying agent (heaters), humidifying the drying agent (nozzles), and ensuring circulation of the drying agent (fans). The majority of these components can be easily coded for automated design. However, for components like material stacks, heaters, humidifying nozzles, and fans, the process becomes more intricate and involves multiple automated design steps. At each phase, relevant 2D sketches (refer to Fig. 1) are created, serving as the foundation for the development of their corresponding 3D models. Subsequently, these 3D models are amalgamated into completed assemblies, the number of which may vary depending on the design of the drying chamber and the technological process requirements [8].

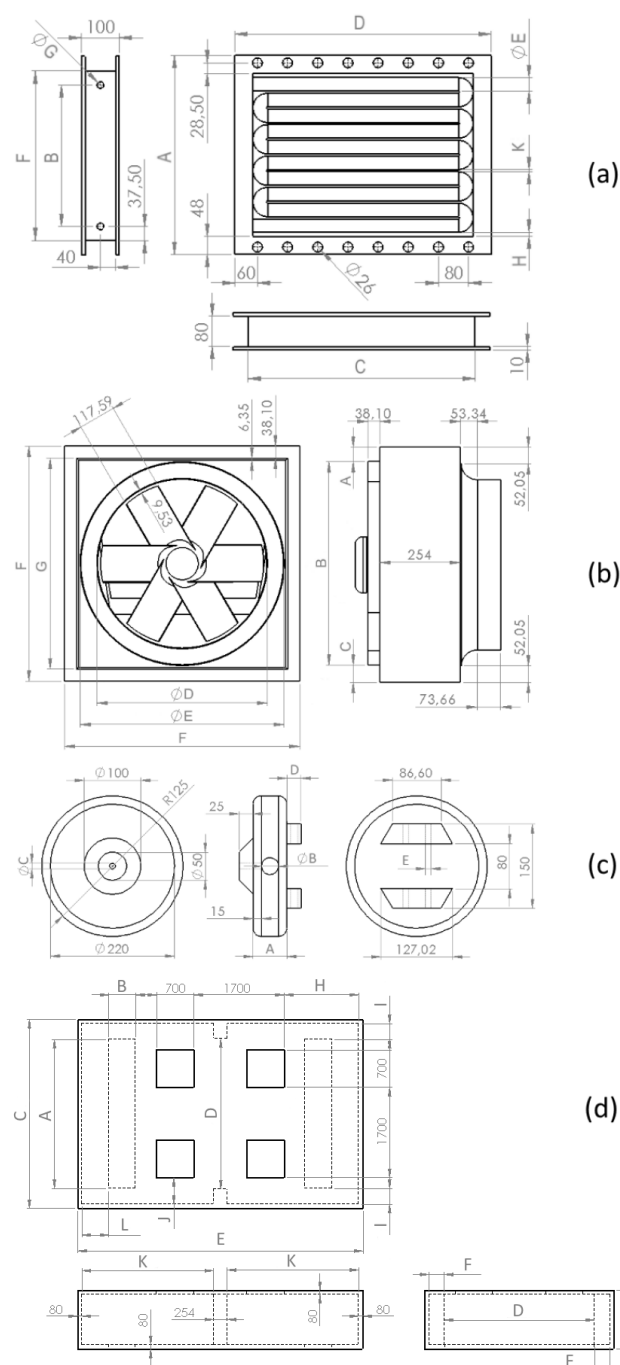


Fig. 1. View of 2D sketches of the water heater (a), axial fan (b), humidifying nozzle (c), and ceiling (d)

For the computer-aided design of the 3D model of the drying chamber, the following dimensions of the body were taken into

account: height 2.25 m, width 5.703 m, length 7.291 m, with a wall thickness of 5 cm, and parameterized dimensions (refer to Tab. 1).

Tab.1. Parameterized dimensions of the main components of the 3D model of the drying chamber

| Component of the 3D model | A, mm | B, mm | C, mm | D, mm | E, mm | F, mm | G, mm | H, mm | I, mm | J, mm | K, mm | L, mm |
|---------------------------|-------|--------|-------|--------|--------|-------|-------|--------|-------|-------|--------|-------|
| Water heater | 555 | 402 | 730 | 808 | 38 | 477 | 19 | 12.5 | - | - | 8 | - |
| Axial fan | 47.74 | 740.83 | 54.43 | 638.53 | 743.94 | 843 | 766.8 | - | - | - | - | - |
| Humidifying nozzle | 55 | 25 | 15 | 30 | 14 | - | - | - | - | - | - | - |
| Ceiling | 4848 | 477 | 5703 | 5058 | 7291 | 242.5 | 1003 | 2365.5 | 347.5 | 547.5 | 3438.5 | 238.5 |

Hence, during automated design, it is essential to utilize the primary window of the software, as depicted in Figure 2. Within this window, users can specify the nominal dimensions of the hygroscopic material, its species, and the quantity per stack. In this case, 16 stacks are designed, each containing 36 pine lumber with a thickness of 32 mm, a width of 75 mm and a length of 2.5 m. The height of the spacer between rows in the stack is automatically determined based on the height of the hygroscopic material.

ed 3D models are stored in the program directory by default, though users can easily customize this location in the software settings.

Through automated design, a 3D model of the drying chamber in SolidWorks can be obtained, as illustrated in Figure 4. The use of the SolidWorks API significantly saves time on this task.

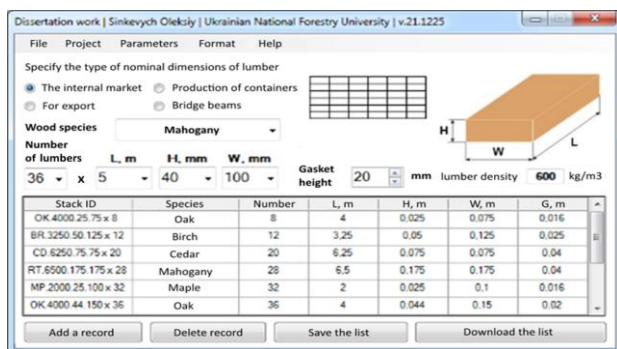


Fig. 2. View of the main window of the developed software

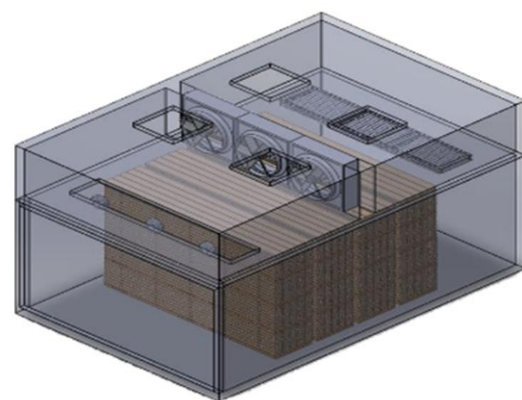


Fig. 4. General view of the drying chamber assembly in SolidWorks

Upon selecting all the requisite parameters and clicking the "Add a record" button, a new stack identifier is appended to the database. Its ID is constructed in the following manner: the initial two letters denote the wood species code, such as "BR" for birch, "CD" for cedar, "RT" for mahogany, "MP" for maple, "OK" for oak, and so forth. The subsequent numbers correspond to the length, height, and width of an individual material, along with their quantities. This comprehensive information is crucial for the automated design of the specified stack.

3. CREATION OF A CELLULAR AUTOMATA FIELD

To create a cellular-automata field, the initial step involves creating a specific graphic scheme (refer to Fig. 5), that illustrating the systematic process of transforming the 3D model of stacks. Similarly, the process of converting the 3D model of the drying chamber will take place.

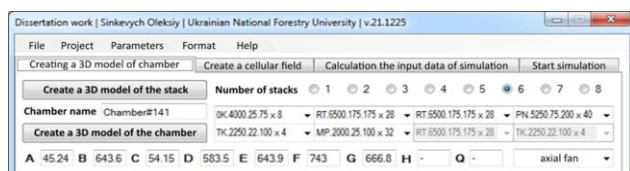


Fig. 3. Tab of the automated design of the 3D model of the drying chamber

However, real drying chambers commonly incorporate multiple stacks. In light of this, the software's first tab (refer to Fig. 3) was developed. This tab enabling users to specify the number of stacks and choose their type from the list created in the main program window (as described earlier). In essence, the user has the option to facilitate the automated design of either a 3D model of individual stacks or an entire assembly of the drying chamber. When opting for the entire assembly, it is necessary to define its name. All creat-

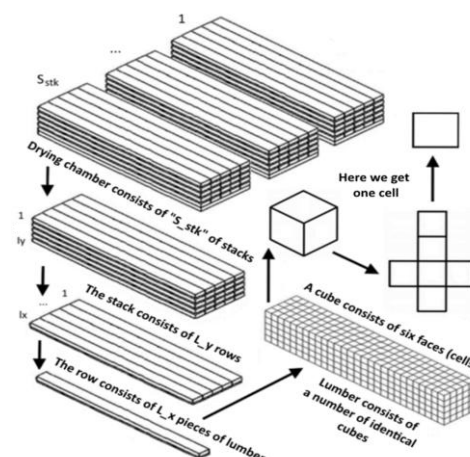


Fig. 5. Scheme of transformation of a 3D model of stacks into a three-dimensional array of cells

The creation of a cellular automata field [9] involves the following steps:

1. The program retrieves the dimensions of the dried materials in stacks, including "L" for length, "H" for height and "W" for width.
2. The program retrieves the maximum allowable division density of the 3D model (d_m), calculated across the greatest common divisor among its dimensions.
3. The program retrieves the desired level of division (d_i), indicating the precision of the calculations. Higher levels of division result in increased time and resource expenditure.
4. The program determines the final division density (d), which

defines the cell sizes. All cells possess identical face dimensions.

5. The program reads the number of drying materials in one stack (S_{imb}) and determines the number of materials in one row (l_x) and the number of rows (l_y) in one stack. Additionally, the program reads the number of stacks (S_{stk}).
6. The program retrieves the total number of cells on the cellular automata field for each of the three coordinates (S_x , S_y , S_z).
7. The program creates a three-dimensional array (a), where the elements represent cells.
8. The program determines the type of each cell on the cellular automata field according to the algorithm (refer to Fig. 6).

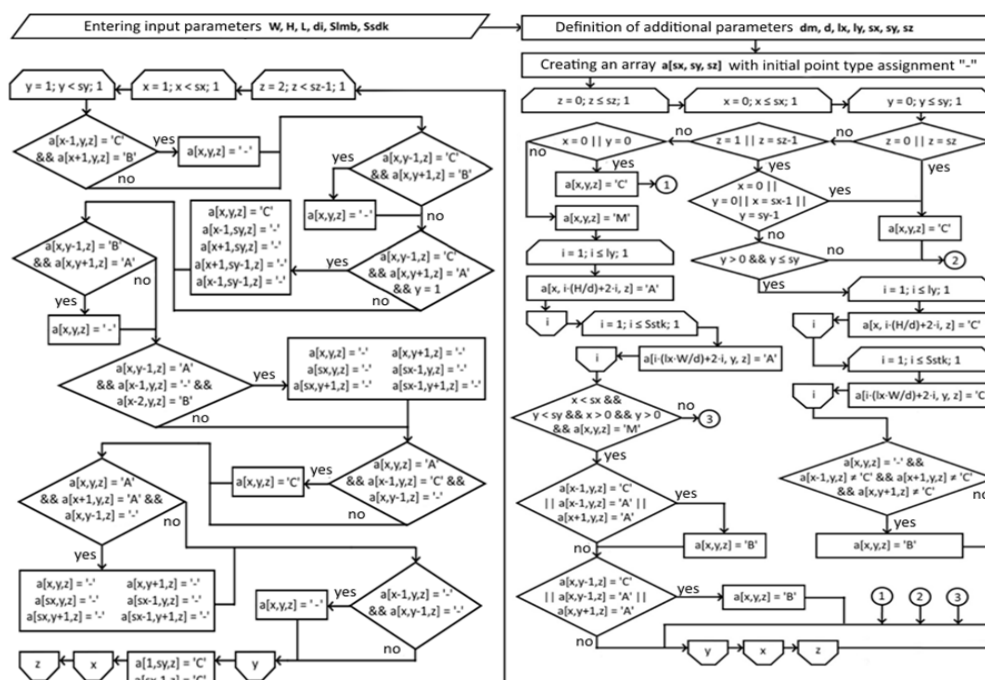


Fig. 6. Algorithm for creating a cellular automata field within stacks

When considering the cellular automata field within the arrangement of the stacks, the cells can have different types, with the main ones being: "A" for the drying agent, "B" for the border of lumber, and "M" for their internal drying zone. To create a cellular automata field by using the software, it is necessary to open the second tab of the main program window (refer to Fig. 7). On this tab, users can inspect the structure of this cellular automata field. To do so, they need to specify one of the coordinates and click the "Check" button. The two-dimensional view of this field will be display in the window below.

The structure of each cell contains information about its moisture content, temperature, coordinates (location), and time. The inclusion of time allows for the observation of changes in all cell parameters over time, a crucial aspect when generating graphic dependencies for a specific cell. Simultaneously, the upper-left vertex of the selected cell determines the coordinates of its location.

Considering the cellular automata field for the entire 3D model of the drying chamber, the cells have the following designations: "G" for the area of humidifying nozzles, "N" for the area of supply-exhaust channels, "V" for the area of axial fans, "H" for the location of water heaters, and "W" for the walls, ceiling, and chamber ceiling. These new designations enable the application of additional transition rules, particularly when the drying agent interacts with various components of the 3D model of the drying chamber. Such a cellular automata field is finite and constitutes one of the two parts of the cellular automata model. However, it's crucial to consider the computational capabilities of computer equipment during its creation. Although fewer resources are utilized compared to the finite difference method (one cell replaces four points), the required resources for its creation remain substantial. Consequently, the constructed cellular automata field accurately replicates the assembly structure of the designed 3D model of the drying chamber (refer to Fig. 8).

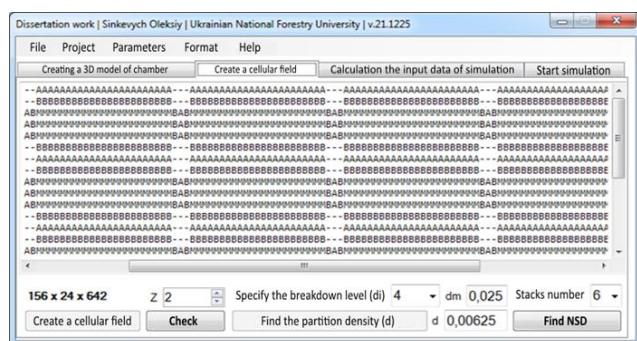


Fig. 7. Tab of the cellular automata field creation

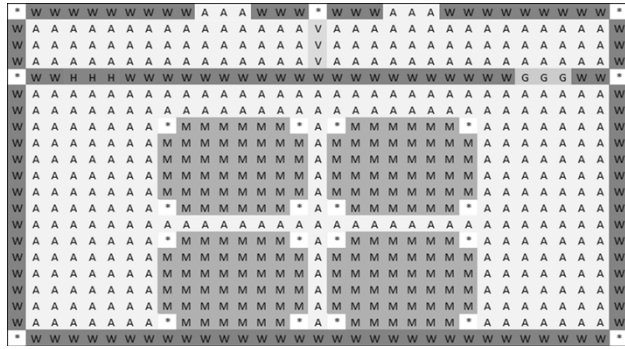


Fig. 8. View of the created cellular automata field

4. ANALYSIS OF MATHEMATICAL MODELS OF HEAT AND MASS TRANSFER PROCESSES IN DRYING CHAMBERS

To create transition rules, it is imperative to initially analyze the pertinent mathematical models describing the heat and mass transfer processes during the drying of hygroscopic materials [10-14]. Those mathematical models must consider the impact of various components of the drying chamber on alterations in the parameters of the drying agent, as well as its influence on the dried material. Additionally, it is advisable to incorporate the influence of the temperature of the walls of the drying chamber and the heater on the temperature of the drying agent. Furthermore, it is crucial to consider the impact of humidifying nozzles on the relative humidity content of the drying agent. Another important task is involves determining the initial speed of movement of the drying agent, a parameter influenced by the characteristics of the axial fans and their quantity.

To modeling the drying process of hygroscopic materials, it is essential to consider the heat transfer among various components within the system. In this context, hygroscopic materials act as the heating object, with water heaters performing as the heat source. The drying agent enables the transfer of heat between them. Unfortunately, the walls, roof, and ceiling absorb a portion of the heat from the drying agent that has traversed from the heaters to the hygroscopic materials. Consequently, it is possible to make certain simplifications by treating all components contributing to heat loss as a unified entity, denoted by a general temperature, T_w . In essence, the heat exchange, as described above, incorporates the heat balance equation [15] for the heater, drying agent, and other components of the drying chamber, and taking the following form:

$$\begin{aligned} & C_h N_h m_h \frac{\partial T_h(x, y, Fo)}{\partial Fo} + N_g G_p I_p + L_{in} (C_n + C_p \varphi_n) T_n - \\ & - G_0 \frac{\partial U_m(x, y, Fo)}{\partial Fo} - \frac{Nu_q \lambda_a}{r l} (T_a(x, y, Fo) - T_m(x, y, Fo)) - \\ & - C_w m_w \frac{\partial T_w(x, y, Fo)}{\partial Fo} - L_{out} (C_n + C_p \varphi_a(x, y, Fo)) \cdot \\ & \cdot T_a(x, y, Fo) = \left(\frac{0.622 V_a P_{bar}(x, y, Fo) (1 + \varphi_a(x, y, Fo)) C_a}{R(273 + T_a(x, y, Fo)) (0.622 + \varphi_a(x, y, Fo))} + \right. \\ & \left. + m_w C_w \right) \frac{\partial T_a(x, y, Fo)}{\partial Fo}, \end{aligned} \quad (1)$$

where: P_{bar} – barometric pressure, V_a – volume of the drying agent, φ_a – relative humidity of the drying agent, L_{out} – the quantity of moist air leaving the chamber through inlet-exhaust channels, m_w – mass of all components of the drying chamber that absorbing heat from the drying agent, except for the hygroscopic material, T_w – temperature on the surface of these components, C_w – average specific heat capacity of materials for all of those components, T_m –

temperature of the hygroscopic material, T_a – temperature of the drying agent, l – size of the hygroscopic material along the movement of the drying agent, r – specific heat of vaporization, λ_a – coefficient of thermal conductivity of air, Nu_q – Nusselt heat transfer criterion, U_m – moisture content of the hygroscopic material, G_0 – mass of absolutely dry hygroscopic material, T_n – temperature of fresh air, φ_n – relative humidity of fresh air, C_p – specific isobaric heat capacity of water vapor, C_n – specific isobaric heat capacity of incoming fresh air, L_{in} – quantity of fresh air entering through inlet-exhaust channels, I_p – enthalpy of 1 kg of water vapor, G_p – quantity of water vapor entering the system through the humidifying nozzle, N_g – number of humidifying nozzles, Fo – Fourier number, T_h – temperature of the surface of the water heaters, m_h – mass of one water heater, N_h – number of water heaters, C_h – specific heat capacity of the metal of the water heaters, R – the universal gas constant, C_a – the specific isobaric heat capacity of the drying agent.

$$\begin{aligned} & C_1 \alpha_t S_t (T_t - T_h(x, y, Fo)) - C_2 \alpha_h S_h (T_h(x, y, Fo) - \\ & - T_a(x, y, Fo)) = C_h m_h \frac{\partial T_h(x, y, Fo)}{\partial Fo}, \end{aligned} \quad (2)$$

where: S_h – heating surface area of the water heaters, α_h – coefficient of heat transfer of the cylindrical surface of the heaters, C_2 – coefficient of the thermal release surface state of the heaters, T_t – temperature of the heat carrier (hot water) in the heaters, S_t – surface area of heat transfer of the hygroscopic material, α_t – coefficient of heat transfer from condensing water vapor to the internal surface of the heaters, C_1 – coefficient of thermal losses of the heaters.

$$\begin{aligned} & \alpha_w (T_a(x, y, Fo) - T_w(x, y, Fo)) - \alpha_s (T_w(x, y, Fo) - \\ & - T_n) = C_w \rho_w l_w \frac{\partial T_w(x, y, Fo)}{\partial Fo}, \end{aligned} \quad (3)$$

where: l_w – dimension of the wall along the movement of the drying agent, ρ_w – average density of wall materials, considering heat insulation layers, α_s – coefficient of heat transfer from the external surface of the walls to the external environment, α_w – coefficient of heat transfer of the drying agent with components of the drying chamber absorbing heat from it, except for the hygroscopic material.

$$Nu_q = 0.0641 Re^{0.8} Gu^2 Pr^{0.333}, \quad (4)$$

where: Pr – Prandtl criterion, Gu – Guhman criterion, Re – Reynolds criterion.

In turn, the moisture balance equation in the drying chamber [14, 15] can accommodate changes in the relative humidity of the drying agent, which changes with its temperature. Essentially, this equation can be formulated as follows:

$$\begin{aligned} & N_g G_p + L_{in} \varphi_n - \frac{Nu_m \lambda_a}{r l} (T_a(x, y, Fo) - T_m(x, y, Fo)) - \\ & - L_{out} \beta_a \varphi_a(x, y, Fo) = \frac{\partial \varphi_a(x, y, Fo)}{\partial Fo} \cdot \frac{0.622 V_a}{R(273 + T_a(x, y, Fo))} \cdot \\ & \cdot \frac{P_{bar}(x, y, Fo)}{\varphi_a(x, y, Fo)^2 + 1.622 \varphi_a(x, y, Fo) + 0.622}, \end{aligned} \quad (5)$$

where: β_a – coefficient of moisture transfer, Nu_m – Nusselt's mass transfer criterion, determined according to A.V. Nesterenko [16].

$$Nu_m = 0.027 Re^{0.9} Gu^{0.175} Pr^{0.333}, \quad (6)$$

According to the law of conservation of energy, the quantity of heat expended on heating and evaporating moisture from the hygroscopic material will always be equivalent to the amount of heat entering it [17]. For this, the heat balance equation within the hygroscopic material being dried can be employed, witch having

the following form:

$$\frac{\partial T_m(x,y,Fo)}{\partial Fo} = (1 + \varepsilon Ko Pn Lu) \left(\frac{\partial^2 T_m(x,y,Fo)}{\partial x^2} + \frac{\partial^2 T_m(x,y,Fo)}{\partial y^2} \right) - \varepsilon Ko Lu \left(\frac{\partial^2 U_m(x,y,Fo)}{\partial x^2} + \frac{\partial^2 U_m(x,y,Fo)}{\partial y^2} \right), \quad (7)$$

At the same time, the moisture content of the hygroscopic material being dried is determined as follows:

$$\frac{\partial U_m(x,y,Fo)}{\partial Fo} = Lu \left(\frac{\partial^2 U_m(x,y,Fo)}{\partial x^2} + \frac{\partial^2 U_m(x,y,Fo)}{\partial y^2} \right) - Lu Pn \left(\frac{\partial^2 T_m(x,y,Fo)}{\partial x^2} + \frac{\partial^2 T_m(x,y,Fo)}{\partial y^2} \right) \quad (8)$$

where: Lu – Luykov criterion, which reflects the ratio of the convective diffusion coefficient (a_m) to the heat diffusion coefficient (a_q), Pn – Posnov criterion, which reflects the relationship between the intensity

of thermodiffusion ($\delta \Delta T_m$) to moisture diffusion transport (ΔU_m), Ko – Kosovych criterion, which represents the dependence between the amount of heat expended on evaporating liquid from the hygroscopic material ($r \Delta U_m$) to the amount spent on its heating $C \Delta T_m$, ε – phase transition coefficient.

Thus, the aforementioned equations constitute a mathematical model of the heat and mass transfer process within the drying chamber. This model allows the determination of the relative humidity and temperature of the drying agent, along with the moisture content and temperature of the hygroscopic material. Similar to any mathematical model, it must incorporate boundary conditions. Given its intricacy, a dedicated diagram (refer to Fig. 9) was devised to illustrate the coordinates of all its borders.

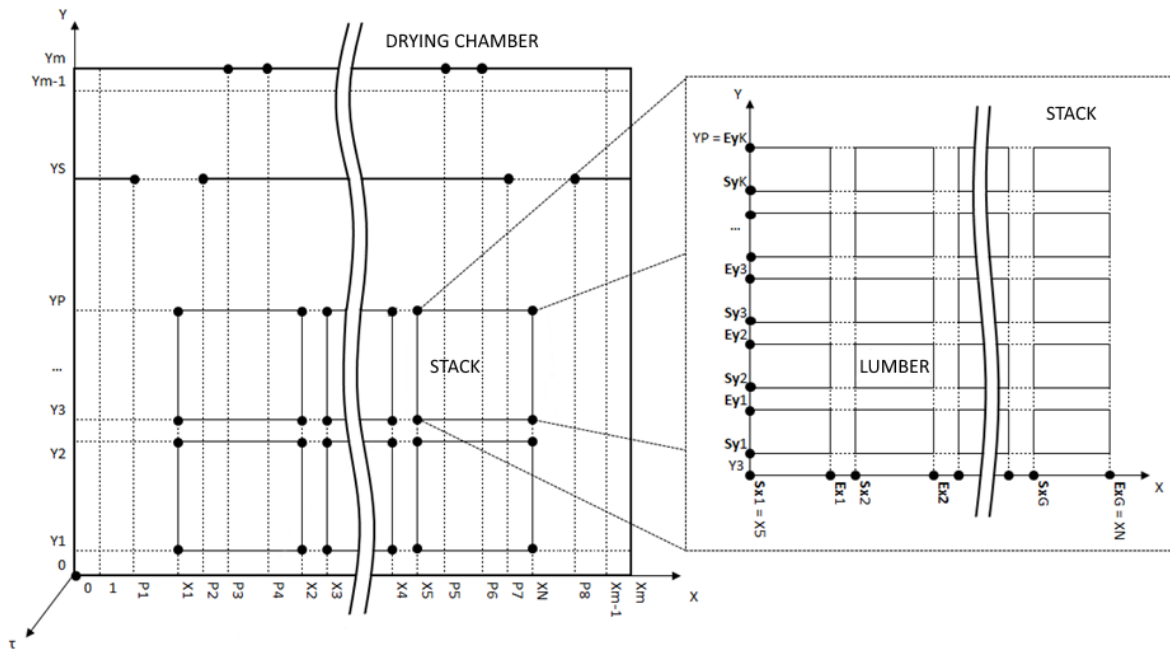


Fig. 9. The diagram illustrating the coordinates for the boundary conditions in the mathematical model

This diagram outlines the overall boundaries of the 3D model of the drying chamber. The X coordinate ranges from [0] to [X_m], and the Y coordinate ranges from [0] to [Y_m]. The position of the supply and exhaust channels is determined by the Y coordinate [Y_m], and X coordinates within [P_3 ; P_4] and [P_5 ; P_6]. The point [Y_s] defines the location of the overlap along the Y coordinate. The diagram also illustrates the placement of side passages containing humidifying nozzles (on the right) and water heaters (on the left). These passages have fixed values, with the Y coordinate [Y_s] and X coordinates within [P_1 ; P_2] and [P_7 ; P_8], respectively.

It is crucial to specify the coordinates of the stack locations, which can change, and their precise [X_n] and [Y_p] coordinates can be determined when their quantity is known. The initial coordinates of the stack location always begin at [X_1], and the end point of the X coordinate will be one step more [$+1$] than the starting point, for instance, [X_2]. The height of one stack corresponds to the distance between points [Y_1] and [Y_2], while the distance between stacks is equivalent to the distance between points [X_2] and [X_3]. Similarly, the width of one stack is equivalent to the length of the interval [X_1 ; X_2].

The coordinates of the location points of hygroscopic materials within a specific stack can be determined using a similar principle. For

instance, the starting coordinate of the material location always begins with "S," and the ending one with "E." The subsequent letter indicates the selected coordinate. Thus, one material has a height equivalent to the interval [S_{y1} ; E_{y1}], and the width is equivalent to the interval [S_{x1} ; E_{x1}]. Simultaneously, the height of one gasket between rows of hygroscopic materials is equivalent to the distance from point [E_{y1}] to [S_{y2}]. Therefore, to initiate the drying process ($\tau = 0$), the following initial conditions, that characterizing the system's initial state, are introduced and have the following form:

$$T_m(x, y, 0) = 20^\circ C, \quad T_a(x, y, 0) = 30^\circ C, \quad T_w(x, y, 0) = 18^\circ C,$$

$$T_h(x, y, 0) = 70^\circ C, \quad T_t = 80^\circ C = const, \quad T_n = 10^\circ C = const,$$

$$U_m(x, y, 0) = 0.4 kg/kg, \quad \varphi_n = 0.6 kg/kg = const,$$

$$\varphi_a(x, y, 0) = 0.6 kg/kg, \quad \rho_s(x, y, 0) = 0.0173 kg/m^3$$

Due to the multitude of coordinates defining the locations of various boundaries, the 3D model segmented into three distinct zones, each with its specific set of boundary conditions. The first zone directly related to hygroscopic materials. It allows the deter-

mination of moisture content and temperature on the surface of a single hygroscopic material undergoing the drying process [12, 15, 16]. In this way, boundary conditions of this zone have the following form:

$$\begin{cases} \frac{\partial T_m(x_{b1}, y_{b1}, Fo)}{\partial x} = (1 - \varepsilon) LuKoKi_m(Fo) - Ki_q(Fo), \\ \frac{\partial T_m(x_{b2}, y_{b2}, Fo)}{\partial y} = (1 - \varepsilon) LuKoKi_m(Fo) - Ki_q(Fo), \\ \frac{\partial U_m(x_{b3}, y_{b3}, Fo)}{\partial x} = Pn \frac{\partial T_m(x_{b3}, y_{b3}, Fo)}{\partial x} + Ki_m(Fo), \\ \frac{\partial U_m(x_{b3}, y_{b3}, Fo)}{\partial y} = Pn \frac{\partial T_m(x_{b3}, y_{b3}, Fo)}{\partial y} + Ki_m(Fo), \end{cases} \quad (9)$$

where: Ki_m – Kirpichov's mass transfer criterion, reflecting the relationship between the liquid flow per length ($j(\tau)l$) to the density on the diffusion coefficient and the difference between the final and initial moisture content ($\rho \Delta U_m$), Ki_q – Kirpichov's heat transfer criterion, representing the dependence of the heat flow per length ($q(\tau)l$) to the thermal conductivity and the difference between the final and initial temperatures ($\lambda \Delta T_m$). In this case, the coordinates of the boundaries of this zone should be within the following limits:

$$((x_{b1} \in [S_x, E_x], y_{b1} = E_y, y_{c1} = E_{y+1}) \cup (x_{b1} \in [S_x, E_x], y_{b1} = S_y, y_{c1} = S_{y-1})) \cap ((x_{b2} = S_x, y_{b2} \in [S_y, E_y], x_{c2} = S_{x-1}) \cup (x_{b2} = E_x, y_{b2} \in [S_y, E_y], x_{c2} = E_{x+1})) \cap ((x_{b3} \in [S_x, E_x], y_{b3} = S_y \cup E_y) \cap (x_{b4} = S_x \cup E_x, y_{b4} \in [S_y, E_y]))$$

The second zone pertains to the positioning of the stacks, where the hygroscopic material undergoing drying exposed to its drying agent. Alterations in the relative humidity and temperature of the drying agent can be assessed within this zone [13-15]. So, the boundary conditions for this zone have the following form:

$$\begin{cases} \frac{\partial T_a(x_{b5}, y_{b5}, Fo)}{\partial x} = \frac{\alpha_m(x)(T_m(x_{b5}, y_{c5}, Fo) - T_a(x_{b5}, y_{b5}, Fo))}{Rv\rho_a C_a}, \\ \frac{\partial T_a(x_{b6}, y_{b6}, Fo)}{\partial y} = \frac{\alpha_m(y)(T_m(x_{c6}, y_{b6}, Fo) - T_a(x_{b6}, y_{b6}, Fo))}{Rv\rho_a C_a}, \\ \frac{\partial \varphi_a(x_{b7}, y_{b7}, Fo)}{\partial x} = \frac{\alpha_m(x)\rho_0(U_m(x_{b7}, y_{c7}, Fo) - U_p)}{Rv\rho_s(x_{b7}, y_{b7}, Fo)} - \frac{\partial \rho_s(x_{b7}, y_{b7}, Fo)}{\partial x} \frac{\varphi_a(x_{b7}, y_{b7}, Fo)}{\rho_s(x_{b7}, y_{b7}, Fo)}, \\ \frac{\partial \varphi_a(x_{b8}, y_{b8}, Fo)}{\partial y} = \frac{\alpha_m(y)\rho_0(U_m(x_{c8}, y_{b8}, Fo) - U_p)}{Rv\rho_s(x_{b8}, y_{b8}, Fo)} - \frac{\partial \rho_s(x_{b8}, y_{b8}, Fo)}{\partial y} \frac{\varphi_a(x_{b8}, y_{b8}, Fo)}{\rho_s(x_{b8}, y_{b8}, Fo)}, \end{cases} \quad (10)$$

where: ρ_s – density of saturated vapor, U_p – equilibrium moisture content, ρ_0 – base density of materials, $\alpha_m(x)$, $\alpha_m(y)$ – moisture diffusion coefficients of materials, ρ_a – density of the drying agent, v – velocity of the drying agent flow, $\alpha_m(x)$, $\alpha_m(y)$ – heat transfer coefficients. In this case, the coordinates of the boundaries of this zone should be within the following limits:

$$((x_{b5} \in [S_x, E_x], y_{b5} = E_{y+1}, y_{c5} = E_y) \cup (x_{b5} \in [S_x, E_x], y_{b5} = S_{y-1}, y_{c5} = S_y)) \cap ((x_{b6} = S_{x-1}, y_{b6} \in [S_y, E_y], x_{c6} = S_x) \cup (x_{b6} = E_{x+1}, y_{b6} \in [S_y, E_y], x_{c6} = E_x)) \cap ((x_{b7} \in [S_x, E_x], y_{b7} = E_{y+1}, y_{c7} = E_y) \cup (x_{b7} \in [S_x, E_x], y_{b7} = S_{y-1}, y_{c7} = S_y)) \cap ((x_{b8} = E_{x+1}, y_{b8} \in [S_y, E_y], x_{c8} = S_x) \cup (x_{b8} = S_{x-1}, y_{b8} \in [S_y, E_y], x_{c8} = E_x))$$

The last third zone encompasses the interaction of the drying agent with other components of the drying chamber. Within this

zone, it is possible to determine the relative humidity and temperature of the drying agent at its various boundaries, such as those in contact with walls, heaters, supply and exhaust ducts, etc. Consequently, the boundary conditions for this zone take on the following form:

$$\begin{cases} T_a(x_{b9}, y_{b9}, Fo) = T_n, \\ T_a(x_{b10}, y_{b10}, Fo) = T_h(x, y, Fo), \\ \varphi_a(x_{b11}, y_{b11}, Fo) = \varphi_n, \\ \frac{\partial T_a(x_{b12}, y_{b12}, Fo)}{\partial x} = -Bi_q(T_w(x_{b12}, y_{c12}, Fo) - T_a(x_{b12}, y_{b12}, Fo)), \\ \frac{\partial T_a(x_{b13}, y_{b13}, Fo)}{\partial y} = -Bi_q(T_w(x_{c13}, y_{b13}, Fo) - T_a(x_{b13}, y_{b13}, Fo)), \end{cases} \quad (11)$$

where: Bi_q – the Bio heat transfer criterion reflects the ratio of the heat transfer coefficient from the body surface to the surrounding environment ($a_m l$) to the thermal conductivity coefficient of the body material (λ_m). In this case, the coordinates of the boundaries of this zone should be within the following limits:

$$\begin{aligned} &(x_{b9} \in [P_3, P_4] \cup [P_5, P_6], y_{b9} = Y_{m-1}) \cap \\ &\cap (x_{b10} \in [P_1, P_2], y_{b10} = Y_{s+1} \cup Y_{s-1}) \cap \\ &\cap (x_{b11} \in [P_3, P_4] \cup [P_5, P_6], y_{b11} = Y_{m-1}) \cap \\ &\cap ((x_{b12} \in (0, X_1) \cup (X_2, X_3) \cup \dots \cup (X_n, X_m), y_{b12} = Y_1, \\ &y_{c12} = 0) \cup (x_{b12} \in (0, P_3) \cup (P_4, P_5) \cup (P_6, X_m), \\ &y_{b12} = Y_{m-1}, y_{c12} = Y_m)) \cap ((x_{b13} = 1, y_{b13} \in (0, Y_m), \\ &x_{c13} = 0) \cup (x_{b13} = X_{m-1}, y_{b13} \in (0, Y_m), x_{c13} = X_n)) \end{aligned}$$

It is worth separately noting the influence of the number of axial fans and their power on the initial velocity of the drying agent. In this regard, it is important to consider the resistance of the stacks, which affects the initial velocity, and can be determined as follows:

$$v_0 = \frac{N_v P_v (1 - e_c)}{(1 - \frac{h_w}{h_g}) l_{st} h_{st} N_{st}} \quad (12)$$

where: N_{st} – total number of stacks, h_{st} – height of one stack, l_{st} – length of one stack, h_g – height of the spacer between rows of materials in a stack, h_w – height of one hygroscopic material, e_c – coefficient of expenditure during the operation of fans, P_v – power of fan, N_v – number of axial fans, v_0 – initial velocity of the drying agent.

5. DEVELOPMENT OF TRANSITION RULES FOR THE CELLULAR AUTOMATA MODEL

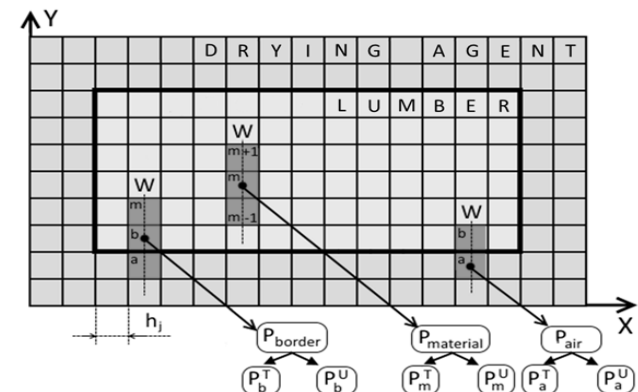


Fig. 10. Cell marking scheme used for transition rules

After analyzing the mathematical model, including its boundary and initial conditions, it becomes possible to formulate transition rules for the cellular automata model [17, 18]. The developed scheme (refer to Fig. 10) utilized to illustrate the conditional designations employed in these transition rules. It provides an example of the interaction among adjacent cells, where the interaction direction "W" corresponds to the Y coordinate.

In general, utilizing the cellular automata model involves the following steps:

- Establishing the direction of interaction "W" according to the normal distribution law;
- Start the iteration, equivalent to a time interval of Δt seconds;
- Choosing the target cell (mc) following the uniform distribution law;
- Verifying the type of neighboring cell (nc) and applying the relevant transition rules;
- Repeating steps 2-4 until all cells are selected;
- Finalizing the execution of the current iteration and assessing termination conditions;
- Concluding the simulation if the test is successfully completed;
- Advancing the simulation time and returning to step one if the test not met.

A satisfactory condition to finish modeling is reaching the specified simulation time or the desired moisture content of the hygroscopic material undergoing drying. The main transition rules have the following form:

IF 'mc' = «M»

AND 'nc' = «M» AND $P_m^T \neq P_{m+1}^T$ AND $P_m^U \neq P_{m+1}^U$
 THEN $P_{m(new)}^U = P_m^U - C_1(P_{m+1}^U - 2P_m^U + P_{m-1}^U +$
 $+\delta(P_{m+1}^T - 2P_m^T + P_{m-1}^T))$ AND $P_{m(new)}^T = P_m^T +$
 $+C_2(P_{m+1}^T - 2P_m^T + P_{m-1}^T) + C_3(P_{m(new)}^U - P_m^U)$

IF 'mc' = «M»

AND 'nc' = «B» AND $P_m^T \neq P_b^T$ AND $P_m^U \neq P_b^U$
 THEN $P_{m(new)}^U = P_m^U - C_1(P_b^U - 2P_m^U + P_{m-1}^U +$
 $+\delta(P_b^T - 2P_m^T + P_{m-1}^T))$ AND $P_{m(new)}^T = P_m^T +$
 $+C_2(P_b^T - 2P_m^T + P_{m-1}^T) + C_3(P_{m(new)}^U - P_m^U)$

IF 'mc' = «B» THEN $P_{b(new)}^U = (C_9(P_m^T - P_b^T) +$
 $+a_j P_m^U + C_{10} P_a^U)/(a_j + C_{10})$ AND $P_{b(new)}^T =$
 $= (P_a^T (C_5 - C_6 - C_4 \delta) + P_m^T (C_8 - C_7) -$
 $-C_1(P_m^U - P_a^U))/(C_5 + C_8 - C_6 - C_7 - C_4 \delta)$

IF 'mc' = «A» AND 'nc' = «B» THEN $P_{a(new)}^T = P_a^T +$
 $+C_{11}(P_b^T - P_a^T)/C_{12}$ AND $P_{a(new)}^U = P_a^U +$
 $+\frac{C_{13}(P_b^U - P_a^U)}{C_{14}} - \frac{P_a^U (P_n - P_s)}{C_{15} P_a^T} + \frac{P_a^U P_s P_{a(new)}^T}{C_{15} (P_a^T)^2} - \frac{P_a^U P_s}{C_{15} P_a^T}$

IF 'mc' = «A» AND 'nc' = «A» THEN

$P_{a(new)}^T = \frac{(P_a^T + P_{a+1}^T)}{2}$ AND $P_{a(new)}^U = \frac{(P_a^U + P_{a+1}^U)}{2}$

IF 'mc' = «A» AND 'nc' = «W» OR 'nc' = «V»

THEN $T_w = P_a^T$

IF 'mc' = «A» AND 'nc' = «H» THEN $P_{a(new)}^T = T_h$

IF 'mc' = «A» AND 'nc' = «N» THEN $P_{a(new)}^T = T_n$

IF 'mc' = «A» AND 'nc' = «G» THEN $P_{a(new)}^U = \frac{P_a^U + P_{a+1}^U}{2}$

Where the value of coefficients C_1 - C_{15} can be calculated as

follows:

$$C_1 = \frac{a_j \Delta t}{h_j^2}, \quad C_2 = \frac{\lambda_j \Delta t}{c_m \rho_m h_j^2}, \quad C_3 = \frac{\varepsilon \rho_0 r}{c_m \rho_m},$$

$$C_4 = a_j \rho_0 (1 - \varepsilon) \beta, \quad C_5 = \beta \lambda_j, \quad C_6 = \frac{a_j \lambda_j}{h_j}, \quad (13)$$

$$C_7 = \alpha_m a_j, \quad C_8 = \alpha_m \beta h_j, \quad C_9 = a_j \delta,$$

$$C_{10} = \beta h_j, \quad C_{11} = \alpha h_j, \quad C_{12} = v c_c \rho_c h_s,$$

$$C_{13} = a_j \rho_0 h_j, \quad C_{14} = v \rho_s h_s, \quad C_{15} = h_s \rho_s,$$

where: h_s – distance between hygroscopic materials in a stack and the gap between two stacks, c_c – specific heat capacity of the condensate, ρ_c – density of the condensate, δ – thermal gradient coefficient, ρ_m – density of materials, c_m – specific heat capacity of materials, λ_j – thermal conductivity coefficient of the material in the specified direction, h_j – size of one cell, Δt – time for one iteration. The value of j can be "1" for "x" and "2" for "y".

6. DEVELOPMENT OF THE DATABASE AND DISTRIBUTION OF ACCESS RIGHTS

To enter the input data of the simulation, it is necessary to open the third tab of the software (refer to Fig. 11).

Fig. 11. Tab of the input data of the simulation and its launch

On this tab, the user enters the initial values of some parameters, in particular: temperature and moisture content of lumber; temperature and relative humidity of the drying agent; specific heat capacity; density and basic density of the material; specific heat of vaporization; simulation time and time step. At the same time, the rest of the parameters, most of which are represented by different coefficients, will be determined automatically. Having all the parameters for the simulation, user can start its execution using the same tab.

To carry out modeling, it is absolutely necessary to have a database in which the results will be stored. To create it, it was decided to use the MySQL Workbench Community Edition environment. The created database is named "dissertation" and consists of several interconnected tables, namely: "lumber", "stack", "chamber", "ca_field", "coefficients" and "results". The "lumber" table contains a unique lumber code that is generated automatically and has the following structure: "XX.LL.HH.WW", where "XX" is the type of wood (birch - "BR", cedar - "CD", Beech - "RT", maple - "MP", oak - "OK", pine - "PN", teak - "TK" and other), "LL" - length, "HH" - height, "WW" - width of lumber in mm. Also in this table there is information about the density of the material. The "stack" table contains a unique stack code that is generated automatically and has the following structure: "XX x LL", where "XX" is the number of lumber in the stack, and "LL" is

the unique lumber code. Also, this table contains data on the number of lumber in the stack, their location, and information on the size and number of spacers between rows of lumber. The "chamber" table contains the unique code of the drying chamber, which is generated automatically and has the following structure: "XX→SS", where "XX" is the number of stacks in the drying chamber, and "SS" is the unique code of the stack. Also, this table contains information about the number of stacks in the chamber and the scheme of their arrangement along it. The "ca_field" table contains information about the cell autofield, including the number and sizes of cells. The "coefficients" table contains information about all modeling parameters, both initial, which are constant, and current, which change with the passage of model time. The last table "results" contains information about the results of the simulation and is the largest among all of them. To display the entities, attributes and relationships between them, an Entity-Relationship (ER) diagram (refer to Fig. 12) was created. It provides an opportunity to better understand how the data will interact with each other in the developed software.

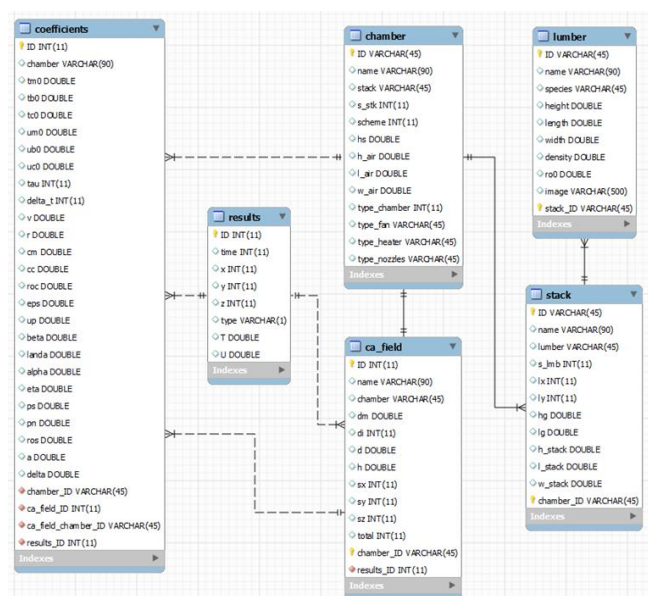


Fig. 12. View of the Entity-Relationship diagram for developed software

To visualize the functionality of the system from the perspective of users and other system agents, a UML use case diagram was created (refer to Fig. 13). It is used to describe how a system interacts with its environment, including users and various processes. By its structure, this diagram has actors that interact with the system. These actors are divided into 4 types, namely "Users", "SolidWorks experts", "Cellular automata experts" and "System administrators". Each of them has its own access rights and certain usage options. Each of these use cases represents a specific scenario that the system supports and can implement. At the same time, each scenario details the sequence of actions and interaction between actors and the system.

To visualize the interaction between system components within a specific usage scenario, a sequence diagram was created (refer to Fig. 14). It helps to understand the sequence of actions and the exchange of messages between different elements of the system involved in a specific process. In turn, this diagram shows three actors and their sequence of actions in the system.

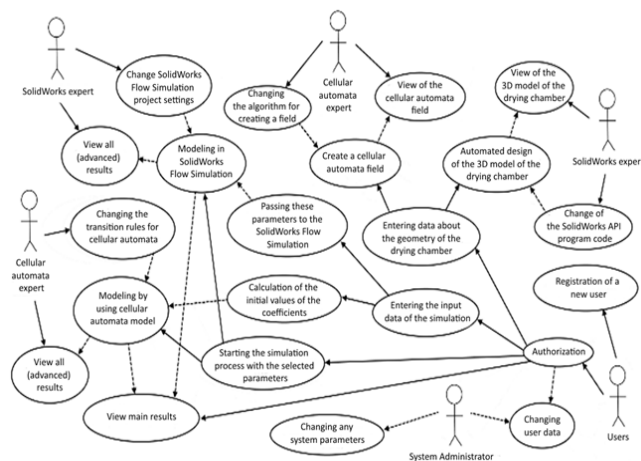


Fig. 13. View of the UML use case diagram

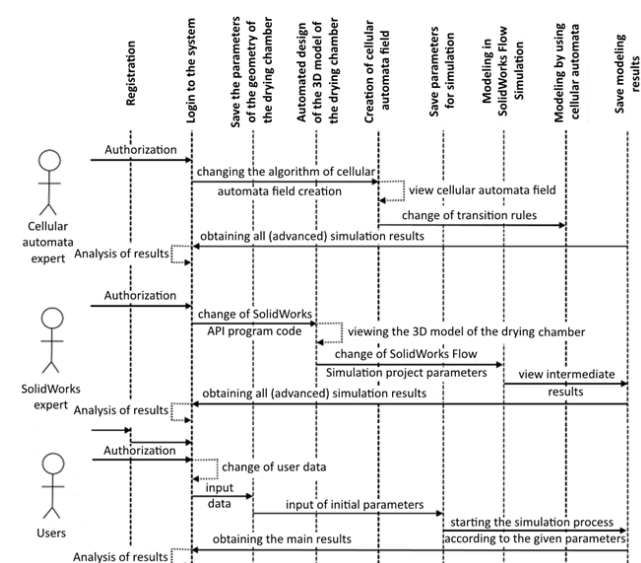


Fig. 14. View of the UML sequence diagram

7. SIMULATION OF THE DRYING PROCESS OF HYGROSCOPIC MATERIALS USING THE CELLULAR AUTOMATA MODEL

After initiating the simulation, an iterative cycle begins, executing transition rules among closely located cells. Through these interactions, the key parameters of both the drying agent and the hygroscopic material undergo changes. As illustrated in Fig. 15, influencing a single cell leads to subsequent alterations in 27 cells after several iterations. This approach effectively illustrates the cellular automata principle [18], where modifying values in specific cells, such as on material surfaces, directly influences internal cell values. To conveniently monitor temperature and moisture content changes in the drying material, users can utilize the "View values" window located in the "Format" section of the software's main menu.

This window helps user to view the changes of parameters in two-dimensional space on the cellular automata field, but for this, they need to specify the starting point of the tracking according to the coordinates (lower left corner of the field). After that, user can see cells that display a given parameter to choose from (temperature or moisture content). For the convenience of obtaining graphical dependencies, the values of the main parameters displayed in

the right part of the window. At the same time, user can select a specific area on the cellular automata field, thus obtaining the value of the desired parameter in space and time.

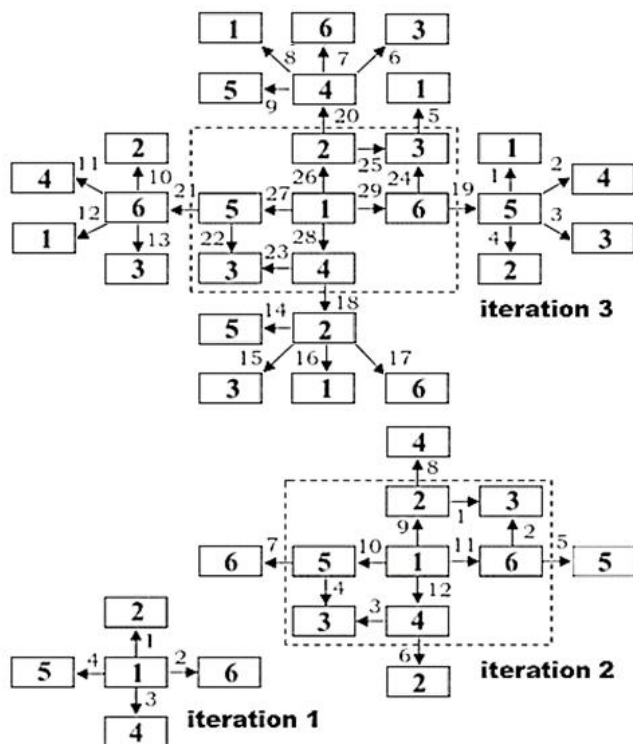


Fig. 15. Start of the iteration cycle

8. ANALYSIS OF THE OBTAINED SIMULATION RESULTS

As a result of the simulation [19], graphical dependences of the main parameters of the hygroscopic material to be dried and the drying agent over time were obtained (refer to Fig. 16 and 17). The main parameters include: the average relative humidity of the drying agent (P_a^U), the average temperature of the drying agent (P_a^T), the average moisture content of the hygroscopic material being dried in the stacks (P_m^U) and its average temperature (P_m^T).

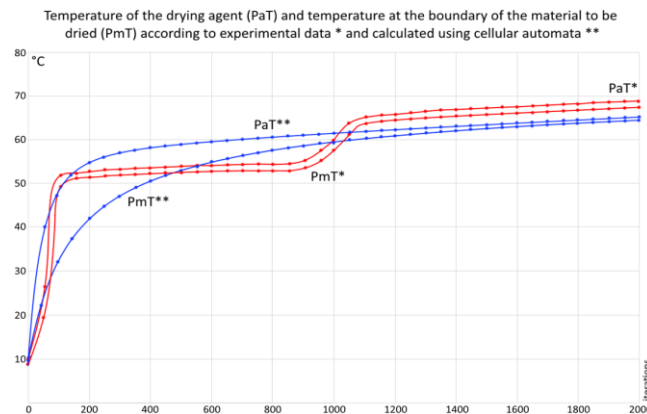
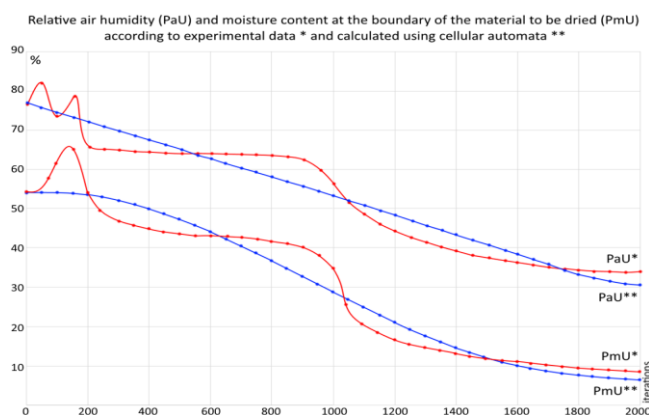


Fig. 16. A chart depicting the variation of the key parameters over time for the first study

To verify the obtained results, they compared with experimental data that obtained using the "LK-ZDR-100" wood drying chamber, located at "Rodors" LLC (Khmelnitskyi region, Ukraine). Data for compared the first study collected using sensors between 29/10/18 and 06/11/18 for 30 mm thick pine material with an initial moisture content of 55%. Data for compared the second study collected between 18/03/23 and 01/04/23 for 45 mm thick pine material with an initial moisture content of 65%.

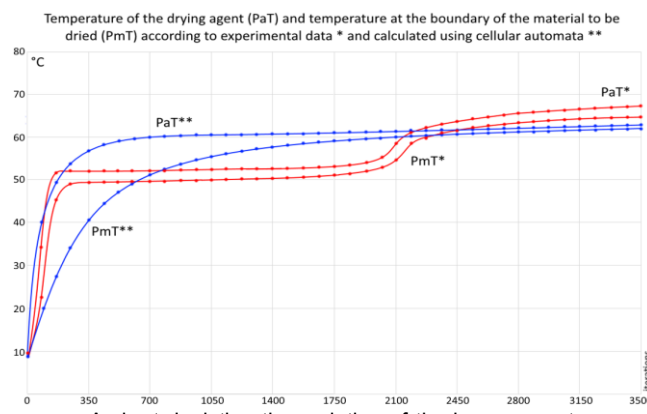
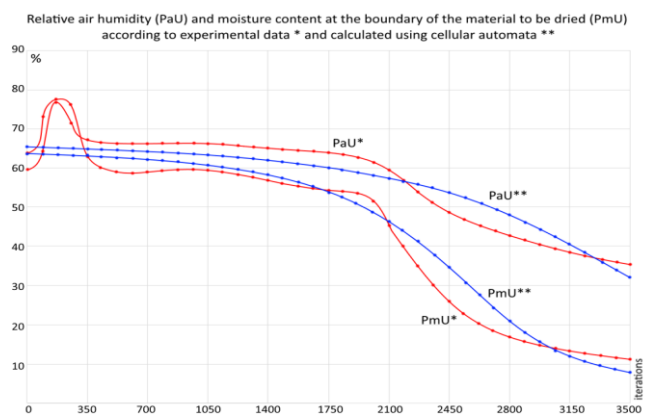


Fig. 17. A chart depicting the variation of the key parameters over time for the second study

The input parameters for comparing the results are as follows: initial relative humidity of the drying agent is 77% / 74%, the temperature of the heat carrier (hot water in the heaters) is 70 °C (for both data sets), the initial temperature of the drying agent is 15 °C / 19 °C, the initial temperature on the surface of the hygroscopic

material is 13 °C / 18 °C, the simulation time is 166 h / 291 h, and the iteration step is 300 s (for both data sets).

Visual evaluation of the results is important, but it doesn't provide a way to determine the accuracy of the modeling. In general, there are many ways to determine accuracy, each of which depends on the context and specifics of the comparative data [20]. In this case, two of the most common methods chosen to assess the accuracy, namely, the mean absolute error (MAE) and the mean absolute percentage error (MAPE). As a result of the calculations, the values of these errors were determined for the temperature and humidity parameters of the drying agent and hygroscopic material for both data sets.

It was established that the average value of MAPE is 13%. The largest values amounting to approximately 24%. This result may indicate that a limited number of cells of cellular automata field and limited transition rules between them were used in the initial phase of the simulation. Over time, the number of cells increases and the accuracy of the results improves significantly. Therefore, MAPE at the end of the simulation doesn't exceed 9%. This analysis confirms the accuracy and correspondence of the obtained results to real drying conditions. In addition, simulation results can be used to determine optimal input parameters for simulation in computational fluid dynamics programs, including SolidWorks Flow Simulation.

In general, the topic of this research is new. In this regard, the research results can be compared with related works of other authors, in particular, in work [3]. In this work, a three-dimensional mathematical model of heat and moisture transfer during drying of wood in drying chambers was developed. This model was successfully verified using numerical simulations and experiments, including the analysis of air movement and moisture. In turn, in [4] heat and mass transfer in the process of high-temperature processing of wood were analyzed. It allows to evaluate the relationship between changes in temperature and moisture content in wood in its drying agent. In addition, some authors [21, 22] also use the capabilities of automated design when performing a related class of tasks. To conduct similar research, some authors also resort to the use of cellular automata models [7].

9. CONCLUSIONS

To summarize, this study makes a significant contribution to the field of CAD design of 3D models of drying chambers by using tools for parameterizing its geometric characteristics. At the same time, the proposed model of cellular automata provides an effective tool for modeling the drying process of hygroscopic materials in such designed 3D models of drying chambers.

The key achievement of this work is the integration of the algorithms for automated 3D design and the cellular automata model. Therefore, the developed software not only simplifies the design process, saving precious time and material resources, but also provides a powerful platform for modeling and studying the dynamics of heat and moisture transfer during the drying of hygroscopic materials.

The validation of the developed cellular automata model was carried out by comparing the obtained results with experimental data, with the average MAPE value not exceeding 13%. This level of error is acceptable, since the processes of heat and mass transfer during the drying of hygroscopic materials characterized by complexity, multifactoriality, and nonlinearity. This makes modeling with absolute accuracy impossible, even with the most advanced approaches. Under such conditions, an error of 15% considered typical for most models in this field, since achieving perfect accuracy

is extremely resource-intensive. At the same time, the proposed cellular automata model demonstrates accuracy comparable to existing models, but characterized by higher computational speed, which makes it practically valuable for real-world applications.

It is also worth noting the possibility of determining changes in the parameters of the hygroscopic material and its drying agent during the modeling process. This was realized due to the improved structure of the cellular automaton field, which takes into account the physical and geometric characteristics of the whole 3D model of the drying chamber. This field structure makes it possible to use different types of cells and the relationships between them, which are realized by the corresponding transition rules.

REFERENCES

1. Sokolovskyy Y, Sinkevych O, Shymanskyi V, Boretska I, Samotii T. Construction of an asynchronous cell-automatic model for investigating the thermal mass transfer process. 2021 IEEE XVIIth Int Conf Perspect Technol Methods MEMS Des MEMSTECH 2021. 2021;29-33. Available from: <https://doi.org/10.1109/MEMSTECH53091.2021.9467930>
2. Mende FF, Shurupov IA. Simple camera for high-quality wood drying. Eng Technol. 2015;2(3):95-117.
3. Zhao J, Cai Y. A comprehensive mathematical model of heat and moisture transfer for wood convective drying. Holzforschung. 2017;71(5):425-35. Available from: <https://doi.org/10.1515/hf-2016-0148>.
4. Kadem S, Lachemet A, Younsi R, Kocaefe D. 3D-transient modeling of heat and mass transfer during heat treatment of wood. Int Commun Heat Mass Transf. 2011;38(6):717-22. Available from: <https://doi.org/10.1016/j.icheatmasstransfer.2011.03.026>
5. Ovsiaik OV, Dendiuk MV. Mathematical modeling of moisture transfer in wood drying for the two-dimensional case. Sci Bull UNFU. 2023;33(5):59-64. Available from: <https://doi.org/10.36930/40330408>.
6. Shumylyak L, Zhikharevych V, Ostapov S. Study of the method of asynchronous cellular automata when applied to heat conduction problems. Inf Process Syst. 2018;1(152):74-9. Available from: <https://doi.org/10.30748/soi.2018.152.11>
7. Boichot R, Luo L, Fan Y. Tree-network structure generation for heat conduction by cellular automaton. Energy Convers Manag. 2009;50(2):376-86. Available from: <https://doi.org/10.1016/j.enconman.2008.09.003>.
8. Sokolovskyy Y, Sinkevych O. Software for automatic calculation and construction of chamber drying wood and its components. XII Int Conf Perspect Technol Methods MEMS Des MEMSTECH. 2016;209-13. Available from: <https://doi.org/10.1109/MEMSTECH.2016.7507544>
9. Chopard B, Droz M. Cellular automata modeling of physical systems. Cambridge: Cambridge University Press; 1998. Available from: <https://doi.org/10.1017/CBO9780511549755>
10. Zhang J, Miao P, Zhong D, Liu L. Mathematical modeling of drying of Masson pine lumber and its asymmetrical moisture content profile. Holzforschung. 2014;68(3):313-21. Available from: <https://doi.org/10.1515/hf-2013-0077>
11. Ravshanov N, Shadmanov I, Kubyashev K, Khikmatullaev S. Mathematical modeling and research of heat and moisture transfer processes in porous media. E3S Web Conf. 2021;264:01038. Available from: <https://doi.org/10.1051/e3sconf/202126401038>
12. Plumb OA, Spolek GA, Olmstead BA. Heat and mass transfer in wood during drying. Int J Heat Mass Transf. 1985;28(9):1669-78. Available from: [https://doi.org/10.1016/0017-9310\(85\)90141-3](https://doi.org/10.1016/0017-9310(85)90141-3)
13. Mnasri F, Abahri K, El GM, Bennacer R, Gabsi S. Numerical analysis of heat, air, and moisture transfers in a wooden building material. Therm Sci. 2017;21(2):785-95. Available from: <https://doi.org/10.2298/TSCI160421248M>
14. Ovsiaik OV, Dendiuk MV. Using cellular automata to simulate external heat and mass transfer in the wood drying process. Sci Bull UNFU. 2023;33(5):63-9. Available from: <https://doi.org/10.36930/40330508>.
15. Hirnyk LM, et al. Mathematical modeling of convective drying processes. Budivelnik. 1993. [In Ukrainian].

16. Hirnyk LM, et al. Automation of wood drying processes in the construction industry. Budivelnik. 1992. [In Ukrainian].
17. Sokolovskyy Y, Sinkevych O. Calculation of the drying agent in drying chambers. 2017 14th Int Conf Exp Des Appl CAD Syst Microelectron CADSM 2017. 2017;27-31. Available from: <https://doi.org/10.1109/CADSM.2017.7916077>
18. Ilachinski A. Cellular automata: a discrete universe. Singapore: World Scientific; 2001. Available from: <https://doi.org/10.1142/4702>
19. Sokolovskyy Y, Sinkevych O. Study of heat and mass transfer into biomaterials by using asynchronous cellular automata. 16th Int Conf Comput Sci Inf Technol CSIT 2021. 2021;274-7. Available from: <https://doi.org/10.1109/CSIT52700.2021.9648826>
20. Nearing TY, Peters-Lidard GS, Harrison CD, Tang L. Performance metrics, error modeling, and uncertainty quantification. Mon Weather Rev. 2016;144(2):607-13. Available from: <https://doi.org/10.1175/MWR-D-15-0087.1>
21. Li G, Li Y, Chen Q. CAD/CAE system for wooden package based on SolidWorks. Appl Mech Mater. 2012;(200):487-91.
22. Kyratsis P, Tzotzis A, Manavis A. Computational design and digital fabrication. Adv Manuf Syst. 2021;1-16.

The authors of the work would like to express special thanks to *Yuriy Guber*, PhD, Associate Professor of the Department of Environmental and Wood Protection Technologies and Life Safety of the Ukrainian National Forestry University, for the opportunity to obtain graphs of experimental data from a real drying chamber.

Yaroslav Sokolovskyy:  <https://orcid.org/0000-0003-4866-2575>

Oleksiy Sinkevych:  <https://orcid.org/0000-0001-6651-5494>



This work is licensed under the Creative Commons BY-NC-ND 4.0 license.

AN OPTIMAL BRAKING FORCE DISTRIBUTION IN THE RIGID DRAWBAR TRAILERS WITH TANDEM SUSPENSION

Zbigniew KAMIŃSKI^{*} 

^{*}Faculty of Mechanical Engineering, Białystok University of Technology, ul. Wiejska 45C, 15-351 Białystok, Poland

z.kaminski@pb.edu.pl

received 15 November 2023, revised 11 November 2024, accepted 15 November 2024

Abstract: Rigid drawbar agricultural trailers with laden weight of up to 13 tonnes have a single axle, up to 19 tonnes tandem axles. Carried out analysis of a tractor semi-mounted trailer combination showed that under ideal braking, the adhesion utilised by all axles and a coupling device are equal. By adopting the concept of treating the coupling device as a conventional front axle, the requirements of EU Directive 2015/68 for multi-axle trailers have been used to develop a new method for selecting the brake force distribution of semi-trailers with different suspensions. First, the forces acting on a single and tandem semi-trailer were analysed during braking. An algorithm based on the quasi-Monte Carlo method was then proposed to solve the constrained optimisation of the linear brake force distribution of semi-trailers equipped with ALB or MLB regulators. Finally, examples of MATLAB calculations were given for a 5 tonne single axle trailer and a 16-tonne trailer with 5 different tandem suspensions: bogie, two leaf spring, two leaf spring and rods, two leaf spring with dynamic equalisation and air spring. The results of the work are expected to provide a reference for the design and evaluation of the braking system of agricultural semi-trailers, especially with different types of tandem axles, to improve braking performance and reduce coupling forces.

Key words: agriculture tractor/semi-trailer combination, tandem axle, air braking system, braking force distribution, optimization

1. INTRODUCTION

The design of the running gear of agricultural trailers with rigid (unbalanced) drawbar depends on their load capacity. Semi-mounted trailers with laden weight of up to 13 tonnes have a single axle, up to 19 tonnes tandem axles and up to 22.5 tonnes triaxle [1]. A multiple-axle unit consists of axles spaced closely together, usually between 1.2 m and 1.85 m [2, 3]. Tandem and triple axles are used to increase the vehicle's load capacity and load distribution between the axles, regardless of road surface irregularities [4]. Generally, two basic tandem suspension arrangements have been developed: a central pivoting single vertical semi-elliptic or parabolic spring which has an axle clamped to it at either end and a pivoting reactive or non-reactive balance beam which interconnects adjacent first and second semi-elliptic springs via their shackle plates [5-7].

During a brake application, all the vehicles of a combination tractor-trailer should be braked with similar intensity to enable efficient deceleration without the risk of the combination losing its directional stability. From 2016, EU legislation on agricultural vehicles [8] has required agricultural trailers travelling at speeds above 30 km/h to comply with the same braking efficiency of 50% as commercial trailers [9]. Furthermore, agricultural balanced trailers with a total mass exceeding 3500 kg (categories R3 and R4) require a specific brake force distribution among the axles. As in the case of commercial vehicles [9], the individual parts of the combination are treated as individual vehicles, so that the coupling interactions between them are not taken into account. No recommendations are made in this respect for semi-trailers. To share the brake force

distribution between a tractor and a towed vehicle, permissible compatibility corridors for the braking rate of the tractor and the towed vehicle refer to the pressure values of the control line between these vehicles that have been introduced. The compliance with compatibility requirements, as well as requirements regarding high-speed operation (response time of less than 0.6 s [8]), contribute to the shortening of stopping distance of tractor-trailer combinations and the reduction of forces in the coupling during emergency braking [10]. The implementation of the new European legislation in the field of agricultural vehicles places high demands on the manufacturers of agricultural trailers, tractors and machines concerning braking systems [11].

Most of the works on agricultural trailer braking deal with various aspects of the braking process of tractor-trailer combinations, mainly with two-axle trailers [12-14]. Papers [15, 16], describe the braking mechanics of a tractor with a single-axle trailer while moving up and down a slope under various operating conditions. The dynamic behaviour during braking of tractor-semitrailer combinations in terms of stability and road safety has been analysed in [17] and [18]. Paper [19], on the other hand, describes the braking of a semitrailer endowed with an inertial braking system, working in aggregate with the tractor. Both the theoretical and practical aspects of the braking performance of tractor-semitrailer combinations were examined in [20] and [21]. To simplify the theoretical considerations in [20], the tandem bogie suspension was replaced by a single axle and the forces from the wheels were applied to the bogie joint without considering the interaction between the tandem axles. From the designer's (manufacturer's) point of view, any analysis of the braking mechanics of a tractor-trailer combination seems to be of little use for the design of semi-trailer braking systems, as it requires

specific assumptions to be made about the geometric and mass parameters of a farm tractor. Moreover, these considerations usually apply to single-axle semi-trailers but not to semi-trailers with tandem suspension. And as is well known [3, 4, 22], when a braking force is applied on a tandem axle, there is often a load transfer among the axles, and the lighter loaded axle tends to lock up before the other. This phenomenon, which is dependent on the tandem suspension type used, harms braking performance and directional stability. If the lock-up occurs on the trailing axle, it can lead to a complete loss of directional stability [3]. Therefore, in this study, the influence of inter-axle load transfer in semitrailers with different tandem suspensions has been considered in the development of the brake force distribution methodology for use by designers and manufacturers of agricultural machinery, thus filling a gap in the literature.

The design process of a new brake system starts with the selection of the distribution of brake forces [23]. The axle load transfer and braking force distribution play an important role in the safety and dynamic stability of road vehicles [24, 25]. In general, for the correct design of a vehicle braking system, it is essential to know the ideal brake force distribution between the axles for laden and unladen vehicles [26]. With the braking distribution at the ideal level, the braking performance is maximized, and the brake stability is then also guaranteed [27]. The optimum braking condition is achieved when each axle has the same utilised adhesion, i.e. the ratio between the braking force on each axle and its vertical load is the same [28, 29]. Under such conditions, the ratio of the longitudinal force and vertical force on the coupling device is also the same [30].

This latter condition became an inspiration to use the brake force distribution strategy for two-axle trailers, according to the EU regulations [8], to determine the braking force distribution in semi-trailers between the axle unit (single or tandem) and the coupling device that attaches the towed vehicle to the farm tractor. With this approach, a semi-trailer can be considered as if it were an individual braked vehicle with braking forces at the axle wheels and the coupling device.

To calculate the brake distribution of a single-axle semi-trailer, the analytical method can be used as for two-axle trailers [31, 32]. However, for tandem semitrailers, the analysis is more complicated because the leading and trailing axle loads are functions of the trailer load and the type and geometry of the tandem axle unit [4]. Therefore, even for vehicles with the simplest of tandem suspensions, such as a walking beam and bogie [31, 33] or a double elliptic leaf spring suspension [34], optimisation methods are used to calculate and select the brake force distribution. To find an optimal linear force distribution, which is mostly used in trailer air brake systems due to the linear characteristics of the brake force regulators, the quasi-Monte Carlo method was used in this paper.

The remainder of the paper is structured as follows: in section 2, the equations of forces acting during braking on a tractor single-axle semi-trailer and a tractor tandem-axle semi-trailer combination are developed to find the condition of ideal braking force distribution; in section 3, the analysis of the forces acting during braking on a semi-trailer with different types of tandem suspension is presented; in section 4, the UE regulations for the brake force distribution adapted to semi-trailers are described; in section 5, the quasi Monte Carlo method and the algorithm of linear brake force distribution are described. The results of optimising the different tandem axles are analysed and discussed in section 6. Finally, a summary and conclusions are drawn in Section 7.

The findings of the work are expected to provide a reference for

the design and evaluation of the air braking system of agricultural semi-trailers, especially with different types of tandem axles, to improve braking performance and reduce coupling forces.

2. IDEAL BRAKING OF TRACTOR AND SEMI-TRAILER

Tractor-semitrailer combination is modelled as two rigid body hinges to each other, and suspension deflection is ignored. The forces acting on a braking farm tractor with single and tandem axle semi-trailers are shown in Figures 1-3. For simplicity, it is assumed that aerodynamic and rolling drag is neglected.

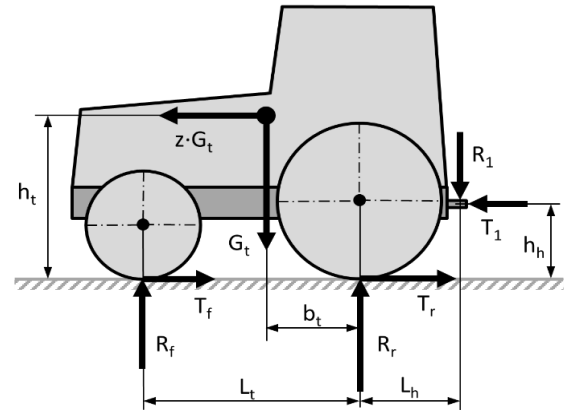


Fig. 1. Forces acting on a farm tractor (ISO coordinate system [35])

Using the notation from Fig. 1, the equations of forces and moments exerted on the decelerating tractor are of the form:

$$\sum X = z \cdot G_t + T_1 - T_f - T_r = 0 \quad (1)$$

$$\sum Z = R_f + R_r - G_t - R_1 = 0 \quad (2)$$

$$\sum M_1 = -R_f(L_t + L_h) - R_r L_h + G_t(L_h + b_t) + z \cdot G_t(h_t - h_h) + (T_f + T_r)h_h = 0 \quad (3)$$

where: T_f , T_r – front and rear axle braking forces, R_f , R_r – axle loads, T_1 , R_1 – horizontal and vertical force on the coupling, L_t – inter-axle spacing, b_t – distance between centre of gravity and rear axle, h_t – height of the centre of gravity, L_h – distance from coupling device to the rear axle, G_t – trailer weight, z – braking rate.

The equilibrium equations of forces and moments exerted on the single-axle semi-trailer shown in Fig. 2 are as follows:

$$\sum X = z \cdot G - T_1 - T_{21} = 0 \quad (4)$$

$$\sum Z = R_1 + R_{21} - G = 0 \quad (5)$$

$$\sum M_1 = R_{21}L_1 - G \cdot a + z \cdot G(h - h_h) + T_{21}h_h = 0 \quad (6)$$

where: T_2 – axle brake force, R_{21} – axle load, L_1 – distance between coupling device and semi-trailer's axle, a – distance from the coupling to the centre of gravity, h – height of the centre of gravity, G – trailer weight.

From the equations (2) and (5) of vertical forces (after elimination of the reaction R_1) and the equation of moments for the tractor (3) and the trailer (6) concerning the coupling, the vertical reactions are obtained:

$$R_f = \frac{G_t}{L_t} [b_t + z(h_t - h_h)] + (T_f + T_r) \frac{h_h}{L_t} - R_1 \frac{L_h}{L_t} \quad (7)$$

$$R_r = \frac{G_t}{L_t} [L_t - b_t - z(h_t - h_h)] - (T_f + T_r) \frac{h_h}{L_t} + R_1 \frac{L_h + L_t}{L_t} \quad (8)$$

$$R_1 = \frac{G}{L_1} [L_1 - a + z(h - h_h)] + T_{21} \frac{h_h}{L_1} \quad (9)$$

$$R_{21} = \frac{G}{L_1} [a - z(h - h_h)] - T_{21} \frac{h_h}{L_1} \quad (10)$$

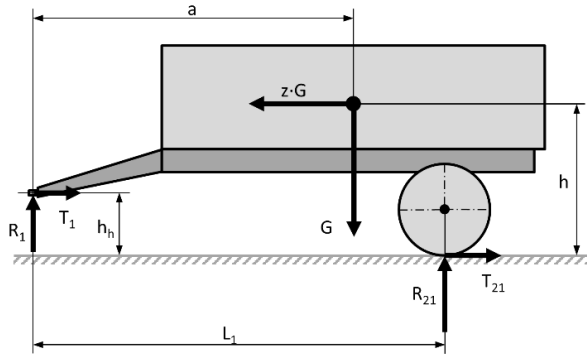


Fig. 2. Forces acting on a single-axle semi-trailer

In the case of ideal braking of a tractor with a single-axle semi-trailer, the adhesion utilisation of each axle is the same and equal to the braking rate of the combination, i.e. $f_1 = f_2 = z$. Hence $T_1 + T_2 = z(R_1 + R_2)$ and $T_{21} = z \cdot R_{21}$. Then the ground reactions to the axle wheels are as follows:

$$R_f = \frac{G_t(b_t + z \cdot h_t) - G(L_h - z \cdot h_h)}{L_t} + \frac{G[a - z(h - h_h)](L_h - z \cdot h_h)}{L_t(L_1 + z \cdot h_h)} \quad (11)$$

$$R_r = G_t + R_1 - R_f \quad (12)$$

$$R_1 = \frac{G[L_1 - a + z \cdot h]}{L_1 + z \cdot h_h} \quad (13)$$

$$R_{21} = \frac{G[a - z(h - h_h)]}{L_1 + z \cdot h_h} \quad (14)$$

So that during ideal braking, the ratio of the tangential force to the vertical force acting on the coupling:

$$f_1 = \frac{T_1}{R_1} = \frac{z \cdot G - T_{21}}{G - R_{21}} = z \quad (15)$$

is the same as the braking rate of the vehicle combination.

The system of equilibrium equations for a braked single-axle semi-trailer with walking beam tandem suspension (Fig. 3) is given as:

$$\sum X = z \cdot G - T_1 - T_{21} - T_{22} = 0 \quad (16)$$

$$\sum Z = R_1 + R_{21} + R_{22} - G = 0 \quad (17)$$

$$\sum M_1 = R_{21}L_1 + R_{22}(L_1 + L_2) - G \cdot a + z \cdot G(h - h_h) + (T_{21} + T_{22})h_h = 0 \quad (18)$$

where: L_2 – tandem axle spread.

From the equations (2), (17) of vertical forces (after elimination of the reaction R_1) and the equation of moments for the tractor (3) and the trailer (18) with respect to the coupling and the relationship between the reactions in the tandem suspension:

$$\sum M_2 = R_{22}d_2 - R_{21}d_1 + (T_{21} + T_{22})h_s = 0 \quad (19)$$

vertical reactions are obtained:

$$R_f = \frac{G_t}{L_t} [b_t + z(h_t - h_h)] + (T_f + T_r) \frac{h_h}{L_t} - R_1 \frac{L_h}{L_t} \quad (20)$$

$$R_r = \frac{G_t}{L_t} [L_t - b_t - z(h_t - h_h)] - (T_f + T_r) \frac{h_h}{L_t} + R_1 \frac{L_h + L_t}{L_t} \quad (21)$$

$$R_1 = \frac{G}{L} [L - a + z(h - h_h)] - (T_{21} + T_{22}) \frac{(h_s - h_h)}{L} \quad (22)$$

$$R_{21} = G[a - z(h - h_h)] \frac{d_2}{L_2 L} + \frac{T_{21} + T_{22}}{L_2 L} [(L_1 + L_2)h_s - d_2 h_h] \quad (23)$$

$$R_{22} = G[a - z(h - h_h)] \frac{d_1}{L_2 L} - \frac{T_{21} + T_{22}}{L_2 L} [L_1 h_s + d_1 h_h] \quad (24)$$

where: d_1 and d_2 – beam length, h_s – height of support position, $L_2 = d_1 + d_2$ and $L = L_1 + d_1$.

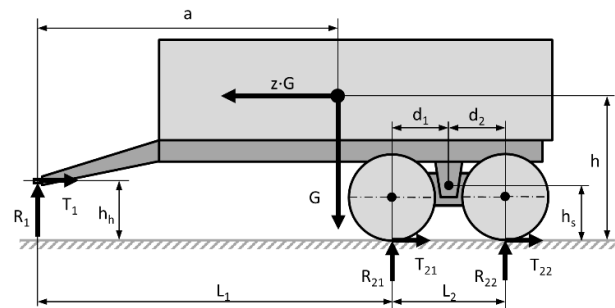


Fig. 3. Forces acting on a tandem-axle semi-trailer

During ideal braking of the combination of tractor-semitrailer with tandem suspension, the adhesion utilisation of each axle is the same and equal to the braking rate: $f_1 = f_2 = f_{21} = f_{22} = z$, which means $T_1 + T_2 = z(R_1 + R_2)$ and $T_{21} + T_{22} = z(R_{21} + R_{22})$. Then, the vertical reactions at the coupling and the wheels of the trailer are as follows:

$$R_1 = \frac{G[L - a + z(h - h_s)]}{L - z(h_s - h_h)} \quad (25)$$

$$R_{21} = \frac{G[a - z(h - h_h)](d_2 + z \cdot h_s)}{L_2[L - z(h_s - h_h)]} \quad (26)$$

$$R_{22} = \frac{G[a - z(h - h_h)](d_1 - z \cdot h_s)}{L_2[L - z(h_s - h_h)]} \quad (27)$$

The quotient of the tangential force to the vertical force on the coupling:

$$f_1 = \frac{T_1}{R_1} = \frac{z \cdot G - (T_{21} + T_{22})}{G - (R_{21} + R_{22})} = z \quad (28)$$

is therefore the same as the adhesion utilisation rate for each axle of the vehicle combination. Similar calculations can be carried out for other types of tandem suspensions, also considering unsprung mass, with the same results. Identical results shall be obtained for the ideal braking conditions of the tractor-trailer combination [30].

Thus, the ideal braking condition is unambiguously defined and to determine the ground reaction and then the distribution of braking forces, it is not necessary to analyse the braking process of the entire combination - only the braking process of the trailer alone may be considered.

3. BRAKING OF SEMI-TRAILERS WITH TANDEM SUSPENSION

A rigid two-dimensional model is used to analyse the brake force distribution of tandem-axle semitrailers (Fig. 3). The braking forces T_{21} and T_{22} of tandem axle are considered to be known functions of the brake line pressure [8, 36]. This model also allows the use of tandem suspensions of a different type and geometry. The model equations (16)-(18) must be completed with an extra relationship between reactions R_{21} and R_{22} , determined from the equilibrium equations for a specific type of tandem suspension.

3.1. Walking beam and bogie suspension

The simplest form of tandem unit is a walking (rigid) beam [37] mounted pivotally to a frame hanger on either side of the vehicle (Fig. 4-a). In the bogie suspension [38], parabolic tapered springs are anchored upside down to the trailer frame in place of walking beams (Fig. 4-b).

The forces exerted on the walking beam and bogie suspension during braking are shown in Fig. 4.

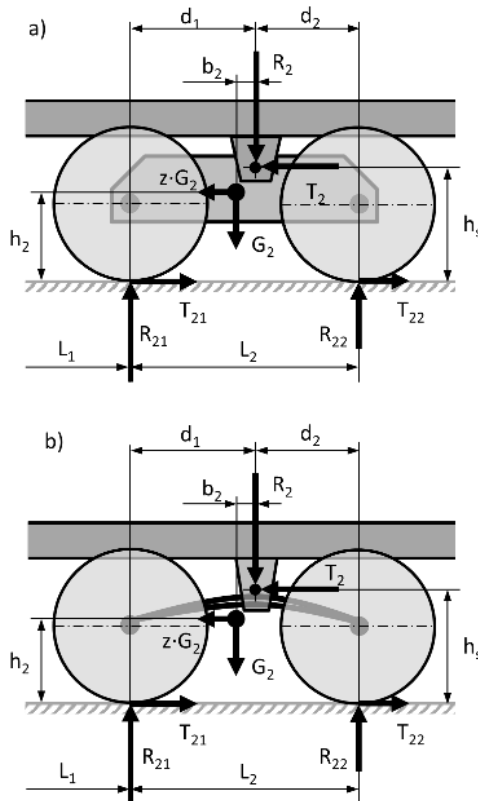


Fig. 4. Forces acting on a walking beam (a) and bogie suspension (b)

The same equilibrium force and moment equations can be used to describe both tandem suspensions:

$$\sum X = z \cdot G_2 - T_{21} - T_{22} + T_2 = 0 \quad (29)$$

$$\sum Z = R_{21} + R_{22} - R_2 - G_2 = 0 \quad (30)$$

$$\sum M_2 = R_{22}d_2 - R_{21}d_1 + G_2b_2 - z \cdot G_2(h_s - h_2) + (T_{21} + T_{22})h_s = 0 \quad (31)$$

where: T_2 and R_2 – horizontal and vertical forces in the single-point support between the suspension and trailer frame, d_1 and d_2 – beam (parabolic spring) length, h_s – height of position, b_2 – distance of centre of unsprung weight from a support, h_2 – height of centre of unsprung weight, G_2 – unsprung weight.

By solving the system of equations (17), (18) and (31) together, considering from equation (16) that $T_{21} + T_{22} = z \cdot G - T_1$, the dynamic axle loads and the vertical coupling force during braking of semi-trailer are obtained:

$$R_1 = G \left(1 - \frac{a}{L} + z \frac{h-h_h}{L} \right) - G_2 \left(\frac{b_2}{L} - z \frac{h_s-h_2}{L} \right) - (T_{21} + T_{22}) \frac{h_s-h_h}{L} \quad (32)$$

$$R_{21} = \left[G \left(\frac{a}{L} - z \frac{h-h_h}{L} \right) - (T_{21} + T_{22}) \frac{h_h}{L} \right] \frac{d_2}{L_2} + \left[G_2 \left(\frac{b_2}{L} - z \frac{h_s-h_2}{L} \right) + (T_{21} + T_{22}) \frac{h_s}{L} \right] \frac{L_1+L_2}{L_2} \quad (33)$$

$$R_{22} = \left[G \left(\frac{a}{L} - z \frac{h-h_h}{L} \right) - (T_{21} + T_{22}) \frac{h_h}{L} \right] \frac{d_1}{L_2} - \left[G_2 \left(\frac{b_2}{L} - z \frac{h_s-h_2}{L} \right) + (T_{21} + T_{22}) \frac{h_s}{L} \right] \frac{L_1}{L_2} \quad (34)$$

where: $L_2 = d_1 + d_2$ is the tandem wheelbase and $L = L_1 + d_1$ is the trailer wheelbase.

3.2. Two leaf spring suspension

In tandem leaf spring suspension, the two most common spring types are the double eye leaf spring and the slipper spring. For agricultural trailers, the second type is more common [37-39]. The front eye of both the leading and trailing springs are hinged directly to the front hanger bracket and the levelling beam, respectively, through pin joints (Fig. 5). The rear end of the springs is captured in the equalizer beam or rear hanger.

The forces applied to the two leaf spring suspensions with two unsprung weights are illustrated in Fig. 5.

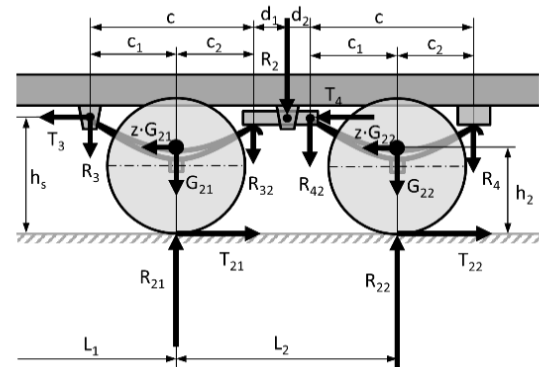


Fig. 5. Forces acting on a two leaf spring suspension

For the unsprung weight G_{21} , the following force and moment equilibrium equations are applicable:

$$\sum X = z \cdot G_{21} - T_{21} + T_3 = 0 \quad (35)$$

$$\sum Z = R_{21} - R_3 - R_{32} - G_{21} = 0 \quad (36)$$

$$\sum M_3 = -R_{32}c + R_{21}c_1 - G_{21}c_1 - z \cdot G_{21}(h_s - h_2) + T_{21}h_s = 0 \quad (37)$$

The equations of the balance of forces and moments for the unsprung weight of the G_{22} suspension are given by:

$$\sum X = z \cdot G_{22} - T_{22} + T_4 = 0 \quad (38)$$

$$\sum Z = R_{22} - R_4 - R_{42} - G_{22} = 0 \quad (39)$$

$$\sum M_4 = R_{42}c - R_{22}c_2 + G_{22}c_2 - z \cdot G_{22}(h_s - h_2) + T_{22}h_s - T_4 \cos \alpha_2 (h_s - h_{r2}) - T_4 \sin \alpha_2 (c_2 + c_{r2}) = 0 \quad (40)$$

Equations (37) and (40) give the reactions at the equalizer beam ends:

$$R_{32} = (R_{21} - G_{21}) \frac{c_1}{c} - z \cdot G_{21} \frac{h_s - h_2}{c} + T_{21} \frac{h_s}{c} \quad (41)$$

$$R_{42} = (R_{22} - G_{22}) \frac{c_2}{c} + z \cdot G_{22} \frac{h_s - h_2}{c} - T_{22} \frac{h_s}{c} \quad (42)$$

After substitution of the expressions (41) and (42) into the equilibrium equation of the force moments on the equalizer beam:

$$R_{32}d_1 = R_{42}d_2 \quad (43)$$

a new relationship is obtained which, together with equations (17) and (18), forms a system of 3 equations which makes it possible to determine the dynamic axle loads and the vertical coupling force during braking of the semi-trailer:

$$R_1 = G - \frac{L_2}{MN} \left\{ [G[a - z(h - h_h)] - (T_{21} + T_{22})h_h] \frac{c_1(d_1 - d_2) + c \cdot d_2}{L_2} + G_{21}d_1[c_1 + z(h_s - h_2)] - G_{22}d_2[c_2 - z(h_s - h_2)] - (T_{21}d_1 + T_{22}d_2)h_s \right\} \quad (44)$$

$$R_{21} = \frac{L_1 + L_2}{MN} \left\{ [G[a - z(h - h_h)] - (T_{21} + T_{22})h_h] \frac{d_2(c - c_1)}{L_1 + L_2} + G_{21}d_1[c_1 + z(h_s - h_2)] - G_{22}d_2[c_2 - z(h_s - h_2)] - (T_{21}d_1 + T_{22}d_2)h_s \right\} \quad (45)$$

$$R_{22} = \frac{L_1}{MN} \left\{ [G[a - z(h - h_h)] - (T_{21} + T_{22})h_h] \frac{c_1d_1}{L_1} - G_{21}d_1[c_1 + z(h_s - h_2)] + G_{22}d_2[c_2 - z(h_s - h_2)] + (T_{21}d_1 + T_{22}d_2)h_s \right\} \quad (46)$$

where: $MN = c_2d_2L_1 + c_1d_1(L_1 + L_2)$.

3.3. Two leaf-two rod suspension

Another version of the tandem axle configuration uses only two springs with slipper ends. Vertical forces are transmitted to the trailer frame via the front and rear hanger brackets and equalizer beam (according to the BPW equalising beam) [37-39]. Longitudinal forces are transferred by connecting the radius rods between the axles and the front and middle hanger brackets (Fig. 6). The parameters α_1 and α_2 , as well as h_{r1} and h_{r2} , have a significant effect on the operation of the suspension. This design uses a reduced radius rod angle α_2 and a reduced pivot height h_{r2} on the rear axle to decrease inter-axle load transfer during braking [22].

The force and moment equations for unsprung weights G_{21} and G_{22} are as follows:

$$\sum X = z \cdot G_{21} - T_{21} + T_3 \cos \alpha_1 = 0 \quad (47)$$

$$\sum Z = R_{21} + T_3 \sin \alpha_1 - R_3 - R_{32} - G_{21} = 0 \quad (48)$$

$$\sum M_3 = -R_{32}c + R_{21}c_1 - G_{21}c_1 - z \cdot G_{21}(h_s - h_2) + T_{21}h_s - T_3 \cos \alpha_1 (h_s - h_{r1}) + T_3 \sin \alpha_1 (c_1 - c_{r1}) = 0 \quad (49)$$

$$\sum X = z \cdot G_{22} - T_{22} + T_4 \cos \alpha_2 = 0 \quad (50)$$

$$\sum Z = R_{22} + T_4 \sin \alpha_2 - R_4 - R_{42} - G_{22} = 0 \quad (51)$$

$$\sum M_4 = R_{42}c - R_{22}c_2 + G_{22}c_2 - z \cdot G_{22}(h_s - h_2) + T_{22}h_s - T_4 \cos \alpha_2 (h_s - h_{r2}) - T_4 \sin \alpha_2 (c_2 + c_{r2}) = 0 \quad (52)$$

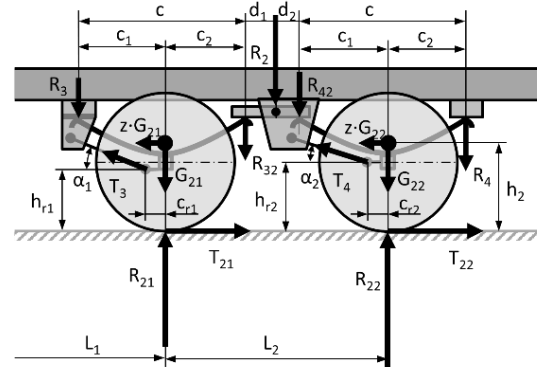


Fig. 6. Forces acting on a two leaf-two rod suspension

From equations (49) and (52), the reactions acting on the ends of the equalizer beam are given:

$$R_{32} = (R_{21} - G_{21}) \frac{c_1}{c} - z \cdot G_{21} \frac{h_{r1} - h_2}{c} + T_{21} \frac{h_{r1}}{c} + (T_{21} - z \cdot G_{21}) \tan \alpha_1 \frac{c_1 - c_{r1}}{c} \quad (53)$$

$$R_{42} = (R_{22} - G_{22}) \frac{c_2}{c} + z \cdot G_{22} \frac{h_{r2} - h_2}{c} - T_{22} \frac{h_{r2}}{c} + (T_{22} - z \cdot G_{22}) \tan \alpha_2 \frac{c_2 + c_{r2}}{c} \quad (54)$$

which are interrelated by the equation of force moments:

$$R_{32}d_1 = R_{42}d_2 \quad (55)$$

Solving equations (17), (18) and (53) - (54) together, the semi-trailer axle loads, and the coupling force are obtained:

$$R_1 = G - \frac{L_2}{MN} \left\{ [G[a - z(h - h_h)] - (T_{21} + T_{22})h_h] \frac{c_1(d_1 - d_2) + c \cdot d_2}{L_2} + G_{21}d_1[c_1 + z(h_{r1} - h_2)] - G_{22}d_2[c - c_1 - z(h_{r2} - h_2)] - (T_{21}d_1h_{r1} + T_{22}d_2h_{r2}) + ED \right\} \quad (56)$$

$$R_{21} = \frac{L_1 + L_2}{MN} \left\{ [G[a - z(h - h_h)] - (T_{21} + T_{22})h_h] \frac{d_2(c - c_1)}{L_1 + L_2} + G_{21}d_1[c_1 + z(h_{r1} - h_2)] - G_{22}d_2[c - c_1 - z(h_{r2} - h_2)] - (T_{21}d_1h_{r1} + T_{22}d_2h_{r2}) + ED \right\} \quad (57)$$

$$R_{22} = \frac{L_1}{MN} \left\{ [G[a - z(h - h_h)] - (T_{21} + T_{22})h_h] \frac{c_1d_1}{L_1} - G_{21}d_1[c_1 + z(h_{r1} - h_2)] + G_{22}d_2[c - c_1 - z(h_{r2} - h_2)] + (T_{21}d_1h_{r1} + T_{22}d_2h_{r2}) - ED \right\} \quad (58)$$

where

$$MN = d_2L_1c_2 + c_1d_1(L_1 + L_2) \quad ED = (T_{22} - z \cdot G_{22}) \tan \alpha_2 d_2(c_2 + c_{r2}) - (T_{21} - z \cdot G_{21}) \tan \alpha_1 d_1(c_1 - c_{r1})$$

Equations (56) - (58) become much simpler when $\alpha_1 = \alpha_2 = 0$, since then $ED = 0$.

3.4. Two leaf spring with equalization

A tandem double leaf spring suspension with equalization [4] has a pair of slipper springs and a mechanical equalisation of the braking load (Fig. 7). The rear end of the front spring is connected to the rear end of the rear spring by a rocker arm which is hinged to a central hanger bracket. This rocker distributes static (and shock) loads evenly between the two axles. An alternative design solution for a non-reactive tandem suspension with a bell crank and a tie-rod linkage is described in [5]. The forces acting on the two leaf spring suspensions with equalisation are presented in Fig. 7.

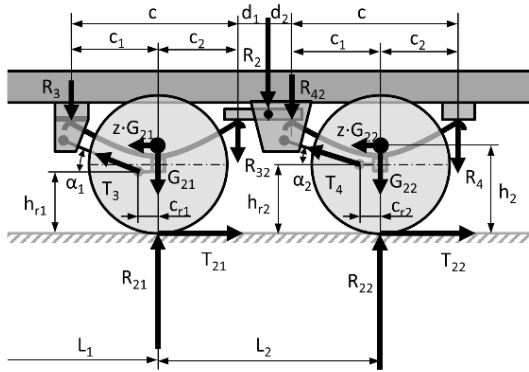


Fig. 7. Forces acting on two leaf spring suspension with equalization

The force and moment equations for the unsprung weights G_{21} and G_{22} of the suspension are given by:

$$\sum X = z \cdot G_{21} - T_{21} + T_3 = 0 \quad (59)$$

$$\sum Z = R_{21} - R_3 - R_{43} - G_{21} = 0 \quad (60)$$

$$\sum M_3 = -R_{43}c + R_{21}c_1 - G_{21}c_1 - z \cdot G_{21}(h_s - h_2) + T_{21}h_s = 0 \quad (61)$$

$$\sum X = z \cdot G_{22} - T_{22} + T_2 = 0 \quad (62)$$

$$\sum Z = R_{22} - R_2 - R_{42} - G_{22} = 0 \quad (63)$$

$$\sum M_4 = -R_{42}c + R_{22}c_1 - G_{22}c_1 - z \cdot G_{22}(h_s - h_2) + T_{22}h_s = 0 \quad (64)$$

Equations (61) and (64) are used to compute the reactions at the ends of the beam:

$$R_{43} = (R_{21} - G_{21}) \frac{c_1}{c} - z \cdot G_{21} \frac{h_s - h_2}{c} + T_{21} \frac{h_s}{c} \quad (65)$$

$$R_{42} = (R_{22} - G_{22}) \frac{c_1}{c} - z \cdot G_{22} \frac{h_s - h_2}{c} + T_{22} \frac{h_s}{c} \quad (66)$$

related by the equation of moments:

$$R_{43}d_1 = R_{42}d_2 \quad (67)$$

By solving the system of equations (17), (18), (65) – (67), the vertical coupling force and the dynamic axle loads are obtained during deceleration of the semi-trailer:

$$R_1 = \frac{1}{c_1 L} \{ G[L - a + z(h - h_h)]c_1 + (T_{21} + T_{22})h_h c_1 - (G_{21}d_1 - G_{22}d_2)[c_1 + z(h_s - h_2)] + (T_{21}d_1 - T_{22}d_2)h_s \} \quad (68)$$

$$R_{21} = \frac{1}{c_1 L} \left\{ G[a + z(h - h_h)] \frac{c_1 d_2}{L_2} - (T_{21} + T_{22})h_h \frac{c_1 d_2}{L_2} + \frac{L_1 + L_2}{L_2} (G_{21}d_1 - G_{22}d_2)[c_1 + z(h_s - h_2)] - \frac{L_1 + L_2}{L_2} (T_{21}d_1 - T_{22}d_2)h_s \right\} \quad (69)$$

$$R_{22} = \frac{1}{c_1 L} \left\{ G[a + z(h - h_h)] \frac{c_1 d_1}{L_2} - (T_{21} + T_{22})h_h \frac{c_1 d_1}{L_2} - \frac{L_1}{L_2} (G_{21}d_1 - G_{22}d_2)[c_1 + z(h_s - h_2)] + \frac{L_1}{L_2} (T_{21}d_1 - T_{22}d_2)h_s \right\} \quad (70)$$

where: $L_2 = d_1 + d_2$ and $L = L_1 + d_1$.

3.5. Air suspension

With air suspension, the air springs are mounted to the trailing arms via a crossmember and attached to the frame at the top (Fig. 8). The trailing arms are hinged to the hanger brackets and axle housings. All the air bags are connected by air lines to balance the axle loads. Vertical forces are distributed between the hanger brackets and the airbags. Longitudinal forces from braking are transferred to the trailer frame through the hanger brackets.

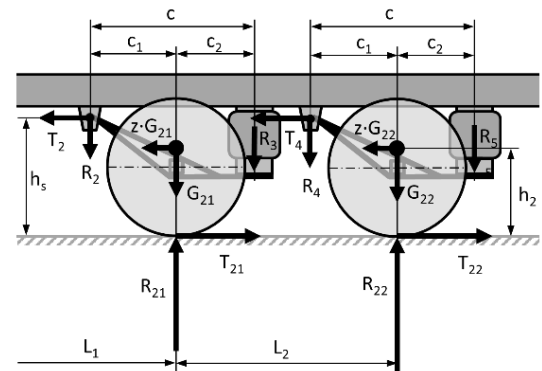


Fig. 8. Forces acting on air tandem suspension

The balance equations for the forces and moments applied to the suspension with unsprung weights G_{21} and G_{22} are calculated as follows:

$$\sum X = z \cdot G_{21} - T_{21} + T_2 = 0 \quad (71)$$

$$\sum Z = R_{21} - R_2 - R_3 - G_{21} = 0 \quad (72)$$

$$\sum M_3 = -R_3c + R_{21}c_1 - G_{21}c_1 - z \cdot G_{21}(h_s - h_2) + T_{21}h_s = 0 \quad (73)$$

$$\sum X = z \cdot G_{22} - T_{22} + T_4 = 0 \quad (74)$$

$$\sum Z = R_{22} - R_4 - R_5 - G_{22} = 0 \quad (75)$$

$$\sum M_4 = -R_5c + R_{22}c_1 - G_{22}c_1 - z \cdot G_{22}(h_s - h_2) + T_{22}h_s = 0 \quad (76)$$

On the assumption that the pressure in the airbags is the same, the vertical reactions transmitted by the air springs will be the same as well: $R_3 = R_5$. Then from equations (73) and (76), where $G_{21} = G_{22}$, the relationship between the loads of the tandem axles is obtained:

$$R_{21}c_1 + T_{21}h_s = R_{22}c_1 + T_{22}h_s \quad (77)$$

The solution of the system of equations (17), (18) and (77) is the vertical coupling force and the trailer axle loads:

$$R_1 = \frac{G}{L} [L - a + z(h - h_h)] + (T_{21} + T_{22}) \frac{h_h}{L} + \frac{L_2}{L} (T_{21} - T_{22}) \frac{h_s}{2c_1} \quad (78)$$

$$R_{21} = \frac{G}{2L} [a - z(h - h_h)] - (T_{21} + T_{22}) \frac{h_h}{2L} - \frac{L_1 + L_2}{L} (T_{21} - T_{22}) \frac{h_s}{2c_1} \quad (79)$$

$$R_{22} = \frac{G}{2L} [a - z(h - h_h)] - (T_{21} + T_{22}) \frac{h_h}{2L} + \frac{L_1}{L} (T_{21} - T_{22}) \frac{h_s}{2c_1} \quad (80)$$

where: $L = L_1 + L_2/2$.

4. BRAKING OF SEMI-TRAILERS WITH TANDEM SUSPENSION

As proved in section 2, the ideal braking condition for semi-trailers is achieved when the rate of utilized adhesion of each axle and the quotient of the horizontal to vertical force at the coupling is equal to the braking rate z of the combination. For semi-trailers with a single or tandem axle, this condition can be expressed as follows:

$$f_1 = f_2 = f_{2i} = z \quad z = \frac{T_1 + \sum T_{2i}}{R_1 + \sum R_{2i}} \quad (81)$$

where T_1, R_1 – braking force and normal reaction on the coupling device, T_{2i}, R_{2i} – braking forces and normal loads on tandem axle, i – axle number in the tandem unit.

The adhesion utilization rates used by the front coupling and the rear axle assembly are calculated based on the relationship:

$$f_1 = \frac{T_1}{R_1} \quad f_2 = \frac{\sum f_{2i} R_{2i}}{\sum R_{2i}} \quad (82)$$

With ideal braking, stopping distance is minimised and braking efficiency requirements are met with reserve ($z \geq 50\%$ at 6.5 bar pressure) as each axle reaches its maximum braking force capability [40].

Due to varying trailer loads, it is virtually impossible to ensure ideal brake distribution, even with the application of brake force regulators. Therefore, for agricultural trailers travelling at speeds above 40 km/h, acceptable limits have been set for the deviation of the adhesion utilisation rates of individual axles from the optimal distribution. When considering brake force distribution, each part of the combination is deemed to be a single vehicle without considering the force at the coupling. The UE regulation allows for two solutions, as shown in Fig. 9 [8].

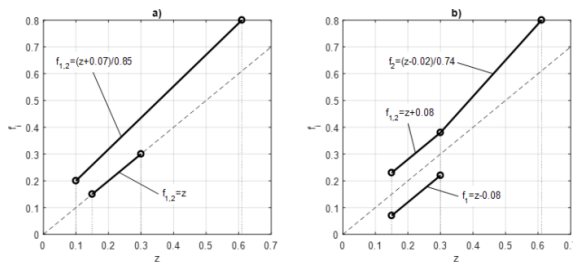


Fig. 9. Limits of adhesion utilization in accordance with Commission Delegated Regulation (EU) 2015/68 [8]: a – first solution, b – second solution

The first solution: the adhesion utilization rate for each axle group must satisfy the condition of ensuring the minimum required braking performance:

$$f_{1,2} \leq \frac{z + 0.07}{0.85} \quad \text{when} \quad 0.1 \leq z \leq 0.61 \quad (83)$$

and the condition of prior locking of the wheels of the front axle to ensure straight-ahead stability:

$$f_1 > z > f_2 \quad \text{when} \quad 0.15 \leq z \leq 0.30 \quad (84)$$

Second solution: the axle adhesion utilization rates should be within a certain range, then the wheel locking limits are established by the following relationships:

$$\begin{aligned} f_1 &\geq z - 0.08 \\ f_{1,2} &\leq z + 0.08 \end{aligned} \quad \text{when} \quad 0.15 \leq z \leq 0.30 \quad (85)$$

Furthermore, the adhesion curve for the rear axle assembly should satisfy the requirement:

$$f_2 \leq \frac{z - 0.02}{0.74} \quad \text{when} \quad 0.30 \leq z \leq 0.61 \quad (86)$$

For accurate calculations, the divisor in inequality (86) should be set to 0.7381.

The requirements concerning the wheel locking sequence are met if the adhesion utilized by the front axle is greater than that utilized by at least one of the rear axles at braking rates between 0.15 and 0.30 [8]:

$$f_1 > f_{2i} \quad \text{for any } i \quad (87)$$

Of course, in the case of the application of these solutions for a semi-trailer, the requirements for the front axle relate to the coupling device.

5. METHOD OF SELECTION OF LINEAR BRAKE FORCE DISTRIBUTION

In the air braking systems of agricultural trailers, various types of load-dependent brake force regulators are used to approximate the ideal brake force distribution. The automatic load-sensing valves (LSVs) currently fitted to heavy trailers are designed to adjust the brake pressure on the axles according to the load condition [41]. If the braking forces are designed correctly, this will prevent the wheels from locking when the vehicle is unladen or only partially laden. On mechanically suspended trailers, the regulation is proportional to the spring deflection, while on air-suspended trailers, it depends on the control pressure of the air springs. If there are technical reasons against equipping the vehicles with an LSV (especially unsuspended vehicles), agricultural trailers or machines should be equipped with a manual brake force regulator. In the most popular three-stage adjustment device (full - half - empty), the regulation of braking force is achieved by pressure limitation in axle brake chambers [41]. Due to the difficulty to comply with the requirements of EU 2015/68 for the distribution of braking forces on vehicles with manual regulators, which were mentioned before, BPW developed a seven-position mechanical load-dependent brake force regulator (MBL), but with linear characteristics [42]. The BPW MLB works with a proportional pressure control. As a result, the output pressure remains proportional to the control pressure. This kind of control fully complies with the requirements of the EU regulation for unsuspended vehicles.

As the pressure distribution characteristic of the ALB and MLB

is essentially a straight line, the distribution of braking forces between the coupling device and the rear axles can also be regarded as linear (radial). The contribution of the coupling device and trailer axles to the braking of the semi-trailer is expressed by the ratio of the partial braking force on the coupling device or individual axle to the total braking force:

$$\beta_1 = \frac{T_1}{z \cdot G} \quad \beta_2 = \frac{T_{2T}}{z \cdot G} \quad \beta_{21} = \frac{T_{21}}{z \cdot G} \quad \beta_{22} = \frac{T_{22}}{z \cdot G} \quad (88)$$

where: T_{2T} – total braking force of the tandem axles.

The values of the braking force distribution coefficients defined in this way can theoretically vary from 0 to 1 and satisfy the following relationships:

$$\beta_1 + \beta_2 = 1 \quad \beta_{21} + \beta_{22} = \beta_2 \quad (89)$$

Using the relations (88) and (89), the braking force of the coupling device and trailer axles can be calculated:

$$\begin{aligned} T_1 &= \beta_1 z \cdot G & T_{2T} &= (1 - \beta_1) z \cdot G & T_{21} &= \beta_{21} z \cdot G \\ T_{22} &= (1 - \beta_1 - \beta_{21}) z \cdot G \end{aligned} \quad (90)$$

A directional coefficient of the brake distribution line, which passes through the origin of the coordinate system $T_{2T} = f(T_1)$, is calculated as follows:

$$i_P = \frac{T_{21} + T_{22}}{T_1} = \frac{T_{2T}}{T_1} \quad (91)$$

Similarly, a linear braking force distribution, variable or fixed (in the absence of a braking force regulator), can be applied to the tandem assembly:

$$i_S = \frac{T_{22}}{T_{21}} \quad (92)$$

Unlike the β coefficients, the values of the i_P and i_S ratios can theoretically range from zero to infinity, especially when the braking force of one axle is close to zero.

To find optimal solutions for the linear brake force distribution, the Quasi Monte Carlo method [43-45] was chosen. Fig. 10 shows an example block diagram of the algorithm for the optimum selection of the braking force distribution coefficients β_1 and β_{21} .

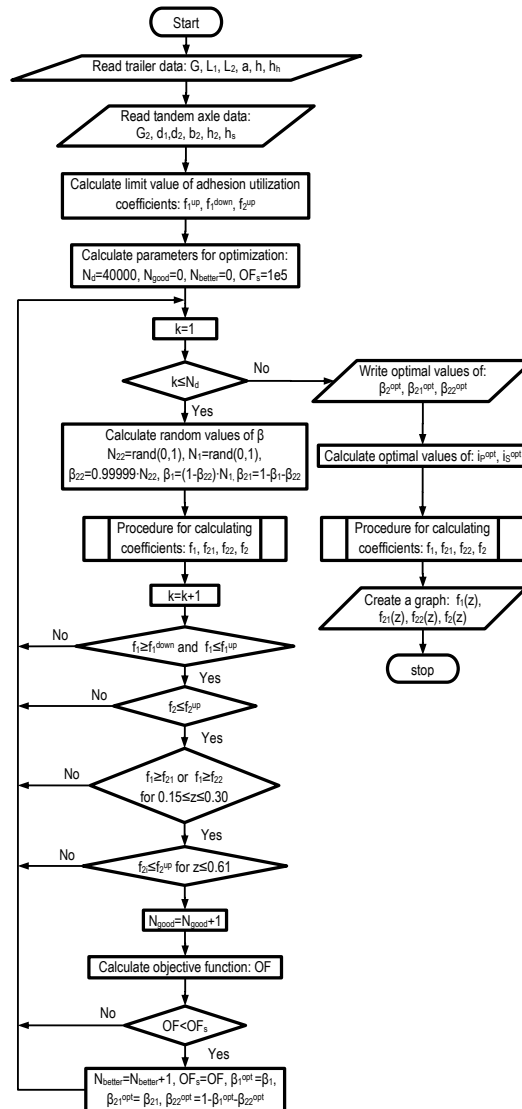


Fig. 10. A block diagram of an algorithm for the optimization of brake forces of a semi-trailer with tandem suspension using the Monte Carlo method (OF_s – initial value of the objective function, N_d – number of draws, N_{good} – number of good solutions, meeting inequality constraints, N_{better} – number of better solutions, reducing the value of the objective function)

The optimal values of the brake force distribution coefficients are determined by minimizing the objective function consisting of the residual sum of squares:

$$OF = \frac{w_1(f_1 - f_2)^2 + w_2(f_{21} - f_{22})^2}{w_1 + w_2} \quad (93)$$

where: w_i – weighting factors.

The OF thus obtained favourable solutions with the smallest differences between the adhesion utilised by each axle. As it is more important to reduce the difference between the values f_1 and f_2 than to reduce the difference between the adhesion values f_{21} and f_{22} utilised by the rear axles to fulfil the requirements (83) - (86), $w_1 > w_2$ should, therefore, be taken in the OF criterion.

Before the computation of the OF, the inequality conditions (83), (84) for the first solution and (85), (86) for the second solution are checked:

$$f_1^{up} \geq f_1 = \frac{T_1}{R_1} \geq f_1^{down} \quad f_2 = \frac{T_{21} + T_{22}}{R_{21} + R_{22}} \leq f_2^{up} \quad (94)$$

To simplify the notation of the boundary equations, they have been expressed as the product of the algebraic and logical equations. For the first solution:

$$f_1^{down} = z \cdot (0.15 \leq z \leq 0.30) \quad (95)$$

$$f_1^{up} = f_2^{up} = (z + 0.07)/0.85 \cdot (0.10 \leq z \leq 0.61) \quad (96)$$

For the second solution:

$$f_1^{down} = (z - 0.08) \cdot (0.15 \leq z \leq 0.30) \quad (97)$$

$$f_1^{up} = (z + 0.08) \cdot (0.15 \leq z \leq 0.30) \quad (98)$$

$$f_2^{up} = (z + 0.08) \cdot (0.15 \leq z \leq 0.30) + \left(\frac{z - 0.3}{0.7381} + 0.36 \right) \cdot (0.3 < z \leq 0.61) \quad (99)$$

Then, the condition (87) for multi-axle trailer is checked:

$$f_1 > f_{21} \quad \text{or} \quad f_1 > f_{22} \quad \text{for} \quad z = 0.15 \div 0.30 \quad (100)$$

In addition, an extra condition has been added to the rear axle adhesion utilisation rates:

$$f_{2i} \leq f_2^{up} \quad \text{for} \quad z \leq 0.61 \quad (101)$$

which limits the unduly high increase of the coefficient f_{22} for $z \leq 0.61$.

6. RESULTS OF OPTIMIZATION CALCULATIONS

Based on the algorithm described above, a computer program was written in MATLAB [46] to calculate the optimum distribution of the braking forces for semi-trailers with tandem suspension. The same algorithm, but without calculating the coefficients f_{21} and f_{22} , was used to calculate the single-axle semi-trailer. The MATLAB procedure of the Hammersley sequence [47] by Burkardt [48] was used to generate the quasi-random numbers N_{22} and N_1 (Fig. 10). The two-dimensional Hammersley point set is one of the simplest sequences with a low discrepancy that is used in both numerical and graphical applications [49]. The number of draws has been set to $N_d = 40.000$. The OFs (93) were calculated for the following values of the weighting factors $w_1 = 0.6$, $w_2 = 0.4$ in the range $0.1 \leq z \leq 0.66$ with a step size of 0.01.

The technical data and calculation results of the brake force distribution for the laden and unladen single axle semi-trailer are shown in Tab. 1.

Tab. 1. The technical data and results of the optimization of brake force distribution in single axle semi-trailer: $L_1 = 4.45$ m, $h_n = 0.7$ m (L – laden, U – unladen, I, II – first and second solution)

| | m [kg] | a [m] | h [m] | OF | β_1 | i_P |
|---------------------|--------|-------|-------|---------------|---------------|---------------|
| U-I-U _{II} | 2250 | 3.895 | 0.98 | 0.0947-0.0947 | 0.2079-0.2079 | 3.8097-3.8097 |
| L-I-L _{II} | 7250 | 3.840 | 1.25 | 0.1272-0.1272 | 0.2445-0.2445 | 3.0901-3.0901 |

In the case of laden and unladen semi-trailers, identical results were obtained for the optimum distribution of braking forces using both solutions. The adhesion utilization curves of the braked axle and the trailer coupling are shown in Fig. 11.

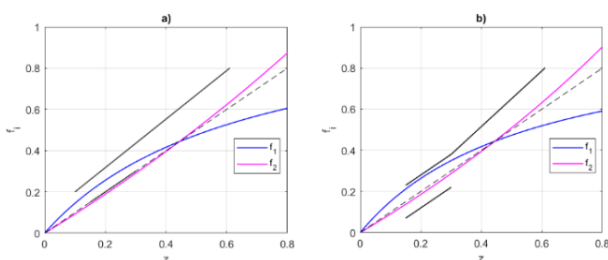


Fig. 11. Adhesion utilization curves $f_i(z)$ for an optimal distribution of brake forces in a single axle semi-trailer: a – an unladen trailer (I solution), b – a laden trailer (II solution)

The technical data of the laden and unladen semi-trailer with different tandem suspensions taken for the optimization calculations are presented in Tab. 2. To achieve comparability of the

calculation results, the same mass $m_2 = 1700$ kg was taken for all types of suspensions, and some geometrical parameters of suspensions obtained from literature data [37-38] were fixed. In addition, no changes were made to some of the suspension dimensions for the laden and unladen trailers. Based on the calculated results of the β_1 , β_{21} , β_{22} , i_P and i_S ratios presented in Tab. 3, the braking force distribution in a tandem semi-trailer depends significantly on the trailer load and the type of tandem suspension.

Following the optimization criterion used (lowest OF values), the air suspension (section 3.5) and the two leaf spring suspensions with equalization (section 3.4) can be regarded as the best. The same optimum brake force distribution ratios were found for these tandem suspensions (Table 3) using the solutions described in Section 2. The values after the dash have been obtained by considering the weight of the tandem axle. Moreover, with equalised values of the β_{21} and β_{22} coefficients (the values of the i_S coefficients are close to 1), the trailer with these suspensions has a uniform, close to ideal, distribution of the braking forces. Therefore, the adhesion utilization curves f_{21} , f_{22} and f_2 almost coincide (Fig. 12-a, c).

Tab. 2. Rigid drawbar trailer and tandem suspension technical data [37-38]

| Semi-trailer with tandem axle | | Tandem suspension | | | | |
|-------------------------------|------------------------|-------------------------|---------------------------------------|---|---|-------------------------|
| unladen | laden | bogie (3.1) | 2 leaf spring (3.2) | 2 leaf 2 rod (3.3) | 2 leaf equal. (3.4) | air susp. (3.5) |
| m=3900 kg | m=19800 kg | d ₁ =0.705 m | c ₁ =0.454 m | c ₁ =0.497 m | c ₁ =0.454 m | c ₁ =0.5 m |
| L ₁ =3.94 m | L ₁ =3.94 m | d ₂ =0.645 m | c=0.93 m | c=0.97 m | c=0.93 m | c=0.88 m |
| L ₂ =1.35 m | L ₂ =1.35 m | h _s =0.567 m | h _s =0.717 m | h _{r1} =h _{r1} =0.467 m | h _s =0.717 m | h _s =0.717 m |
| a=4.26 m | a=4.055 m | h ₂ =0.547 m | h ₂ =0.567 m | h ₂ =0.567 m | h ₂ =0.567 m | h ₂ =0.567 m |
| h=1.19 m | h=1.62 m | b ₂ =0.03 m | d ₁ =d ₂ =0.21m | d ₁ =d ₂ =0.19 m | d ₁ =d ₂ =0.675 m | |
| h _h =0.59 m | h _h =0.59 m | | | α ₁ = α ₂ =15° | | |

Tab. 3. The results of the optimization of brake force distribution in a tandem axle semi-trailer (L –laden, U – unladen, L_w, U_w – laden and unladen with weight of suspension)

| Suspension | | OF | β ₁ | β ₂₁ | β ₂₂ | i _p | i _s |
|--|------------------|---------------|----------------|-----------------|-----------------|----------------|----------------|
| Bogie (3.1) I and II solution | U-U _w | 0.3040-0.3115 | 0.1629-0.1588 | 0.5740-0.5793 | 0.2631-0.2619 | 5.1402-5.2971 | 0.4583-0.4521 |
| | L-L _w | 0.3006-0.3015 | 0.2301-0.2301 | 0.5286-0.5286 | 0.2412-0.2412 | 3.3456-3.3456 | 0.4564-0.4564 |
| 2 leaf 2 rod (3.3) I solution II solution | U-U _w | 0.6716-0.8831 | 0.2313-0.2307 | 0.1803-0.1527 | 0.5884-0.6166 | 3.3239-3.3354 | 3.2635-4.0377 |
| | L-L _w | 0.5841-0.6991 | 0.3117-0.3267 | 0.1674-0.1644 | 0.5209-0.5189 | 2.2086-2.1574 | 3.1116-3.1573 |
| | U-U _w | 0.9446-1.2169 | 0.2075-0.2065 | 0.1705-0.1444 | 0.6220-0.6490 | 3.8198-3.8417 | 3.6483-4.4935 |
| | L-L _w | 0.7531-0.7893 | 0.2806-0.2818 | 0.1577-0.1525 | 0.5617-0.5657 | 2.5635-2.5490 | 3.5631-3.7096 |
| 2 leaf equal. (3.4) I solution II solution | U-U _w | 0.2512-0.2512 | 0.1951-0.1951 | 0.4031-0.4031 | 0.4018-0.4018 | 4.1265-4.1265 | 0.9969-0.9969 |
| | L-L _w | 0.2099-0.2099 | 0.2605-0.2605 | 0.3710-0.3710 | 0.3685-0.3685 | 2.8388-2.8388 | 0.9935-0.9935 |
| | U-U _w | 0.3002-0.3002 | 0.1803-0.1803 | 0.4040-0.4040 | 0.4156-0.4156 | 4.5449-4.5449 | 1.0288-1.0288 |
| | L-L _w | 0.2117-0.2117 | 0.2561-0.2561 | 0.3721-0.3721 | 0.3717-0.3717 | 2.9046-2.9046 | 0.9989-0.9989 |
| air susp. (3.5) I solution II solution | U-U _w | 0.2511-0.2511 | 0.1951-0.1951 | 0.4031-0.4031 | 0.4018-0.4018 | 4.1265-4.1265 | 0.9969-0.9969 |
| | L-L _w | 0.2098-0.2098 | 0.2605-0.2605 | 0.3710-0.3710 | 0.3685-0.3685 | 2.8388-2.8388 | 0.9935-0.9935 |
| | U-U _w | 0.3003-0.3003 | 0.1803-0.1803 | 0.4040-0.4040 | 0.4156-0.4156 | 4.5449-4.5449 | 1.0288-1.0288 |
| | L-L _w | 0.2117-0.2117 | 0.2561-0.2561 | 0.3721-0.3721 | 0.3717-0.3717 | 2.9046-2.9046 | 0.9989-0.9989 |
| 2 leaf (3.2) only I solution | U-U _w | 5.3013-3.5221 | 0.2271-0.2337 | 0.0017-0.0218 | 0.7712-0.7446 | 3.4025-3.2798 | 458.23-34.199 |
| | L-L _w | 4.6761-4.5855 | 0.3230-0.3202 | 0.0018-0.0030 | 0.6752-0.6768 | 2.0957-2.1233 | 376.30-222.04 |

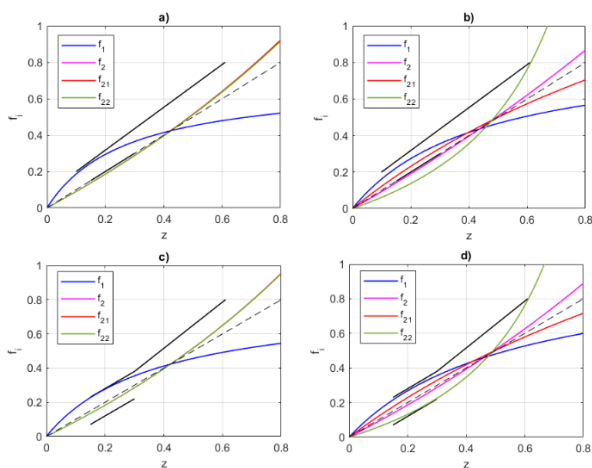


Fig. 12. Adhesion utilization curves $f_i(z)$ for an optimal distribution of brake forces in a tandem semi-trailer (considering the weight of the tandem suspension): a – an unladen trailer with air suspension (I solution), c – a laden trailer with air suspension (II solution), b – an unladen trailer with bogie suspension (I solution), d – a laden trailer with bogie suspension (II solution)

Larger values of the OF were obtained for the bogie suspension (section 3.1) and even higher values for the two leaf-two rod suspension (section 3.3). In both cases, this causes a greater deviation of the adhesion utilization curves from the ideal distribution of braking forces (Fig. 12-b, d and Fig.13-a, c).

For the two-leaf suspension (section 3.2), the calculation of the distribution of braking forces was only obtained from the first solution, with values of the OF objective function an order of magnitude higher (from 3.5 to 5.3) than for the other tandem suspensions. However, this solution cannot be considered correct either, as the leading tandem axle is braked to a very small extent (β_{21} values range from 0.003 to 0.022 - Table 3). In addition, once the z -value exceeds 0.6, the wheels of this axle start to come off the ground (the f_{21} values go to infinity and then fall below zero - Fig.13-b, d). Thus, f_i curves for braking rates above 0.6 make no physical sense. Braking at very low vertical loads can, according to the literature [3, 4], cause wheel lock on the leading axle. It should be noted that qualitatively similar results were obtained when calculating the braking force distribution on three-axle trailers with tandem axles [33].

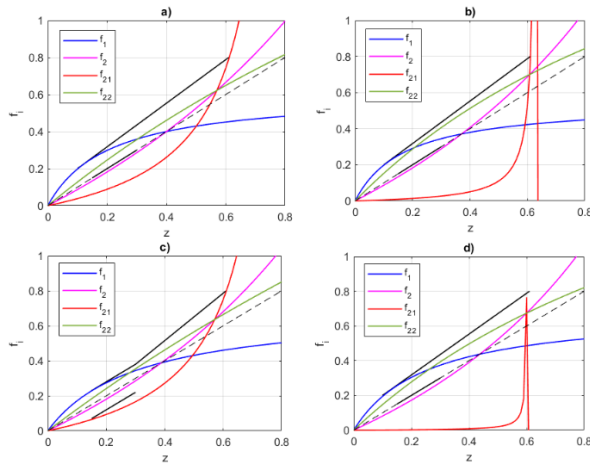


Fig. 13. Adhesion utilization curves $f(z)$ for an optimal distribution of brake forces in a tandem axle semi-trailer (considering the weight of the tandem suspension): a – an unladen trailer with two leaf-two rod suspension (I solution), c – a laden trailer with two leaf-two rod suspension (II solution), b – an unladen trailer with two leaf suspension (I solution), d – a laden trailer with two leaf suspension (I solution)

A comparison of the results obtained without and with the weight of the tandem shows that for most tandems, the effect of this weight on the distribution of braking forces has been negligible. The differences in the brake force distribution ratios are no more than 5%. But for suspension 3.3, the differences in the calculated values of the β_{21} ratio are about 18%, and for suspension 3.2, they are even up to 92%. Omitting the weight of the tandem suspension in the calculation of the braking force distribution considerably simplifies the relationships for the vertical reactions of the braked axles and, above all, avoids the many time-consuming steps over determining the mass of the tandem suspension and the position of its centre of gravity.

7. SUMMARY AND CONCLUSIONS

The method described for optimising the choice of linear brake force distribution for rigid drawbar agricultural trailers with single and tandem axles can be used in the initial design phase of air braking systems using the ALB or MLB regulator with radial characteristic. The calculation of the braking force distribution considered the requirements of EU Directive 2015/68 [8] for multi-axle trailers, treating the coupling device of a rigid drawbar trailer as a contractual front axle. It should be noted that although optimising the brake force distribution improves the braking performance and directional stability of agricultural vehicle combinations on different road surfaces, it does not prevent individual wheels from lockup, particularly on slippery and uneven surfaces. Therefore, agricultural vehicles travelling at speeds above 60 km/h must be equipped with ABS systems [8].

Optimization calculations using the Quasi Monte Carlo method for a rigid drawbar trailer with a payload of approximately 16 tonnes showed that the distribution of braking forces depends significantly on the type of tandem suspension. The lowest values of the minimized objective function were obtained for tandem axles with air suspension and two leaf springs suspension with equalization. For these two tandem assembly, the adhesion utilizations of the individual axles are closest to the straight line representing the ideal brake force distribution (Fig. 12-a,c), where the adhesion utilized by

each tandem axle is the same and equal to the braking rate. Higher values of OF were found for the bogie suspension (Fig. 12-b, d), and even higher for the two leaf-two rod suspension (Fig. 13-a, c). In both cases, this leads to a greater deviation of the adhesion utilisation curves from the ideal distribution of the braking forces. The two leaf spring suspension (Figure 13-b, d) produced the highest OF values. These results are in qualitative agreement with Limpert's analysis of the braking dynamics of a vehicle combination with tandem axles [4]. In addition, calculations for the two leaf spring suspension have shown that the load transfer between the tandem axles can lead to premature locking of the leading axle wheels at a braking rate of about 0.6, which is also confirmed in the literature [3, 4]. The results of the optimisation calculations show that for most tandem suspensions, the effect of the suspension mass on the brake force distribution is negligible.

REFERENCES

1. Revised standards for agricultural vehicles. RSA Guide. Road Safety Authority; 2015. Available from: https://www.rsa.ie/docs/default-source/road-safety/r1.6-agricultural-vehicles/revised-standards-for-agricultural-vehicles.pdf?Status=Master&sfvrsn=670b2fb7_5
2. Gillmann R. Axle Spacing and Load Equivalency Factors. Transportation Research Record 1998;(1655):227–232. <https://doi.org/10.3141/1655-29>.
3. Harwood DW. Review of truck characteristics as factors in roadway design. The National Academies Press; 2003. <https://doi.org/10.17226/23379>
4. Limpert R. Brake design and safety. SAE International, 2011. <https://doi.org/10.4271/R-398>
5. Heisler H. Advanced vehicle technology. Elsevier, 2002. <https://doi.org/10.1016/b978-0-7506-5131-8.x5000-3>
6. Nunney MJ. Light and heavy vehicle technology. Elsevier; 2007. <https://doi.org/10.4324/9780080465753>
7. Van Straelen B. Lastverlagerung und Bremskraftverteilung bei Einachs- und Doppelachsanhängern. Grundlehren Der Landtechnik 1983; 33(6): 183–189.
8. Commission Delegated Regulation (EU) 2015/68 of 15 October 2014 Supplementing Regulation (EU) No 167/2013 of the European Parliament and of the Council with Regard to Vehicle Braking Requirements for the Approval of Agricultural and Forestry Vehicles.
9. ECE Regulation No. 13. Uniform Provisions Concerning the Approval of Vehicles of Categories M, N and O with Regard to Braking. UN Economic Commission for Europe; Switzerland 2001.
10. Radlinski R, Flick M. Tractor and trailer brake system compatibility. SAE Technical Paper 861942; 1986. <https://doi.org/10.4271/861942>
11. Glišović J, Lukić J, Šušteršič V, Čatić D. 2015. Development of tractors and trailers in accordance with the requirements of legal regulations. In: Proc. of 9th International Quality Conference. Kragujevac, Serbia 2015; 193–202.
12. Nastasoiu M, Ispas N. Comparative analysis into the tractor-trailer braking dynamics: tractor with single axle brakes, tractor with all wheel brakes. Central European Journal of Engineering 2014; 4(2): 142–147. <https://doi.org/10.2478/s13531-013-0155-0>
13. Janulevičius A, Giedra K. The evaluation of braking efficiency of tractor transport aggregate. Transport 2002; 17(4): 152–158. <https://doi.org/10.3846/16483840.2002.10414033>
14. Aykan H, Çarman K, Canlı E, Ekinci Ş. Evaluation of tractor-trailer combination braking performance in different operating conditions. Journal of Natural and Applied Sciences. 2023; 27(2): 219–25.
15. Abu-Hamdeh NH. Stability and computer simulation of trailed implement under different operating conditions. Applied Mechanics and Materials. 2016; 826 :61–5. <https://doi.org/10.4028/www.scientific.net/amm.826.61>

16. Bădescu M, Iordache S, Ivancu B, Persu C, Bunduchi G, Epure M, Vlăduț V. Theoretical study of the system of forces and moments acting on tractor-semitrailer aggregate, into rectilinear motion. *Annals of the Faculty of Engineering Hunedoara - International Journal of Engineering* 2014; 12(3): 221-228.
17. Popescu S, Candea I, Csatlós C. Influence of the tractor and semitrailer mass ratio on braking stability. *Commission of Motorization and Power Industry in Agriculture* 2004; 4: 7-13.
18. Ogunjirin OA, Ogunlela AO. An appraisal of safety of tractor-trailer braking system. *Nigerian Journal of Technological Development*. 2011; 8(1): 10-22.
19. Ciuperca R, Popa L, Nedelcu A, Borisov B, Atanasov A. Braking of trailer endowed with inertial braking system, working in aggregate with tractor. *INMATEH Agricultural Engineering*. 2010;32(3): 51-58.
20. Ahokas J, Kosonen S. Dynamic behaviour of a tractor-trailer combination during braking. *Biosystems Engineering*. 2002; 85(1): 29–39. [https://doi.org/10.1016/S1537-5110\(03\)00035-7](https://doi.org/10.1016/S1537-5110(03)00035-7)
21. Dwyer MJ. The braking performance of tractor-trailer combinations. *Journal of Agricultural Engineering Research*. 1970; 15(2): 148–162. [https://doi.org/10.1016/0021-8634\(70\)90086-7](https://doi.org/10.1016/0021-8634(70)90086-7)
22. Pierce P. Controlled load transfer during braking on a four-spring trailer suspension. *SAE Technical Paper 85234*; 1985. <https://doi.org/10.4271/852344>
23. Mital A, Desai A, Subramanian A, Mital A. Product development: A structured approach to consumer product development, design, and manufacture. Elsevier Science; 2014. <https://doi.org/10.1016/B978-0-12-799945-6.00015-6>
24. Goodarzi A, Mehmashhadi J, Esmailzadeh E. Optimised braking force distribution strategies for straight and curved braking. *International Journal of Heavy Vehicle Systems IJHVS*. 2009; 16(1): 78-89. <https://doi.org/10.1504/IJHVS.2009.023856>
25. Zhang N, Wu J, Li T, Zhao Z, Yin G. Influence of braking on dynamic stability of car-trailer combinations. *Proceedings of the Institution of Mechanical Engineers, Part D: Journal of Automobile Engineering* 2021; 235(2-3): 455-464. <https://doi.org/10.1177/09544070209598>
26. Limpert R. An investigation of the brake force distribution on tractor-semitrailer combinations. *SAE Technical Paper 710044*; 1971. <https://doi.org/10.4271/710044>
27. Nakazawa M, Isobe O, Takahashi S, Watanabe Y. Braking force distribution control for improved vehicle dynamics and brake performance. *Vehicle System Dynamics*. 1995;24(4-5):413-426. <https://doi.org/10.1080/00423119508969101>
28. Nakazawa M, Isobe O, Takahashi S, Watanabe Y. Braking force distribution control for improved vehicle dynamics and brake performance. *Vehicle System Dynamics*. 1995;24(4-5):413-426. <https://doi.org/10.1080/00423119508969101>
29. Zheng H, Liu Z, Xu W. Braking force distribution strategy for comfort of tractor and semi-trailer combination. In: *Proc. of the 2012 International Conference on Automobile and Traffic Science Materials, Metallurgy Engineering*. Wuhan China 2012; 0108-0112. <https://doi.org/10.2991/mmat.2013.21>
30. Beyer C, Schramm H, Wrede J. Electronic braking System EBS - status and advanced functions. *SAE Technical Paper 982781*; 1998. <https://doi.org/10.4271/982781>
31. Kamiński Z, Radzajewski P. Calculations of the optimal distribution of brake force in agricultural vehicles categories R3 and R4. *Eksploatacja i Niezawodność - Maintenance and Reliability*. 2019; 21(4): 645–653. <https://doi.org/10.17531/ein.2019.4.14>
32. Miatluk M, Kamiński Z. Brake Systems of Road Vehicles. Calculations. Wydawnictwo Politechniki Białostockiej; 2005. Kamiński Z. Calculation of the optimal braking force distribution in three-axle trailers with tandem suspension. *Acta Mechanica et Automatica*. Sciendo. 2022;16(3):189-199. <https://doi.org/10.2478/ama-2022-0023>
33. Tang G, Zhao H, Wu J, Zhang Y. Optimization of braking force distribution for three-axle Truck. *SAE Technical Paper*; 2013. <https://doi.org/10.4271/2013-01-0414>
34. ISO 8855: 2011. Road vehicles - vehicle dynamics and road-holding ability - vocabulary.
35. Bryant D, Day A. Braking of road vehicles. Elsevier; 2022. <https://doi.org/10.1016/C2019-0-04185-4>
36. BPW. Agriculture equipment brochure; 2015. Available from: http://www.bpwtranspec.com.au/wp-content/uploads/2013/03/BPW_Agriculture_Equipment_brochure.pdf
37. Colaert Essieux. General catalogue; 2023. Available from: <https://www.adraxles.com/gallery/catalogue-colaert-essieux-2023-v22-11-18-lr.pdf>
38. Titan agricultural catalogue – tires, wheels, tracks, axles; 2015. Available from: http://titanaust.com.au/wp-content/uploads/2015/10/TITA0053-C1L3P2-Agricultural-Catalogue-COMPLETE_LR.pdf
39. NHTSA Heavy duty vehicle brake research program: Report no. 1 – Stopping capability of air braked vehicles. National Highway Traffic Safety Administration; 1985. Available from: <https://books.google.pl/books?id=pfBzvgEACAAJ>
40. Pneumatic braking system. Agriculture and forestry. Product catalogue. Wabco; 2017. Available from: <https://www.wabco-customercentre.com/catalog/docs/8150100823.pdf>
41. BPW. Mechanical load-dependent brake force regulator. The unique solution for the requirements imposed by Regulation EU 2015/68. Available from: <https://bpwagrar.comen/mlb/>
42. Dimov IT. Monte Carlo methods for applied scientists. World Scientific Publishing Co; 2007. <https://doi.org/10.1142/2813>
43. Kroese DP, Taimre T, Botev ZI. Handbook of Monte Carlo methods. John Wiley & Sons; 2011. <https://doi.org/10.1002/9781118014967>
44. Morton DP, Popova E. Monte-Carlo simulations for stochastic optimization. In: *Encyclopedia of Optimization*. Springer; 2001. https://doi.org/10.1007/0-306-48332-7_305
45. Venkataraman P. Applied optimization with MATLAB programming. John Wiley & Sons, Inc.; 2009.
46. Hammersley J.M. Monte Carlo methods for solving multivariable problems. *Annals of the New York Academy of Sciences*. 1960; 86(3): 844-874. <https://doi.org/10.1111/j.1749-6632.1960.tb42846.x>
47. Burkhardt J. Various software. MATLAB source codes. The Hammersley Quasi Monte Carlo (QMC) sequence 2020. Available from: https://people.sc.fsu.edu/~jburkardt/m_src/hammersley/hammersley.html
48. Wong TT, Luk WS, Heng PA. Sampling with Hammersley and Halton points. *Journal of Graphics Tools*. 2012; 2(2): 9-24. <https://doi.org/10.1080/10867651.1997.10487471>

Acknowledgements: This research was funded through a subsidy from the Ministry of Science and Higher Education of Poland, for the discipline of mechanical engineering at the Faculty of Mechanical Engineering at Białystok University of Technology (WZ/WM-IIM/5/2023).

Zbigniew Kamiński:  <https://orcid.org/0000-0003-2693-5077>



This work is licensed under the Creative Commons BY-NC-ND 4.0 license.

MOVING OBJECT DETECTION: A NEW METHOD COMBINING BACKGROUND SUBTRACTION, FUZZY ENTROPY THRESHOLDING AND DIFFERENTIAL EVOLUTION OPTIMIZATION

Oussama BOUFARES*, Mohamed BOUSSIF*, Wajdi SAADAOU**, Imed MIRAOU**

*Faculty of sciences of Tunis, Department physics, University of Tunis El Manar, El Manar 2092

**Faculty of sciences of Gafsa, Department electronics, University of Gafsa, Zarrok 2112

tsm.oussema@gmail.com, boussifmohamed1989@gmail.com, wajdi.enit@gmail.com, aimed_mir@yahoo.fr

received 28 March 2024, revised 15 September 2024, accepted 25 September 2024

Abstract: Detecting moving objects in videos is an evolving area of research, with important implications in many computer vision applications. In this paper, we propose a new detection approach by combining background subtraction and multi-level image thresholding based on fuzzy entropy, powered by the differential evolution (DE) algorithm. The first step of our method is background subtraction, aiming to isolate moving objects by eliminating the static background. However, this approach can be sensitive to lighting variations and background changes, thus limiting its accuracy. To overcome these limitations, we introduce multi-level image thresholding based on fuzzy entropy. This method exploits the intrinsic variability of moving objects rather than simply differentiating against the background. By adjusting thresholds locally, our approach better adapts to changing environmental conditions. The key element of our proposal lies in the optimization of the fuzzy entropy threshold parameters using the differential evolution algorithm. We chose DE for its robustness and efficiency in handling continuous optimization problems, which makes it well-suited for complex tasks like multi-level image thresholding. By iteratively adjusting the thresholds, we maximize the detection of moving objects while minimizing false positives, thereby improving the robustness and accuracy of the method. Our experiments on test video sequences demonstrate the effectiveness of our approach, highlighting a significant improvement in moving object detection compared to traditional methods. This promising methodology paves the way for future advances in moving object detection, with potential applications in surveillance, robotics, and computer vision in general.

Key words: detecting moving objects; fuzzy entropy; differential evolution; object segmentation

1. INTRODUCTION

In the ever-evolving realm of computer vision, accurately segmenting objects in video streams remains a pivotal challenge with profound implications across numerous domains. This task, crucial for applications spanning from video surveillance to human-machine interaction, including personal safety and industrial process monitoring, necessitates robust methodologies capable of dynamically adapting to changing environmental conditions.

Background subtraction [1, 2] has emerged as a widely recognized technique in video object segmentation, aiming to distinguish foreground objects from a dynamic background. Among these approaches, the median background model stands out for its effectiveness in adapting to dynamic scenes, capturing median pixel values to provide a stable background representation amidst variations such as lighting changes and moving shadows.

However, the effectiveness of background subtraction methods, including the median background model, is impeded by persistent challenges such as false positives and negatives. False positives occur when non-object regions are erroneously identified, while false negatives result from the failure to detect real objects, often due to complex variations in lighting or background dynamics.

To address these challenges, this article proposes an innovative post-processing scheme by combining the median background model with the gamma correction factor and the Ma-

halanobis distance metric. This synergistic approach aims to mitigate both false positives and negatives. Gamma correction enhances image contrast, facilitating the differentiation between foreground and background elements, while the Mahalanobis distance metric offers a robust statistical measure assessing the dissimilarity between pixels in difference images.

The primary contribution of this article lies in introducing an innovative post-processing scheme that significantly enhances the accuracy of video object segmentation. Focusing on the object segmentation process, we exploit enhanced difference images using fuzzy entropy and differential evolution. Fuzzy Entropy [3] resolves inherent uncertainty in difference frames, while Differential Evolution [4, 5] optimizes the segmentation process, enhancing the accuracy and efficiency of object delineation in the video stream. Subsequent sections will delve deeper into the methodology, experimental setup, and results, demonstrating how this post-processing scheme synergistically integrates with the median background model to establish a refined segmentation framework.

The paper is structured as follows: it begins by reviewing previous work on foreground detection, encompassing deep learning-based methods and traditional approaches. Subsequently, Section 3 elaborates on our MOD-BFDO method for foreground detection, which integrates background subtraction, fuzzy entropy thresholding, and differential evolution optimization. Experimental results and discussion are presented in Section 4, followed by concluding remarks in Section 5.

2. RELATED WORK

Detecting moving objects in video is a dynamic area of research, marked by notable advances in multi-level image thresholding and the integration of fuzzy entropy with metaheuristic algorithms like differential evolution, as demonstrated in works such as [6]. The choice of Differential Evolution (DE) among various metaheuristic algorithms stems from its balance between exploration and exploitation, making it particularly effective for optimization problems in image segmentation. DE has shown strong adaptability in handling continuous optimization problems, which aligns well with the complexity of multi-level thresholding in dynamic video sequences. These results have driven our exploration in the specific context of moving object detection. Localized approaches outlined in [7] have further piqued our interest in detecting objects within well-defined areas in video sequences. Meanwhile, global approaches to multi-level thresholding, as discussed in [8], offer crucial insights for improving detection across sequences. Li et al. (2023) introduced an approach based on the Improved Slime Mould Algorithm (SMA) combined with symmetric cross-entropy for multi-level thresholding, achieving greater accuracy in complex image segmentation tasks [9]. Additionally, Zhou et al. (2023) proposed a complex-valued encoding golden jackal optimization for multilevel thresholding image segmentation, further enhancing the robustness of image segmentation techniques [10].

Recent developments in fuzzy-based methods also play an essential role in this domain. For example, [11] introduces a robust approach to moving object detection by fusing Atanassov's Intuitionistic 3D Fuzzy Histon Roughness Index and texture features, enhancing performance in diverse conditions. Similarly, [12] uses Atanassov's intuitionistic fuzzy histon for robust detection in noisy environments. Another notable contribution is [13], which proposes a novel feature descriptor for moving object detection, showcasing improvements in robustness, particularly in complex scenes.

In addition to fuzzy-based approaches, the exploration of synergies between differential evolution, fuzzy entropy, and alternative entropy measures, as highlighted in [14], has broadened our understanding of multi-level image thresholding techniques. These advanced approaches can be categorized into two broad classes: methods based on deep learning and traditional unsupervised learning.

In the realm of deep learning, [15] presents a novel approach using deep neural networks for detecting moving objects, offering superior accuracy and generalization. Similarly, [16] highlights the potential of convolutional neural networks (CNNs) for robust moving object detection, while [17] uses generative adversarial networks (GANs) to generate improved training data for enhanced detection performance. Another contribution, [18], applies transfer learning to improve detection generalization across various scenarios.

In the domain of moving object detection, traditional unsupervised learning methods, such as background subtraction, temporal segmentation, and clustering, have proven effective due to their simplicity and low computational requirements. Techniques like adaptive thresholding using wavelet transforms and principal component analysis (PCA) capture spatial and temporal features, making them reliable in dynamic environments. For example, [19] introduces a method using stationary wavelet transforms for background subtraction, showing high accuracy. Similarly, [20] demonstrates temporal segmentation's effectiveness, while [21]

emphasizes the robustness of traditional approaches in specific conditions. These methods underscore the resilience and adaptability of unsupervised learning, maintaining relevance despite the rise of deep learning. Additionally, [22] explores unsupervised clustering to group objects based on temporal similarities, and [23] highlights the application of PCA for detecting moving objects in complex sequences. Traditional methods, despite their limitations, continue to be valuable in scenarios where deep learning models may be less practical due to computational or data constraints.

By consolidating these related works, our paper offers an integrated methodology for detecting moving objects in videos, emphasizing the synergies between fuzzy entropy, differential evolution, and multi-level image thresholding.

3. METHODOLOGY

This study focuses on improving object segmentation in video streams by combining the median background model, an innovative post-processing scheme, and advanced segmentation techniques based on entropy and differential evolution. The main goal is to achieve accurate segmentation of moving objects while overcoming the challenges of false positives and false negatives in the object delineation process.

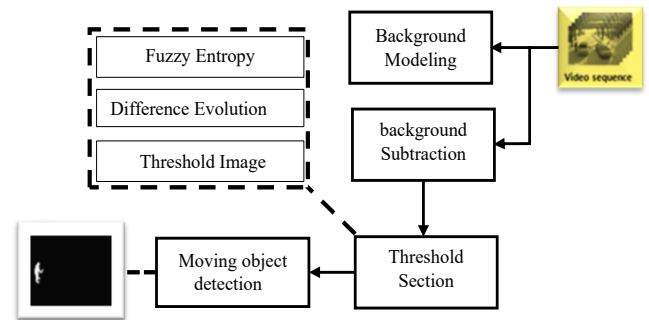


Fig. 1. General flow chart of the proposed method

3.1. Calculation of Difference Images Using Median Background Model

Calculating image difference using the Median Background Model is a fundamental step in our methodology. This phase involves capturing the dynamic changes in a video sequence by subtracting the median background from each frame. The Median Background Model is presented as a robust representation of the static scene, adapting to variations in lighting, shadows, and gradual environmental changes

3.1.1. Background Model Initialization

This step begins by initializing the median background model using a set of consecutive frames from the video sequence. Median pixel values are calculated independently for each pixel position on this set, creating a stable background representation.

$$Bkg(x, y) = \frac{\sum_{n=1}^N I(x, y)}{N} \quad (1)$$

In this context, $Bkg(x, y)$ represents the pixel intensity of the background model at coordinates (x, y) , while $I(x, y)$ denotes the pixel intensity at (x, y) within the frame. The background model is constructed using N frames, where N signifies the number of frames incorporated within the process.

3.1.2. Frame-wise Subtraction

For each subsequent frame in the video sequence, we mainly perform a per-pixel subtraction of the average background calculated from the current frame. The result is a different image that highlights the dynamic elements of the scene that stand out from the static background.

$$\Delta t = |I(x, y) - Bkg(x, y)| \quad (2)$$

When detecting moving objects, updating the background is a crucial step. With each iteration of the algorithm, the background model is dynamically adjusted. This adaptation concerns each pixel of the matrix, and each pixel is modified according to the dynamic matrix resulting from the subtraction between the current image and the initial background. For maintaining an accurate and up-to-date representation of the background, it is essential to adopt an adaptive method. This approach takes into consideration changes observed in the scene over time. More precisely, it adjusts the values of the dynamic matrix according to new information coming from the current image. Thus, updating the dynamic matrix not only makes it possible to detect moving objects. Nonetheless, to intelligently adapt to variations in the scene to ensure robust and precise detection.

When looking closely at the difference images, it becomes apparent that some background pixels may be misclassified, thereby leading to inaccurate segmentation of foreground objects. This imprecision can compromise the overall quality of the segmentation and introduce false positive regions. It is imperative to undertake additional processing on the different images to rectify this situation. This processing process aims to eliminate these false positive areas, thereby improving the reliability of object segmentation and obtaining more accurate results in identifying elements of interest. Adopting this approach strengthens the algorithm's ability to correctly discern the edges and details of foreground objects, thereby contributing to more robust and reliable segmentation.



Fig. 2. The first row shows the original images, the second row shows the generated difference images

3.2. Post-processing diagram

A new post-processing scheme is introduced to improve the results obtained by background subtraction. This system comprises two basic elements.

3.2.1. Gamma correction

For enhancing contrast, the difference images use the gamma correction factor. By improving the ability to distinguish between foreground and background items, this improvement helps to lower the number of false positives.

Our approach consists of first defining a gamma correction factor higher than 1, which maps intensity values to lower output values, and then defining a value below 1, which extends intensity values to higher levels. Figure 3 shows the change in the output image's intensity with the input image's intensity values for a fixed gamma value. This lessens the low-value gris noise concentration zones.

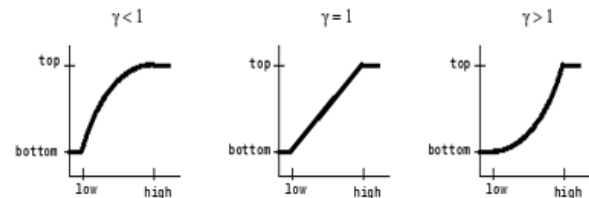


Fig. 3. Change in intensity of the input image along the x-axis relative to the output image along the y-axis, when gamma is less than or equal to 1 and b gamma is greater than or equal to 1

3.2.2. Mahalanobis Distance Metric

The produced different images are, then, subjected to a Mahalanobis distance calculation, which produces a refined difference image free of outlier pixels. The sample mean and covariance of the difference image—whose mean value skews toward the higher gray level values—are used in this approach. As a result, this averaging effect helps to remove ambiguity or unclearness from areas with low-valued gray levels. When it comes to reducing the impact of large covariance directions—especially those brought on by noisy components—the Mahalanobis distance is essential. Therefore, any noise is seen as an outlier and is essentially averaged out. The Mahalanobis distance metric uses the spatial orientation of the variables, taking into consideration their covariance between them.

The post-processing schemes eliminated most of the gray areas present in the output. The representation of the moving object in Figure 4 is significantly more defined compared to the smudged output observed in Figure 2. The results obtained in Figure 4 also facilitate segmentation due to the elimination of several outliers.



Fig. 4. The first row shows the original images, and the post-processing scheme improves the difference images

3.3. Object Segmentation using Fuzzy Entropy and Differential Evolution

The next stage of our process is object segmentation, which is essential to fine-tuning the initial difference images. We utilize two sophisticated methods, Differential Evolution, and Fuzzy Entropy, to improve the accuracy and stability of the segmentation procedure. The local Fuzzy Entropy and Differential Evolution thresholding approach is carried out in two major stages as depicted in Fig. 5.

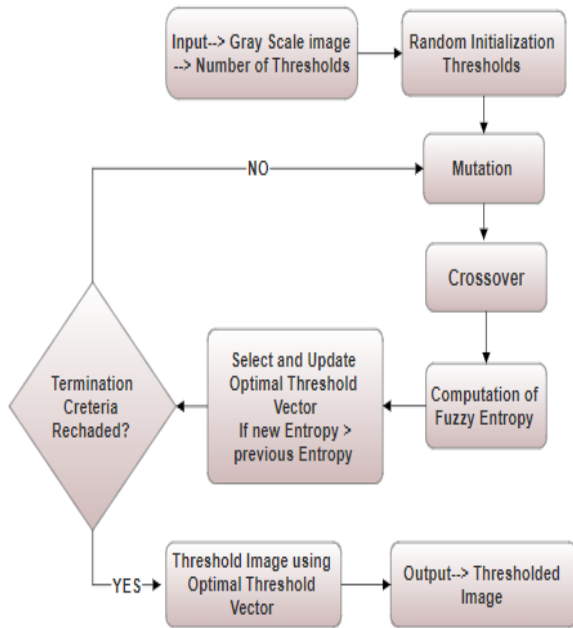


Fig. 5. Flowchart of segmentation process

3.3.1. Fuzzy Entropy

Fuzzy entropy is presented as a powerful tool for dealing with the uncertainty inherent in different images. In scenarios where pixel values may be fuzzy or ambiguous, fuzzy entropy captures the complexity of the pixel distribution. By incorporating the principles of fuzzy logic, it provides a nuanced measure of entropy, enabling more adaptive and accurate segmentation in regions with varying degrees of certainty.

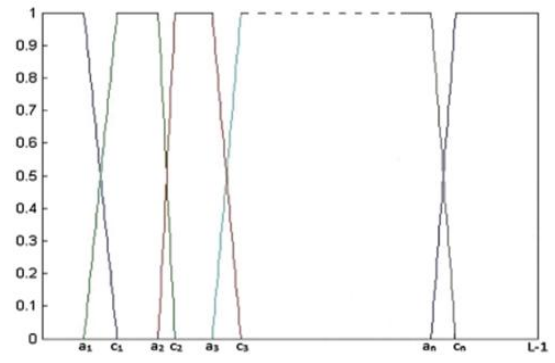


Fig. 6. Fuzzy membership function for n - level segmentation

A classical set, denoted as A , is essentially a collection of elements that may or may not be members of set A . In the realm of fuzzy sets, which is an extension of classical sets, an element can exhibit partial membership within set A . The definition of A could be stated as follows:

$$A = \{(x, \mu_A(x)) | x \in X\} \quad (3)$$

where $0 < \mu_A(x) < 1$ and $\mu_A(x)$ is the membership function, which measures x 's proximity to A .

In this study, a trapezoidal membership function; as depicted in Fig. 6, is utilized to estimate the membership of n segmented areas, $\mu_1, \mu_2, \dots, \mu_n$, by employing $2(n-1)$ unknown fuzzy parameters, namely $a_1, c_1, \dots, a_{n-1}, c_{n-1}$, where $0 < a_1 < c_1 < \dots < a_{n-1} < c_{n-1} < L-1$. Then, for n -level thresholding, the following membership function can be obtained.

$$\mu_1(k) = \begin{cases} 1 & k < a_1 \\ \frac{k-a_1}{a_1-c_1} & a_1 \leq k \leq c_1 \\ 0 & k > c_1 \end{cases} \quad (4)$$

$$\mu_{n-1}(k) = \begin{cases} 0 & k < a_{n-2} \\ \frac{k-a_{n-2}}{c_{n-2}-a_{n-2}} & a_{n-2} \leq k < c_{n-2} \\ 1 & c_{n-2} \leq k \leq a_{n-1} \\ \frac{k-c_{n-2}}{a_{n-1}-c_{n-2}} & a_{n-1} \leq k \leq c_{n-1} \\ 0 & k > c_{n-1} \end{cases} \quad (5)$$

$$\mu_n(k) = \begin{cases} 1 & k < a_{n-1} \\ \frac{k-a_{n-1}}{a_n-c_n} & a_{n-1} \leq k \leq c_{n-1} \\ 1 & k > c_{n-1} \end{cases} \quad (6)$$

The maximization of fuzzy entropy at multiple levels of the image, i.e., background and foreground areas, can be formulated as follows.

$$H_n = H_1 + H_2 + \dots + H_n = - \sum_{x=0}^{L-1} \frac{P_1 \mu_1(i)}{P_1} \ln \frac{P_1 \mu_1(i)}{P_1} - \sum_{x=0}^{L-1} \frac{P_2 \mu_2(i)}{P_2} \ln \frac{P_2 \mu_2(i)}{P_2} - \dots - \sum_{x=0}^{L-1} \frac{P_n \mu_n(i)}{P_n} \ln \frac{P_n \mu_n(i)}{P_n} \quad (7)$$

where

$$P_1 = \sum_{i=0}^{L-1} p_i \mu_1(i), P_1 = \sum_{i=0}^{L-1} p_i \mu_2(i), \dots, P_n = \sum_{i=0}^{L-1} p_i \mu_n(i)$$

and P_i is the probability measure of the occurrence of gray levels.

Maximizing the total entropy gives the optimal value for the parameters.

$$\varphi(a_1, c_1, \dots, a_{n-1}, c_{n-1}) = \text{Argmax}(H_1 + H_2 + \dots + H_n) \quad (8)$$

It is essential to apply a global optimization technique to effectively optimize equation (8) and simultaneously reduce the time complexity of the proposed method. The (n-1) threshold values can be obtained using the fuzzy parameters as follows:

$$T_1 = (\frac{a_1+c_1}{2}); T_2 = (\frac{a_2+c_2}{2}); \dots; T_{n-1} = (\frac{a_{n-1}+c_{n-1}}{2}) \quad (9)$$

3.3.2. Differential Evolution Optimization

In our approach, the optimization phase has a crucial position in perfecting the object segmentation process. To do this, we exploit differential evolution; a global optimization technique proposed by Storn [4]. This robust method adaptively adjusts the parameters of the segmentation algorithm, aiming to search for a global optimal point in a real parameter space of dimension R^D . More precisely, we use a simple version of differential evolution, called the DE/rand/1 scheme, where the i^{th} individual of the population, represented as a vector of dimension D , contributes significantly to improving the accuracy of the segmentation process.

$$\vec{X}_i(t) = [\vec{X}_{i,1}(t), \vec{X}_{i,2}(t), \dots, \vec{X}_{i,D}(t)] \quad (10)$$

The first step is initialization. the set is randomly initialized in the search space, according to the following:

$$\vec{X}_{i,j}(t) = [X_{jmin} + rand * (X_{jmax} - X_{jmin})] \quad (11)$$

$i = 1$ to NP and $j = 1$ to D

Where (X_{jmax}) and (X_{jmin}) define the maximum and minimum limits of the search space respectively. NP represents the total population engaged in the search process, and a $rand$ is a random number between 0 and 1. At each iteration, for each parent, a mutant vector, called a donor vector, emerges through the differential mutation operation. Creating the i^{th} donor vector $\vec{Y}_i(t)$ for the i^{th} parent vector involves choosing three other parent vectors (e.g., the $a1, a2$, and $a3 - th$ vectors, where $a1, a2, a3 \in [1, NP]$ and $a1 \neq a2 \neq a3$ are selected randomly from the current population). Thus, the donor vector can be formulated as follows:

$$\vec{Y}_i(t) = \vec{X}_{a1}(t) + F * (\vec{X}_{a2}(t) - \vec{X}_{a3}(t)) \quad (12)$$

Where F (scalar quantity called a weighting factor) exerts its influence. The next step involves optimizing the potential diversity of donor vectors to create test vectors. A binomial crossing operation is methodically applied to each of the D variables of a vector, following a rigorous protocol.

$$R_{i,j}(t) = \begin{cases} Y_{i,j}(t), & \text{if } rand_j(0,1) \leq Cr \text{ or } j = j_{rand} \\ X_{i,j}(t), & \text{Otherwise} \end{cases} \quad (13)$$

Each j , from 0 to D , and $rand_j$ in the interval $[0,1]$, represents the j^{th} evaluation of a uniform random generator. The component of $\vec{X}_i(t)$ and Cr symbolizes the crossover rate. The test vector evolves as a renewed parental progenitor for iteration $t + 1$ if it outperforms, in terms of the fitness function value (in case of maximization), the current parental vector in iteration t .

$$\vec{X}_i(t+1) = \begin{cases} \vec{R}_i(t), & \text{if } f(\vec{R}_i(t)) \geq f(\vec{X}_i(t)) \\ \vec{X}_i(t), & \text{if } f(\vec{R}_i(t)) < f(\vec{X}_i(t)) \end{cases} \quad (14)$$

The previous steps are iterated until the termination criterion is met, which is defined by the number of iterations.

4. EXPERIMENT RESULTS

In this section, we demonstrate the intrinsic relevance of our advanced methodology through a detailed presentation of experimental results. A comprehensive comparison was made between the performance of our approach (MOD-BFDO) and other methods, including five background subtraction-based approaches: the SuBSENSE [24] approach, the SC_SOBS [25] approach, the GMM_Zivkovic [26] approach, the GMM [31] approach, and the Cuevas [32] approach, as well as a deep learning-based approach, namely DeepBS [27]. All evaluations were conducted on three distinct datasets: the SBI [29], CDnet 2014 [28], LASIESTA [30], BMC2012 [33] databases. These datasets consist of sequences captured by cameras deployed in both public and private environments, containing various moving or stationary entities within the scene, such as vehicles, individuals, and others.

4.1. Qualitative Measurement

4.1.1. Qualitative evaluation using the CDnet 2014 and SBI datasets

During this step, we proceed to analyze and evaluate the detection results obtained using our approach, while and comparing these results with those obtained by other front-end detection methods in various contexts. Experimental scenes are classified based on different criteria, such as homogeneous illumination, light contrast, presence of shadows, range, occlusion, presence of multiple targets, weak signals, and baseline. A detailed analysis of these scenes is presented as follows.

4.1.1.1. Illumination changes

Figure 7 shows the experimental results obtained under uniform illumination. The first row presents the original image, the second row exposes the ground truth image and the seventh row reveals the result of our approach. Lines 7(3) to 7(6) show the results of the DeepBS [27], SC_SOBS [25], SuBSENSE [24], and GMM_Zivk [26] methods, respectively. For the HallAndMonitor-HM video, the presented results were obtained with optimal thresholds automatically calculated by our method based on differential evolution. For NThr=4, the optimal thresholds averaged are 63.5, 128, 190.5, and 254. This choice of NThr indicates that the algorithm has determined four thresholds to segment the

image. These thresholds maximize the detection of moving objects while reducing noise and false positives, offering a good compromise between accuracy and computational complexity.

After carrying out experiments on the “HumanBody1-HB” and “HallAndMonitor-HM” videos, our approach, as well as DeepBS [27], demonstrated satisfactory performance without requiring specific quality measurements as a reference. But when it came to the detailed rendering of the target object, other leading detection methods showed less convincing results, particularly methods that tend to overlook detailed information, thus leading to detection errors.

Compared to these methods, our approach stands out for its effectiveness in eliminating slight deformations while preserving target details. This efficiency arises from the use of a multi-scale fusion model, which more adequately preserves the contours and details of the target objects.



Fig. 7. Comparative analysis of our approach with state-of-the-art methods by exploiting specific videos such as “HumanBody1-HB” and “HallAndMonitor-HM” from the SBI2015 dataset. The left-to-right layout shows results for: original, ground truth, DeepBS [27], SC_SOBS [25], SuBSENSE [24], GMM_Zivk [26], as well as our method. The results for NThr=4 are displayed in this figure

4.1.1.2. Dynamic background

Figure 8 presents the experimental results obtained in various situations (dynamic background (CE), bad weather (SF), and shadow (BS)). The first row of Figure 8 shows the original image, the second row shows the ground truth image and the seventh row shows the result of our approach. Lines 8(3) to 8(6) correspond respectively to the results of the DeepBS [27], SC_SOBS [25], SuBSENSE [24], and GMM_Zivk [26] methods.

Analyzing videos with dynamic backgrounds represents a significant challenge in the field of object detection. Our approach was designed specifically to deal with this complexity, and the results obtained are very promising. Compared to several other methods, notably DeepBS [27], our approach stands out remarkably. Videos demonstrating scenes with constantly changing backgrounds are often subject to slight distortions and complex movements, making object detection difficult.

In our experiments, the results obtained by our approach and

DeepBS [27] outperformed those of other methods. Figures revealing frames extracted from videos with dynamic backgrounds show exceptional clarity and accuracy in detecting target objects. Our approach, like DeepBS [27], managed to maintain satisfactory performance, even in complex conditions where other methods showed limitations.

Using Differential Evolution models in our approach has proven effective in removing slight deformations and retaining details of target objects, which is crucial in dynamic environments. These results suggest that our approach, in tandem with DeepBS [27], constitutes a particularly robust and satisfactory solution for object detection in videos with dynamic backgrounds, thus opening new perspectives for various applications, such as video surveillance and real-time computer vision.

4.1.1.3. Bad weather

The figure shows the performance of seven object detection methods on a video sequence captured under bad weather conditions. The first two rows present the original images and the ground truth, respectively. The results of the different detection methods are displayed in rows 3 to 7.

In general, deep learning-based detection methods, such as DeepBS and our approach, achieve better results compared to non-deep learning methods like GMM_Zivk [26], SuBSENSE [24], and SC_SOBS [25]. This is likely due to the ability of deep learning-based methods to learn object characteristics, allowing for more accurate identification in challenging conditions.

In this experiment, our approach determined four thresholds to segment the bad weather video, with the optimal values averaging 56.5, 107, 178.5, and 254.5. These thresholds were specifically selected to enhance the detection of moving objects while minimizing noise and false positives, ensuring a robust trade-off between detection accuracy and computational efficiency

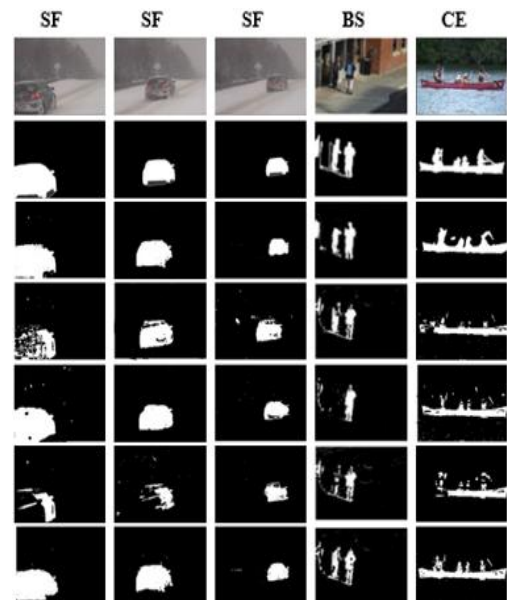


Fig. 8. Comparative analysis of our approach with state-of-the-art methods by exploiting specific videos such as “SnowFall-SF”, “BusStation-BS” and “Canoe-CE” from the CDnet 2014 dataset. The left-to-right layout shows results for original, ground truth, DeepBS [27], SC_SOBS [25], SuBSENSE [24], GMM_Zivk [26], as well as our method. The results for NThr=4 are displayed in this figure

Specifically, the DeepBS [27] method delivers the best performance on the bad weather video sequence, followed closely by our method. SuBSENSE [24] performs similarly to our method, though it is slightly less accurate than DeepBS [27]. SC_SOBS [25] produces the weakest results, though it still manages to detect some objects.

The GMM_Zivk [26] method yields the poorest performance on the bad weather video sequence, likely due to its reliance on simplifying assumptions about the object distribution. These assumptions may not hold in real-world conditions, leading to a significant loss in accuracy.

4.1.1.4. Baseline

The figure shows the results of seven object detection methods on two video sequences, one of road traffic and one of pedestrians. Rows 1 and 2 of the figures show the original images and the ground truth, respectively. Lines 3 to 7 show the results of the different detection methods.

In general, deep learning-based detection methods (DeepBS [27]) and our method achieve better results than non-deep learning-based methods SC_SOBS [25], SuBSENSE [24], and GMM_Zivk [26]. Probably, it is because our method and deep learning-based methods can learn the characteristics of the objects to be detected, which allows them to detect objects under difficult conditions accurately.

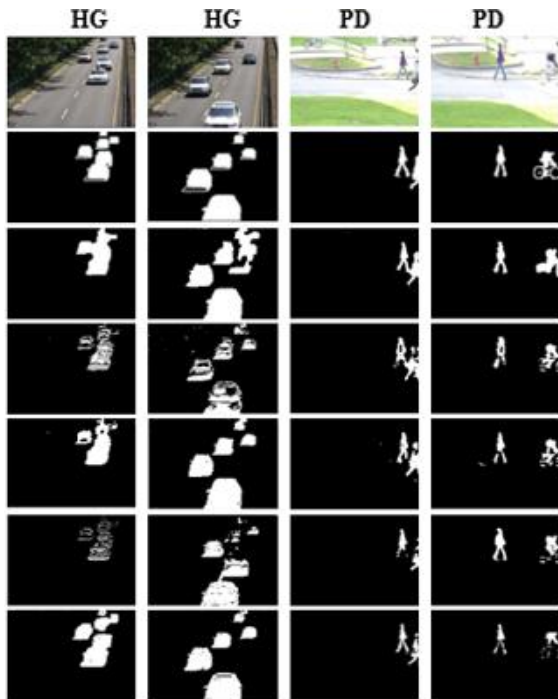


Fig. 9. Comparative analysis of our approach with state-of-the-art methods by exploiting specific videos such as "Highway-HG" and "Pedestrians-PD" from the CDnet 2014 dataset. The left-to-right layout shows results for original, ground truth, DeepBS [27], SC_SOBS [25], SuBSENSE [24], GMM_Zivk [26], as well as our method. The results for NThr=4 are displayed in this figure

Specifically, our method obtains the best results on the road traffic sequence, followed by the DeepBS [27] method. The SuBSENSE [24] method obtains good results on both sequences, but

it is slightly less precise than DeepBS [27] and our method. The SC_SOBS [25] method obtains results comparable to those of SuBSENSE [24]. The GMM_Zivk [26] method obtains the worst results on both sequences because the GMM_Zivk [26] method relies on simplifying assumptions about the distribution of the tracked objects. These assumptions may not be valid in real-world conditions, resulting in a loss of accuracy.

4.1.2. Qualitative evaluation using the LASIESTA and BMC2012 dataset

Figures 10 and 11 demonstrate the performance of the MOD-BFDO approach on two challenging sequences from the LASIESTA dataset. In Figure 10, the method handles moderate shadows effectively, accurately detecting and segmenting moving objects with minimal errors, showing robustness in controlled indoor environments. In contrast, Figure 11 highlights the method's challenges with dynamic backgrounds, camouflage, and hard shadows, where some moving objects are not fully detected. Despite these limitations, the approach still performs reasonably well in such complex scenarios. Overall, the results indicate that the MOD-BFDO approach is effective for object detection but may struggle in environments with high background complexity.

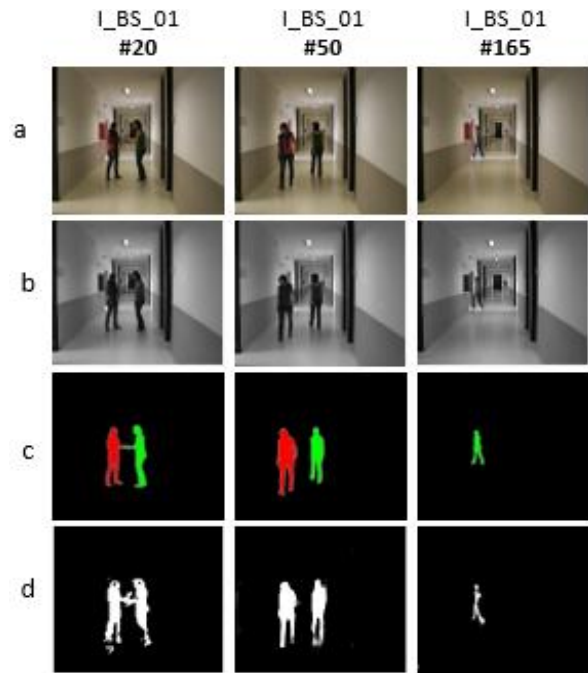


Fig. 10. Qualitative Performance of the MOD-BFDO Approach on I_BS_01 (Bootstrap, Moderate Shadows): (a) Original Image, (b) Grayscale Image, (c) Ground Truth, (d) Proposed Approach. The results for NThr=4 are displayed in this figure

Figure 12 showcases our approach's capability in outdoor environments, where varying lighting and small-scale movements often present challenges. The sequence images #276, #317, #352, and #228 reveal that our approach is proficient at detecting prominent moving objects even against complex urban backdrops, though smaller or distant objects may sometimes be less accurately captured, with the optimal values averaging 56.5, 107, 178.5 and 254.5.

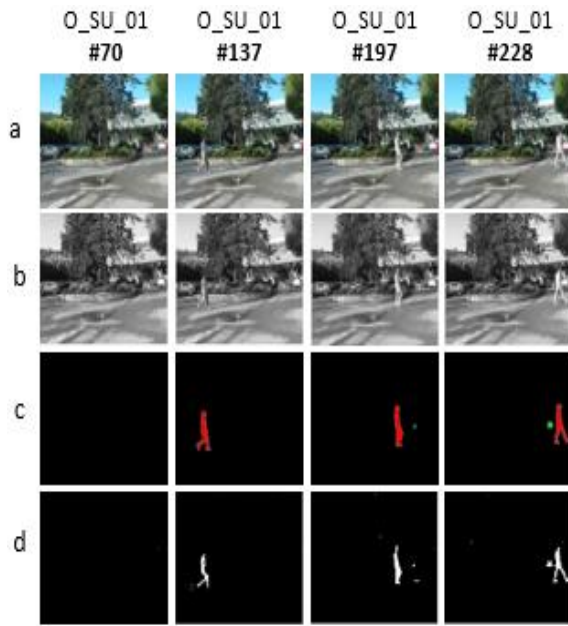


Fig. 11. Qualitative Performance of the MOD-BFDO Approach on O_SU_01 (Dynamic background, camouflage, hard shadows.): (a) Original Image, (b) background model, (c) Ground Truth, (d) Proposed Approach. The results for NThr=4 are displayed in this figure

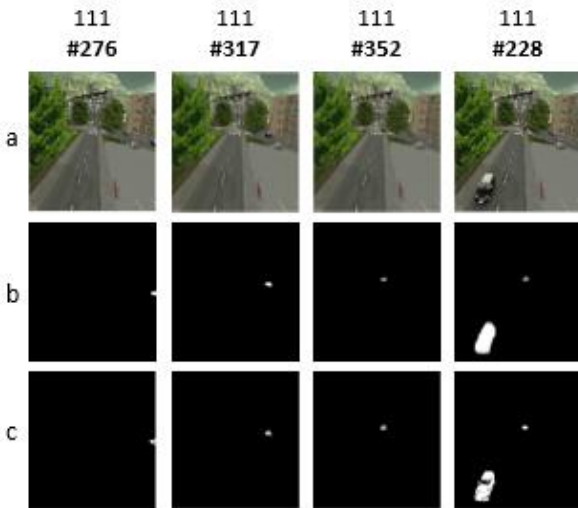


Fig. 12. Qualitative performance of the MOD-BFDO approach on the "111" synthetic videos from the BMC2012 dataset. This figure shows: (a) the original image, (b) the background model, and (c) the results obtained with the proposed approach. The results displayed correspond to NThr=4

4.2. Quantitative Measurement

In this section, we provide a detailed quantitative evaluation of the MOD-BFDO method. The performance is assessed using various metrics that measure the accuracy and reliability of the detection results. These metrics offer a clear indication of how well the proposed approach distinguishes moving objects from the background in different scenarios. By comparing our results to existing methods, we highlight the effectiveness and robustness of MOD-BFDO in both controlled and complex environments. The following subsections provide the mathematical definitions and full forms of each metric used in our evaluation.

- RE (Recall): Measures the proportion of actual positives correctly identified.

$$RE = \frac{TP}{TP + FN}$$

where TP represents true positives and FN represents false negatives

- SP (Specificity): Represents the proportion of actual negatives correctly identified.

$$SP = \frac{TN}{TN + FP}$$

where TN represents true negatives and FP represents false positives.

- FPR (False Positive Rate): The proportion of false positives among all actual negatives.

$$FPR = \frac{FP}{FP + TN}$$

- FNR (False Negative Rate): The proportion of false negatives among all actual positives.

$$FNR = \frac{FN}{TP + FN}$$

- PWC (Percentage of Wrong Classifications): Indicates the percentage of incorrectly classified instances (false positives and false negatives) out of the total number of classifications.

$$PWC = \frac{100 * (FN + FP)}{TP + FN + FP + TN}$$

- F-M (F-Measure): The harmonic mean of precision and recall, providing a balance between the two

$$F - measure = \frac{2 * Precision * Recall}{Precision + Recall}$$

- PR (Precision): Measures the proportion of correctly predicted positives out of all predicted positives.

$$PR = \frac{TP}{TP + FP}$$

4.2.1. Quantitative evaluation using the CDnet 2014 dataset

Table 1 shows seven evaluation metrics for our moving object detection approach based on background subtraction, fuzzy entropy thresholding, and differential evolution optimization (MOD-BFDO) using the CDnet 2014 dataset. Our methodology has been tested in various scenarios, including uniform lighting conditions, shadow areas, long-range scene occlusion environments, the presence of multiple targets, and weak signals. MOD-BFDO effectively adapts to dynamic backgrounds and fast-moving objects, as well as slow background changes and static objects in scenes.

Tab. 1. Evaluation of our method on the CDnet 2014

| Category | RE | SP | FPR | FNR | PWC | F-M | PR |
|-------------|--------|--------|--------|--------|--------|--------|--------|
| Baseline | 0.9577 | 0.9911 | 0.0021 | 0.0423 | 0.3634 | 0.9409 | 0.9432 |
| Bad weather | 0.8950 | 0.9970 | 0.0004 | 0.1053 | 0.5212 | 0.8834 | 0.8723 |
| Dy. Backg | 0.8839 | 0.9989 | 0.0013 | 0.2332 | 0.6121 | 0.9051 | 0.9272 |
| Shadow | 0.8704 | 0.9917 | 0.0082 | 0.1295 | 1.6663 | 0.8785 | 0.8869 |
| Cam. Jitter | 0.8154 | 0.9945 | 0.0057 | 0.1864 | 1.2627 | 0.8332 | 0.8515 |
| Law. Fram | 0.7610 | 0.9934 | 0.0061 | 0.2492 | 0.9064 | 0.6800 | 0.6146 |
| Average | 0.8639 | 0.9944 | 0.0039 | 0.1576 | 0.7220 | 0.8535 | 0.8492 |

The advantages of MOD-BFDO are supported by the high precision, recall, F-measure and PWC scores shown in Table 2. Notably, MOD-BFDO shows higher recall and F-measure, as well as lower PWC, highlighting its ability to detect foreground and background pixels while minimizing errors. Compared to many traditional approaches, including those outside the deep learning domain, our method also outperforms deep learning-based models, approaching the performance of the SuBSENSE [24] algorithm in terms of accuracy.

Tab. 2. Comparative assessment of F-measure in six categories using four methods. Each row presents results specific to each method; each column displays the average scores in each category

| Methods | F-M | | | | | | |
|---------------|----------|-------------|-----------|--------|-------------|----------|---------|
| | Baseline | Bad weather | Dy. Backg | Shadow | Cam. Jitter | Law Fram | Overall |
| DeepBS [27] | 0.9580 | 0.8301 | 0.8761 | 0.9304 | 0.8990 | 0.6002 | 0.8490 |
| SC_SOBS [25] | 0.9333 | 0.6620 | 0.6686 | 0.7786 | 0.7051 | 0.5463 | 0.7158 |
| SuB-SENSE[24] | 0.9503 | 0.8619 | 0.8177 | 0.8646 | 0.8152 | 0.6445 | 0.8257 |
| GMM_Zivk [26] | 0.8382 | 0.7406 | 0.6328 | 0.7322 | 0.5670 | 0.5065 | 0.6696 |
| MOD-BFDO | 0.9409 | 0.8834 | 0.9051 | 0.8785 | 0.8332 | 0.6800 | 0.8535 |

In comparison with other ranked methods on the dataset in Table 3, MOD-BFDO stands out once again, especially in terms of F-measure scores, which combine recall and precision. Even in the Law framerate category, where some approaches use more sophisticated frame-level motion analysis techniques, our method excels. Overall, we maintain the highest F-measure scores in four out of six categories, surpassing the second-best method with an 8.53% relative improvement in the overall F-measure, exclusively for the CDnet 2014 dataset. These results highlight the exceptional flexibility of our method, capable of adapting to the most challenging change detection scenarios.

Tab. 3. A comparison between our method and some of the most important existing methods on CDnet 2014 dataset

| Methods | Overall | | | |
|---------------|---------|---------|----------|----------|
| | Avg. RE | Avg. PR | Avg. PCW | Avg. F-M |
| DeepBS [27] | 0.8312 | 0.8712 | 0.6373 | 0.8490 |
| SC_SOBS [25] | 0.8068 | 0.7141 | 2.1462 | 0.7158 |
| SuBSENSE [24] | 0.8615 | 0.8606 | 0.8116 | 0.8257 |
| GMM_Zivk [26] | 0.7155 | 0.6722 | 1.7052 | 0.6696 |
| MOD-BFDO | 0.8639 | 0.8492 | 0.72202 | 0.8535 |

4.2.2. Statistical Stability Test

In this part, we present a comparative analysis of the performance of the MOD-BFDO method against other object detection methods, based on the mean F-measure and standard deviations calculated for each method. We then apply a z-test to assess the statistical significance of the differences between these methods.

Tab. 4. Mean F-measure and standard deviations for different methods

| Methods | Mean F-M (μ) | Standard Deviation (σ) |
|---------------|--------------------|---------------------------------|
| MOD-BFDO | 0.8535 | 0.0920 |
| SuBSENSE [24] | 0.8257 | 0.1013 |
| DeepBS [27] | 0.8490 | 0.1296 |
| SC_SOBS [25] | 0.7158 | 0.1306 |
| GMM_Zivk [26] | 0.6696 | 0.1232 |

The standard deviation σ for each method is calculated using the following formula:

$$\sigma = \sqrt{\frac{1}{n-1} \sum_{i=1}^n (X_i - \bar{X})^2}$$

where:

X_i : is the F-measure for each category.

\bar{X} : is the mean F-measure for the method.

n : is the number of categories.

To compare the performance of MOD-BFDO with other methods, we use the following z-test equation:

$$z = \frac{\bar{X}_{MOD} - \bar{X}_{compared}}{\sqrt{\frac{\sigma_{MOD}^2}{n_{MOD}} + \frac{\sigma_{compared}^2}{n_{compared}}}}$$

where:

\bar{X}_{MOD} : is the mean F-measure for MOD-BFDO.

$\bar{X}_{compared}$: is the mean F-measure for the compared method.

σ_{MOD} and $\sigma_{compared}$ are the standard deviations of the respective methods

n_{MOD} and $n_{compared}$ are the number of samples (here $n=6$ for each method).

Tab. 5. Z-scores for MOD-BFDO vs other methods

| Comparison | z-Score |
|----------------------|---------|
| MOD-BFDO vs SuBSENSE | 0.498 |
| MOD-BFDO vs DeepBS | 0.069 |
| MOD-BFDO vs SC_SOBS | 2.11 |
| MOD-BFDO vs GMM_Zivk | 2.93 |

The z-test was applied to assess whether the performance differences in terms of F-measure between MOD-BFDO and the other methods are statistically significant at the 95% confidence level. For this confidence level, the critical value is 1.96, meaning that any z-score greater than 1.96 or less than -1.96 indicates a significant difference.

The results show that the differences between MOD-BFDO and SuBSENSE ($z = 0.498$) as well as DeepBS ($z = 0.069$) are not significant, as the z-scores are below 1.96. However, the differences with SC_SOBS ($z = 2.11$) and GMM_Zivk ($z = 2.93$) are statistically significant, indicating that MOD-BFDO significantly outperforms these two methods at the 95% confidence level. These results confirm the robustness and effectiveness of MOD-BFDO in complex environments, particularly in comparison with older methods such as SC_SOBS and GMM_Zivk.

4.2.3. Quantitative evaluation using the LASIESTA dataset

Tab. 6. Results obtained by the proposed algorithm on the LASIESTA dataset

| Category | RE | PWC | F-M | PR |
|----------|--------|--------|--------|--------|
| I_SI | 0.8969 | 0.5501 | 0.9089 | 0.9219 |
| I_CA | 0.7930 | 1.2835 | 0.8415 | 0.9250 |
| I_BS | 0.7015 | 0.4164 | 0.7120 | 0.7457 |
| O_SU | 0.8868 | 0.1917 | 0.8938 | 0.9038 |
| Average | 0.8195 | 0.6104 | 0.8390 | 0.8741 |

Tab. 7. Comparative assessment of F-measure across four categories using four methods on the LASIESTA dataset. Each row presents the results for a specific method, while each column displays the average scores for each category

| Methods | F-M | | | | |
|---------------|--------|--------|---------|--------|---------|
| | I_SI | I_CA | I_BS | O_SU | Overall |
| GMM [31] | 0.8328 | 0.8272 | 0.36941 | 0.7240 | 0.6880 |
| GMM_Zivk [26] | 0.9054 | 0.8320 | 0.5330 | 0.7100 | 0.7450 |
| Cuevas [32] | 0.8805 | 0.8440 | 0.6809 | 0.8568 | 0.8155 |
| Our approach | 0.9089 | 0.8415 | 0.7021 | 0.8938 | 0.8390 |

The results from both tables provide a comparative evaluation of different methods applied to the LASIESTA dataset. In Table 6, our proposed approach demonstrates strong performance, with an average F-measure of 0.8390 and high scores in categories I_SI (0.9089) and O_SU (0.8938), indicating robust capability in detecting objects in diverse environments. In comparison, Table 7 shows the results of other methods. Our method outperforms the GMM [31] and GMM_Zivkovic [26] approaches in terms of overall F-measure (0.8390 vs. 0.6880 and 0.7450, respectively) and slightly surpasses the Cuevas approach (0.8390 vs. 0.8155). This highlights the enhanced efficiency of our algorithm in handling complex and heterogeneous scenes.

4.2.4. Real-time assessment

In this section, we compare the average frames per second (FPS) across several algorithms using videos from the SBI2015, CDnet 2014 and LASIESTA datasets. To assess processing speed, we selected four videos with resolutions of (320x240, 352x288 and 720x480). All videos were recorded at 25 fps, and frames were converted to grayscale before applying the algorithms. Table V summarizes the average FPS results obtained on our system, equipped with an Intel(R) Core (TM) i7-4700MQ CPU @ 2.40GHz and implemented in C++.

For real-time applications, GMM_Zivkovic [26] emerges as the most suitable method due to its high FPS performance. MOD-BFDO offers a balanced alternative, providing a compromise between speed and accuracy. On the other hand, SC_SOBS [25] and SuBSENSE show lower FPS, especially for larger videos, which makes them less ideal for real-time scenarios involving high-resolution content.

Tab. 8. Comparison of Average Frames Per Second (FPS) Across Three Source Video Sequences

| Methods | Size of video | | |
|---------------|---------------|---------|---------|
| | 320x240 | 352x288 | 720x480 |
| SC_SOBS [25] | 9.8 | 8.7 | 3.4 |
| SuBSENSE [24] | 3.3 | 2.8 | 1.6 |
| GMM_Zivk [26] | 21.6 | 18.1 | 13.8 |
| MOD-BFDO | 5.5 | 4.7 | 3.2 |

5. CONCLUSION

In conclusion, our experimental results conclusively demonstrate that our MOD-BFDO method represents a significant advance in detecting moving objects in videos. Compared to object detection algorithms, whether based on deep learning or not, our approach stands out for its ability to provide superior performance, especially in difficult conditions such as lighting variations, long ranges, baseline changes, and other complex scenarios.

The innovative combination of background subtraction, fuzzy entropy-based multi-level image thresholding, and differential evolution algorithm achieved remarkable results. Background subtraction provides a crucial first step to isolating moving objects, while multi-level image thresholding based on fuzzy entropy improves robustness to environmental variations.

The optimization of the fuzzy entropy threshold parameters by the differential evolution algorithm was instrumental in obtaining superior performance. This iterative approach made it possible to maximize the detection of moving objects, while minimizing false positives, thus strengthening the precision and reliability of our method.

In summary, the results of our experiments position our MOD-BFDO method as a promising and competitive solutions for detecting moving objects. These advances open up exciting prospects for applying our method in areas such as surveillance, robotics, and computer vision, demonstrating its potential to address the complex challenges of detecting moving objects in dynamic and varied environments.

REFERENCES

1. Tsai DM, Lai SC. Independent component analysis-based background subtraction for indoor surveillance. *IEEE Trans Image Process.* 2009;18(1):158-67. Available from: <https://doi.org/10.1109/tip.2008.2007558>
2. Stauffer C, Grimson WEL. Adaptive background mixture models for real-time tracking. *Proc IEEE Comput Vis Pattern Recognit.* 2003;246-52. Available from: <https://doi.org/10.1109/cvpr.1999.784637>
3. Xing-ju W, Yu-wei H, Ran-hang O. Method, model and application for the conversion from vague sets to fuzzy sets. *Proc Int Conf Artif Intell Comput Intell AICI.* 2009;510-3. Available from: <https://doi.org/10.1109/aici.2009.397>
4. Storn R, Price K. Differential evolution—a simple and efficient heuristic for global optimization over continuous spaces. *J Glob Optim.* 1997;11:341-59. Available from: <https://doi.org/10.1023/A:1008202821328>
5. Das S, Ponnuthurai S. Differential evolution: a survey of the state-of-the-art. *IEEE Trans Evol Comput.* 2011;15(1):4-31. Available from: <https://doi.org/10.1109/tevc.2010.2059031>
6. Sarkar S, Paul S, Burman R, Das S, Chaudhuri S. A fuzzy entropy-

- based multi-level image thresholding using differential evolution. Int Conf Swarm Evol Memet Comput. 2014;386–95. Available from: https://doi.org/10.1007/978-3-319-20294-5_34
7. Nihal P, Ashish S, Abhishek M, Partha P, Debi D. Moving object detection using modified temporal differencing and local fuzzy thresholding. J Supercomput. 2017;73:1120–39. Available from: <https://doi.org/10.1007/s11227-016-1815-7>
8. Charansiripaisan K, Sirapat C, Khamron S. A global multilevel thresholding using differential evolution approach. Math Probl Eng. 2014;1–23. Available from: <https://doi.org/10.1155/2014/974024>
9. Yuanyuan J, Dong Z, Wenchang Z, Li W. Multi-level thresholding image segmentation based on improved slime mould algorithm and symmetric cross-entropy. Entropy. 2023;25(1):178. Available from: <https://doi.org/10.3390/e25010178>
10. Jinzhong Z, Tan Z, Duansong W. A complex-valued encoding golden jackal optimization for multilevel thresholding image segmentation. Appl Soft Comput. 2024;165:112108. Available from: <https://doi.org/10.1016/j.asoc.2024.112108>
11. Giveki D. Robust moving object detection based on fusing Atanassov's intuitionistic 3D fuzzy histogram roughness index and texture features. Int J Approx Reason. 2021;135:1–20. Available from: <https://doi.org/10.1016/j.ijar.2021.04.007>
12. Giveki D, Montazer A, Soltanshahi A. Atanassov's intuitionistic fuzzy histogram for robust moving object detection. Int J Approx Reason. 2017;91:80–95. Available from: <https://doi.org/10.1016/j.ijar.2017.08.014>
13. Giveki D, Soltanshahi A, Yousefvand M. Proposing a new feature descriptor for moving object detection. Optik. 2020;209:164563. Available from: <https://doi.org/10.1016/j.ijleo.2020.164563>
14. Hathiram N, Ravi J. Hybridizing sine cosine algorithm with differential evolution for global optimization and object tracking. Appl Soft Comput. 2018;62:1019–43. Available from: <https://doi.org/10.1016/j.asoc.2017.09.039>
15. Yi W, Zhiming L, Pierre-Marc J. Hybridizing sine cosine algorithm with differential evolution for global optimization and object tracking. Appl Soft Comput. 2018;62:1019–43. Available from: <https://doi.org/10.1016/j.asoc.2017.09.039>
16. Cao W, Yuan J, He Z. Fast deep neural networks with knowledge guided training and predicted regions of interests for real-time video object detection. IEEE Access. 2018;6:8990–9. Available from: <https://doi.org/10.1109/access.2018.2795798>
17. Garcia-Aguilar I, Jorge G, Rafael M, Ezequiel L. Automated labeling of training data for improved object detection in traffic videos by fine-tuned deep convolutional neural networks. Pattern Recognit Lett. 2023;167:45–52. Available from: <https://doi.org/10.1016/j.patrec.2023.01.015>
18. Talukdar J, Gupta S, Rajpura P, Hegde R. Transfer learning for object detection using state-of-the-art deep neural networks. Int Conf Signal Process Integr Netw SPIN. 2018. Available from: <https://doi.org/10.1109/spin.2018.8474198>
19. Boufares O, Aloui N, Cherif A. Adaptive threshold for background subtraction in moving object detection using stationary wavelet transforms 2D. Int J Adv Comput Sci Appl. 2016;7(8). Available from: <https://doi.org/10.14569/ijacsa.2016.070805>
20. Lu G, Kudo M, Toyama J. Temporal segmentation and assignment of successive actions in a long-term video. Pattern Recognit Lett. 2013;34(15):1936–44. Available from: <https://doi.org/10.1016/j.patrec.2012.10.023>
21. Yong X, Jixiang D, Bob Z, Daoyun X. Background modeling methods in video analysis: A review and comparative evaluation. CAAI Trans Intell Technol. 2016;1(1):43–60. Available from: <https://doi.org/10.1016/j.trit.2016.03.005>
22. Carolina R, Roberto L. Unsupervised learning from videos using temporal coherency deep networks. Comput Vis Image Underst. 2019;179:79–89. Available from: <https://doi.org/10.1016/j.cviu.2018.08.003>
23. Oliver N, Rosario B, Pentland A. A Bayesian computer vision system for modeling human interactions. IEEE Trans Pattern Anal Mach Intell. 2000;22(8):831–43. Available from: <https://doi.org/10.1109/34.868684>
24. Pierre-Luc S, Guillaume B, Robert B. SUBSENSE: A universal change detection method with local adaptive sensitivity. IEEE Trans Image Process. 2015;24(1):359–73. Available from: <https://doi.org/10.1109/tip.2014.2378053>
25. Maddalena L, Petrosino A. The SOBS algorithm: What are the limits? Proc IEEE Workshop Change Detect CVPR. 2012. Available from: <https://doi.org/10.1109/cvprw.2012.6238922>
26. Zivkovic Z. Improved adaptive Gaussian mixture model for background subtraction. Proc 17th Int Conf Pattern Recognit ICPR. 2004. Available from: <https://doi.org/10.1109/icpr.2004.1333992>
27. Bouwmans T, Javed S, Sultana M, Jung S. Deep neural network concepts for background subtraction: A systematic review and comparative evaluation. arXiv. 2018. Available from: <https://arxiv.org/pdf/1811.05255>
28. Wang Y, Jodoin PM, Porikli F, Konrad J, Benezeth Y, Ishwar P. CDnet 2014: An expanded change detection benchmark dataset. Proc IEEE Conf Comput Vis Pattern Recognit Workshops. 2014;387–94. Available from: <https://www.opencv.org>
29. Maddalena L, Petrosino A. Towards benchmarking scene background initialization. Proc ICIAP Workshops. 2015;469–76. Available from: <http://sbmi2015.na.icar.cnr.it/>
30. Cuevas C, Yez EM, García N. Labeled dataset for integral evaluation of moving object detection algorithms: LASIESTA. Comput Vis Image Underst. 2016;152:103–17. Available from: <https://doi.org/10.1016/j.cviu.2016.01.012>
31. Stauffer C, Grimson WEL. Learning patterns of activity using real-time tracking. IEEE Trans Pattern Anal Mach Intell. 2000;22(8):747–57. Available from: <https://doi.org/10.1109/34.868684>
32. Berjón D, Cuevas C, Morán F, García N. Real-time non-parametric background subtraction with tracking-based foreground update. Pattern Recognit. 2018;74:156–70. Available from: <https://doi.org/10.1016/j.patcog.2017.09.009>
33. Vacavant A, Chateau T, Wilhelm A, Lequievre L. A benchmark dataset for outdoor foreground/background extraction. Proc Asian Conf Comput Vis ACCV. 2012.

Oussama Boufares:  <https://orcid.org/0000-0003-2488-0666>

Mohamed Boussif:  <https://orcid.org/0000-0003-3198-7605>

Wajdi Saadaoui:  <https://orcid.org/0000-0001-8977-9652>

Imed Miraoui:  <https://orcid.org/0000-0001-5003-6683>



This work is licensed under the Creative Commons BY-NC-ND 4.0 license.

FORCED CONVECTION HEAT DISSIPATION FROM PIN FIN HEAT SINKS MODIFIED BY RINGS AND CIRCULAR PERFORATION

Karima ALEM^{*✉}, Djamel SAHEL^{**✉}, Warda BOUDAUD^{***✉}, Redouane BENZEGUIR^{*✉}

^{*}Laboratoire des Carburants Gazeux et Environnement, Faculté de Génie Mécanique, USTO-Mohamed Boudiaf, Oran, Algeria

^{**}Département du Tronc commun des Sciences et de Technologie, Faculté de Technologie, Université Amar Telidji de Laghouat, Algeria

^{***}Laboratoire des Science et Ingénierie Maritimes, Faculté de Génie Mécanique, USTO-Mohamed Boudiaf, Oran, Algeria

Karima.alem@univ-usto.dz, d.sahel@lagh-univ.dz, warda.boudaoud@univ-usto.dz, benzeguiouane@gmail.com

received 15 June 2024, revised 10 August 2024, accepted 02 September 2024

Abstract: The primary factors to be managed in the design of heat sinks include enhancing the heat dissipation rate, minimizing occupied volume and mass, and eliminating lower heat transfer areas behind the pin fins. This study focuses on numerically analysing the impact of combining perforation technique and ring inserts on the heat dissipation and turbulent fluid flow characteristics of pin fin heat sinks. The rings are positioned around the cylindrical pin fins (CPFs). The perforation technique allows fluid flow to pass through the pin fins (PFs) and agitate the stagnant zones of flow behind PFs. These configurations are denoted as case 0 (no perforation) to case 4. Results show that fitted with rings and perforation (case 4), as an optimal configuration, demonstrates a 180.82% increase in Nusselt number and a 154.54% decrease in thermal resistance compared to CPFs. Fortunately, this configuration contributes to a significant decrease in the pressure drop by 62.19%. Furthermore, under the same conditions, the occupied volume and mass of case 4 are reduced by 77.5% and 77.65%, respectively. Additionally, the optimal configuration exhibits the highest hydrothermal performance factor (η) of 3.29 at $Re = 8740$.

Key words: Heat sink; heat dissipation; perforated space; pin fins; ring

1. INTRODUCTION

In recent years, there has been a trend in electronic devices towards higher frequencies and smaller sizes, resulting in a significant increase in power density. This has led to chip-level heat dissipation exceeding 1000 W/cm² for compound semiconductor devices (1). The elevated temperatures resulting from inadequate heat dissipation pose a significant challenge to device reliability, and improper thermal management can result in complete device failure. It is empirically observed that for every 10 degrees Celsius reduction in the temperature of electronic components, the failure rate is halved (2). Therefore, in order to achieve optimal performance, electronic devices must be equipped with advanced cooling technologies that offer enhanced heat dissipation capabilities to improve cooling efficiency and maintain the device at an appropriate temperature level to ensure proper system functionality (3,4). A heat sink is an important component that fixed on heated electronic devices to cool them. Through conductive and convective heat transfer, heat sink effectively dissipates generated heat by electronic devices(5).

There are several fluids used for cooling electronic systems, such as nanofluids (6–10), hybrid nanofluids (11–15) and phase change materials (PCM) (16–19). However, the latter fluids still pose economic costs and technological challenges. Usually utilized air-cooling technologies are becoming inadequate in meeting the cooling requirements of modern high-power small-sized devices. Air is free, available in nature, does not pose any technical problems to electronic devices, such as leaks(20,21).

Vortex generators (VGs)(22,23), perforation (24,25) and splitters insert (26,27) have become efficient strategies that

are favored techniques of cooling by air. Alam et al (28) tested heat transfer characteristics of PFHS by using triangular vortex generator mounted on heat sink of central processing unit (CPU). They showed that Nusselt number (Nu) increases with increasing of air velocity which is enhances the thermal performance of CPU. In this context, the wavy way of channel heat sinks can also enhance heat dissipation rates by developing of the flow structure (29).

Bezaatpour and Goharkhah (30) analyzed the impact of porous media on the performance of two conventional pin fins heat sink (circular and rectangular). They used Fe₃O₄ nanofluid as a working fluid. In the presence of porous media, the two cases showed an increase in Nusset number by 450% and 547%. Chin et al (31) numerically and experimentally studied the effect of number (N) and diameter (DP) of perforation on heat transfer and fluid flow behaviors of CPFHSs. They reported that $N=5$ and $DP=3mm$ offer the best performance by an increase in Nusselt number by 45% compared to the conventional pin fins (CPFes).

Sajedi et al (32) numerically studied the effect of splitters on the performance of PFHS. They showed that splitters insert behind the cylindrical pin fins (CPFes) reduces pressure drop by 13.4 %, thermal resistances decrease by 36.8 %. In addition, they reported that splitters can reduces the formation of flow recirculation zones behind CPFes. Abdemohimen et al (33) analyzed the influence of splitters with different deviation angles which are varied from 0° to 90° than the flow direction. For staggered arrangements of CPFes, the angle of 22.5° achieved better hydro thermal performance factor. In this context, several papers were confirmed that the perforation technique not only enhance heat transfer coefficient by its also reduce pressure drops in different shapes of heat sinks (34,35). Meganathan et al(36) reported that the best design of heat sinks consists to consider some geometric parameters such as the height,

length, the thickness, the number of the fins and the material of the construction. Haque et al (37) analyzed different shapes of perforation and budes for create better mixture of flow. The studies are conducted using a CFD program for Reynolds numbers (Re) varying from 8547 to 21,367. They indicate that elliptical pin fins significantly improve the hydro-thermal performance factor (HTPF).

Specifically, the circular perforated elliptical pin fin achieves a peak HTPF of 1.72 as the Re varies from 8547 to 21,367.

This study proposes a new design that integrates perforation

through CPFHSs fitted with rings located around CPFs. In this new design, perforation and rings were combined in different configurations. Rings augments heat transfer surface, where the perforation technique helps also augments heat transfer area, reduces mass of heat sink and develop the flow structure behind the pin fins. The simulation was carried out using Comsol Multiphysics v.5.4 software to model turbulent fluid flow and heat transfer within the heat sinks.

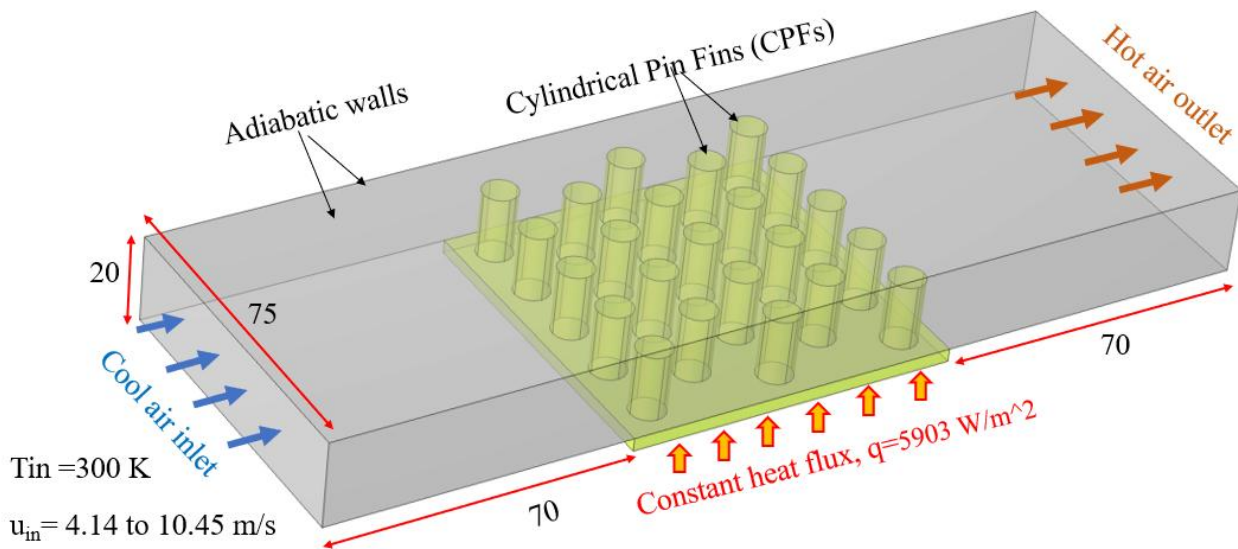


Fig. 1. General illustration and dimensions (in mm) of air flow channel heat sink

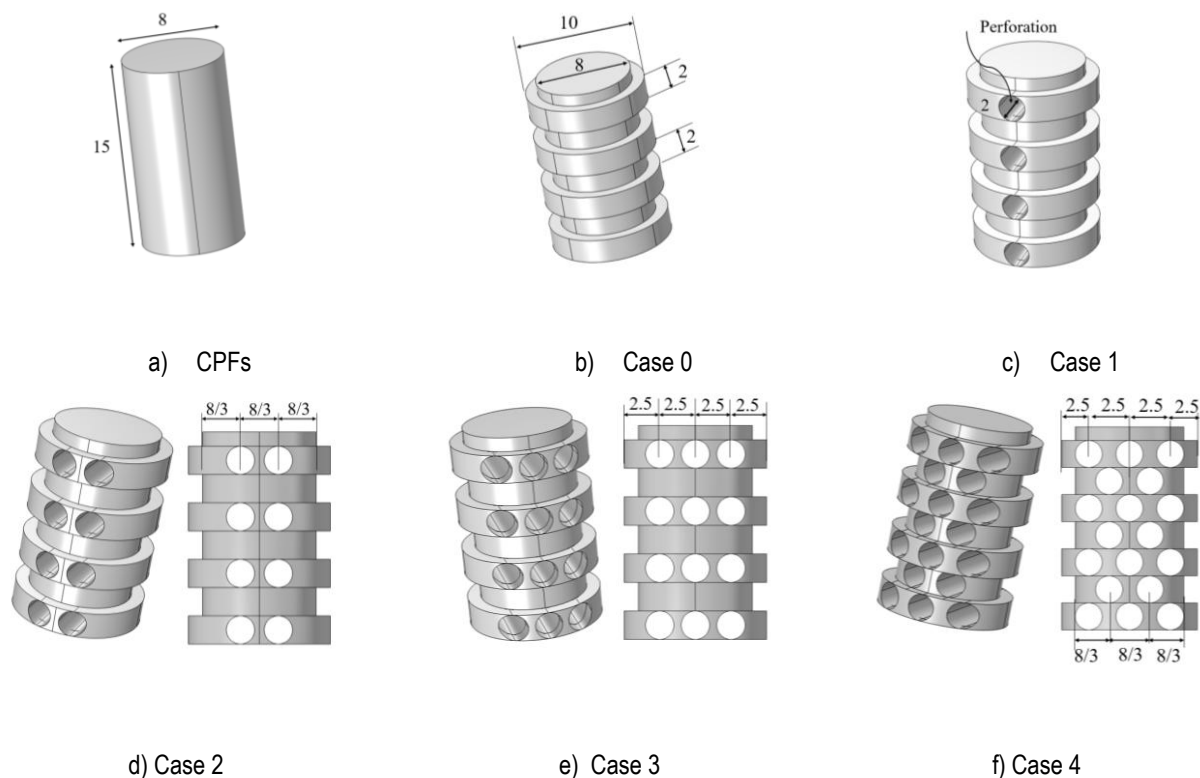


Fig. 2. Detailed dimensions (in mm) of different heat sink configurations

2. NUMERICAL METHODOLOGY

2.1. Physical model

A set of three-dimensional Computational Fluid Dynamics (CFD) simulations were conducted to study the hydro-thermal efficiency of different pin-fin heat sinks (PFHSs), as illustrated in Figures 1 and 2. These PFHSs consist of a base plate with fins arranged in a staggered manner, placed within a channel as depicted in Fig. 1. The dimensions of the base plate are $75 \times 75 \times 2 \text{ mm}^3$ and of the channel are $215 \times 75 \times 20 \text{ mm}^3$. Both the base plate and fins were constructed from A8350P aluminum. The staggered cylindrical pin fin (CPFs) heat sink from a previous study was used as a benchmark to validate the methodology employed in this research. Combination between ring and perforation techniques was analyzed parametrically under fully turbulent flow conditions using three-dimensional CFD simulations. This combination was results five cases named as: case 0, case 1, case 2, case 3, case 4. Simulation was realized for Reynolds number (Re) ranging from 8740 to 22,060. The longitudinal and transversal distances of the pins are set to 15 mm. all dimensions of channel and heat sinks were illustrated in Figs.1 and 2.

2.2. Governing formulation and boundary conditions

The fluid flow state is considered to be turbulent flow with single-phase characteristics. In the context of fluid-solid conjugate heat transfer in channel heat sinks, several assumptions are employed to simplify the numerical calculation process as:

- Both air flow and heat transfer are assumed to be in steady states.
- The air is treated as single-phase, Newtonian and incompressible.
- Radiation heat transfer is neglected.
- The influence of gravity is ignored.
- The thermo-physical properties of the fluid are assumed to be constants.
- No-slip conditions are assumed at the solid-fluid interface.

These assumptions lead to the formulation of control equations appropriate for the analysis of steady states fluid flow and heat transfer (38) (39), which includes the continuity equation, momentum equation, energy equation, and conduction energy equation (27).

$$\frac{\partial u_i}{\partial x_i} = 0 \quad (1)$$

$$\frac{\partial}{\partial x_i} (\rho u_i u_j) = \frac{\partial}{\partial x_i} \left[\mu \left(\frac{\partial u_i}{\partial x_j} - \overline{\rho u'_i u'_j} \right) \right] - \frac{\partial p}{\partial x_i} \quad (2)$$

$$\frac{\partial (u_j T)}{\partial x_j} = \alpha \nabla^2 T + \frac{\partial}{\partial x_j} (-\overline{u'_j \theta}) \quad (3)$$

$$\nabla \cdot (\lambda_s \nabla T_s) = 0 \quad (4)$$

Where, λ_s is the thermal conductivity of A8350P Aluminum ($167 \text{ W/m} \cdot \text{K}$), T_s is the temperature field in the Aluminum-solid heat sink.

For closing the equation system, standard k- ϵ turbulence model was used in this study. This model is largely used to estimate heat

transfer and fluid flow in thermal systems(20,33,40,41). Also, this model is better to predict turbulent flow in channels(42).

In order to evaluate heat transfer, performance and fluid flow behaviors of different PFHSs, we used some parameters which are summarized as follows (20).

Nusselt number (Nu):

$$Nu = \frac{q D_h}{\lambda_{air}(T_W - (T_{in} + T_{out})/2)} \quad (5)$$

Where, q is the constant heat flux on the base plate of heat sink (5903 W/m^2), λ_{air} is the thermal conductivity of air ($0.024 \text{ W/m} \cdot \text{K}$). T_{in} , T_{out} is the temperatures in the inlet and outlet of channel respectively. T_W is the mean temperature of walls of the base plate and pin fins.

Thermal resistance (R_{th}):

$$R_{th} = (T_W - T_{in})/q \quad (6)$$

Pressure drops (Δp):

$$\Delta p = p_{in} - p_{out} \quad (7)$$

Hydro thermal performance factor (η);

$$\eta = \left(\frac{Nu}{Nu_{CPFHS}} \right) / \left(\frac{\Delta p}{\Delta p_{CPFHS}} \right)^{\frac{1}{3}} \quad (8)$$

Pumping power (P_p):

$$P_p = u_{in} \times A_c \times \Delta p \quad (9)$$

Where, u_{in} is the speed in the inlet of channel, A_c is the contact solid-fluid surface, Δp is the pressure difference between inlet (p_{in}) and outlet (p_{out}) of channel heat sink.

The regime of the air turbulent flow can be determined by using Reynolds number (Re):

$$Re = \frac{u_{in} \times D_h}{\nu} \quad (10)$$

Reynolds number (Re) is determined at the hydraulic diameter (D_h) and it ranging from 8740 to 22060 corresponding of inlet velocity interval of 4.14 to 10.45 m/s. Where the temperature in the inlet is set to 300K.

2.3. Numerical method and procedure

The simulation of conjugate heat transfer and turbulent fluid flow characteristics was conducted using the CFD software COMSOL Multi-Physics v. 5.4. The Reynolds Average Navier Stocks (RANS) and energy equations were discretized through the finite element method (FEM). Convergence criteria of 10^{-6} and 10^{-9} were set for the RANS and energy equations, respectively.

Grid sensitivity analyzes were performed to ensure the accuracy of the numerical model. Tetrahedral and unstructured grid were generated for each case to determine the most efficient independent grid mesh (Fig.3).

A free tetrahedral type mesh was utilized for all numerical domains. Different grid sizes were tested for validation, for example, for CPFHSs arrangement, the grid of 1,367,577 was selected for following simulation.

Because, this case illustrated that Nusselt number (Nu) results showed that its deviation does not less than 1% compared to the refined grid cases. Similar grid independence assessments were carried out for other cases, resulting in the selection of specific grid sizes for each case.

Fig.4 show an example of the test of the grid sensibility for the case 4. The simulations were run on a computing station with a CPU i7 and a frequency of 2.6 GHz and 16 Go of RAM, with each simulation typically taking around 4 hours.

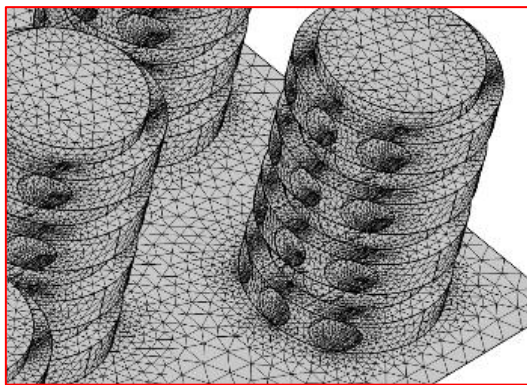
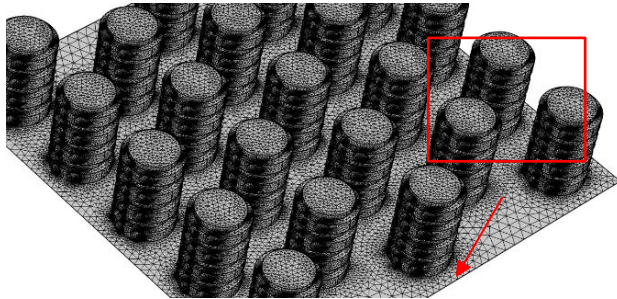


Fig. 3. Example of generated tetrahedral mesh, Case 4

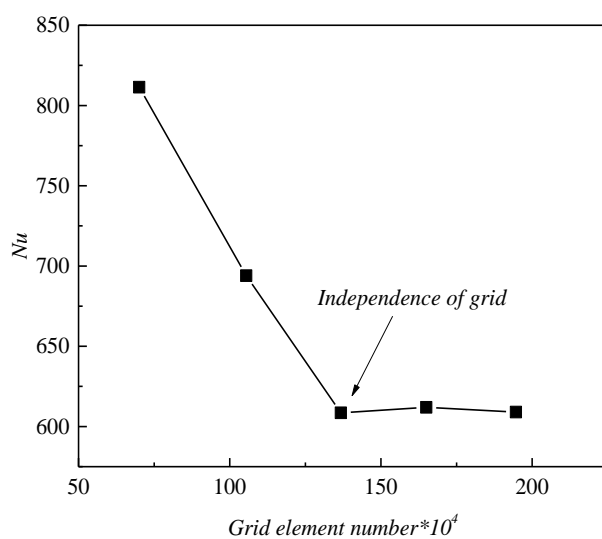


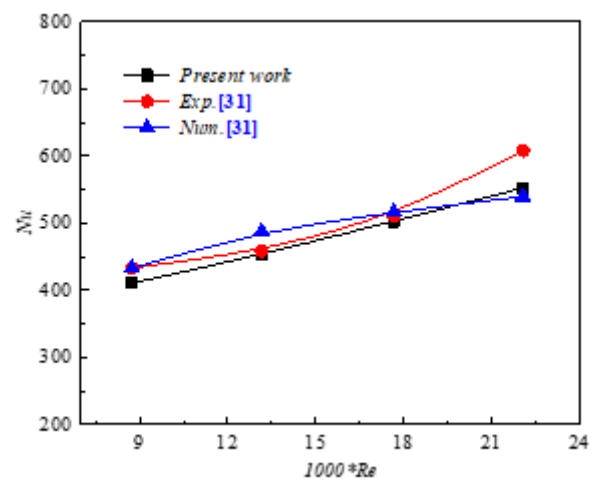
Fig. 4. Test of grid independence for CPFs

3. RESULTS AND DISCUSSION

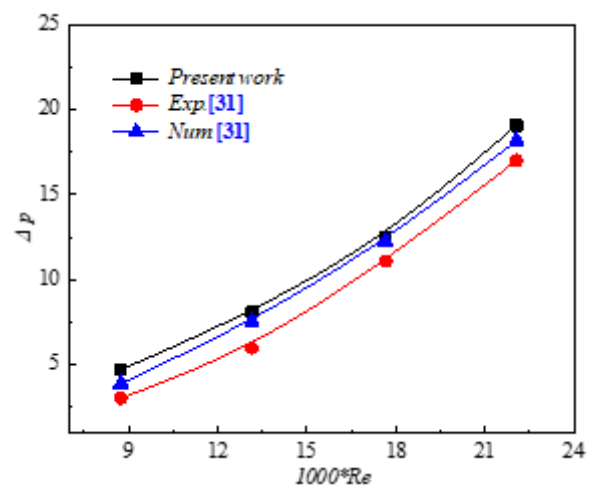
3.1. Validation of results

It is crucial to evaluate the accuracy of the current model for realized the following simulations. This evaluation includes confirming the results by comparing them with available data from literature (31). For the validation, we utilized both Nusselt number (Nu) and pressure drop (Δp).

Figs 5(a) and 5(b) depict the variation of Nu and Δp versus Reynolds number (Re), respectively. The examination of Nu results indicated a maximum deviation of 11.51% and 2.60% in comparison to the experimental and numerical results of Chin et al (31). Similarly, the assessment of Δp results displayed a deviation of 15.83% and 8.21%. These deviations due to the utilization of three thermocouples in the inlet of the channel and other three thermocouples in the outlet by Chin et al (31). Where, in the present study, we used the mean surfaces of the inlet and outlet to evaluate the temperatures.



a) Nusselt number (Nu) results



b) Pressure difference (Δp) results

Fig. 5. Validation of results for CPFs

3.2. Hydraulic and thermal aspects

One factor that can reduce the effectiveness of CPFs is the creation of air vortices behind the pin at very low speeds (43), resulting in the formation of hot points or lower heat transfer areas (LHTAs)(44,45). Figs. 6 and 7 show the distribution of velocity streamlines and temperature contours for cases 0 and 4 as typical arrangements. In Fig. 6, the airflow splits into two regions as it passes over the sides of the cylindrical pins, with one region having high speeds that are conducive to heat transfer due to the turbulence of air molecules. The second region, located directly behind the pin fins, experiences low-velocity eddies, leading to the formation of hot spots and decreased heat transfer rates.

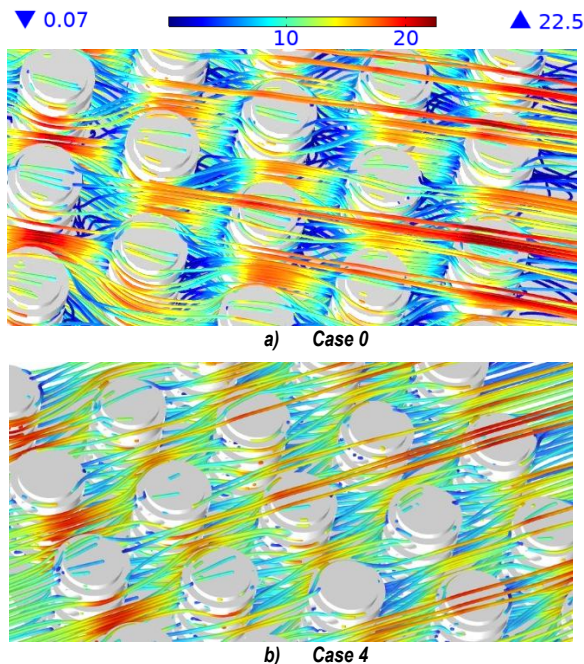
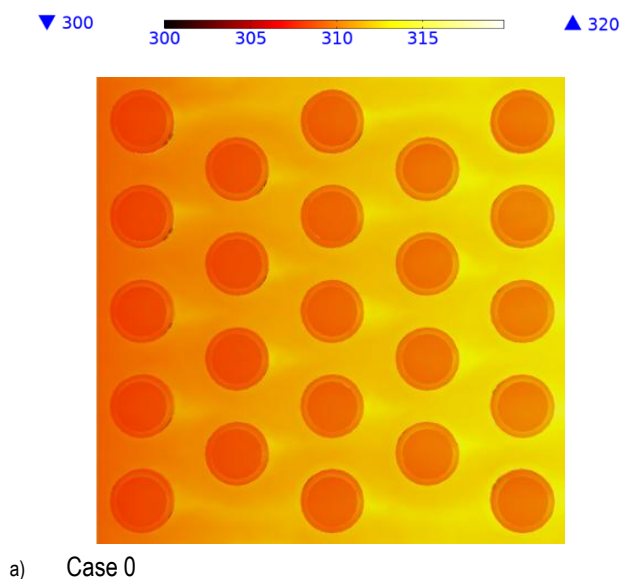


Fig. 6. Velocity streamline distribution (m/s) for a) case 0 b) and case 4 at $Re=22060$



b) Case 4

Fig. 7. Contours of local temperature distribution (K) for a) case 0 b) and case 4 at $Re=22060$

To address this issue, solutions such as adding rings insert and perforation space have been proposed, as depicted in these figures. By adding rings around CPFs, the area of low-velocity regions can be reduced, decreasing recirculation flow zones and increasing heat transfer areas. Finally, the use of perforation techniques helps to reduce recirculation flow zones with low velocity, thereby decreasing LHTAs behind the pin fins. The flow pattern significantly influences thermal characteristics, with CPFs showing the mean highest temperatures due to the presence of LHTAs. However, by implementing solutions such as increasing perforation number, the occurrence of hot spots and LHTAs can be reduced, leading to improved heat transfer coefficient.

3.3. Nusselt number (Nu) and thermal resistance (R_{th})

Fig.8 displays the variation of the Nusselt number (Nu) versus Reynolds number (Re) for various PFHS arrangements. The graph demonstrates that Nu augments with increasing Re, attributed to the increased inlet velocity and enhanced inertial shears near the walls. The findings reveal that Nu values increased by of 66.32%, 116.58%, 146.80%, 127.63%, and 180.82% for case 0, case 1, case 2, case 3 and case 4, respectively, compared to cylindrical pin fins at $Re = 22,060$. Therefore, case 4 ensures better augmentation of heat transfer coefficient of 180.82% due to the perforated space which is helps not only augment heat transfer areas but also significantly reduces the formation of the lower heat transfer areas (LHTAs) behind of the pin fins.

The variation of thermal resistance (R_{th}) against Re for different PFHS configurations was depicted in Fig.9. It is evident from this illustration that an increase in Re results in a decline in R_{th} , consistent with the trends observed for Nu in Fig. 8. A remarkable reduction in thermal resistance is achieved at the highest Reynolds number (i.e., $Re = 22,060$).

The percentage reductions in R_{th} for case 0, case 1, case 2, case 3, and case 4 are 58.49%, 102.41%, 69.56%, 108.95%, and 154.54% compared to the cylindrical pin fins (CPF), respectively.

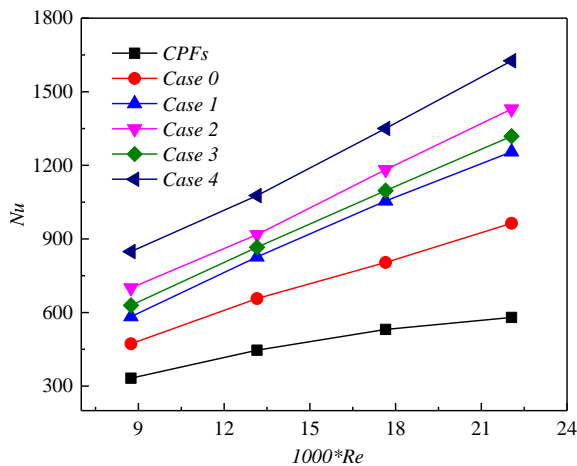


Fig. 8. Variation of Nusselt number (Nu) versus Reynolds number (Re)

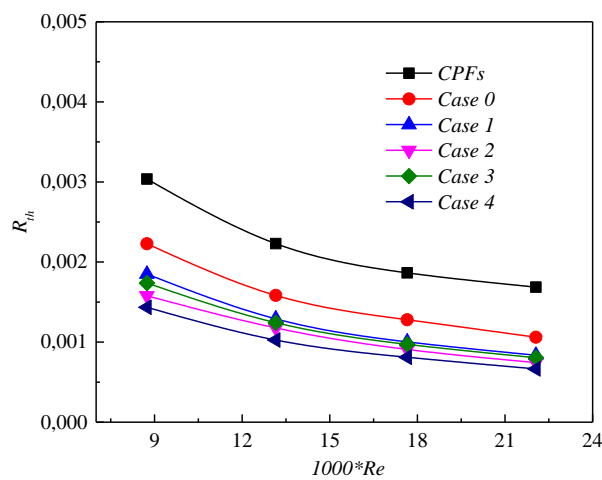


Fig. 9. Variation of thermal resistance (R_{th}) versus Reynolds number (Re)

As a consequence, the location of rings around CPFs augment heat transfer areas which are participate to reduce the thermal resistance of PFHSs, where the perforation space obviously enhances conjugate heat transfer by augmenting heat transfer surfaces and diminishing hot spots behind the pin fins. From these results, case 4 ensures a significant reduction in the thermal resistance by 154.54% compared to CPFs at $Re = 22,060$.

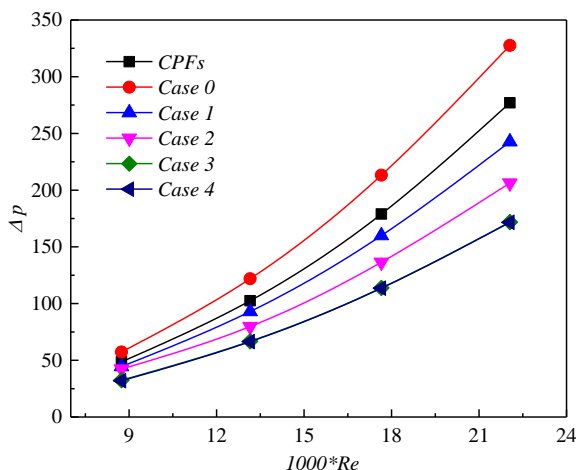


Fig. 10. Variation of pressure difference (Δp) versus Reynolds number (Re)

3.4. Pressure drops (Δp) and pumping power (P_p)

Fig.10 illustrates the variation of the pressure drop (Δp) and Reynolds number (Re) across different PFHS arrangements. These configurations present prominent advantages over conventional or cylindrical pin fin heat sinks (CPF), resulting in a significant reduction in pressure losses despite the enhanced heat transfer coefficients except case 0. The graph indicates that with an increase in Reynolds number (Re), there is a corresponding increase in pressure drop due to the emergence of flow blocking phenomena and heightened inertial shears near the wall of pin fins (PFs) and the base plate. The findings reveal that in comparison to CPFs at $Re = 22,060$, there is a remarkable reduction in Δp by 14.46 %, 34.46 %, 61.04%, and 62.19% for case 1, case 2, case 3, and case 4, respectively. Except, case 0 creates a pressure drop penalty of 29.22% for the same comparison. These results demonstrate that the perforation space helps to reduce pressure drop due to the diminution in blockage flow before the pin fins.

The integration of rings around the CPFs and perforation methods has partially removed recirculation zones behind the pin fins, which are responsible for reducing pressure drop. The pumping power (P_p) is directly related to the pressure drop (Δp), inlet velocity (u_{in}), and frontal area (A_c) as depicted in equation 9. Fig. 11 shows the linking between P_p and Re for various PFHS configurations. It is obvious that an increase in Re leads to an evolution in P_p due to the amplified inlet velocity. Nevertheless, a substantial increase in P_p is observed in the proposed configurations compared to CPFs, attributed to the augmentation in frontal area (A_c). For the highest Reynolds number ($Re = 22,060$), P_p augments by 39.56%, 31.67%, 32.43%, 26.91%, and 41.29% for case 0, case 1, case 2, case 3, and case 4, respectively, compared to CPFs at $Re = 22,060$.

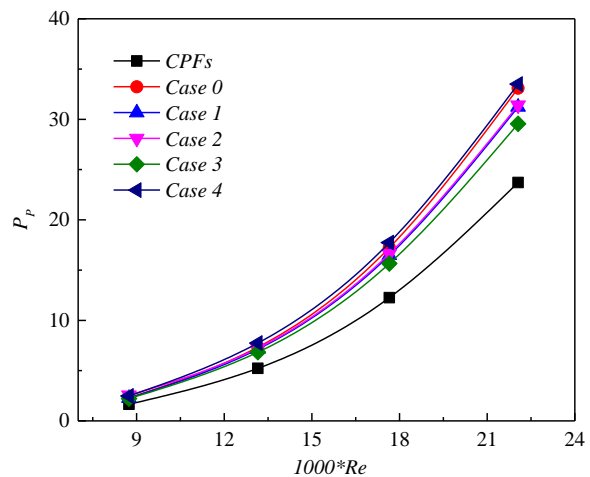


Fig. 11. Variation of pumping power (P_p) versus Reynolds number (Re)

3.5. Hydro thermal performance, volume and mass optimization

Fig. 12 illustrates the change in hydro thermal performance factor (η) with Reynolds number for pin fin heat sinks (PFHSs) featuring different perforation and rings arrangements. The figure indicates that η values are consistently above 1 for all configurations of PFHS, suggesting that these configurations exhibit superior performance compared to the reference case

(CPFs). This underscores the effectiveness of the perforation technique and rings insert in enhancing the thermal performance of the PFHSs, at least within the scope of this study. Furthermore, in the presence of rings insert, the results reveal that rings increases both with higher Reynolds number and an increased number of perforations. Specifically, for Cases 0 to 4 at Reynolds number of 22,060, the corresponding η values are approximately 1.57, 2.26, 2.72, 2.67 and 3.29, respectively. Based on these findings, it is determined that case 4 demonstrates the highest performance, achieving an η of 3.29 at Reynolds number of 22,060, and is thus identified as the optimal configuration. Compared with the reference case (31), the optimal configuration (case 4) ensures an reduction of 77.5% and 77.65% for the volume and mass of heat sink, respectively, leading to space and cost savings in addition to improved hydrothermal performance.

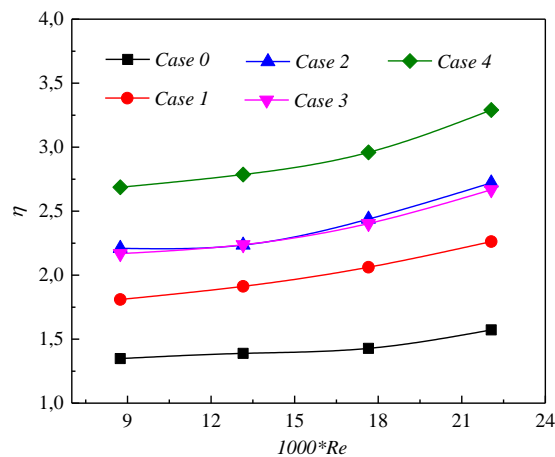


Fig. 12. Variation of thermal resistance (η) versus Reynolds number (Re)

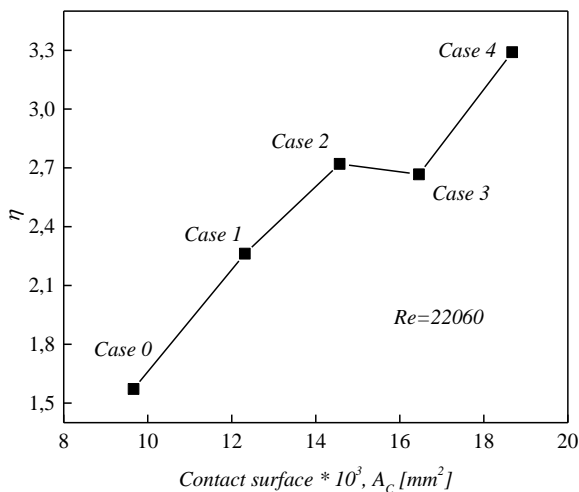


Fig. 13. Variation of the hydrothermal performance factor (η) versus contact surface (A_c)

Fig. 13 depicts the variation of the hydrothermal performance factor versus contact surface. The first observation from this figure is insertions of ring and perforation augment the surface of contact. Usually, the increase in the surface of contact between air flow and the solid let to an augmentation in the performance of heat sink. In addition, the perforation in external rings leads to slight diminution in the thermal performance as shown in case 2 to case 3. But, the perforation in the rings and grooves helps to augment the hydrothermal performance factor.

4. CONCLUSION

A series of 3D numerical simulations were conducted to optimize the design of a heat sink. The study investigated the performance of five different heat sink configurations at Reynolds number (Re) ranging from 8740 to 22060 and compared to a cylindrical pin fin (CPFs). Some conclusions were reported and summarized as follows:

- The use of both perforated and ring inserts can enhance heat transfer rates and decrease the size and weight of heat sinks. Also, this combination helps to creates better mixture of flow around of PFHS.
- For the case 4, the Nusselt number increased by 180.82%, leading to a 154.54% reduction in thermal resistance compared to traditional CPFs. Fortunately, this configuration participates in important reduction in the pressure drop by 62.19%. Furthermore, it achieved the highest η of 3.29 at Re = 22,060.
- Compared with the conventional CPFs (31), the optimal configuration (case 4) ensures a reduction of 77.5% and 77.65% for the volume and mass of heat sink.
- For the same optimal case, the pumping power increased by 41.29% under the same conditions of comparison.

Nomenclature

| | |
|--------------------------|---|
| $\overline{u'_i u'_j}$ | Reynolds stress [m ² /s ²] |
| $\overline{u'_i \theta}$ | Turbulent heat flux [m.K/s] |
| x | Cartesian coordinate vector [m] |
| ν | Kinematic viscosity [m ² /s] |
| \bar{p} | Modified kinematic pressure [m ² /s ²] |
| Δp | Pressure drops [Pa] |
| α | Thermal diffusivity [m ² /s] |
| k | Turbulent kinetic energy [m ² /s ²] |
| i, j | Velocity vector [m/s] |
| q | Constant heat flux [W/m ²] |
| μ | Dynamic viscosity [kg/m.s] |
| A_c | Frontal heat transfer area [m ²] |
| C_p | Specific heat [J/kg.K] |
| D_h | Hydraulic diameter [m] |
| Nu | Nusselt number |
| Re | Reynolds number |
| R_{th} | Thermal resistance [K.m ² /W] |
| T | Temperature [K] |
| u | Mean speed [m/s] |
| λ | Thermal conductivity [W/m ² .K] |

Subscript

| | |
|--------|--------------|
| i, j | Tensor index |
| in | Inlet |
| out | Outlet |
| s | Solid |
| w | Wall |

Abbreviations


| | |
|-------|---------------------------------|
| CPFs | Cylindrical pin fins |
| CPFHS | Cylindrical pin fins heat sinks |
| PFHSs | Pin fins heat sinks |


REFERENCES

- Yuan J, Qu Y, Deng N, Du L, Hu W, Zhang X, et al. Three-dimensional numerical simulation of heat transfer enhancement of electronic devices by single crystal diamond rhombus-shaped pin fin microchannel heat sink. *Diam Relat Mater*. 2024;143(February):110887.
- Ahmed HE, Salman BH, Kherbeet AS, Ahmed MI. Optimization of thermal design of heat sinks: A review. *Int J Heat Mass Transf*. 2018;118:129–53.
- Kumar S, Kumar A, Darshan Kothiyal A, Singh Bisht M. A review of flow and heat transfer behaviour of nanofluids in micro channel heat sinks. *Therm Sci Eng Prog*. 2018;8(June):477–93.
- Chingulpitak S, Wongwises S. A review of the effect of flow directions and behaviors on the thermal performance of conventional heat sinks. *Int J Heat Mass Transf*. 2015;81:10–8.
- Wang Q, Tao J, Cui Z, Zhang T, Chen G. Passive enhanced heat transfer, hotspot management and temperature uniformity enhancement of electronic devices by micro heat sinks: A review. *Int J Heat Fluid Flow*. 2024;107(December 2023):109368.
- Castillo E, Santos A, Gonzalez A. Numerical study of the use of shear-thinning nanofluids in a microchannel heat sink with different pin densities and including vortex generator. *Case Stud Therm Eng*. 2024;57(March):104328.
- Ho CJ, Pan J, Yang TF, Rashidi S, Yan WM. Experimental study on thermal performance of water/nano-phase change emulsion through a mini- and micro-channel stacked double-layer heat sink. *Int J Heat Mass Transf*. 2023;217(September).
- Cheng J, Tang D, Li X, Tang Z. Multi-objective optimization of a combined heat sink with triangular protrusion and corrugated surface impinged by a nanofluid slit-confined jet. *Int J Heat Mass Transf*. 2024;218(September 2023):124769.
- Ho CJ, Peng JK, Yang TF, Rashidi S, Yan WM. Comparison of cooling performance of nanofluid flows in mini/micro-channel stacked double-layer heat sink and single-layer micro-channel heat sink. *Int J Therm Sci*. 2023;191(May 2022).
- Panja SK, Das B, Mahesh V. Numerical study of parabolic trough solar collector's thermo-hydraulic performance using CuO and Al₂O₃ nanofluids. *Appl Therm Eng*. 2024;248(PB):123179.
- Gaur SK, Sahoo RR, Sarkar J. Numerical investigation on assessing the influence of diverse-shaped hybrid nanofluids on thermal performance of triple tube heat exchanger. *Powder Technol*. 2024;439(January):119690.
- Tian MW, Rostami S, Aghakhani S, Gordanlou AS, Qi C. A techno-economic investigation of 2D and 3D configurations of fins and their effects on heat sink efficiency of MHD hybrid nanofluid with slip and non-slip flow. *Int J Mech Sci*. 2021;189(July 2020):105975.
- Ghaneifar M, Arasteh H, Mashayekhi R, Rahbari A. Thermohydraulic analysis of hybrid nanofluid in a multilayered copper foam heat sink employing local thermal non-equilibrium condition: Optimization of layers thickness. *Appl Therm Eng*. 2020;181(June):115961.
- Tang Z, Yin C, Xiang Y, Yu P, Cheng J. Multi-objective optimization of a hybrid nanofluid jet impinging on a microchannel heat sink with semi-airfoil ribs based on field synergy principle. *Int J Heat Mass Transf*. 2024;225(November 2023):125431.
- Alnaqi AA, Alsarraf J, Al-Rashed AAAA, Afrand M. Thermal-hydraulic analysis and irreversibility of the MWCNTs-SiO₂/EG-H₂O non-Newtonian hybrid nanofluids inside a zigzag micro-channels heat sink. *Int Commun Heat Mass Transf*. 2021;122(February):105158.
- Chen J, Jiang J, Ma A, Song D. Research progress of phase change materials (PCMs) embedded with metal foam (a review). *Procedia Mater Sci*. 2014;4:389–94.
- Cui W, Si T, Li X, Li X, Lu L, Ma T, et al. Heat transfer enhancement of phase change materials embedded with metal foam for thermal energy storage: A review. *Renew Sustain Energy Rev*. 2022;169(September):112912.
- Heo JH, Rohini AK, Kim SM. Thermal design limits for flow boiling of R-134a in large mini/micro-channel heat sinks with wall temperature deviation restriction. *Int J Multiph Flow*. 2024;175(January):104783.
- Rehman T, Woo Park C. Optimising heat sink performance with porous media-PCM integration: An experimental investigation. *Appl Therm Eng*. 2024;242(January):122506.
- Sahel D, Bellahcene L, Yousfi A, Subasi A. Numerical investigation and optimization of a heat sink having hemispherical pin fins. *Int Commun Heat Mass Transf*. 2021;122(February):105133.
- Souda S, Sahel D, Ameer H, Yousfi A. Numerical simulation of heat transfer behaviors in conical pin fins heat sinks. *Acta Mech Slovaca*. 2022;26(3):32–41.
- Vilarubí M, Regany D, Camarasa J, Ibañez M, Rosell JI, Barrau J. Numerical evaluation of doubly clamped self-adaptive fins acting as vortex generators inside micro heat sinks (MHS). *Int J Heat Mass Transf*. 2024;220(November 2023).
- Al-Asadi MT, Al-damook A, Wilson MCT. Assessment of vortex generator shapes and pin fin perforations for enhancing water-based heat sink performance. *Int Commun Heat Mass Transf*. 2018;91(December 2017):1–10.
- Al-Sallami W, Al-Damook A, Thompson HM. A numerical investigation of the thermal-hydraulic characteristics of perforated plate fin heat sinks. *Int J Therm Sci*. 2017;121:266–77.
- Abdollahi SA, Basem A, Alizadeh A, Jasim DJ, Ahmed M, Sultan AJ, et al. Combining artificial intelligence and computational fluid dynamics for optimal design of laterally perforated finned heat sinks. *Results Eng*. 2024;21(November 2023):102002.
- Huang CH, Huang YR. An optimum design problem in estimating the shape of perforated pins and splitters in a plate-pin-fin heat sink. *Int J Therm Sci*. 2021;170(September 2020):107096.
- Bencherif B, Sahel D, Benzeguir R, Ameer H. Performance analysis of central processing unit Heat sinks fitted with perforation technique and splitter inserts. *ASME J Heat Mass Transf*. 2023;145(1).
- Alam MW, Bhattacharyya S, Souayah B, Dey K, Hammami F, Rahimi-Gorji M, et al. CPU heat sink cooling by triangular shape micro-pin-fin: Numerical study. *Int Commun Heat Mass Transf*. 2020;112.
- Hajjalilabaei M, Saghir MZ, Dincer I, Bicer Y. Optimization of heat dissipation in novel design wavy channel heat sinks for better performance. *Energy*. 2024;297(March):131155.
- Bezaatpour M, Goharkhah M. Three dimensional simulation of hydrodynamic and heat transfer behavior of magnetite nanofluid flow in circular and rectangular channel heat sinks filled with porous media. *Powder Technol*. 2019;344:68–78.
- Chin SB, Foo JJ, Lai YL, Yong TTK. Forced convective heat transfer enhancement with perforated pin fins. *Heat Mass Transf*. 2013;49(10):1447–58.
- Sajedi R, Osanloo B, Talati F, Taghilou M. Splitter plate application on the circular and square pin fin heat sinks. *Microelectron Reliab*. 2016;62:91–101.
- Abdelmohimen MAH, Hussien MA, Algarni S, Karali MA, Ahamed Saleel C, Ahmed GMS, et al. Numerical investigation of thermal performance enhancement of pin fin heat sink using wings with different angles. *Ain Shams Eng J*. 2024;15(3):102584.
- Zohora FT, Haque MR, Haque MM. Numerical investigation of the hydrothermal performance of novel pin-fin heat sinks with hyperbolic, wavy, and crinkle geometries and various perforations. *Int J Therm Sci*. 2023;194(March).
- Haque MR, Hridi TJ, Haque MM. CFD studies on thermal performance augmentation of heat sink using perforated twisted, and grooved pin fins. *Int J Therm Sci*. 2022;182(August).
- Meganathan S, Arunkumar R, Ponshanmugakumar A. Numerical analysis of passive heat sink for different shapes. *Mater Today Proc*. 2020;46(1):3749–55.
- Haque MR, Redu RR, Rafi MAAA, Haque MM, Rahman MZ. Numerical investigation of heat transfer performance for rectangular, elliptical, and airfoil shaped pin fin heatsinks through the novel combination of perforation and bulge inserts. *Int Commun Heat Mass Transf*. 2022;138.
- Introduction To Comsol Multiphysics. Users Guid Multiphysics Model with Finite Elem Methods. 2006;1–26.
- Interface P, User B. Comsol Multiphysics. Interface. 2012.

40. Sahel D. Thermal performance assessment of a tubular heat exchanger fitted with flower baffles. *J Thermophys Heat Transf.* 2021;35(4):726–34.
41. Bencherif B, Sahel D, Ameer H, Benzeguir R. Investigation of the hydrothermal enhancement of grooved pin fins heat sinks. *Int J Ambient Energy.* 2022;43(1):8505–15.
42. Anli EC, Teş AA, Bilir Ş. Derivation of Dimensionless Governing Equations for Axisymmetric Incompressible Turbulent Flow Heat Transfer Based on Standard k- ϵ Model Standart k- ϵ Modeli Temelinde Eksenel Simetrik Sıkıştırılmaz Türbülanslı Akış Isı Transferi i çin Boyutsuz Ana Denk. *Afyon Kocatepe Üniversitesi Fen ve Mühendislik Bilim Derg.* 2020;20:1096–111.
43. Ate A, Bilir Ş. Developing Turbulent Flow in Pipes and Analysis of Entrance Region. *Acad Platf J Eng Sci.* 2021;9–2:332–53.
44. Ali A, Ozdemir M, Canli E. Effects of pin fin height , spacing and orientation to natural convection heat transfer for inline pin fin and plate heat sinks by experimental investigation. *Int J Heat Mass Transf.* 2021;177:121527.
45. Hakan A, Nacak H, Canli E. Effects of trapezoidal and twisted trapezoidal tapes on turbulent heat transfer in tubes. *Appl Therm Eng.* 2022;211:118386.

Karima Alem:  <https://orcid.org/0009-0006-3603-7974>

Djamel Sahel:  <https://orcid.org/0000-0002-6754-0082>

Warda Boudaoud:  <https://orcid.org/0009-0008-3900-7089>

Redouane Benzeguir:  <https://orcid.org/0000-0002-1576-8528>



This work is licensed under the Creative Commons BY-NC-ND 4.0 license.

COMPOSITE ANTI-DISTURBANCE SWITCHED \mathcal{H}_2 CONTROL DESIGN FOR SWITCHED SYSTEMS

Emre KEMER*, Hasan BAŞAK**

*Engineering and Natural sciences, Electrical-Electronics Engineering, Uşak University, Uşak, Turkey

** Engineering, Electrical-Electronics Engineering, Artvin Çoruh University, Artvin, Turkey

emre.kemer@usak.edu.tr, hasanbasak@artvin.edu.tr

received 04 July 2024, revised 09 October 2024, accepted 10 October 2024

Abstract: This article addresses the challenge of integrated switched H_2 control with disturbance rejection capabilities for switched systems, particularly when external disturbances are present. A novel anti-disturbance switched H_2 control strategy is formulated, leveraging estimated disturbance values. The formulation is given in Linear Matrix Inequalities (LMIs), establishing sufficient conditions to ensure H_2 performance while maintaining closed-loop stability. To validate the effectiveness of the proposed methodology, it is applied to a practical aero-engine model. Through simulations, it is demonstrated that the closed-loop aero-engine model exhibits remarkable transient performance even in the face of external disturbances. These results underscore the efficacy of the developed approach in enhancing the robustness and performance of switched systems subjected to disturbances. The integration of anti-disturbance capabilities within the H_2 control framework offers a promising avenue for addressing real-world control challenges, particularly in systems characterized by switching dynamics and external perturbations.

Key words: composite anti-disturbance control, switched systems, dwell time, \mathcal{H}_2 -switched control, aero-engine model

1. INTRODUCTION

There are several system disturbances, which can lead to instability or poor performance. Therefore, several anti-disturbance control techniques have been developed by researchers to enhance the anti-disturbance performance of systems. For example, [1] developed a H_∞ control with an observer for eliminating a norm-bounded disturbance and a disturbance defined by an exogenous system on an aircraft model. [2] proposed a methodology for Markovian jump systems under the influence of multiple disturbances. A sliding mode observer and a feedback control law based on the backstepping method were employed in [3] for flexible spacecraft systems. [4] designed a flight controller for a helicopter system using a disturbance observer and a backstepping controller. A disturbance rejection control method was proposed by [5] using H_∞ control and the equivalent input disturbance method for an aircraft system. The equivalent input disturbance method was employed in [6] to estimate exogenous perturbations with the Lyapunov-based state feedback control law and in [7], authors improved the disturbance estimation performance of modelling equivalent input perturbations for a missile autopilot design. [8] developed a sliding mode controller in conjunction with a disturbance observer for a quadrotor helicopter where the disturbance observer estimates the impact of persistent and gradually changing disturbances. [9] suggested a methodology combining a sliding mode controller and a dual disturbance observer to manage spacecraft position and attitude dynamics, where the dual disturbance observer based controller attenuates both the external disturbances characterized by the exogenous model and the bounded disturbances. The helicopter slung load system was governed by a composite anti-disturbance model reference controller, which ensured asymptotic stability and L_2 —

L_∞ performance in [10]. A composite control strategy comprising a disturbance observer and a robust controller was designed by [11] to handle with multiple disturbances in a rigid spacecraft system, aiming to achieve anti-disturbance performance. A hybrid control approach was presented in [12] for Markovian jump systems affected by multiple disturbances. This approach specifically addresses an energy-bounded disturbance alongside an event-triggered sinusoidal disturbance characterized by unknown frequencies and amplitudes. An anti-disturbance control was designed in [13] which tackles the challenges of finite-time boundedness and disturbance rejection in takagi-sugeno fuzzy networked systems, particularly those susceptible to actuator faults, linear fractional uncertainties, and multiple disturbances. In [14], researchers investigate a distributed extended state observer design and a dual-side dynamic event-triggered output feedback anti-disturbance control strategy for interconnected systems facing quantization issues and multi-source disturbances.

In another research domain, there has been a notable rise in interest regarding the analysis of stability and design of controllers for switched systems [15], because switched systems find wide-ranging applications across various industries, including but not limited to the automotive industry, aviation, air traffic control systems, switching power converters, and so on [16]. At present, numerous significant findings have emerged regarding the stability and control synthesis of switched systems. Generally, the most prevalent approaches to designing switching laws involve state- and time-dependent switching rules [17,18,19]. A state-dependent switching law refers to a switching function that depends on the system state. Even though individual subsystems exhibit instability, the overall stability of the switched system can be preserved. Nevertheless, the chattering phenomenon [20] may be revealed because any

dwell-time constraint cannot be guaranteed between switching instants. A few examples of dwell-time switching laws [21, 22, 23] which are formulated based on time-dependent rules. The amplitude changes in switching controllers may lead to control bumps, negatively affecting transient performance and potentially causing instability. This issue was addressed in [24,25], where the authors proposed an H_∞ bumpless transfer controller specifically designed for switched interval type-2 (IT2) fuzzy systems. A fault tolerance and anti-disturbance attenuation using a two-dimensional modified repetitive control system was investigated in [26] for switched fuzzy systems with multiple disturbances.

Various disturbances occur during flight, which can significantly impact the performance of aero-engine systems. Consequently, developing anti-disturbance controllers for these systems is imperative. However, the challenge of implementing effective disturbance-rejection control in aero-engine systems especially in the presence of multiple disturbances remains largely unaddressed. This gap in the existing literature serves as the main motivation behind our study. By focusing on the unique challenges faced by aero-engine systems, we aim to contribute a robust framework for designing anti-disturbance controllers that can effectively manage multiple disturbances. Our research not only addresses this critical need but also provides innovative solutions that enhance the stability and performance of aero-engine systems in dynamic flight conditions. This work lays the groundwork for future advancements in control strategies within the aerospace industry, promoting greater safety and efficiency in aircraft operations. In this paper, we address the challenge of composite disturbance-rejection \mathcal{H}_2 control for switched systems. Many control systems encounter significant challenges from external disturbances that can compromise operational stability. Traditional control strategies often struggle to maintain performance under such conditions, leading to increased instability and inefficiency. To address these issues, developing an anti-disturbance approach is essential for ensuring consistent performance and reliability. The anti-disturbance switched \mathcal{H}_2 control method specifically enhances system performance and optimizes operational efficiency. We propose a composite anti-disturbance control scheme to effectively manage multiple disturbances. The need for effective control of time-varying systems, particularly those subjected to external disturbances, has led to the development of advanced control strategies. In this context, our composite anti-disturbance control approach integrates disturbance observer-based control with robust switching strategies, offering superior disturbance rejection compared to traditional methods. A key advantage of our method is the use of a state-dependent switching law, which makes the system highly adaptable to time-varying dynamics—a significant improvement over static or less adaptive control schemes. Additionally, the integration of an \mathcal{H}_2 based controller ensures optimal tracking performance. When combined with the disturbance observer, it outperforms standard \mathcal{H}_2 methods, providing better tracking accuracy while maintaining comparable levels of robustness. The proposed design also tackles common challenges in switching systems by carefully managing dwell times and switching conditions, ensuring both stability and high performance without typical drawbacks like chattering. The key contributions of this work are as follows: We propose a disturbance observer-based control approach and a switched state feedback \mathcal{H}_2 control method for a class of switched systems experiencing multiple disturbances. Here, the disturbance observer is designed to estimate the external disturbances described by an exogenous system. The outputs of the disturbance observer and the switched \mathcal{H}_2 state feedback controller are integrated to form a composite anti-disturbance switched

controller. We present conditions, formulated as LMIs, that guarantee robust stability of the closed-loop system while maintaining the specified \mathcal{H}_2 -norm. A growing number of articles has focused on control problems in aero-engine systems, highlighting the significance of this area in engineering. To demonstrate the effectiveness of our proposed composite anti-disturbance control scheme, we apply it to an aero-engine system. We achieve stability of the controlled aero-engine system by applying minimum dwell-time theory.

The structure of this paper is as follows: In the subsequent section, we provide the preliminaries and problem formulation. We then detail a composite anti-disturbance \mathcal{H}_2 control scheme using LMIs in Section 3. Application of the proposed control approach to an aero-engine model is detailed in Section 4. Following this, simulation results are presented in the subsequent section to show the effectiveness of the developed control scheme. Lastly, the conclusions of this paper are given.

Notation: The function $Tr(\cdot)$ represents the trace operation for square matrices. $He\{A\} = A + A'$ is called $He\{\cdot\}$. P are symmetric matrices and $P > 0$ (≥ 0) indicates positive definiteness (semi-definiteness). A symmetric matrix of the form $\begin{bmatrix} P & Q \\ Q' & P \end{bmatrix}$ is denoted as $\begin{bmatrix} P & Q \\ * & P \end{bmatrix}$. We denote \mathbb{R}^n as the n -dimensional Euclidean space and $\mathbb{R}^{p \times q}$ as the set of all $p \times q$ real matrices. Additionally, \mathbb{N} denotes the set of natural numbers.

2. PRELIMINARIES AND PROBLEM FORMULATION

Consider a dynamic system described by:

$$\frac{dx(\theta)}{d\theta} = A(\theta)x(\theta) + B(\theta)(\delta_1(\theta) + u(\theta)) + B_w(\theta)\delta_2(\theta) \quad (1)$$

in which the state denoted by $x(\theta)$ belongs to the n -dimensional real space, \mathbb{R}^n , the control signal represented as $u(\theta)$ resides in the k -dimensional real space, \mathbb{R}^k . External disturbances are an unknown disturbance, $\delta_2(\theta) \in \mathbb{R}^l$ and the disturbance, $\delta_1(\theta) \in \mathbb{R}^m$ generated by the following system:

$$\begin{aligned} \dot{w}(\theta) &= E(\theta)w(\theta) + F(\theta)\delta_3(\theta) \\ \delta_1(\theta) &= G(\theta)w(\theta) \end{aligned} \quad (2)$$

in which the state of the external disturbance system is $w(\theta) \in \mathbb{R}^p$ and the perturbations and uncertainties of the exogenous system are denoted by $\delta_3(\theta) \in \mathbb{R}^r$.

In this paper, the disturbance observer is formulated as:

$$\begin{aligned} \dot{\hat{w}}(\theta) &= (E(\theta) + LB(\theta)G(\theta))\hat{w}(\theta) + L(A(\theta)x(\theta) + B(\theta)u(\theta)) \\ \hat{w}(\theta) &= v(\theta) - Lx(\theta) \\ \hat{\delta}_1(\theta) &= G(\theta)\hat{w}(\theta) \end{aligned} \quad (3)$$

where $L \in \mathbb{R}^{p \times n}$ is the disturbance observer gain. In the composite disturbance observer-based control scheme, the state feedback controller is defined here with the form

$$u(\theta) = Kx(\theta) - \hat{\delta}_1(\theta) \quad (4)$$

where $\hat{\delta}_1$ signifies the estimated external disturbance and $K \in \mathbb{R}^{k \times n}$ is the controller. Also, it is assumed that all system states are accessible for measurement.

The disturbance estimation error can be calculated as

$$e_w(\theta) = w(\theta) - \hat{w}(\theta) \quad (5)$$

Combining (2), (3) and (5), we have

$$\begin{aligned} \dot{e}_w(\theta) &= (E(\theta) + LB(\theta)G(\theta))e_w(\theta) + LB_w(\theta)\delta_2(\theta) \\ &\quad + F(\theta)\delta_3(\theta) \end{aligned} \quad (6)$$

Thus, the output is given such:

$$z(\theta) = C_1x(\theta) + C_2e_w(\theta) \quad (7)$$

Therefore, using (6) and (7) with (1) the augmented system is obtained

$$\begin{aligned} \dot{\tilde{x}}(\theta) &= \tilde{A}(\theta)\tilde{x}(\theta) + \tilde{B}(\theta)\delta(\theta) \\ z(\theta) &= \tilde{C}\tilde{x}(\theta) \end{aligned} \quad (8)$$

where

$$\tilde{x}(\theta) = [x'(\theta), e'(\theta)]', \delta(\theta) = [\delta_2'(\theta), \delta_3'(\theta)]'$$

$$\tilde{A}(\theta) = \begin{bmatrix} A(\theta) + B(\theta)K & B(\theta)G(\theta) \\ 0 & E(\theta) + LB(\theta)G(\theta) \end{bmatrix},$$

$$\tilde{B}_w(\theta) = \begin{bmatrix} B_w(\theta) & 0 \\ LB_w(\theta) & F(\theta) \end{bmatrix},$$

$$\tilde{C} = [C_1 \quad C_2].$$

2.1. Switched System Case

A nominal linear switching system emerges as a special case of system (1),

$$\begin{aligned} \frac{dx(\theta)}{d\theta} &= A_{\xi(\theta)}(\theta)x(\theta) + B_{\xi(\theta)}(\theta)(u(\theta) + \delta_1(\theta)) \\ &\quad + B_{w,\xi(\theta)}(\theta)\delta_2(\theta), \end{aligned} \quad (9)$$

where the switching rule function $\xi(\theta)$ defined for $\theta \geq 0$. $\xi(\theta)$ takes values from $1, \dots, M$, here M is the time-varying subsystems' number. Assuming that the system matrices of (9) are contained within the collective polytopes $\zeta_i(\theta)$ of the subsystems:

$$\zeta(\theta) = \bigcup_{i=1}^M \zeta_i(\theta) \quad (10)$$

where the definition of $\zeta_i(\theta)$ is as follows:

$$\zeta_i(\theta) = [A_i(\theta) \quad B_i(\theta) \quad B_{w,i}(\theta)] = \sum_{j=1}^N \kappa_j(\theta) \zeta_i^j, \quad (11)$$

where

$$\sum_{j=1}^N \kappa_j(\theta) = 1, \kappa_j(\theta) \geq 0, \theta \geq 0 \quad (12)$$

and

$$\zeta_i^j = [A_i^j \quad B_{u,i}^j \quad B_{w,i}^j] \quad (13)$$

Remark 1. In the preceding definition, the sub-polytopes are indexed by the variable i , which ranges from 1 to M . Additionally, j indexes the vertices of the corresponding sub-polytope, with each

sub-polytope assumed to possess N vertices. The convex combinations of these vertices give the matrices of the related sub-system. It is assumed that the sub-polytopes share some common regions and that the rates of change with respect to time for the polytopic coordinates $\kappa_j(\theta)$, $\forall j = 1, \dots, N$, are bounded.

Then, the external disturbance, $\delta_1(\theta)$ in (2) defined as:

$$\begin{aligned} \dot{w}(\theta) &= E_{\xi(\theta)}(\theta)w(\theta) + F_{\xi(\theta)}(\theta)\delta_3(\theta) \\ \delta_1(\theta) &= G_{\xi(\theta)}(\theta)w(\theta) \end{aligned} \quad (14)$$

Therefore, the disturbance observer is formulated such

$$\begin{aligned} \dot{\hat{w}}(\theta) &= (E_{\xi(\theta)}(\theta) + L_{\xi(\theta)}B_{\xi(\theta)}(\theta)G_{\xi(\theta)}(\theta))\hat{w}(\theta) \\ &\quad - L_{\xi(\theta)}(A_{\xi(\theta)}(\theta)x(\theta) + B_{\xi(\theta)}(\theta)u(\theta)) \\ \hat{w}(\theta) &= v(\theta) - L_{\xi(\theta)}x(\theta) \\ \hat{\delta}_1(\theta) &= G_{\xi(\theta)}(\theta)\hat{w}(\theta) \end{aligned} \quad (15)$$

and the state feedback control law is

$$u(\theta) = K_{\xi(\theta)}x(\theta) - \hat{\delta}_1(\theta) \quad (16)$$

Combining (14), (15) and the disturbance estimation error $e_w(\theta) = w(\theta) - \hat{w}(\theta)$, we have

$$\begin{aligned} \dot{e}_w(\theta) &= (E_{\xi(\theta)}(\theta) + L_{\xi(\theta)}B_{\xi(\theta)}(\theta)G_{\xi(\theta)}(\theta))e_w(\theta) \\ &\quad + L_{\xi(\theta)}B_{w,\xi(\theta)}(\theta)\delta_2(\theta) + F_{\xi(\theta)}(\theta)\delta_3(\theta) \end{aligned} \quad (17)$$

Finally, the augmented system is obtained based on the system in (9) and the system output

$$\begin{aligned} z(\theta) &= C_{1,\xi(\theta)}(\theta)x(\theta) + C_{2,\xi(\theta)}(\theta)e_w(\theta), \\ \dot{\tilde{x}}(\theta) &= \tilde{A}_{\xi(\theta)}\tilde{x}(\theta) + \tilde{B}_{\xi(\theta)}\delta(\theta) \\ z(\theta) &= \tilde{C}_{\xi(\theta)}\tilde{x}(\theta) \end{aligned} \quad (18)$$

where

$$\tilde{x}(\theta) = [x'(\theta), e'(\theta)]', \delta(\theta) = [\delta_2'(\theta), \delta_3'(\theta)]'$$

$$\tilde{A}_{\xi(\theta)}(\theta) =$$

$$\begin{bmatrix} A_{\xi(\theta)}(\theta) + B_{\xi(\theta)}(\theta)K_{\xi(\theta)} & B_{\xi(\theta)}(\theta)G_{\xi(\theta)}(\theta) \\ 0 & E_{\xi(\theta)}(\theta) + L_{\xi(\theta)}B_{\xi(\theta)}(\theta)G_{\xi(\theta)}(\theta) \end{bmatrix},$$

$$\tilde{B}_{w,\xi(\theta)}(\theta) = \begin{bmatrix} B_{w,\xi(\theta)}(\theta) & 0 \\ L_{\xi(\theta)}B_{w,\xi(\theta)}(\theta) & F_{\xi(\theta)}(\theta) \end{bmatrix},$$

$$\tilde{C}_{\xi(\theta)}(\theta) = [C_{1,\xi(\theta)}(\theta) \quad C_{2,\xi(\theta)}(\theta)]$$

The augmented system parameters are uncertain and presumed to reside in the union of the subsystems' polytopes as in (10). For simplicity, the notation θ will be dropped in the following sections.

Remark 2. In this paper, we employ a state-dependent switching law, as given in [18], which adheres to a dwell time constraint with a specified dwell time. This approach effectively manages the switching between different modes, thereby enhancing the overall stability and performance of the control system.

Definition 1. Throughout this paper, we adopt the assumption of a minimum dwell time constraint on the switching signal $\xi(\theta)$. This constraint implies that if the minimum dwell time is denoted by T , and the system's switching instants are represented as

$(\theta_1, \theta_2, \dots)$, then it holds that $\theta_{k+1} - \theta_k \geq T \forall k \geq 1$. Here, we define the time instants $\theta_{k,h} := \theta_k + hT/H$, where h ranges from 0 to H , and $\theta_{k,0} := \theta_k, \forall k$. Consequently, the minimum dwell time constraint T ensures that $\theta_{k,H} \leq \theta_{k+1,0}$. This definition is explained in Fig. 1.

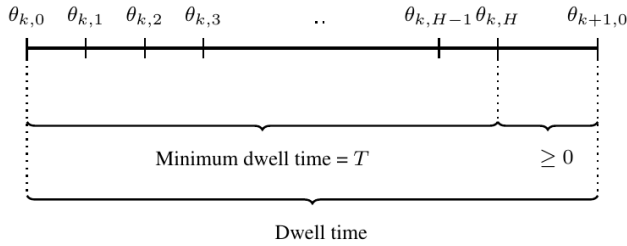


Fig. 1. Splitting the minimum dwell-time into H equal segments

3. COMPOSITE ANTI-DISTURBANCE CONTROL SCHEME

\mathcal{H}_2 control design is often adopted to deal with the transient performance of closed-loop systems. The \mathcal{H}_2 -norm in terms of LMIs can be defined as in the following lemma.

Lemma 1. (\mathcal{H}_2 -norm [27]) Given that A in the system (1) is Hurwitz and the corresponding transfer function is represented by $G(s) = C(sI - A)^{-1}B + D$, the following statements are equivalent:

\mathcal{H}_2 -norm of the system, $\|G\|_2^2 < \gamma^2$,

there exist symmetric matrices, $Y > 0$ and Z such that $Tr(Z) < \gamma^2$, $\begin{bmatrix} P & C' \\ * & Z \end{bmatrix} > 0$, $\begin{bmatrix} PA + A'P & PB \\ * & -I \end{bmatrix} < 0$.

Lemma 2. For the system (8), the following statements are equivalent to Lemma 1;

there exist symmetric matrices, $Q > 0, P > 0$ and Z such that

$$\begin{aligned} Tr(Z) &< \gamma^2, \\ \begin{bmatrix} Q & 0 & QC_1' \\ * & P & C_2' \\ * & * & Z \end{bmatrix} &> 0, \\ \begin{bmatrix} He\{A_c Q\} & BG & B_w & 0 \\ * & He\{PE_c\} & PLB_w & PF \\ * & * & -I & 0 \\ * & * & * & -I \end{bmatrix} &< 0, \end{aligned}$$

Given positive scalars α and β , if there exist matrices X and Y , along with symmetric matrices $Q > 0, P > 0$, and Z , such that

$$\begin{aligned} Tr(Z) &< \gamma^2, \\ \begin{bmatrix} Q & 0 & QC_1' \\ * & P & C_2' \\ * & * & Z \end{bmatrix} &> 0, \\ \begin{bmatrix} He\{A_c Y\} & BG & B_w & 0 & \theta & 0 \\ * & He\{XE_c\} & XLB_w & XF & 0 & \Phi \\ * & * & -I & 0 & 0 & \beta(XLB_w)' \\ * & * & * & -I & 0 & \beta(XF)' \\ * & * & * & * & -\alpha(Y + Y') & 0 \\ * & * & * & * & * & -\beta(X + X') \end{bmatrix} &< 0, \end{aligned}$$

where

$$A_c = A + BK, E_c = E + LBG, \theta = Q - Y' + \alpha A_c Y \text{ and } \Phi = P - X + \beta(XE_c)'.$$

Proof: Denoting $P = \text{diag}(P_1, P_2)$ and replacing the system matrices in Lemma 1(ii) with the augmented system matrices (8), then the following equivalent conditions are obtained:

$$Tr(Z) < \gamma^2,$$

$$\begin{bmatrix} P_1 & 0 & C_1' \\ * & P_2 & C_2' \\ * & * & Z \end{bmatrix} > 0, \quad (19)$$

$$\begin{bmatrix} He\{P_1 A_c\} & P_1 BG & P_1 B_w & 0 \\ * & He\{P_2 E_c\} & P_2 LB_w & P_2 F \\ * & * & -I & 0 \\ * & * & * & -I \end{bmatrix} < 0 \quad (20)$$

where

$$A_c = A + BK, E_c = E + LBG.$$

Denoting $\tilde{P} = \text{diag}(P_1^{-1}, I, I)$ and $\bar{P} = \text{diag}(P_1^{-1}, I, I)$, multiplying (19) and (20) by respectively \tilde{P} and \bar{P} from both sides, then the conditions in Lemma 2(ii) are obtained.

The proof of Lemma 2(ii) relies on applying the Finsler lemma in conjunction with Lemma 2(i). Also, multiplying Lemma 2(ii) the left by Y and from the right Y' the condition of Lemma 2(i) are obtained, where:

$$Y = \begin{bmatrix} I & 0 & 0 & 0 & A_c & 0 \\ 0 & I & 0 & 0 & 0 & E_c' \\ 0 & 0 & I & 0 & 0 & (LB_w)' \\ 0 & 0 & 0 & I & 0 & F' \end{bmatrix}$$

For the switched linear time-varying (LTV) system(18), the conditions in Lemma 2(i) can be rewritten as follows:

$$Tr(Z) < \gamma^2$$

$$\begin{aligned} \begin{bmatrix} Q_i^j & 0 & Q_i^j(C_{1,i}^j)' \\ * & P_i^j & (C_{2,i}^j)' \\ * & * & Z \end{bmatrix} &> 0 \\ \begin{bmatrix} -\dot{Q}_i^j + He\{A_c\} & B_i^j G_i^j & B_{w,i}^j & 0 \\ * & \dot{P}_i^j + He\{E_c\} & R_i^j B_{w,i}^j & P_i^j F_i^j \\ * & * & -I & 0 \\ * & * & * & -I \end{bmatrix} &< 0 \end{aligned}$$

where $A_c = A_i^j Q_i^j + B_i^j S_i^j, E_c = P_i^j E_i^j + R_i^j B_i^j G_i^j$ and the matrices $P_i^j(\theta)$ and $Q_i^j(\theta)$ are assumed to be time-varying, hence the time derivative of $P_i^j(\theta)$ and $Q_i^j(\theta)$ are considered in the last condition. Also, it is assumed that the matrices $P_i^j(\theta)$ and $Q_i^j(\theta)$ can be expressed as convex combinations of the $P_i^j(\theta)$ and $Q_i^j(\theta)$, respectively.

As in [28], positive-definite Lyapunov matrices dependent on time and parameters, $Q_{\xi(\theta)}^j(\theta) \in \{Q_1^j(\theta), \dots, Q_M^j(\theta)\}$ and $P_{\xi(\theta)}^j(\theta) \in \{P_1^j(\theta), \dots, P_M^j(\theta)\}$, are defined as:

$$Q_i^j(\theta) = \begin{cases} Q_{i,h}^j + (Q_{i,h+1}^j - Q_{i,h}^j) \frac{\theta - \theta_{i,h}}{T/H} & \theta \in [\theta_{k,h}, \theta_{k,h+1}) \\ Q_{i,H}^j & \theta \in [\theta_{k,H}, \theta_{k+1}) \end{cases} \quad (21)$$

$$P_i^j(\theta) = \begin{cases} P_{i,h}^j + (P_{i,h+1}^j - P_{i,h}^j) \frac{\theta - \theta_{i,h}}{T/H} & \theta \in [\theta_{k,h}, \theta_{k,h+1}) \\ P_{i,H}^j & \theta \in [\theta_{k,H}, \theta_{k+1}) \end{cases} \quad (22)$$

Theorem 1. If a scalar $T > 0$ is given, and there exist matrices $S_{i,h}^j$, $R_{i,h}^j$, as well as positive-definite symmetric matrices Z , $P_{i,h}^j$, and $Q_{i,h}^j$ that satisfy the following LMIs minimization program $\forall i = 1, \dots, M$ and $j = 1, \dots, N$:

minimise $Tr(Z)$

subject to

$$\begin{bmatrix} Q_{i,h}^j & 0 & Q_{i,h}^j (C_{1,i}^j)' \\ * & P_{i,h}^j & (C_{2,i}^j)' \\ * & * & Z \end{bmatrix} > 0, \forall h \in \{0, \dots, H\},$$

$$\begin{bmatrix} \frac{Q_{i,h}^j - Q_{i,h+1}^j}{T/H} + He\{A_i^j Q_{i,h}^j + B_i^j S_{i,h}^j\} & B_i^j G_i^j & B_{w,i}^j & 0 \\ * & \frac{P_{i,h+1}^j - P_{i,h}^j}{T/H} + He\{P_{i,h}^j E_i^j + R_{i,h}^j B_i^j G_i^j\} & R_{i,h}^j B_{w,i}^j & P_{i,h}^j F_i^j \\ * & * & -I & 0 \\ * & * & * & -I \end{bmatrix} < 0, \quad (23a)$$

$$\begin{bmatrix} \frac{Q_{i,h}^j - Q_{i,h+1}^j}{T/H} + He\{A_i^j Q_{i,h+1}^j + B_i^j S_{i,h+1}^j\} & B_i^j G_i^j & B_{w,i}^j & 0 \\ * & \frac{P_{i,h+1}^j - P_{i,h}^j}{T/H} + He\{P_{i,h+1}^j E_i^j + R_{i,h+1}^j B_i^j G_i^j\} & R_{i,h+1}^j B_{w,i}^j & P_{i,h+1}^j F_i^j \\ * & * & -I & 0 \\ * & * & * & -I \end{bmatrix} < 0, \quad (23b)$$

where $h = 0, \dots, H-1$,

$$\begin{bmatrix} He\{A_i^j Q_{i,H}^j + B_i^j S_{i,H}^j\} & B_i^j G_i^j & B_{w,i}^j & 0 \\ * & He\{P_{i,H}^j E_i^j + R_{i,H}^j B_i^j G_i^j\} & R_{i,H}^j B_{w,i}^j & P_{i,H}^j F_i^j \\ * & * & -I & 0 \\ * & * & * & -I \end{bmatrix} < 0, \quad (23c)$$

$$\begin{bmatrix} Q_{s,0}^j - Q_{i,H}^j & 0 \\ * & P_{i,H}^j - P_{s,0}^j \end{bmatrix} \geq 0, \forall s \in \{1, \dots, M\} \text{ and } s \neq i \quad (23d)$$

then gains of the switched state-feedback controller and the disturbance observer gains are computed as:

$$K_{\xi}^j(\theta) = \begin{cases} \left(S_{i,h}^j + (S_{i,h+1}^j - S_{i,h}^j) \frac{(\theta - \theta_{k,h})}{T/H} \right) (Q_{i,h}^j + (Q_{i,h+1}^j - Q_{i,h}^j) \frac{(\theta - \theta_{k,h})}{T/H})^{-1}, & \theta \in [\theta_{k,h}, \theta_{k,h+1}), \\ \bar{S}_{i,H}^j \bar{Q}_{i,H}^{j-1}, & \theta \in [\theta_{k,H}, \theta_{k+1}), \end{cases} \quad (24)$$

$$L_{\xi}^j(\theta) = \begin{cases} \left(P_{i,h}^j + (P_{i,h+1}^j - P_{i,h}^j) \frac{(\theta - \theta_{k,h})}{T/H} \right)^{-1} (R_{i,h}^j + (R_{i,h+1}^j - R_{i,h}^j) \frac{(\theta - \theta_{k,h})}{T/H}), & \theta \in [\theta_{k,h}, \theta_{k,h+1}), \\ \bar{P}_{i,H}^{j-1} \bar{R}_{i,H}^j, & \theta \in [\theta_{k,H}, \theta_{k+1}), \end{cases} \quad (25)$$

Then it guarantees that the closed-loop system (18) exhibits global stability, while the closed-loop \mathcal{H}_2 -gain from d to z is maintained at $\sqrt{\text{Tr}(Z)}$ or less for any switching rule with a dwell-time equal to or greater than T .

Based on the above conditions and Lyapunov matrices, the following theorem is defined to provide solutions to the composite anti-disturbance control problem within the framework of the switched linear time-varying (LTV) system (18).

It is notable that prior to the initial switching event, the Lyapunov function experiences a decrease due to the conditions (23c). This indicates that the control strategy effectively preserves the Lyapunov function in the absence of switching, ensuring system stability and performance. Throughout the time span $\theta_k \leq \theta \leq \theta_k + T$, conditions (23a, 23b) derived from (21 and 22) ensure a consistent monotonous decrease in the Lyapunov function. Following this, conditions (23c) ensure the continuous decrease of $V(\theta, x)$ after $\theta_k + T$ and before the subsequent switching event. The non-increasing property of the Lyapunov function between any two arbitrary switching events is guaranteed by the conditions (23d).

Remark 3. According to Theorem 1, the state-feedback gains $K_i^j(\theta)$ and the disturbance observer gains $L_i^j(\theta)$ vary over time and depend on vertices. Nonetheless, these gains are often impractical for real-world use. Instead of those, time-invariant state-feedback gains and disturbance observer gains are often preferred. Therefore, the following theorem is formulated by using the conditions in Lemma 2(ii).

Remark 4. The computational complexity is given by $N(3MH + 3M - 1)$, where N represents the number of vertices, M is the number of subsystems, and H is the number of time instants. From this equation, we can conclude that both N and M contribute linearly to the overall computational complexity. This implies that if either the number of vertices or the number of subsystems increases, the computational effort will increase proportionately.

Theorem 2. For the given scalars $T > 0$, $\alpha > 0$, and $\beta > 0$, if there are matrices $S_{i,h}^j$, $R_{i,h}^j$, $X_{i,h}^j$, $Y_{i,h}^j$, and positive-definite symmetric matrices Z , $P_{i,h}^j$, and $Q_{i,h}^j$; $\forall i = 1, \dots, M$ and $j = 1, \dots, N$ that satisfy the following LMI minimization conditions:

minimise $Tr(Z)$
subject to

$$\begin{bmatrix} Q_{i,h}^j & 0 & Q_{i,h}^j (C_{1,i}^j)' \\ * & P_{i,h}^j & (C_{2,i}^j)' \\ * & * & Z \end{bmatrix} > 0, \forall h \in \{0, \dots, H\} \quad (26)$$

$$\begin{bmatrix} \Gamma_h & B_i^j G_i^j & B_{w,i}^j & 0 & Q_{i,h}^j - Y_{i,h}^{j'} + \alpha(A_i^j Y_{i,h}^j + B_i^j S_{i,h}^j) & 0 \\ * & \vartheta_h & R_{i,h}^j B_{w,i}^j & X_{i,h}^j F_i^j & 0 & P_{i,h}^j - X_{i,h}^j + \beta(X_{i,h}^j E_i^j + R_{i,h}^j B_i^j G_i^j)' \\ * & * & -I & 0 & 0 & \beta(R_{i,h}^j B_{w,i}^j)' \\ * & * & * & -I & 0 & \beta(X_{i,h}^j F_i^j)' \\ * & * & * & * & -\alpha(S_{i,h}^j + S_{i,h}^{j'}) & 0 \\ * & * & * & * & * & -\beta(X_{i,h}^j + X_{i,h}^{j'}) \end{bmatrix} < 0, \quad (27a)$$

$$\begin{bmatrix} \Gamma_{h+1} & B_i^j G_i^j & B_{w,i}^j & 0 & Q_{i,h+1}^j - Y_{i,h+1}^{j'} + \alpha(A_i^j Y_{i,h+1}^j + B_i^j S_{i,h+1}^j) & 0 \\ * & \vartheta_{h+1} & R_{i,h+1}^j B_{w,i}^j & P_{i,h+1}^j F_i^j & 0 & P_{i,h+1}^j - X_{i,h+1}^j + \beta(X_{i,h+1}^j E_i^j + R_{i,h+1}^j B_i^j G_i^j)' \\ * & * & -I & 0 & 0 & \beta(R_{i,h+1}^j B_{w,i}^j)' \\ * & * & * & -I & 0 & \beta(X_{i,h+1}^j F_i^j)' \\ * & * & * & * & -\alpha(S_{i,h+1}^j + S_{i,h+1}^{j'}) & 0 \\ * & * & * & * & * & -\beta(X_{i,h+1}^j + X_{i,h+1}^{j'}) \end{bmatrix} < 0, \quad (27b)$$

where

$$\Gamma_h = \frac{Q_{i,h}^j - Q_{i,h+1}^j}{T/H} + He\{A_i^j Y_{i,h}^j + B_i^j S_{i,h}^j\}, \quad \Gamma_{h+1} = \frac{Q_{i,h+1}^j - Q_{i,h+2}^j}{T/H} + He\{A_i^j Y_{i,h+1}^j + B_i^j S_{i,h+1}^j\},$$

$h = 0, \dots, H-1$ and

$$\vartheta_h = \frac{P_{i,h+1}^j - P_{i,h}^j}{T/H} + He\{X_{i,h}^j E_i^j + R_{i,h}^j B_i^j G_i^j\}, \quad \vartheta_{h+1} = \frac{P_{i,h+2}^j - P_{i,h+1}^j}{T/H} + He\{X_{i,h+1}^j E_i^j + R_{i,h+1}^j B_i^j G_i^j\},$$

$$\begin{bmatrix} \Gamma_H & B_i^j G_i^j & B_{w,i}^j & 0 & Q_{i,H}^j - Y_{i,H}^{j'} + \alpha(A_i^j Y_{i,H}^j + B_i^j S_{i,H}^j) & 0 \\ * & \vartheta_H & R_{i,H}^j B_{w,i}^j & X_{i,H}^j F_i^j & 0 & P_{i,H}^j - X_{i,H}^j + \beta(X_{i,H}^j E_i^j + R_{i,H}^j B_i^j G_i^j)' \\ * & * & -I & 0 & 0 & \beta(R_{i,H}^j B_{w,i}^j)' \\ * & * & * & -I & 0 & \beta(X_{i,H}^j F_i^j)' \\ * & * & * & * & -\alpha(S_{i,H}^j + S_{i,H}^{j'}) & 0 \\ * & * & * & * & * & -\beta(X_{i,H}^j + X_{i,H}^{j'}) \end{bmatrix} < 0, \quad (27c)$$

where

$$\Gamma_H = He\{A_i^j Y_{i,H}^j + B_i^j S_{i,H}^j\} \text{ and } \vartheta_H = He\{X_{i,H}^j E_i^j + R_{i,H}^j B_i^j G_i^j\},$$

$$\begin{bmatrix} Q_{s,0}^j - Q_{i,h}^j & 0 \\ * & P_{i,h}^j - P_{s,0}^j \end{bmatrix} \geq 0, \forall s \in \{1, \dots, M\} \text{ and } s \neq i \quad (27d)$$

then gains of the switched state-feedback controller and the disturbance observer gains are computed as:

$$K_{\xi}^j(\theta) = \begin{cases} (S_{i,h}^j + (S_{i,h+1}^j - S_{i,h}^j) \frac{(\theta - \theta_{k,h})}{T/H}) (Y_{i,h}^j + (Y_{i,h+1}^j - Y_{i,h}^j) \frac{(\theta - \theta_{k,h})}{T/H})^{-1}, & \theta \in [\theta_{k,h}, \theta_{k,h+1}), \\ \bar{S}_{i,H}^j \bar{Y}_{i,H}^{j-1}, & \theta \in [\theta_{k,H}, \theta_{k+1}), \end{cases} \quad (28)$$

$$L_{\xi}^j(\theta) = \begin{cases} (X_{i,h}^j + (X_{i,h+1}^j - X_{i,h}^j) \frac{(\theta - \theta_{k,h})}{T/H})^{-1} (R_{i,h}^j + (R_{i,h+1}^j - R_{i,h}^j) \frac{(\theta - \theta_{k,h})}{T/H}), & \theta \in [\theta_{k,h}, \theta_{k,h+1}), \\ \bar{X}_{i,H}^{j-1} \bar{R}_{i,H}^j, & \theta \in [\theta_{k,H}, \theta_{k+1}), \end{cases} \quad (29)$$

where, ensures that the closed-loop system (18) maintains global stability. Additionally, In scenarios where the dwell-time is T or greater, the closed-loop \mathcal{H}_2 -gain from d to z is limited to $\sqrt{\text{Tr}(Z)}$ or lower.

Remark 5. Theorem 2 provides vertex-dependent and time-varying state-feedback gains, $K_i^j(\theta)$, and disturbance observer gains, $L_i^j(\theta)$. However, if $S_{i,h}^j$, $Y_{i,h}^j$, $X_{i,h}^j$, and $R_{i,h}^j$ are selected independently of h and j , then these gains become time-invariant. They can be computed as $K_i = S_i Y_i^{-1}$ and $L_i = X_i^{-1} R_i$.

Remark 6. The \mathcal{H}_2 controller ensures optimal tracking performance by minimizing the quadratic cost function associated with tracking error and control effort. Integrating a disturbance observer enhances this performance by compensating for disturbances, improving tracking accuracy and overall system effectiveness. This combination allows the controller to adapt to varying disturbance levels, making it more versatile in handling unpredictable real-world scenarios.

It is important to note that as the size of the LMIs increases, there is a potential for a greater computational burden. Larger LMIs can introduce higher complexity in the numerical solving process, requiring more computational resources and time. However, advancements in modern computing technology have made it feasible to manage these challenges effectively. Furthermore, this computational complexity primarily arises during the initial design phase. Once the control strategies are established, the size of the LMIs becomes less significant, as they do not affect real-time implementation. Consequently, the initial investment in computational resources can yield robust and efficient control solutions that perform effectively in practice.

4. APPLICATION TO AERO-ENGINE MODEL

In this section, we showcase the implementation of the proposed anti-disturbance control scheme on the speed control system of the GE-90 aero-engine. We begin by presenting the GE-90 aero-engine model and then delve into the discussion of simulation results.

4.1. Aero-engine model

The aero-engine is comprised of essential components such as a combustion chamber, turbine, and compressor. Both the compressor and turbine feature high-pressure and low-pressure stages with rotating blades. The high-pressure compressor and turbine are concentrically aligned via a separate shaft, while the low-pressure compressor and turbine, along with the fan, rotate synchronously. Positioned at the inlet, the fan facilitates airflow, and a variable bleed valve is employed to extract gas from the core. Additionally, variable stator vanes aid in reducing flow separation within the compressor blades. Further details can be found in [29, 30]. The aero-engine has complex and highly non-linear dynamics. In the literature, different models of aero-engines have been developed. For this study we will use an LPV model of aero-engine (GE-90) which has been proposed by [29]. The altitude is normalized by 10000 and the fan speed by 3000. An LPV model of the uncertain state-space presentation is

$$\begin{bmatrix} \Delta \dot{N}_f \\ \Delta \dot{N}_c \end{bmatrix} = A(m, h, f) \begin{bmatrix} \Delta N_f \\ \Delta N_c \end{bmatrix} + B(m, h, f) (\Delta W_F + \delta_1) + B_w \delta_2 \quad (30)$$

and the external disturbance system

$$\begin{aligned} \dot{w}(\theta) &= E_{\xi(\theta)} w(\theta) + F_{\xi(\theta)} \delta_3(\theta) \\ \delta_1(\theta) &= G_{\xi(\theta)} w(\theta) \end{aligned} \quad (31)$$

where m , h and f denote the Mach number, altitude and fan speed respectively. $\Delta N_f = N_f - N_{f0}$ is the fan speed increment, $\Delta N_c = N_c - N_{c0}$ is the core speed increment and $\Delta W_F = W_F - W_{F0}$ is the fuel flow increment. Also, δ_1 is the external disturbance, $\delta_2 = t e^{-t}$ is another disturbance and $\delta_3 = t e^{-t}$ is an additional disturbance which results from the perturbations and uncertainties in the external disturbance. The engine pressure ratio (EPR) increment is

$$EPR = C \begin{bmatrix} \Delta N_f \\ \Delta N_c \end{bmatrix}$$

Here, the Mach number, the altitude and the fan speed parameters vary between $[0 - 0.84]$, $[0 - 42000]$ and $[1497 - 2432]$ respectively. Using these parameters, the system has been partitioned into four intersecting cells, as illustrated in Fig. 2. Model parameters can be obtained for each vertex and cell according to [23].

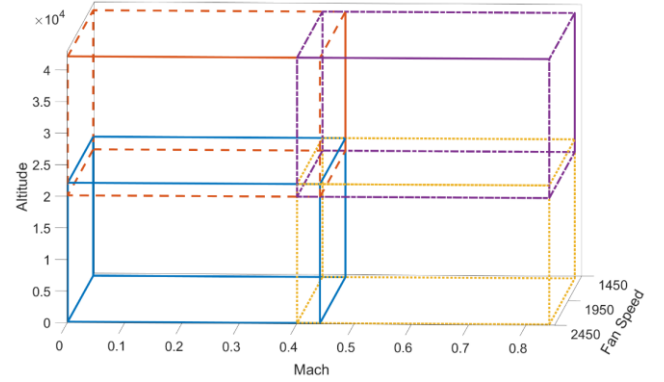


Fig. 2. The cell divisions of the parameters

Then, using LPV model in (30) with vertices of each cell, the switch system matrices A_i^j , B_i^j and C_i^j in (9) are obtained and the matrices $B_{w,i}^j$, E_i^j , F_i^j , G_i^j and $C_{2,i}^j$ for $i \in \{1, \dots, 4\}$ and $j \in \{1, \dots, 8\}$ are given as:

$$\begin{aligned} B_{w,i}^j &= \begin{bmatrix} 0.1 \\ 0.2 \end{bmatrix}, \quad E_i^j = \begin{bmatrix} 0 & -1 \\ 1 & 0 \end{bmatrix}, \quad F_i^j = \begin{bmatrix} 0.002 \\ 0.001 \end{bmatrix}, \\ G_i^j &= \begin{bmatrix} 3 & 2 \end{bmatrix}, \quad C_{2,i}^j = \begin{bmatrix} 0.1 & 1 \end{bmatrix} \end{aligned}$$

Then, solving Theorem 2 by using these matrices with the scalars $\alpha = \beta = 0.04$, $T = 0.1$ and $H = 1$, from equations (28) and (29), the gains of the switched controller and disturbance observer are computed as:

$$\begin{aligned} K_1 &= [0.0013 \quad -0.0064], \quad K_2 = [-0.0633 \quad 0.0090] \\ K_3 &= [0.0034 \quad -0.0066], \quad K_4 = [-0.0643 \quad 0.0085] \\ L_1 &= \begin{bmatrix} -0.0090 & -0.0043 \\ -0.0043 & -0.0025 \end{bmatrix}, \quad L_2 = \begin{bmatrix} -0.0076 & -0.0036 \\ -0.0036 & -0.0022 \end{bmatrix} \\ L_3 &= \begin{bmatrix} -0.0090 & -0.0042 \\ -0.0042 & -0.0025 \end{bmatrix}, \quad L_4 = \begin{bmatrix} -0.0064 & -0.0030 \\ -0.0030 & -0.0019 \end{bmatrix}. \end{aligned}$$

4.2. Simulation results and discussion

This section presents the simulation results of the proposed control scheme with the non-linear model of the GE-90 aero-engine. Initially, we adopt the non-linear validation model of the GE-90 aero-engine from [23] as:

$$\begin{aligned}\Delta \dot{N}_f &= -5.4452\Delta N_f - 3.1335\Delta N_f\Delta N_c + 5.1842\Delta N_f^2 \\ &\quad + 2.2142\Delta N_c + 0.2273\Delta N_c^2 + 230.6739\Delta W_F \\ &\quad - 86.2131\Delta N_f\Delta W_F + 25.0211\Delta N_c\Delta W_F \\ \Delta \dot{N}_c &= -0.1849\Delta N_f + 8.7942\Delta N_f\Delta N_c + 2.0938\Delta N_f^2 \\ &\quad - 7.0882\Delta N_c - 0.7456\Delta N_c^2 + 653.5547\Delta W_F \\ &\quad - 395.5347\Delta N_f\Delta W_F + 112.0966\Delta N_c\Delta W_F.\end{aligned}$$

To analyze the effectiveness of the proposed control approach, a standard H_2 controller is designed using the $h2syn$ function in the MATLAB Toolbox. Two scenarios were examined for the standard H_2 control approach. In the first scenario, the GE-90 aero-engine model was simulated using the standard H_2 control without a disturbance estimation. The fan speed and core speed are depicted in Fig. 3, while the EPR increment for the GE-90 aero-engine is shown in Fig. 4. It is evident that the standard H_2 control does not mitigate the disturbance effect. Next, the same model was simulated with the incorporation of the following disturbance observer:

$$L = \begin{bmatrix} -0.0090 & -0.0043 \\ -0.0043 & -0.0025 \end{bmatrix}.$$

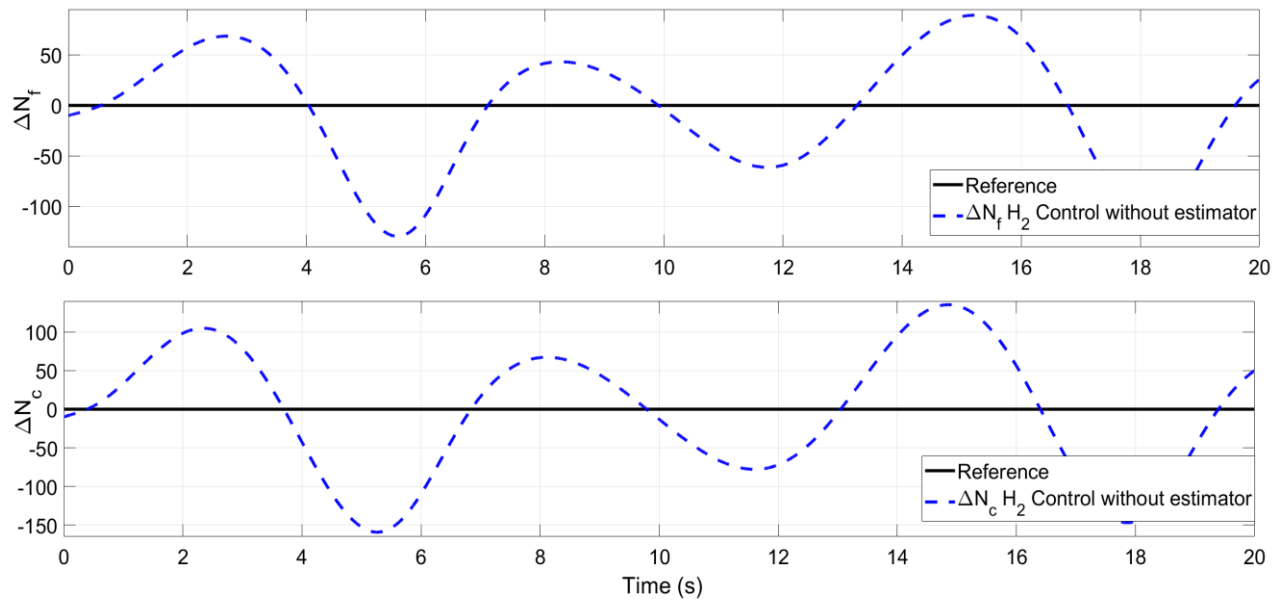


Fig. 3. The \mathcal{H}_2 control responses of the fan and core speed increments without an estimator

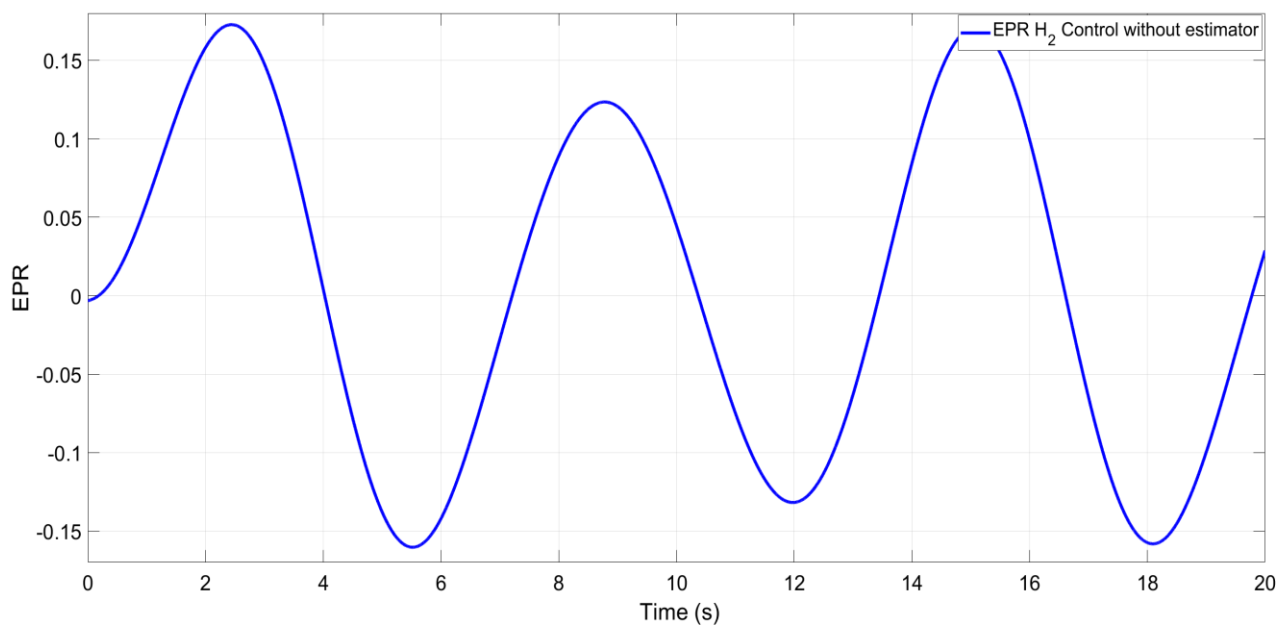


Fig. 4. \mathcal{H}_2 control response of the EPR increment without an estimator

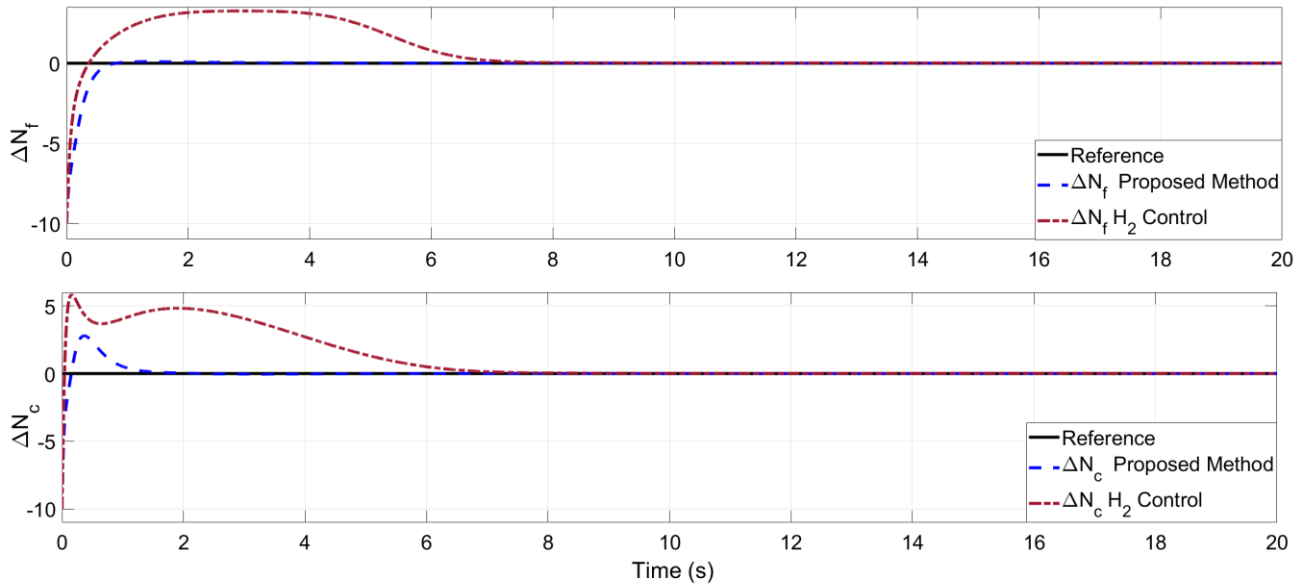


Fig. 5. The fan and core speed increments

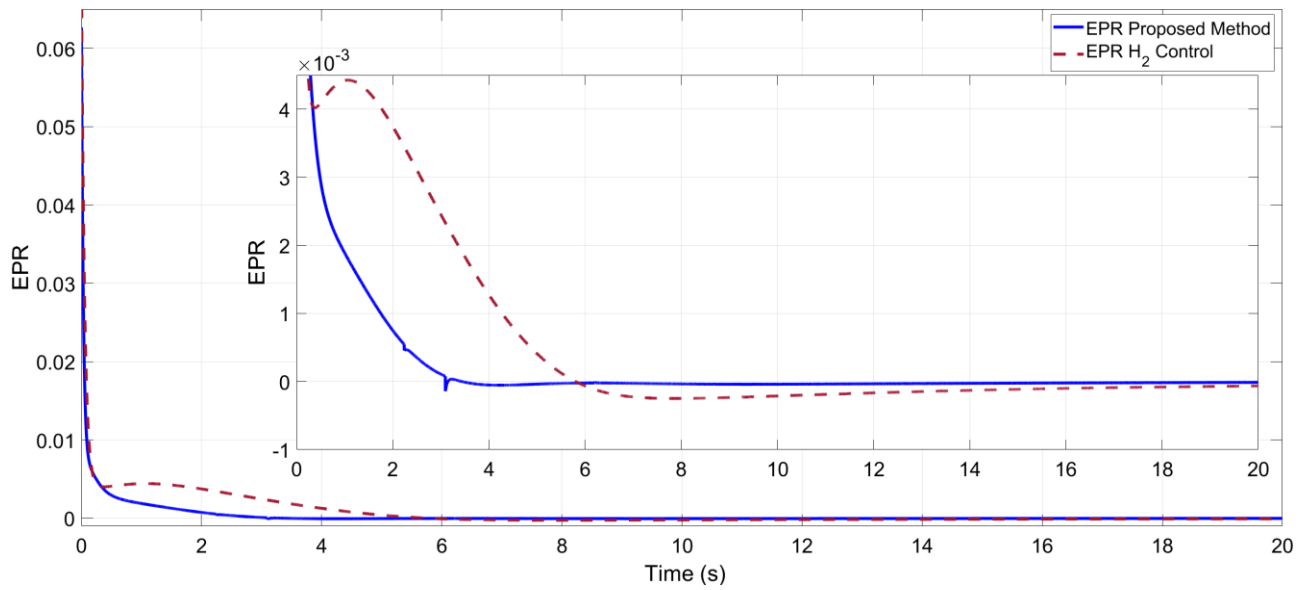


Fig. 6. EPR increment

Furthermore, we compare the simulation results of the proposed method and the standard H_2 controller with a disturbance observer. The responses of the fan speed and the core speed are presented in Fig. 5, while the EPR increment of the GE-90 aero-engine is depicted in Fig. 6. In addition, the comparison of the variation between the external disturbance and its estimation is illustrated in Fig. 7. The performance of the disturbance observer, showing that the estimated disturbance closely matches the actual disturbance profile. The system successfully maintains stability and performance, with settling times of $EPR = 3.5\text{ s}$, $\Delta N_c = 1.5\text{ s}$, and $\Delta N_f = 0.8\text{ s}$ using the proposed control structure. In comparison, under the standard H_2 control, the system exhibits settling times of $EPR = 20\text{ s}$, $\Delta N_c = 7\text{ s}$, and $\Delta N_f = 7\text{ s}$. This demonstrates the effectiveness of the observer in real-time disturbance estimation. Additionally, the switching function under the dwell-time is displayed in Fig. 8. Incorporating dwell time enhances


control performance by reducing energy fluctuations and ensuring system stability. By allowing brief pauses during the switching process, our method mitigates the oscillations typically associated with abrupt transitions, fostering a more stable operational environment. Notably, the time-varying nature of our approach facilitates smoother transitions, avoiding the harsh shifts that can destabilize the system. This smoothness not only improves overall responsiveness but also contributes to a more reliable control strategy, reinforcing the advantages of our proposed method compared to existing techniques. Overall, the simulation results confirm that the proposed anti-disturbance control scheme effectively eliminates the external disturbance given in (31) and stabilizes the nonlinear validation model of the GE-90 aero-engine.

5. CONCLUSION

This paper tackles the composite anti-disturbance switched control problem for switched systems. The dwell time approach has been used to analyze the robust stability with \mathcal{H}_2 -norm performance index using the linear matrix inequalities conditions. The gains of the switched \mathcal{H}_2 controller and the gain of the disturbance observer are computed by solving a convex LMI optimization problem. Then, the proposed control scheme is successfully implemented in an aero-engine model. A standard \mathcal{H}_2 controller method is used to analyse the efficiency of the proposed control approach. Simulation results validate the effectiveness of the proposed control scheme under the external disturbance. In future works, we will consider the disturbance suppression with input saturation problem in the application of aerospace systems.

REFERENCES

- Wei X, Guo L. Composite disturbance-observer-based control and H_∞ control for complex continuous models. *International Journal of Robust and Nonlinear Control: IFAC-Affiliated Journal*. 2010; 20(1): 106-118.
- Yao X, Guo L. Composite anti-disturbance control for Markovian jump nonlinear systems via disturbance observer. *Automatica*. 2013; 49(8): 2538-2545.
- Sun H, Hou L, Zong G, et al. Composite anti-disturbance attitude and vibration control for flexible spacecraft. *IET Control Theory & Applications*. 2017; 11(14): 2383-2390.
- Li Y, Chen M, Ge SS, et al. Anti-disturbance control for attitude and altitude systems of the helicopter under random disturbances. *Aerospace Science and Technology*. 2020; 96: 105561.
- Li T, Yang H, Tian J, et al. Improved disturbance rejection control based on H_∞ synthesis and equivalent-input-disturbance for aircraft longitudinal autopilot design. *Proceedings of the Institution of Mechanical Engineers, Part G: Journal of Aerospace Engineering*. 2018; 233(9): 3323-3335.
- Gao F, Wu M, She J, et al. Disturbance rejection in nonlinear systems based on equivalent-input-disturbance approach. *Applied Mathematics and Computation*. 2016; 282: 244-253.
- Li T, Zhang S, Yang H, et al. Robust missile longitudinal autopilot design based on equivalent-input-disturbance and generalized extended state observer approach. *Proceedings of the Institution of Mechanical Engineers, Part G: Journal of Aerospace Engineering*. 2016; 229(6): 1025-1042.
- Aboudonia A, Rashad R, El-Badawy A. Composite hierarchical anti-disturbance control of a quadrotor UAV in the presence of matched and mismatched disturbances. *Journal of Intelligent & Robotic Systems*. 2018; 90(1): 201-216.
- Zengbo L, Yukai Z, JianzhongnQ. Composite anti-disturbance position and attitude control for spacecraft with parametric uncertainty and flexible vibration. *Chinese Journal of Aeronautics*. 2022; 35(12): 242-252.
- Liu L, Chen M, Li T, et al. Composite Anti-Disturbance Reference Model $L_2 - L_\infty$ Control for Helicopter Slung Load System. *Journal of Intelligent & Robotic Systems*. 2021; 102(1): 1-21.
- Cao S, Guo L, Ding Z. Event-triggered anti-disturbance attitude control for rigid spacecrafts with multiple disturbances. *International Journal of Robust and Nonlinear Control*. 2021; 31(2): 344-357.
- Yao X, Wen X. Composite hierarchical hybrid anti-disturbance control for Markovian jump systems with event-triggered disturbance. *Systems & Control Letters*. 2024;185:105734.
- Sakthivel R, Elayabharath VT, Satheesh T, et al. Design of anti-disturbance reliable control for fuzzy networked control systems with multiple disturbances. *International Journal of Fuzzy Systems*. 2024; 26(1): 105-120.
- Sun H, Liu Y, Jiao T, et al. Distributed extended state observer design and dual-side dynamic event-triggered output feedback anti-disturbance control for nonlinear interconnected systems with quantization. *Journal of the Franklin Institute*. 2024; 106847.
- Lin H, Antsaklis PJ. Stability and stabilizability of switched linear systems: a survey of recent results. *IEEE Transactions on Automatic control*. 2009; 54(2): 308-322.
- Liberzon D, Morse AS. Basic problems in stability and design of switched systems. *IEEE control systems magazine*. 1999; 19(5): 59-70.
- Geromel JC, Colaneri P. Stability and stabilization of continuous-time switched linear systems. *SIAM Journal on Control and Optimization*. 2006; 45(5): 1915-1930.
- Allerhand LI, Shaked U. Robust control of linear systems via switching. *IEEE Transactions on Automatic Control*. 2012; 58(2): 506-512.
- Liu F, Chen M, Li T. Resilient H_∞ control for uncertain turbofan linear switched systems with hybrid switching mechanism and disturbance observer. *Applied Mathematics and Computation*. 2022; 413: 126597.
- Deaecto GS, Souza M, Geromel JC. Chattering free control of continuous-time switched linear systems. *IET Control Theory & Applications*. 2014; 8(5): 348-354.
- Gershon E, Shaked U. Robust State-Dependent Switching of Linear Systems with Dwell Time. In *Advances in H_∞ Control Theory*. Springer Cham. 2019; 27-41.
- Wang J, Huang Z, Wu Z, et al. Extended dissipative control for singularly perturbed PDT switched systems and its application. *IEEE Transactions on Circuits and Systems I: Regular Papers*. 2020; 67(12): 5281-5289.
- Xiang W. Stabilization for continuous-time switched linear systems: A mixed switching scheme. *Nonlinear Analysis: Hybrid Systems*. 2020; 36:100872.
- Zhang S, Zhao J. Dwell-Time-Dependent H_∞ Bumpless Transfer Control for Discrete-Time Switched Interval Type-2 Fuzzy Systems. *IEEE Transactions on Fuzzy Systems*. 2021; 30(70): 2426-2437.
- Zhang S, Zhao J. Membership-function-dependent H_∞ bumpless transfer control for switched interval type-2 fuzzy systems with time-delay. *Nonlinear Analysis: Hybrid Systems*. 2024; 52: 101457.
- Priyanka S, Sakthivel R, Mohanapriya S, et al. Composite fault-tolerant and anti-disturbance control for switched fuzzy stochastic systems. *ISA transactions*. 2022;125: 99-109.
- Scherer C, Weiland S. Linear matrix inequalities in control. *Lecture Notes in Dutch Institute for Systems and Control*. Delft. The Netherlands. 2000; 3.
- Kemer E, Başak H, Prempain E. Switched H_2 -state-feedback control with application to a fighter aircraft. *Proceedings of the Institution of Mechanical Engineers, Part G: Journal of Aerospace Engineering*. 2019; 233(14): 5428-5437.
- Richter H. *Advanced control of turbofan engines*. Springer Science & Business Media; 2011.
- Jaw L, Mattingly J. *Aircraft engine controls: Design, System Analysis and Health Monitoring*. Reston VA. USA: American Institute of Aeronautics and Astronautics; 2009.

Emre Kemer:  <https://orcid.org/0000-0001-8716-1971>

Hasan Başak:  <https://orcid.org/0000-0002-3724-6819>



This work is licensed under the Creative Commons BY-NC-ND 4.0 license.

THE FORMATION AND PROPAGATION OF SOLITON WAVE PROFILES FOR THE SHYNARAY-IIA EQUATION

Muhammad Ishfaq KHAN^{*✉}, Waqas Ali FARIDI^{**✉}, Muhammad Amin Sadiq MURAD^{***✉},
 Mujahid IQBAL^{****✉}, Ratbay MYRZAKULOV^{*****✉}, Zhanar UMURZAKHOVA^{*****✉}

^{*}College of Mechanics and Engineering Science, Hohai University, Nanjing 211100, P. R., China

^{**}Department of Mathematics, University of Management and Technology, Lahore, Pakistan

^{***}Department of Mathematics, College of Science, University of Duhok, Duhok, Iraq

^{****}School of Mathematical Sciences, Jiangsu University, Zhenjiang, 212013, China

^{*****}Ratbay Myrzakulov Eurasian International Centre for Theoretical Physics, Astana, Kazakhstan

m.ishfaqkhan032@gmail.com, wa966142@gmail.com, muhammad.murad@uod.ac, mujahidiqbal399@gmail.com,
 rmyrzakulov@gmail.com, zhumurzhakhova@gmail.com

received 06 August 2024, revised 18 September 2024, accepted 25 September 2024

Abstract: This study examines a novel use of the Jacobi elliptic function expansion method to solve the Shynaray-IIA equation, a significant nonlinear partial differential equation that arises in optical fiber, plasma physics, surface symmetry geometry, and many other mathematical physics domains. This kind of solution has never been attained in research prior to this study. Numerous properties of a particular class of solutions, called the Jacobi elliptic functions, make them useful for the analytical solution of a wide range of nonlinear problems. Using this powerful method, we derive a set of exact solutions for the Shynaray-IIA equation, shedding light on its complex dynamics and behaviour. The proposed method is shown to be highly effective in obtaining exact solutions in terms of Jacobi elliptic functions, such as dark, bright, periodic, dark-bright, dark-periodic, bright periodic, singular, and other various types of solitons. Furthermore, a detailed analysis is conducted on the convergence and accuracy of the obtained solutions. The outcomes of this study extend the applicability of the Jacobi elliptic function approach to a novel class of non-linear models and provide valuable insights into the dynamics of Shynaray-IIA equation. This study advances the creation of efficient mathematical instruments for resolving intricate nonlinear phenomena across a range of scientific fields.

Key words: soliton theory, integrable partial differential equation, analytical approach, propagation of solitary waves

1. INTRODUCTION

The Shynaray-IIA is a coupled partial differential equation, a significant nonlinear partial differential equation (PDE), arises in numerous branches of physical and mathematical sciences, like as fluid mechanics, quantum physics and plasma physics. Its complex nonlinear nature presents a substantial challenge in finding exact analytical solutions, leading researchers to explore innovative and efficient methods for resolution such as tanh method [1], extended auxiliary equation method [2 – 4], variational method [5], modified and extended simple equation method [6 – 8], direct algebraic method [9], generalized exponential rational function technique [10], extended F-expansion scheme [11, 12], G/G' – expansion algorithm [13], sine-Gordon expansion method [14], modified sub-equation method [15], dar-boux method [16], homogeneous balance [17], and so on [18 – 33]. Among the abundance of mathematical tools available, the Jacobi elliptic function approach has emerged as a promising scheme for solving the non-linear partial differential equations (PDEs). This technique is particularly valuable in handling nonlinear equations with high nonlinearity, as it enables researchers to obtain exact solutions by transforming the original equation into a more manageable elliptic equation. In this research article,

we focus on investigating the application of the Jacobi elliptic function approach to handle the Shynaray-IIA equation. The considered model is given as,

$$\begin{aligned}iq_t + q_{xt} - i(vq)_x &= 0, \\ir_t - r_{xt} - i(vr)_x &= 0, \\v_x - \frac{n^2}{\alpha}(rq)_t &= 0.\end{aligned}\tag{1}$$

We aimed to construct exact analytical solutions that shed light on the intricate dynamics described by the equation. The obtained solutions not only contribute to a deeper understanding of underlying physical processes but also offer a valuable standard for validating numerical and approximate method in solving this challenging PDE. The Jacobi elliptic function expansion method serves as a powerful mathematical tool to solve the Shynaray-IIA (S-IIA) equation, allowing us to gain deeper insight into the behavior of complex physical systems. The exact analytical solutions obtained through this research contribute to the existing body of knowledge, paving the way for further advancement in the study of nonlinear Partial differential equations (PDEs) and their implications in diverse scientific disciplines. Sachin et al. [34 – 38] have examined the Konopelchenko–Dubrovsky (KD) equation, generalized complex coupled Schrödinger–Boussinesq equations, Sakovich equation, Zakharov–Kuznetsov–Benjamin–Bona–Mahony (ZK-BBM) equation and Vakhnenko–Parkes equa-

tion to develop the solitary wave solution and visualized their propagation by utilizing the distinct analytical techniques. Rani et al. [39] constructed exact analytical solutions for complex modified Kortewegde-Vries. Nonlaopon et al. [40] performed Painlevé analysis to form the exact soliton solutions.

The remainder of this article is presented in the following structure: Section 1, provides a brief overview of the Shynaray-IIA equation and its relevance in various scientific fields. Section II outlines the theoretical basis of considered method. In Section III, we present the step-by-step implementation of the method to obtain exact solutions for the Shynaray-IIA equation. In section IV, provide the analysis of graphs for direct study. Section V, discusses the conclusion and applicability of the proposed approach.

2. DESCRIPTION OF ANALYTICAL TECHNIQUE

An overview of the Jacobi elliptic function methodology is given in this section. We will use nonlinear partial differential equations, which typically have the following mathematical conclusion,

$$N(u, \frac{\partial u}{\partial t}, \frac{\partial u}{\partial x}, \frac{\partial^2 u}{\partial t^2}, \frac{\partial^2 u}{\partial x^2}, \dots) = 0. \quad (2)$$

Utilizing the following wave transformation to convert Eq. (1) into an ordinary differential equation,

$$u = u(\xi), \xi = k(x - ct), \quad (3)$$

where the symbols for frequency and wave number, respectively, are c and k . Equation (1) has been successfully transformed into an ordinary differential equation (ODE) by the procedure described in Equation (2).

$$\frac{\partial(\cdot)}{\partial t} = -ck \frac{d(\cdot)}{d\xi}, \quad \frac{\partial(\cdot)}{\partial x} = k \frac{d(\cdot)}{d\xi}, \quad (4)$$

$$N(u', u'', u''', \dots) = 0. \quad (5)$$

Tab. 1. The chosen value of P , Q and R

| | P | Q | R | F |
|----|---------------------|-----------------------|--------------------------|--------------|
| 1 | m^2 | $-(1 + m^2)$ | 1 | sn, cd |
| 2 | $-m^2$ | $2m^2 - 1$ | $1 - m^2$ | cn |
| 3 | -1 | $2 - m^2$ | $m^2 - 1$ | dn |
| 4 | 1 | $-(1 + m^2)$ | m^2 | ns, dc |
| 5 | $1 - m^2$ | $2m^2 - 1$ | $-m^2$ | nc |
| 6 | $m^2 - 1$ | $2 - m^2$ | -1 | nd |
| 7 | $1 - m^2$ | $2 - m^2$ | 1 | sc |
| 8 | $-m^2(1 - m^2)$ | $2m^2 - 1$ | 1 | sd |
| 9 | 1 | $2 - m^2$ | $1 - m^2$ | cs |
| 10 | 1 | $2m^2 - 1$ | $-m^2(1 - m^2)$ | ds |
| 11 | $-\frac{1}{4}$ | $\frac{m^2 + 1}{2}$ | $\frac{-(1 - m^2)^2}{4}$ | $mcn \mp dn$ |
| 12 | $\frac{1}{4}$ | $\frac{-2m^2 + 1}{2}$ | $\frac{1}{4}$ | $ns \mp cs$ |
| 13 | $\frac{1 - m^2}{4}$ | $\frac{m^2 + 1}{2}$ | $\frac{1 - m^2}{4}$ | $nc \mp sc$ |
| 14 | $\frac{1}{4}$ | $\frac{m^2 - 2}{2}$ | $\frac{m^4}{4}$ | $ns \mp ds$ |

| | | | | |
|----|-------------------------|----------------------|----------------------|---|
| 15 | $\frac{m^2}{4}$ | $\frac{m^2 - 2}{2}$ | $\frac{m^2}{4}$ | $sn \mp icn, \frac{sn}{\sqrt{1 - m^2}sn}$ |
| 16 | $\frac{1}{4}$ | $\frac{1 - 2m^2}{2}$ | $\frac{1}{4}$ | $mcn \mp idn, \frac{sn}{1 \mp cn}$ |
| 17 | $\frac{m^2}{4}$ | $\frac{m^2 - 2}{2}$ | $\frac{1}{4}$ | $\frac{sn}{1 \mp dn}$ |
| 18 | $\frac{m^2 - 1}{4}$ | $\frac{m^2 + 1}{2}$ | $\frac{m^2 - 1}{4}$ | $\frac{dn}{1 \mp msn}$ |
| 19 | $\frac{1 - m^2}{4}$ | $\frac{m^2 + 1}{2}$ | $\frac{-m^2 + 1}{4}$ | $\frac{cn}{1 \mp sn}$ |
| 20 | $\frac{(1 - m^2)^2}{4}$ | $\frac{m^2 + 1}{2}$ | $\frac{1}{4}$ | $\frac{sn}{dn \mp cn}$ |
| 21 | $\frac{m^4}{4}$ | $\frac{m^2 - 2}{2}$ | $\frac{1}{4}$ | $\frac{cn}{\sqrt{1 - m^2} \mp dn}$ |

In conjunction with utilizing this advanced directed technique, the underlying principle entails augmenting the likelihood of resolving an auxiliary ODE, namely first-order Jacobian problem with the three parameters. This method aims to produce a multitude of Jacobian elliptic solutions for the given issue. Visualizing the auxiliary equation is a feasible step in understanding this process.

$$(F')^2(\xi) = PF^4(\xi) + QF^2(\xi) + R. \quad (6)$$

Let $F' = \frac{dF}{d\xi}$, where $\xi = \xi(x, t)$, and the constants P , Q and R are involved. The solution for equation (5) is provided in Tab. 1. It is important to note that $i^2 = -1$. Additionally, the Jacobi elliptic functions are denoted as $sn\xi = sn(\xi, m)$, $cn\xi = cn(\xi, m)$, and $dn\xi = dn(\xi, m)$, where m lies in the range $0 < m < 1$ and represents the modulus.

Tab. 2. Analysis of Jacobi elliptic functions in the limit of $m \rightarrow 0$ and $m \rightarrow 1$.

| | | $m \rightarrow 1$ | $m \rightarrow 0$ | | | $m \rightarrow 1$ | $m \rightarrow 0$ |
|---|-------|-------------------|-------------------|----|-------|-------------------|-------------------|
| 1 | snu | \tanhu | \sinu | 7 | dcu | 1 | $secu$ |
| 2 | cnu | $sechu$ | \cosu | 8 | ncu | \coshu | $secu$ |
| 3 | dnu | $sechu$ | 1 | 9 | scu | \sinhu | \tanu |
| 4 | cdu | 1 | \cosu | 10 | nsu | \cothu | $cscu$ |
| 5 | sdu | \sinhu | \sinu | 11 | dsu | $cschu$ | $cscu$ |
| 6 | ndu | \coshu | 1 | 12 | csu | $cschu$ | $cotu$ |

The elliptic functions exhibit a distinctive double periodic, processing distinct properties as outline below:

$$sn^2\xi + cn^2\xi = 1,$$

$$dn^2\xi + m^2sn^2\xi = 1,$$

$$\frac{d}{d\xi} sn\xi = cn\xi dn\xi,$$

$$\frac{d}{d\xi} cn\xi = -sn\xi dn\xi,$$

$$\frac{d}{d\xi} dn\xi = -m^2sn\xi cn\xi.$$

With reference to Tab. 2, this reduction makes it possible to derive the solutions for the given problem using the trigonometric function and solitons. The Jacobi elliptic function expansion method can be used to describe the function as a finite series of Jacobi elliptic functions.

$$u(\xi) = \sum_{i=0}^n a_i F^i(\xi). \quad (7)$$

Here the function $F(\xi)$ represents solution to the non-linear ordinary equation denoted as Eq. 5. The constants n and a_i (where $i = 0, 1, 2, \dots, n$) are parameters that have to be found. The determination of the integer n in Eq. 6 involves an analysis of the highest order linear term.

$$O\left(\frac{d^p u}{d\xi^p}\right) = n + p, \quad p = 0, 1, 2, 3, \dots, \quad (8)$$

thus, the most significant nonlinear terms at the highest order are $O\left(u^q \frac{d^p u}{d\xi^p}\right) = (q + 1)n + p, \quad p = 0, 1, 2, 3, \dots,$

$$q = 1, 2, 3, \dots, \quad (9)$$

in Eq. 4.

Utilizing Eq. 6 and setting all coefficients of powers F to zero, we derive a set of nonlinear algebraic equations for the variables a_i , (where $i = 0, 1, 2, 3, \dots$). Employing Mathematica, we proceed to solve this system of algebraic equations and put all the values for P , Q , and R as per Eq. 5 in Tab. 1. This approach, integrating the information from Eq. 6 with the selected auxiliary equation, allows for the determination of exact solutions for Eq. 1.

3. THE CONSTRUCTION OF SOLITONS OF SHYNARAY-IIA EQUATION (S-IIAE)

The precise solutions to Shynaray-IIA Eq. 1 using the Jacobi elliptic function expansion approach are shown in this section,

$$iq_t + q_{xt} - i(vq)_x = 0,$$

$$ir_t - r_{xt} - i(vr)_x = 0,$$

$$v_x - \frac{n^2}{\alpha}(rq)_t = 0.$$

In case when $\epsilon = \epsilon \bar{q}$ ($\epsilon = \pm 1$), the S-IIAE takes the following form:

$$iq_t + q_{xt} - i(vq)_x = 0,$$

$$v_x - \frac{n^2 \epsilon}{\alpha}(|q|^2)_t = 0. \quad (10)$$

In the above equation m , n and ϵ are constants. By using the traveling wave transformation Eq. 11 is reduced into the following ODE:

$$q(x, t) = U(\eta)e^{i\xi(x, t)}, v(x, t) = G(\eta), \quad \xi(x, t) = -\delta x + \omega t + \theta, \eta = x - ct, \quad (11)$$

where $v, \theta, \omega, \delta$ characterize the frequency, the phase constant, the wave number and the velocity, respectively. The Eq. 27 is plugging into the first part of Eq. 26 and getting the real and imaginary parts,

$$cU''(\eta) + \omega(1 - \delta)U(\eta) + \delta G(\eta)U(\eta) + i(\omega - c(1 - \delta))U'(\eta) - G(\eta)U'(\eta) - G'(\eta)U(\eta) = 0,$$

$$G'(\eta) + \frac{2c\epsilon n^2}{\alpha}U(\eta)U'(\eta) = 0. \quad (12)$$

The second Eq. 28 is integrated, and we get

$$G(\eta) = -\frac{c\epsilon n^2}{\alpha}U^2(\eta). \quad (13)$$

Substitute the Eq. 13 into the first part of 12 and separating the real and imaginary parts as

$$cU''(\eta) + \omega(1 - \delta)U(\eta) - \frac{\delta c\epsilon n^2}{\alpha}U^3(\eta) = 0. \quad (14)$$

And we have the imaginary part as,

$$(\omega - c(1 - \delta))U'(\eta) + \frac{3c\epsilon n^2}{\alpha}U''(\eta)U'(\eta) = 0. \quad (15)$$

By using the homogeneous balancing procedure, we obtained $n = 1$, the determine value of n is substituted in Eq. 7 we obtained the simple form of the solution as:

$$U(\eta) = a_0 + a_1 F(\eta), \quad (16)$$

$$U^3(\eta) = a_0^3 + a_1^3 F^3(\eta) + 3a_0 a_1^2 F^2(\eta) + 3a_0^2 a_1 F \quad (17)$$

and

$$U''(\eta) = a_1(2PF^3(\eta) + QF(\eta)). \quad (18)$$

Substitute Eq. 16-18 into Eq. 15, we get,

$$c a_1(2PF^3(\eta) + QF(\eta)) + \omega(1 - \delta)(a_0 + a_1 F(\eta)) - \frac{\delta c\epsilon n^2}{\alpha}(a_0^3 + a_1^3 F^3(\eta) + 3a_0 a_1^2 F^2(\eta) + 3a_0^2 a_1 F(\eta)) = 0. \quad (19)$$

By collecting the various coefficients of $F^i(\eta)$, we get the system of equations,

$$U^0: (\omega(1 - \delta) - \frac{\delta c\epsilon n^2}{\alpha}a_0^2) a_0 = 0, \quad (20)$$

$$U^1: (cQ + \omega(1 - \delta) - 3a_0^2 \frac{\delta c\epsilon n^2}{\alpha})a_1 = 0, \quad (21)$$

$$U^2: -3a_0 a_1^2 \frac{\delta c\epsilon n^2}{\alpha} = 0, \quad (22)$$

$$U^3 = (2Pc - a_1^2 \frac{\delta c\epsilon n^2}{\alpha})a_1 = 0. \quad (23)$$

Upon solving the aforementioned system by using Maple software, we obtain the coefficients pertaining to the series 16,

$$a_0 = 0, \quad a_1 = \pm \sqrt{\frac{2\alpha P}{\delta \epsilon}}. \quad (24)$$

The obtained solution is of the form,

$$U = \pm \sqrt{\frac{2\alpha P}{\delta \epsilon}} F(\eta). \quad (25)$$

When the values $P = m^2$, $Q = -(1 + m^2)$, and $R = 1$ are chosen, table 1 provides the corresponding values of $F = sn$. Therefore, the periodic solution of Equation 1 can be represented as,

$$q_{1,1} = \pm \sqrt{\frac{2\alpha m^2}{\delta \epsilon}} \frac{sn(x - ct)}{n}, \quad (26)$$

$$v_{1,1} = -\frac{2cm^2}{\delta} sn^2(x - ct). \quad (27)$$

Supposing $m \rightarrow 1$, hence, by referring to table 2, one may derive the solitary wave solution of Eq. 1.

$$q_{1,2} = \pm \sqrt{\frac{2\alpha}{\delta \epsilon}} \tanh(x - ct), \quad (28)$$

$$v_{1,2} = -\frac{2c}{\delta} \tanh^2(x - ct). \quad (29)$$

Choosing $P = -m^2, Q = 2m^2 - 1, R = 1 - m^2$, based on the data supplied in Table 1, it can be inferred that the variable F can be mathematically expressed as $F = cn$. Consequently, the periodic solution of Equation (1) can be derived as follows:

$$q_{1,3} = \pm \sqrt{\frac{-2\alpha m^2}{\delta \epsilon}} cn(x - ct), \quad (30)$$

$$v_{1,3} = \frac{2cm^2}{\delta} cn^2(x - ct). \quad (31)$$

Considering $m \rightarrow 1$ the solitary wave solution of Eq. 1 can be expressed as per the information provided in Tab. 2.

$$q_{1,4} = \pm \sqrt{\frac{-2\alpha}{\delta \epsilon}} \operatorname{sech}(x - ct), \quad (32)$$

$$v_{1,4} = \frac{2c}{\delta} \operatorname{sech}^2(x - ct). \quad (33)$$

Setting $P = -1, Q = 2 - m^2, R = m^2 - 1$, based on the data shown in Tab. 1, it can be inferred that the periodic solution of Eq. 1 can be mathematically represented as follows:

$$q_{1,5} = \pm \sqrt{\frac{-2\alpha}{\delta \epsilon}} dn(x - ct), \quad (34)$$

$$v_{1,5} = \frac{2c}{\delta} dn^2(x - ct). \quad (35)$$

In the context of $m \rightarrow 1$ from Tab. 2, the similarity between the solution shown and the solution derived in Eq. 27 is clearly demonstrated.

While $P = 1, Q = -(1 + m^2), R = m^2, F = ns$, according to the data presented in Tab. 1, the answer to Eq. 1 can be represented as follows:

$$q_{1,6} = \pm \sqrt{\frac{2\alpha}{\delta \epsilon}} ns(x - ct), \quad (36)$$

$$v_{1,6} = -\frac{2c}{\delta} ns^2(x - ct). \quad (37)$$

Additionally, when $m \rightarrow 1$ the solitary wave solution of Eq. 1 is presented in Tab. 2.

$$q_{1,7} = \pm \sqrt{\frac{2\alpha}{\delta \epsilon}} \coth(x - ct), \quad (38)$$

$$v_{1,7} = -\frac{2c}{\delta} \coth^2(x - ct). \quad (39)$$

Using Tab. 2, the periodic solution of Eq. 1 can be stated as follows if $m \rightarrow 0$:

$$q_{1,8} = \pm \sqrt{\frac{2\alpha}{\delta \epsilon}} \csc(x - ct), \quad (40)$$

$$v_{1,8} = -\frac{2c}{\delta} \csc^2(x - ct). \quad (41)$$

Supposing $P = 1, Q = -(1 + m^2), R = m^2$.

Thus, $F = dc$,

$$q_{1,8} = \pm \sqrt{\frac{2\alpha}{\delta \epsilon}} dc(x - ct), \quad (42)$$

$$v_{1,8} = -\frac{2c}{\delta} dc^2(x - ct). \quad (43)$$

Using Tab. 2, the periodic solution of Eq. 1 can be stated as follows if $m \rightarrow 0$:

$$q_{1,10} = \pm \sqrt{\frac{2\alpha}{\delta \epsilon}} \sec(x - ct), \quad (44)$$

$$v_{1,10} = -\frac{2c}{\delta} \sec^2(x - ct). \quad (45)$$

When $P = 1 - m^2, Q = 2m^2 - 1, R = -m^2$. Thus, $F = nc$ and the solution of periodic nature of Eq. 1 as:

$$q_{1,11} = \pm \sqrt{\frac{2\alpha(1-m^2)}{\delta \epsilon}} nc(x - ct), \quad (46)$$

$$v_{1,11} = -\frac{2c(1-m^2)}{\delta} nc^2(x - ct). \quad (47)$$

As $m \rightarrow 0$ from Tab. 2, it is shown that the solution found as that of 33.

Also regarding $P = 1 - m^2, Q = 2 - m^2, R = 1$.

Thus, $F = sc$:

$$q_{1,12} = \pm \sqrt{\frac{2\alpha(1-m^2)}{\delta \epsilon}} sc(x - ct), \quad (48)$$

$$v_{1,12} = -\frac{2c(1-m^2)}{\delta} sc^2(x - ct). \quad (49)$$

Furthermore, we find the periodic solution of Eq. 1 as follows for $m \rightarrow 0$, as shown in Tab. 2:

$$q_{1,13} = \pm \sqrt{\frac{2\alpha}{\delta \epsilon}} \tan(x - ct), \quad (50)$$

$$v_{1,13} = -\frac{2c}{\delta} \tan^2(x - ct). \quad (51)$$

Considering $P = 1, Q = 2 - m^2, R = 1 - m^2$ and $F = cs$, thus:

$$q_{1,14} = \pm \sqrt{\frac{2\alpha}{\delta \epsilon}} cs(x - ct), \quad (52)$$

$$v_{1,14} = -\frac{2c}{\delta} cs^2(x - ct). \quad (53)$$

The solitary wave solution Eq. (1) is given as follows as $m \rightarrow 1$, per Tab. 2:

$$q_{1,15} = \pm \sqrt{\frac{2\alpha}{\delta \epsilon}} \operatorname{csch}(x - ct), \quad (54)$$

$$v_{1,15} = -\frac{2c}{\delta} \operatorname{csch}^2(x - ct). \quad (55)$$

The solitary wave solution Eq. 1 is given as follows as $m \rightarrow 0$, per Tab. 2,

$$q_{1,16} = \pm \sqrt{\frac{2\alpha}{\delta \epsilon}} \cot(x - ct), \quad (56)$$

$$v_{1,16} = -\frac{2c}{\delta} \cot^2(x - ct). \quad (57)$$

Also assigning $P = 1, Q = 2m^2 - 1, R = m^4 - m^2$ and $F = ds$. Thus,

$$q_{1,17} = \pm \sqrt{\frac{2\alpha}{\delta \epsilon}} ds(x - ct), \quad (58)$$

$$v_{1,17} = -\frac{2c}{\delta} ds^2(x - ct). \quad (59)$$

In this family, the soliton solution is the similar to Eq. 30. If the limit of $m \rightarrow 0$, the solution can be articulated as per Eq. 38 with reference to Tab. 2.

Assuming P, Q, R as $P = \frac{-1}{4}, Q = \frac{m^2+1}{2}, R = \frac{-(1-m^2)}{4}$, according to Tab. 1, F formulated as $F = mcn \mp dn$, the solution is determined as,

$$q_{1,18} = \pm \sqrt{\frac{-\alpha}{2\delta\epsilon}} mcn(x-ct) \mp dn(x-ct), \quad (60)$$

$$v_{1,18} = \frac{c}{2\delta} (mcn(x-ct) \mp dn(x-ct))^2. \quad (61)$$

Additionally, when $m \rightarrow 1$, the obtained solution is similar the solution found in Eq. (25).

If we select P, Q, R as $P = \frac{1}{4}, Q = \frac{-2m^2+1}{2}, R = \frac{1}{4}$, and evaluate F from table 1 where $= ns \mp cs$, thus solution of Eq. (1) can be indicated as,

$$q_{1,19} = \pm \sqrt{\frac{\alpha}{2\delta\epsilon}} (ns(x-ct) \mp cs(x-ct)), \quad (62)$$

$$v_{1,19} = -\frac{c}{2\delta} (ns(x-ct) \mp cs(x-ct))^2. \quad (63)$$

The solitary wave solution for $m \rightarrow 1$ in Eq. 1 is identified as,

$$q_{1,20} = \pm \sqrt{\frac{\alpha}{2\delta\epsilon}} \coth(x-ct) \mp csch(x-ct), \quad (64)$$

$$v_{1,20} = -\frac{c}{2\delta} (\coth(x-ct) \mp csch(x-ct))^2. \quad (65)$$

Additionally, in the case where $m \rightarrow 0$, based on Tab. 2, obtaining a periodic solution is evident.

$$q_{1,21} = \pm \sqrt{\frac{\alpha}{2\delta\epsilon}} csc(x-ct) \mp cot(x-ct), \quad (66)$$

$$v_{1,21} = -\frac{c}{2\delta} (csc(x-ct) \mp cot(x-ct))^2. \quad (67)$$

If $P = \frac{1-m^2}{4}, Q = \frac{m^2+1}{2}, R = \frac{1-m^2}{4}$ and $F = nc \mp sc$, the solution of Eq. (1) can be found as,

$$q_{1,22} = \pm \sqrt{\frac{\alpha(1-m^2)}{2\delta\epsilon}} (nc(x-ct) \mp sc(x-ct)), \quad (68)$$

$$v_{1,22} = \frac{-c(1+m^2)}{2\delta} (nc(x-ct) \mp sc(x-ct))^2. \quad (69)$$

The solitary wave solution for $m \rightarrow 0$ in Eq. 1 is identified as,

$$q_{1,23} = \pm \sqrt{\frac{\alpha}{2\delta\epsilon}} (\sec(x-ct) \mp \tan(x-ct)), \quad (70)$$

$$v_{1,23} = -\frac{c}{2\delta} (\sec(x-ct) \mp \tan(x-ct))^2. \quad (71)$$

Setting $P = \frac{m^2}{4}, Q = \frac{m^2-2}{2}, R = \frac{m^2}{4}$, as per Table 1, $F = sn \mp icn$, due to this setting the solution of Eq. 1 can be found as:

$$q_{1,24} = \pm \sqrt{\frac{\alpha m^2}{2\delta\epsilon}} (sn(x-ct) \mp icn(x-ct)), \quad (72)$$

$$v_{1,24} = -\frac{cm^2}{2\delta} (sn(x-ct) \mp icn(x-ct))^2. \quad (73)$$

The solitary wave solution for $m \rightarrow 1$ in Eq. (1) is identified as,

$$q_{1,25} = \pm \sqrt{\frac{\alpha}{2\delta\epsilon}} (\tanh(x-ct) \mp \operatorname{sech}(x-ct)), \quad (74)$$

$$v_{1,25} = \frac{-c}{2\delta} (\tanh(x-ct) \mp \operatorname{sech}(x-ct))^2. \quad (75)$$

Regarding $P = \frac{1}{4}, Q = \frac{-2m^2+1}{2}, R = \frac{1}{4}$, and $F = msn \mp idn$ from the Table 1, thus, the solution of Eq. 1 can be expressed as,

$$q_{1,26} = \pm \sqrt{\frac{\alpha}{2\delta\epsilon}} (msn(x-ct) \mp idn(x-ct)), \quad (76)$$

$$v_{1,26} = \frac{-c}{2\delta} (msn(x-ct) \mp idn(x-ct))^2. \quad (77)$$

For $m \rightarrow 1$, the solution obtained as that of 48.

Considering

$$P = \frac{1}{4}, Q = \frac{1-2m^2}{2}, R = \frac{1}{4},$$

and

$$F = \frac{sn}{1 \mp cn},$$

from Tab. 1, thus, the solution of Eq. 1 can be found as,

$$q_{1,27} = \pm \sqrt{\frac{\alpha}{2\delta\epsilon}} \frac{sn(x-ct)}{1 \mp cn(x-ct)}, \quad (78)$$

$$v_{1,27} = \frac{-c}{2\delta} \left(\frac{sn(x-ct)}{1 \mp cn(x-ct)} \right)^2. \quad (79)$$

If we take a look at Tab. 2, we can determine the solitary wave solution of Eq. 1 for $m \rightarrow 1$,

$$q_{1,28} = \pm \sqrt{\frac{\alpha}{2\delta\epsilon}} \frac{\tanh(x-ct)}{1 \mp \operatorname{sech}(x-ct)}, \quad (80)$$

$$v_{1,28} = \frac{-c}{2\delta} \left(\frac{\tanh(x-ct)}{1 \mp \operatorname{sech}(x-ct)} \right)^2. \quad (81)$$

If we take a look at Tab. 2, we can determine the solitary wave solution of Eq. 1 for $m \rightarrow 0$,

$$q_{1,29} = \pm \sqrt{\frac{\alpha}{2\delta\epsilon}} \frac{\sin(x-ct)}{1 \mp \cos(x-ct)}, \quad (82)$$

$$v_{1,29} = \frac{-c}{2\delta} \left(\frac{\sin(x-ct)}{1 \mp \cos(x-ct)} \right)^2. \quad (83)$$

Supposing $P = \frac{m^2}{4}, Q = \frac{m^2-2}{2}, R = \frac{1}{4}$ it can be concluded from Tab. 1 $F = \frac{sn}{1 \mp dn}$, so the solution of Eq. 1 can be found as,

$$q_{1,30} = \pm \sqrt{\frac{\alpha m^2}{2\delta\epsilon}} \frac{sn(x-ct)}{1 \mp dn(x-ct)}, \quad (84)$$

$$v_{1,30} = -\frac{cm^2}{2\delta} \left(\frac{sn(x-ct)}{1 \mp dn(x-ct)} \right)^2. \quad (85)$$

When $m \rightarrow 1$, the solution is determined by the solution in equation 52.

From Tab. 1, allocating $P = \frac{1-m^2}{4}, Q = \frac{m^2+1}{2}, R = \frac{1-m^2}{4}$ and

$$F = \frac{cn}{1 \mp sn},$$

thus,

$$q_{1,31} = \pm \sqrt{\frac{\alpha(1-m^2)}{2\delta\epsilon}} \frac{cn(x-ct)}{1 \mp sn(x-ct)}, \quad (86)$$

$$v_{1,31} = \frac{-c(1+m^2)}{2\delta} \left(\frac{cn(x-ct)}{1 \mp sn(x-ct)} \right)^2. \quad (87)$$

If we take a look at Tab. 2, we can determine the solitary wave solution of Eq. 1 for $m \rightarrow 0$,

$$q_{1,32} = \pm \frac{\sqrt{\frac{\alpha}{2\delta\epsilon}}}{n} \frac{\cos(x-ct)}{1 \mp \sin(x-ct)}, \quad (88)$$

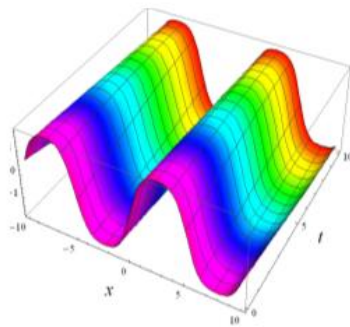
$$v_{1,32} = \frac{-c}{2\delta} \left(\frac{\cos(x-ct)}{1 \mp \sin(x-ct)} \right)^2. \quad (89)$$

Choosing $P = \frac{(1-m^2)^2}{4}$, $Q = \frac{m^2+1}{2}$, $R = \frac{1}{4}$ and $F = \frac{sn}{dn \mp cn}$, so that the solution of Eq. 1 can be obtained as,

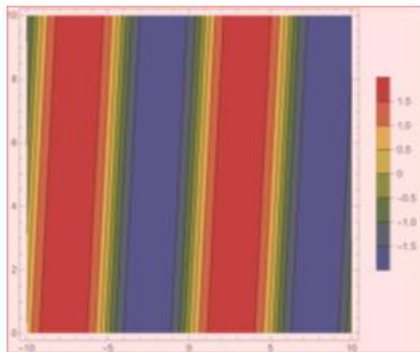
$$q_{1,33} = \pm \frac{\sqrt{\frac{\alpha(1-m^2)^2}{2\delta\epsilon}}}{n} \frac{sn(x-ct)}{dn(x-ct) \mp cn(x-ct)}, \quad (90)$$

$$v_{1,33} = \frac{-c(1+m^2)^2}{2\delta} \left(\frac{sn(x-ct)}{dn(x-ct) \mp cn(x-ct)} \right)^2. \quad (91)$$

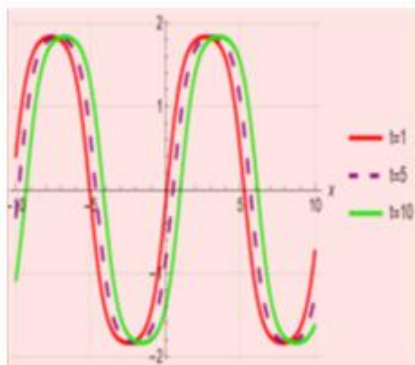
For $m \rightarrow 0$, the solution is obtained as that of 51.



a) 3-D visualization

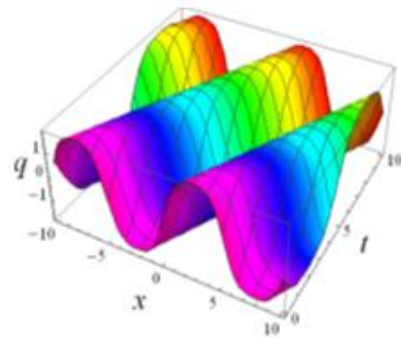


b) contour visualization

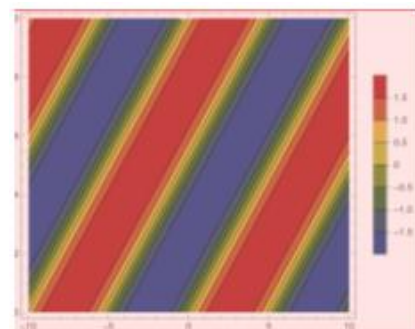


c) 2-D visualization

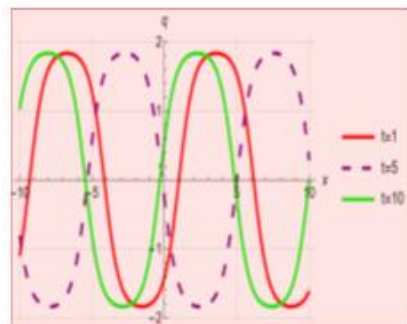
Fig. 1. 3-D, contour visualization and 2-D propagation of $q_{1,1}$ for specific values of the parameters are $\epsilon = 1.2$, $\alpha = 1.3$, $\delta = 0.5$, $m = 0.9$, $c = 0.1$



a) 3-D visualization

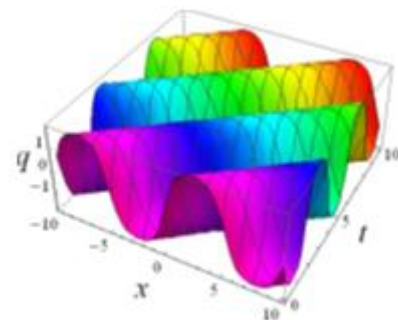


b) contour visualization



c) 2-D visualization

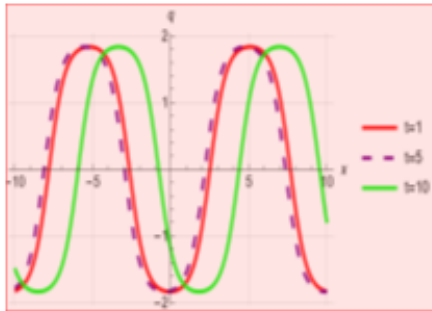
Fig. 2. 3-D, contour visualization and 2-D propagation of $q_{1,1}$ for specific values of the parameters are $\epsilon = 1.2$, $\alpha = 1.3$, $\delta = 0.5$, $m = 0.9$, $c = 01$



a) 3-D visualization

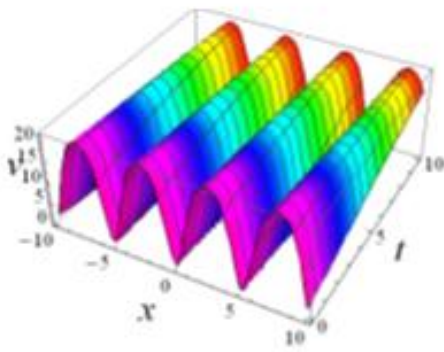


b) contour visualization

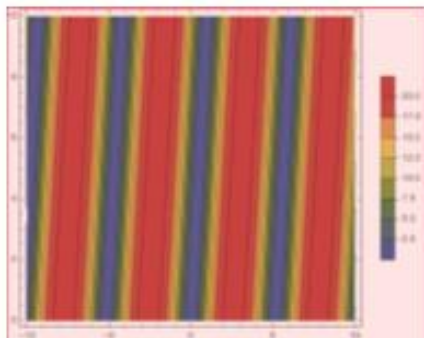


c) 2-D visualization

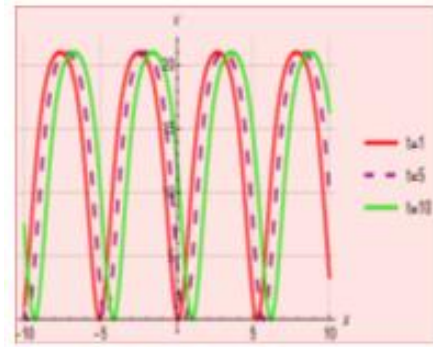
Fig. 3. 3-D, contour visualization and 2-D propagation of $q_{1,1}$ for specific values of the parameters are $\epsilon = 1.2$, $\alpha = 1.3$, $\delta = 0.5$, $m = 0.9$, $c = 2.5$



a) 3-D visualization

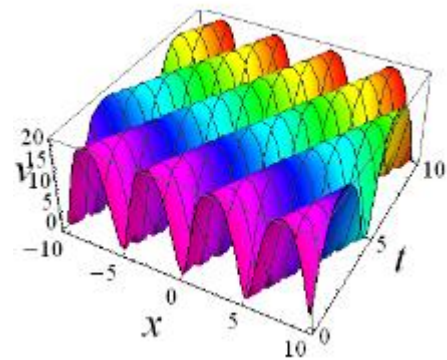


b) contour visualization

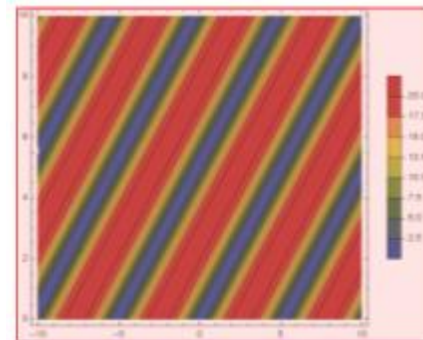


c) 2-D visualization

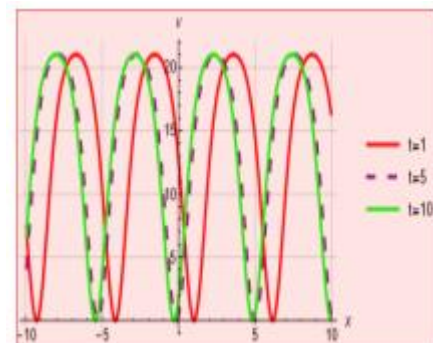
Fig. 4. 3-D, contour visualization and 2-D propagation of $v_{1,1}$ for specific values of the parameters are $\epsilon = 1.2$, $\alpha = 1.3$, $\delta = 0.5$, $n = 1.5$, $c = -1.5$, $m = 0.9$, $c = 0.1$.



a) 3-D visualization

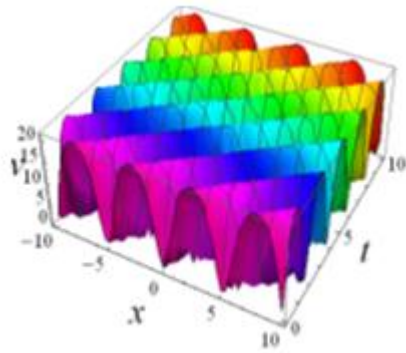


b) contour visualization

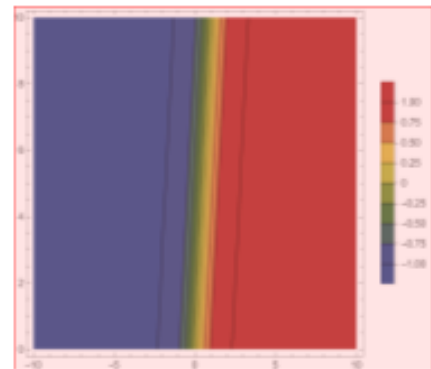


c) 2-D visualization

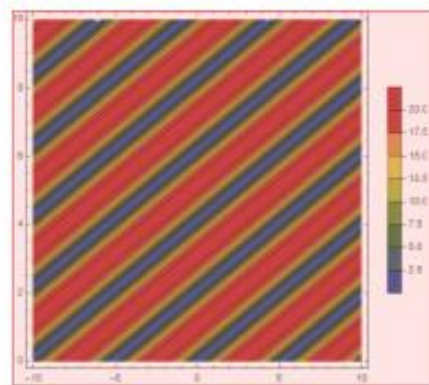
Fig. 5. 3-D, contour visualization and 2-D propagation of $v_{1,1}$ for specific values of the parameters are $\epsilon = 1.2$, $\alpha = 1.3$, $\delta = 0.5$, $n = 1.5$, $c = -1.5$, $m = 0.9$, $c = 01$



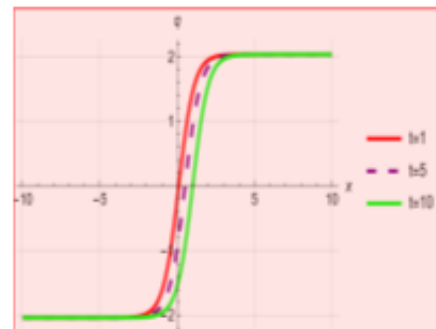
a) 3-D visualization



b) contour visualization

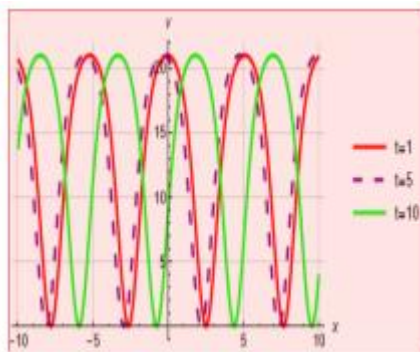


b) contour visualization



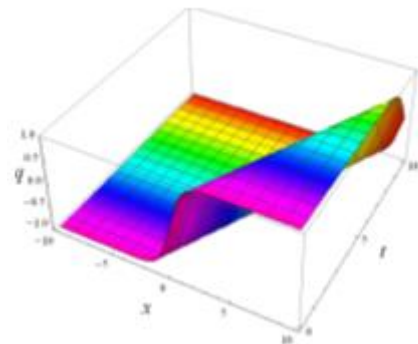
c) 2-D visualization

Fig. 7. 3-D, contour visualization and 2-D propagation of $q_{1,2}$ for specific values of the parameters are $\epsilon = 1.2$, $\alpha = 1.3$, $\delta = 0.5$, $m = 0.5$, $c = 0.1$

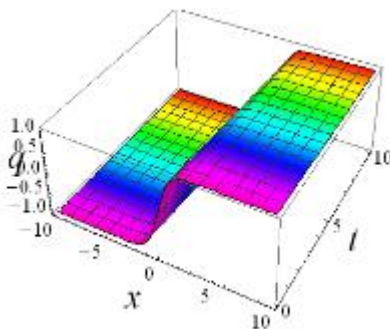


c) 2-D visualization

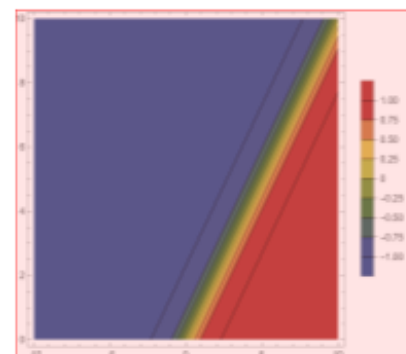
Fig. 6. 3-D, contour visualization and 2-D propagation of $v_{1,1}$ for specific values of the parameters are $\epsilon = 1.2$, $\alpha = 1.3$, $\delta = 0.5$, $n = 1.5$, $c = -1.5$, $m = 0.9$, $c = 2.5$



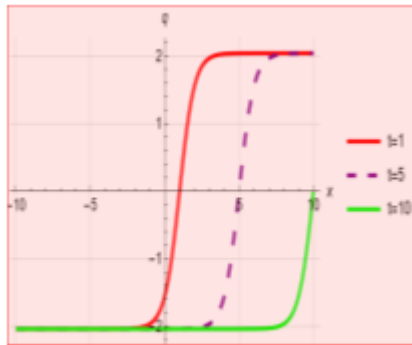
a) 3-D visualization



a) 3-D visualization

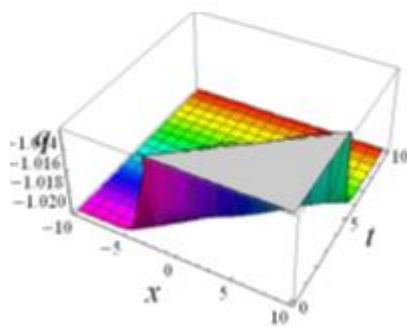


b) contour visualization

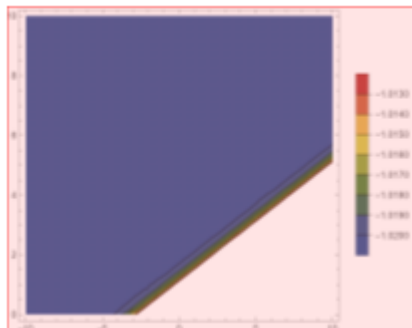


c) 2-D visualization

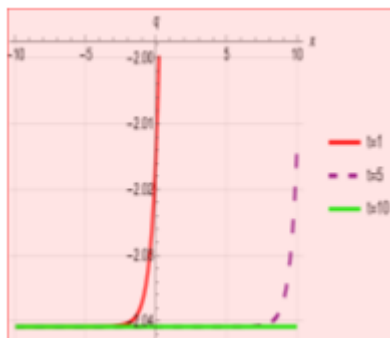
Fig. 8. 3-D, contour visualization and 2-D propagation of $q_{1,2}$ for specific values of the parameters are $\epsilon = 1.2$, $\alpha = 1.3$, $\delta = 0.5$, $m = 0.5$, $c = 01$



a) 3-D visualization

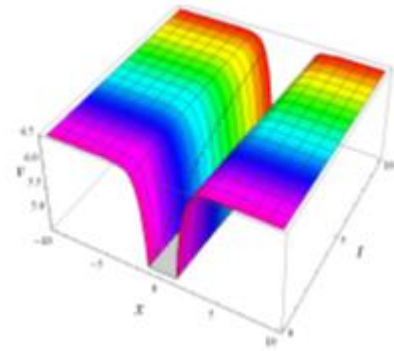


b) contour visualization

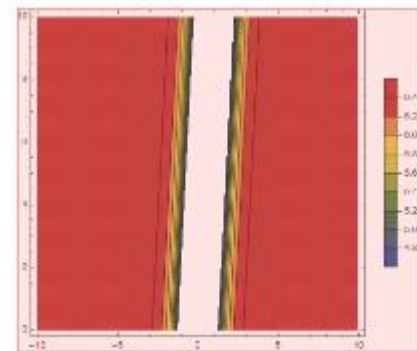


c) 2-D visualization

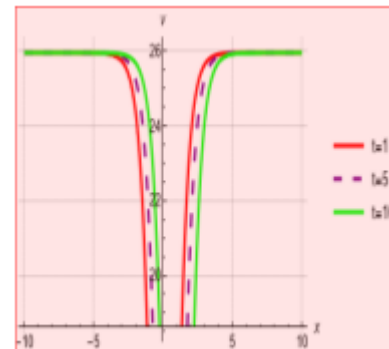
Fig. 9. 3-D, contour visualization and 2-D propagation of $q_{1,2}$ for specific values of the parameters are $\epsilon = 1.2$, $\alpha = 1.3$, $\delta = 0.5$, $m = 0.5$, $c = 2.5$



a) 3-D visualization

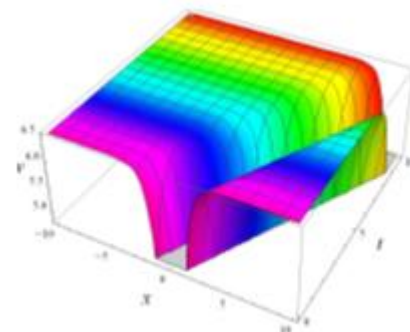


b) contour visualization

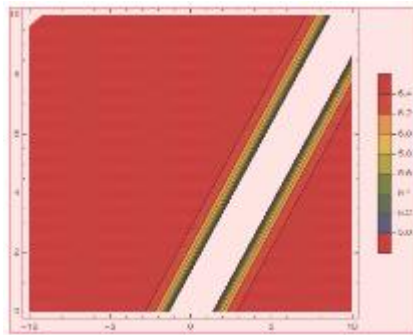


c) 2-D visualization

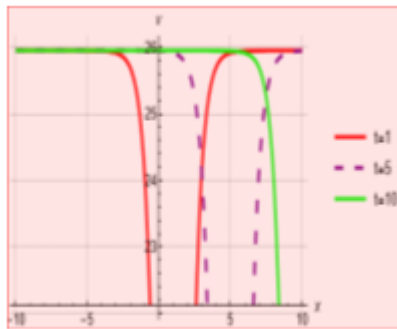
Fig. 10. 3-D, contour visualization and 2-D propagation of $v_{1,2}$ for specific values of the parameters are $\epsilon = 1.2$, $\alpha = 1.3$, $\delta = 0.5$, $n = 1.5$, $c = -1.5$, $m = 0.5$, $c = 0.1$



a) 3-D visualization

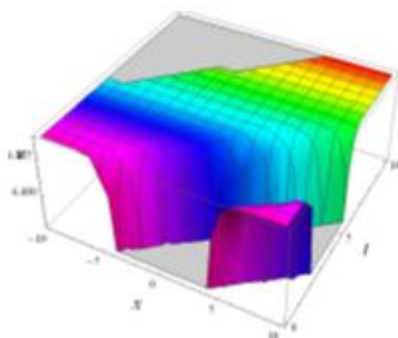


b) contour visualization

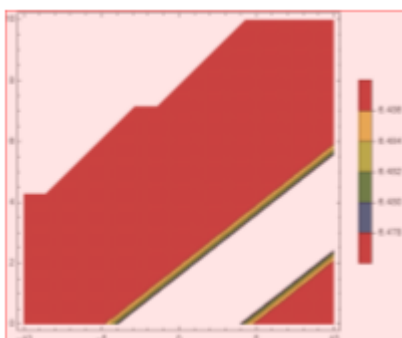


c) 2-D visualization

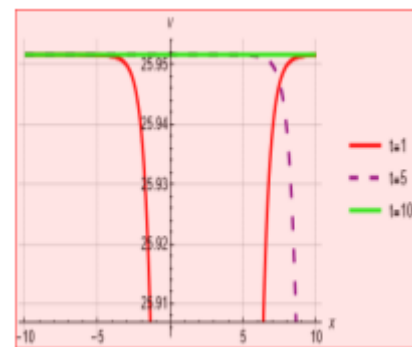
Fig. 11. 3-D, contour visualization and 2-D propagation of $v_{1,2}$ for specific values of the parameters are $\epsilon = 1.2$, $\alpha = 1.3$, $\delta = 0.5$, $n = 1.5$, $c = -1.5$, $m = 0.5$, $c = 01$



a) 3-D visualization



b) contour visualization



c) 2-D visualization

Fig. 12. 3-D, contour visualization and 2-D propagation of $v_{1,2}$ for specific values of the parameters are $\epsilon = 1.2$, $\alpha = 1.3$, $\delta = 0.5$, $n = 1.5$, $c = -1.5$, $m = 0.5$, $c = 2.5$

4. PHYSICAL EXPLANATIONS

This section offers physical explanation of Figure [1-12] and selection of wave solutions that have been obtained by applying the Jacobi elliptic function expansion method to the S-IIAE equation. In order to create visual representations of different soliton wave patterns, we have carefully selected and used certain parameter values. These patterns are illustrated in the accompanying figures. For every scenario, we have produced surface and contour visualization plots in two and three dimensions. These visual aids are important because they can verify that the theoretical conclusions, we came to earlier are accurate. It's important to keep in mind that these graphs and figures were produced using Mathematica. Consequently, one can notice that, the above-mentioned graphics are presenting the dark-bright, periodic, composite and bright soliton behavior respectively, under the influence of variation of wave number. On the other hand, the influence of wave is also discussed and noticed that, researchers and physicists can acquire their required results by controlling the propagation of soliton with wave number.

5. CONCLUSION

In conclusion, this research article explored the application of the Jacobi elliptic function expansion method for the Shynaray-IIA Equation (S-IIAE). The partial differential model is transformed into ordinary differential equation by employing the next travelling wave transformation according to considered analytical technique. Numerous properties of a particular class of solutions, called the Jacobi elliptic functions, make them useful for the analytical solution of a wide range of nonlinear problems. Using this powerful method, we derive a set of exact solutions for the Shynaray-IIA (S-IIA) equation, shedding light on its complex dynamics and behavior. The proposed method is shown to be highly effective in obtaining exact solutions in terms of Jacobi elliptic functions, such as dark, bright, periodic, dark-bright, dark-periodic, bright periodic, singular, and other various types of solitons. Additionally, a thorough examination of the accuracy and convergence of the obtained solutions is carried out. Overall, this research enriches the theoretical framework for the S-IIAE and presents a valuable tool for researchers and practitioners working in the field of nonlinear differential equations and mathematical physics.

REFERENCES

6. Wazwaz AM. Abundant solitons solutions for several forms of the fifth-order KdV equation by using the tanh method. *Applied Mathematics and Computation*. 2006;182(1):283-300.
7. Seadawy AR. Travelling-wave solutions of a weakly nonlinear two-dimensional higher-order Kadomtsev-Petviashvili dynamical equation for dispersive shallow-water waves. *Eur. Phys. J. Plus*. 2017;132:29. <https://doi.org/10.1140/epjp/i2017-11313-4>.
8. Akram U, Seadawy AR, Rizvi STR, Younis M, Althobaiti S, Sayed S. Traveling wave solutions for the fractional Wazwaz–Benjamin–Bona–Mahony model in arising shallow water waves. *Results in Physics*. 2021;20:103725. <https://doi.org/10.1016/j.rinp.2020.103725>
9. Rizvi STR, Kashif A, Marwa A. Optical solitons for Biswas–Milovic equation by new extended auxiliary equation method. *Optik*. 2020;204:164181. <https://doi.org/10.1016/j.jleo.2020.164181>
10. Seadawy AR. New exact solutions for the KdV equation with higher order nonlinearity by using the variational method. *Computers & Mathematics with Applications*. 2011; 62(10):2011;3741-3755. <https://doi.org/10.1016/j.camwa.2011.09.023>
11. Asghar A, Seadawy AR, Dianchen L. Soliton solutions of the nonlinear Schrödinger equation with the dual power law nonlinearity and resonant nonlinear Schrödinger equation and their modulation instability analysis. *Optik*. 2017; 145;79-88. <https://doi.org/10.1016/j.jleo.2017.07.016>
12. Arshad M, Seadawy AR, Dianchen L. Exact bright–dark solitary wave solutions of the higher-order cubic–quintic nonlinear Schrödinger equation and its stability. *Optik*. 2017;138;40-49. <https://doi.org/10.1016/j.jleo.2017.03.005>
13. Arnous AH, Seadawy AR, Alqahtani RT, Biswas A. Optical solitons with complex Ginzburg–Landau equation by modified simple equation method. *Optik*. 2017;144:475-480. <https://doi.org/10.1016/j.jleo.2017.07.013>
14. Seadawy AR, El-Rashidy K. Traveling wave solutions for some coupled nonlinear evolution equations. *Mathematical and Computer Modelling*. 2013;57(5-6):1371-1379. <https://doi.org/10.1016/j.mcm.2012.11.026>
15. Younas U, Younis M, Seadawy AR, Rizvi STR, Althobaiti S, Sayed S. Diverse exact solutions for modified nonlinear Schrödinger equation with conformable fractional derivative. *Results in Physics*. 2021;20:103766. <https://doi.org/10.1016/j.rinp.2020.103766>
16. Bhrawy AH, Abdelkawy MA, Kumar S, Biswas A. Solitons and other solutions to Kadomtsev–Petviashvili equation of B-type. *Rom. J. Phys.* 2013; 58(7-8):729-748.
17. Ebadi G, Fard NY, Bhrawy AH, Kumar S, Triki H, Yildirim A, Biswas A. Solitons and other solutions to the (3+ 1)-dimensional extended Kadomtsev–Petviashvili equation with power law nonlinearity. *Rom. Rep. Phys.* 2013; 65(1):27-62.
18. Iqbal MA, Wang Y, Miah MM, Osman MS. Study on date–Jimbo–Kashiwara–Miwa equation with conformable derivative dependent on time parameter to find the exact dynamic wave solutions. *Fractal and Fractional*. 2021; 6(1):4.
19. Ali KK, Wazwaz AM, Osman MS. Optical soliton solutions to the generalized nonautonomous nonlinear Schrödinger equations in optical fibers via the sine-Gordon expansion method. *Optik*. 2020; 208:164132.
20. Akinyemi L, Houwe A, Abbagari S, Wazwaz AM, Alshehri HM, Osman MS. Effects of the higher-order dispersion on solitary waves and modulation instability in a monomode fiber. *Optik*. 2023; 288: 171202. <https://doi.org/10.1016/j.jleo.2023.171202>
21. Mani Rajan MS, Saravana Veni S, Wazwaz AM. Self-steepening nature and nonlinearity management of optical solitons with the influence of generalized external potentials. *Opt Quant Electron*. 2023; 55:703. <https://doi.org/10.1007/s11082-023-04912-8>
22. Jafari H, Tajadodi H, Baleanu D. Application of a homogeneous balance method to exact solutions of nonlinear fractional evolution equations. *Journal of Computational and Nonlinear Dynamics*. 2014;9(2): 021019.
23. Kumar S, Malik S, Rezazadeh H, Akinyemi L. The integrable Boussinesq equation and its breather, lump and soliton solutions. *Nonlinear Dynamics*; 2022;1-14.
24. Kumar S, Kumar A., Samet B, Gómez-Aguilar JF, Osman MS. A chaos study of tumor and effector cells in fractional tumor-immune model for cancer treatment. *Chaos, Solitons & Fractals* 2020; 141: 110321.
25. Khan MI, Asghar S, Sabi'u J. Jacobi elliptic function expansion method for the improved modified Korteweg-de Vries equation. *Optical and Quantum Electronics*. 2022; 54: 734.
26. Osman MS. One-soliton shaping and inelastic collision between double solitons in the fifth-order variable-coefficient Sawada–Kotera equation. *Nonlinear Dynamics*. 2019; 96(2):1491-1496.
27. Osman MS, Rezazadeh H., Eslami M. Traveling wave solutions for (3+1) dimensional conformable fractional Zakharov–Kuznetsov equation with power law nonlinearity. *Nonlinear Engineering*. 2016; 8(1):559-567.
28. Alquran M, Jarrah A. Jacobi elliptic function solutions for a two-mode KdV equation. *J King Saud Univ Sci*. 2019;31:485–9. <https://doi.org/10.1016/j.jksus.2017.06.010>
29. Jaradat HM, Syam M, Alquran M. A two-mode coupled Korteweg-de Vries: multiple-soliton solutions and other exact solutions. *Nonlinear Dyn*. 2017;90:371–7. <https://doi.org/10.1007/s11071-017-3668-x>
30. Alquran M, Jaradat HM, Syam MI. A modified approach for a reliable study of new nonlinear equation: two-mode Korteweg-de Vries–Burgers equation. *Nonlinear Dyn*. 2018;91:1619–26. <https://doi.org/10.1007/s11071-017-3968-1>
31. Jaradat HM, Awawdeh F, Al-Shara S, Alquran M, Momani S. Controllable dynamical behaviors and the analysis of fractal burgers hierarchy with the full effects of inhomogeneities of media. *Rom. J. Phys.* 2015; 60:324–43.
32. Syam M, Jaradat HM, Alquran M. A study on the two-mode coupled modified Korteweg-de Vries using the simplified bilinear and the trigonometric-function methods. *Nonlinear Dyn*. 2017; 90:1363–71. <https://doi.org/10.1007/s11071-017-3732-6>
33. Alquran M, Jaradat HM, Al-Shara S, Awawdeh F. A new simplified bilinear method for the N-soliton solutions for a generalized F mKdV equation with time-dependent variable coefficients. *Int J Nonlinear Sci Numer Simul*. 2015;16:259–69. <https://doi.org/10.1515/ijnsns-2014-0023>
34. Rezazadeh H, Vahidi J, Zafar A, Bekir A. The functional variable method to find new exact solutions of the nonlinear evolution equations with dual-power-law nonlinearity. *Int J Nonlinear Sci Numer Simul*. 2020; 21:249– 57. <https://doi.org/10.1515/ijnsns-2019-0064>
35. Yépez-Martínez H, Gómez-Aguilar JF. Fractional sub-equation method for Hirota–Satsuma-coupled KdV equation and coupled mKdV equation using the Atangana's conformable derivative. *Waves Ran Comp Med*. 2019;29:678–93. <https://doi.org/10.1080/17455030.2018.1464233>
36. Yépez-Martínez H, Gómez-Aguilar JF, Baleanu D. Beta-derivative and sub equation method applied to the optical solitons in medium with parabolic law nonlinearity and high order dispersion. *Optik*. 2018;155:357– 65. <https://doi.org/10.1016/j.jleo.2017.10.104>
37. Yépez-Martínez H, Gómez-Aguilar JF. M-derivative applied to the soliton solutions for the Lakshmanan–Porsezian–Daniel equation with dual-dispersion for optical fibers. *Optical Quant Electron*. 2019; 51:31. <https://doi.org/10.1007/s11082-018-1740-5>
38. Akinyemi L. Two improved techniques for the perturbed nonlinear Biswas–Milovic equation and its optical solutions. *Optik-International Journal for Light and Electron Optics*. 2021;243;167477.
39. Kumar S, Mann N, Kharbanda H, Inc M. Dynamical behavior of analytical soliton solutions, bifurcation analysis, and quasi-periodic


- solution to the (2+1)-dimensional Konopelchenko–Dubrovsky (KD) system. *Analysis and Mathematical Physics*. 2023;13(3):40.
40. Kumar S, Mann N. A variety of newly formed soliton solutions and patterns of dynamic waveforms for the generalized complex coupled Schrödinger–Boussinesq equations. *Optical and Quantum Electronics*. 2023;55(8):723.
41. Kumar S, Rani S, Mann N. Diverse analytical wave solutions and dynamical behaviors of the new (2+1)-dimensional Sakovich equation emerging in fluid dynamics. *The European Physical Journal Plus*. 2022;137(11):1226.
42. Kumar S, Niwas M, Mann N. Abundant analytical closed-form solutions and various solitonic wave forms to the ZK-BBM and GZK-BBM equations in fluids and plasma physics. *Partial Differential Equations in Applied Mathematics*. 2021;4:100200.
43. Kumar S, Mann N. Abundant closed-form solutions of the (3+1)-dimensional Vakhnenko–Parkes equation describing the dynamics of various solitary waves in ocean engineering. *Journal of Ocean Engineering and Science*; 2022.
44. Rani S, Kumar S, Mann N. On the dynamics of optical soliton solutions, modulation stability, and various wave structures of a (2+1)-dimensional complex modified Korteweg–de–Vries equation using two integration mathematical methods. *Optical and Quantum Electronics*. 2023;55(8):731.
45. Nonlaopon K, Mann N, Kumar S, Rezaei S, Abdou MA. A variety of closed-form solutions, Painlevé analysis, and solitary wave profiles for modified KdV–Zakharov–Kuznetsov equation in (3+1)-dimensions. *Results in Physics*. 2022;36:105394.

Authors are thankful to University of Management and Technology for supporting this research work.


Muhammad Ishfaq Khan:  <https://orcid.org/0009-0002-2160-9002>

Waqas Ali Faridi:  <https://orcid.org/0000-0003-0713-5365>

Muhammad Amin Murad:  <https://orcid.org/0000-0002-3402-1796>

Mujahid Iqbal:  <https://orcid.org/0000-0002-7323-601X>

Ratbay Myrzakulov:  <https://orcid.org/0000-0002-5274-0815>

Zhanar Umurzakhova:  <https://orcid.org/0000-0002-1388-9377>



This work is licensed under the Creative Commons BY-NC-ND 4.0 license.

THE INFLUENCE OF MOLAR EXTRACTION IN MANDIBLE ON THE BONE REMODELING PROCESS UNDER DIFFERENT CHEWING CONDITIONS

Anna TOMASZEWSKA*

*Institute of Biomedical Engineering, Faculty of Mechanical Engineering, Białystok University of Technology, Wiejska 45A, 15-345 Białystok

anna.tomaszewska@sd.pb.edu.pl

received 03 December 2024, revised 11 January 2025, accepted 12 January 2025

Abstract: The aim of this study is to analyze the process of remodeling the mandibular bone in the context of functional adaptation after tooth extraction. The mandible, as a bone structure, undergoes continuous remodeling, allowing it to adapt to changing mechanical conditions. After tooth loss, significant changes occur in the distribution of loading, which can lead to bone resorption in areas with reduced mechanical stimulation and to excessive loading of the remaining teeth. The study utilizes a geometric model of the mandible, taking into account different chewing conditions before and after tooth extraction, as well as numerical simulations to assess changes in bone density. The results show significant changes in stress and bone density in the region of the extracted tooth, including an increase in the density of cortical and cancellous bone, confirming hypotheses regarding adaptive mechanisms. Understanding these processes is crucial for dental practice, enabling doctors to better plan therapy after tooth extractions and to avoid complications associated with tooth loss.

Key words: tooth extraction, mandible, bone remodeling simulation, finite-element-analysis

1. INTRODUCTION

The mandible undergoes a process of functional adaptation of bone. As a bone structure, it combines the properties of living tissue with the strength necessary to withstand large loads resulting from muscle contractions during chewing. It undergoes continuous remodeling of its structure, allowing for the ongoing exchange of old bone material for new(1). In addition to systematic renewal, a process of functional adaptation may occur, allowing the bone structure to adjust to changes in the mechanical environment(2). This corresponds with the 19th-century theory known as Wolff's law(3). Its further development has been contributed to by researchers such as Cowin(4, 5), Carter and Beaupre(6), Huiskes(7, 8), and Frost, who formulated the "mechanostat" hypothesis(9). According to all these studies, the value of the so-called mechanical stimulus beyond a threshold level (the "lazy zone") can disrupt the equilibrium state of bone, leading to "functional adaptation": a value of the stimulus below the threshold level can cause resorption, while a value above the threshold level leads to additional bone formation. This mechanistic approach is very straightforward and is often applied in bioengineering analyses.

The process of functional adaptation of the mandible can be disrupted in the event of the loss of one or more teeth. The mandible adapts to new working conditions, for instance, when a tooth or teeth are extracted. As a result, changes occur in the transfer of loads through the mandible. After tooth loss, the distribution of loading changes, which can lead to excessive loading on the remaining teeth and areas of bone. This situation is the opposite of the case when a full dentition is present, where the chewing forces are evenly distributed across all teeth, providing optimal stimulation of the bone(10). After tooth loss, the mandible may respond through the process of resorption in areas where there is a lack of mechanical stimulus, which can lead to a decrease in its volume and a loss

of bone density(11).

Unfortunately, tooth removal, also known as tooth extraction, is one of the most commonly performed dental procedures in clinical practice. Tooth extraction is a common dental procedure in adult populations, often performed due to caries or periodontal disease [12]. The most common reasons for this dental procedure include dental caries, misalignment of teeth, teeth damaged by trauma, or the need to prepare teeth for orthodontic treatment. Furthermore, the teeth most frequently subjected to this procedure are molars [13].

Understanding the processes of bone remodeling and functional adaptation is crucial for dental practice, enabling dentists to properly plan and conduct therapy after tooth extraction, which is essential for maintaining the integrity and health of the stomatognathic system(12). Additionally, the research context suggests that a better understanding of these processes is necessary to improve the effectiveness of therapy and to avoid complications after tooth extraction. The study conducted in this article aims to investigate the state of bone strain before and after tooth removal under various chewing conditions. By utilizing numerical simulations and current scientific knowledge, we can understand the impact of tooth extraction on the biomechanics of the stomatognathic system and identify potential risk factors for the state of the mandible.

2. METHODS

2.1. Geometrical and material model

The mandible model was developed based on imaging data from computed tomography and processed using the 3D Slicer Image Computing Platform. Both the trabecular bone and the surrounding cortical bone were modeled, reflecting the structure of the

mandible visible in the tomographic data. Two geometric models were prepared: 1) a basic anatomical model, which included all the teeth, such as incisors, premolars, and molars; and 2) an anatomical model following the extraction of a right-side molar from the mandible (Fig. 1)

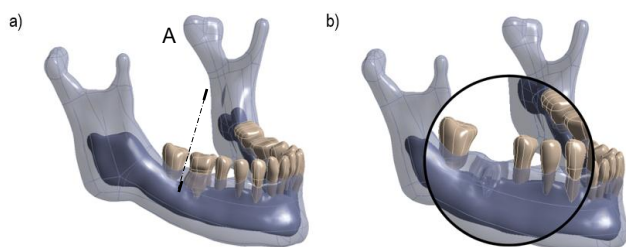


Fig. 1. Geometric models prepared for the study: a) basic anatomical model before extraction; b) anatomical model after tooth extraction

In the studies, it was assumed that the Young's modulus for cancellous bone is 1.37 GPa, for cortical bone 13.7 GPa, for dental enamel 80 GPa and for dentine 20 GPa, (Fig. 2). The initial density for cancellous bone is 0.71 g/cm³ and for cortical bone is 1.37 g/cm³. The Poisson ratio was assumed to be 0.3 for all materials.(13-15).

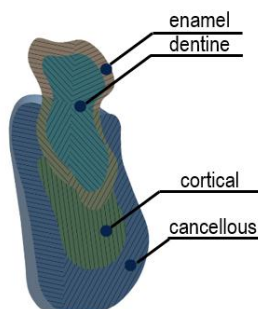


Fig. 2. The cross-section A-A of the molar tooth and the mandibular bone

The discretization of the model was carried out using the ANSYS system preprocessor, utilizing 10-node tetrahedral elements (Solid187). A quality mesh test was conducted to evaluate the maximum Huber-Mises-Hencky (HMH) stresses. Given the complex anatomy of the mandible, the mesh was optimized globally and locally. A Jacobian test was also performed, where it was determined that the coefficient was 0.4, which is consistent with literature data(16). The optimized mesh comprised approximately 56,000 elements, distributed over about 80,000 nodes.

2.2. Boundary conditions

During the modeling of boundary conditions, the conditions prevailing in the temporomandibular joint during chewing were assumed. To this end, a cylindrical coordinate system was introduced along the main axis of the joint, which was used to define the boundary conditions, allowing rotation around the Z-axis while blocking the other two degrees of freedom, namely displacement along the X-axis and displacement along the Z-axis. The study was

conducted for four support variants, considering the conditions present when during chewing the following occurs:

- incisors resting on the maxillary teeth (Fig. 3a),
- symmetric lower and upper molars (Fig. 3b),
- lower and upper molars on the side of the deficiency (Fig. 3c),
- lower and upper molars on the opposite side of the deficiency (Fig. 3d).

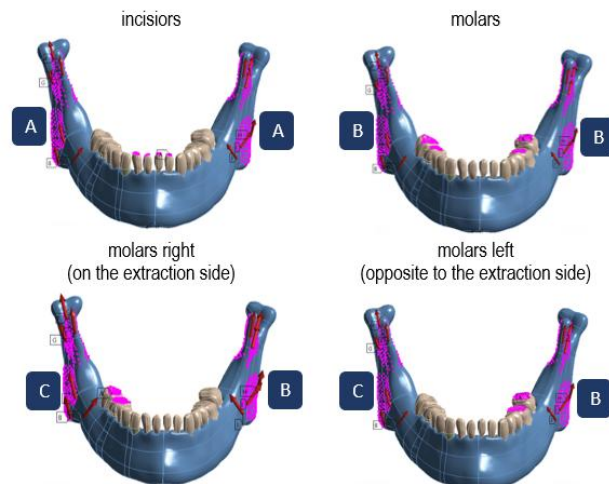


Fig. 3. Representation of the force vectors exerted by the main muscles acting on the mandible. The vectors are labeled (e.g. RM: Right Masseter, LT: Left Temporalis) to correspond with the muscle names listed in Table 1. The directions and magnitudes of the vectors were determined based on the values provided in Tab. 1

Analyzing the anatomy of the musculoskeletal system, the locations of the forces exerted by the main muscles acting on the mandible were identified (Fig. 3), namely: right masseter, left masseter, right temporalis, left temporalis, right lateral pterygoid, and left lateral pterygoid. It was taken into account that changes in contact between the teeth also vary the values of the muscle forces. Therefore, for four different chewing conditions, appropriate muscle force actions were designed, indicated in Figure 3 by the letters A-A, B-B, B-C, and C-B. The corresponding muscle forces were assigned to the letter designations in Table 1.

Tab. 1. Values exerted by the muscles(17)

| Muscles description | A | B | C |
|--------------------------|-------|-------|-------|
| Middle - temporalis [N] | 5.7 | 64.0 | 63.0 |
| Deep masseter [N] | 21.2 | 48.9 | 17.1 |
| Superficial masseter [N] | 76.1 | 114.2 | 137.0 |
| Anterior temporalis [N] | 1.6 | 91.6 | 115.4 |
| Medial pterygoid [N] | 136.4 | 104.9 | 146.9 |

2.3. Bone remodelling

Research on bone regeneration utilizes Huiskes' algorithm(7), developed by Weinans(8). The model integrates bone density ρ with strain energy density U , which is called as mechanical stimulus and described by the equation:

$$S = \frac{U}{\rho} \quad (1)$$

The bone remodeling algorithm takes into account the process of bone resorption, the dead zone, where the processes of resorption and bone formation are in equilibrium, and the process of bone formation:

$$\frac{d\rho}{dt} = \begin{cases} B \frac{U}{\rho} - (1 - S)k, & \frac{U}{\rho} < (1 - S)k \\ 0, & (1 - s)k \leq \frac{U}{\rho} \leq (1 + S)k \\ B \frac{U}{\rho} - (1 + S)k, & \frac{U}{\rho} > (1 + S)k \end{cases} \quad (2)$$

The constant values used in the algorithm were as follows: $s = 0.1$, $B = 10$, and $k = 0.002$. Initial material values for the bone and the implant were assumed, which are described in the "Geometrical and Material Model" section. The material model of the bone underwent remodeling:

for cortical bone according to the relationship(18):

$$E = 0.014\rho^3 - 6.142 \quad (3)$$

gdzie: C – constans = 3790, ρ - bone density at the given step, for cancellous bone according to the relationship(19):

$$E = 1.02\rho^{1.22} . \quad (4)$$

The bone remodeling algorithm was implemented in ANSYS APDL language. Numerical calculations were performed using the finite element method in ANSYS v. 24R1 (Ansys Inc., Canonsburg, Pennsylvania, United States).

3. RESULTS

The results are presented as maps of HMH stress for cancellous bone (Fig. 4a) and cortical bone (Fig. 4b) in the region surrounding the root of molar tooth number 6. The bone remodeling process was modeled based on Equations (1) and (2). The change in material properties of cortical and cancellous bone was conducted according to equations 3 and 4, respectively.

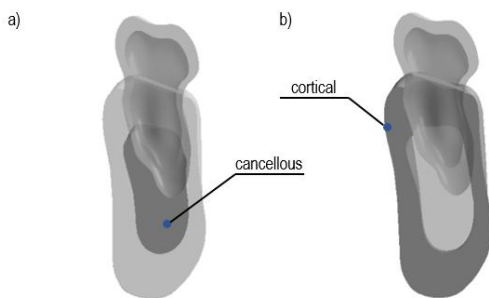


Fig. 4. Cross-section of the tooth and mandibular bone highlighting the zone: a) for cancellous bone; b) for cortical bone

Below are the results for trabecular bone in the presence of a tooth (Fig. 5), trabecular bone after the extraction of the molar (Fig. 6), cortical bone in the presence of the molar (Fig. 7), and cortical bone after the extraction of the molar (Fig. 8), during different chewing conditions, namely for:

- incisors – when contact occurs between the incisors of the mandible and the incisors of the maxilla,
- molars – when contact occurs between the molars of the mandible and the molars of the maxilla,

- left molars – when contact occurs on the left side between the molars of the mandible and the molars of the maxilla,
- right molars – when contact occurs on the right side between the molars of the mandible and the molars of the maxilla.

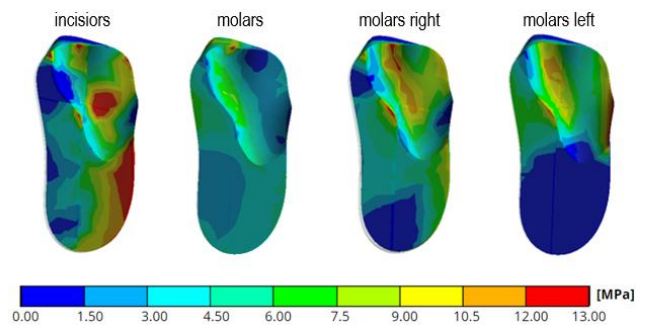


Fig. 5. Distribution of HMH stress [MPa] in cancellous bone before tooth extraction

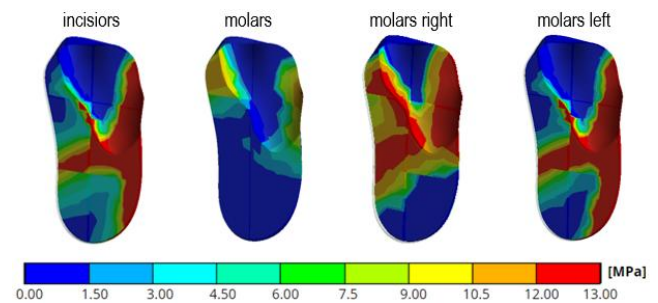


Fig. 6. Distribution of HMH stress [MPa] in cancellous bone after tooth extraction

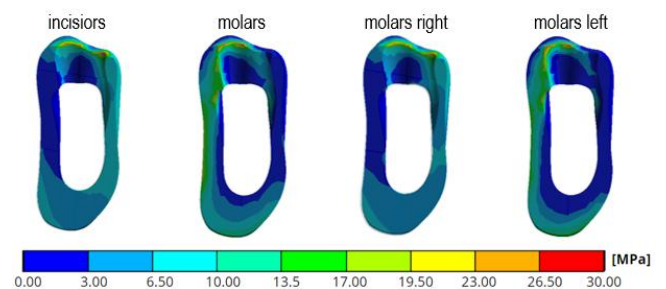


Fig. 7. Distribution of HMH stress [MPa] in cortical bone before tooth extraction

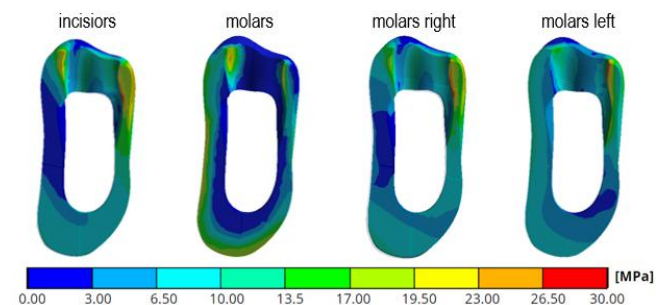


Fig. 8. Distribution of HMH stress [MPa] in cortical bone after tooth extraction

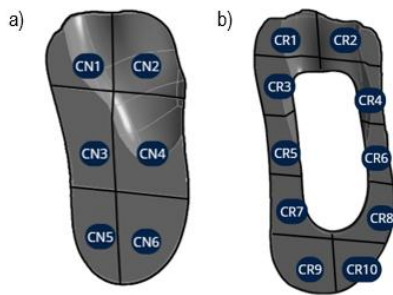


Fig. 9. Division into areas for: a) cancellous bone; b) cortical bone

Tab. 2. Change in cancellous bone density in the analyzed areas [g/cm³] for the model after tooth extraction compared to the model before tooth extraction

| Region | Incisors | Molars | Molars right | Molars left |
|---------|----------|--------|--------------|-------------|
| CN1 [%] | 938 | -72 | 505 | 27 |
| CN2 [%] | 82 | -56 | 103 | 725 |
| CN3 [%] | 80 | 0 | 59 | 483 |
| CN4 [%] | -24 | -18 | 28 | 1415 |
| CN5 [%] | 37 | 0 | 189 | 49 |
| CN6 [%] | 68 | 0 | 2059 | 0 |

Tab. 3. Change in cortical bone density [g/cm³] in the analyzed areas for the model after tooth extraction compared to the model before tooth extraction

| Region | Incisors | Molars | Molars right | Molars left |
|----------|----------|--------|--------------|-------------|
| CR1 [%] | 0 | 102 | -9 | -12 |
| CR2 [%] | -12 | 27 | -9 | -2 |
| CR3 [%] | 285 | 28 | 52 | 2 |
| CR4 [%] | -7 | 49 | -5 | 3 |
| CR5 [%] | 323 | -4 | 127 | 0 |
| CR6 [%] | -72 | 181 | 0 | 0 |
| CR7 [%] | -10 | -4 | 9 | 0 |
| CR8 [%] | 0 | 48 | 0 | -17 |
| CR9 [%] | 0 | 3 | 0 | 0 |
| CR10 [%] | 0 | 8 | 0 | 0 |

4. DISCUSSION

The results of the analysis of the area around the molar tooth (Fig. 5) indicate significantly higher stresses in the trabecular bone at the moment of contact between the incisors, reaching values from 4.50 to 13.00 MPa. The maximum HMH stress are located at the end of the root, where a phenomenon of stress shielding is observed. Slightly lower stress values are noted in the case of contact with molars, especially the left molars, where the maximum values reach up to 10.50 MPa. After tooth extraction, the distribution of H-M-H stress changes in each of the four chewing conditions, wherein for aliquots as well as for molars on the left and right sides, stress shielding is noted in the area around the extraction site (Fig. 6). Stresses accumulate on the posterior wall of the socket where the root of the molar tooth was supported. There is also a decrease in H-M-H stresses on the lateral wall of the tooth deficiency.

In the cortical bone, a concentration of stresses was observed

around the upper boundary between the bone and the molar tooth. In the analyzed area, the maximum HMH stress reach approximately 30 MPa across the four different chewing conditions. The distribution of stresses changes after tooth extraction. In the case of incisors, stresses increase to 26.5 MPa from both the anterior and posterior sides of the tooth (Figs. 7, 8). A similar phenomenon occurs with contact between the right and left molars, with the maximum HMH stress being localized at the anterior side within the cortical bone and the socket, in the area of support between the molars, a minimum of H HMH stress was noted.

The results of the analysis of cortical and trabecular bone density after tooth extraction confirm the mechanisms of functional adaptation of the bone, consistent with Wolff's law. The mandible undergoes intense remodeling after tooth removal, evidenced by changes in bone density in the analyzed areas. In the cortical bone, particularly around the socket (CR1–CR4), significant increases in density were recorded, especially in CR3 (+285%) and CR5 (+323%) (Tab. 3). This increase can be explained by the increased mechanical stimulation of the remaining areas that must take on additional loads after extraction. In contrast, the decreases in density in areas such as CR6 (-72%) may indicate diminished loads, leading to bone resorption in line with Frost's "mechanostat" hypothesis (Tab. 3). This indicates that a lack of adequate mechanical stimulus leads to a decrease in bone density. Similar phenomena occur in the trabecular bone, where the most significant changes were observed in the alveoli (CN1, CN2, CN4) and surrounding areas. An extreme increase in density in CN1 (+938% for incisors, +505% on the right side) and CN6 (+2059% on the right side of the molars) indicates intense remodeling of these regions, acting as an adaptive response to the altered loading conditions (Tab. 2). In contrast, areas such as CN4 (-24% for incisors, -18% for molars) experienced a decrease in density, suggesting reduced mechanical stimulation and associated resorption.

These results clearly show that in regions where force transmission increases after extraction, bone density rises, consistent with Wolff's law. Conversely, in areas with reduced loading, such as CR6 and CN4, resorption occurs due to the lack of mechanical stimulation. This phenomenon illustrates how crucial the balance between loading and bone remodeling is. From a clinical perspective, these findings highlight the importance of understanding the processes involved in the functional adaptation of bone following tooth extraction. Proper planning of therapy and rehabilitation, including appropriate mechanical stimulation, can support bone regeneration and prevent excessive resorption in areas with reduced loading. This is vital for maintaining the health and integrity of the mandible after tooth removal, which has significant implications for the long-term health of the patient.

5. CONCLUSION

Both cortical and trabecular bone undergo intensive remodeling processes after tooth extraction. In areas of increased loading, there is a rise in bone density, whereas in places with reduced stimulation, resorption is observed.

After tooth extraction, bone density increases in the areas surrounding the socket, particularly in regions that take on greater loads. This phenomenon was especially noted in CR3, CR5, as well as in CN1 and CN6.

In some areas, such as CR6 and CN4, there was a decrease in bone density, suggesting that the lack of an adequate mechanical stimulus leads to bone resorption.

The results of the study confirm the crucial role of mechanical stimulation in maintaining the health and density of the mandible. Proper rehabilitation after tooth extraction should include a bone stimulation strategy to prevent resorption and promote regeneration.

The findings are significant for planning dental treatment after tooth extractions. Understanding the adaptive mechanisms of bone can aid in developing effective therapies that minimize the loss of bone density and support the regeneration process.

REFERENCES

1. Allena R, Scerrato D, Bersani A, Giorgio I. Functional adaptation of bone mechanical properties using a diffusive stimulus originated by dynamic loads in bone remodelling. *Zeitschrift Fur Angewandte Mathematik Und Physik*. 2024;75. <https://doi.org/10.1007/s00033-024-02230-x>
2. Addessi D, D'Annibale F, Placidi L, Giorgio I. A bone remodeling approach encoding the effect of damage and a diffusive bio-mechanical stimulus. *Continuum mechanics and thermodynamics*. 2024;36:993-1012. <https://doi.org/10.1007/s00161-024-01308-1>
3. Cowin S. Wolff's law of trabecular architecture at remodeling equilibrium. *Journal of biomechanical engineering*. 1986;108:83-88.
4. Cowin SC, Hegedus DH. Bone remodeling 1. Theory of adaptive elasticity. *Journal of Elasticity*. 1976; 6: 313-326. <https://doi.org/10.1007/bf00041724>
5. Cowin SC. The mechanical and stress adaptive properties of bone. *Annals of Biomedical Engineering*. 1983;11:263-295. <https://doi.org/10.1007/bf02363288>
6. Beaupre GS, Orr TE, Carter DR. An approach for time-dependent bone modeling and remodeling - application - a preliminary remodeling simulation. *Journal of Orthopaedic Research*. 1990;8:662-670. <https://doi.org/10.1002/jor.1100080507>
7. Huiskes R, Weinans H, Grootenboer HJ, Dalstra M, Fudala B, Slooff TJ. Adaptive bone-remodeling theory applied to prosthetic-design analysis. *Journal of Biomechanics*. 1987;20:1135-1150. [https://doi.org/10.1016/0021-9290\(87\)90030-3](https://doi.org/10.1016/0021-9290(87)90030-3)
8. Weinans H, Huiskes R, Grootenboer HJ. The behavior of adaptive bone-remodeling simulation-models. *Journal of Biomechanics*. 1992; 25:1425-1441. [https://doi.org/10.1016/0021-9290\(92\)90056-7](https://doi.org/10.1016/0021-9290(92)90056-7)
9. Frost HM. Bone mass and the mechanostat - a proposal. *Anatomical Record*. 1987; 219:1-9. <https://doi.org/10.1002/ar.1092190104>
10. Elleuch S, Jrad H, Wali M, Dammak F. Mandibular bone remodeling around osseointegrated functionally graded biomaterial implant using three dimensional finite element model. *International journal for numerical methods in biomedical engineering*. 2023;39. <https://doi.org/10.1002/cnm.3750>
11. Wang LJ, You XL, Zhang LL, Zhang CQ, Zou WG. Mechanical regulation of bone remodeling. *Bone Research*. 2022;10. <https://doi.org/10.1038/s41413-022-00190-4>
12. Passarelli P, Pagnoni S, Piccirillo GB, Desantis V, Benegiamo M, Liguri A, Papa R, Papi P, Pompa G, D'addona A. Reasons for Tooth Extractions and Related Risk Factors in Adult Patients: A Cohort Study. *International Journal of Environmental Research and Public Health*. 2020;17. <https://doi.org/10.3390/ijerph17072575>
13. Hatami A, Dreyer C. The extraction of first, second or third permanent molar teeth and its effect on the dentofacial complex. *Australian Dental Journal*. 2019. <https://doi.org/10.1111/adj.12716>
14. Sato E, Shigemitsu R, Mito T, Yoda N, Rasmussen J, Sasaki K. The effects of bone remodeling on biomechanical behavior in a patient with an implant-supported overdenture. *Computers in Biology and Medicine*. 2021;129. <https://doi.org/10.1016/j.compbimed.2020.104173>
15. Morgan E, Unnikrisnan G, Hussein A. Bone Mechanical Properties in Healthy and Diseased States. *Annual review of biomedical engineering*. 2018;20:119-143. <https://doi.org/10.1146/annurev-bioeng-062117-121139>
16. Zhang Y, Du W, Zhou X, Yu H. Review of research on the mechanical properties of the human tooth. *International Journal Of Oral Science*. 2014; 6: 61-69. <https://doi.org/10.1038/ijos.2014.21>
17. Park S, Wang D, Dongsheng Z, Romberg E, Arola D. Mechanical properties of human enamel as a function of age and location in the tooth. *Journal Of Materials Science-Materials In Medicine*. 2008;19:2317-2324. <https://doi.org/10.1007/s10856-007-3340-y>
18. Gryko A, Prochor P. Numerical evaluation of scaffolds as a method to restore continuity of a long bone. *Journal of computational science*. 2024;79. <https://doi.org/10.1016/j.jocs.2024.102314>
19. Huang HL, Su KC, Fuh LJ, Chen MYC, Wu J, Tsai MT, Hsu JT. Biomechanical analysis of a temporomandibular joint condylar prosthesis during various clenching tasks. *Journal of Cranio-Maxillofacial Surgery*. 2015;43;1194-1201. <https://doi.org/10.1016/j.jcms.2015.04.016>
20. Hobatho MC, Rho JY, Ashman RB. Anatomical variation of human cancellous bone mechanical properties in vitro. *Bone Research in Biomechanics*. 1997;40:157-173.
21. Rho JY, Hobatho MC, Ashman RB. Relations of mechanical-properties to density and ct numbers in human bone. *Medical Engineering & Physics* 1995;17:347-355. [https://doi.org/10.1016/1350-4533\(95\)97314-f](https://doi.org/10.1016/1350-4533(95)97314-f)

Anna Tomaszewska:  <https://orcid.org/0000-0002-9913-2171>



This work is licensed under the Creative Commons BY-NC-ND 4.0 license.

THE IMPACT OF THE GAS TURBINE BLADE HEATING TEMPERATURE IN THE PRESENCE OF AVIATION KEROSENE ON COATING AND ALLOY MICROSTRUCTURE

Mariusz BOGDAN^{*✉}, Artur KUŁASZKA^{**✉}, Dariusz ZASADA^{***✉}

^{*}Faculty of Mechanical Engineering, Białystok Technical University, 45 Wiejska Street, 15-333 Białystok, Poland

^{**}Air Force Institute of Technology, 6 Księcia Bolesława Street, 01-494 Warsaw, Poland

^{***}Faculty of Advanced Technologies and Chemistry, Military University of Technology, 2 Kaliskiego Street, 00-908 Warszawa, Poland

m.bogdan@pb.edu.pl, artur.kulaszka@itwl.pl, dariusz.zasada@wat.edu.pl

received 15 July 2024, revised 30 October 2024, accepted 30 November 2024

Abstract: Under operating conditions, gas turbine blades may experience overheating. The degree of unfavourable modifications of the condition of both the protective insulating coating and the alloy (microstructure degradation) depends, among other factors, on the temperature and its exposure time. In this study, under laboratory conditions, in the presence of aviation kerosene exhaust gases, the influence of temperature (mainly outside the range of nominal operating temperatures) on the condition of uncooled polycrystalline rotor blades of aircraft turbine jet engines was examined. The object of the research were new gas turbine blades of the SO-3 aircraft engine made of the EI-867 WD alloy, which were exposed to high temperatures for a period of two hours in a laboratory furnace in the temperature range $T = 1123 - 1523\text{K}$, every 100K. The article determines the nature of changes (modifications) both in the state of the coatings and in the core material (alloy). A multifactor analysis was taken into account, including in the case of coatings modifications: morphological microstructure of the coating, chemical composition of oxides and roughness parameters, and in the case of the alloy mainly grain growth, and modification of the strengthening γ' phase. As a result of exposure to high temperatures in the surroundings of exhaust gases, the roughness of the surface changes and various types of oxides are formed, and its thickness increases. An increasing number of carbides appeared in the EI-867 WD alloy and grain growth was found as a function of the heating temperature. In particular, the blade alloy structure experienced the growth of the reinforcing γ' phase, which is adverse in terms of heat resistance, and the percentage-wise depletion of this phase in the alloy structure. Due to the aforementioned changes, heated blades experiences significant reduction in heat resistance and high-temperature creep resistance. The article also indicates the possibility of using the characteristics of microstructural changes to determine the technical condition of the tested turbine element in a non-destructive way.

Key words: gas turbine blade, temperature, coating structure, alloy structure

1. INTRODUCTION

In aviation, the gas turbine has found wide application due to the relatively high efficiency of the energy conversion process, amounting to 30-45%. Its most important feature is the high operating temperature of the blades. Nickel-based superalloys are widely used due to their particular combination of very good mechanical properties and good structural stability at high temperatures [1÷3]. However, increasing the operating temperature of blades made of nickel superalloys is limited. This is due to the barrier of reducing the heat resistance of the superalloy in the presence of high exhaust gas temperature. A number of measures are taken to reduce the temperature of the blade superalloy, such as allowing internal cooling and applying coatings [4÷11].

During the operation of gas turbine blades, and especially the rotor blades of the manoeuvring aircraft engine, the blades are subjected to complex stress and thermal loads, as well as oxidation and hot corrosion processes. Extreme and complex operating conditions of the blades may intensify the basic destructive processes, which mainly include: creep, overheating and melting, corrosion and fatigue cracking, intergranular and thermal corrosion, low- and high-cycle fatigue: thermal and thermo-mechanical, erosion, and burnout [13÷16]. Among the factors that degrade the

blades, high operating temperature is of particular importance, as it rapidly accelerates the diffusion processes taking place in the blades. Under operating conditions, an excessive increase in exhaust gas temperature, which has a long-term effect, has a destructive effect on the technical condition of the blades [17÷22]. It is closely related to the material criterion, because the strength properties of superalloys are an appropriate microstructure that is not subject to weakening changes during operation, which is the main criterion for the durability of gas turbine blades [1, 3, 22÷26].

The process of destruction of blades during operation begins with the destruction of the coating, which is the first barrier of "contact" of exhaust gases (high temperature, pressure, chemical interaction) with the blade surface. High-temperature, highly oxidizing environments contain large amounts of chemical impurities. Therefore, heat-resistant coatings are mainly characterized by high resistance to high-temperature corrosion in a gaseous environment. Other features include low thermal conductivity and high structural stability [8, 11, 17]. To protect blades made of nickel alloys, mainly heat-resistant coatings made of metal alloys are used: (Ni, Co)-Cr-Al-Y or Al-Si-Ni-Y. Among the aluminium compounds that are created during the coating process, the intermetallic phase β -(NiAl) turns out to be the best compromise because it is a very good mix of mechanical properties and is characterized by high resistance to high temperatures [8, 11, 17]. In order to increase the thermal stability of this phase, the

composition of the covering material is supplemented with alloy additives. Under operating conditions, a layer of aluminium oxides Al_2O_3 is formed on the surface of the β -NiAl layer, significantly reducing the oxidation rate. Degradation of the coatings occurs as a result of diffusion processes causing oxidation and an increase in the thickness of the oxide layer, as well as the progressive burning of alloy additions from the coating material, which impairs the self-regeneration capabilities of the coating (healing of micro-damages). Depletion of the covering material may also be caused by the diffusion of alloy additives into the substrate [4, 11, 27].

Assessment of the technical condition of turbine blades is a very important aspect in the process of operating aircraft turbine engines and is carried out using various techniques and methods [28, 29]. One of the techniques developed by M. Bogdan et al. [30–32] is the possibility of assessing or computer-aided assessment of the technical condition of the blades based on operational colour changes of the blade coating surface.

In this context, one of the main goals of this work was to describe the structural changes in both the coating and the alloy, reflecting a significant deterioration in the technical condition of the test object defined on the basis of the material criterion. This approach is important for specifying the procedure of the proposed non-destructive testing (NDT) for operational blades.

The article examined in laboratory conditions in the environment of exhaust gases the influence of increased temperature (outside the nominal operating range of the blades) on the modification of the alloy material as well as the condition of the coating of the blades made of the EI-867 WD alloy with a diffusion-applied aluminized coating. In section 2, the research object (the method of its production and selected features) and the implementation of the experiment were characterized. Section 3 specifies the changes occurring in the coating in terms of changes in surface roughness, its chemical composition, morphological structure and coating thickness. Section 4 draws attention to selected aspects related to the change of the alloy structure. Changes in grain size, carbide precipitates and the strengthening γ' phase were determined. Section 5 discusses the test results in the context of linking material changes in the blades with the deterioration of strength properties. In section 6, practical implications of the findings and their limitations are outlined. The final part of the article contains final conclusions.

2. CHARACTERISTICS OF THE TESTED OBJECT AND DESCRIPTION OF THE EXPERIMENT

A set of new blades (Fig. 1) from one production batch was used for laboratory tests. Five blades were exposed to temperatures ranging from 1123K to 1523K, every 100K, by heating them for two hours in an FCF 60 chamber furnace filled with continuously generated aviation kerosene exhaust gases. Cooling took place in the furnace. The heating time and temperature affect both coagulation and the growth kinetics of γ' phase particles, as well as modifying the thickness of the blade's protective coating. The duration of temperature exposure was selected experimentally based on the results of the analysis of data obtained from the operational flight parameter recorder of the Ts-11 Iskra training aircraft (with an SO-3W turbojet engine installed). The profile of the flights performed and the engine service life of 400 hours were taken into account. Additionally, based on the metallographic tests carried out, it was found that the differences between heating for 2 hours and 3 hours at a temperature above the maximum

temperature after the turbine, i.e. 1323 K, do not significantly affect the change in the coating thickness or the average particle size of the γ' phase.



Fig. 1. Example of blade convex (suction face) surfaces

The EI-867 WD alloy is characterized by a structure typical of nickel superalloys. It consists of carbides, γ phase and γ' reinforcing phase and borides. The γ phase is a solid solution in nickel of elements such as chromium, molybdenum, aluminium, cobalt and tungsten. The relative volume of the γ' phase (Ni_3Al), which takes the shape of cubic particles, does not exceed 31–34%. The distinguishing feature is that the EI-867 WD alloy (chemical composition given in Tab. 1) does not contain titanium. In addition, it is characterized by a lower chromium content compared to other superalloys, which translates into greater susceptibility to corrosion. Therefore, elements made of these alloys require protective and insulating coatings. They are produced using thermochemical treatment, i.e. in the aluminization process. Aluminizing is carried out using the out-of-pack method at a temperature of 1223 K and for 12 hours.

Tab 1. Chemical composition of the superalloy used in the present study (wt.%)

| C | Mn | Si | Cr | Co | Mo | W | Al | B | Fe | Ni |
|-----|-----|-----|-----|------|------|-----|-----|------|-----|------|
| max | max | max | | | | | | max | | |
| 0.1 | 0.3 | 0.6 | 9.0 | 14.0 | 10.3 | 5.0 | 4.5 | 0.02 | 4.0 | Rest |

The desired properties of the alloy (increase in mechanical strength, yield strength with increasing temperature, corrosion resistance required in special, demanding working conditions) are formed in a complex technological process of alloy production and include heat treatment involving precipitation hardening. Heat treatment includes supersaturation and aging. Supersaturation takes place at a temperature of 1473 ± 283 K for 4 to 6 hours, causing the dissolution of some carbides and intermetallic phases in the matrix. Cooling in air during supersaturation leads to the separation of small particles of the γ' phase, the relative volume of which is approximately 20%. The aging process affects the further secretion of γ' phase particles and the growth of previously isolated particles. Among the carbides whose relative volume in the alloy does not exceed 2%, the M_{23}C_6 carbide dominates. It is formed during heat treatment or is released during operation, usually at the grain boundaries in the temperature range of $933 \text{ K} \div 1253 \text{ K}$. M_6C carbide occurs inside the grains [25].

3. STUDYING THE BLADE COATING MICROSTRUCTURAL CONDITION

3.1. Surface roughness tests

One of the parameters, the value of which can change due to blade heating at different temperatures is surface roughness. It is

defined as a non-conformity or deviation from the product profile assumed in the drawing. This parameter is measured at small surface sections. It is described by two basic parameters: R_a and R_z [8]. The R_a parameter is privileged in testing and is most often measured. There is the $R_z \approx 4R_a$ relationship between these parameters. The 2D assessment of the surface geometric structure was conducted in the blade ridge area, using a PGM-1C profilometer with a BS 1000-10-1 WAT head. To define the surface profile, its roughness in the form of profile ordinate arithmetic means (R_a , R_z) were determined.

A sample roughness profile measured on the ridge in the middle part of a new blade profile is shown in Fig. 2. Based on the obtained measurement data presented in the form of graphs (Figs. 3 and 4), the authors concluded that heating temperature increase entails a decrease in R_a and R_z roughness first for a temperature of 1223 K and 1323 K, followed by a clear increase of said parameters at a temperature of 1523 K.

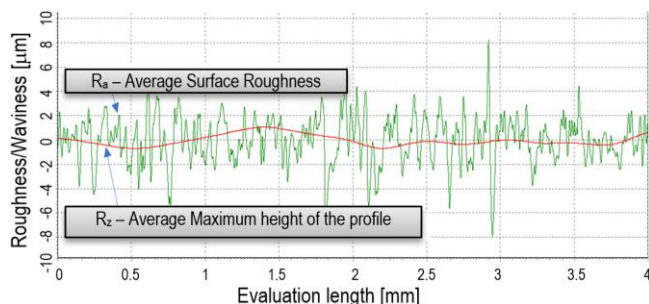


Fig. 2. Sample roughness and undulation profile – new blade

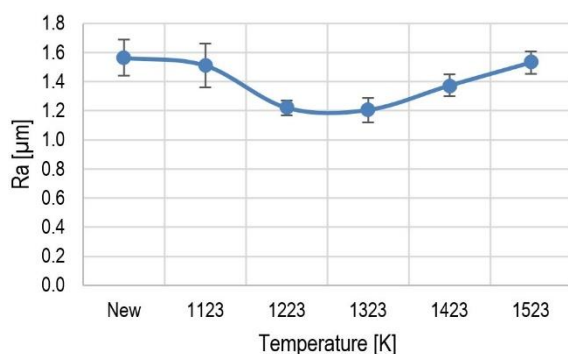


Fig. 3. Impact of heating temperature on roughness profile changes – R_a

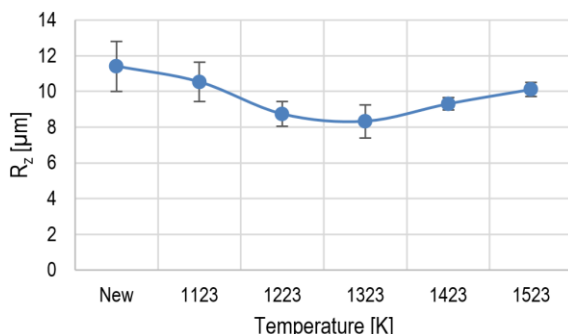


Fig. 4. Impact of heating temperature on roughness profile changes – R_z

The recorded roughness changes directly translate to changes on the surface of the analysed blades under the influence of temperature and the environment. Based on the conducted microscopic examinations, chemical composition and surface distribution testing related to the elements, it was concluded that

scale made of an external aluminium, nickel and chromium oxide layer and fuel combustion products is formed on the surface of the described alloys.

3.2. Surface structure tests

The surface morphology of the analysed blades was tested and microstructural changes within the coatings were observed using a high-resolution scanning electron microscope Quanta 3D FEG. Quanta 3D FEG combines emission scanning electron microscope (SEM) with focused ion beam (FIB). It was concluded that scale was formed on the surface, leading to very significant morphological changes (imaging of surface topography using backscattered electrons (BSE) and topographic separation (BSE-TOPO)) - Figs. 5 ÷ 10. The surface of the new blade is relatively undeveloped with few defects in the scale formed on it. Cracks and delamination of the scale were observed in a few areas. As the heating temperature increases, on the one hand, the scale increases, which causes its delamination and, consequently, falling off. In this case, the morphological changes of the surface are caused by coagulant oxides forming on the scale surface, especially visible in Fig. 8b. A further increase in temperature only accelerates this process, causing the scale to fall off and, as a consequence, the native material is exposed (compare Fig. 5 with Fig. 10). It was found that increasing heating temperature on the surface of the analysed blades leads to the formation of, mainly, Al_2O_3 and NiO oxides (Fig. 11). They form a surface layer protecting against further oxidation. The Al_2O_3 oxide has a morphologically heterogeneous structure and a tendency to uneven growth and exfoliation, which reduces roughness at higher heating temperatures. Furthermore, there were areas observed on blade surfaces that are highly rich in carbon and sulphur, the presence of which is directly associated with aviation fuel components. The most undesirable aviation fuel component in this case is surface layer sulphur, which can occur in free or bound form (e.g., sulphides, disulphides, hydrogen sulphide and other). Furthermore, it was found that sulphur-enriched areas have products of partial or complete fuel combustions, e.g., SO_2 , SO_3 , H_2S , etc., which cause the formation of sulphides based on the coating material.

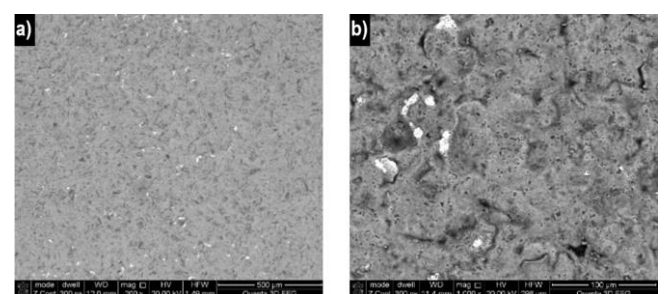


Fig. 5. Blade surface morphology – new, not heated: a) BSE-TOPO; b) BSE

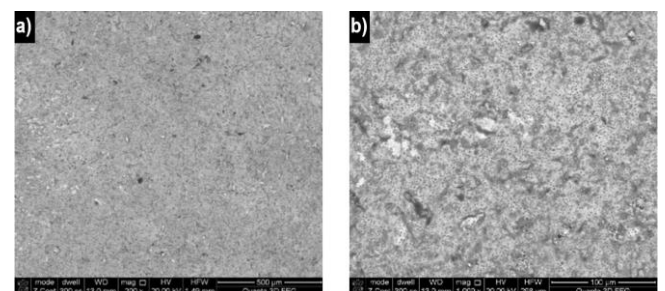


Fig. 6. Blade surface morphology at 1123 K: a) BSE-TOPO; b) BSE

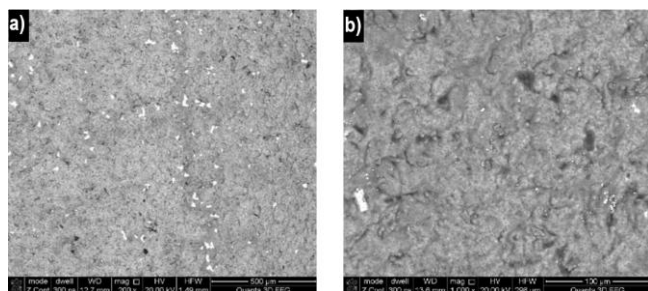


Fig. 7. Blade surface morphology at 1223 K: a) BSE-TOPO; b) BSE

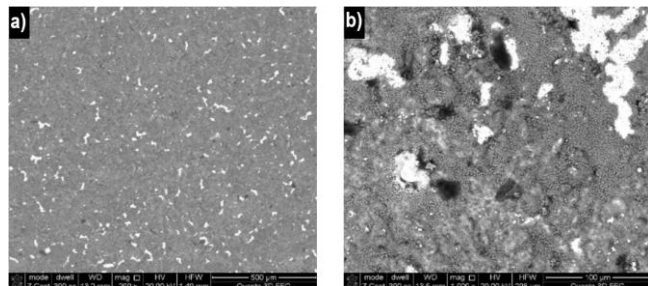


Fig. 8. Blade surface morphology at 1323 K: a) BSE-TOPO; b) BSE

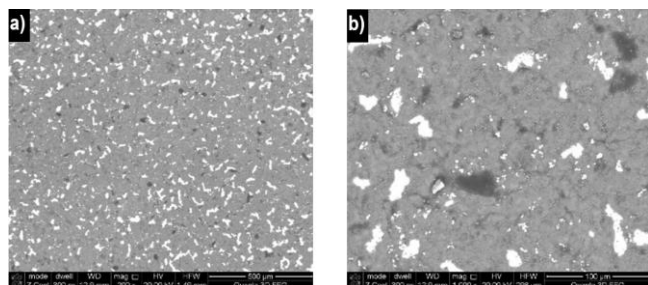


Fig. 9. Blade surface morphology at 1423 K: a) BSE-TOPO; b) BSE

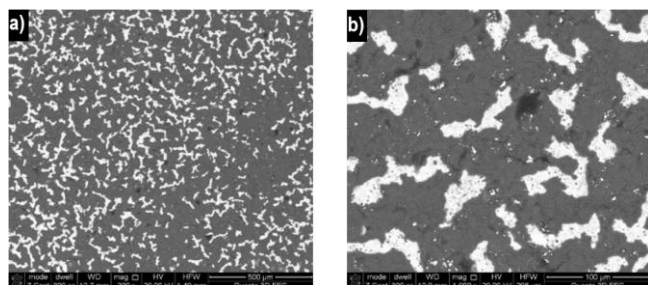


Fig. 10. Blade surface morphology at 1523 K: a) BSE-TOPO and b) BSE

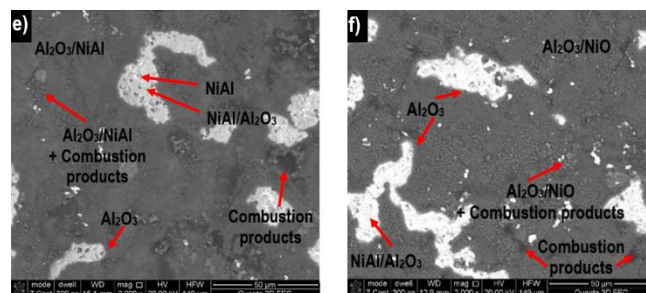
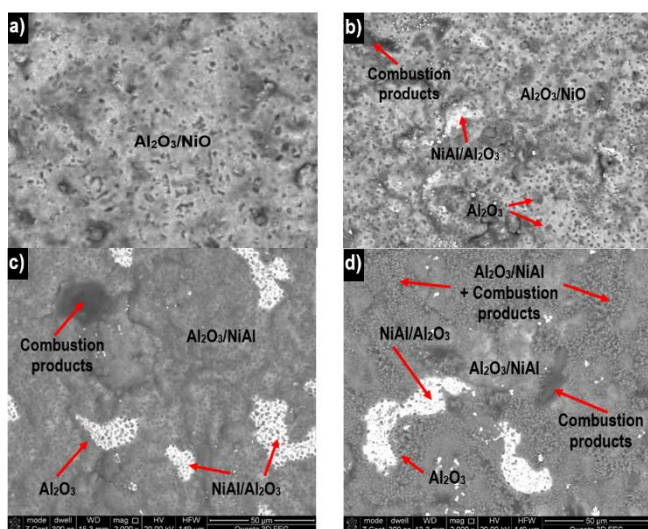


Fig. 11. Blade surface morphology: a) new; b) 1123 K; c) 1223 K; d) 1323 K; e) 1423 K; f) 1523 K

3.3. Area share of elements and oxides

Recorded structural changes ongoing on the surface of the analysed blades under the impact of temperature lead to very significant difference in the chemical and phase composition. It was found, among others, that a blade heating temperature increase results in considerable changes in the content of individual surface elements, primarily oxygen, chromium, nickel and carbon (Fig. 12-13). The observed changes are confirmed by independent EDS (Energy Dispersive Spectroscopy) and element mapping testing.

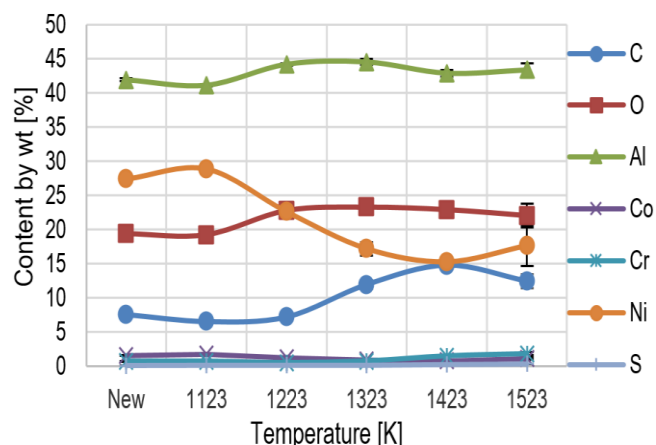


Fig. 12. Percentage share by weight of elements on the surface of tested blades – (SEM/EDS)

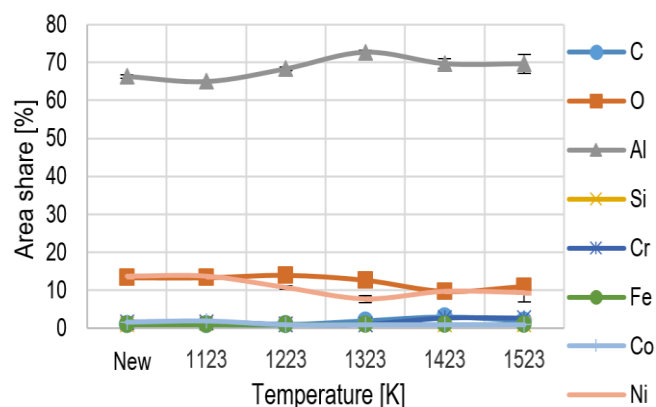


Fig. 13. Percentage share of elements on the surface of tested blades – element mapping method

Changes in the content of individual elements also translate to phase changes. They are particularly emphasized if we analyse the impact of temperature on the percentage content share of oxides on the surface of tested blades (Fig. 14). Based on the obtained data, it can be clearly seen that with increasing temperature, the mass oxide share reaches its maximum for a blade heated at 1423 K. In this case, the total oxide share exceeds 50% of the weight content. Furthermore, the recorded changes in oxide share directly translate to changes in their type. The impact of temperature on nickel oxide share changes is particularly noticeable in this case (Fig. 15). NiO content share changes impacted by temperature are primarily associated with the creation of the Al_2O_3 scale on the surface of the analysed blades.

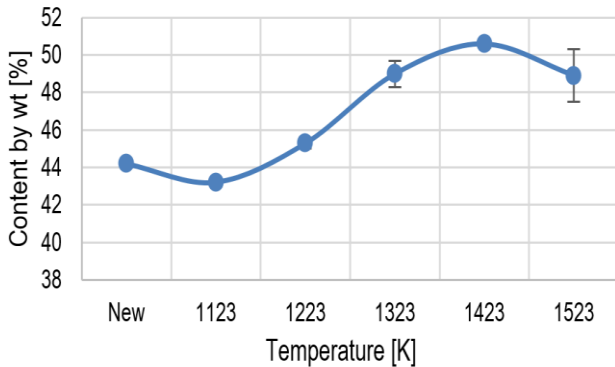


Fig. 14. Total percentage share of oxides measured on the surfaces of tested blades

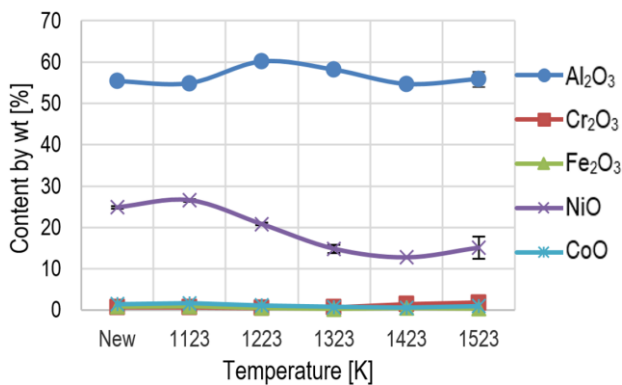


Fig. 15. Percentage share of individual oxides measured on the surfaces of tested blades

3.4. Microstructural tests

Thickness measurements were conducted using computer software for processing and analysing images from a Quanta 3D FEG microscope. Coating thickness was measured at characteristic blade locations, i.e., its edge of attack, trough surface and blade ridge – both inside and near the blade vane profile trailing edge. This provided an averaged aluminium thickness layer for each recorded (analysed) image (Fig. 16). Measured coating thickness values of a new blade (not heated) and a blade heated at different temperatures are shown in Fig. 17.

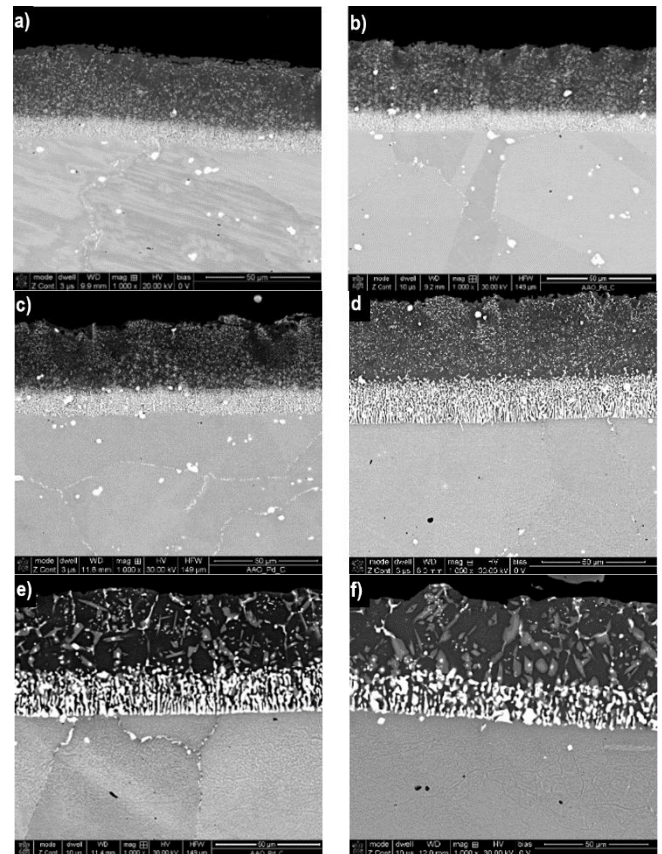


Fig. 16. Blade coating microstructures by heating temperature: a) new; b) 1123 K; c) 1223 K; d) 1323 K; e) 1423 K; f) 1523 K

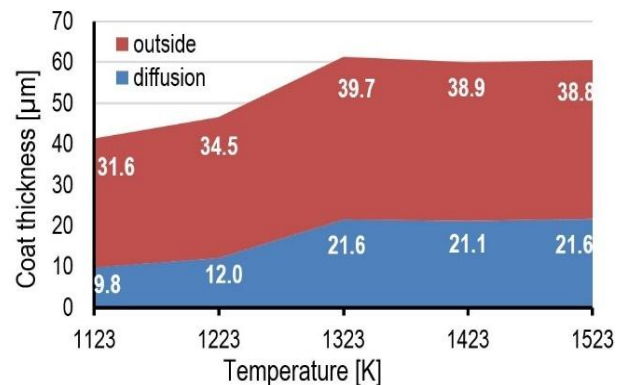


Fig. 17. Changes in the thickness of the external and diffusion coating exposed to different temperatures

3.5. Elemental composition of the internal and diffusion layers

The tests demonstrated that increased blade heating temperature leads to significant changes in the content of individual coating elements, nickel, chromium and aluminium in particular. Cumulative test results for a new blade and blades heated at 1123 K – 1523 K are shown in graphs (Figs. 18 and 19).

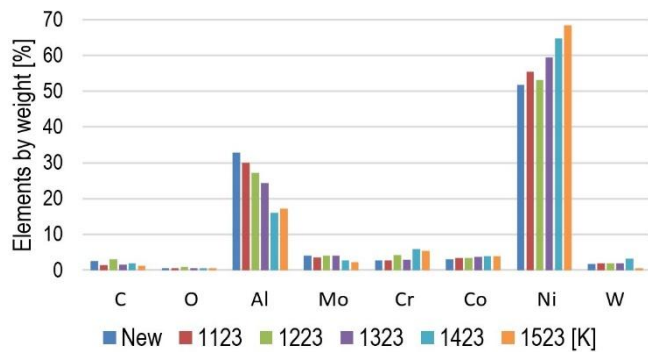


Fig. 18. Chemical composition of the external coating part of a new blade and heated blades

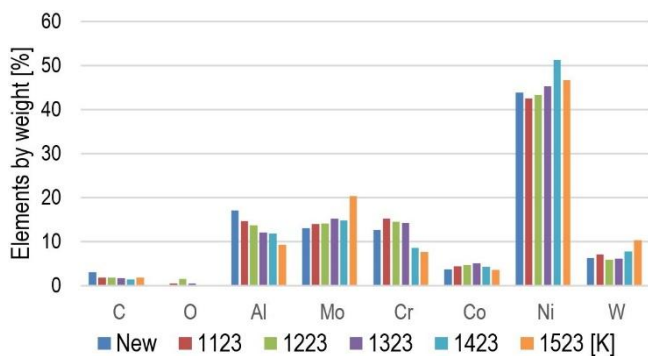


Fig. 19. Chemical composition of the diffusion coating part of a new blade and heated blades

4. MICROSTRUCTURAL TESTS OF THE BLADE EI-867 WD ALLOY

4.1. Grain size tests

Metallographic microsections were tested under a Nikon MA-200 optical microscope and a Quanta 3D FEG and XL30 LaB6 scanning (SEM) microscopes by Philips. Using NIS Elements AR material microstructure image analysis software, the authors determined the mean size (area) of the alloy grain and reinforcing phase γ' , expressed as the diameter of a circle with an area equal to the surface area of the measured object ($E_{qdia} = \sqrt{4 \cdot \text{Area} / \pi}$). Images depicting alloy grain size by heating temperature can be seen in Fig. 20, and a change in its average size as a heating function can be seen in the graph in Fig. 21.

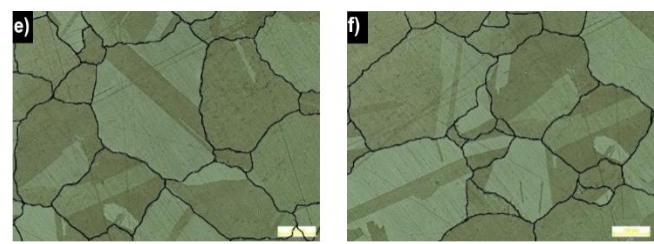
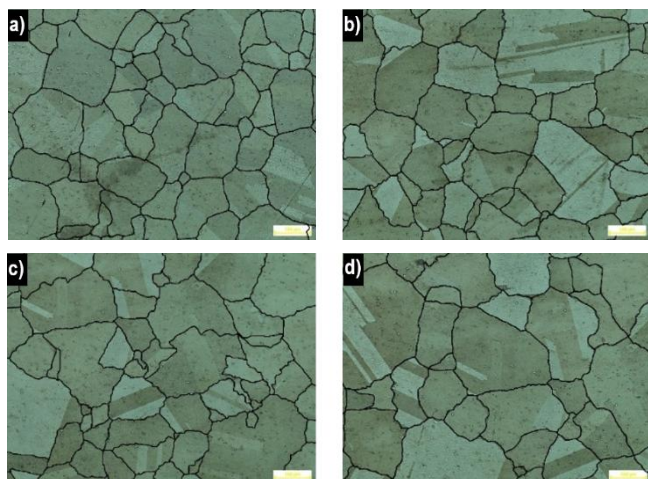


Fig. 20. Blade alloy grain size by heating temperature: a) new; b) 1123 K; c) 1223 K; d) 1323 K; e) 1423 K; f) 1523 K

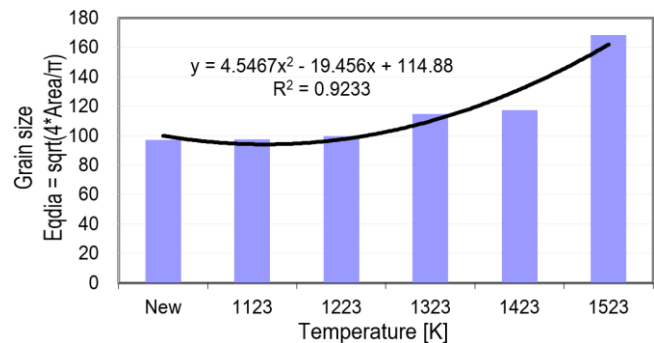
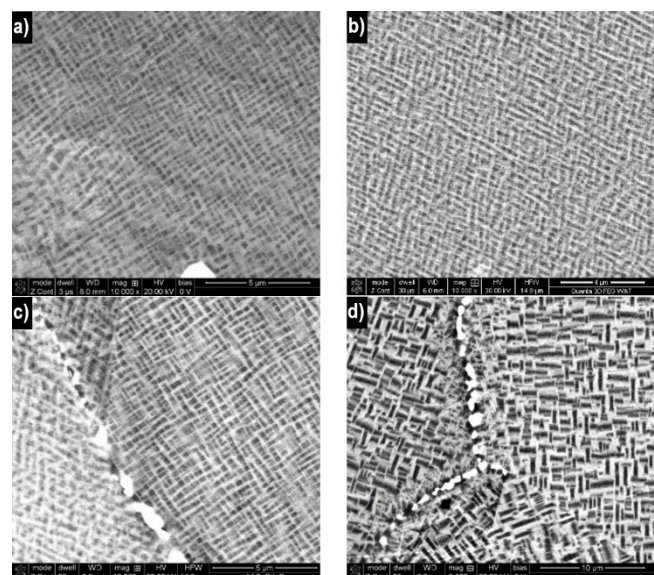


Fig. 21. The dependence of a change in the average blade alloy grain size on heating temperature, expressed by an equivalent diameter of a circle with an area equal to the grain surface area

4.2. Reinforcing γ' phase and carbide precipitate tests

The presence of carbides, even in a non-heated blade, can be observed in the alloy microstructure. Carbide content increases during heating, especially on grain boundaries. Carbides are stand-alone and in the form of "Chinese writing". A change in the γ' precipitate morphology was also found. The exposure of turbine blade alloy to high temperature also impacted their microstructural change, leading to a modification and distribution of the dispersive γ' phase. Fig. 22 shows sample images of microsections demonstrating the phase γ' precipitate morphology and the presence of stand-alone carbides. Based on analysing the microsections, the authors calculated a percentage content of individual phase γ' size classes in the blade alloy (Fig. 23) and the content of average-sized precipitates of this phase (Fig. 24).



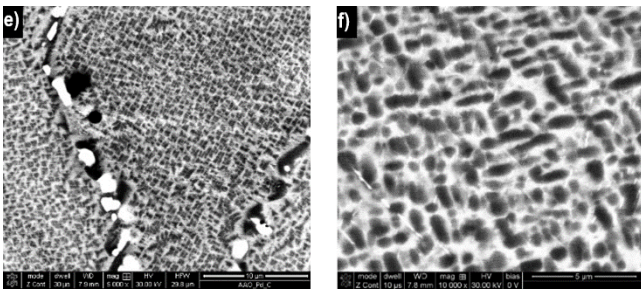


Fig. 22. Blade alloy phase γ' precipitate morphology by heating temperature: a) new; b) 1123 K; c) 1223 K; d) 1323 K; e) 1423 K; f) 1523 K

In the course of heating, the reinforcing γ' phase experiences significant changes, and its structure is modified (Fig. 23). A temperature of 1123 K favours the growth of phase γ' particles.

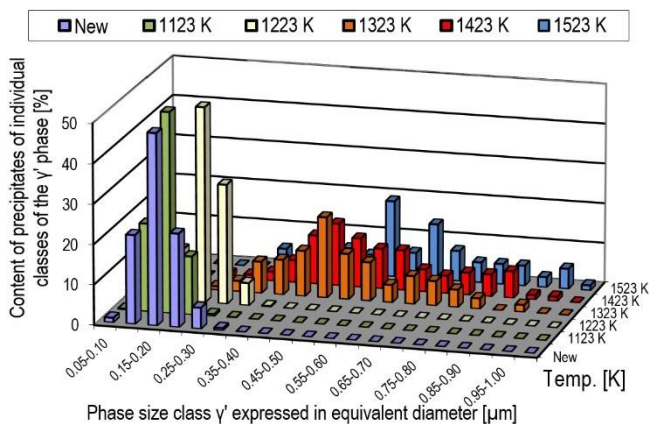


Fig. 23. Percentage precipitate content of individual phase γ' molecule size classes in the alloy

The average size of this phase molecules increases at a temperature of 1323 K (Fig. 23, Fig. 24). While at 1423 K, due to coagulation, the molecules with the largest initial dimensions increase (Fig. 23, Fig. 24).

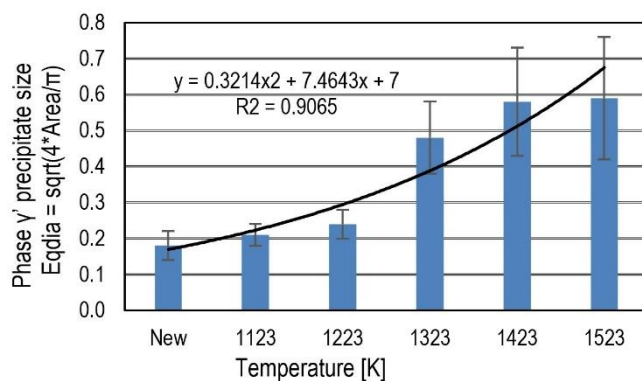


Fig. 24. Dependence of the average phase γ' precipitation in the alloy

It was found that temperature increase entails a reduction in the number of molecules with the largest dimensions relative to material microstructure changes in a new blade and a blade heated at 1123 K (Fig. 23). An increasing distance between γ' phase molecules is simultaneously seen. The observed growth, merging and wavy shape of the γ' phase particles are characteristic of an

overheated alloy and significantly reduce its heat resistance. Assuming the change in the phase γ' precipitate structure (Fig. 25) as a material criterion that enables further operation of the material, one can determine the suitability threshold for their further operation. According to the test results, after the temperature exceeds 1223 K and after an even relatively short exposure time, an intensive growth of the γ' precipitate occurs due to the bonding of fine-grained cubic phase γ' molecules into lamellas. This leads to the loss of cubic shape stability and the formation of irregular and undulated lamellas (Fig. 25).

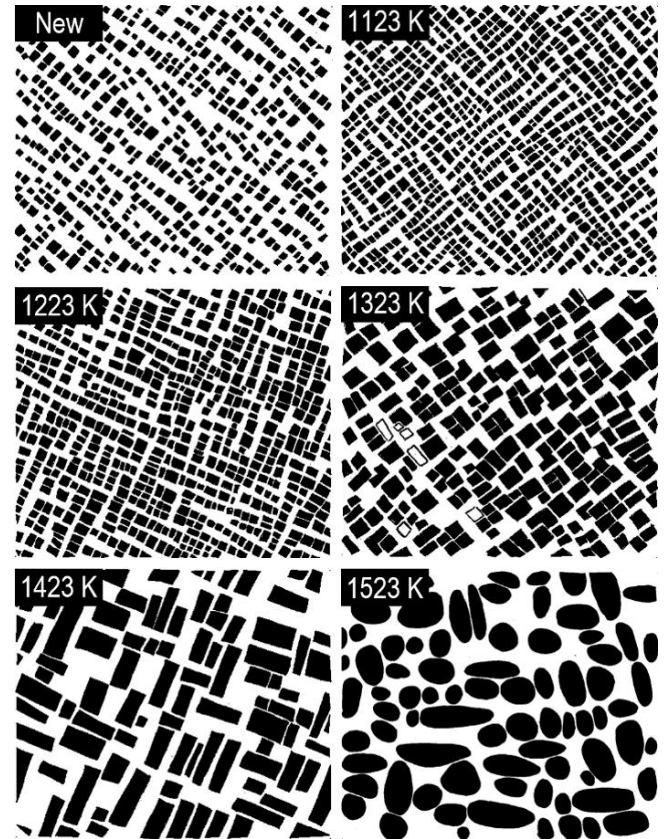


Fig. 25. Phase γ' precipitate microstructure of a new blade and heated blades (20000x zoom) – with visible coagulation, change of shape from cubic to irregular and phase precipitate undulation

5. DISCUSSION OF TEST RESULTS

In the course of the tests, it was found that coating surface morphology, as well as the chemical composition microanalysis spectrum and results indicate that these values significantly, and above all adversely, changed after heating. In the article [33] for the same material but under different experimental conditions, based on SEM/TEM studies in connection with the possibility of strengthening the physical basis of non-destructive testing of blades, microstructural processes occurring in the upper, most external layer of the coating were identified. It was found that above the temperature of 1223 K, a layer of aluminium oxide Al_2O_3 is formed, the microstructure of the coatings is coarsened, pores are formed, Fe and Cr diffuse to the surface and Fe-Cr particles are formed and subsequently coarsened on the surface of the aluminium oxide layer. In the context of non-destructive inspection of blades exposed to high temperatures, the last process mentioned above is of particular importance, because it explains the changes in the light reflected from the blade surface.

The impact of increasing temperature causes the R_a and R_z roughness parameters initially decrease up to a temperature of 1223 K, followed by a slight increase up to 1323 K. The increase in R_a and R_z parameters is caused by the growing thickness of the heat-resistant coating, which considerably impacts the deterioration of its heat and corrosion resistance. Furthermore, various Al_2O_3 and NiO oxides are formed on the blade coating surface together with increasing heating temperature. Aluminium oxide protects the coating surface against further oxidation. It has a morphologically heterogeneous structure and a tendency to uneven growth and exfoliation. Fluctuations in the parameters determining surface roughness are related to the processes of thermal softening, oxidation and microstructural changes. The presence of areas highly rich in carbon and sulphur was found on the coating surface. Their occurrence is directly associated with aviation fuel components. The most undesirable aviation fuel component is sulphur, which can occur in free or bound form of sulphides, disulfides and hydrogen sulphide. In the course of tests, the authors found that the total percentage share of oxides on coating surfaces initially grows, followed by a decrease at the highest heating temperature. The percentage weight share of the elements making up the coating is modified due to heating. A significant content difference can be seen, primarily in relation to the following elements: W, Mo, Ni and Al.

When testing the EI-867 WD alloy, it was found that MC carbides appeared when producing the blades in the alloy. They were found as stand-alone and in the form of "Chinese writing", mainly at grain boundaries. Carbides of such type can cause instabilities that reduce plasticity at low temperatures. The second of the identified carbides, M_6C , is more stable at higher temperatures. The M_6C carbide was mainly observed near grain boundaries. The next carbide, $M_{23}C_6$, precipitates during low-temperature heat treatment or in the course of alloy operation at temperatures from the 1033 K – 1253 K range. It is shaped as large, irregular precipitates at grain boundaries, in the form of lamellas or polygons. A $M_{23}C_6$ carbide significantly impacts nickel-based superalloy properties. Grains grow in the alloy, which adversely impacts its mechanical properties. The observed transformation of $M_{23}C_6$ carbides into M_6C in an alloy exposed to prolonged high temperatures (above 1223 K) is related to the diffusion of atoms, primarily molybdenum and tungsten present in the tested alloy, into the carbide structures. This high-temperature transformation from $M_{23}C_6$ to M_6C leads to a decrease in creep resistance, as the process reduces the amount of stable reinforcing particles along the grain boundaries. Larger and less homogeneous M_6C carbides limit the alloy's ability to resist deformation under creep conditions. Additionally, the growth and transformation of carbides contribute to microstructural degradation, as M_6C carbides are less effective than $M_{23}C_6$ in binding carbon at grain boundaries. This results in unfavourable changes in the alloy's microstructure, which in turn weakens its corrosion and oxidation resistance.

The expansion of the phase γ' particles leads to the loss of their stability, resulting in coagulation of some particles and dissolving of others. That process occurs above certain temperatures and heating time, characteristic for a given phase. According to the test results, after the temperature exceeds 1223 K and after an even relatively short exposure time, an intensive growth of the γ' precipitate occurs due to the bonding of fine-grained cubic phase γ' molecules into lamellas. This leads to the loss of cubic shape stability and the formation of irregular and undulated lamellas. This conclusion is also confirmed by the results in [34]. A similar conclusion was drawn by the authors of [25, 27, 35]. Based on the

example of the Udimet 700 alloy, lamellar-form precipitates above a temperature of 1093 K significantly deteriorate the yield strength. The kinetics of phase γ' precipitation depends on the supersaturation of the matrix, i.e., phase γ , with alloy elements. Exudation shape depends on the degree of mismatch between their grid with the warp grid. The authors of [34, 36] concluded that the precipitates of the γ' phase are coherent with the matrix, and the morphology is related to the degree of mismatch between phase γ and phase γ' lattice parameters. Furthermore, they found that the phase γ , with mismatch of the grid $\Delta a = 0.2\%$ exudes in spheroid shape, at $\Delta a = 0.5 - 1\%$ takes the cuboid form and at $\Delta a = 1.2\%$ - tile form. A number of alloy properties depend on the phase γ' precipitate shape and amount. These include, e.g., the value of yield strength of weakening of adverse action of brittle phases – e.g., Laves. The exudation hardening theory shows that the factors deciding the hardening degree are diameter of phase γ' particles and distance between them. These parameters depend on the growth rate (controlled by volumetric diffusion) and coagulation of these molecules. Phase γ' chemical composition significantly impacts the value of its $a_{\gamma'}$ lattice and the associated degree of mismatch between Δa and the a_{γ} lattice matrix. Wherein $\Delta a = (a_{\gamma} - a_{\gamma'})/a_{\gamma}$. This impact phase γ' precipitate morphology and its durability range. It turns out that the degree of mismatch of phase lattice parameters is a function of temperature. According to [34], the highest high-temperature creep resistance is exhibited by alloys with positive phase lattice mismatch. The chemical composition, morphology and microstructural arrangement of phase γ' precipitates have a decisive impact on alloy strength properties.

According to [25], the change in $R_{0.2}$ and R_m strength properties for an analogous EI-867 alloy and for various test temperature values is of similar nature. A minor change in these two parameters is observed up to a temperature of 473 K. The value slightly increases up to approximately 673 K, followed by low fluctuation up until a temperature of ca. 1073 K, above which a clear reduction in tensile strength and yield strength can be seen.

6. PRACTICAL IMPLICATIONS OF THE FINDINGS AND THEIR LIMITATIONS

The tested turbine element, due to its core material, is classified as a nickel-based alloy, polycrystalline alloy with reduced chromium content and titanium-free. The lower chromium content requires the use of a coating – a coating that increases heat resistance properties and operating temperature by about 100 K. The tested object can be representative of a wide range of polycrystalline alloys with a similar chemical and volumetric composition of the γ' phase, which are used in heat exchangers, cooling systems or renewable energy systems. Certain findings, despite limitations resulting from tests conducted in laboratory conditions, have practical significance in relation to the group of alloys and coated materials characterized above:

- The γ' phase determines the mechanical properties of the alloy (durability of turbine blades).
- The microstructural modification of the γ' phase, carbides and grain boundaries depends on the temperature and time of its action and may constitute a parameter of the degree of microstructural degradation.
- Based on changes in the size of γ' , the approximate working temperature of the nickel alloy can be determined. The γ' phase precipitates change their size and shape during long-term

exposure to high temperature, which allows them to be used as indicators of the material's working temperature.

- In order to verify the technical condition of the blades, a comparative method can be used, in which the size and shape of the γ' phase of the new blade (standard values) are compared to the blade considered unfit for further operation during the technical inspection. On this basis, it can be stated, for example, that the damaged turbine blade (or superalloy in general) operated at an exhaust gas temperature above the maximum permissible temperature. Unfortunately, such tests are carried out using destructive methods. The proposed methodology for identifying damage to the gas turbine blade may prove helpful in the event of an engine failure, if the information on its operating conditions is insufficient.
- Diffusion processes (movement of aluminium from the interior of the coating to its surface) are more intensive the higher the temperatures. Additionally, long-term exposure to high temperatures leads to strong depletion of aluminium from the surface layer, which translates into a significant reduction in its resistance.
- Combustion products appear on the outer layer of the coating, and the presence of sulphur in exhaust gases intensifies corrosive processes. Sulphur reacts with aluminium, creating unstable compounds (e.g. sulphides), which weaken the coating and contribute to its degradation. Sulphur corrosion can lead to the formation of cracks and microcracks in the coating (acceleration of the coating degradation process). To some extent, combustion products affect the surface colour.
- Increase in coating thickness due to exposure to high temperatures is related to thermal expansion, phase changes and its oxidation. "Coating swelling" translates into a strong deterioration of its protective properties (in operating conditions, all destructive processes are intensified). Microstructural changes of the coating affecting the colour of its surface.

Several selected operational aspects that affect the limitations in formulating generalizations of the discussion of the results of the conducted laboratory experiment:

- Often, in real conditions, overheating of blades is local because the degree of impact of exhaust gases, thermal loads on the blade surface, is not uniform over the entire surface. The highest temperature values occur on the leading edge of the blade, because it is often accompanied by the process of stagnation of the exhaust gas temperature (dependence of the static value of the exhaust gas stream with defined thermodynamic properties and the flow rate value).
- The morphology of the γ' phase particles also depends on the sign of the mechanical stress. The tensile stress occurring axially of the blade during the rotation of the turbine rotor promotes the growth of the γ' phase in the plane perpendicular to the direction of stress. As a result, plates are formed from the original cuboid shape, the wider walls of which are located perpendicular to the direction of stress.
- There are several factors that increase the acceleration of the degradation processes of aluminium-based coatings. The working environment can be considered as particularly important. In coastal areas (even 40 kilometres from the reservoir) due to the increased concentration of chloride ions (Cl^-), aluminized coatings are subject to accelerated degradation and destruction due to hot corrosion and oxidation. Under the influence of sea salts and high temperatures, they lose their protective properties. The coating loses thickness, which results in the gradual exposure of the basic blade

material, exposing it to further corrosion and operation at elevated temperatures despite the nominal operating conditions.

7. CONCLUSIONS

Gas turbine blades are exposed to high-temperature corrosion and cyclic thermal stresses, which lead to surface damage and thermomechanical fatigue. Prolonged exposure to this process, along with the adverse effects of elevated temperatures, causes blade overheating (significant microstructural degradation of the superalloy). Under operational conditions, this results in the formation of microstructural zones with locally diminished mechanical properties—namely, reduced heat resistance and creep resistance of the alloy. Excessively high temperatures relative to the nominal operating temperature, combined with tensile stresses during rotation, lead to creep in the superalloy. An important aspect of this issue is an attempt to determine the extent of modification in the state of the coating and the blade alloy material due to the effects of supercritical temperatures. Additionally, to approximate real conditions, the experiment was conducted in an exhaust gas environment. The research conducted could contribute to defining criteria for determining the suitability or unsuitability of the tested turbine element for further operation, based on information obtained through endoscopic devices without the need to dismantle the blades from the turbine. The technical condition of the blades can be indirectly assessed, i.e., based on the correlation between the light signal reflected from the coating surface (or, in its absence, the alloy surface) and the microstructural state of the alloy/coating.

The article describes the material changes (alloy and coating) in gas turbine blades of jet engines caused by high temperatures. Additionally, to simulate real conditions to some extent, the experiment was conducted in an exhaust environment. Microstructural studies performed, along with quantitative and qualitative results obtained, help in identifying significant material changes in both the coating and the alloy. They represent an attempt to comprehensively describe the material modifications in the blades (demonstrating differences compared to the material characteristics of a new blade). Section 6 presents practical implications of the results and certain limitations. The generalizations in this section attempt to point out potential applications in engineering practice while also considering certain limitations due to the experimental conditions and the interpretation of results in the context of real, complex working conditions of superalloys. The reflected light signal (colour) is influenced by factors such as the position and nature of the light source, as well as the surface roughness and chemical composition (see section 3). In terms of gas turbine blade durability, this material criterion is a decisive factor in defining strength properties (section 4 and discussion of results, see section 5).

1. Coating surface morphology, as well as the chemical composition microanalysis spectrum and results indicate that these values significantly changed after heating.
2. Due to the impact of increasing temperature, the R_a and R_z roughness parameters initially decrease up to a temperature of 1223 K, followed by a slight increase up to 1323 K. The increase in R_a and R_z parameters is impacted by growing thickness of the heat-resistant coating. Therefore, its heat and corrosion resistance deteriorates.
3. Various Al_2O_3 and NiO oxides are formed on the blade coating surface together with increasing heating temperature.

Aluminium oxide has a morphologically heterogeneous structure and a tendency to uneven growth and exfoliation.

4. Furthermore, there are areas on blade surfaces that are highly rich in carbon and sulphur, the presence of which is directly associated with aviation fuel components.
5. The total percentage share of oxides on coating surfaces initially grows, followed by a decrease at the highest heating temperature. The percentage weight share of the elements making up the coating is modified due to heating.
6. There is little carbide presence when creating blades using the EI-867WD alloy, with the process dominated by the $M_{23}C_6$ carbide, both in grains and at grain boundaries. The size and structure of the carbides changed in the course of heating, ultimately transforming into M_6C , and found primarily at grain boundaries.
7. Alloy grain growth was identified under the impact of high temperature, mainly above 1223 K.
8. The most significant microstructural changes were found in the precipitate morphology of the reinforcing γ' phase. The growth of molecules in this phase led to the loss of their stability.
9. The growth (adverse for heat resistance) and the percentage depletion of the reinforcing γ' phase in the alloy structure appeared at a temperature above 1223 K. This was caused by coagulation, a change of the shape from cubic to irregular and undulation of the reinforcing γ' phase precipitation.
10. The aforementioned changes in the microstructure of the EI-867WD changes led to significantly deteriorated strength properties in the course of heating at a temperature above 1223 K.

Further work will continue in the area of material characterization, focusing on single-crystal alloys and various types of coatings. On the other hand, diagnosing blades using videoscopes without removing them from the turbine remains challenging. The quality of the image obtained from the videoscope depends on the lighting and the device itself. Improper lighting settings, light reflections, or variable lighting conditions can affect the image coloration, which may lead to incorrect conclusions regarding the condition of the coating or the alloy surface.


REFERENCES


1. Pollock TM, Tin S. Nickel-based superalloys for advanced turbine engines: Chemistry, microstructure, and properties. *J. Propuls. Power.* 2006; 22: 361–374.
2. Gudivada G, Pandey AK. Recent developments in nickel-based superalloys for gas turbine applications: review. *J Alloy Compd.* 2023;963.
3. Sims CT, Stoloff NS, Hagel WC. *Superalloys II-High-Temperature Materials for Aerospace and Industrial Applications.* New York (NY): John Wiley & Sons; 1987.
4. DeMasi-Marcin JT, Gupta DK. Protective coatings in the gas turbine engine. *Surf Coat Technol.* 1994;68:1–9.
5. Kadir A, Bég O, Gendy EIM, Bég TAB, Shamshuddin MD. Computational fluid dynamic and thermal stress analysis of coatings for high-temperature corrosion protection of aerospace gas turbine blades. *Heat Transf Asian Res.* 2019;48. doi:10.1002/htj.21493
6. Singh I, Tiwari AC. A revisit to different techniques for gas turbine blade cooling. *Mater Today Proc.* 2023.
7. Chowdhury TS, Mohsin FT, Tonni MM, Mita MNH, Ehsan MM. A critical review on gas turbine cooling performance and failure analysis of turbine blades. *Int J Thermofluids.* 2023;18:100329.
8. Hetmańczyk M, Swadźba L, Mendala B. Advanced materials and protective coatings in aero-engines application. *JAMME.* 2007;24:372–81.
9. Grimme C, Oskay C, Mengis L, Galetz MC. High temperature wear behavior of δ - Ni_2Al_3 and β - $NiAl$ coatings formed on pure nickel using pack cementation process and diffusion heat treatment. *Wear.* 2021;477:203850.
10. Han J, Dutta S, Ekkad S. *Gas Turbine Heat Transfer and Cooling Technology.* New York (NY): Taylor and Francis; 2012.
11. Rajendran R. Gas turbine coatings—An overview. *Eng Fail Anal.* 2012;26:355–69.
12. Darolia R. Development of strong, oxidation and corrosion resistant nickel-based superalloys: critical review of challenges, progress and prospects. *Int Mater Rev.* 2018;64:355–80.
13. Azevedo C, Sinatora A. Erosion-fatigue of steam turbine blades. *Eng Fail Anal.* 2009;16:2290–303.
14. Laguna-Camacho JR, Villagran Y, Martínez-García H, Juárez-Morales G, Cruz-Orduña MI, Manuel VT, et al. A study of the wear damage on gas turbine blades. *Eng Fail Anal.* 2015;61:88–99.
15. Dubiel B, Moskalewicz T, Swadźba L, Czyrska-Filemonowicz A. Analytical TEM and SEM characterisation of aluminide coatings on nickel based superalloy CMSX-4. *Surf Eng.* 2008;24:327–31.
16. Carter TJ. Common failures in gas turbine blades. *Eng Fail Anal.* 2005;12:237–47.
17. Kopec M. Recent advances in the deposition of aluminide coatings on nickel-based superalloys: a synthetic review (2019–2023). *Coatings.* 2024;14:630. doi:10.3390/coatings14050630
18. Qu S, Fu CM, Dong C, Tian JF, Zhang ZF. Failure analysis of the 1st stage blades in gas turbine engine. *Eng Fail Anal.* 2013;32:292–303.
19. Kolagar AM, Tabrizi N, Cheraghzadeh M, Shahriari MS. Failure analysis of gas turbine first stage blade made of nickel-based superalloy. *Case Stud Eng Fail Anal.* 2017;8:61–8.
20. Belan J, Vaško A, Tillová E. Microstructural analysis of DV-2 Ni-base superalloy turbine blade after high temperature damage. *Procedia Eng.* 2017;177:482–7.
21. García-Martínez M, Del Hoyo Gordillo JC, Valles González MP, Pastor Muro A, González Caballero B. Failure study of an aircraft engine high pressure turbine (HPT) first stage blade. *Eng Fail Anal.* 2023;149:107251. doi:10.1016/j.engfailanal.2023.107251
22. Bogdan M, Blachnio J, Spychała J, Zasada D. Assessment of usability of the exploited gas turbine blade heat resistant coatings. *Eng Fail Anal.* 2019;105:337–46. doi:10.1016/j.engfailanal.2019.07.016
23. Villada JA, Bayro-Lazcano RG, Martínez-Franco E, Espinosa-Arbelaes DG, Gonzalez-Hernandez J, Alvarado-Orozco JM. Relationship between γ' phase degradation and in-service GTD-111 first-stage blade local temperature. *J Mater Eng Perform.* 2019;28:1950–7.
24. Zhu J, An C, Lu Y, Zhu M, Xuan F. Research progress on effect of γ' phase on strength, fatigue and creep properties of nickel-based superalloys. *Mater Mech Eng.* 2023;7(6):1–7. doi:10.11973/jxgccl202306001
25. Ponańska A. *Żywotność łopatek silników lotniczych ze stopu EI-867 w aspekcie odkształcenia niejednorodnego i zmian strukturalnych [doctoral dissertation].* Rzeszów: Rzeszów University of Technology; 2000.
26. Xiaotong G, Weiwei Z, Chengbo X, Longfei L, Stoichko A, Yunrong Z, Qiang F. Evaluation of microstructural degradation in a failed gas turbine blade due to overheating. *Eng Fail Anal.* 2019;103:308–18.
27. Skočovský P, Podrábský T, Belan J. Degradacja w wyniku eksploatacji warstwy aluminiowo-krzemowej łopatek turbinowych wykonanych na bazie Ni. *Archiwum Technologii Maszyn i Automatyzacji.* 2004;24(1):45–52.
28. Mevissen F, Meo M. A review of NDT/structural health monitoring techniques for hot gas components in gas turbines. *Sensors.* 2019;19:711.
29. Kukla D, Kopec M, Sitek R, Olejnik A, Kachel S, Kiszowskiak Ł. A novel method for high temperature fatigue testing of nickel superalloy turbine blades with additional NDT diagnostics. *Materials.* 2021;14:1392.

- doi:10.3390/ma14061392
30. Bogdan M, Derlatka M, Blachnio J. Concept of computer-aided assessment of the technical condition of operated gas turbine vanes. *Pol Marit Res.* 2018;3(99):104–12. doi:10.2478/pomr-2018-0101
 31. Bogdan M, Blachnio J, Kułaszka A, Zasada D. Investigation of the relationship between degradation of the coating of gas turbine blades and its surface colour. *Materials.* 2021;14:2478. doi:10.3390/ma14247843
 32. Bogdan M, Blachnio J, Kułaszka A, Derlatka M. Assessing the condition of gas turbine rotor blades with the optoelectronic and thermographic methods. *Metals.* 2019;9:31.
 33. Bogdan M, Zieliński W, Płociński T, Kurzydłowski KJ. Electron microscopy characterization of the high temperature degradation of the aluminide layer on turbine blades made of a nickel superalloy. *Materials (Basel).* 2020;13:3240. doi:10.3390/ma13143240
 34. Paton B. *Żaropropczność litiejnych nikielowych spławów i zaszczuta ich ot okislenija.* Kijew: Naukowa Dumka; 1997.
 35. Swadźba L. *Kształtowanie struktury oraz właściwości powłok ochronnych na wybranych stopach stosowanych w lotniczych silnikach turbinowych.* Katowice: Wydawnictwo Politechniki Śląskiej; 2007.
 36. Nikitin WI. *Korozja i zaszczuta łopatek gazowych turbin.* Leningrad; 1987.

This research was financed by the Ministry of Science and Higher Education of Poland with allocation to the Faculty of Mechanical Engineering Białystok University of Technology for the WZ/WM-IIM/4/2023 academic project in the mechanical engineering discipline.

Mariusz Bogdan:  <https://orcid.org/0000-0002-9960-7210>

Artur Kułaszka:  <https://orcid.org/0000-0002-8318-5877>

Dariusz Zasada:  <https://orcid.org/0000-0002-3138-5105>



This work is licensed under the Creative Commons BY-NC-ND 4.0 license.

ASSESSING COMPANY FINANCIAL HEALTH USING AN INTEGRATED BSC-DEA FRAMEWORK WITH A FOCUS ON PROCESS DIGITIZATION

Michaela KOČIŠOVÁ*, Milan FILO*, Jaroslava KÁDÁROVÁ*, Alžbeta SUHÁNYIOVÁ*

*Faculty of Mechanical Engineering, Department of Business Management and Economics,
 Technical University of Košice, Letná 1/9, 042 00 Košice, Slovakia

jaroslava.kadarova@tuke.sk, milan.filo@tuke.sk, alzbeta.suhanyiova@tuke.sk, michaela.kocisova@tuke.sk

received 23 August 2024, revised 17 October 2024, accepted 30 October 2024

Abstract: The integration of the Balanced Scorecard and Data Envelopment Analysis offers a powerful method for evaluating a company's financial health in a multi-dimensional manner, with a strong emphasis on digitization. By combining strategic performance metrics from BSC with the efficiency-focused analysis of DEA, organizations can gain deeper insights into both financial and operational aspects of their business. Digitization plays a crucial role in this approach by automating data collection, enabling real-time monitoring, and improving the accuracy of performance assessments. This digital transformation not only enhances decision-making but also allows for scalable and flexible implementations across various departments. Ultimately, the integrated BSC-DEA approach, supported by digital tools, helps companies optimize their resources, align with strategic goals, and ensure long-term financial sustainability. This research paper also explores the process, mathematical formulation and benefits of using this integrated approach to evaluate company financial health.

Key words: financial health, Balanced Scorecard, Data Envelopment Analysis, model, digitization, software

1. INTRODUCTION

The implementation of the integrated Balanced Scorecard (BSC) and Data Envelopment Analysis (DEA) model in an industrial company involves aligning strategic objectives with measurable performance indicators across key perspectives, such as financial health, customer satisfaction, and operational efficiency. Accurate data collection and validation are critical, followed by the integration of this data into the Data Envelopment Analysis framework to assess the relative efficiency of different decision-making units. The process includes benchmarking performance, identifying areas for improvement, and implementing targeted action plans to enhance efficiency. By leveraging digital tools, companies can automate data collection, enhance real-time monitoring, and make more informed decisions, ultimately aligning with strategic goals and ensuring long-term financial sustainability.

2. INTEGRATED BSC-DEA MODEL

Despite the popularity of both the BSC and DEA approaches, there are very few studies that examine their integration for better evaluation of the performance and efficiency of industrial enterprises and their financial health. Given the proposed systematic relationship between these two methods, it is essential to first summarize their fundamental differences, weaknesses and strengths. In general, DEA evaluates inputs and outputs, while BSC utilizes qualitative or quantitative multi-criteria assessment, DEA does not take into account the company's strategy, whereas in BSC, strategy is the foundation for decision-making process. More weaknesses of BSC and strengths of DEA method are summarized in Table 1.

Tab. 1. BSC weaknesses and strengths of DEA [1]

| Weaknesses of BSC |
|---|
| One of the challenges in BSC is having the baseline which performance is measured against. Evaluation is impossible without a benchmark. First, a baseline for evaluation should be determined and then we should do the evaluation against the baseline. However, baselines and benchmarks are hard to determine and can be ambiguous. As DEA is based on relative comparison, the DMUs are evaluated against each other. By combining the BSC with DEA we can answer this important challenge of BSC. |
| BSC confronts managers with an extraordinarily complex optimization problem because of BSC has complexity and the interrelated indicators. This complexity also rises from the large number of variables. Big companies, which should try to track hundreds of measures in BSC, state that BSC lacks a single complex index to summarize the interaction between these measures of performance. |
| Lack of a common scale of measurement causes more complexity. Moreover, in BSC, we may have dimensionless ratios and index numbers. |
| Strengths of DEA |
| DEA permits to analyze multiple inputs and output factors simultaneously. This ability is very helpful in real-world management situations because there are usually multiple, multidimensional inputs and outputs. From this perspective, DEA is better in comparison with traditional approaches that can only deal with multiple inputs and a single output. Managers can use the results of DEA to improve and increase corporate performance, efficiency and competitiveness. |
| DEA solves an optimization problem and gains its weights result. Hence, DEA is only dependent on the empirical observations. This fact gives the DEA a great advantage over usual optimization procedures. |
| DEA is a non-parametric approach so it does not need to have an explicit functional form to relate inputs to outputs. |

As for the mathematical model, BSC does not provide a mathematical model or a complex index to summarize the interaction between performance indicators for inter-company comparison or comparison of several companies between each other. The use of the non-parametric DEA method offers an overall view of the efficiency of the compared companies based on the calculated efficiency value.

2.1. Comparison of the integrated BSC-DEA model with other performance measurement systems

The choice between these systems depends on the company's specific needs, resources, and objectives. Compared to next systems, the integrated BSC - DEA model offers a more comprehensive view of performance, both strategic alignment and efficiency analysis and a balance of qualitative and quantitative measures. However, it also requires more expertise to implement and interpret, may be more resource-intensive and could be overly complicated for smaller organizations or companies.

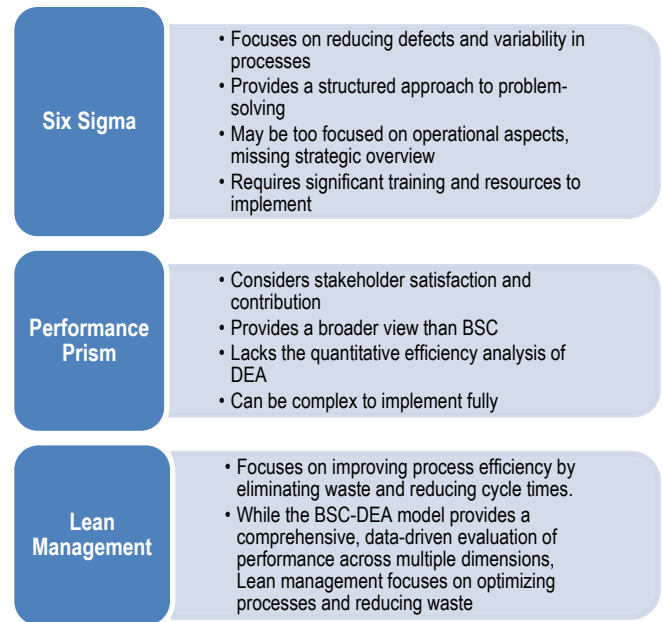
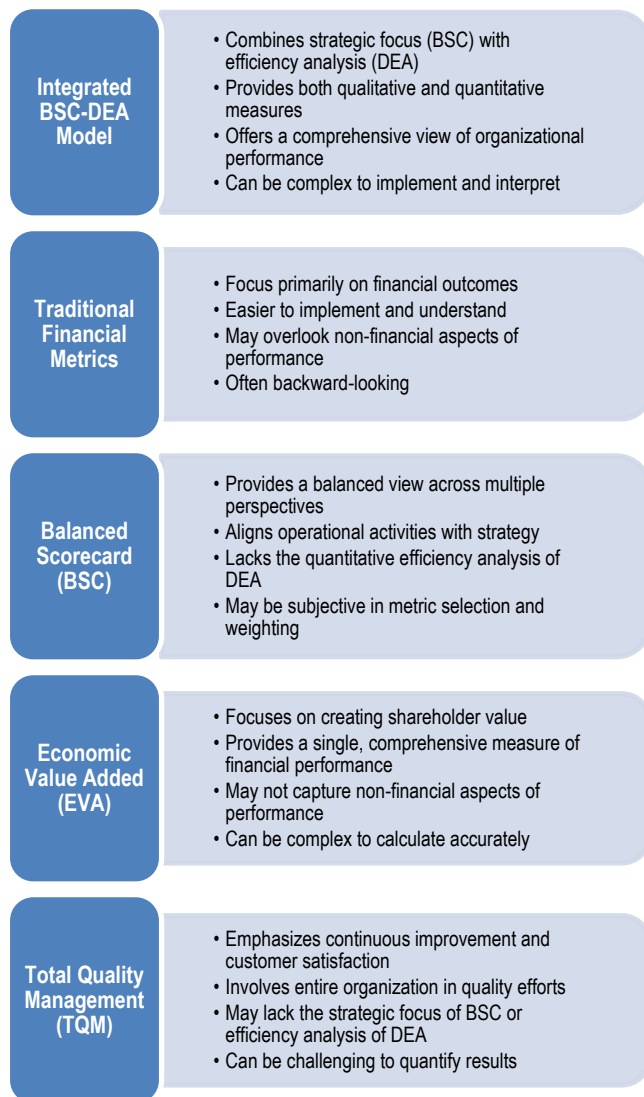


Fig. 1. Comparison BSC-DEA model with other systems [2]

Each performance measurement system offers unique benefits and is suited to different organizational needs. While the BSC - DEA model provide a complete strategic, performance and efficiency-focused approach, other systems like Six Sigma, TQM, and EVA offer more specialized management tools. The choice of system depends on the business's goals, resources and strategic priorities.

2.2. Company's financial health

A financially healthy company typically demonstrates consistent profitability, a strong balance sheet with manageable debt levels, positive and stable cash flows, the ability to invest in growth opportunities, resilience to economic downturns, and good credit standing [3].

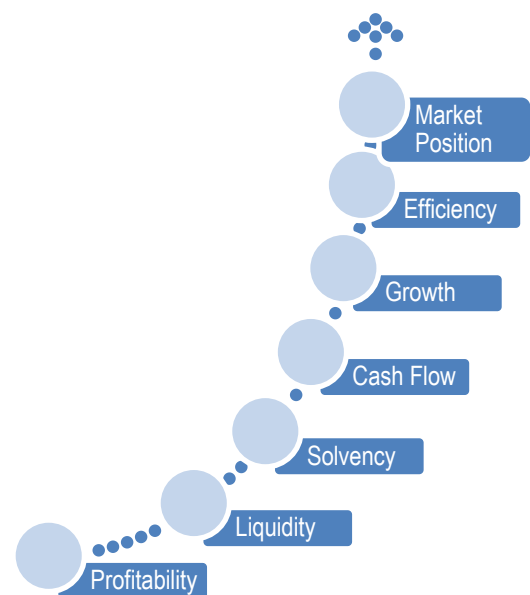


Fig. 2. Key aspects of a company's financial health

Regularly monitoring the financial health of a company is essential for investors, creditors, management, and other stakeholders. It enables them to evaluate the company's performance, identify potential risks and opportunities, and make informed decisions regarding investment, lending, strategic planning, and resource allocation. By staying informed about the company's financial position, stakeholders can proactively address challenges and capitalize on growth opportunities [4].

3. PROCESS PROPOSAL FOR IMPLEMENTING THE INTEGRATED BSC-DEA MODEL FOR ASSESING A COMPANY'S FINANCIAL HEALTH

Assessing a company's financial health involves analysing financial statements, market performance, and industry trends. The implementation of an integrated BSC-DEA model offers a comprehensive approach to evaluating this issue. Below is a proposal outlining how the integrated BSC-DEA model can be applied in a company to assess its financial health (Figure 3).

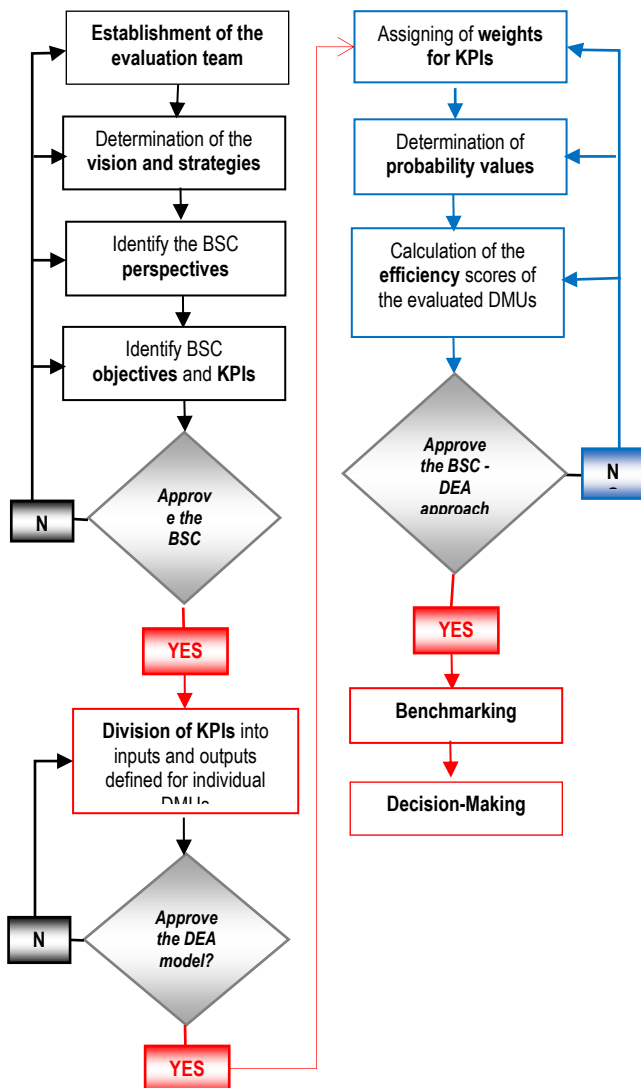


Fig. 3. Decision – making process of BSC - DEA model

The integrated BSC-DEA model offers a robust framework for assessing and improving the financial health of companies and their viability. From the DEA method's perspective, the integrated model formalizes the way to calculate the efficiency of business processes based on identified inputs and outputs, which are the KPIs assigned to specific strategic goals within the BSC perspectives.

From the BSC perspective, the integrated model proposes a new approach to performance evaluation using quantitative analysis that combines KPI values within each perspective into a single value. As a result, the BSC-DEA model for industrial enterprises provides a comprehensive view of the company from both financial and non-financial, as well as short-term and long-term perspectives, and provides valuable insights for managers and stakeholders in understanding and enhancing business performance [4].

3.1. Assessing company financial health using an integrated BSC-DEA model

The specification of the individual steps from the point of view of evaluating the financial health of the company is as follows:

1. BSC framework for evaluation of a company financial health

The BSC provides a structured framework for evaluating company performance across multiple perspectives. When applied to assess financial health, the BSC typically includes the following perspectives, objectives and KPIs [8]:

- Financial Perspective:
 - a) Objectives: Increase profitability, optimize costs, improve cash flow, and manage debt.
 - b) Key Indicators: Return on Equity (ROE), Return on Assets (ROA), Debt-to-Equity Ratio, and Liquidity.
- Customer Perspective:
 - a) Objectives: Enhance customer satisfaction, increase customer loyalty, and grow market share.
 - b) Key Indicators: Customer Satisfaction Index, Customer Retention Rate, and Market Share.
- Internal Process Perspective:
 - a) Objectives: Improve internal process efficiency and optimize operational costs.
 - b) Key Indicators: Inventory Turnover, Production Cycle Time, and Operational Costs as a percentage of revenue.
- Learning and Growth Perspective:
 - a) Objectives: Foster innovation, develop employees, and ensure long-term sustainability.
 - b) Key Indicators: R&D Expenditure, Training Hours per Employee, and Employee Engagement Index.
- Social Perspective:
 - a) Objectives: Enhance social responsibility, community engagement, and employee well-being.
 - b) Key Indicators: Corporate Social Responsibility (CSR) initiatives, community investment, diversity and inclusion metrics, employee satisfaction, and turnover rates.
- Environmental Perspective:
 - a) Objectives: Minimize environmental impact, improve resource efficiency, and support sustainability.
 - b) Key Indicators: Carbon footprint, energy consumption, waste reduction, water usage, and compliance with environmental regulations.

2. DEA Framework for evaluation of a company financial health

DEA is a non-parametric method used to evaluate the relative

efficiency of decision-making units (DMUs) within an organization. When applied in conjunction with the BSC, DEA can assess how efficiently different departments, branches, or business units convert inputs (e.g., costs, resources) into desired outputs (e.g. profits, customer satisfaction) [5]:

- Inputs: In the context of financial health, inputs might include operational costs, capital expenditures, and employee-related expenses. These are resources which the company uses to generate financial outcomes.
- Outputs: Outputs are the financial results achieved, such as profitability, revenue growth, and market share. DEA evaluates the efficiency of converting inputs into these financial outputs.

By integrating the KPIs from the BSC into the DEA model, the company can compare the efficiency of different units in achieving financial health. DEA provides an efficiency score for each unit, highlighting which units are performing well and which require improvement.

Tab. 2. Comparing different DEA models [6]

| Model | Scale Assumption | Efficiency Focus | Applicability | Key Advantage |
|------------------|---------------------------|-------------------------|--|---|
| CCR | Constant Returns | Overall Technical | Standardized processes | Simple and widely applicable |
| BCC | Variable Returns | Pure Technical | Units of varying sizes | Handles scale effects |
| Additive | Non-radial | Slack-based | Input-output balance critical | Measures input and output inefficiency |
| Malmquist Index | Time-based | Productivity Change | Longitudinal performance studies | Measures efficiency over time |
| Super-Efficiency | Constant/Variable Returns | Ranking Efficient Units | Competitive benchmarking | Ranks DMUs beyond efficiency frontier |
| Network DEA | Multi-stage Process | Process-based | Complex operations (e.g., supply chains) | Evaluates internal processes separately |

Comparing different DEA models involves evaluating how they handle various aspects of efficiency measurement, including their focus, assumptions, and applicability.

3. The integrated BSC - DEA approach

The integrated BSC-DEA approach combines the qualitative and quantitative strengths of both models to provide a more comprehensive assessment of financial health.

Step 1: Identify and measure KPIs

- Define KPIs for each BSC perspective relevant to financial health.
- Collect data for these KPIs across different DMUs within the company.

Step 2: Build a DEA model that uses these inputs and outputs to each DMU.

Step 3: Calculate efficiency scores

- Run the DEA model to compute efficiency scores. These scores indicate how well each DMU is utilizing its resources to achieve financial health.
- A score of 1 indicates that the unit is efficient (on the efficiency

frontier), while scores less than 1 indicate inefficiency.

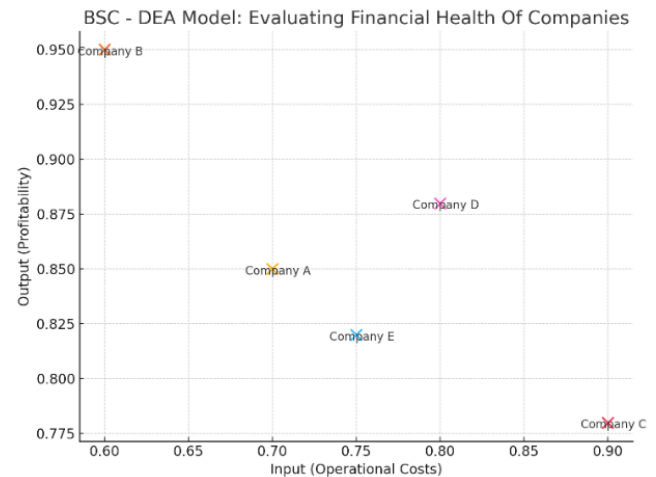


Fig. 4. Visualization of efficiency scores in BSC-Dea model

This graph visualizes the relationship between inputs (operational costs) and outputs (profitability) for different companies, helping to evaluate their financial health through the integrated BSC-DEA approach.

4. Benchmarking

This step includes benchmarking and analysis of:

- the efficiency scores across DMUs to identify best practices and areas for improvement,
- the results to understand which factors are contributing to inefficiencies and how they can be addressed.

5. Strategic insights and decision-making

The integrated BSC-DEA approach provides valuable insights that can guide strategic decision-making.

| Resource Allocation | Process Improvement | Strategic Investments |
|---|---|---|
| <ul style="list-style-type: none"> • Allocate resources more effectively by understanding which units are making the best use of their inputs to achieve financial health. | <ul style="list-style-type: none"> • Identify specific areas where internal processes can be optimized to reduce costs and improve financial outcomes. | <ul style="list-style-type: none"> • Use insights from the Learning and Growth perspective to make strategic investments in employee development, innovation, and technology that will drive future financial performance. |

Fig. 5. Strategic Insights of BSC-DEA model

6. Continuous Improvement

One of the strengths of the integrated BSC-DEA model is its flexible nature. By continuously updating the BSC and DEA models with the latest data, companies can monitor their financial health over time and make ongoing adjustments to strategies and operations.

- Implement feedback loops to regularly assess performance, adjust targets, and refine strategies based on the latest insights from the BSC-DEA analysis.
- As the business environment changes, the integrated model can be adapted to incorporate new KPIs, inputs, and outputs, ensuring that the company remains agile and responsive to market conditions.

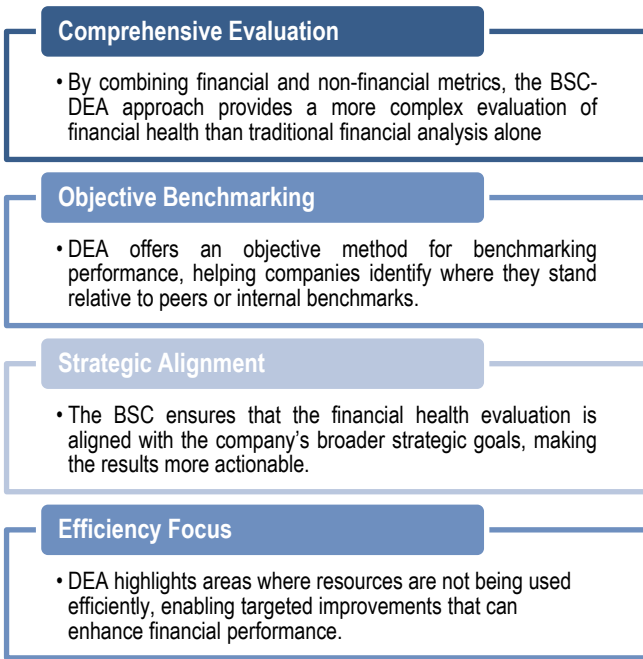


Fig. 6. Benefits of the Integrated Approach

By leveraging the strategic focus of the Balanced Scorecard and the efficiency analysis of Data Envelopment Analysis, companies can gain deeper insights into their financial performance and make more informed, data-driven decisions. This integrated approach not only helps in assessing current financial health but also provides a framework for continuous improvement and long-term financial sustainability.

3.2. Mathematical formulation of the proposed integrated BSC-DEA Model

To mathematically express the integrated BSC-DEA model, which includes the financial, customer, internal process, learning and growth, social, and environmental perspectives, we will construct the model to evaluate the efficiency of DMUs using multiple inputs and outputs derived from the BSC framework.

1. Model variables

- X_{ik} is the i -th input for DMU k
- Y_{rk} is the r -th output for DMU k
- v_i is the weight assigned to input i
- u_r is the weight assigned to output r
- θ_k is the efficiency score for DMU k

2. Inputs and outputs categorization

The inputs and outputs will be categorized based on the perspectives of the expanded BSC framework:

Inputs X_{ik} :

- Financial Inputs: Operating costs, capital expenditures.
- Customer Inputs: Marketing expenditures, customer service costs.
- Internal Process Inputs: Manufacturing costs, operational expenses.
- Learning and Growth Inputs: Employee training costs, R&D expenses.
- Social Inputs: CSR expenditures, community investments.

- Environmental Inputs: Costs related to energy consumption, waste management.

Outputs Y_{rk} :

- Financial Outputs: Profitability, Return on Investment (ROI), cash flow.
- Customer Outputs: Customer satisfaction, market share, customer retention.
- Internal Process Outputs: Process efficiency, cost savings, production output.
- Learning and Growth Outputs: Innovation (e.g., new products developed), employee satisfaction.
- Social Outputs: Community impact, employee well-being.
- Environmental Outputs: Reduced carbon footprint, waste reduction.

3. Objective function

The DEA model aims to maximize the efficiency score θ_k for each DMU. The efficiency score θ_k is defined as the ratio of the weighted sum of outputs to the weighted sum of inputs:

$$\theta_k = \frac{\sum_{r=1}^R u_r Y_{rk}}{\sum_{i=1}^I v_i X_{ik}} \quad (1)$$

R is the total number of outputs across all perspectives.

I is the total number of inputs across all perspectives.

4. Constraints

To ensure fair evaluation and normalization of efficiency scores, the following constraints are applied:

Efficiency Constraint:

For all DMUs $j = 1, 2, \dots, N$, the efficiency score must be less than or equal to 1, indicating that no DMU can exceed 100% efficiency:

$$\frac{\sum_{r=1}^R u_r Y_{rk}}{\sum_{i=1}^I v_i X_{ik}} \leq 1 \quad \forall j = 1, 2, \dots, N \quad (2)$$

Normalization Constraint:

For the DMU under evaluation (DMU k), the sum of the weighted inputs is normalized to 1:

$$\sum_{i=1}^I v_i X_{ik} = 1 \quad (3)$$

Non-Negativity Constraint:

The weights assigned to the inputs and outputs must be non-negative:

$$v_i \geq 0 \quad \forall i = 1, 2, \dots, I \quad (4)$$

$$u_r \geq 0 \quad \forall r = 1, 2, \dots, R \quad (5)$$

These constraints ensure that the DEA model remains consistent and that the efficiency scores are meaningful across all DMUs.

5. Linear Programming Formulation

To solve the DEA model using linear programming, we transform the objective function into a minimization problem, which is equivalent to maximizing efficiency. The goal is to minimize the sum of weighted inputs while ensuring that the weighted outputs are maximized relative to all other DMUs.

Objective Function:

$$\text{Minimize } \theta_k = \sum_{i=1}^I v_i X_{ik} \quad (6)$$

Subject to the following constraints:

a) Output Constraints:

$$\sum_{r=1}^R u_r Y_{rj} \leq \sum_{i=1}^I v_i X_{ij} \quad \forall j = 1, 2, \dots, N \quad (7)$$

b) Normalization Constraint:

$$\sum_{i=1}^I v_i X_{ik} = 1 \quad (8)$$

c) Non-Negativity Constraints:

$$v_i \geq 0 \quad \forall_i \quad (9)$$

$$u_r \geq 0 \quad \forall_r \quad (10)$$

7. Interpretation Of Results

- Efficient DMUs: DMUs with an efficiency score of $\theta_k = 1$ are considered efficient, meaning they use resources optimally to achieve their outputs.
- Inefficient DMUs: DMUs with efficiency scores $\theta_k < 1$ indicate place for improvement, as they are not utilizing their resources as effectively as the benchmark DMUs.

The complete mathematical formulation of the integrated BSC-DEA model incorporates a wide range of inputs and outputs across various perspectives.

This model enables companies to evaluate performance comprehensively and identify specific areas for improvement. The resulting efficiency scores offer actionable insights for optimizing resource allocation and achieving long-term sustainability.

4. THE IMPORTANCE OF DIGITIZATION FOR THE INTEGRATED BSC-DEA MODEL IN EVALUATING FINANCIAL HEALTH OF COMPANIES

Digitization plays a critical role in the implementation of the integrated BSC-DEA model for evaluating the financial health of companies. As companies increasingly rely on data-driven decision-making, digitization enhances the accuracy, efficiency, and scalability of performance evaluation models like the BSC-DEA in various areas, which we identify as follows:

- Automated Data Gathering: Digitization enables the automation of data collection from various sources, such as financial systems, customer relationship management (CRM) tools, enterprise resource planning (ERP) systems, and environmental monitoring systems. This ensures that the data used in the BSC-DEA model is timely, accurate, and comprehensive.
- Centralized Data Repositories: By digitizing data management, companies can create centralized databases that integrate financial, operational, customer, social, and environmental data. This centralization facilitates the seamless flow of information across departments, making it easier to apply the BSC-DEA model.
- Dynamic Performance Tracking: Digitization allows for real-time monitoring of KPIs across all BSC perspectives. This enables companies to track their financial health continuously rather than relying on periodic assessments. Real-time updates ensure that the DEA model is always using the most current data for efficiency analysis.
- Immediate Feedback: With digital tools, companies can receive immediate feedback on their performance, allowing for quicker adjustments to strategies and operations. This ability is crucial for maintaining financial health in a rapidly changing business environment.
- Advanced Analytics: Digitization enables the use of advanced analytics, such as machine learning and artificial intelligence, to enhance the predictive power of the BSC-DEA model. These tools can identify patterns, forecast trends, and suggest optimal

resource allocations, making the DEA model more powerful and accurate.

- Scenario Analysis: Digital platforms can simulate various scenarios, allowing companies to evaluate how changes in inputs (e.g., costs, investments) might affect outputs (e.g., profitability, customer satisfaction). This capability is essential for strategic planning and risk management.
- Scalable Solutions: Digitization allows the BSC-DEA model to be scaled across multiple departments, business units, or even global operations. As companies grow, digital tools can handle the increased data volume and complexity, ensuring that the model remains effective at evaluating financial health at scale.
- Customization and Flexibility: Digital platforms enable companies to customize the BSC-DEA model to their specific needs, allowing them to focus on the most relevant KPIs for their industry or business model. This flexibility enhances the model's relevance and applicability.
- Dashboards: Digitization enables the creation of interactive dashboards that present BSC-DEA results in a clear and accessible format. Stakeholders can easily visualize efficiency scores, compare performance across business units, and track progress toward strategic goals.
- Automated Reporting: Digital tools can automate the generation of reports, ensuring that stakeholders receive regular updates on financial health without manual intervention. This improves transparency and keeps all parties informed.
- Data-Driven Decisions: With digitization, companies can base their strategic decisions on accurate, real-time data from the BSC-DEA model. This reduces the reliance on intuition and ensures that decisions are backed by quantitative analysis.
- Strategic Alignment: Digitization helps ensure that the insights derived from the BSC-DEA model are aligned with the company's overall strategy. By integrating digital tools into the decision-making process, companies can ensure that their strategies are consistently executed across all levels of the organization.

Figure 7 summarizes the possible digitization tools for implementation of BCS-DEA method in company and the comparison of the software options suitable for BSC-DEA digitalization with visualization features is processed in Table 3.

Digitalizing the BSC-DEA method involves leveraging digital tools and technologies to streamline, automate, and enhance the process of evaluating a company's financial health.

The specific characteristics of individual industries significantly impact the selection of digitization tools when applying the BSC-DEA model.

- Automation and robotics: The use of IoT sensors, AI analytics, and predictive maintenance enables fast and accurate performance evaluation of individual processes.
- Mechanical engineering: The focus on optimizing production processes leads to the deployment of ERP systems and digital twins to simulate production efficiency.
- Biomedical engineering: This sector relies on clinical data management software, ensuring regulatory compliance and efficiency analysis in product development.

Digital tools play a different role in each sector and influence how the BSC-DEA model is practically implemented. This variability underscores the importance of sector-specific approaches to digitization within the BSC-DEA framework.

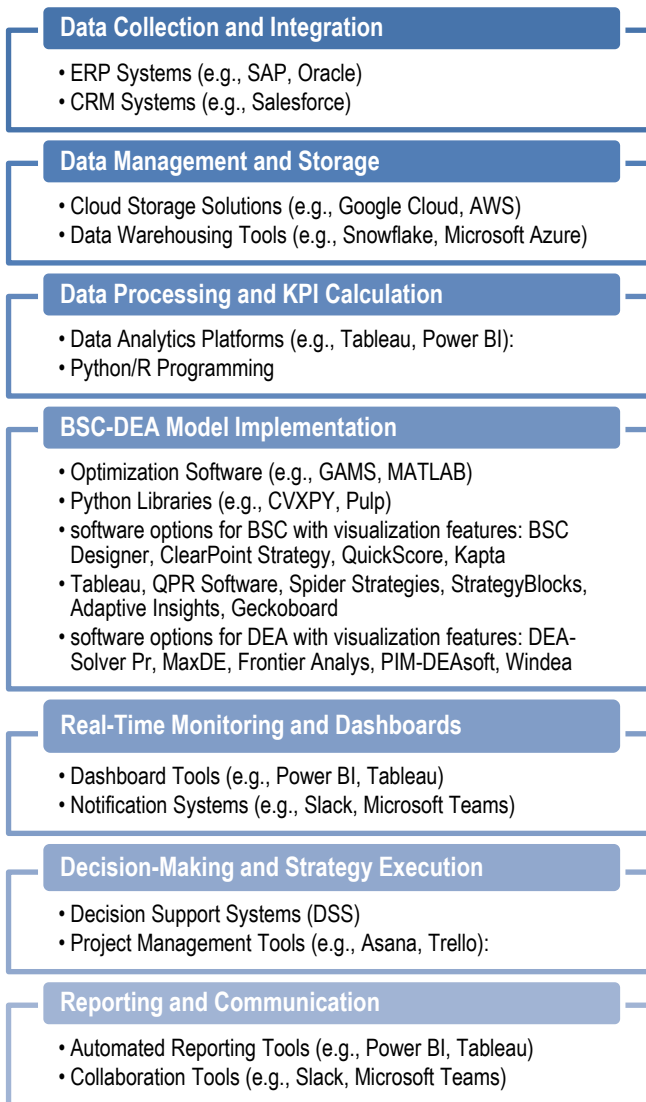


Fig. 7. Digitization tools for BSC-DEA model

Tab. 3. Software options suitable for BSC-DEA digitalization [6]

| Software | Best For | Strengths | Limitations |
|----------------------------|--|--|--|
| BSC Designer | BSC implementation with strategy maps and KPI tracking | User-friendly, good visualization for BSC | May lack advanced DEA functionalities |
| ClearPoint Strategy | Comprehensive strategy management with reporting and visualization | Strong BSC features, extensive reporting | May not provide detailed DEA analysis |
| MaxDEA | Dedicated DEA analysis with advanced models | Specialized in DEA, strong visualization | Lacks BSC functionalities |
| DEA-Solver Pro | Advanced DEA modeling with a focus on efficiency analysis | Highly regarded for DEA, advanced modeling | Requires expertise, not focused on BSC |

| | | | |
|---|--|--------------------------------------|------------------------------------|
| PIM-DEAsoft | Intuitive DEA tool with solid visualization features | Good for DEA, intuitive interface | Doesn't focus on BSC |
| QPR Software | Integrated performance management across BSC and other methodologies | Versatile, strong BSC features | May not have the same depth in DEA |
| Tableau (customized for BSC-DEA) | Customizable and advanced data visualization | Powerful visualization, customizable | Requires manual setup for DEA |
| R with Benchmarking Package | Users comfortable with programming and customization | Flexible, advanced analysis | Requires coding skills |
| MATLAB with DEA Toolbox | Advanced users needing custom DEA solutions | Powerful analytics, customizable | Requires significant expertise |
| Frontier Analyst | Performance benchmarking with DEA | Strong DEA focus, good visualization | Limited BSC functionality |

5. CONCLUSION

By integrating the Balanced Scorecard with Data Envelopment Analysis, companies can comprehensively assess their financial health. This model not only evaluates financial performance but also incorporates the influence of customer satisfaction, internal processes, learning and growth, social and environmental aspects on financial outcomes. It provides a holistic approach to improving financial health by identifying inefficiencies and guiding strategic improvements.

Digitization is essential for maximizing the effectiveness of the integrated BSC-DEA model in evaluating the financial health of companies. It enhances data accuracy, enables real-time monitoring, supports advanced analytics, and facilitates scalability and customization. By leveraging digital tools, companies can make more informed, data-driven decisions that align with their strategic goals, ultimately improving their financial performance and long-term viability.

Despite the widespread use of BSC and DEA models across various industrial sectors, their application differs depending on the industry in which a company operates. In mechanical engineering, performance is primarily evaluated through production quality, cost optimization, and sustainability. DEA methodology provides an advantage in benchmarking the efficiency of production lines, while BSC ensures a strategic framework for long-term management. In biomedical engineering, compliance with strict regulatory requirements and the development of innovative healthcare technologies are top priorities. When applying the BSC-DEA model, it is crucial to incorporate parameters related to regulatory compliance, technological innovation, and patient satisfaction. These differences indicate that industry specificity influences the way the BSC-DEA model is implemented, with various sectors emphasizing different performance parameters.

REFERENCES

1. Niknazar P. Evaluating the use of BSC-DEA method in measuring organization's efficiency. Borås: University of Borås, School of Business and Informatics; 2010. Available from: <http://bada.hb.se/bitstream/2320/7976/1/2010MI09.pdf>
2. Bain & Company. Management tools and trends [Internet]. Available from: <https://www.bain.com/insights/topics/management-tools-and-trends/>
3. Understanding the financial health of a company [Internet]. Available from: <https://www.schoolofmoney.co/blog/understanding-the-financial-health-of-a-company>
4. Comparison of the Results of a Data Envelopment Analysis Model and Logit Model in Assessing Business Financial Health [Internet]. Available from: https://www.researchgate.net/publication/339989154_Comparison_of_the_Results_of_a_Data_Envelopment_Analysis_Model_and_Logit_Model_in_Assessing_Business_Financial_Health/link/5e7188db4585152cdbfa80c3/download
5. Lai M-C, Huang H-C, Wang W-K. Designing a knowledge-based system for benchmarking: A DEA approach. Knowledge-Based Systems. 2011;24(5):662-671. Available from: <https://doi.org/10.1016/j.knosys.2011.02.006>
6. Kohl S, Brunner JO. Benchmarking the benchmarks: Comparing the accuracy of Data Envelopment Analysis models in constant returns to scale settings. Eur J Oper Res. 2020;285(3):1042-1057. Available from: <https://doi.org/10.1016/j.ejor.2020.02.031>
7. Zarei M, Emrouznejad A. Balanced performance assessment under uncertainty: an integrated CSW-DEA and balanced scorecard (BSC). Annals of Operations Research. 2022. Available from: 10.1007/s10479-022-04637-z.
8. The Excitant Fourth Generation Balanced Scorecard Approach [Internet]. Available from: <http://www.excitant.co.uk/resources/white-papers/the-fourth-generation-balanced-scorecard-approach>
9. Jaber Hafshjani M, Najafi SE, Hosseinzadeh Lotfi F, Hajimolana SM, Mahmood T. A hybrid BSC-DEA model with indeterminate information. J Math. 2021;72:1-14. Available from: https://www.researchgate.net/publication/350598187_A_hybrid_BSC-DEA_model_with_indeterminate_information
10. Banker DR, Chang H, Pizzini MJ. A Balanced Scorecard analysis of performance metrics. Eur J Oper Res. 2004;154(2):423-36.
11. Bet G, Dainelli F, Fabrizi E. The Financial Health of a Company and the Risk of its Default: Back to the Future SSRN. Available from: https://papers.ssrn.com/sol3/papers.cfm?abstract_id=4351506
12. Karpac D, Bartosova V. Prediction of Financial Health of Business Entities of Selected Sector Using Balance Analysis II. by Rudolf Doucha and Verification of Its Predictive Ability through ROC. SHS Web of Conferences. 2021;91:01006. Available from: <https://doi.org/10.1051/shsconf/20219101006>
13. Small business financial health analysis [Internet]. Available from: <https://www.frbsf.org/wp-content/uploads/sites/3/small-business-financial-health-analysis.pdf>
14. Measuring Financial Health [Internet]. Available from: <https://cenfri.org/wp-content/uploads/Measuring-Financial-Health.pdf>
15. Eilat H, Golany B, Shtub A. Constructing and evaluating balanced portfolios of R&D projects with interactions: a DEA based methodology. Eur J Oper Res. 2006;172:1018-39. Available from: http://ie.technion.ac.il/Home/Users/golany/EJOR_06.pdf.
16. Eilat H, Golany B, Shtub A. R&D project evaluation: An integrated DEA and balanced scorecard approach. Omega. 2008;36(5):895-912.
17. Chen TY, Chen L. DEA performance evaluation based on BSC indicators incorporated: the case of semiconductor industry. Int J Product Perform Manag. 2007;56(4):335-57. ISSN: 1741-0401.

This paper was prepared within the grant scheme VEGA No. 1/0340/21 (The impact of the pandemic and the subsequent economic crisis on the development of digitalization of companies and society in Slovakia).

Michaela Kočíšová:  <https://orcid.org/0009-0004-6611-290X>

Milan Filo:  <https://orcid.org/0009-0002-8724-3701>

Jaroslava Kádárová:  <https://orcid.org/0000-0002-5101-0773>

Alžbeta Suhányiová:  <https://orcid.org/0000-0001-6537-0000>



This work is licensed under the Creative Commons BY-NC-ND 4.0 license.

3K METHOD: TIME-OPTIMAL PATH PLANNING FOR FIELD ROBOT

Konrad K. KWAŚNIEWSKI^{*}, Zdzisław GOSIEWSKI^{*}

^{*} Faculty of Electrical Engineering, Białystok University of Technology, ul. Wiejska 45 C, 15-351 Białystok, Poland

kwasniewski.konrad.krzysztof@gmail.com, gosiewski@post.pl

received 10 October 2023, revised 31 May 2024, accepted 25 July 2024

Abstract: In this study, a hybrid genetic-geometrical path finding method is presented. Its main feature is the division of the path-finding process into global and local path-finding to achieve a trajectory optimized under the shortest travel time condition in an environment filled with obstacles. To improve the reliability of the algorithm, a safety zone around obstacles is included. In this zone, the maximum velocity allowed for a robot is additionally limited to decrease the probability of collision due to noise in obstacle mapping, distraction from terrain irregularities or malfunction of the steering system. The simulation and real world experiment results are presented in another paper.

Key words: mobile robot, path planning, path optimization, robot rover, autonomous, genetic algorithm

1. INTRODUCTION

Nowadays, the usage of robots in production services is constantly increasing. This trend extends even to domestic applications, such as vacuum cleaners and lawnmowers. The expanding range of fields where autonomous robots can be employed presents us with new challenges. Widely known are autonomous cars, which are specifically adapted to road environments. However, off-road areas are much more prevalent on Earth. Tasks such as rescue actions, emergency transportation, patrol, and exploration in natural disaster areas often occur in regions with limited or nonexistent transportation infrastructure. Therefore, robust navigation methods that consider travel time constraints are crucial for further development in these types of terrains. Path planning and obstacle avoidance methods are often based on graph algorithms such as A* [22, 1], Dijkstra [14], or D* [20]. The path obtained by those methods has to be smoothed before applying it to a controller [5]. Another approach is to use artificial neural networks (ANN) [3, 19, 21, 25]. An alternative way is to use optimization methods. Biology-inspired genetic algorithms [10, 7, 9, 14], ant colony optimization [22], particle swarm optimization [24], chicken swarm optimization [6], cuckoo search optimization [2], grey wolf algorithm [16], whale optimization algorithm [17]. Other noteworthy approaches are potential fields [11] and fuzzy-based potential fields [4]. An interesting field of path planning are methods based on the Dubins path. Worth mentioning are especially methods using the coverage path planning approach, which can be used for both a priori known [12] and unknown [13] environments.

2. 3K METHOD OVERVIEW

When it comes to avoiding an obstacle, the solution is trivial. The robot can ride on its left or right side. The problem becomes more complex when there are multiple obstacles. But if we want to go from point A to point B as fast as possible, the task becomes

very complex. When a robot knows only about obstacles in its surroundings it does not have enough knowledge to choose the best path in the general context. On the other hand, if it follows a path, that was found using only previously mapped obstacles, it cannot omit a new object in the working area. The 3K method combines two strategies: it finds a global path using a priori known obstacles from maps and optimizes it under the travel time criterion; then, during the ride, it uses the global path as a set of waypoints and corrects the trajectory by finding a local obstacle-free path. These local obstacles are detected autonomously by the robot. The local path is also selected under the shortest travel time condition.

The characteristic features of the 3K method in comparison to the other ones are obstacles modeled as circles, division of the problem to the local and the global scales and introduction of the velocity reduction area around obstacles for more precise navigation in the immediate vicinity of obstacles, especially those not known a priori, for safety reasons.

The main algorithm is presented in Fig. 1. The current robot position is considered a start position, while the ordered travel point is considered a destination point. At first, the map of a priori known obstacles is loaded. Then the global path is found, and the travel begins. The robot moves along the sequence of the global path waypoints. If at least one obstacle is detected, the local path between the current robot position and one of the more distant global waypoints is determined, and the robot starts following the local path. The local path computation is repeated as long as at least one local obstacle is in the robot's view range. When the robot has avoided all the obstacles, it continues following the global waypoints. The 3K method ends when the last global waypoint, the destination point, is reached.

2.1. Map and obstacle models

The map is modeled in a 2D Cartesian coordinate system. This simplification, in relation to the real form of Earth, facilitates

its mathematical description and is a good approximation on short distances on the planet surface. The map is stored as a list of obstacles. It is shown in Fig. 2.

All obstacles are modeled as circles. In the case of bigger obstacles or those of complex shape, they can be either circumscribed by a large circle or covered by multiple smaller ones. Each i -th circle O_i is described by two values: radius $O_{r,i}$ [m] and center point $O_{C,i}$ [m, m] where $O_{C,i} \in C$. The axis of the real part is identical to the X axis of the robot-centered coordinate system and, similarly, the imaginary part to the Y axis of the robot-centered coordinate system. The advantage of this model is its mathematical simplicity, which allows for easy collision detection.

Around each obstacle, the velocity reduction area is applied. It is the additional circle, in which the velocity of the robot has to be reduced to provide better precision of steering when the robot moves close to the obstacle. This approach reduces the probability of a collision in the case of an error in the obstacle position estimation.

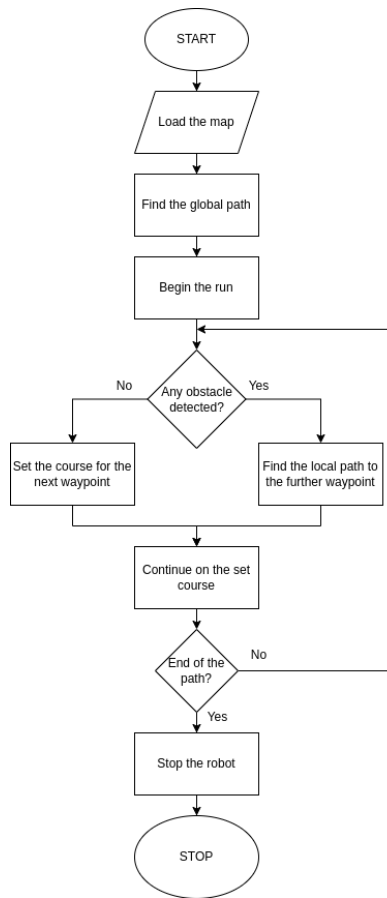


Fig. 1. Flowchart of 3K method

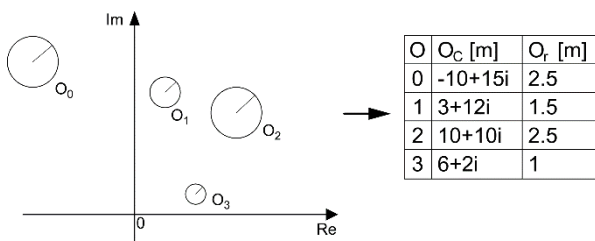


Fig. 2. Example of map model

2.2. Path model

The path of the global path method is modeled using a B-spline curve, which is a special case of a NURBS curve (Non-Uniform Rational B-Spline) [18]. The B-spline has uniformly distributed knots, unlike the NURBS, in which the knots can be distributed non-uniformly. The shape of the B-spline is defined by a vector of control points and a degree of the curve. The number of control points has to be at least greater by one than the curve degree. In curves of a higher degree, more control points are considered when particular points of the curve are computed. The main advantage of the B-spline is its property, that translation of a control point of a curve modifies it only to a limited distance from the control point (depending on the curve degree). The size of the shape modification depends on the distance of the translation. It makes the B-spline very well suited to be a model of a path that undergoes operations of an optimization algorithm.

2.3. Collision detection

A collision between the B-spline and a circle can be detected by computing a set of equidistant curve points S and testing, if any of them lies inside the currently considered circle (Fig. 3). In the case of obstacle avoidance, however, where an optimization algorithm is used, the binary information is not enough. A smoother solution is required. Hence, the collision depth is adopted instead. It is computed as follows. Firstly, the closest point p_c of the S set to the obstacle center O_c is selected. Then the collision depth is the difference between the obstacle radius O_r and the distance between the obstacle center O_c and the p_c point, divided by the radius O_r . Then the collision depth value is always in the range $[0; 1]$. It is shown in Fig. 4 and given by the formula (1).

$$m_k = \frac{O_r - |O_c p_c|}{O_r}, |O_c p_c| \leq O_r, O_r \neq 0 \quad (1)$$

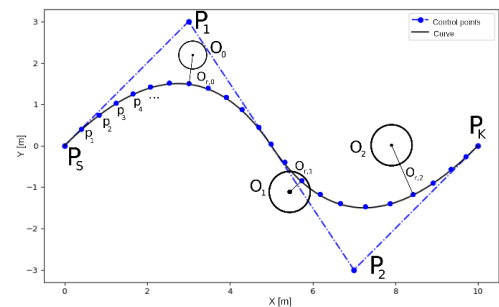


Fig. 3. Example of collision detection between B-spline and circle-shaped obstacles

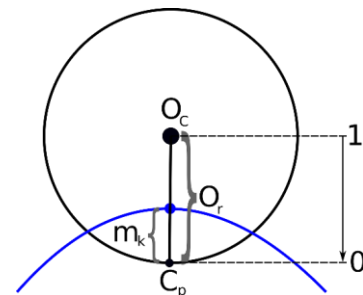


Fig. 4. Visualization of the collision depth

3. VELOCITY PROFILER

To find a path of the shortest travel time, it is necessary to know the path travel time itself. To estimate it, the velocity profile of a path is needed. The travel, however, has to fulfill certain constraints:

- the robot must not exceed the given maximum velocity,
- the robot must not exceed the maximum velocity of considered segment of the path, to secure the robot against skidding,
- the acceleration must not exceed the maximal acceleration value, either set or achievable by the robot,
- the deceleration, as in the case of the acceleration, must not exceed the maximal acceleration value, either set or achievable by the robot.

The acceleration and deceleration rate in the 3K method are considered as constant in time. The difference between the constant rates and the real ones is negligible because of many other factors present in a real environment, which can greatly affect the robot during the journey.

The computation of the velocity profile consists of the following steps:

1. computation of the maximum permissible velocities on all the segments of the path (between waypoints) – the maximum velocities profile,
2. reduction of velocities from the maximum velocities profile in such a way that the given acceleration value is maintained,
3. reduction of velocities from the reduced velocities profile in such a way that the given deceleration value is maintained,
4. computation of the travel time of the individual path segments and the total travel time.

The main factor limiting the robot's velocity is the friction between the robot wheels and the ground. The speed must be low enough to prevent the robot from getting out of a track due to the centrifugal force. The formula for the maximum velocity v_{max} on the particular path segment (4) is derived from the formulae for the friction T (2) and the centrifugal F_c (3) forces. The maximum velocity is a velocity of the state where both forces are equal, i.e. $T = F_c$.

$$T = \mu N = \mu mg \quad (2)$$

$$F_c = \frac{mv^2}{r} \quad (3)$$

$$v_{max} = \sqrt{\mu gr} \quad (4)$$

where m is the mass of the robot [kg], g is standard gravity acceleration [m/s²], v - velocity [m/s], r - radius of the path segment [m]. In the case of a straight segment the maximum velocity is infinite, which is in fact the maximum velocity allowed for the robot to reach.

In the velocity reduction steps, the new velocity for the $i + 1$ -th waypoint is computed from the formula (5). The start and the end point velocities are set at the beginning of the algorithm and are equal to 0. They remain intact during the whole process.

$$v_{i+1} = \sqrt{2ad_i + v_i^2}, i \in [0, n - 2], a \leq 0 \quad (5)$$

where a - a set acceleration or deceleration [m/s²], d_i - Euclidean distance between i -th and $i + 1$ -th waypoint, n - number of waypoints. This formula is derived from the equation (6) [8].

$$v^2 = v_0^2 + 2a(x - x_0) \quad (6)$$

The acceleration and deceleration steps are computed in the same manner, although as the deceleration is a reverse operation to the acceleration, the reduction process has to proceed from the last waypoint to the first one.

The partial travel times, which mean times between each pair of the following waypoints, is computed by formula (8) which is derived from (7) [8].

$$(x - x_0) = \frac{1}{2}(v_0 + v)t \quad (7)$$

$$t_i = \frac{2d_i}{v_i + v_{i+1}}, i \in [0, n - 2] \quad (8)$$

where in (7): x - current distance, x_0 - initial distance, v_0 - initial velocity, v - current velocity, t - travel time; in (8): t_i - travel time between i -th and $i + 1$ -th waypoints, d_i - distance between i -th and $i + 1$ -th waypoints, v_i velocity at i -th waypoint, v_{i+1} velocity at $i + 1$ -th waypoint, n - number of waypoints.

Total travel time t_c [s] is a sum of all the partial times (9).

$$t_c = \sum_{i=0}^{n-2} t_i \quad (9)$$

4. GLOBAL PATH METHOD

The global path method is based on a genetic algorithm (GA). It is used for finding a collision free path, whose shape is optimized to minimize the travel time. The features of the used GA are:

- roulette parents selection operator,
- arithmetical non-symmetric crossing operator,
- population size of 100 individuals,
- elitism: the best individual of a current generation is transferred into a next one,
- mutation operator of low probability and a narrow range of a gene value change,
- a chromosome is a sequence of following B-spline control points,
- control points are defined as complex numbers,
- optimization takes place under two criteria: collision (obstacle avoidance) and travel time.

The collision criterion is measured with a collision depth value which is introduced by the formula (1). It is a sum of the collision depths between the considered path and all the obstacles. The travel time is computed for the considered path by the velocity profiler. Sets of the fitness values, that mean the collision and the travel time, of the all individuals are then remapped to a new domain [0; 1] separately. Then they are weighted and summed. It is shown by the equation (10).

$$F = M_k c_m + T c_p; c_m + c_p = 1; c_m, c_p > 0 \quad (10)$$

where F is a vector of the fitness values of the whole population, M_k is a vector of the remapped collision criteria, T is a vector of the remapped travel times, c_m and c_p are coefficients of the collision criterion and the travel time respectively.

The initial population is generated by random modifications of the curve, that is built of equidistant control points, which are located on the straight line between the first and the last control point. The first point is equal to the robot start position and the last point is equal to the destination point. The robot start position and the destination point are converted from the ECEF coordinates system to the local coordinates system of the robot. The initial

straight line variant of the curve is always included in the initial population. The modification range is limited to the area around known obstacles. The algorithm stops when the differences between the individuals become smaller than a set threshold.

When the algorithm stops, the result path is returned, that means the path with the lowest fitness value in the last generation of the individuals. Before use, it is converted to a set of the following waypoints.

5. LOCAL PATH METHOD

The local path is computed in a geometrical way. The general idea of the method is presented in the Fig. 5. The map and obstacle models are the same as described in section 2. The method looks for a path constructed with two straight line segments between the local start P_S and the local destination P_K points. At first, rays, $l_{s,i}$ from P_S and $l_{k,i}$ from P_K , tangent to each obstacle are computed. It gives two pairs of the rays for each obstacle. To this set, a straight path between P_S and P_K points is added. Next, the intersection points D_i between the rays are calculated. This process is shown in the Fig. 6. The paths are created from segments of intersecting rays from the points P_S and P_K , which ends at their intersection point. Each path is then tested for a collision. If it is detected for at least one obstacle, the path is removed from the set.

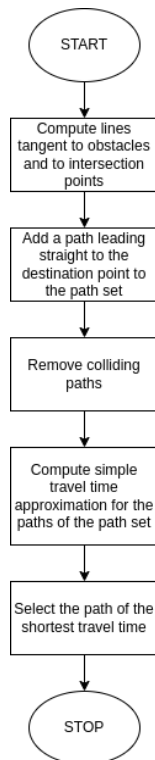


Fig. 5. Flowchart of the local path finding method

The same process is done for the velocity reduction areas instead of the obstacles. Collisions, however, still are computed for the obstacles.

For the remaining paths, approximate travel times are computed. The approximate travel time t_j for the j -th path is described by the formula (11).

$$t_j = \frac{l_j - c_j}{v_{max}} + \frac{c_j}{v_{min}} \quad (11)$$

where l_j is the length of the j -th path, c_j is the sum of the chord lengths in the velocity reduction areas i.e. these parts of the path, that lie in the circles of the velocity reduction areas, v_{max} is the maximum allowed velocity for the robot, v_{min} is the maximum allowed velocity in the velocity reduction areas.

When the approximated travel times of every path are known, then the path of the shortest time is selected from the set as a result path and the local path algorithm ends.

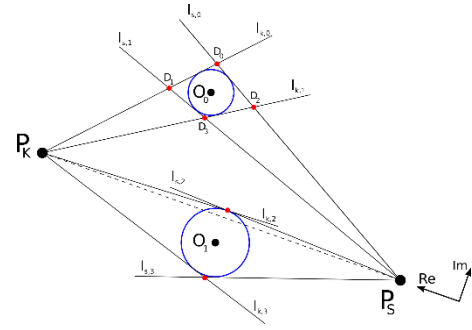


Fig. 6. Visualization of local path computation

6. ROBOT NAVIGATION METHOD

The robot navigation method joins the results of the global path method (sec. 4) and the local path method (sec. 5). It consists of three layers: movement along the global path, deviation from the global path to avoid local obstacles (movement along the local path), return to the global path.

6.1. Movement along the global path

The global path is set for the algorithm as a sequence of the waypoints. The robot sets the course to the following waypoints. The current waypoint is changed to the next one, when the distance between the current waypoint and the robot is shorter than the given one. This distance is named point change distance. It is often set up to several meters. A shorter distance forces the robot to follow the path more strictly, a longer one is less prone to errors of losing the path.

Before beginning, the velocity profile for the global path is computed. During the ride, the robot velocity is set to the value from the profile that corresponds to the currently selected waypoint.

6.2. Movement along the local path

If at least one obstacle is detected, then the local path method is used to create a path. The local destination point is set to a distant point from the set of not yet reached waypoints. The minimal distance for the selection is set by the robot operator. The result is a navigation point, which the robot sets the course to. The algorithm is frequently repeated while any obstacles are in sight. The robot velocity is set dependently on the local path - if it goes through the velocity reduction area (v_{max} (11)) or not (v_{min} (11)).

6.3. Return to the global path

When again no obstacle is detected, the closest global way-point to the robot is set as the navigation point. The point change distance smooths the return to the global path, because of the navigation point changing to the next waypoints as the robot comes closer to them.

6.4. Termination

The algorithm stops along with the robot, when the global destination point is reached within the given accuracy.

7. SUMMARY

The 3K method described in the paper divides the path planning problem into two cases: the global context and the local context. Two distinct methods to both global and local path finding were developed in order to achieve necessary performance for successfully controlling the robot.

The global method is based on a genetic algorithm, and it uses the map of a priori known obstacles to produce a path. The local method is based on the geometrical path planning approach with numerous simplifications of the problem model. It uses the data about the obstacles that are detected during the run.

The third method was designed to control the robot using data obtained from the global and the local path finding methods. It leads the robot along the global path, but when an unknown obstacle is found, the local path is used to avoid it.

The main purpose of the 3K method is to minimize travel time of the robot in partially unknown environments. The results of the experiments in simulations and in the real world are described in a following paper.

REFERENCES

- Alazzam H, AbuAlghanam O, Sharieh A. Best path in mountain environment based on parallel A* algorithm and apache spark. *The Journal of Supercomputing*. 2022; 1–20.
- Alymani M, Alsolai H, Maashi M, Alhebi A, Alshahrani H, Al-Wesabi FN, Mohamed A, Hamza MA. Dispersal foraging strategy with cuckoo search optimization based path planning in unmanned aerial vehicle networks. *IEEE Access* 11. 2023; 31365–31372.
- Bozek P, Karavaev YL, Ardentov AA, Yefremov KS. Neural network control of a wheeled mobile robot based on optimal trajectories. *International journal of advanced robotic systems* 2020;17: 2.
- Cao X, Zuo F. A fuzzy-based potential field hierarchical reinforcement learning approach for target hunting by multi-auv in 3-d underwater environments. *International Journal of Control* 2021;94(5):1334–1343.
- Duan S, Wang Q, Han X. Improved a-star algorithm for safety insured optimal path with smoothed corner turns. *Journal of Mechanical Engineering*. 2020;56(18): 205–215.
- Fu W, Wang B, Li X, Liu L, Wang Y. Ascent trajectory optimization for hypersonic vehicle based on improved chicken swarm optimization. *IEEE Access* 7. 2019;151836–151850.
- Gosiewski Z, Kwaśniewski K. Time minimization of rescue action realized by an autonomous vehicle. *Electronics* 9. 2020;12: 2099.
- Halliday D, Resnick R, Walker J. *Fundamentals of physics*. John Wiley & Sons; 2013.
- Jiang A, Yao X, Zhou J. Research on path planning of real-time obstacle avoidance of mechanical arm based on genetic algorithm. *The Journal of Engineering*. 2018;16: 1579–1586.
- Kwaśniewski KK, Gosiewski Z. Genetic algorithm for mobile robot route planning with obstacle avoidance. *acta mechanica et automatica*. 2018; 12(2): 151–159.
- Li G, Yamashita A, Asama H, Tamura Y. An efficient improved artificial potential field based regression search method for robot path planning. In 2012 IEEE International Conference on Mechatronics and Automation. 2012; 1227–1232.
- Li L, Shi D, Jin S, Yang S, Zhou C, Lian Y, Liu H. Exact and Heuristic Multi-Robot Dubins Coverage Path Planning for Known Environments. *Sensors*. 2023;23(5):2560.
- Li L, Shi D, Jin S, Yang S, Lian Y, Liu H. SP2E: Online spiral coverage with proactive prevention extremum for unknown environments. *Journal of Intelligent & Robotic Systems*; 2023; 108(2): 30.
- Lo CC, Yu SW. A two-phased evolutionary approach for intelligent task assignment & scheduling. In 2015 11th international conference on natural computation (ICNC). 2015; 1092–1097.
- Norhafez K, Nurfadziana A, Megawati O. Simulation of municipal solid waste route optimization by dijkstra's algorithm. *Journal of Fundamental and Applied Sciences* 9. 2017; 732–747.
- Pawłowski A, Romaniuk S, Kulesza Z, Petrović M. Trajectory optimization using learning from demonstration with meta-heuristic grey wolf algorithm. *IAES International Journal of Robotics and Automation (IJRA)*. 2022; 11(4): 263–277.
- Petrović M, Miljković Z, Jokić A. A novel methodology for optimal single mobile robot scheduling using whale optimization algorithm. *Applied Soft Computing* 81. 2019;105520.
- Piegl L, Tiller W. *The NURBS book*. Springer Science & Business Media; 1996.
- Salt L, Howard D, Indiveri G, Sandamirskaya Y. Parameter optimization and learning in a spiking neural network for uav obstacle avoidance targeting neuromorphic processors. *IEEE transactions on neural networks and learning systems*. 2019; 31(9): 3305–3318.
- Shi J, Liu C, Xi H. Improved d* path planning algorithm based on CA model. *Journal of Electronic Measurement & Instrumentation*; 2016.
- Singla A, Padakandla S, Bhatnagar S. Memory-based deep reinforcement learning for obstacle avoidance in uav with limited environment knowledge. *IEEE Transactions on Intelligent Transportation Systems*. 2019; 22(1): 107–118.
- Wang Z, Zeng G, Huang B, Fang Z. Global optimal path planning for robots with improved A* algorithm. *Journal of Computer Applications*. 2019;39(9): 2517.
- Yi Z, Yanan Z, Xiangde L. Path planning of multiple industrial mobile robots based on ant colony algorithm. In 2019 16th International Computer Conference on Wavelet Active Media Technology and Information Processing. 2019; 406–409.
- Zhang T, Xu J, Wu B. Hybrid path planning model for multiple robots considering obstacle avoidance. *IEEE Access* 10. 2022;71914–71935.
- Zhu H, Ouyang H, Xi H. Neural network-based time optimal trajectory planning method for rotary cranes with obstacle avoidance. *Mechanical Systems and Signal Processing* 185. 2023;109777.

Konrad K. Kwaśniewski:  <https://orcid.org/0000-0003-2528-8904>

Zdzisław Gosiewski:  <https://orcid.org/0000-0002-7437-2574>


This work is licensed under the Creative Commons BY-NC-ND 4.0 license.